NUMERICAL STUDIES OF INCOMPRESSIBLE RICHTMYER-MESHKOV INSTABILITY IN A STRATIFIED FLUID

Thesis by

Thu Pham

In Partial Fulfillment of the Requirements

for the Degree of

Doctor of Philosophy

California Institute of Technology

Pasadena, California

1991

(Submitted October 17, 1990)

ACKNOWLEDGMENTS

The completion of this thesis would not have been possible without the support of Professors Daniel I. Meiron and Philip G. Saffman. I would like to express my sincere gratitude for their guidance and advice throughout the work. Their enthusiasm and experience have greatly inspired my research.

I would like to thank Professor Donald S. Cohen, and Ms. Sheila K. Shull for making my transition from Chemical Engineering to Applied Mathematics possible and smooth.

During my initial residency at Caltech, I have also been benefited from interaction with Professor L. Gary Leal. I would like to thank him for his support and lectures which has demonstrated to me the beauty of fluid mechanics.

My technical discussions with fellow students at Caltech have been very fruitful and educational. I would like to thank them all. In particular, I would like to thank my best friend and colleague Hoanh X. Vu for his interest and insights into my research, Vidyadhar Y. Mudkavi for his computer expertise, and Alex W. Ho for his generous computing support. Last, but not least, I would like to thank In Seok Kang whom I regard as an older brother, and teacher who led me in the first solid steps of an advanced degree.

The financial support for this project was provided by the U.S. Department of Energy, Lawrence Livermore National Laboratory, under project agreement DOE W-7405-ENG-48.

Finally, the birth of a particular event is only a temporary point enclosed as well as encapsulated in a self complete time–space continuum; the existence of this work must owe its conception to the events which began from the abyss of time, and

its completion to the ones born in the inmeasurable future. The next essay includes some beautiful flowers of emotional support which I have collected during the last few years at Caltech, which can only then partially form the whole of a reality.

MỘT ÍT GHI DẤU

Cuộc đời rồi như một giấc chiêm bao, ra đi tay trắng trở về tay không. Nhưng mà dù không đi nữa, sự hiện hữu tròn đầy của nó trong một hiện tại nào đó vẫn luôn luôn có một ý nghĩa miên viễn trường tồn. Năm năm qua, dòng đời có biến động đổi thay, nhưng thỉnh thoảng tôi vẫn may mắn gặp được những gì gần như không thay đổi, đó là tình cảm chân thành cuộc sống này đã cho tôi trong đó có anh, có chị, có bạn, có lẽ có cả những người không quen biết như một lần Tế Hanh đã viết trong bài thơ "Nhớ con sông quê hương", mặc dầu khác với thi sĩ, con sông của tôi là cả một dòng đời bất tận mênh mông. Ngày tôi đi, mẹ tôi buồn không nói, giận con cả mấy tháng trường. Vậy mà cứ hai tuần, mẹ đã già vẫn còn cặm cụi làm chả gởi cho tôi ăn. Làm sao tôi có thể nói hết được những âu yếm thương yêu gói gém kín đáo trong những tấm bánh chưng ngày Tết, miếng bánh dẻo ngày Trung Thu. Mỗi lần tôi gọi dây nói về thăm nhà, trong niềm lo âu tha thiết, hăng hái tràn trề mẹ lại dạy tôi nấu những món này món kia. Mẹ làm bánh, Ba đi gởi bánh. Chị và các em yêu thương, trìu mến, kính trọng. Năm năm có gì thay đổi, nhưng tình Ba Mẹ, Chị Em vẫn chan chứa nồng nàn như ngày nào. Tôi là người có diễm phúc nhất trên đời. Có lẽ người ta nói đúng, nước mắt chảy xuôi, nhưng mà làm sao được tôi cũng chỉ là người, vẫn trôi theo nhánh sông rẽ của đời mình.

Bác Cả Hồng và chị Thúy ra đón tôi ở phi trường Ontario trong cơn nắng hơi gắt của buổi chiều cuối hè 85. Nhưng có lẽ những hơi ấm thật sự của Cali là tấm chân tình gia đình Bác đã dành cho tôi, cũng như của hai bác Kiên, của Bill

Constantine, của anh chị Trường Sinh, Xuân Tô. Có đi xa mới biết mình không là gì cả, tôi học được rất nhiều từ những người bạn mới Arthur Lee, Chris Koh, Ken Wolfenbarger. Những ngày rong chơi ở Chinatown với Ricky và Alex hoặc trên chiếc xe cũ mèm của Alex, hoặc của Ricky mang cho tôi êm đềm của những ngày xa xưa cũ thuở còn là học trò Petrus Ký ngây ngô. Thời gian qua kỷ niệm lớn dần với những ngày tập võ say mê cùng Evan, học đàn với Hoành, những đêm không ngủ với anh Vĩnh, Hùng, Trường, có Minh Thủy làm điệu, Ngọc Diệp thông minh chăm chỉ, những ngày kèm học tận tụy cho Kim Linh nhút nhát, cho bé Cúc ranh mãnh, cho ba chàng Ngự Lâm pháo thủ Thu, Trang, Trinh, cho Mai Thanh siêng năng lém lỉnh. Cả một VSA thương yêu trong sự thân mật đầm ấm của gia đình cô chú Tuyến, có Nguyên Thao hay làm dáng, có Thái lầm lì, có bé Thảo mắc cỡ duyên dáng.

Cuộc sống nào rồi cũng có những khúc quanh ngõ rẽ, tôi dọn về sống chung với Hùng. Tôi đi vào thế giới của Hùng với những đêm nằm bên anh Hoan vừa nói chuyện vừa ngủ, chứng kiến sức sống mãnh liệt của anh Hướng bên sự kiêu kỳ non dại của Quỳnh, và sự trầm lặng mộc mạc hy sinh chịu đựng của anh Hải trong sự sốt sắng của vợ. Tôi và Hùng thân thiết, thế giới của tôi và Hùng quyện lẫn vào nhau trong sự chăm sóc thân thương của chị Yến Tuyết, sự thân mật tự nhiên của Minh Tiến, sự thận trọng của Tina Trinh, và sự khôn ngoan sâu sắc của Hoàng Liên. Chúng tôi đi mãi, rong chơi trên chiếc xe con con của Hùng. Đôi khi tôi tự hỏi có bao giờ tôi thương Hùng chưa? Rồi chúng tôi dừng lại, Hùng dừng lại, tôi dừng lại. Tôi may mắn gặp lại cô giáo cũ của tôi, chị Kim Phượng (chị thích tôi gọi chị ấy bằng chị, tôi thích gọi chị bằng cô). Gia đình của chị với Phước Lộc, Ngọc Mai, Thiên Nga, Trâm Thư, Quang Vinh, Quang Huy trở thành gia đình thứ hai của tôi, của Hùng. Mỗi khi chúng tôi đến chơi ra về, chị cẩn thận gói gém cho chúng tôi từng trái cam, trái đào thật tươi, đôi ly chè dịu ngọt mà Thiên Nga đã chăm sóc với cái tài nếm của cô nàng Trâm Thư. Sau này lúc Hùng đã ra trường, tôi đã sống nhờ đồ ăn của chị và Nga nấu. Làm sao để diễn tả tình cảm gia đình

chị đã dành cho tôi, và sự thân thương tôi đã dành cho gia đình chị, cùng cô học trò chân thật dễ ghét Thiên Nga? Những ngày cuối của tôi ở Cali, tôi lại được may mắn có thêm ba người bạn mới lúc nào cũng khuyến khích lo lắng cho công việc của tôi. Mặc dầu thèm rủ tôi đi chơi chung, Lưu Thuận khi nào cũng đốc thúc để cho tôi làm. Cái chăm sóc kín đáo và ý tứ của Thuận đôi lúc làm tôi cảm động. Tuấn cũng vậy, thỉnh thoảng mới dám đến chơi sợ tôi bận học. Tuấn có nhiều tâm sự, những lời kể chân tình và tha thiết của Tuấn gợi cho tôi nhiều nhớ nhung và suy nghĩ về một quê hương chỉ còn tồn tại lu mờ trong ký ức. Còn một Lưu nữa, Lưu Quốc. Anh chàng to lớn mà hay mắc cỡ. Nụ cười tươi và đẹp của Quốc lúc nào cũng làm tôi khuây đi những nỗi buồn, nhất là tấm postcard thật đẹp gởi từ South Africa.

Tất cả đến để rồi tất cả đi. Có ai giữ lại được hương hoa của một gì thật đẹp? Hay là có lẽ đúng hơn, hương hoa đầu xuân nào cũng quyện lẫn làm cho nổi bật hay tự nổi bật cùng sắc hương mùa hoa sau. Nhánh sông cuộc đời tôi lại một lần nữa rẽ nhánh. Năm năm cũng chẳng là bao, nhưng chuyện đổi thay phải chăng là ít. Có những người bạn của tôi đã không bao giờ còn nữa, có những người tôi không bao giờ còn gặp hay liên lạc nữa, nhưng mà thực tại của quá khứ bao giờ cũng có một ý nghĩa nào đó, vì sự hiện hữu của nó đã viên thành bắt đầu từ những ngày vô thủy, và kéo dài miên viễn tới tận ngày vô chung. Đó mới thật là chân ý nghĩa của lần học hỏi này. Nó đã giúp tôi khai phá một phần nào toàn thể nhân tính của một kiếp người ẩn sâu trong từng hơi thở. Cho đóa đại liên hoa Lăng Vân yêu thương và tất cả thế giới loài người mộng cũng như thực, tôi viết,

Cuộc nhân thế chao ôi nhiều biến loạn
Vẫn thì thầm tiếng nói cuộc tình xưa
Hoa lá vấn vương chiều rất mộng
Ai có về ươm nắng bóng ngày qua?
Ánh mắt non xanh bên trời xa lạ
Chút hững hờ chua xót dậy niềm thương
Ai ra đi ai về ai có biết
Một ít lòng cho ấm tặng cùng nhau.

ABSTRACT

Theory and calculations are presented for the evolution of Richtmyer-Meshkov instability in continuously stratified fluid layers. The initial acceleration and subsequent instability of the fluid layer are induced by means of an impulsive pressure distribution. It is shown that such an initial condition is an adequate approximation of the effect of a weak shock impinging on a stratified layer of fluid. We then calculate the subsequent dynamics of the fluid layer numerically using the incompressible equations of motion.

Both initial conditions having single scale perturbations and multiple scale random perturbations are considered. It is found that the growth rates for Richtmyer-Meshkov instability of stratified fluid layers are substantially lower than those predicted by Richtmyer for a sharp fluid interface with an equivalent jump in density. The initial behavior is linear over a time equivalent to the traversal of several layer thicknesses. It is observed that the nonlinear development of the instability results in the formation of plumes of penetrating fluid. Late in the process, the initial momentum deposited by the shock is primarily used in the internal mixing of the layer rather than in the overall growth of the stratified layer.

At intermediate time, the existence of a weak scaling behavior in the width of the mixing layer of the instability is observed for the multiple scale random perturbations, but not for the single scale perturbations. The time variation of the layer thickness differs from the scaling hypothesized by Barenblatt even at low Atwood ratio, presumably because of the inhomogeneity and anisotropy due to the excitation of vortical plumes. The emergence of these plumes at the boundaries of the density layer is characterized by the elongation of the internal spikes which have

weak interactions and grow proportionally to their intial perturbed amplitudes. It is conjectured that the formations of the plumes may correspond to weakly interacting single scale modes.

TABLE OF CONTENTS

TABLE OF CONTENTS *(cont'd)*

TABLE OF CONTENTS *(cont'd)*

LIST OF FIGURES

CHAPTER 3

profile, A = −0.8, $t = 16$ using the linear model. The contours are at $\rho = 0.11, 0.2, 0.3, 0.4, 0.5, 0.6, 0.7, 0.8, 0.89$.

LIST OF TABLES

CHAPTER 1

INTRODUCTION

It is well known that in a gravitational field directed downwards, a surface separating two fluids of different densities is stable provided the heavy fluid is at the bottom, and the lighter fluid is at the top. Any ripple on the surface due to perturbations will soon disappear and the surface returns to its normal flat shape. On the other hand, if we accelerate the whole system at a downward acceleration of magnitude greater than that of the gravitational field, any ripple on the surface will grow exponentially fast. Late in the process, spikes of heavy fluid penetrate the lighter fluid. This is an example of the well-known Rayleigh-Taylor instability, which is a type of baroclinic instability.

Lord Rayleigh (1900) was the first to study this problem. He obtained the initial flow field both for a sharp interface and a stratified fluid with an exponential density profile. Taylor (1950) extended this result to include a general acceleration and applied his result to the study of a liquid sheet of finite thickness. Birkhoff (1955) has given an extensive report of this instability that includes the effects of surface tension and discusses the different stages of the resultant laminar and ultimately turbulent mixing. The effects of viscosity are considered by Bellman and Pennington (1954), of gradual density gradient by LeLevier *et al.* (1955) and Case (1960), and of molecular diffusion by Duff *et al.* (1962). The growth rate of the instability is reduced with the inclusion of these effects. Recently, Sharp (1984) has given a survey of Rayleigh-Taylor instability and suggests important issues which require further investigations such as the three-dimensional nature,

the role of statistically distributed heterogeneities, as well as the possible chaotic limit due to the fractal geometric structure of this instability.

The baroclinic instability arises from the misalignment between the pressure gradient and the density gradient and this is responsible for the generation of the vorticity in the flow. In addition to Rayleigh-Taylor instability, other examples of baroclinic instability are the Landau-Darrieus instability due to the mass transfer across an interface, and the Richtmyer-Meshkov instability due to a normal shock wave passing normally to a perturbed interface.

In this thesis we are concerned with the study of the Richtmyer-Meshkov instability due to its importance in many technical applications. Some examples of its occurrence are in the laser implosion of deuterium-tritium (DT) fusion targets (Lindl & Mead 1975), in supersonic combustion (Marble *et al.* 1987), and in the interaction between pressure waves and flame fronts (Markstein 1957). The performance of the implosion of a DT pellet depends, among other factors, upon the behavior of the Richtmyer-Meshkov instability at the ablating pellet surface. In an oversimplified view of the process, a spherical DT pellet is surrounded by a glass or metal tamper. When this tamper is irradiated with intense laser light, it accelerates inwards. The outer surface of the tamper is the interface between a heavy fluid (metal or glass) and a light fluid (vaporized tamper) and is unstable during the initial phase of the implosion. At late times, when the pellet is compressed to about 1000 times its normal density, its pressure increases enough to slow down the inward motion of the tamper, and the inner surface between the tamper and the deuterium-tritium becomes unstable. If the modes of the instability reach large amplitude, they will cause a breakup of the shell and gross mixing of high- and low-density matter. In the other mentioned applications, the instability produces pockets of unburned gases to deteriorate the flame front or to reduce the efficiency of the combustion process. A fundamental understanding of the physics underlying the instability is therefore useful in tempering these undesirable effects.

If compressibility of the fluids is neglected, the Richtmyer-Meshkov instability

can be considered as the limit of the Rayleigh-Taylor instability when the acceleration is impulsive, *i.e.*, it acts for almost zero time but the magnitude of the acceleration is very large so that a finite amount of momentum is transferred to the fluid as in the case of a shock. This approximation is reasonable when the shock strength is weak. Its validity has been verified by Ritchmyer (1960) in his consideration of the effect of the compressibility to the inital growth rate of a perturbed sharp interface. He concluded that for a weak shock, the extension of the Rayleigh-Taylor formula for a constant acceleration of finite magnitude to an impulsive one yields results which are accurate to within 5% to 10% of the results obtained from a full compressible calculation.

Saffman and Meiron (1989) used this approximation in a slightly different way for a continuously stratified fluid, and showed that the growth of the instability is reduced when one decreases the density gradient across the interface. It is important to note that a fundamental difference between the two instabilities, Rayleigh-Taylor and Richtmyer-Meshkov, is that in the absence of the gravity, the Rayleigh-Taylor instability occurs only when a light fluid is accelerated into a heavy one but not in the opposite direction, while there is no directional dependency for Richtmyer-Meshkov instability. This difference, according to Saffman and Meiron (1989), is due to the line of action of the pressure gradient which is responsible for the generation of the vorticity. In the Rayleigh-Taylor instability, this pressure gradient is parallel to the direction of the flow, while it is perpendicular in the Richtmyer-Meshkov instability due to the action of the impulsive acceleration on the transverse density fluctuations. Hence, in the Richtmyer-Meshkov instability, the direction of the acceleration is not important. Note also that the growth of the R-M layer is initially linear in time, in contrast to Rayleigh-Taylor instability.

Meshkov (1969) experimentally observed the linear growth rate predicted by Richtmyer theory, and confirmed the directional independence of this instability. Recently, Brouillette (1989) have investigated the shock-induced Richtmyer-Meshkov instability of a sharp and continuous interface, and verified the rate re-

duction due to a decreasing density gradient.

The theory of Richtmyer, and of Saffman and Meiron are applicable to a small perturbed interface. In the present investigation, we examine both small and finite amplitude perturbations of the interface. We perform long-time numerical simulations of the instability. We consider the effect of the density gradient on the growth rate, the detailed structure of the time evolution of a single scale perturbation, and of a random perturbed interface. We also attempt to answer the question of the existence of a self-similar long-time asymptotic limit of the Richtmyer-Meshkov instability, which is known to exist for the Rayleigh-Taylor instability.

From a dimensional analysis for the dominating length scale in the late stage of the Rayleigh-Taylor instability when memory of inital configurations has been lost, it can be shown that the width of the mixed region is proportional to gt^2, where g is the constant acceleration, and t is time. Youngs (1984) numerically verifies this scaling behavior at late times for the penetration of the instability into the denser fluid provided the initial perturbation is random and uniformly distributed. In other words, the quadratic law ceases to be valid if large amplitude long wavelength perturbations are initially present. This result is also confirmed experimentally by Read (1984).

In contrast to the Rayleigh-Taylor instability in which there is a continuous flow of energy into the system, *i.e.*, constant acceleration of finite amplitude, in Richtmyer-Meshkov instability the momentum is only deposited at the interface initially by the impingement of the shock. Moreover, as noted by Brouillette (1989), for a single scale perturbation, the deposited energy is a function of the initial wavelength for Richtmyer-Meshkov instability, but not for the Rayleigh-Taylor instabililty. From these considerations, Brouillette conjecture that a power law governing the mixing of Richtmyer-Meshkov instability can hardly exist at late times. In their experiments, they found that perturbations of a sharp interface evolve quickly into the non-linear turbulent mixing regime, while those of a continuous interface exhibit growth only at late times. For both cases, scaling behavior is not

obtained.

On the other hand, from a consideration of the time evolution of inital turbulent energy deposited at a plane interface, there seems to be another possibility as indicated by the work of Barenblatt (1983). Using a turbulent energy balance equation whose closure is accomplished by certain Kolmogorov-type similarity hypotheses, together with an assumption that the turbulence length scale is equal to a certain fixed part of actual turbulent layer depth, Barenblatt is able to show that there exists a self-similar asymptotic solution for the propagation of turbulence from an instantaneous plane source originally concentrated in a horizontal plane layer of finite depth.

For an idealized problem of an incompressible homogeneuous fluid, *i.e.*, zero Atwood number, initially having an infinitely thin instantaneous turbulence source of finite bulk intensity, Barenblatt shows that the depth of the turbulent layer grows as $t^{2/3}$ purely from a dimensional argument. For a viscous fluid, he finds that a self-similar solution can only be obtained if the initial depth of the turbulent layer is different from zero. The self-similarity, however, is incomplete, *i.e.*, it only exists for intermediate time, and of the second kind so that the time exponent in self-similar variables cannot be determined from a purely dimensional consideration. The value of this exponent is instead obtained from a nonlinear eigenvalue problem, and shown to range from 0 to 2/3.

Results of our simulation seem to indicate the existence of a weak scaling behavior at intermediate time for the width of the stratified layer having initial multiple scale perturbation. The scaling shows a weak dependency on the initial configurations with the time exponent lying in the neighborhood of 1/4. On the other hand, results from single scale perturbations definitely show a lack of universality relative to the initial conditions. This verifies the observation of Brouillette (1989) on the behavior of a single scale perturbation, namely the instability depends strongly on the initial wavelength. However, the extension of this behavior to multiple scale perturbations should be taken with extreme care. Due to limits

of our present computational resources, a much longer simulation and higher resolution is not possible. The question of whether a steepening of the time exponent from 1/4 in our present simulation to the value of 2/3 as predicted by Barenblatt (1983) could ever be reached can only be answered with a much longer simulation. The discrepancy of 1/4 and 2/3 in the time exponent even at low Atwood ratio is presumably due to the existence of inhomogeneity and anisotropy arising from the excitation of vortical plumes as opposed to the uniform character of the random turbulence assumed in the work of Barenblatt (1983).

In the rest of this thesis, the topics considered are presented in the following manner. In Chapter 2, we review the theories related to the Richtmyer-Meshkov instability. We verify the applicability of the flow generated by an initial impulsive acceleration as an approximation to one produced by a weak shock by applying methods of analysis from the work of Paterson (1948) and Chisnell (1955) to a one-dimensional problem. We also formulate and summarize the important dimensionless groups in our problem. In Chapter 3, we discuss the time-dependent numerical scheme used for the simulation, and describe in detail the different numerical tests used to validate the algorithm. The results are discussed in Chapter 4, and Chapter 5 concludes the work with some possible future extensions.

CHAPTER 2

THEORETICAL CONSIDERATIONS

When a plane shock wave passes normally or obliquely through a flat interface separating two fluids of different densities, any perturbation on the interface will grow in time. This interfacial instability is known as Richtmyer-Meshkov instability. It is an example of baroclinic instability, due to the misalignment between the pressure gradient and the density gradient. In order to understand and quantify the growth of this instability, experimental results, for example, work by Meshkov (1969) and recently Brouillette (1989), have been analyzed based on Richtmyer's extension of Rayleigh-Taylor instability.

Lord Rayleigh (1900), and G. I. Taylor (1950) studied the instability of a liquid interface subjected to a finite acceleration in a gravitational field. They found that in the absence of gravity, the interface undergoes instability whenever the lighter fluid is accelerated into the heavier fluid, and the growth is initially exponential in time. Richtmyer (1960) extended the incompressible theory of Rayleigh and Taylor to the case of an impulsive acceleration, i.e., an acceleration having large magnitude and acting for a short time, such as one generated when a shock wave impinges normally on a planar interface. He showed that the instability develops independently of the direction of the acceleration and grows linearly in time. Since the magnitude of the shock-induced impulsive acceleration is large, the initial compressibility effects cannot be neglected. However, as the shock moves a large distance away from the interface, one expects this effect to be less important, and the growth rate of the instability will qualitatively follow that predicted by incompressible theory.

Richtmyer studied the growth rate of the instabilty taking into account the initial compressibility effects, and showed that his results are within 5% to 10% of that given by incompressible theory.

On the experimental side, using the shock tube, Meshkov (1969), and recently Brouillette (1989), studied the instability resulting from the impingement of a shock on a perturbed interface separating two different gases such as air, helium, Freon-22, and carbon dioxide.

Meshkov (1969) verified the initially linear growth and the independence on the direction of the instability. His result on the growth rate, however, was lower by more than 10% than predicted from Richtmyer theory. He suggested that among other experimental factors, such as asymmetry of the form of the disturbance, the impurity of the test gases, and the porosity of the film membrane separating the gases, the marked diffusion of the gas interface during the experiment is one of the important factors contributing to this discrepancy.

Brouillette (1989) studied this effect in detail, and observed a reduction in growth rate by lowering the density gradient at the interface. He found that the initial growth rate for a single scale perturbation can be reduced as much as tenfold if the discontinuous interface is replaced by a continuous one for which the ratio between the thickness of the continuous stratified layer to the initial perturbed wavelength is around three. For a discontinuous interface formed by a thin plastic membrane, Brouillette (1989) found that the perturbation introduced on the interface by the rupture of the membrane due to the passage of a shock evolves rapidly into the non-linear turbulent mixing regime. Due to a large uncertainty in his data at early times, he could not determine a power law describing the time evolution of the interface. For a diffuse interface, perturbations are introduced as gravitational waves by retracting a plate initially separating two gases. The results from this experiment show a dramatic reduction in the growth of a possible turbulent mixing zone. After an initial compression, the thickness of the layer remains essentially the same, and it exhibits growth only at late times, after the development of perturba-

tions introduced by the reverberation of waves between the end wall, the side walls and the distorted interface under the influence of boundary layers.

In this study, we hope to gain some insights into the long time behavior as well as the effect of the smoothness of the interface on the growth rate of the instability using a full 2-D numerical simulation of the time dependent incompressible equations. We model the initial effect of compressibility by approximating the action of the shock as an impulsive pressure using an incompressible impulsive theory. This idea was used by Saffman and Meiron (1989) to study the kinetic energy deposited by an impulse at a layer of stratified fluid with a weak density perturbation in the transverse direction to the flow. This incompressible approximation is a reasonable one for an impulsive acceleration induced by a weak shock, since the induced velocity is subsonic. Moreover, one expects that for such weak shocks, the effect of the compressibility is limited to some initial modification of the density distribution, since the residence time of the shock in the nonuniform region is very small compared to the characteristic time for the evolution of the instability.

In section 1, we summarize the theory of Rayleigh-Taylor instability for finite acceleration and its extension by Richtmyer to the system subjected to an impulsive acceleration. The justification for the use of the discussed incompressible impulsive approximation as well as an assessment of its range of validity are done by examining the solution of a planar shock passing a region of non-uniform density distribution using one-dimensional gas dynamics. In section 2, we review the basic theory of one-dimensional normal shocks, and summarize the Rankine-Hugoniot relations for later reference. Sections 3 and 4 present the results from our study on a normal planar shock passing through a sharp and continuous interface using the methods of analysis due to Paterson (1948) and Chisnell (1955). The incompressible impulsive theory of Saffman and Meiron is reviewed in Section 5. Finally, in section 6, we describe the geometry and the governing equations for our problem.

2.1 Linear Theory

2.1.1 Rayleigh-Taylor Instability

Lord Rayleigh (1900) considered the nature of the equilibrium of a system containing incompressible stratified fluid in a gravitational field. The well-known condition for equilibrium for this system is that the fluid must be arranged in horizontal strata, i.e., the density σ is only a function of the vertical distance, z. In the following discussion, z is the vertical coordinate pointing upward. If this state of equilibrium is altered slightly, a stability criterion can be obtained using linear theory.

Let u, v, and w be the perturbed velocity components in the x, y, and z direction respectively, and let ρ and p be the perturbed density and pressure. To the first order of amplitude perturbation ϵ in a regular expansion, the continuity equation becomes,

$$\frac{\partial u}{\partial x} + \frac{\partial v}{\partial y} + \frac{\partial w}{\partial z} = 0. \tag{2.1}$$

The three momentum equations are

$$\frac{\partial p}{\partial x} = -\sigma \frac{\partial u}{\partial t}, \tag{2.2}$$

$$\frac{\partial p}{\partial y} = -\sigma \frac{\partial v}{\partial t}, \tag{2.3}$$

$$\frac{\partial p}{\partial z} = -g\rho - \sigma \frac{\partial w}{\partial t}. \tag{2.4}$$

The condition of incompressibility for a system of stratified fluid requires the material derivative of the density be identically zero, thus we have

$$\frac{\partial \rho}{\partial t} + w \frac{d\sigma}{dz} = 0. \tag{2.5}$$

Since the above sytem of equations is linear, we can use the superposition principle. Using Fourier theory, the dependence of the flow variables on x, y, and t can be expanded respectively into the eigenmodes $e^{ik_x x}$, $e^{ik_y y}$, and e^{int}, where

k_x, and k_y are the wavenumbers in the x- and y-direction respectively. If the disturbances in time, and in the x-, and y-direction are decomposed into these eigenmodes, then for a particular set of k_x, k_y, and n, the above set of equations is reduced to a second order O.D.E. for the perturbed velocity component w as follows,

$$\frac{d^2w}{dz^2} - ({k_x}^2 + {k_y}^2)w + \frac{1}{\sigma}\frac{d\sigma}{dz}\left\{\frac{dw}{dz} - \frac{g({k_x}^2 + {k_y}^2)}{n^2}w\right\} = 0. \tag{2.6}$$

In the case of a flat interface ($z = 0$) separating two fluids of uniform density σ_1, and σ_2, neglecting any disturbances in the y direction, (*i.e.*, a two dimensional problem), for each region of fluid, the general equation (2.6) is reduced to

$$\frac{d^2w}{dz^2} - {k_x}^2 w = 0, \tag{2.7}$$

of which the general solution is

$$w = Ae^{k_x z} + Be^{-k_x z}. \tag{2.8}$$

Since the fluid is at rest as $z \to +\infty$ for the upper fluid, and as $z \to -\infty$ for the lower fluid, we have $A = 0$ for upper fluid, and $B = 0$ for lower fluid. Due to the continuity of w across the interface, the solution for the upper fluid is $w = Be^{-k_x z}$, and that for the lower fluid is $w = Be^{k_x z}$. The eigenvalue for the time disturbance n is related to the wave number k_x by integrating equation (2.6) across the interface. One obtains,

$$n^2 = gk_x\frac{\sigma_1 - \sigma_2}{\sigma_1 + \sigma_2} = -gk_xA, \tag{2.9}$$

where A is known as the Atwood number.

If $F(x, y, z, t) = 0$ is the equation of the interface, then at every point we must have,

$$\frac{DF}{Dt} = 0. \tag{2.10}$$

For the two-dimensional case we have considered, the equation of the surface is

$$z - \eta(x, t) = 0, \tag{2.11}$$

where η is the perturbed position for a given point on the surface relative to the equilibrium position ($z = 0$). Substituting (2.11) into (2.10), and neglecting small quantities of the second order, the evolution equation for the interface becomes

$$\frac{d\eta}{dt} = w|_{z=0}. \tag{2.12}$$

If the initial perturbation of the interface from the equilibrium position is

$$\eta_0 = a_0 \cos(k_x x), \tag{2.13}$$

and the initial velocity is zero, (2.12) can be integrated to give

$$\eta = a_0 \exp(int) \cos(k_x x), \tag{2.14}$$

where n is the positive root of n^2 in equation (2.9). If we let

$$a(t) = a_0 \exp(int) \tag{2.15}$$

denote the amplitude of the disturbance at time t, then the evolution equation for $a(t)$ is

$$\frac{d^2}{dt^2} a(t) = -n^2 a(t) = g k_x A a(t). \tag{2.16}$$

From equation (2.15), one sees that a flat interface subjected to an infinitesimal disturbance will oscillate about the equilibrium state when n^2 is positive, *i.e.*, the density of the upper fluid (σ_2) is smaller than that of the lower fluid (σ_1). On the other hand, if the density gradient is reversed, then the system is unstable. As long as the amplitude of the disturbance remains small compared with its wavelength, the instability grows exponentially in time and the growth rate of the disturbance increases with increasing k_x, i.e., smaller wavelength. If the motion is not limited to two dimensions, then as can be seen from equation (2.6), the relation between n, and k_x is the same with k_x replaced by $\sqrt{{k_x}^2 + {k_y}^2}$. Hence, in the later discussion, we will only use k to stand for wave number in general.

Taylor (1950) considered an extension to this problem. Instead of a system at rest, he assumed the whole system is accelerated vertically upward with an uniform acceleration g_1. If we choose the reference frame to be fixed relative to the interface, i.e., uniform accelerating moving frame, then the governing equations are the same except the body force $g\rho$ in equation (2.4) is replaced by $(g + g_1)$. Taylor used the velocity potential formulation for the perturbed system and arrived at the same stability criteria (2.9) with the modified gravity, $(g + g_1)$. The stability of a flat interface now depends not only on the densities, σ_i, $i = 1, 2$, but also on the magnitude of g_1 relative to g, and the direction of the acceleration, g_1. When the upper fluid is lighter than the lower fluid, the stability of the interface disappears when the whole system is accelerated downward faster than free fall. Vice versa, the instability of the interface when $\sigma_1 < \sigma_2$ will become stable if the liquid were given a downward acceleration greater than that of gravity. In the case of no gravitational acceleration, the system is unstable when accelerated from light to heavier fluid, and is stable when accelerated in the opposite direction. This is the well-known Rayleigh-Taylor instability.

It should be noted that the above analysis is valid for an ideal case of two incompressible fluids without viscosity, diffusion, or surface tension, with an infinite density gradient at their interface. As shown in equation (2.14) and (2.9), an infinitesimal perturbation with wave number k will increase exponentially in amplitude with the exponent being proportional to $k^{1/2}$. Hence, the growth rate of the amplitude increases without limit with increasing wave number. This unrealistic situation is resolved by the inclusion of the effects of surface tension (Chandrasekhar, 1961), viscosity (Bellman and Pennington, 1954), finite interface density gradient (Case, 1960), or diffusion (Duff *et al.*, 1962). For an extensive list of references, see Sharp (1984). The resulting eigenvalue n is then bounded for all values of k, and has a maximum for some particular wave number. If the initial perturbation has a fairly complete spectrum of harmonic wave numbers, then after some time, a particular wave number (k_{max}, or wavelength λ_{max}) will dominate the overall

growth. This development of the instability is usually known as the first stage of the overall evolution of the Rayleigh-Taylor instability.

The next two stages of the instability are discussed by Youngs (1984) as follows. After the amplitude of the dominant wave number has reached about half of its wavelength ($\frac{1}{2}\lambda_{max}$), the exponential growth of short wavelength perturbation slows down and longer wavelength perturbations begin to grow more rapidly. This stage is characterized by the appearance of larger and larger structures which emerge from the nonlinear interaction and competition of bubbles. If a bubble of the lighter fluid penetrating the denser fluid is slightly larger than its neighbors it grows more rapidly and eventually overtakes the surrounding bubbles. This stage ends when the memory of the initial conditions is lost, and the dominant wavelength λ_d has reached about $10\lambda_{max}$.

In the final mixing stage of the Rayleigh-Taylor instability, the growth of the large-scale structures is weakly affected by the viscosity. Since the memory of the initial conditions is lost, from a dimensional analysis, it can be shown that the dominant length scale is of the order $O(gt^2)$. Hence, the width of the mixed region must be proportional to t^2. This quadratic scaling has been confirmed numerically by Youngs (1984), and experimentally by Read (1984) for the penetration of the denser fluid, *i.e.*, the growth of the bubbles of light fluid, provided no initial large amplitude long wavelength perturbations are initially present. Read (1984) and Youngs (1984) also noticed that the experimental values of the growth rate tend to be higher than the values obtained from two-dimensional calculations. They attribute this effect to the two-dimensional constraint of the numerical calculations, which presumably inhibits the growth of the large scale structure, as opposed to the more rapid growth observed in three-dimensional experiments. This phenomenology of low constant acceleration of the bubbles penetrating the heavy fluid clearly does not correspond to the instability evolved from a pure sinusoidal perturbation. In the later case it is known that at late times a single bubble of light fluid penetrates the heavy fluid with a constant velocity in proportion to $\sqrt{g\lambda}$, and the spike of

heavy fluid falls with constant acceleration (Davies and Taylor, 1950). This fact is observed experimentally in the work of Lewis (1950).

Recently, using moving source singularities and a scheme for the competition between bubbles, Zufiria (1987) successfully modeled the dynamics of Rayleigh-Taylor instability for the case in which the density ratio between the two fluids is infinity. His results suggest that the constant acceleration observed in the motion of the interface is due to the competition among the different bubbles which form the front. He also found that the averaged motion of the front is very insensitive to the initial conditions, even though the detailed structure of the bubbles is quite sensitive. In a subsequent investigation using a numerical scheme known as the vortex in cell method (VIC), Zufiria (1987) includes surface tension in his calculation, and obtains results in agreement with the experimental results of Read (1984). He concludes that surface tension is the mechanism for the final selection of the number of bubbles at the front. He also observes that the motion of these bubbles is not affected by the behavior of the spikes, and hence he could obtain acceptable results with a very poor resolution in the region of the spikes.

Later, in this work, we will analyse the results of our numerical simulation in parallel with the features quoted above for the Rayleigh-Taylor instability for both single and random multiple scale perturbations. In the next section, we summarize the extension of Richtmyer (1960) to the case of an impulsive acceleration.

2.1.2 Richtmyer-Meshkov Instability

Richtmyer (1960) investigated the effect of compressibility on the instability of an interface undergoing shock-induced impulsive acceleration. When the acceleration g in the above theory of Rayleigh and Taylor is impulsive, i.e., $g = g(t)$ is very large during a short time interval and zero or small outside that interval, then one can integrate equation (2.16) over this time interval to obtain the evolution equation for the disturbance amplitude $a(t)$.

Let v_0 be the induced velocity of the fluid due to the impulsive acceleration $g(t)$,

$$v_0 = \int g(t)dt.$$

If the condition of the interface before the arrival of the acceleration is

$$a = a_0, \qquad \frac{da}{dt} = 0, \tag{2.17}$$

then by integrating (2.16), immediately after passage of the impulse, we have

$$a = a_0, \qquad \frac{da}{dt} = kv_0a_0A. \tag{2.18}$$

Thus, the amplitude of the disturbance grows linearly in time. Notice that in contrast to the case of finite magnitude acceleration, this instability exists independently of the direction of the acceleration. When the acceleration is directed from a light fluid into a heavy one, the amplitude simply increases. In the reverse direction, from heavy to light, the amplitude first decreases then reverses its phase and increases. The underlying physics of this difference is due to the line of action of the pressure gradient that is responsible for the generation of the vorticity. In Rayleigh-Taylor instability, this pressure gradient is parallel to the direction of the flow, while it is perpendicular in the Richtmyer-Meshkov instability due to the action of the impulsive acceleration on the transverse density fluctuation. Hence, Richtmyer-Meshkov instability occurs independently of the direction of the acceleration.

Equation (2.18) is obtained using the assumption of incompressibility. That is, any disturbance in the flow field is communicated instantaneously to the other parts of the domain. Therefore, there exists a discontinuity in the rate of change of the amplitude as shown above. In reality, since the magnitude of the acceleration is large, the fluid will first be compressed, and there will not be any communication to the other part of the fluid until there has been time for the shock to pass through a distance of the order several wave lengths of the disturbance. One expects that

the compressibility effect will be restricted to this initial state as long as the shock is weak, and after which the growth of the instability will be qualitatively the same as that predicted by equation (2.18).

In his first order theory, Richtmyer considered a plane shock wave passing normally to a corrugated interface separating two fluids of different densities as shown in Figure 2.1. Before the arrival of the shock, the system is at rest and thus equation (2.17) is applicable. Initially, when the shock impinges on the interface, $a(t)$ is less than a_0 due to the compression, and $\dot{a}(t)$ is zero because the induced velocity at the crest of the disturbance and the trough are the same. To the first order of approximation, the transmitted and reflected shocks are also corrugated. The transmitted shock is slightly converging at the crest, and diverging at the trough of the disturbance. The opposite is true for the reflected shock. Thus pressure gradients are generated across the crest and the trough in such a way to hold back the crest and accelerate the trough further into the heavy fluid.

Richtmyer derived a set of linear partial differential equations for these pressure perturbations, along with a set of initial, and boundary conditions. He then solved the linearized problem numerically using finite difference methods, and obtained the solution of $\dot{a}(t)$ as a function of time. As shown in Figure 2.2, it increases monotonically from zero, then after several oscillations, it reaches an asymptotic limit. The oscillation is physical and has been observed experimentally by Meshkov (1969). Thus, the corrugation in a shock are superstable, *i.e.*, they oscillate in a damped fashion. Richtmyer observed that the asymptotic value of $\dot{a}(t)$ is comparable to that given by the incompressible theory, i.e., equation (2.18), if the post shock values for the densities, and the initial $a(0+)$, are used. On the other hand, the incompressible theory overpredicts the value of $\dot{a}(+\infty)$ by a factor of 2 if the pre-shock values are used.

Meshkov (1969) experimentally observed the linear growth rate of Richtmyer's theory for single-scale perturbations. However, the disagreement between his measured growth rate and that based on the theory is more than 10%. He suggested

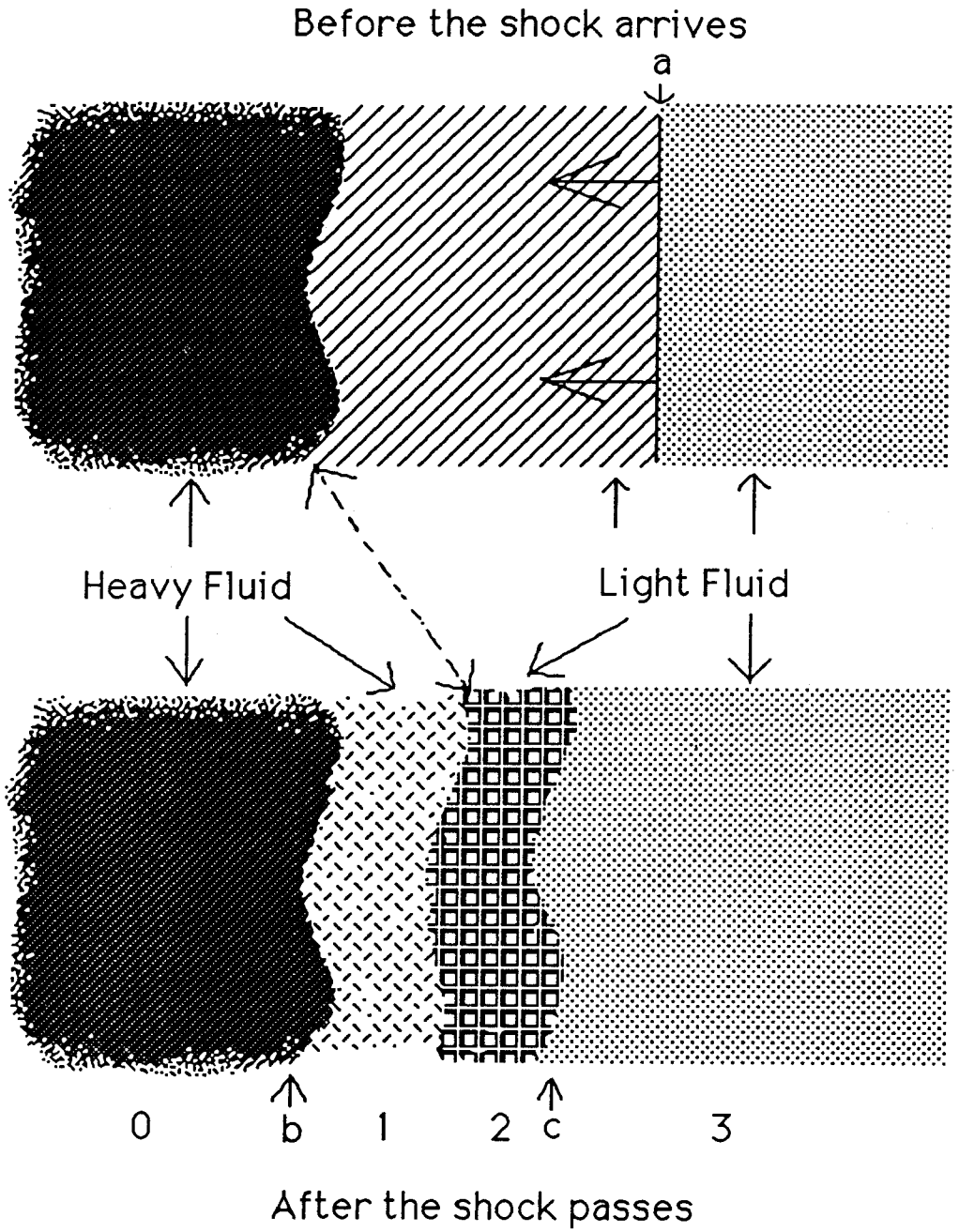

Figure 2.1 Shock impinges on a sharp two-dimensional perturbed interface.

Figure 2.2 Qualitative behavior of the growth rate from Richtmyer's full compressible calculation.

several experimental factors contributing to this discrepancy, one of which is the marked diffusion of the gas interface while Richtmyer's theory is derived for a sharp interface. Sturtevant (1988) pointed out that Meshkov's results can be made close to the theoretical prediction by using the correct post-shock parameters.

Recently, Brouillette (1989) reported experimental results for the Richtmyer-Meshkov instability in the case of continuous stratified fluid. Due to the lack of a theoretical study on this problem, they have developed a model based on equation (2.18), and the so-called growth reduction factor ψ used by Duff *et al.* (1962). Since they can not determine the initial amplitude of the disturbance accurately, they can not validate their model directly. However, indirectly, from the results of different set of experiments, they found good agreement between their experimental and analytical results. This work shows that the shock induced growth of a continuous

interface can be reduced as much as tenfold compared to that of a discontinuous interface.

Mikaelian (1988) has performed full compressible calculations of the Richtmyer-Meshkov instability using an Arbitrary Lagrangian-Eulerian (ALE) code. In his numerical experiment, the geometry of the problem is the same as the configuration used in Brouillette's experiment. Three kinds of perturbations are considered including single scale, double scale, and random multiple scale perturbations. For a shock going from a heavy fluid to a light one, the time at which the perturbation undergoes a phase reversal as predicted by equation (2.18) is in fair agreement with the numerical simulation. For example, for a shock of Mach number 1.2 passing from air into helium, the numerical simulation predicts 2.5cm for the distance travelled by the interface when a phase reversal occurs as opposed to the value of 2.1cm predicted by equation (2.18).

As in the work of Meshkov (1969), Mikaelian's results also indicate the overprediction of equation (2.18) on the growth rate of a single scale perturbation. The penetration of the bubbles of light fluid into the heavier fluid is observed to be at a slower rate than the falling of the spikes of heavy fluid regardless of the direction of the shock. The asymmetric development in the shape of the bubbles and the spikes are clearly seen with the bubble having a round front, while that of the spike rolling-up is in the form of a mushroom's head. In addition to sinusoidal profiles of the initial perturbations, Mikaelian (1988) also studies initial profiles that are composed of parabolic curves. He observes that, except for a small difference in the initial growth of the two profiles, at late times, the growth only depends on the initial amplitudes. Different profiles initially having equal amplitudes will evolve into the same height at late times. It should be noted that these qualitative features of compressible Rictmyer-Meshkov instability will be observed in our simulation of the incompressible Richtmyer-Meshkov instability presented in Chapter 4.

In contrast to Rayleigh-Taylor instability, there seems to be no experimental or theoretical evidence that the non-linear development of the Richtmyer-Meshkov

instability will ever reach an asymptotic stage of self-similar turbulent growth. For the special case of zero Atwood number and of an inviscid fluid, using a turbulence model, Barenblatt (1983) is able to construct a self-similar asymptotic solution to the mixing of uniform turbulence originally concentrated in a horizontal plane layer of zero thickness. A time exponent of 2/3 is obtained purely from a dimensional argument. For a viscous fluid, self-similar intermediate asymptotics can only be obtained for a layer initially having a finite thickness. The self-similarity is of the second kind so that the time exponent is obtained from solving a nonlinear eigenvalue problem. In this case, the time exponent ranges from 0 to 2/3. It should be noted that a fundamental difference between the turbulence propagation in Barenblatt's analysis and the development of the Richtmyer-Meshkov instability is the emergence of larger and larger structures in the later process, while the turbulence layer considered by Barenblatt remains uniformly distributed for all times. If a self-similar development of the Richtmyer-Meshkov instability does exist, the time exponent of the scaling variables may not correspond to the values 2/3 obtained by Barenblatt, but indeed should be lower. This upper bound can be rationalized by the fact that a fraction of energy has been transferred to the internal motion of these larger structures and hence reduces the energy available for the expansion of the overall layer. In an attempt to explore the possibility of scaling behavior, we develop a model to study the Richtmyer-Meshkov instability using the incompressible impulsive theory of Saffman and Meiron (1989).

The fundamental ideas behind this theory as a model for the flow generated by a weak shock wave impinging normally on a continuous stratification are the following.

1. The induced speed of the gas by a weak shock is subsonic and much less than the speed of the transmitted and reflected shock. Thus, the residence time of the shocks in the neighborhood of the interface is small, and the compressibility effects are limited to a short time interval initially. Hence, the motion of the interface can be modeled as the response to an incompressible impulsive

acceleration.

2. When the transmitted and reflected shocks have travelled a large distance away from the region of non-uniform density, the state of the gas will be similar to that of a shock impinging on a sharp interface. Hence, the velocities of the gas far away from the interface are uniform. This provides simple boundary conditions for the impulsive model.

In the following sections, we will give some justifications for the above ideas using one-dimensional gas dynamics, and a summary of the Saffman and Meiron formulation along with their results for a small density disturbance.

2.2 Normal Shock Relations for a Perfect Gas

It is well-known that some solutions of the one-dimensional inviscid equation, which are initially continuous, cannot remain continuous for all time; one has to allow discontinuities of velocity, pressure, density, specific entropy, and temperature in its solution. Such a discontinuity is called a shock front. It is a mathematical idealization of a very thin region containing fluid of very high temperature gradient, and viscous stress. Courant and Friedrichs (1948) give an interesting account of the historical development on the ideas of shock waves. They also discussed how the shock conditions can be derived from the differential equations for viscous and heat-conducting fluids. The thickness of the shock has been estimated to be of the order of the mean free path of the gas molecules (see for example, Landau and Lifshitz (1959)). Thus for practical calculation, it is sufficient to consider the shock as a discontinuity and calculate the jumps in the equilibrium values across the shock. For a flow across the shock as shown in Figure 2.3, the three conservation equations, or the jump conditions for mass, momentum, energy, and the entropy condition take the following forms:

$$\rho_1 u_1 = \rho_2 u_2, \tag{2.19}$$

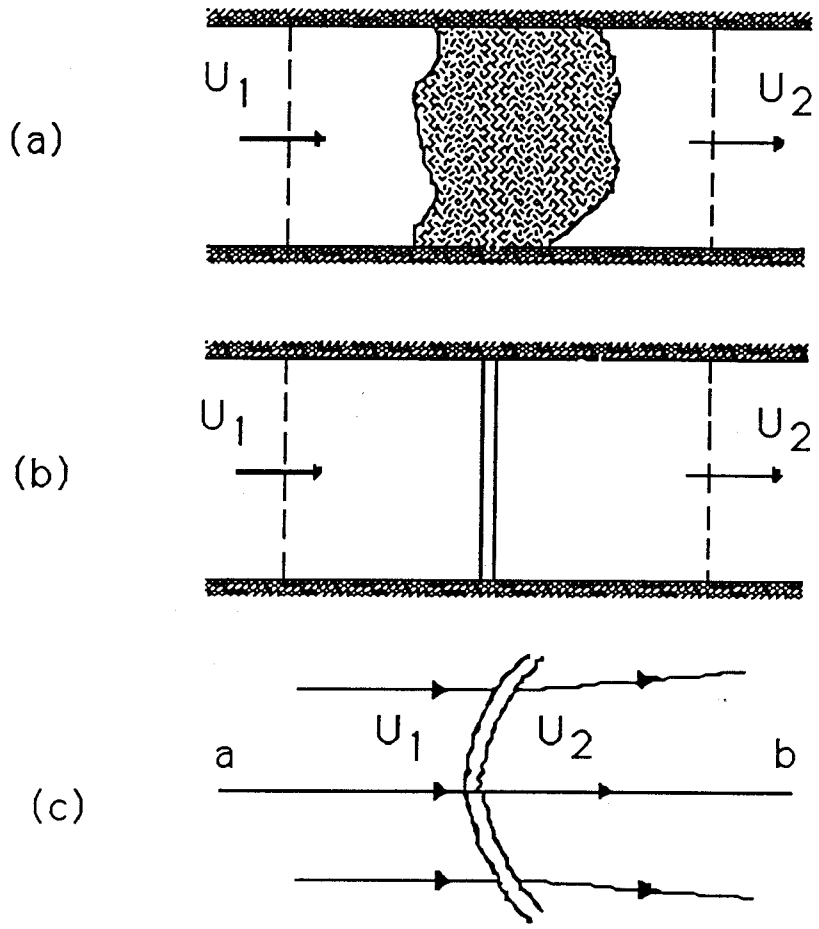

Figure 2.3 Idealization of a normal shock a) flow across a region of nonuniformity, b) normal shock wave, and c) shock wave normal to the streamline a–b.

$$p_1 + \rho_1 u_1^2 = p_2 + \rho_2 u_2^2, \tag{2.20}$$

$$h_1 + \frac{1}{2}u_1^2 = h_2 + \frac{1}{2}u_2^2, \tag{2.21}$$

$$s_1 \leq s_2, \tag{2.22}$$

where h, and s are respectively the enthalpy and the entropy of the fluid in the equilibrium regions denoted by the subscripts 1, and 2.

For a real gas, it is usually necessary to solve the above general equations by numerical methods. However, for an ideal gas undergoing an adiabatic process (gas with equation of state $p/p_0 = (\rho/\rho_0)^\gamma$), its state behind the shock (those having subscript 2) can be obtained in terms of the shock strength, $z_{12} = p_2/p_1$, and the state of the gas in the front of the shock. The resulting equations are known as the Rankine-Hugoniot relations, which may be written in the following form:

$$\rho_2 = \rho_1 \frac{(\lambda^2 + z_{12})}{(1 + \lambda^2 z_{12})}, \tag{2.23}$$

$$u_2 = u_1 \pm \phi(z_{12}, p_1, \rho_1), \tag{2.24}$$

$$U = u_1 \pm \sqrt{\frac{p_1(\lambda^2 + z_{12})}{\rho_1(1 - \lambda^2)}}, \tag{2.25}$$

where

$$\phi(z_{12}, p_1, \rho_1) = (z_{12} - 1)\sqrt{\frac{p_1(1 - \lambda^2)}{\rho_1(\lambda^2 + z_{12})}}, \tag{2.26}$$

$$\lambda^2 = \frac{(\gamma - 1)}{(\gamma + 1)}. \tag{2.27}$$

Here U is the velocity of the shock front, and γ is the ratio of specific heats of the assumed ideal gas. For simplicity, in this work, γ is taken to be 1.4, the value for air. The plus (minus) sign in the above equations applies to the forward (backward) shock, that is a shock moving in the positive (negative) x-direction in the usual x-t coordinate.

Since we are interested in the state of the gas when the shock is inside the non-uniform region as well as its asymptotic behavior when the shock has been a large distance away, in the following discussions, we will consider two related problems of a normal shock wave passing through a sharp interface, and through a non-uniform one-dimensional medium.

2.3 Shock Passing a Sharp Interface

The theory of a plane shock wave impinged normally on an ideally thin and light partition separating two perfect gases of different molecular weights, and specific heat constants has been studied by Paterson (1948). In our work, we will consider two gases otherwise identical having different densities ρ_{0L} on the left of the partition, and ρ_{0R} on the right side as shown in Figure 2.4, with

$$\rho_{0L} < \rho_{0R}, \quad \text{and} \quad \delta = \frac{\rho_{0R}}{\rho_{0L}}. \tag{2.28}$$

We consider a plane shock wave S_1 passing through the gases initially at rest and falling normally on the interface. Since the flow is one-dimensional, after S_1 impinges upon the interface, there is a reflected wave S_3, and a transmitted wave S_2 leaving it. In his work, Paterson shows that the transmitted wave is always a shock wave, and the reflected wave can be either a shock wave, or a rarefaction wave. For the system we consider, the reflected wave is always a shock wave.

Let the subscript 0 denote the initial state of both gases, and $i = 1, 2, 3$ the steady state behind the incident shock (S_1), the transmitted shock (S_2), and the reflected shock (S_3), respectively. And let u_i denote the gas velocity behind the shock, S_i, U_i, the shock speed, and z_i the pressure ratio across the shock, so that $z_1 \equiv p_1/p_0$, $z_2 \equiv p_2/p_0$, $z_3 \equiv p_3/p_1$. By the jump conditions (2.23) to (2.27), we have for S_1

$$\frac{\rho_1}{\rho_{0L}} = \frac{\lambda^2 + z_1}{1 + \lambda z_1}, \tag{2.29}$$

$$u_1 = \phi(z_1, p_0, \rho_{0L}), \tag{2.30}$$

$$U_1 = \sqrt{\frac{p_0(\lambda^2 + z_1)}{\rho_{0L}(1 - \lambda^2)}}, \tag{2.31}$$

for S_2

$$\frac{\rho_2}{\rho_{0R}} = \frac{\lambda^2 + z_2}{1 + \lambda z_2}, \tag{2.32}$$

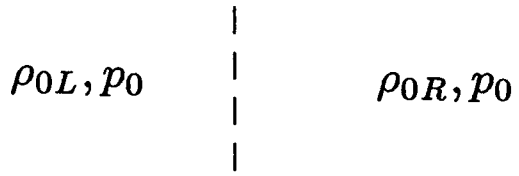

a) Initial state, gases are at rest.

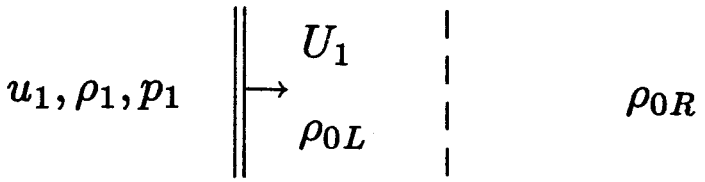

S_1-incident shock

b) Before the incident shock arrived.

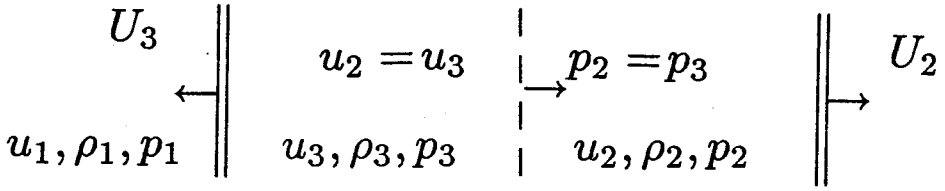

S_3-reflected shock S_2-transmitted shock

c) After the shock passed.

Figure 2.4 Shock passing a sharp one-dimensional interface.

$$u_2 = \phi(z_2, p_0, \rho_{0R}), \tag{2.33}$$

$$U_2 = \sqrt{\frac{p_0(\lambda^2 + z_2)}{\rho_{0R}(1-\lambda^2)}}, \tag{2.34}$$

and for S_3

$$\frac{\rho_3}{\rho_1} = \frac{\lambda^2 + z_3}{1 + \lambda z_3}, \tag{2.35}$$

$$u_3 = u_1 - \phi(z_3, p_1, \rho_1), \tag{2.36}$$

$$U_3 = u_1 - \sqrt{\frac{p_1(\lambda^2 + z_3)}{\rho_1(1-\lambda^2)}}, \tag{2.37}$$

where the function ϕ is given in equation (2.26).

At the interface, by continuity of the velocity and the pressure, *i.e.*, $u_2 = u_3$, and $p_2 = p_3$, we obtain a nonlinear equation for z_3

$$(z_3 z_1 - 1)\sqrt{\frac{1}{\lambda^2 + z_3 z_1}} - (z_1 - 1)\sqrt{\frac{\delta}{\lambda^2 + z_1}} + (z_3 - 1)\sqrt{\frac{z_1\delta(1 + \lambda^2 z_1)}{(\lambda^2 + z_1)(\lambda^2 + z_3)}} = 0. \tag{2.38}$$

For given shock strength z_1, density ratio δ, and λ^2, this equation is solved for z_3 by the bisection method. Once, z_3 is obtained, all flow properties of the gas can be determined. The ratios of the shock speed U_i to the speed u_i of the gas behind it are,

$$\frac{U_1}{u_1} = \frac{1}{2}\frac{\gamma + 1}{z_1 - 1}(\lambda^2 + z_1), \tag{2.39}$$

$$\frac{U_2}{u_2} = \frac{1}{2}\frac{\gamma + 1}{z_2 - 1}(\lambda^2 + z_2), \tag{2.40}$$

$$\frac{U_3}{u_3} = \frac{1 - \dfrac{\gamma + 1}{2(z_1 - 1)}\sqrt{z_1(\lambda^2 + z_3)(1 + \lambda^2 z_1)}}{1 - \dfrac{z_3 - 1}{z_1 - 1}\sqrt{\dfrac{z_1(1 + \lambda^2 z_1)}{\lambda^2 + z_3}}}. \tag{2.41}$$

The density and temperature ratio of the gases across the interface after the passage of the shock are respectively,

$$\frac{1}{\delta}\frac{\rho_2}{\rho_3} = \Pi, \tag{2.42}$$

$$\frac{T_2}{T_3} = \frac{1}{\Pi}, \tag{2.43}$$

where

$$\Pi = \frac{\lambda^2 + z_2}{1 + \lambda^2 z_2} \frac{1 + \lambda^2 z_1}{\lambda^2 + z_1} \frac{1 + \lambda^2 z_3}{\lambda^2 + z_3},$$

and T_i is the temperature of the gas behind the shock S_i.

2.3.1 Motion of the shock away from the partition or a measure of shock residence time

For six density ratios, δ of 1.22, 1.5, 3, 9, 19, 39, corresponding to the six Atwood numbers A of 0.1, 0.2, 0.5, 0.8, 0.9, 0.95, the solutions to the problem of a shock passing a sharp interface are obtained with the arriving shock strength z_1 ranging from 1 to 1000.

Figure 2.5 shows a plot of the speed ratios of equations (2.39) to (2.41) versus the shock strength z_1. For both of the transmitted and reflected shocks, at a given incident shock strength, as the density ratios increase, the speed ratios decrease. That is, the speed of the transmitted shock relative to the partition decreases, while that of the reflected shock increases. As z_1 increases, the speed ratios of the incident and transmitted shocks decreases, while that of the reflected one increases. These ratios quickly approach a limit for $z_1 < 10$. For the incident shock, the final limit can be shown to be

$$\frac{U_1}{u_1} = \frac{\gamma + 1}{2}. \tag{2.44}$$

For $\gamma = 1.4$, the limit is 1.2. The limit for the transmitted shock is also in the neighborhood of 1.2. For the reflected shock the limit ranges from -0.18 to 0.45 for the corresponding values of δ from 39 to 1.22 (in decreasing order). Thus for a very strong incident shock, the transmitted shock leaves the interface at a rate 20% faster than the speed of the interface, and the reflected shock moves out at a rate 60% to more than 100% backward depending on the density ratios.

In Figure 2.6, we show a detail variation of these speed ratios for $z_1 \leq 4$. Up to $z_1 = 1.8$, the speed of the transmitted shock is more than double the speed of the gas for all density ratios. This is also true for the reflected shock, except that

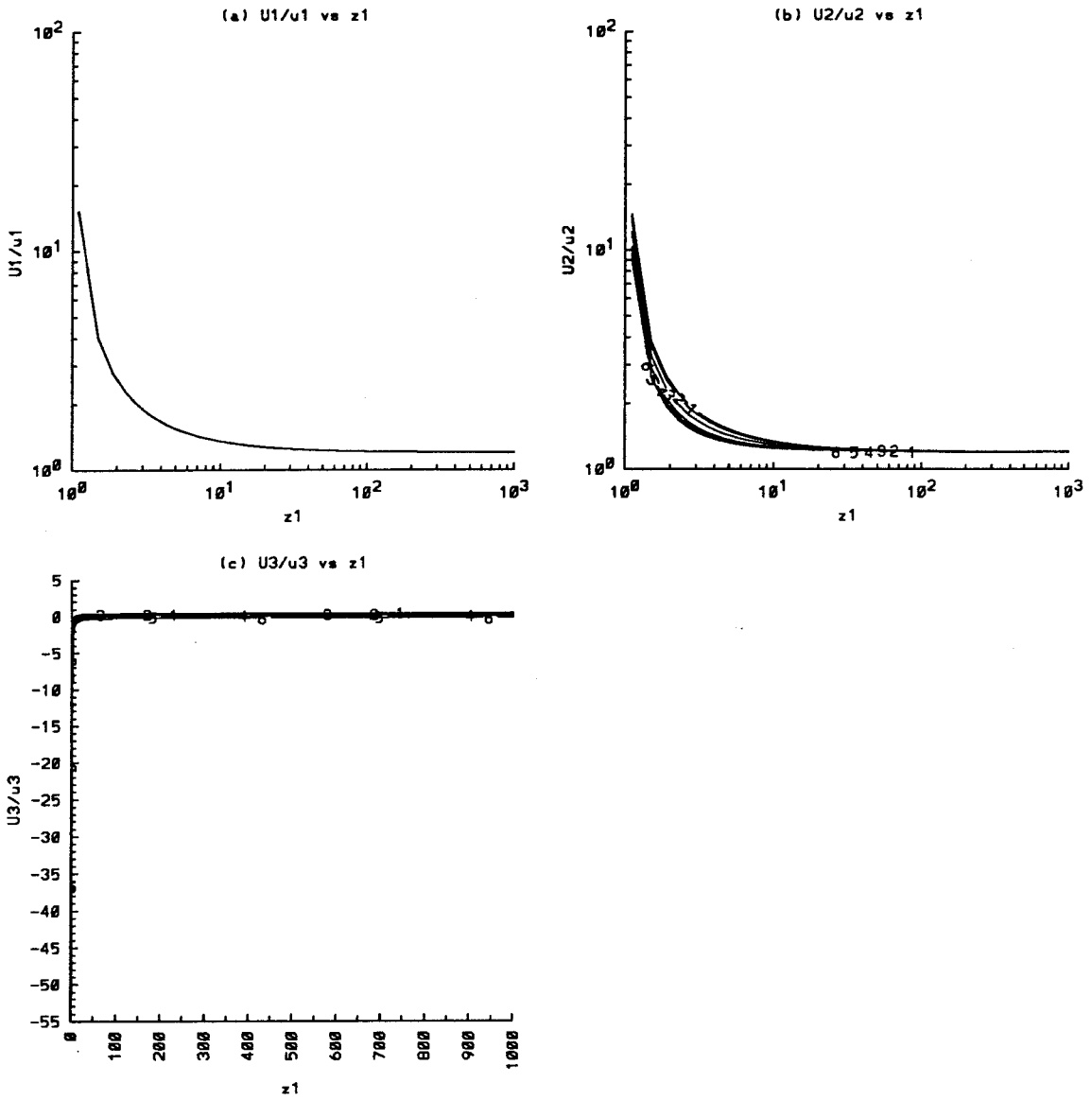

Figure 2.5 Speed ratio as function of the shock strength z for the ranges from 1 to 1000. a) U_1/u_1 b) U_2/u_2 c) U_3/u_3. The numbers 1, 2, 3, 4, 5, and 6 on the curves refer to the Atwood numbers 0.1, 0.2, 0.5, 0.8, 0.9, and 0.95 respectively.

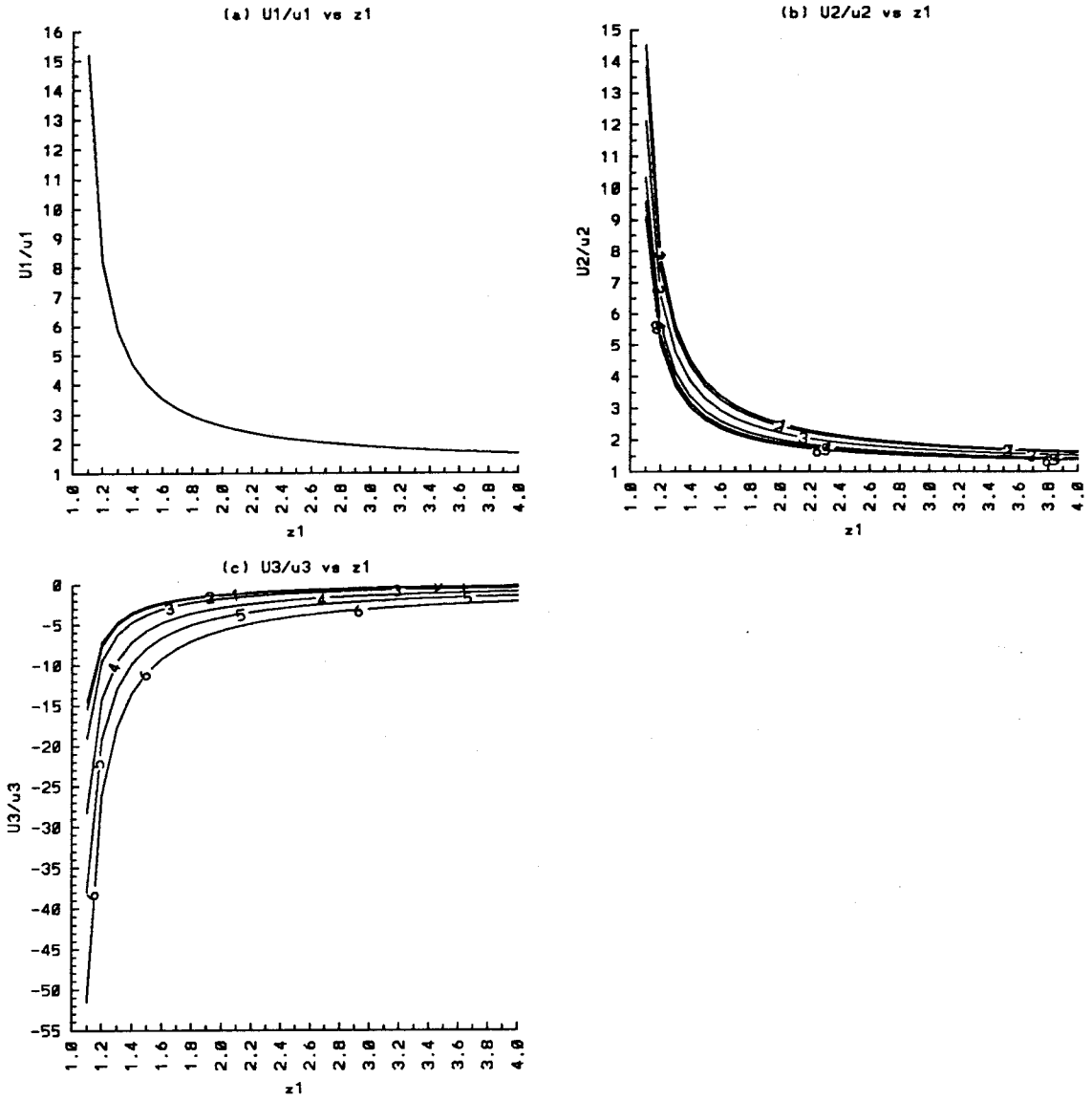

Figure 2.6 Speed ratio as function of the shock strength z for the ranges from 1 to 4. a) U_1/u_1 b) U_2/u_2 c) U_3/u_3. The numbers 1, 2, 3, 4, 5, and 6 on the curves refer to the Atwood numbers 0.1, 0.2, 0.5, 0.8, 0.9, and 0.95 respectively.

the velocities of the reflected shock and the gas are in the opposite direction. Thus, relative to the interface, the reflected shock is moving away from it twice as fast as the transmitted one. For $z_1 = 1.1$, the speed ratio U_2/u_2 is 9 for $A = 0.95$, and 14.5 for $A = 0.1$. The corresponding values for U_3/u_3 are -14.5, and -52.0.

From this result, we conclude that the residence time of the shocks in the neighborhood of a sharp interface is small for a weak shock. For a shock of moderate to strong strength, the residence times quickly approach a limit. The density ratio has more effect on the residence time of a weak shock than a moderate or strong one.

2.3.2 Gas properties after passage of the shocks or a measure of the compressibility effects

Similar to Figure 2.5, and 2.6, as functions of the incident shock strength z_1, we plot in Figure 2.7, and 2.8 plots of the density ratios as given in equation (2.42), the temperature ratios (equation 2.43), and the strength of the transmitted and reflected shock.

For a given z_1, the density ratios decrease for increasing δ. After the passage of an incident shock with strength less than or equal to 3, the density ratio normalized by its initial value is more than 90% for all values of δ. As z_1 increases to 1000, this ratio decreases to a limit of 40% for $\delta = 39$, and 92% for $\delta = 1.22$. Thus, except for a very strong shock, the initial density gradient across a sharp interface is slightly altered.

Before the arrival of the shock, the gases on the either side of the partition are at the same temperature, and pressure. Because of the continuity condition at the interface, the pressures remain the same on both sides of the partition. On the other hand, there exists a temperature gradient across the interface in the direction of the shock motion. This effect is large for large δ, and quickly approaches a limit as z_1 increases. Up to $z_1 = 1.4$, the temperature difference on the two sides of

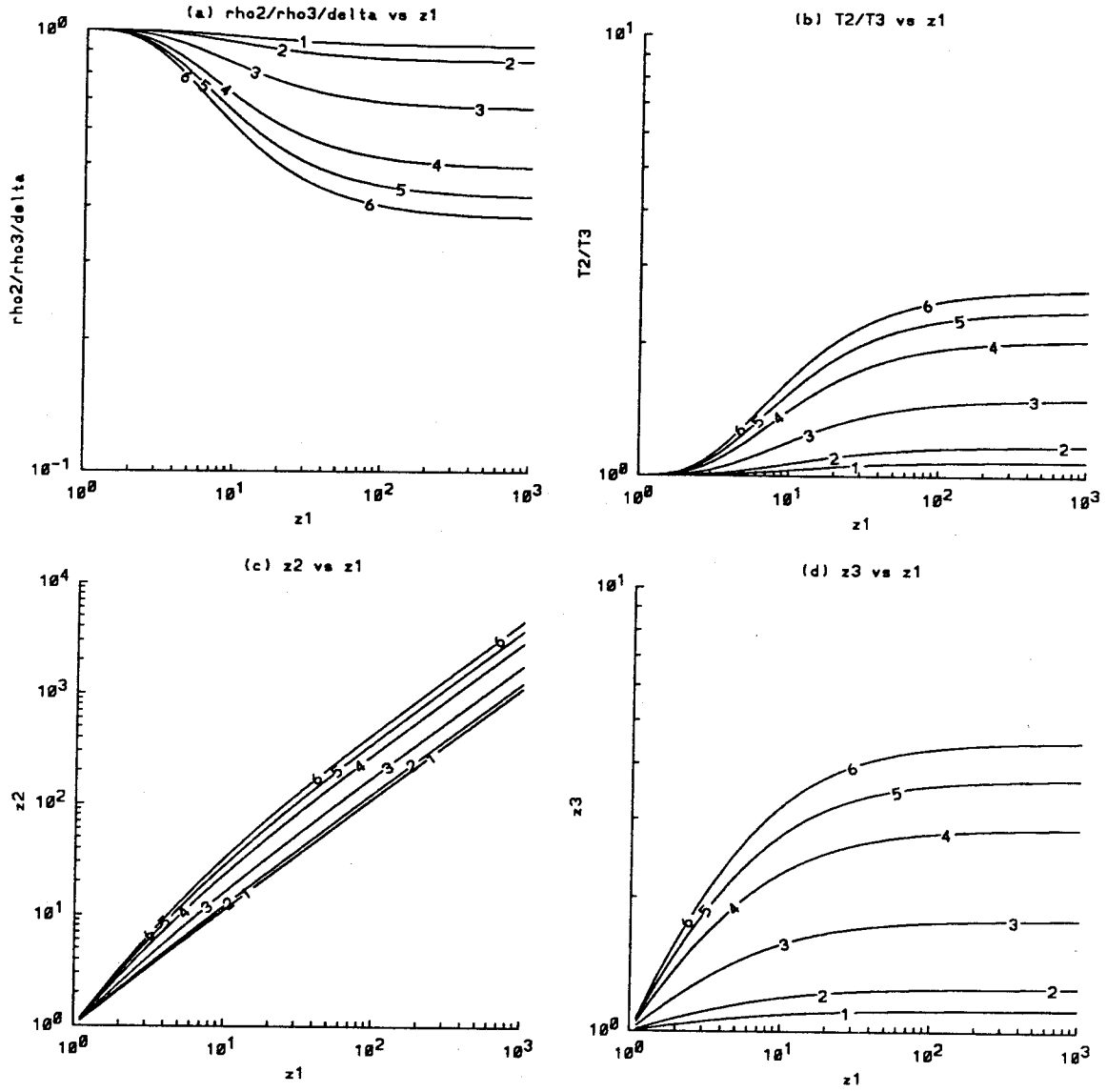

Figure 2.7 Gas properties after passage of the shock for the shock strength from 1 to 1000. a) density ratio $\rho_2/\rho_3/\delta$, b) temperature ratio T_2/T_3, c) transmitted shock strength z_2, and d) reflected shock strength z_3. The numbers 1, 2, 3, 4, 5, and 6 on the curves refer to the Atwood numbers 0.1, 0.2, 0.5, 0.8, 0.9, and 0.95 respectively.

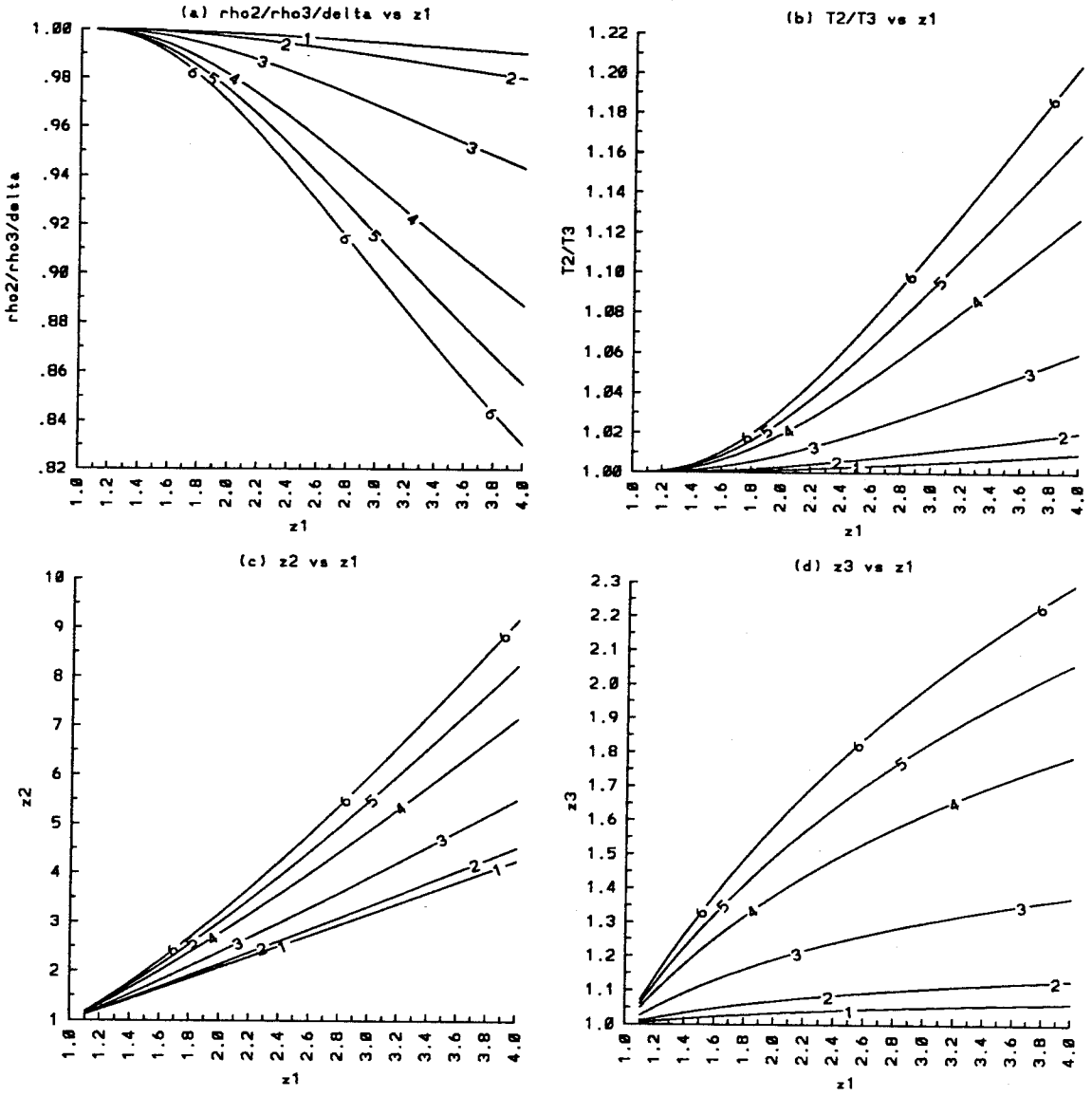

Figure 2.8 Gas properties after passage of the shock for the shock strength from 1 to 4. a) density ratio $\rho_2/\rho_3/\delta$, b) temperature ratio T_2/T_3, c) transmitted shock strength z_2, and d) reflected shock strength z_3. The numbers 1, 2, 3, 4, 5, and 6 on the curves refer to the Atwood numbers 0.1, 0.2, 0.5, 0.8, 0.9, and 0.95 respectively.

the interface normalized to the gas temperature on the left side is less than 0.5% for all density ratios. The corresponding value at $z_1 = 2.0$ is 3%. At $z_1 = 1000$, T_2/T_3 is around 2.62 for $\delta = 39$, and 1.06 for $\delta = 1.22$. Hence, we conclude that after the passage of a weak and even moderate shock, the temperature of the gas is essentially constant across a sharp interface.

2.3.3 Effect of the reflected shock

It is important to see how much the reflected shock will enhance the compressibility effects. For a sharp interface, this effect is clearly seen by observing the reflected shock strength. As shown in Figure 2.7 and 2.8, the strengths of both the transmitted and reflected shock increase as the density ratios increase. For increasing z_1, the strength of the transmitted shock is of the same order of magnitude as that of the incident shock or greater, while that of the reflected shock remains $O(1)$ and is always smaller than the strength of the incident shock. This suggests that when a shock passes through a region of non-uniform density, the strengths of the complicated reverberating waves quickly reduce after several bounces. This consideration gives strong support for the results obtained using Chisnell theory for a shock passing a non-uniform region given in the next section.

In conclusion, when a shock wave impinges normally on a sharp interface, the compressibility effect and the residence time of the transmitted, and reflected shocks in the neighborhood of the interface is very small for a weak shock. For a moderate shock, the state of the gases is modified slightly, and the residence time of the shock quickly approaches a final limit as it would for a very strong shock. For a given incident shock strength, the change in the state of the gases across the interface normalized to its initial state is small for small initial density ratio δ.

These results can be considered as the asymptotic limits for the case of a shock passing through a region of non-uniform density distribution a large distance compared to the characteristic width of the region. Next, we will study in details

the response of the gases in this region as the shock moves through it.

2.4 Shock Passing a Continuous Interface

Chisnell (1955) considers the normal motion of a shock wave through a non-uniform one-dimensional medium. In this theory, he regards the region as a succession of small-density discontinuities separated by uniform regions, with the density distribution being a monotonic function of the distance. A full description of the flow due to the reflected wave of the incident shock is formulated. This reflected wave in turn generates a doubly reflected wave which eventually catches up to the transmitted shock. Due to the complexity of the wave interactions, Chisnell only considers the effect of this doubly reflected wave on the strength of the transmitted shock. Its effect on the strength of the reflected shock and the flow is not given. However, in comparision with the results given by Paterson's theory, Chisnell concludes that his theory is satisfactory even though it only takes into account the first and double reflections.

In this work, we apply Chisnell's theory to a normal shock passing in the positive y direction through a region having the following density distribution,

$$\rho(y) = \frac{1}{2}\left(1 + A\tanh(y)\right), \tag{2.45}$$

where A is the Atwood number. Note that this density profile is used later in our work as the average density distribution on which a sinusoidal perturbation in the x direction is imposed. Figure 2.9 shows a picture of the possible wave interactions at a weak contact discontinuity. There are three types of incident waves, a shock, an element of a forward-facing wave, and an element of a backward-facing wave. After the interaction, the waves are modified in their strengths and propagating speeds. The element of forward-facing wave is absorbed into the transmitted shock.

Using the general theory of one-dimensional gas dynamics (for example, see Courant and Friedrichs (1948)), it is possible to prove an important theorem com-

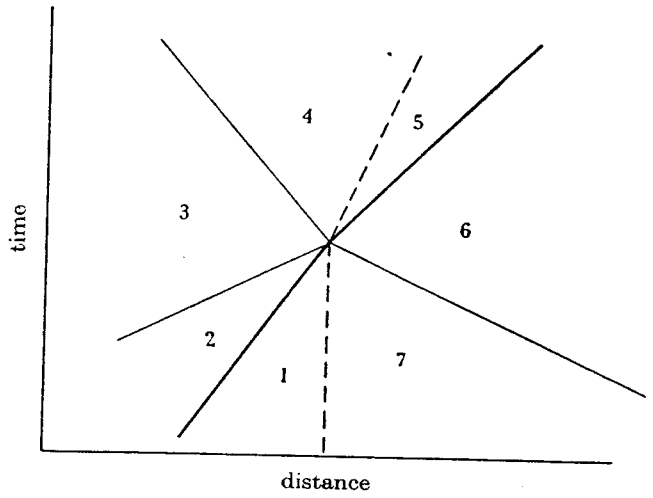

Figure 2.9 Possible wave patterns at a weak contact discontinuity. A shock wave separating regions 1, 2; similarly, an element of a forward-facing wave 2, 3, an element of a backward-facing wave 6, 7, and a weak contact discontinuity 1, 7. After the interaction there is a transmitted shock 5, 6, with a velocity nearly equal to the velocity of the incident shock, a contact discontinuity 4, 5, moving in the same direction as the shock, and a small disturbance 3, 4, , moving in the opposite direction. — shock wave, – – – weak contact discontinuity, — small disturbance.

paring the discontinuous transition through a shock with a continuous transition through a simple wave. Suppose a shock and a simple wave transform a gas in the initial state given by (τ_0, p_0, u_0) into the states given by (τ, p, u), and (τ^*, p^*, u^*) respectively, where τ is the volume per unit mass. If the shock strength is measured by any of the three differences $\tau - \tau_0$, $p - p_0$, or $u - u_0$, then a simple wave and a shock are considered to have equal strength if $\tau^* = \tau$, or $p^* = p$, or $u^* = u$. The theorem then states:

For a shock transition and a simple wave transition with the same initial state and the same strength the quantities τ^* and τ, p^* and p, u^* and u agree up to second order in the shock strength and differ in third order.

So far we have called z the shock strength. In regard to this theorem, the appropriate shock strength is $z-1$. However, in the following discussion, we will use both of the terms interchangeably, and its connotation will be clear from the context. In Chisnell's approximate theory, the Rankine-Hugoniot relations whenever used are expanded to the first and second order in $z-1$. Therefore, these jump conditions are valid even for the simple waves, i.e., there is no distinction between shocks and waves in this theory. In addition to the jump conditions, at the contact discontinuity, the continuity of the pressures and the velocities gives,

$$p_1 = p_7, \quad p_4 = p_5, \quad u_1 = u_7, \quad u_4 = u_5, \tag{2.46}$$

where p and u denote the pressure and velocity with the subscripts indicating the regions shown in Figure 2.9. In term of the shock strength z, and ϕ, these conditions become,

$$z_{12} z_{23} z_{34} = z_{76} z_{65}, \tag{2.47}$$

$$\phi(z_{12}, p_1, \rho_1) + \phi(z_{23}, p_2, \rho_2) - \phi(z_{34}, p_3, \rho_3) = -\phi(z_{76}, p_7, \rho_7) + \phi(z_{65}, p_6, \rho_6), \tag{2.48}$$

where $z_{mn} = p_n/p_m$.

In the following discussion, equations (2.47) and (2.48) are used to obtain the solution of a shock passing a one-dimensional stratified layer of gas. Both the zeroth, and first order solution (*i.e.*, only the first reflected shock is included) are considered.

2.4.1 Strength of the transmitted shock

Flow at the zeroth order of approximation

At the zeroth order of approximation, as the shock moves through the non-uniform region, the strength z of the incident shock will depend only on the density

ρ it encounters. This can be seen in Figure 2.9, where there are no backward-facing waves 6, 7 because the shock moves into a undisturbed region, and the forward-facing waves 2, 3 will only appear at the next order of approximation. Thus, we have $z_{23} = z_{76} = 1$. Since the contact discontinuity is weak, let $\rho_7 = \rho_1 + d\rho_1$, and $z_{65} = z_{12} + dz_{12}$. The continuity equations (2.47) and (2.48) then give,

$$z_{34} = 1 + \frac{dz_{12}}{z_{12}}, \tag{2.49}$$

$$\phi(z_{12}, p_1, \rho_1) - \phi(1 + \frac{dz_{12}}{z_{12}}, p_3, \rho_3) = \phi(z_{12} + dz_{12}, p_6, \rho_6). \tag{2.50}$$

Applying the appropriate Rankine-Hugoniot relations, and expanding ϕ to the first order in dz_{12}, and $d\rho_1$, we obtain an O.D.E. relating the incident shock strength at any point of the non-uniform region to the density there :

$$\frac{1}{\rho_1}\frac{d\rho_1}{dz_{12}} = \frac{2}{z_{12}-1} - \frac{1}{\lambda^2 + z_{12}} + \frac{2}{z_{12}-1}\sqrt{\frac{1+\lambda^2 z_{12}}{z_{12}(1+\lambda^2)}}. \tag{2.51}$$

This equation can be integrated into

$$\rho(z) = Cf(z), \tag{2.52}$$

where

$$f(z) = \frac{(z-1)^2}{(\lambda^2+z)} \left\{ \frac{\lambda + \sqrt{\lambda^2 + \frac{1}{z}}}{-\lambda + \sqrt{\lambda^2 + \frac{1}{z}}} \right\}^{\frac{2\lambda}{\sqrt{\lambda^2+1}}} \left\{ \frac{\sqrt{\lambda^2+1} - \sqrt{\lambda^2 + \frac{1}{z}}}{\sqrt{\lambda^2+1} + \sqrt{\lambda^2 + \frac{1}{z}}} \right\}^2 \tag{2.53),}$$

and z_{12} and ρ_1 have been replaced by the current z and ρ. If the incident shock strength before entering the variable media is known to be z_1, then the constant C is determined as

$$C = \frac{\rho_1}{f(z_1)}, \tag{2.54}$$

where ρ_1 now denotes the density at the beginning of the variable density region.

For the density distribution given in equation (2.45), we obtain the shock strength z as a function of the position by solving equation (2.52). The results for the incoming shock strength of $z_1 = 1.001, 1.01, 1.1, 2.0, 5.0$ are shown in Figures 2.10-b through 2.14-b, each with $A = 0.1, 0.2, 0.5, 0.8, 0.9, 0.95$. Since at this order of approximation, we have neglected any effect of the reflected waves as well as the interactions between the reverberating waves, the flow variables of the gas behind the shock depend only on the shock strength z through the Rankine-Hugoniot relations. Figures 2.10-c to 2.14-c present the density distributions of the gases after the passage of the shock. For comparison, the initial density distributions are shown in Figures 2.10-a to 2.14-a. The ratios U/u_2 of the shock velocity to the velocity of the gas immediately behind the shocks are plotted in Figures 2.10-d to 2.14-d.

For a weak shock $z_1 = 1.001, 1.01, 1.1$ the density distributions are not modified significantly, especially at low Atwood number, A. The speed of the shock is very large compared to the gas speed, and this effect magnifies for smaller A. For the highest Atwood number $A = 0.95$ and $z_1 = 1.001$, the speed ratio U/u_2 decreases from 1400 to 561 as the shock goes through the non-uniform region. The corresponding patterns for $z_1 = 1.01, 1.1$ are from 141 to 57, and from 15.2 to 6.5 respectively. Thus, the residence time of the shock in the non-uniform region relative to the characteristic time for the motion of the gas is very short. Hence, for a weak shock, the compressibility effects are small and restricted to a short initial time interval, and the assumption of impulsive motion is a good one.

As the strength of the incoming shock increases, the density distribution is increasingly modified, especially for high Atwood number. The speed of the shock front exceeds the gas speed by at least 26% for Atwood number $A = 0.95$, and the incoming shock strength $z_1 = 5.0$. Since at this order of approximation, the effects of the reverberating waves are not yet considered, the speed ratios as shown in Figure 2.12-d to 2.14-d are close to the results obtained in the last section for a shock passing a sharp interface as shown in Figure 2.5-b, and 2.6-b only for the

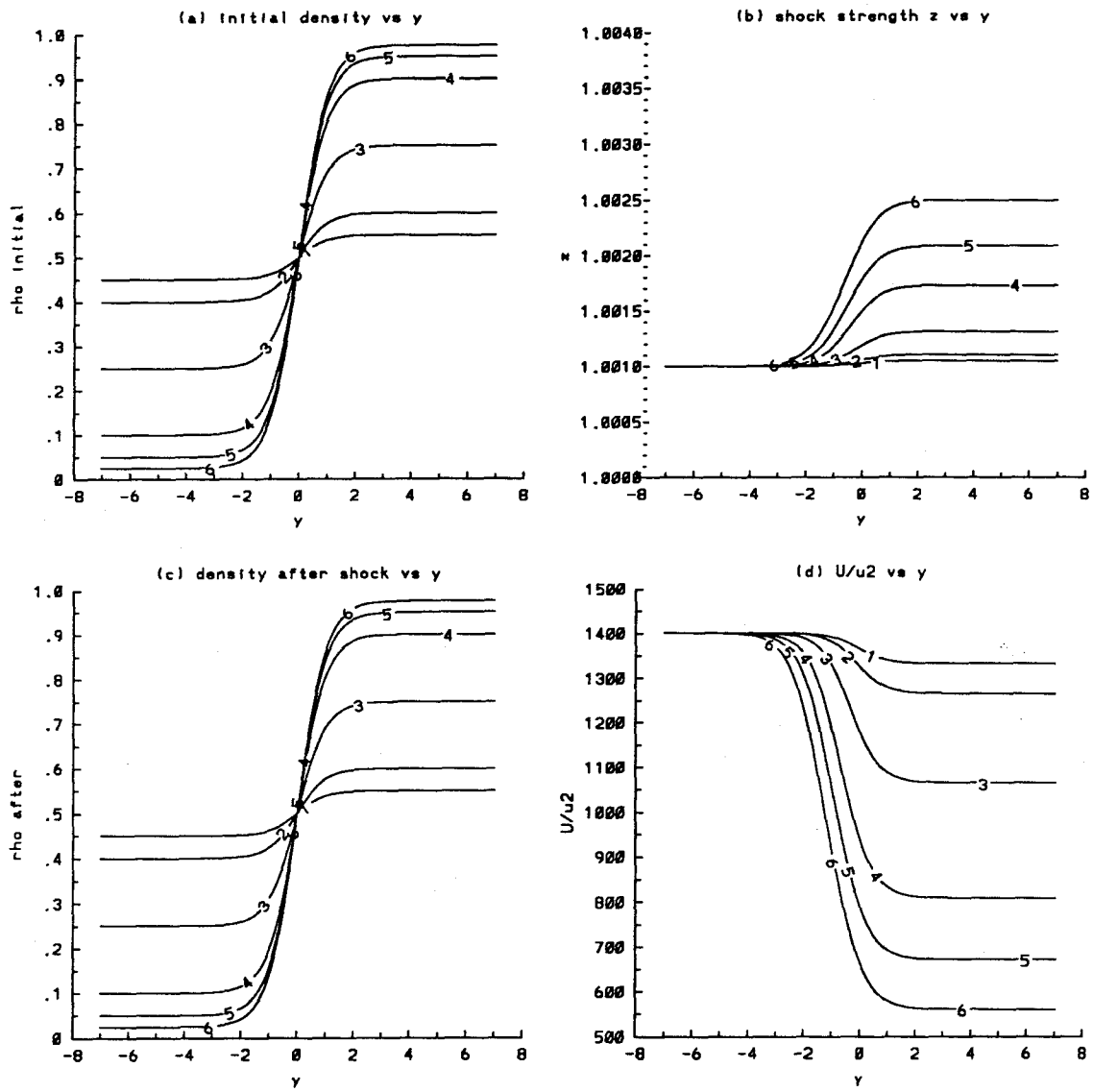

Figure 2.10 Zeroth order solution from Chisnell's theory for $z_1 = 1.001$ a) initial density profile b) shock strength z along y c) zeroth order solution of the density profile after the passage of the shock d) speed ratio U/u_2 along y. The numbers 1, 2, 3, 4, 5, and 6 on the curves refer to the Atwood numbers 0.1, 0.2, 0.5, 0.8, 0.9, and 0.95 respectively.

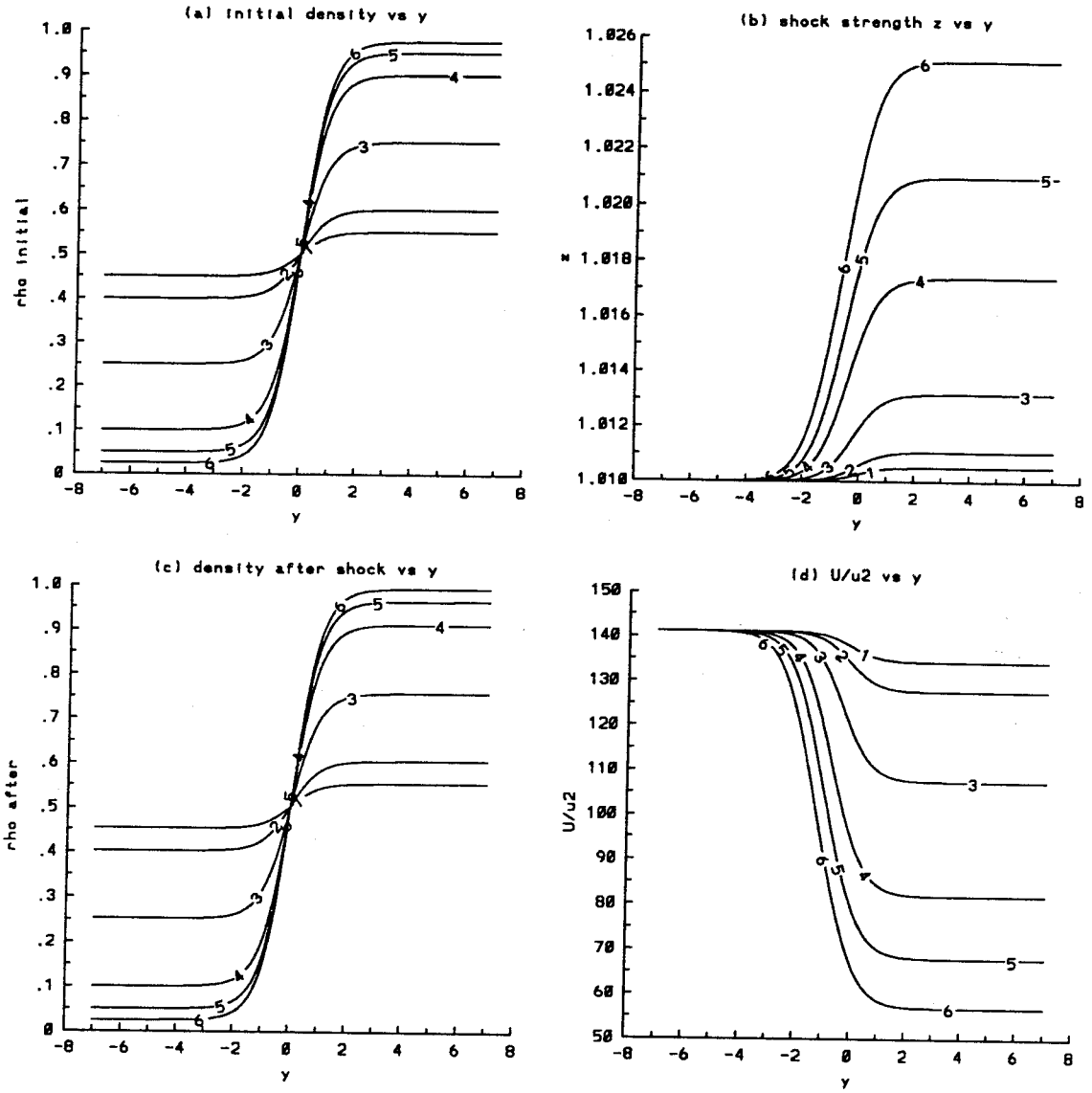

Figure 2.11 Zeroth order solution from Chisnell's theory for $z_1 = 1.01$ a) initial density profile b) shock strength z along y c) zeroth order solution of the density profile after the passage of the shock d) speed ratio U/u_2 along y. The numbers 1, 2, 3, 4, 5, and 6 on the curves refer to the Atwood numbers 0.1, 0.2, 0.5, 0.8, 0.9, and 0.95 respectively.

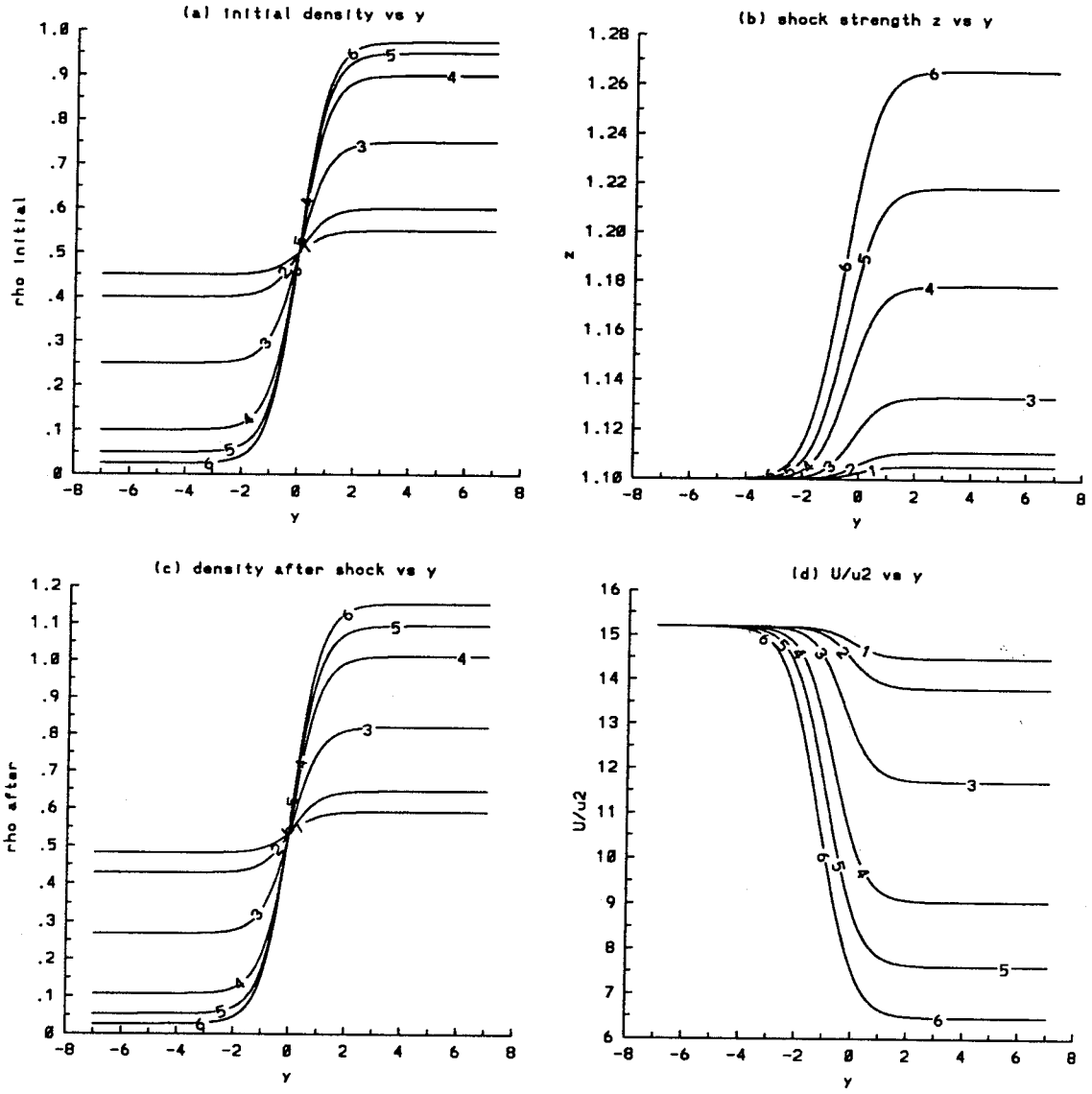

Figure 2.12 Zeroth order solution from Chisnell's theory for $z_1 = 1.1$ a) initial density profile b) shock strength z along y c) zeroth order solution of the density profile after the passage of the shock d) speed ratio U/u_2 along y. The numbers 1, 2, 3, 4, 5, and 6 on the curves refer to the Atwood numbers 0.1, 0.2, 0.5, 0.8, 0.9, and 0.95 respectively.

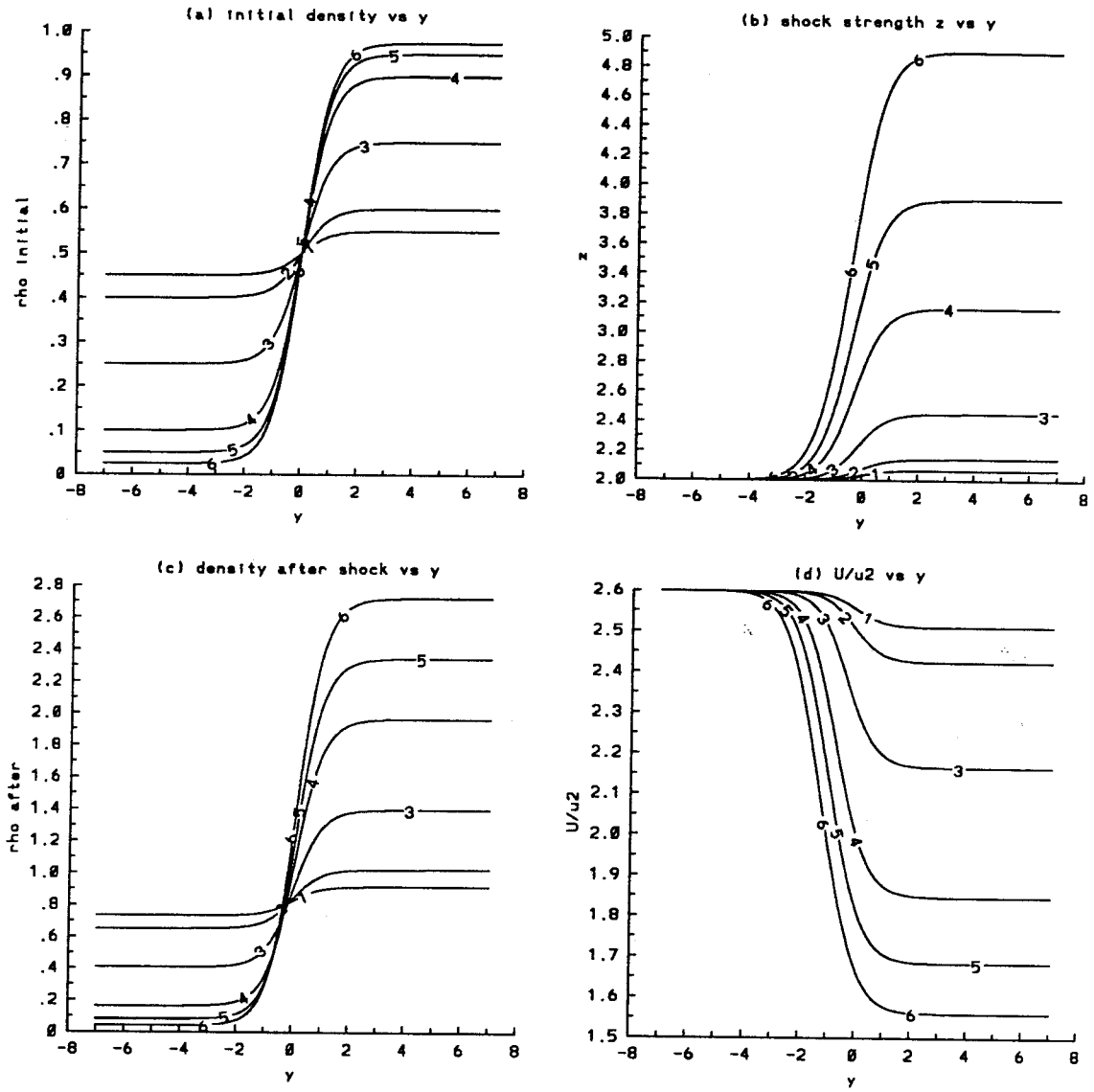

Figure 2.13 Zeroth order solution from Chisnell's theory for $z_1 = 2.0$ a) initial density profile b) shock strength z along y c) zeroth order solution of the density profile after the passage of the shock d) speed ratio U/u_2 along y. The numbers 1, 2, 3, 4, 5, and 6 on the curves refer to the Atwood numbers 0.1, 0.2, 0.5, 0.8, 0.9, and 0.95 respectively.

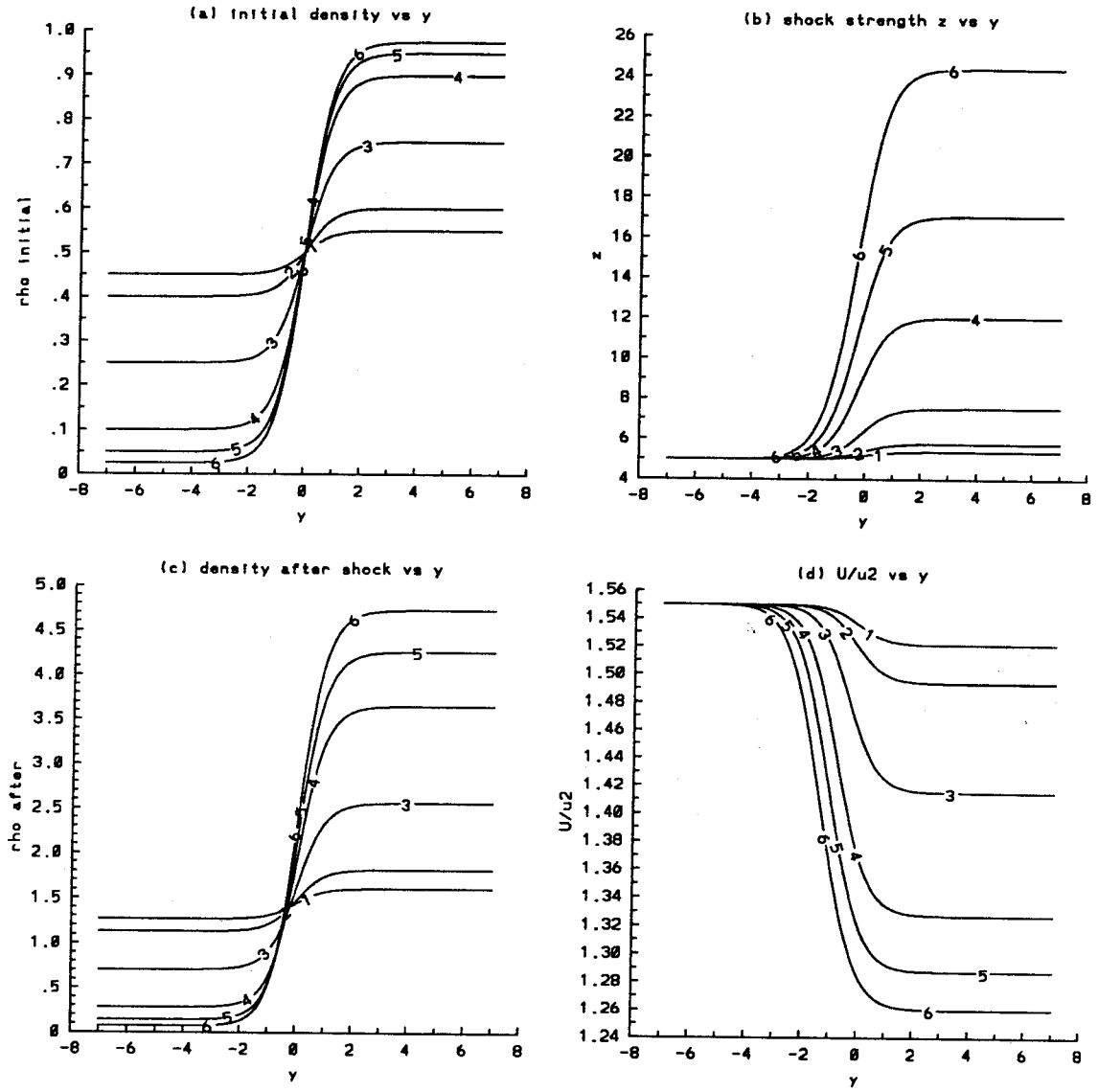

Figure 2.14 Zeroth order solution from Chisnell's theory for $z_1 = 5.0$ a) initial density profile b) shock strength z along y c) zeroth order solution of the density profile after the passage of the shock d) speed ratio U/u_2 along y. The numbers 1, 2, 3, 4, 5, and 6 on the curves refer to the Atwood numbers 0.1, 0.2, 0.5, 0.8, 0.9, and 0.95 respectively.

cases with small jump in density, *i.e.*, small Atwood number. For example, at $z_1 = 1.1$, from Figure 2.12-d, the shock leaves the non-uniform region at the speed ratios U/u_2 of 6.5 and 14.5 for $A = 0.95$ and 0.1 respectively. From Figure 2.6-b, the corresponding values for the same shock strength and density ratio are 9 and 14.5. Similarly, at $z_1 = 2$, the zero order of Chisnell theory gives the values U/u_2 of 1.56 and 2.52 as compared to the values of 1.8, and 2.52 obtained from Paterson's theory. Hence, the speed ratios U/u_2 as calculated from the two theories are very close to each other for small Atwood numbers, and slightly different for the large ones.

As reverberating waves are considered, one expects that the first reflected wave (*i.e.*, the singly reflected wave) will slow down the gas in the non-uniform region, while the second reflected wave will speed it up, and so on. Ideally, a final state of the gas can be solved for if we include the effects of all reverberating waves. However, as noted in section 2.3.3, for a sharp interface, the strength of the reflected shock remains at $O(1)$ even for a strong incident shock, and is always smaller than the strength of the incident shock. Thus, for the cases when the strength of the singly reflected shocks decrease fast enough, a reasonable final solution can be obtained if we only include the effects of the first reflected wave. In the next section, we will consider the effects of the singly reflected wave on the flow variables.

2.4.2 Flow induced by the singly reflected wave

As shown by Chisnell, when the density gradient is large (*i.e.*, high Atwood number), at the zeroth order of approximation, this theory predicts a higher transmitted shock strength than that of Paterson's theory. This conclusion is confirmed in our work by comparing results plotted in Figure 2.7-c, 2.8-c using Paterson's theory to those in Figure 2.13-b, 2.14-b using Chisnell's theory. At $z_1 = 2$, for $A = 0.95$, Paterson's theory predicts $z_2 = 3.25$ as compared to 4.9 by the other theory. Similarly, at $z_1 = 5$, the corresponding values are 13 and 24. When Chisnell takes

into account the effect of the doubly reflected wave on the strength of the transmitted shock, this discrepancy is reduced significantly. However, due to the complexity of the calculation, Chisnell's theory only considers the effects of the singly reflected wave but not those of the doubly reflected wave on the properties of the gas behind the shock. In this discussion, we present briefly a summary of Chisnell's results.

To describe the motion of a particular fluid element, he labels the path of the fluid particle which originally was at density $\rho(z)$, related to z by equation (2.52) to be the '$z-$*particle path*'. The flow variables behind the shock are thus functions of two variables, the shock strength z and the particular particle path, z_0. For example, the density on the z_0-particle path is $\rho(z_0, z_0)$ immediately behind the shock when the shock passes the z_0-particle path. The density $\rho(z_0, z_0)$ reaches the values of $\rho(z, z_0)$ when the incident shock moved from the z_0 to the z-particle path.

Consider an element of the first reflected wave generated when the shock moves from a particle path labeled by z to one labeled by $(z + dz)$. By equation (2.23), the density $\rho(z, z)$ of the fluid particles on the z-particle path immediately behind the shock is

$$\rho(z, z) = \rho(z)\frac{(\lambda^2 + z)}{(1 + \lambda^2 z)}. \tag{2.55}$$

From equation (2.49), the strength of the reflected shock immediately behind the shock is

$$1 + \frac{dz}{z}. \tag{2.56}$$

As discussed earlier, to the first and second order in the shock strength, there is no distinction between shocks and waves. Since equation (2.52) is derived from a first order expansion in the shock strength, we can also apply it to the reflected wave. Let the strength of the reflected wave when it reaches the z_0-particle path be:

$$1 + \alpha(z, z_0)\frac{dz}{z}, \tag{2.57}$$

where $\alpha(z, z_0)$ is an unknown. Applying equations (2.52) to (2.54) to the reflected wave, we have

$$\rho(z, z_0) = B(z) f\left(1 + \alpha(z, z_0)\frac{dz}{z}\right), \tag{2.58}$$

where

$$B(z) = \frac{\rho(z,z)}{f\left(1+\frac{dz}{z}\right)}. \tag{2.59}$$

Using equation (2.53) for $f(z)$, equation (2.58) can be expanded in power of $(z-1)$, and $\alpha(z,z_0)$ is found to be

$$\alpha(z,z_0) = \left\{\frac{\rho(z,z_0)}{\rho(z_0,z_0)}\right\}^{\frac{1}{4}}. \tag{2.60}$$

Another relation between $\alpha(z,z_0)$ and $\rho(z,z_0)$ can be obtained by the Rankine-Hugoniot relations as follows. When the reflected wave with the strength given in equation (2.57) reaches the z_0-particle path, it will raise the density $\rho(z,z_0)$ by an amount determined by the jump condition (2.23). Keeping only the first order term, it is possible to show that

$$\frac{\partial\rho(z,z_0)}{\partial z}dz = \frac{1}{\gamma}\rho(z,z_0)\alpha(z,z_0)\frac{dz}{z}. \tag{2.61}$$

Substituting equation (2.60) into the above equation, and integrating from z_0 to z, the density $\rho(z,z_0)$ of the fluid on the z_0-particle path when the incident shock moves from the z_0 to the z-particle path is

$$\rho^{-\frac{1}{4}}(z,z_0) = \rho^{-\frac{1}{4}}(z_0,z_0) - \frac{1}{4\gamma}\int_{x=z_0}^{z}\rho^{-\frac{1}{4}}(x,x)\frac{dx}{x}. \tag{2.62}$$

Let the interval of the shock strength from z_0 to z be divided into n equal subintervals such that $z_0 < z_i < z$, $i = 1$ to $n-1$, and $z_i = z_0, z_n$ for $i = 0, n$ respectively. By the definition of the reflected shock z, *i.e.*, $z = z_{34} = p_4/p_3$, we have

$$\frac{p(z,z_0)}{p(z_0,p_0)} = z_{rflct}(z,z_0) = \prod_{i=0}^{i=n}\left(1+\alpha(z_i,z_0)\frac{\Delta z}{z_i}\right), \tag{2.63}$$

where $\Delta z = z_i - z_{i-1}$. Let $n \to \infty$. Taking the logarithm of both sides of the above equation, and using the expansion $\ln(1+x) = x + O(x^2)$, the total strength

of the singly reflected wave, z_{rflct}, along the z_0-particle path when the element of the reflected wave generated at the z-particle path has arrived is

$$z_{rflct}(z, z_0) = \exp\left\{\int_{y=z_0}^{z} \rho^{-\frac{1}{4}}(y, y)\rho^{\frac{1}{4}}(y, z_0)\frac{dy}{y}\right\}. \tag{2.64}$$

The pressure field $p(z, z_0)$ in term of the initial constant pressure p_{int} of the fluid and the fluid velocity at the same point are respectively,

$$p(z, z_0) = z_0 p_{int} z_{rflct}, \tag{2.65}$$

$$u_2(z, z_0) = (z_0 - 1)\sqrt{\frac{p(1-\lambda^2)}{\rho(z_0)(\lambda^2 + z_0)}} - \int_{y=z_0}^{z} \gamma^{-\frac{1}{2}} p^{\frac{1}{2}}(y, z_0)\rho^{-\frac{1}{4}}(y, y)\rho^{-\frac{1}{4}}(y, z_0)\frac{dy}{y}, \tag{2.66}$$

since the pressure of the z_0-particle path immediately after the passage of the shock $p(z_0, z_0) = z_0 p_{int}$.

For a given density profile, we integrate the above equations for the density $\rho(z, z_0)$, the reflected shock strength $z_{rflct}(z, z_0)$, and the velocity of the gas $u_2(z, z_0)$ as follows. First, equation (2.52) is solved for z as a function of the distance. To calculate the flow variables u, p, ρ, we keep the transmitted shock strength z fixed at the value z_f, obtained when the shock leaves the non-uniform region, and vary z_0 from the value of the incident shock strength z_1 to z_f. The integrals are evaluated using the trapezoidal rule. In all calculations, we use 100 grid points for y ranging from -6.0 to 6.0. The above description of the flow field is expressed in terms of the shock strength parameters z, and z_0. In order to plot the results as a function of the fluid particle position y, we need to obtain y as a function of z, and z_0:

$$y(z, z_0) = \int_{x=z_1}^{z_0} \frac{dy(x)}{dx}dx + \int_{x=z_0}^{z} \frac{u_2(x, z_0)}{U(x)}\left\{1 + \frac{U(x) - u_2(x, x)}{a(x, x)}\right\} \times \exp\left\{\int_{z'=z_0}^{x} a^{-1}(x, z')\frac{\partial u_2(x, z')}{\partial z'}dz'\right\}\frac{dy(x)}{dx}dx, \tag{2.67}$$

where $U(x)$ is the shock velocity, $y(z)$ is the location of the shock as a function of the strength z, and $a(z, z_0)$ is the speed of sound,

$$a^2(z, z_0) = \gamma\frac{p(z, z_0)}{\rho(z, z_0)}. \tag{2.68}$$

In Figures 2.15-a to 2.15-g, we plot respectively the density, the pressure p/p_{int}, the gas velocity $u_2/\sqrt{p_{int}}$, the speed ratio U/u_2 of the transmitted shock over the gas speed, the initial density distribution, the ratio of the reflected shock velocity over the gas velocity, and the strength of the reflected shock versus $y(z, z_0)$ for A = 0.1, 0.2, 0.5, and an incident shock of strength 1.1. Figures 2.16-a to 2.16-g are the corresponding plots for the same flow variables but we have assumed that every fluid particle is affected instantaneously after the passage of the shock. That is, the shock only changes the properties of the gas particle but not its location. Equivalently, we do not use equation (2.67) in plotting the results. Comparing the two plots, we see that the width of the stratified layer is slightly compressed with the use of equation (2.67). Apart from this small compression, the variations of the flow variables in the two plots are identical. The little indentations at the left sides of the curves in Figures 2.15-a to 2.15-g are due to the difficulty in resolving that region for the integration of the position $y(z, z_0)$ in equation (2.67).

Clearly, the profiles of the velocity and the pressure resemble that of the density. The higher the Atwood number, the more deviations of the velocity and the pressure from the mean value become. For $A = 0.5$, the variation of the velocity is within 5% of the mean velocity. Thus even for a moderate density ratio of 3:1, the assumption that the gas undergoes an incompressible impulsive motion, *i.e.*, that the velocity is constant and that the pressure varies linearly with the distance in one dimension, is a good one. As observed in plots 2.15-d and 2.15-f, the ratios of the velocity of the transmitted and reflected shock compared to the velocity of the gas are at least more than 10. Thus, the residential time of the shocks in the non-uniform region is short.

Extensive results similar to Figure 2.16 are plotted in Figures 2.17 to 2.20 for the case of z_1 = 1.001, 1.01, 1.1, 2.0 and A = 0.1, 0.2, 0.5, 0.8, 0.9, 0.95, corresponding to the density ratios 1.22:1, 1.5:1, 3:1, 9:1, 19:1, and 39:1. Again, as the Atwood number increases, the velocity gradient in the non-uniform region increases. The strength of the incident shock modifies the magnitudes of the velocities, but not the

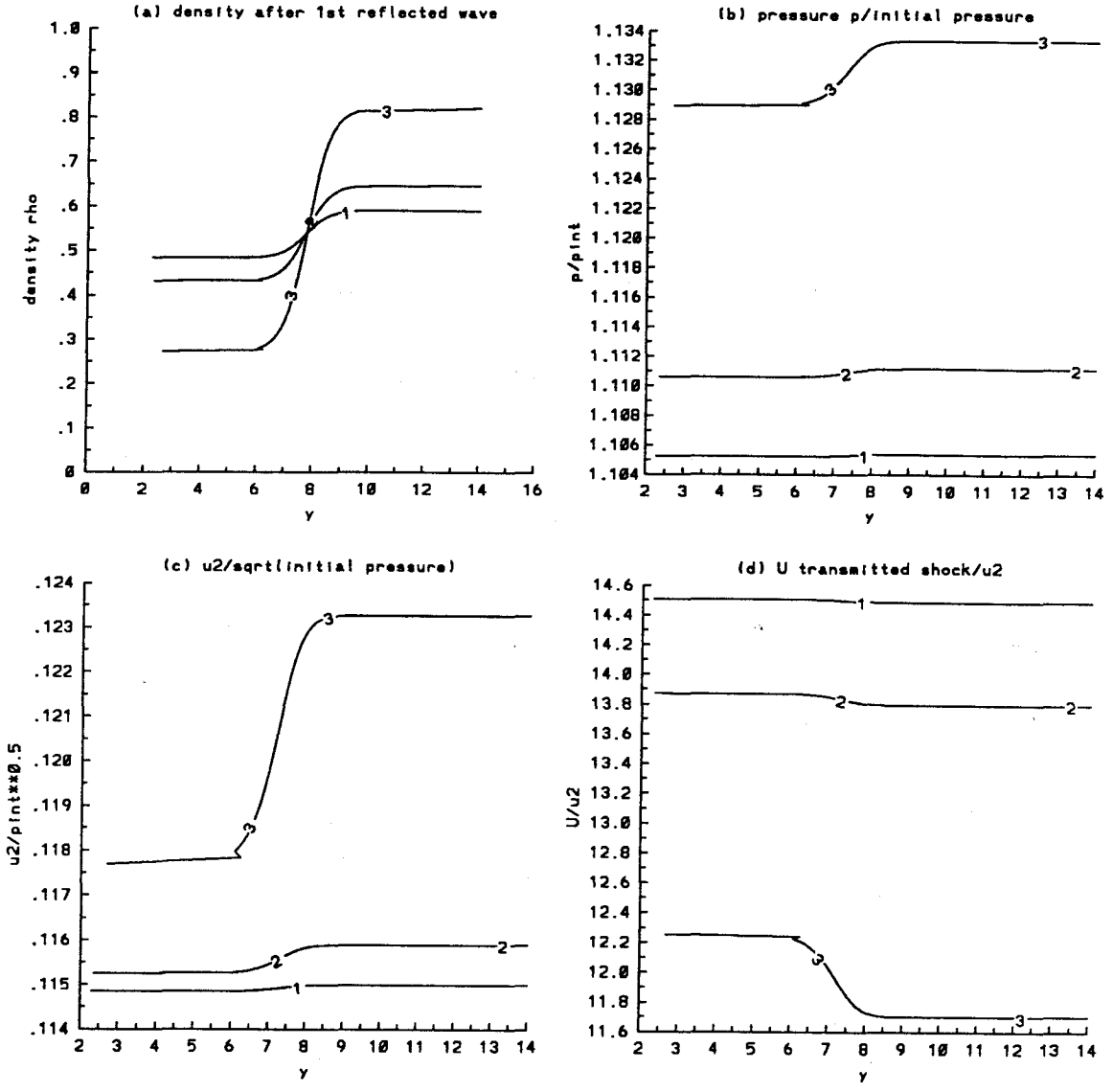

Figure 2.15 Solution including the effects of the singly reflected wave for $z_1 = 1.1$ using (2.67) for y a) density profile b) ratio of the pressure over the initial one c) $u_2/\sqrt{p_{int}}$ d) U of transmitted shock/u_2. The numbers 1, 2, and 3 on the curves refer to the Atwood numbers 0.1, 0.2, and 0.5 respectively.

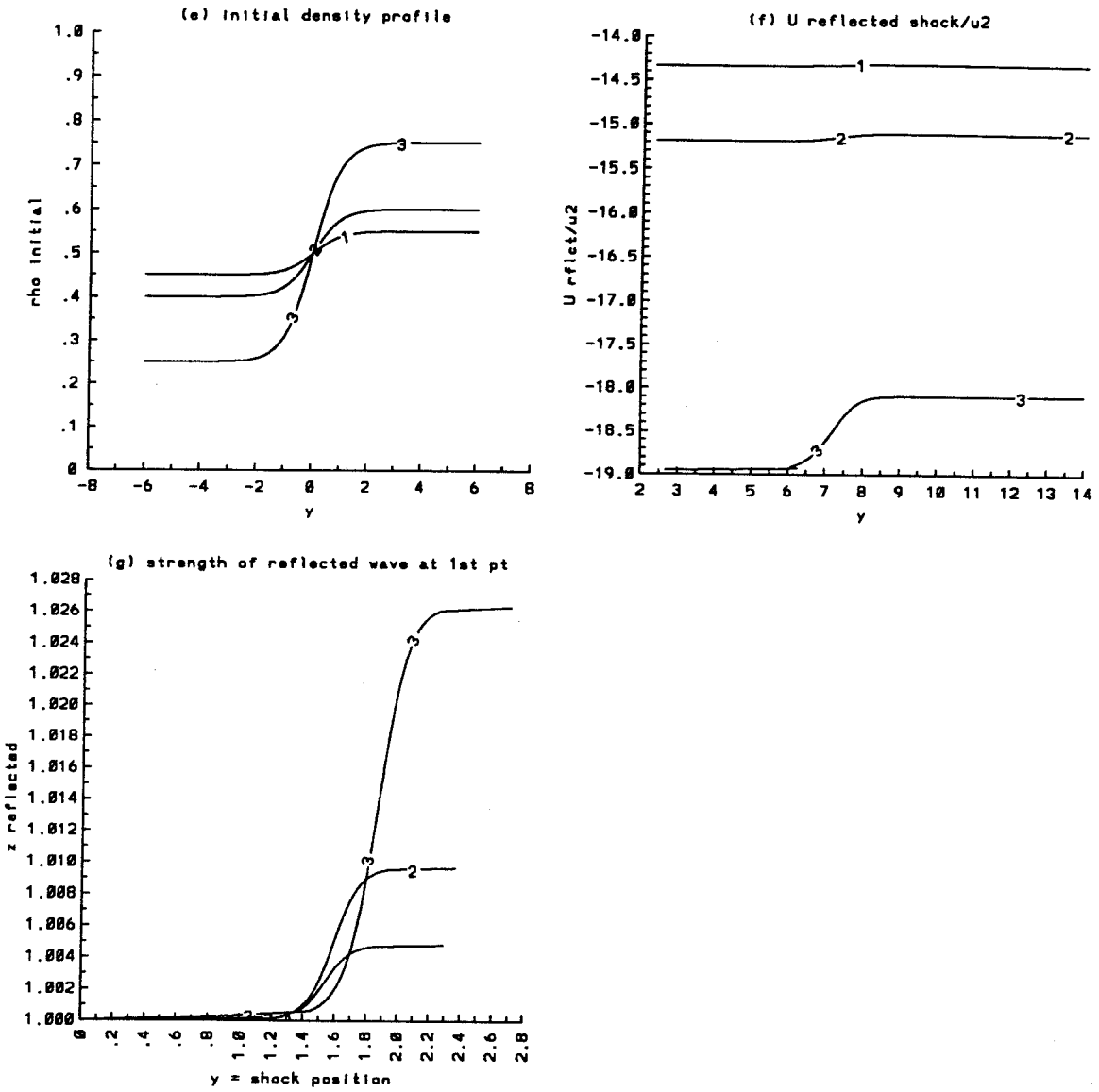

Figure 2.15 *(cont'd)* Solution including the effects of the singly reflected wave for $z_1 = 1.1$ using (2.67) for y e) initial density profile f) U of reflected shock $/u_2$ g) strength of the reflected shock at the beginning of the non-uniform region as a function of the transmitted shock's position. The numbers 1, 2, and 3 on the curves refer to the Atwood numbers 0.1, 0.2, and 0.5 respectively.

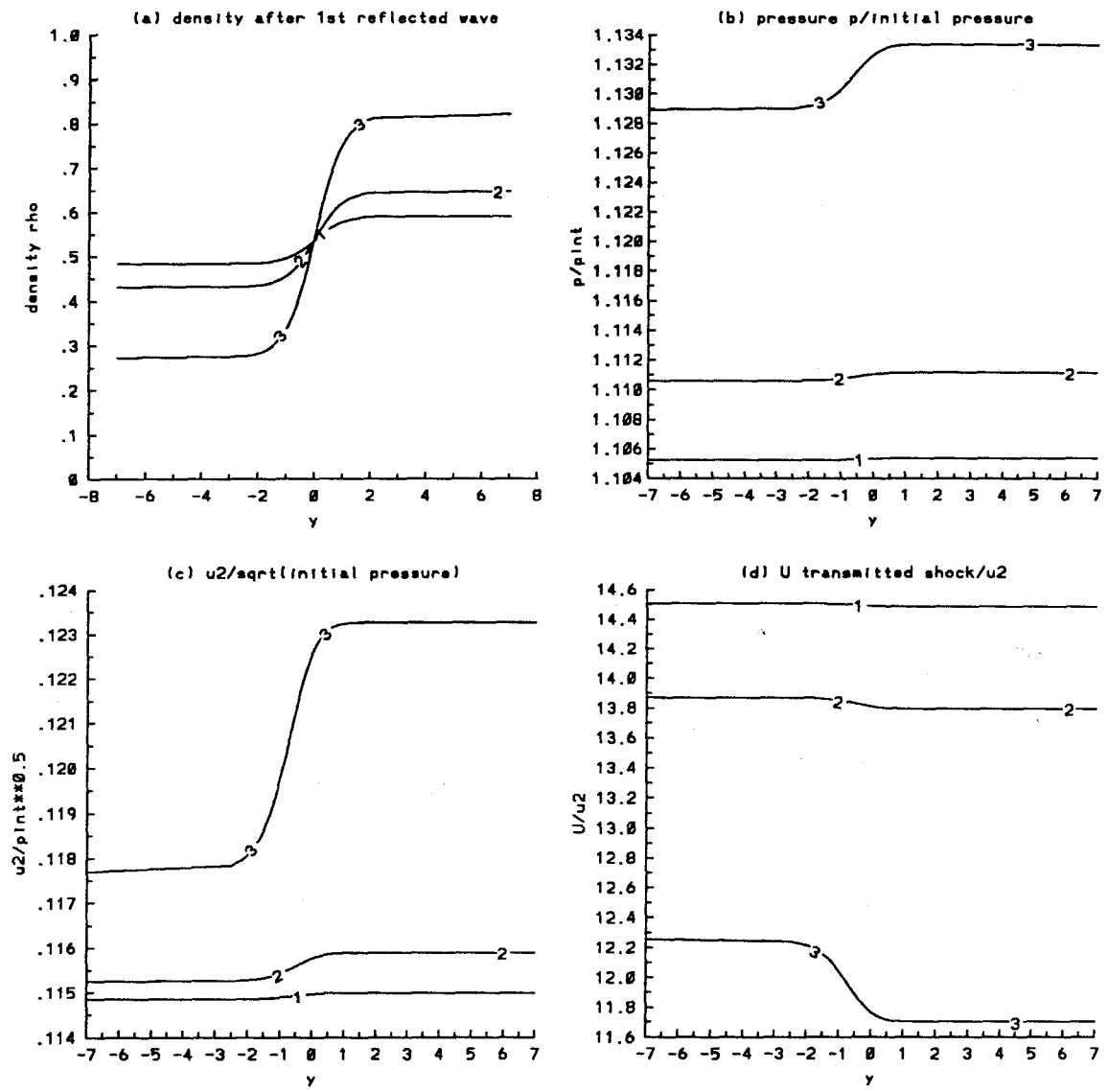

Figure 2.16 Solution including the effects of the singly reflected wave for $z_1 = 1.1$ without using (2.67) for y a) density profile b) ratio of the pressure over the initial one c) $u_2/\sqrt{p_{int}}$ d) U of transmitted shock/u_2. The numbers 1, 2, and 3 on the curves refer to the Atwood numbers 0.1, 0.2, and 0.5 respectively.

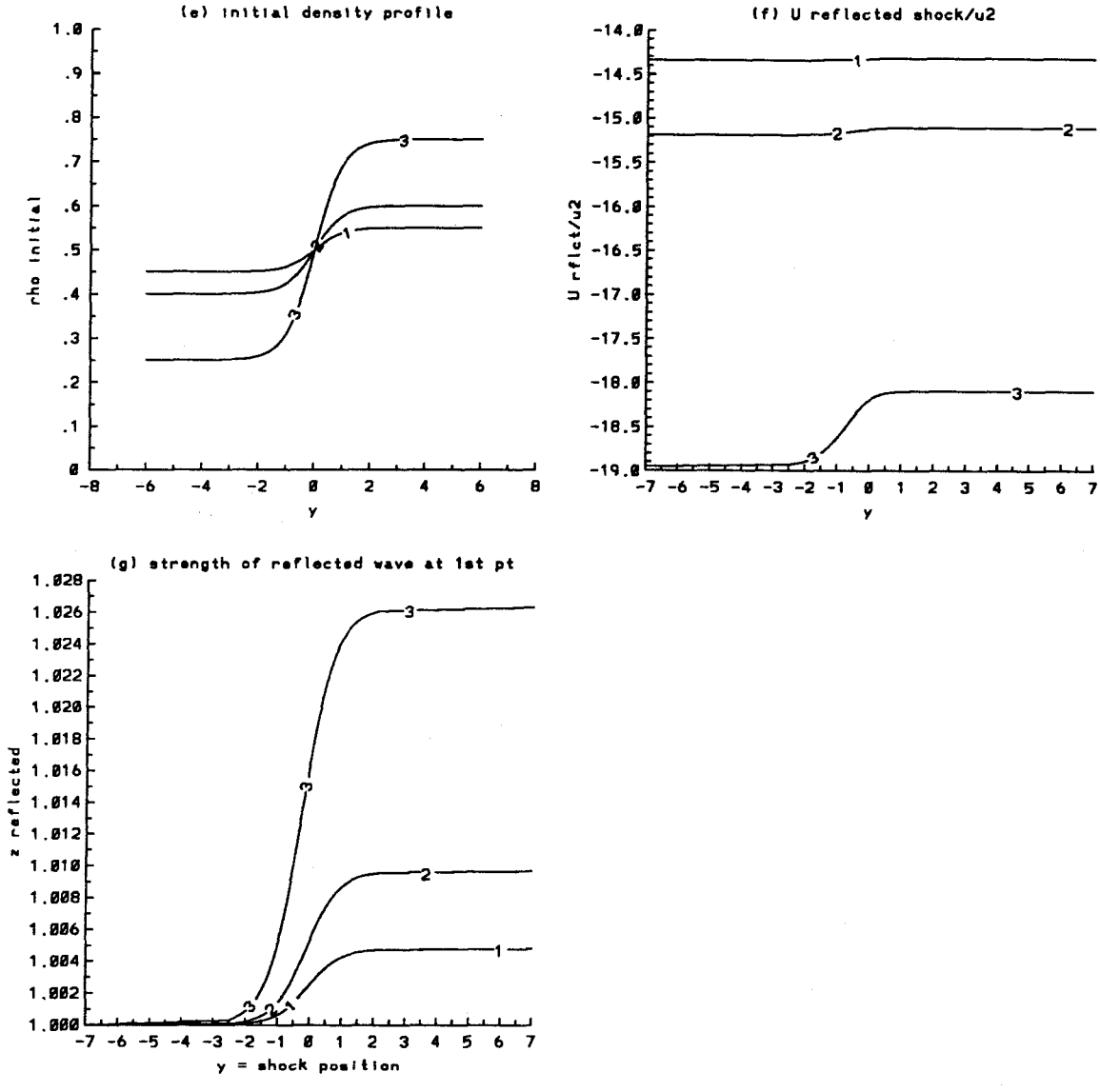

Figure 2.16 *(cont'd)* Solution including the effects of the singly reflected wave for $z_1 = 1.1$ without using (2.67) for y e) initial density profile f) U of reflected shock $/u_2$ g) strength of the reflected shock at the beginning of the non-uniform region as a function of the transmitted shock's position. The numbers 1, 2, and 3 on the curves refer to the Atwood numbers 0.1, 0.2, and 0.5 respectively.

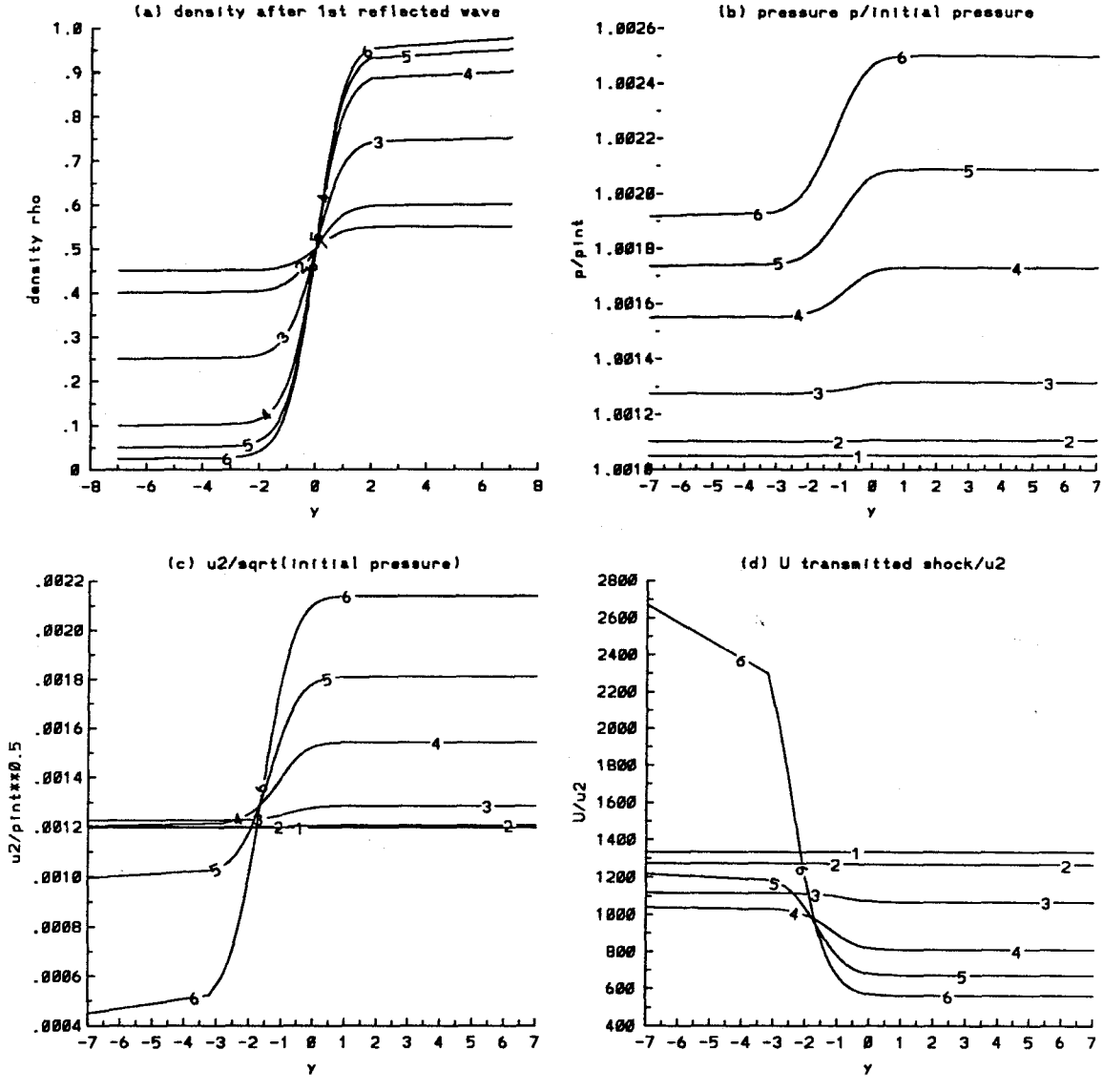

Figure 2.17 Solution including the effects of the singly reflected wave for $z_1 = 1.001$ without using (2.67) for y a) density profile b) ratio of the pressure over the initial one c) $u_2/\sqrt{p_{int}}$ d) U of transmitted shock/u_2. The numbers 1, 2, 3, 4, 5, and 6 on the curves refer to the Atwood numbers 0.1, 0.2, 0.5, 0.8, 0.9, 0.95 respectively.

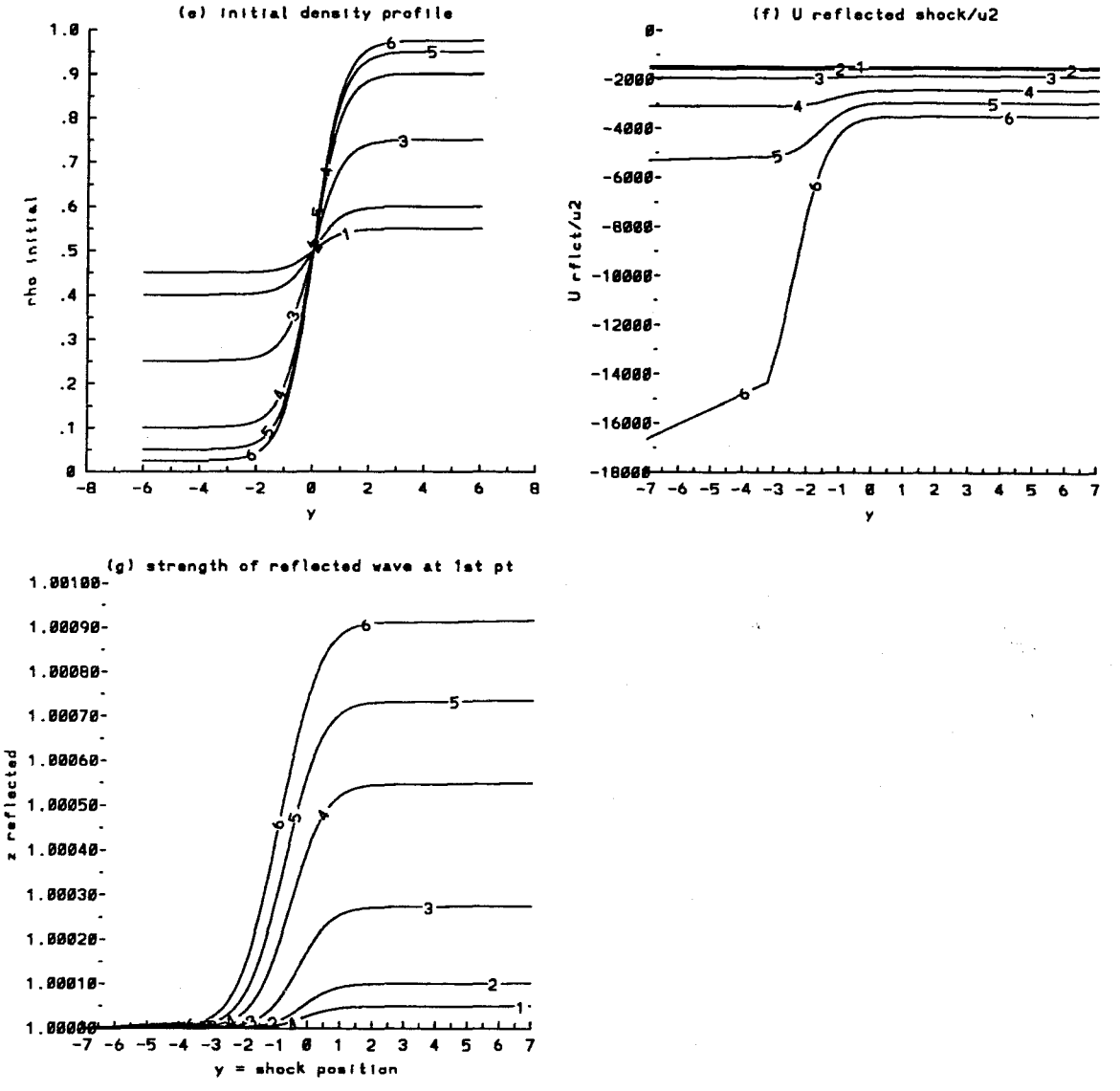

Figure 2.17 *(cont'd)* Solution including the effects of the singly reflected wave for $z_1 = 1.001$ without using (2.67) for y e) initial density profile f) U of reflected shock $/u_2$ g) strength of the reflected shock at the beginning of the non-uniform region as a function of the transmitted shock's position. The numbers 1, 2, 3, 4, 5, and 6 on the curves refer to the Atwood numbers 0.1, 0.2, 0.5, 0.8, 0.9, 0.95 respectively.

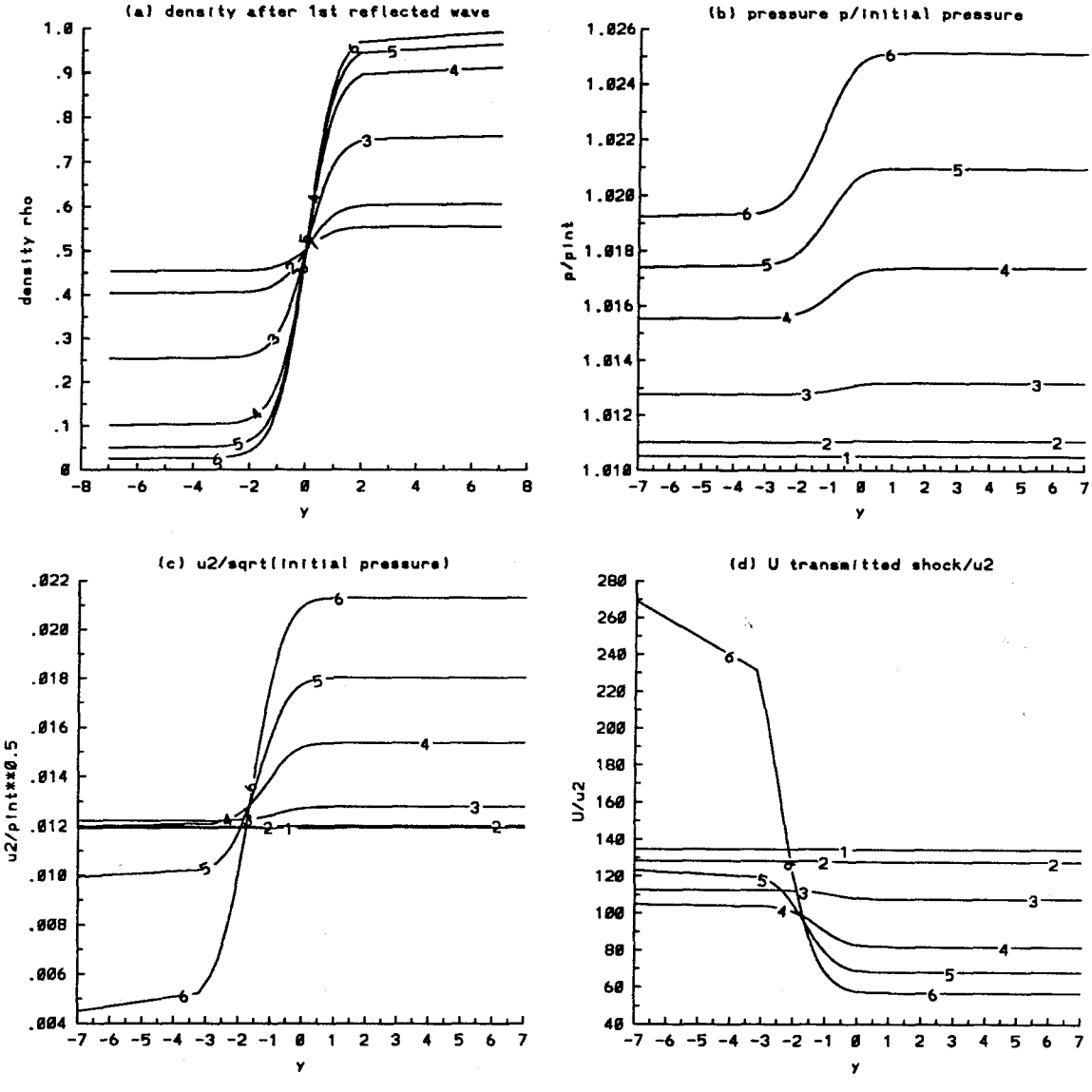

Figure 2.18 Solution including the effects of the singly reflected wave for $z_1 = 1.01$ without using (2.67) for y a) density profile b) ratio of the pressure over the initial one c) $u_2/\sqrt{p_{int}}$ d) U of transmitted shock/u_2. The numbers 1, 2, 3, 4, 5, and 6 on the curves refer to the Atwood numbers 0.1, 0.2, 0.5, 0.8, 0.9, 0.95 respectively.

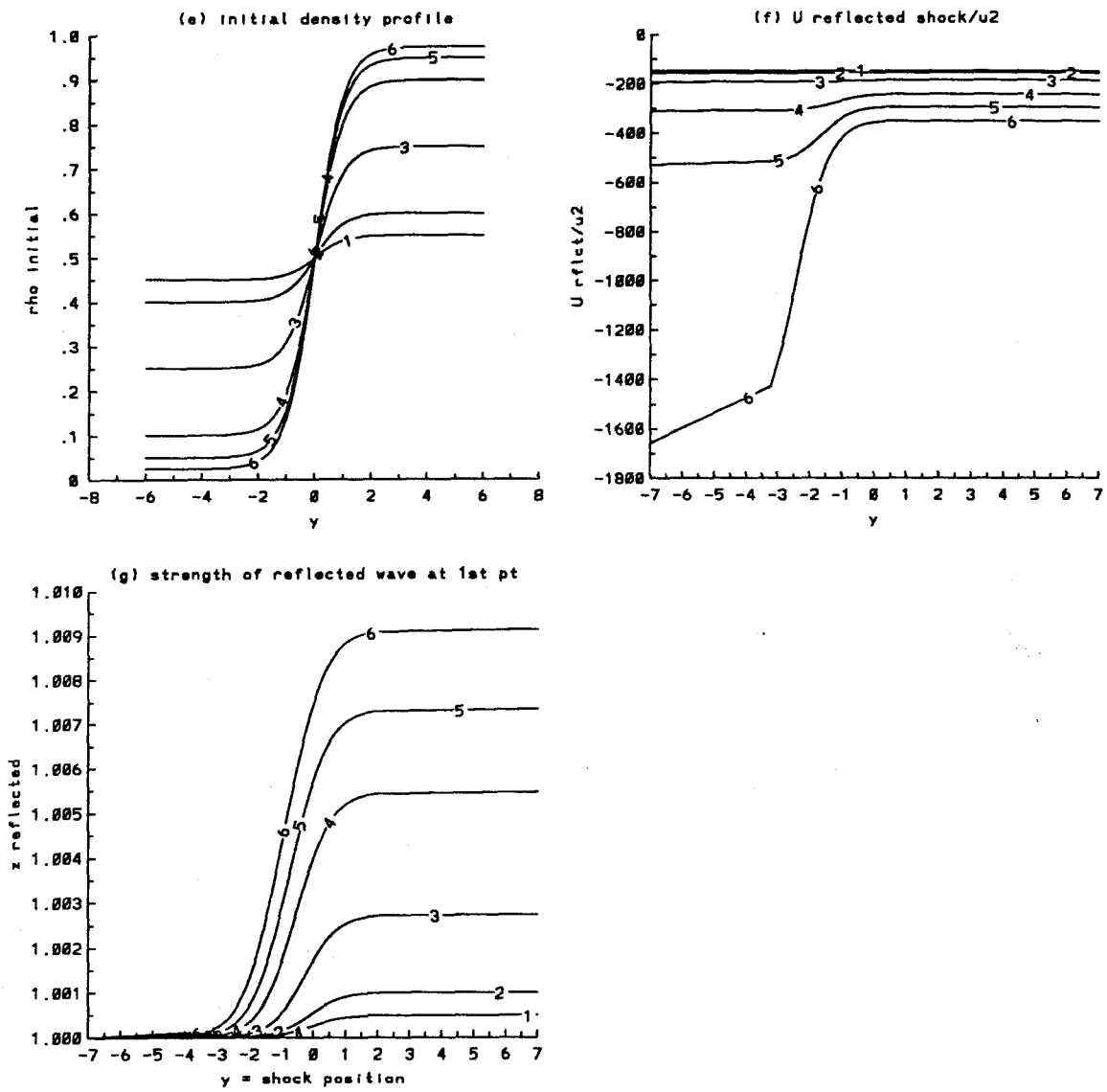

Figure 2.18 *(cont'd)* Solution including the effects of the singly reflected wave for $z_1 = 1.01$ without using (2.67) for y e) initial density profile f) U of reflected shock $/u_2$ g) strength of the reflected shock at the beginning of the non-uniform region as a function of the transmitted shock's position. The numbers 1, 2, 3, 4, 5, and 6 on the curves refer to the Atwood numbers 0.1, 0.2, 0.5, 0.8, 0.9, 0.95 respectively.

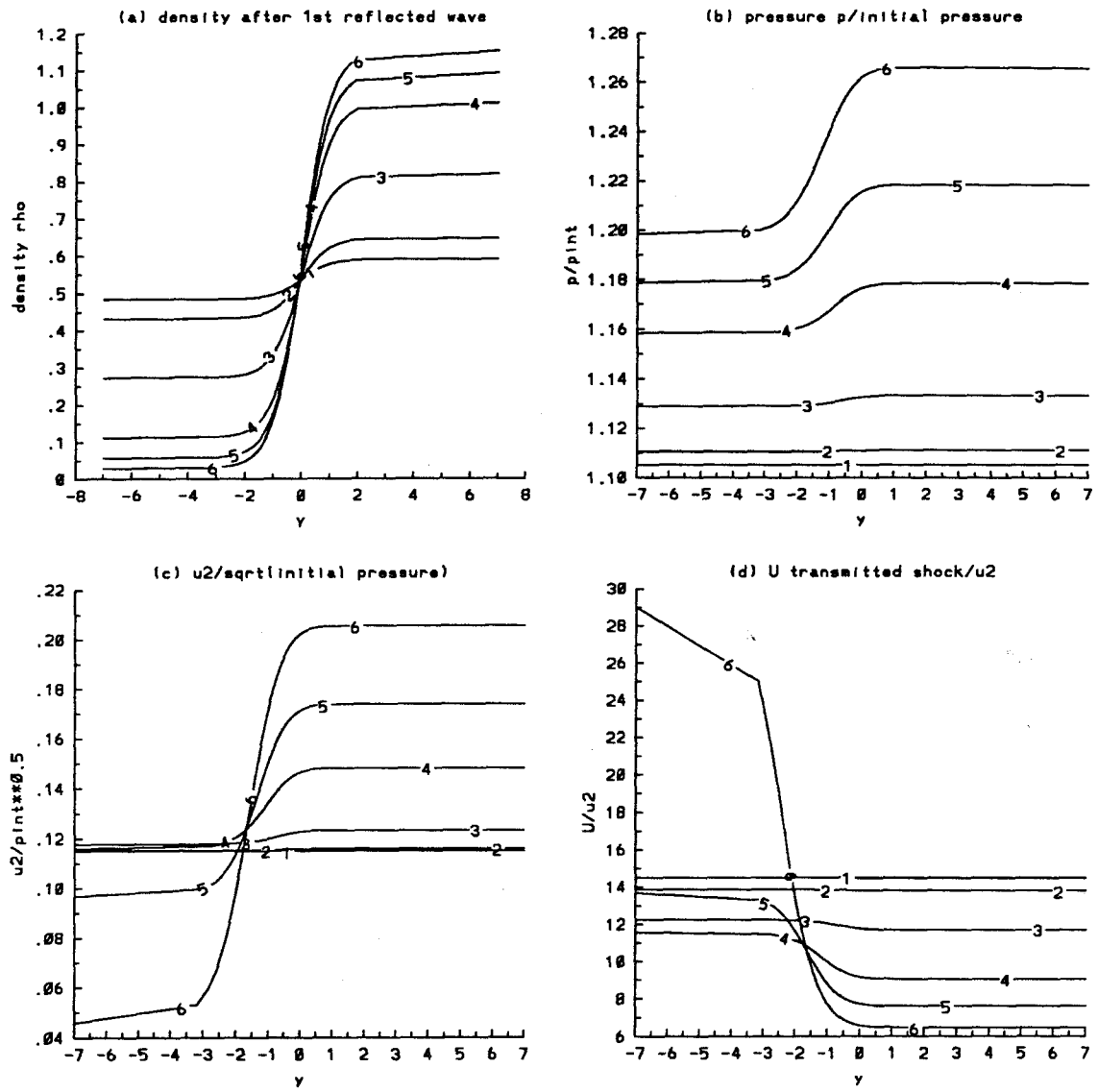

Figure 2.19 Solution including the effects of the singly reflected wave for $z_1 = 1.1$ without using (2.67) for y a) density profile b) ratio of the pressure over the initial one c) $u_2/\sqrt{p_{int}}$ d) U of transmitted shock/u_2. The numbers 1, 2, 3, 4, 5, and 6 on the curves refer to the Atwood numbers 0.1, 0.2, 0.5, 0.8, 0.9, 0.95 respectively.

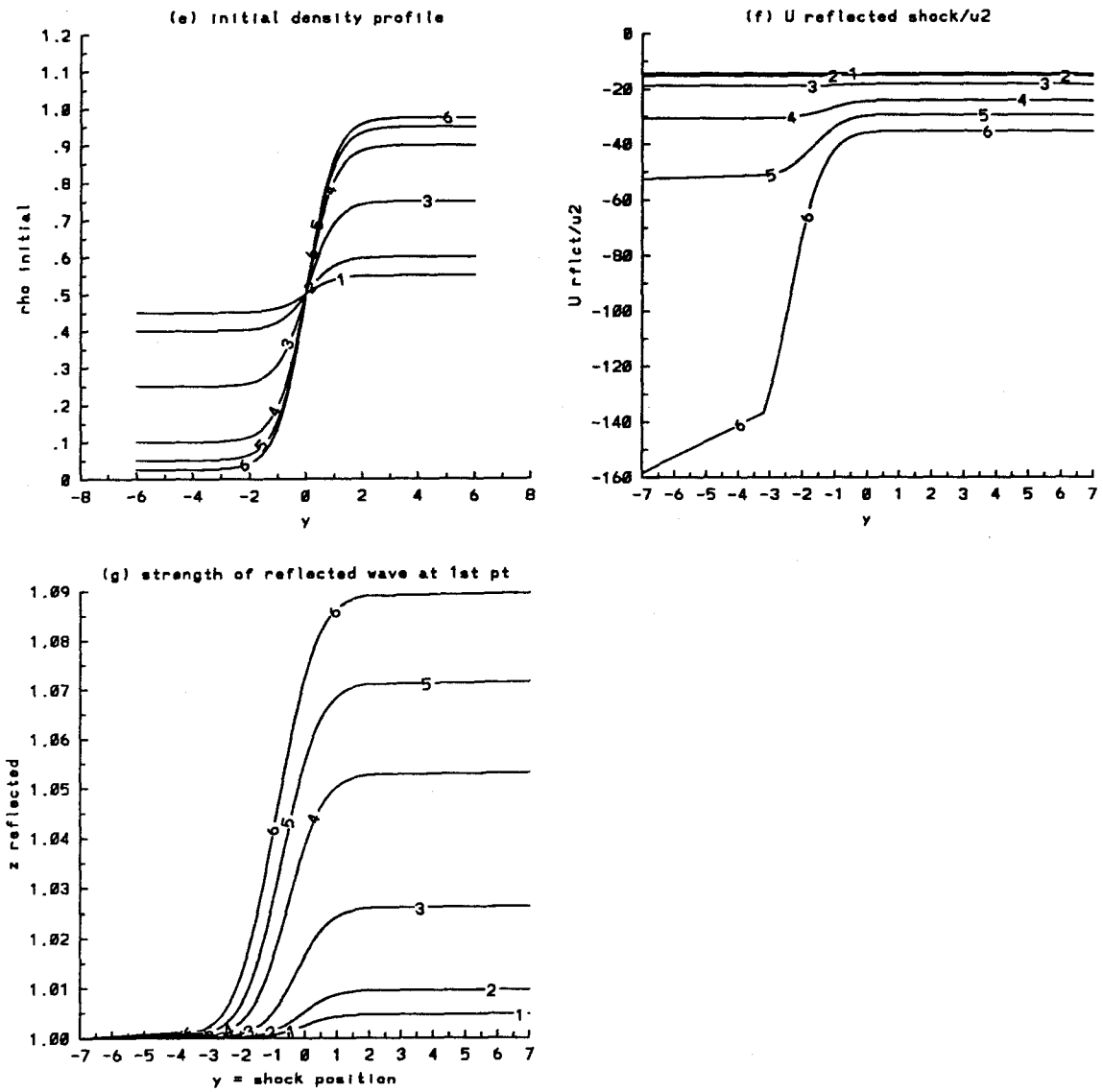

Figure 2.19 *(cont'd)* Solution including the effects of the singly reflected wave for $z_1 = 1.1$ without using (2.67) for y e) initial density profile f) U of reflected shock $/u_2$ g) strength of the reflected shock at the beginning of the non-uniform region as a function of the transmitted shock's position. The numbers 1, 2, 3, 4, 5, and 6 on the curves refer to the Atwood numbers 0.1, 0.2, 0.5, 0.8, 0.9, 0.95 respectively.

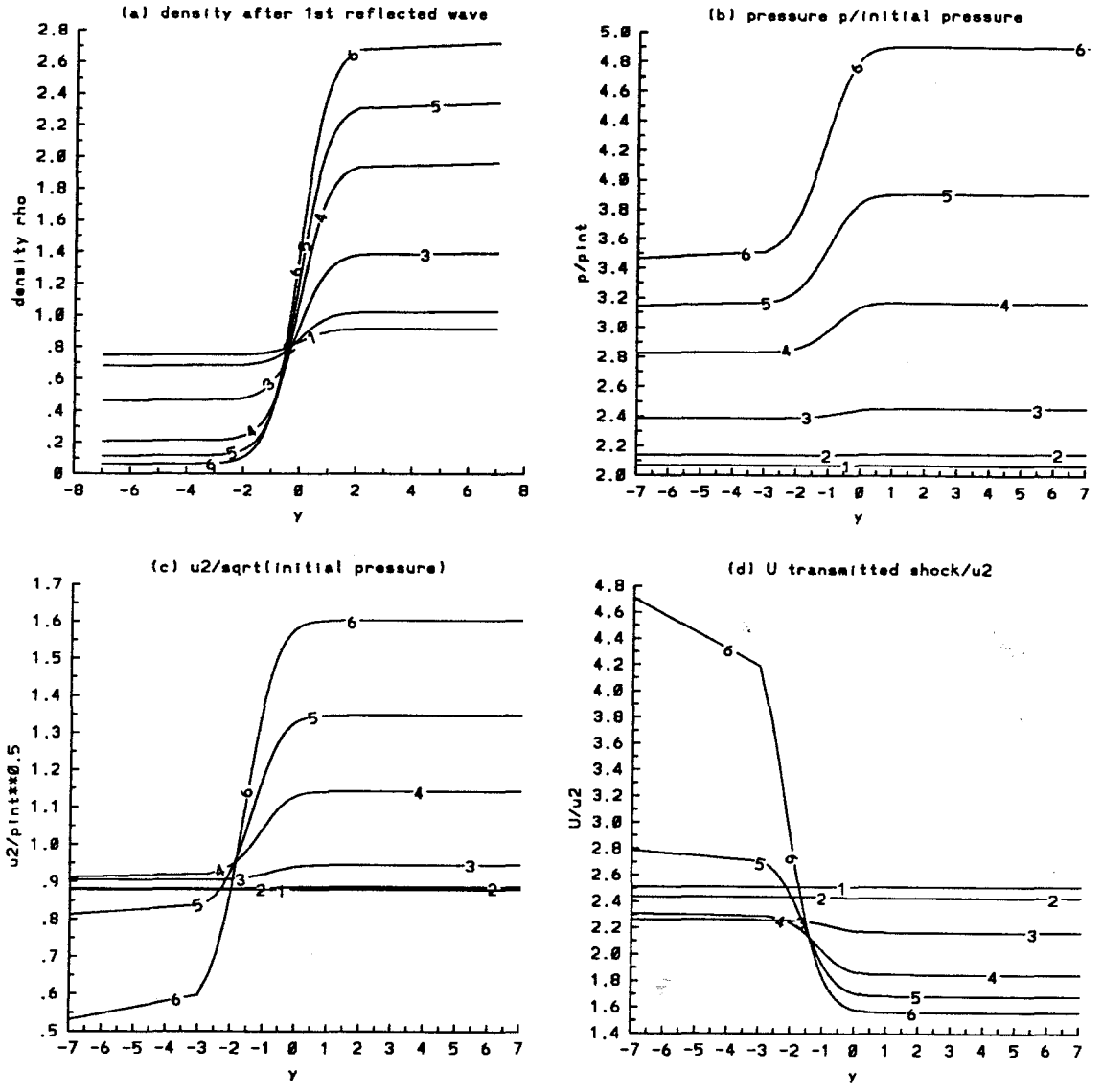

Figure 2.20 Solution including the effects of the singly reflected wave for $z_1 = 2.0$ without using (2.67) for y a) density profile b) ratio of the pressure over the initial one c) $u_2/\sqrt{p_{int}}$ d) U of transmitted shock/u_2. The numbers 1, 2, 3, 4, 5, and 6 on the curves refer to the Atwood numbers 0.1, 0.2, 0.5, 0.8, 0.9, 0.95 respectively.

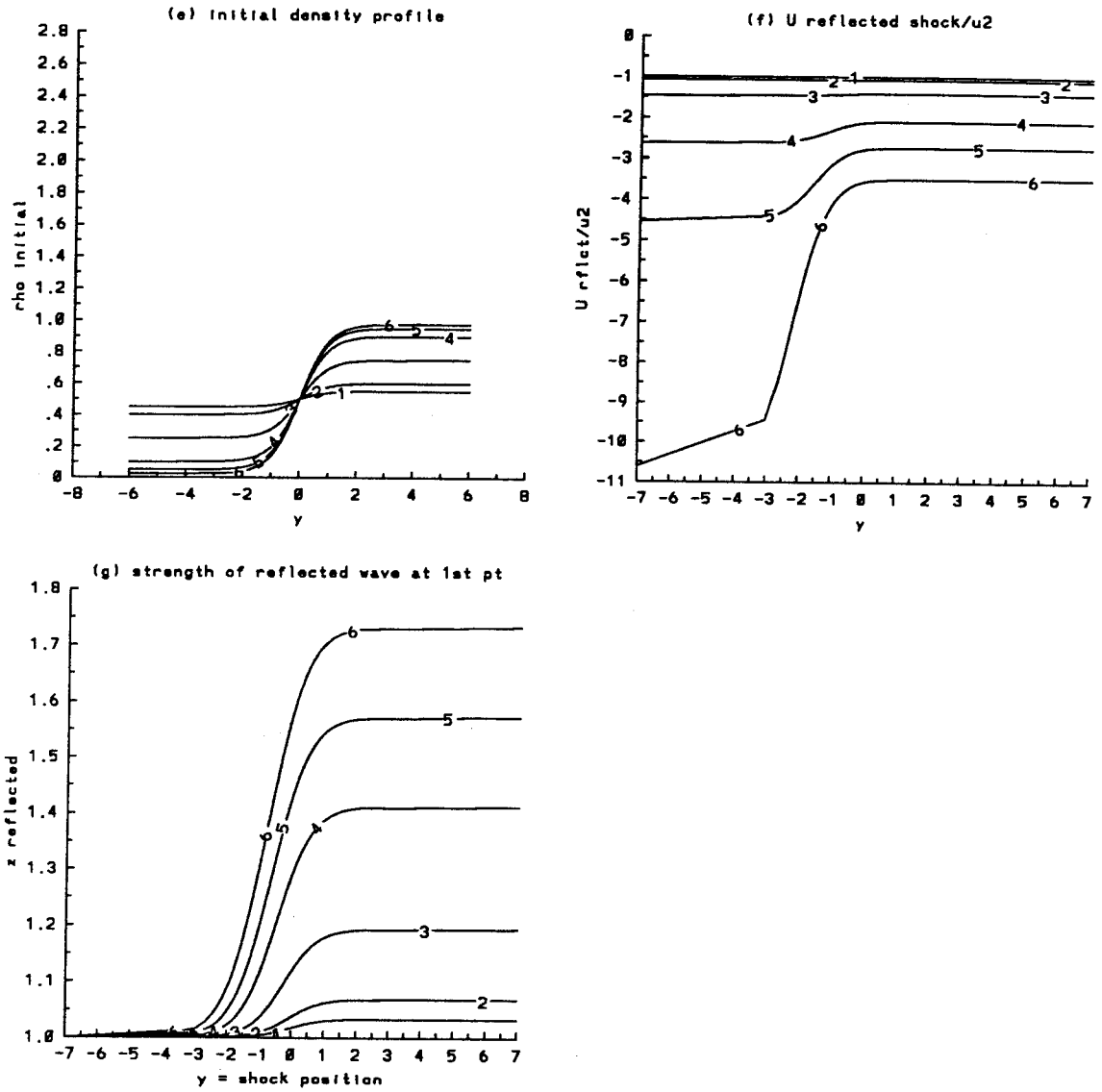

Figure 2.20 *(cont'd)* Solution including the effects of the singly reflected wave for $z_1 = 2.0$ without using (2.67) for y e) initial density profile f) U of reflected shock $/u_2$ g) strength of the reflected shock at the beginning of the non-uniform region as a function of the transmitted shock's position. The numbers 1, 2, 3, 4, 5, and 6 on the curves refer to the Atwood numbers 0.1, 0.2, 0.5, 0.8, 0.9, 0.95 respectively.

velocity gradients. Increasing the shock strength also lengthens significantly the residential time of the shock.

Similar to the zeroth order solution, for small Atwood number, the solution from this calculation is very close to the solution obtained by Paterson theory. From Figure 2.6-b, at $z_1 = 1.1$, the speed ratios of the transmitted shock to the gas speed are 14.5, 13.9, 12.1 for $A = 0.1, 0.2, 0.5$ respectively. The corresponding values at $y = 2.5$ from Figure 2.15-d are 14.5, 13.88, and 12.27. At $y = 14.0$, they are 14.5, 13.8, and 11.7. Similarly, from Figure 2.6-c, at $z_1 = 1.1$, the velocity ratios of the reflected shock to the gas velocity are -14.5, -15.4, -19.0 for $A = 0.1, 0.2, 0.5$. From Figure 2.15-f, the corresponding values at $y = 2.5$ are -14.35, -15.2, and -18.95. At $y = 14.0$, they are -14.35, -15.1, and -18.1. Moreover, from Figure 2.15-g, the total strength of the reflected shock when the transmitted shock has left the region is less than 1.028. For $z_1 = 2.0$, from Figure 2.20-g, it is less than 1.2 for A less than 0.5. The effects of doubly and higher reverberating waves are therefore small. Thus, we can conclude that the solution obtained from a sharp interface gives a good approximation to the solution of a shock passing a continuous interface for low Atwood number.

In conclusion, the constancy of the gas velocity depends strongly on the density gradient. The smaller the gradient, the more uniform the velocity of the gas becomes. After the passage of the shock, when the incident shock strength is weak, the density profile is essentially the same except for a reduction in the characteristic length of the width of the density layer. The higher the shock strength, the more the density profile is altered. The assumption of incompressible impulsive motion is excellent for a weak shock, and small density ratio. For a moderate strength, and density ratio, it is a reasonable assumption.

2.5 Saffman and Meiron Impulsive Model

With the justifications discussed in sections 2.3, and 2.4, Saffman and Meiron

(1989) modeled the motion of a perturbed planar interface undergoing a shock-induced acceleration as one generated by the impulsive motion of the containing walls with a velocity V directed parallel to the undisturbed density gradient. Since the fluid is incompressible, this motion induces instantaneously a pressure field $P(x,y)\delta(t)$, where $\delta(t)$ is the delta function, and there exists a balance between the pressure gradient and the acceleration (viscous and inertial terms are negligible). Note that the function $P(x,y)$ has units of pressure times time.

Let y be the vertical axis parallel to the undisturbed density gradient, and x be the horizontal axis. The upper fluid has density ρ_+, and the lower fluid has density ρ_- as $y \to \pm\infty$ respectively. Integrating the momentum equations, one obtains the equations for the induced initial velocities,

$$\begin{aligned} u &= -\frac{1}{\rho_0}\frac{\partial P}{\partial x}H(t), \\ v &= -\frac{1}{\rho_0}\frac{\partial P}{\partial y}H(t), \end{aligned} \tag{2.69}$$

where $H(t)$ is the Heaviside function, and ρ_0 is the density distribution at the time $t = 0^-$. Using the continuity equation, the impulsive pressure is determined by

$$\frac{\partial}{\partial x}\Big(\frac{1}{\rho_0}\frac{\partial P}{\partial x}\Big) + \frac{\partial}{\partial y}\Big(\frac{1}{\rho_0}\frac{\partial P}{\partial y}\Big) = 0. \tag{2.70}$$

The boundary conditions are

$$\begin{aligned} \frac{\partial P}{\partial y} &\to -\rho_+ V, \quad as \quad y \to +\infty, \\ \frac{\partial P}{\partial y} &\to -\rho_- V, \quad as \quad y \to -\infty. \end{aligned} \tag{2.71}$$

At a vertical wall $x =$ constant, there is no flux. Hence $\partial P/\partial x = 0$. Saffman and Meiron solved this system of equation for a density profile of the form,

$$\rho_0 = \bar{\rho}(y) + \epsilon\rho'(x,y), \tag{2.72}$$

where ϵ is a small perturbation parameter. This particular distribution enables them to analyze the problem using perturbation theory. The dependency of ρ'

on x is essential, since there is no generation of vorticity unless there is a density perturbation in the x-direction.

For small disturbances, they predict that less kinetic energy is generated when the width of the undisturbed density distribution is increased. Hence, in order to reduce the Richtmyer-Meshkov instability, one should decrease the density gradient along the direction of the shock.

In the following study, the solution of the incompressible impulsive model is used as the initial condition for a fully nonlinear simulation of the finite-amplitude stage of the instability. The next section summarizes the equations of motion and the boundary conditions considered.

2.6 Problem formulation

In this section, we present a model for the study of the Richtmyer-Meshkov instability along a continuous interface. As we have shown in the previous sections, for a weak shock, the compressibility effects are small and restricted to a short time interval after the passage of the shock. The initial action of the shock on the interface can be approximated reasonably well by the motion induced due to an incompressible impulsive acceleration. We consider a planar periodic flow as shown in Figure 2.21. For $t = 0^-$, the fluid is at rest with a density,

$$\rho_0 = 1 + A \tanh\left(\frac{y}{L}\right) + \left(\frac{\epsilon}{2L}\right) \operatorname{sech}^2\left(\frac{y}{L}\right) \cos(kx), \tag{2.73}$$

where L is the characteristic width of the stratified layer. This initial density profile had been considered by Saffman and Meiron. It includes the first two terms of the Taylor expansion of a more general profile,

$$\rho_0 = 1 + A \tanh\left\{\frac{1}{L}\left(y - \epsilon' \cos(kx)\right)\right\}, \tag{2.74}$$

where ϵ' is related to ϵ by

$$\epsilon' = -\frac{\epsilon}{2A}. \tag{2.75}$$

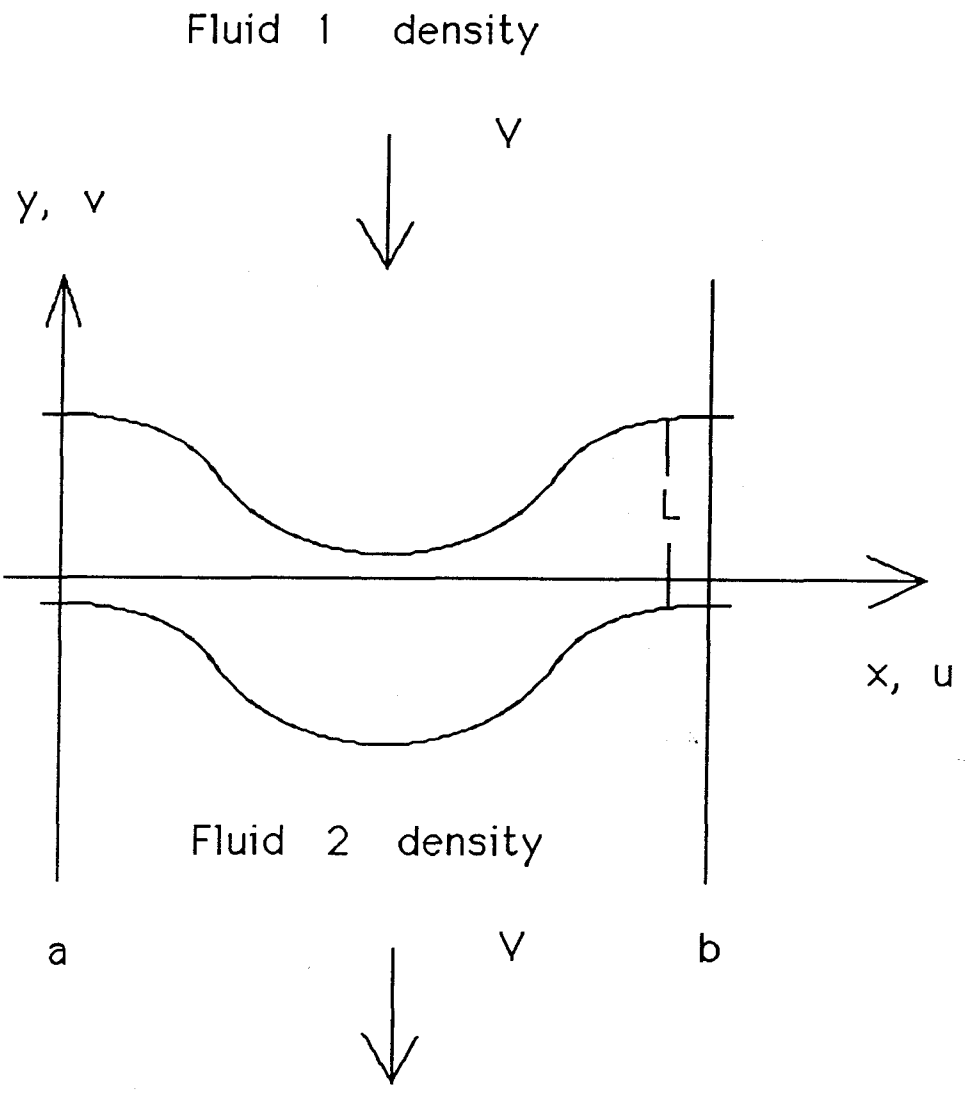

Figure 2.21 Geometry of the flow field. Two imaginary periodic boundaries are labelled a and b.

At time $t = 0$, the whole fluid is accelerated impulsively with a uniform velocity V as $y \to \pm\infty$. This corresponds to the Neumann boundary conditions given in equations (2.71). From the divergence theorem, it can be shown that the solution of the Poisson equation (2.70) is unique up to an arbitrary constant if the boundary

conditions satisfy the compatibility condition,

$$\int_\omega \nabla \cdot \left(\frac{1}{\rho}\nabla p\right) d\omega = \int_S \frac{1}{\rho}\nabla p \cdot \mathrm{n} dS.$$

The boundary conditions (2.71) meet this requirement, and hence, the solution for the initial velocity of the impulsive problem is well-posed and unique.

For the subsequent motion, the flow is governed by the two dimensional unsteady Navier-Stokes equations,

$$\frac{\partial \rho}{\partial t} + \mathbf{u} \cdot \nabla \rho = 0, \tag{2.76}$$

$$\rho \frac{\partial \mathbf{u}}{\partial t} + \rho \mathbf{u} \cdot \nabla \mathbf{u} = -\nabla P + \mu \nabla^2 \mathbf{u}, \tag{2.77}$$

$$\nabla \cdot \mathbf{u} = 0, \tag{2.78}$$

where μ is the viscosity of the fluid. The above equations are solved subject to the boundary conditions,

$$\mathbf{u} \to (0, V) \quad as \quad y \to \pm\infty, \tag{2.79}$$

$$\rho \to \rho_\pm \quad as \quad y \to \pm\infty, \tag{2.80}$$

and $\mathbf{u}$, and ρ are periodic in x, with the period $2\pi/k$. Since we are interested in the inviscid regime, the magnitude of the viscosity used is very small. Its presence is solely for the stability of the numerical scheme. In some of the testing calculations, we scale the above equations using the following characteristic quantities

$$u_c = |V|, \quad l_c = L, \quad p_c = \rho_c u_c^2,$$

$$\rho_c = \rho_+ + \rho_-, \quad \text{and} \quad t_c = \frac{L}{u_c}.$$

In both cases, the equations have the same forms as shown in equations (2.76) to (2.78), except that in the non-dimensional momentum equation the viscosity μ in equation (2.77) is replaced by the factor Re^{-1}, where $Re = \rho_c u_c l_c/\mu$ is the Reynold number. In the actual simulations, we choose $V = -1$, $k = 1$, and $\mu = 10^{-6}$.

The above nonlinear set of equations is solved numerically. This is the topic of the next chapter.

CHAPTER 3

NUMERICAL METHOD FOR SIMULATION

A numerical scheme for solving the unsteady two-dimensional incompressible Richtmyer-Meshkov problem is presented in this chapter. Due to the sharp gradient of the initial density profile in some parts of the flow domain, we use a non-uniform grid in a moving frame in order to resolve this region. We use a finite difference discretization with a staggered grid and with the primitive variables as the unknowns. The system of equations is discretized in time with an implicit Crank-Nicolson scheme applied to all terms. Central differencing is used to compute spatial derivatives. The resulting nonlinear set of equations is solved by an iterative technique, the artificial compressibility method described below.

3.1 Specification of the non-uniform grid

Following Saffman and Meiron (1989), we consider a particular form of the initial density as given in equations (2.73) and (2.74). This density profile has a small variation in the tranverse x-direction while it changes rapidly around the origin along the flow (y-direction). Hence in the y-direction, we use the following coordinate transformation:

$$\eta = \tanh(\gamma y), \tag{3.1}$$

where γ is a controlling parameter for stretching.

A uniform distribution of the grid points in the η computational domain corresponds to a non-uniform distribution over an increasing range in y in the physical

domain. As $\gamma \to 0$, we have a linear transformation and the discretization in y becomes uniform. As $\gamma \to \infty$, we have a very dense distribution of grid points around $y = 0$. This transformation is convenient because of the monotonicity and the smoothness of the hyperbolic tangent. The transformed equations are described below.

The inversion for y in term of η is

$$y = \frac{1}{\gamma} \ln \sqrt{\frac{1+\eta}{1-\eta}}. \tag{3.2}$$

The first and second y-derivative of a flow variable are transformed as follows

$$\frac{\partial}{\partial y} = \frac{d\eta}{dy} \frac{\partial}{\partial \eta}, \tag{3.3}$$

$$\frac{\partial^2}{\partial y^2} = \left(\frac{d\eta}{dy}\right)^2 \frac{\partial^2}{\partial \eta^2} + \frac{d\eta}{dy} \left[\frac{\partial}{\partial \eta}\left(\frac{d\eta}{dy}\right)\right] \frac{\partial}{\partial \eta}, \tag{3.4}$$

where

$$\frac{d\eta}{dy} = \gamma\left(1-\eta^2\right),$$

$$\frac{d\eta}{dy}\left[\frac{\partial}{\partial \eta}\left(\frac{d\eta}{dy}\right)\right] = -2\gamma^2\eta\left(1-\eta^2\right).$$

In all of the calculations, we use a staggered grid in the x, η domain as shown in Figure 3.1. The flow region is divided up three different ways resulting in three kinds of computational cells: the u, v, and p-cell. For the u-cell, the center of the cell is the node point for the u-component of the velocity. The density and the pressure equation are discretized at the center of the p-cell. The u-momentum equation, and the v-momentum equation are discretized at the center of the u, and v cells respectively.

3.2 Velocity field generated by the impulsive acceleration

The initial velocity field is obtained by first solving equation (2.70) and the corresponding boundary conditions (2.71) for the impulsive pressure $P(x, y)$. Note

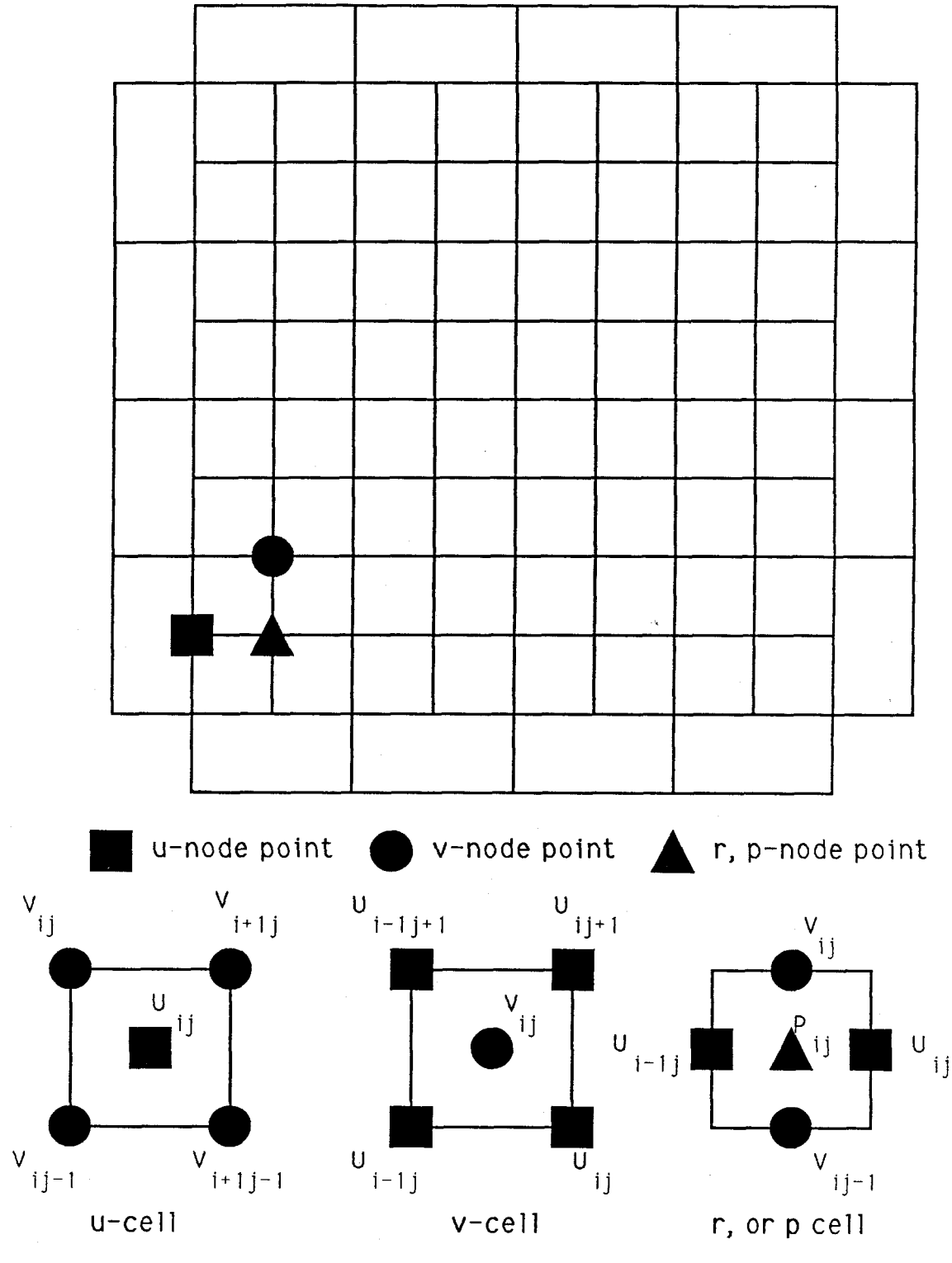

Figure 3.1 Staggered grid and its three cells.

that $P(x,y)$ has the unit of pressure times time. It only has physical meaning when used along with the Heaviside function for computing the initial velocity field. These equations in the transformed coordinate are,

$$\frac{\partial}{\partial x}\left(\frac{1}{\rho_0}\frac{\partial P}{\partial x}\right)+\frac{d\eta}{dy}\frac{\partial}{\partial \eta}\left(\frac{1}{\rho_0}\frac{d\eta}{dy}\frac{\partial P}{\partial \eta}\right)=0, \tag{3.5}$$

and

$$\frac{d\eta}{dy}\frac{\partial P}{\partial \eta}=-\rho_{\pm}V \quad as \quad \eta\to\pm 1.$$

Let h denote the uniform spacing of the grid points in the x-direction, and $\triangle\eta$ that in the η-direction. Equation (3.5) is discretized at the center of the p-cell, and after rearrangement becomes,

$$\begin{aligned} 0=&\left\{-\frac{1}{h^2}\left(\frac{1}{\rho_{oi+\frac{1}{2}j}}+\frac{1}{\rho_{oi-\frac{1}{2}j}}\right)-\eta'_{uj}\left(\frac{\eta'_{vj}}{\rho_{oij+\frac{1}{2}}}+\frac{\eta'_{vj-1}}{\rho_{oij-\frac{1}{2}}}\right)\right\}P_{ij}\\ &+\frac{1}{h^2}\frac{1}{\rho_{oi+\frac{1}{2}j}}P_{i+1j}+\frac{1}{h^2}\frac{1}{\rho_{oi-\frac{1}{2}j}}P_{i-1j}+\frac{\eta'_{uj}\eta'_{vj}}{\rho_{oij+\frac{1}{2}}}P_{ij+1}+\frac{\eta'_{uj}\eta'_{vj-1}}{\rho_{oij-\frac{1}{2}}}P_{ij-1}, \end{aligned} \tag{3.6}$$

where

$$\eta'_u=\frac{d\eta}{dy}\Big|_u\frac{1}{\triangle\eta},$$
$$\eta'_v=\frac{d\eta}{dy}\Big|_v\frac{1}{\triangle\eta}.$$

The subscripts u, and v denote the evaluation of the derivatives at the center of the u-cell and v-cell respectively. Equation (3.6) yields a banded matrix, with a band width of twice the number of the grid points in the x-direction. This matrix is solved using a band LU decomposition. Since the solution is arbitrary up to a constant, we have the freedom to fix the value of P at one particular grid point. We choose $P_{22}=0$; this grid point is shown in Figure 3.1, the only one being marked by a triangle. After solving for the impulsive pressure P, the initial velocity field is obtained by using equation (2.69),

$$u=-\frac{1}{\rho_0}\frac{\partial P}{\partial x}H(t),$$
$$v=-\frac{1}{\rho_0}\frac{\partial P}{\partial y}H(t),$$

where $H(t)$ is the Heaviside function, and ρ_0 is the density distribution at the time $t = 0^-$. Then, the initial pressure is determined automatically by the momentum equations. Before discussing the numerical solution for this initial pressure, however, we would like to formulate the problem in a reference frame moving with the fluid flow.

3.3 Equations of motion in a moving reference frame

In a fixed reference frame, as the flow evolves, the fine resolution of the region with a sharp density gradient along the flow (y-direction) will deteriorate in time. To avoid this difficulty, we solve the problem in a frame moving along with the flow in the negative y-direction with the far field velocity V. The governing equations in a general moving coordinate are given in Lamb (1932). For our problem, the equations of motion become:

$$\frac{\partial u}{\partial t} + \frac{\partial}{\partial x}\left(u^2\right) + \frac{\partial}{\partial y}\left(u\left(v - V\right)\right) + \frac{1}{\rho}\frac{\partial p}{\partial x} - \frac{1}{\rho Re}\nabla^2 u = 0, \tag{3.7}$$

$$\frac{\partial v}{\partial t} + \frac{\partial}{\partial x}\left(u\left(v - V\right)\right) + \frac{\partial}{\partial y}\left(\left(v - V\right)^2\right) + \frac{1}{\rho}\frac{\partial p}{\partial y} - \frac{1}{\rho Re}\nabla^2 v = 0, \tag{3.8}$$

$$\frac{\partial \rho}{\partial t} + u\frac{\partial \rho}{\partial x} + \left(v - V\right)\frac{\partial \rho}{\partial y} = 0, \tag{3.9}$$

$$\frac{\partial u}{\partial x} + \frac{\partial v}{\partial y} = 0. \tag{3.10}$$

The boundary conditions for the velocity and the density in this moving frame remain the same as those given in the last section of Chapter 2. In the remaining parts of this chapter, we will discuss the numerical solution of these equations for the calculation of the initial pressure and subsequent motion.

3.4 Pressure field after the impulsive acceleration

The initial pressure is computed by using the method of Harlow and Welch (1965). We first discretize the u, and v-momentum equation at the center of the u,

and v-cell respectively. The resulting equations are then used in the discretization of the equation,

$$\nabla \cdot \mathbf{u}_t = 0, \tag{3.11}$$

at the center of the p-cell, where $\mathbf{u}_t$ are derived from equations (3.7), and (3.8). Imposing the continuity condition at time step $(n+1)$, we obtain a discretized Poisson equation for the pressure,

$$\begin{aligned}
&\frac{1}{h^2}\left\{\frac{1}{\rho_{uij}}p_{i+1j} - \left(\frac{1}{\rho_{uij}} + \frac{1}{\rho_{ui-1j}}\right)p_{ij} + \frac{1}{\rho_{ui-1j}}p_{i-1j}\right\} \\
&+ \eta'_{uj}\left\{\frac{1}{\rho_{vij}}\eta'_{vj}p_{ij+1} - \left(\frac{\eta'_{vj}}{\rho_{vij}} + \frac{\eta'_{vj-1}}{\rho_{vij-1}}\right)p_{ij} + \frac{\eta'_{vj-1}}{\rho_{vij-1}}p_{ij-1}\right\} \\
=&-\left\{\frac{u^n_{ij} - u^n_{i-1j}}{h\triangle t} + \frac{1}{h^2}\left[\left(uu^{+2} - uu^{-2}\right)_{uij} - \left(uu^{+2} - uu^{-2}\right)_{ui-1j}\right]\right. \\
&\left.+ 2\frac{\eta'_{uj}}{h}\left[\left(uv^+vv^+ - uv^-vv^-\right)_{uij} - \left(uv^+vv^+ - uv^-vv^-\right)_{ui-1j}\right]\right\} \\
&-\left\{-\frac{1}{h^3Re}\left(\frac{D_x^2u_{ij}}{\rho_{uij}} - \frac{D_x^2u_{i-1j}}{\rho_{ui-1j}}\right) - \frac{\eta'^{\,2}_{uj}}{hRe}\left(\frac{D_y^2u_{ij}}{\rho_{uij}} - \frac{D_y^2u_{i-1j}}{\rho_{ui-1j}}\right)\right. \\
&- \frac{\eta''_{2uj}}{hRe}\left(\frac{D_yu_{ij}}{\rho_{uij}} - \frac{D_yu_{i-1j}}{\rho_{ui-1j}}\right) - \eta'_{uj}\left(\frac{v^n_{ij} - v^n_{ij-1}}{\triangle t}\right) \\
&+ \eta'_{uj}\left[\eta'_{vj}\left(vv^{+2} - vv^{-2}\right)_{vij} - \eta'_{vj-1}\left(vv^{+2} - vv^{-2}\right)_{vij-1}\right] \\
&- \frac{\eta'_{uj}}{h^2Re}\left(\frac{D_x^2v_{ij}}{\rho_{vij}} - \frac{D_x^2v_{ij-1}}{\rho_{vij-1}}\right) - \frac{\eta'_{uj}}{Re}\left(\frac{\eta'^{\,2}_{vj}D_y^2v_{ij}}{\rho_{vij}} - \frac{\eta'^{\,2}_{vj-1}D_y^2v_{ij-1}}{\rho_{vij-1}}\right) \\
&\left.- \frac{\eta'_{uj}}{Re}\left(\frac{\eta''_{2vj}D_yvij}{\rho_{vij}} - \frac{\eta''_{2vj-1}D_yv_{ij-1}}{\rho_{vij-1}}\right)\right\},
\end{aligned} \tag{3.112}$$

where u, and v are the initial velocities obtained from solving the impulsive acceleration problem. The spatial operators D_x^2, D_y^2, and D_y are defined by,

$$\begin{aligned}
D_x^2u_{ij} &= u_{i+1j} - 2u_{ij} + u_{i-1j}, \\
D_y^2u_{ij} &= u_{ij+1} - 2u_{ij} + u_{ij-1}, \\
D_yu_{ij} &= \frac{u_{ij+1} - u_{ij-1}}{2},
\end{aligned}$$

with

$$\eta''_{2u} = \frac{1}{\Delta\eta}\frac{d\eta}{dy}\left(\frac{\partial}{\partial\eta}\left(\frac{d\eta}{dy}\right)\right)\Big|_u,$$

and a similar expression for $\eta''_{2v}(j)$. The velocity uu^+ (uu^-) is the forward (backward) average of the u-component in the x-direction, and uv^+ (uv^-) is that of the u-component in the y-direction. For example,

$$uu^+ = \frac{u_{ij} + u_{i+1j}}{2}$$

Similarly, vv^+ (vv^-) is that of $(v - V)$ in the y-direction. The subscript uij (vij) of a particular quantity indicates the discretization of that quantity at the uij (vij)-cell.

Equation (3.12) is applied at each center of the p-cell, and similar to the above impulsive problem, the resulting equations are arranged in a band matrix. It is well known that boundary conditions for the pressure are not needed for a specified velocity field. For the purpose of the numerical implementation, however, we impose an artificial pressure boundary condition using the Neumann compatibility condition for the Poisson equation, namely the modified normal pressure gradient $\frac{1}{\rho}\nabla p \cdot \mathbf{n}$ at the boundary. With the staggered mesh, this condition is satisfied automatically as long as a consistent discretization is used both at the boundary and in the governing equations. Let nux be the number of the centers of the u-cells in the x-direction , nuy be that in the y-direction, and similarly for nvx, nvy. Using the momentum equations, we have at the boundary,

$$p_{1j} = p_{2j} + \rho_{u1j}h\Big\{\frac{{uu^+}^2_{u1j}}{h} + \eta'_{uj}(uv^+vv^+ - uv^-vv^-)_{u1j}$$
$$- \frac{1}{\rho_{u1j}Re}\Big(\frac{u_{2j} - 2u_{1j}}{h^2} + {\eta'_{uj}}^2 D_y^2 u_{1j} + \eta''_{2uj}D_y u_{1j}\Big)\Big\},$$

$$p_{nux+1j} = p_{nuxj} - \rho_{unuxj}h\Big\{\frac{({uu^+}^2 - {uu^-}^2)_{unuxj}}{h} + \eta'_{uj}(uv^+vv^+ - uv^-vv^-)_{unuxj}$$
$$- \frac{1}{\rho_{unuxj}Re}\Big(\frac{D_x^2 u_{nuxj}}{h^2} + {\eta'_{uj}}^2 D_y^2 u_{nuxj} + \eta''_{2uj}D_y u_{nuxj}\Big)\Big\},$$

$$p_{invy+1} = p_{invy} - \frac{\rho_{vinvy}}{\eta'_{vnvy}}\Big\{\frac{(uu^{+}vu^{+} - uu^{-}vu^{-})_{vinvy}}{h} + \eta'_{vnvy}(vv^{+2} - vv^{-2})_{vinvy}$$
$$- \frac{1}{\rho_{vinvy}Re}\Big(\frac{D_x^2 v_{invy}}{h^2} + \eta'^{\,2}_{vnvy} D_y^2 v_{invy} + \eta''_{2vnvy} D_y v_{invy}\Big)\Big\},$$
$$p_{i1} = p_{i2} + \frac{\rho_{vi1}}{\eta'_{v1}}\Big\{\frac{(uu^{+}vu^{+} - uu^{-}vu^{-})_{vi1}}{h} + \eta'_{v1})vv^{+2}_{vi1}$$
$$- \frac{1}{\rho_{vi1}Re}\Big(\frac{D_x^2 v_{i1}}{h^2} + \eta'^{\,2}_{v1}(v_{i2} - 2v_{i1}) + \eta''_{2v1}\Big(\frac{v_{i2}}{2}\Big)\Big)\Big\}. \tag{3.13}$$

The pressure obtained in this section and the velocity field generated in section 3.2 provide the necessary initial conditions for a full numerical simulation. In the next section, we will discuss the unsteady two-dimensional Navier-Stokes incompressible scheme used in this work.

3.5 Numerical solution

A well-known difficulty for incompressible calculations is the need to satisfy the zero divergence constraint. This condition, which implicitly couples the pressure to the velocity field, does not appear in a time evolution form. The different ways to satisfy this constraint yield different numerical methods for solving the unsteady incompressible equations. Presently, there are many approaches in the literature, but they can be classified into three main techniques. The first technique uses the vorticity and the stream function as the primary unknowns. The second one developed by Harlow and Welch (1965), also by Chorin (1968) is known as the fractional step method or the projection method. The third technique can be viewed as a direct coupling between the momentum and the continuity equation. In this study, this last technique is used with an iterative scheme proposed by Soh and Goodrich (1988) in which the velocity and the pressure are the primitive variables. This method is chosen because it shows potential robustness, and stability in the time dependent calculation. In addition, the extension of the algorithm to include

the density equation is straightforward and convenient. The overall iteration can be summarized as follows. First all terms of equations (3.7) to (3.10) are discretized using the Crank-Nicolson scheme with central differencing for the space derivatives. Between two given physical time steps, this results in a non-linear set of equations, which is formulated into a fictitious continuous "pseudo-time" system, and is solved by the well-known artificial compressibility method.

The Crank-Nicolson approximation to equations (3.7) to (3.10) gives,

$$\begin{aligned} \frac{\rho^{n+1}-\rho^n}{\triangle t}+\frac{1}{2}\left[F\left(\mathbf{u}^{n+1},\rho^{n+1}\right)+F\left(\mathbf{u}^n,\rho^n\right)\right]&=0,\\ \frac{\mathbf{u}^{n+1}-\mathbf{u}^n}{\triangle t}+\frac{1}{2}\left[\mathbf{G}\left(\mathbf{u}^{n+1},p^{n+1},\rho^{n+1}\right)+\mathbf{G}\left(\mathbf{u}^n,p^n,\rho^n\right)\right]&=0,\\ \nabla\cdot\mathbf{u}^{n+1}&=0, \end{aligned} \tag{3.14}$$

where

$$\begin{aligned} F(\mathbf{u},\rho)&=u\frac{\partial\rho}{\partial x}+(v-V)\frac{\partial\rho}{\partial y},\\ \mathbf{G}(\mathbf{u},p,\rho)&=\left[G_1,G_2\right]^{\mathrm{T}},\\ G_1&=\frac{\partial}{\partial x}\left(u^2\right)+\frac{\partial}{\partial y}\left(u\left(v-V\right)\right)+\frac{1}{\rho}\frac{\partial p}{\partial x}-\frac{1}{\rho Re}\nabla^2 u,\\ G_2&=\frac{\partial}{\partial x}\left(u\left(v-V\right)\right)+\frac{\partial}{\partial y}\left(\left(v-V\right)^2\right)+\frac{1}{\rho}\frac{\partial p}{\partial y}-\frac{1}{\rho Re}\nabla^2 v. \end{aligned} \tag{3.15}$$

Let $\hat{\mathbf{u}}^{n+1}=\mathbf{u}^{n+1}-\mathbf{u}^n$, $\hat{p}^{n+1}=p^{n+1}-p^n$, $\hat{\rho}^{n+1}=\rho^{n+1}-\rho^n$, $\alpha=\triangle t/2$, then the above equations become,

$$\begin{aligned} \hat{\rho}^{n+1}+\alpha F\left(\hat{\mathbf{u}}^{n+1}+\mathbf{u}^n,\hat{\rho}^{n+1}+\rho^n\right)&=-\alpha F\left(\mathbf{u}^n,\rho^n\right),\\ \hat{\mathbf{u}}^{n+1}+\alpha\mathbf{G}\left(\hat{\mathbf{u}}^{n+1}+\mathbf{u}^n,\hat{p}^{n+1}+p^n,\hat{\rho}^{n+1}+\rho^n\right)&=-\alpha\mathbf{G}\left(\mathbf{u}^n,p^n,\rho^n\right),\\ \nabla\cdot\hat{\mathbf{u}}^{n+1}&=0. \end{aligned} \tag{3.16}$$

This nonlinear set of equations for the unknown variables with the superscript $n+1$ at the next physical time step is solved by considering it to be the steady

solution of the following fictitious pseudo-time problem,

$$\begin{aligned}
\frac{\partial \hat{\rho}}{\partial \tau} + \hat{\rho} + \alpha F(\hat{\mathbf{u}} + \mathbf{u}, \hat{\rho} + \rho) &= -\alpha F(\mathbf{u}, \rho), \\
\frac{\partial \hat{\mathbf{u}}}{\partial \tau} + \hat{\mathbf{u}} + \alpha \mathbf{G}(\hat{\mathbf{u}} + \mathbf{u}, \hat{p} + p, \hat{\rho} + \rho) &= -\alpha \mathbf{G}(\mathbf{u}, p, \rho), \\
\beta \frac{\partial \hat{p}}{\partial \tau} + \nabla \cdot \hat{\mathbf{u}} &= 0,
\end{aligned} \tag{3.17}$$

where the superscripts n, and $n+1$ have been dropped for simplicity.

The initial and boundary conditions for this problem are

$$(\hat{u}, \hat{v}, \hat{p}, \hat{\rho}) = 0 \qquad at \quad \tau = 0,$$

$$\hat{u}, \hat{v}, \hat{\rho} \to 0 \quad as \quad \eta \to \pm 1, \quad \tau > 0,$$

along with the periodicity of the velocity and the density in the x direction.

Let k denote the k^{th} iteration of the pseudo-time problem. Then, one way to solve this fictious system is by the following iterative scheme:

1. Sweep in the y direction for the $\hat{v}^{k+1}$ equation. This expression has the following implications. For a fixed i, along a vertical line of grid points, we discretize the $\hat{v}^{k+1}$ equation with the y derivatives evaluated at step $k+1$. The x derivatives and all of the nonlinearities are lagged at the pseudo-time step k. The resulting unknowns can be arranged in the form of a tridiagonal matrix. The pressure in the artificial compressibility equation is coupled with the v momentum equation. Thus, the v momentum equation becomes,

$$\begin{aligned}
&\frac{\partial \hat{v}}{\partial \tau} + \hat{v} + \alpha \left[\frac{d\eta}{dy} \frac{\partial}{\partial \eta} \left(2\hat{v}(v - V) \right) + \frac{1}{\hat{\rho} + \rho} \frac{d\eta}{dy} \frac{\partial \hat{p}}{\partial \eta} \right. \\
&\left. - \frac{1}{(\hat{\rho} + \rho) Re} \left(\left(\frac{d\eta}{dy} \right)^2 \frac{\partial^2 \hat{v}}{\partial \eta^2} + \frac{d\eta}{dy} \left(\frac{\partial}{\partial \eta} \left(\frac{d\eta}{dy} \right) \right) \frac{\partial \hat{v}}{\partial \eta} \right) \right] = H_v,
\end{aligned} \tag{3.18}$$

where

$$\begin{aligned}
H_v = -\alpha \left[\frac{\partial}{\partial x} \left(u(v - V) + (\hat{u} + u)(\hat{v} + v - V) \right) + \frac{d\eta}{dy} \frac{\partial}{\partial \eta} \left(2(v - V)^2 + \hat{v}^2 \right) \right. \\
\left. + \left(\frac{1}{\rho} + \frac{1}{\hat{\rho} + \rho} \right) \frac{d\eta}{dy} \frac{\partial p}{\partial \eta} - \frac{1}{(\hat{\rho} + \rho) Re} \left(\frac{\partial^2 \hat{v}}{\partial x^2} + \nabla^2 v \right) - \frac{1}{\rho Re} \nabla^2 v \right],
\end{aligned} \tag{3.19}$$

and

$$\nabla^2 = \frac{\partial^2}{\partial x^2} + \left(\frac{d\eta}{dy}\right)^2 \frac{\partial^2}{\partial \eta^2} + \frac{d\eta}{dy}\left(\frac{\partial}{\partial \eta}\left(\frac{d\eta}{dy}\right)\right)\frac{\partial}{\partial \eta}. \tag{3.20}$$

2. Sweep the density equation in the y-direction one half pseudo-time step, $\frac{1}{2}\Delta\tau$ to obtain $\hat{\rho}^{k+\frac{1}{2}}$. The density equation for this sweep is,

$$2\frac{\partial \hat{\rho}}{\partial \tau} + \hat{\rho} + \alpha(\hat{v} + v - V)\frac{d\eta}{dy}\frac{\partial \hat{\rho}}{\partial \eta} = H_{r1}, \tag{3.21}$$

where

$$H_{r1} = -\alpha\Big[(2u + \hat{u})\frac{\partial \rho}{\partial x} + (2(v - V) + \hat{v})\frac{d\eta}{dy}\frac{\partial \rho}{\partial \eta} + (\hat{u} + u)\frac{\partial \hat{\rho}}{\partial x}\Big]. \tag{3.22}$$

3. Sweep the $\hat{u}$-equation in the x-direction. The pressure in the artificial compressibility equation is coupled with the u-momentum equation. Only x-derivatives are considered and all of the y derivatives and the nonlinearities are lagged. The u momentum equation for this sweep is then,

$$\frac{\partial \hat{u}}{\partial \tau} + \hat{u} + \alpha\Big[\frac{\partial}{\partial x}(2u\hat{u}) + \frac{1}{\hat{\rho} + \rho}\frac{\partial \hat{p}}{\partial x} - \frac{1}{(\hat{\rho} + \rho)Re}\frac{\partial^2 \hat{u}}{\partial x^2}\Big] = H_u, \tag{3.23}$$

where

$$\begin{aligned} H_u = -\alpha\Bigg[&\frac{\partial}{\partial x}\left(2u^2 + \hat{u}^2\right) + \frac{d\eta}{dy}\frac{\partial}{\partial \eta}\left(u(v - V) + (u + \hat{u})(v + \hat{v} - V)\right) \\ &+ \left(\frac{1}{\rho} + \frac{1}{\hat{\rho} + \rho}\right)\frac{\partial p}{\partial x} - \frac{1}{(\hat{\rho} + \rho)\,Re}\left(\left(\frac{d\eta}{dy}\right)^2 \frac{\partial^2 \hat{u}}{\partial \eta^2} + \frac{d\eta}{dy}\frac{\partial}{\partial \eta}\left(\frac{d\eta}{dy}\right)\frac{\partial \hat{u}}{\partial \eta} + \nabla^2 u\right) \\ &- \frac{1}{\rho Re}\nabla^2 u\Bigg]. \end{aligned} \tag{3.24}$$

4. Sweep in the x direction for the remaining half pseudo-time step for the density equation. The density equation is

$$2\frac{\partial \hat{\rho}}{\partial \tau} + \hat{\rho} + \alpha(\hat{u} + u)\frac{\partial \hat{\rho}}{\partial x} = H_{r2}, \tag{3.25}$$

where

$$H_{r2} = -\alpha\Big[(2u+\hat{u})\frac{\partial \rho}{\partial x} + (2(v-V)+\hat{v})\frac{d\eta}{dy}\frac{\partial \rho}{\partial \eta} + (\hat{v}+v-V)\frac{d\eta}{dy}\frac{\partial \hat{\rho}}{\partial \eta}\Big]. \quad (3.26)$$

5. Obtain the pressure $\hat{p}^{k+1}$ by the artificial compressibility equation.

$$\beta\frac{\partial \hat{p}}{\partial \tau} = -\Big[\frac{\partial \hat{u}}{\partial x} + \frac{d\eta}{dy}\frac{\partial \hat{v}}{\partial \eta}\Big]. \quad (3.27)$$

6. Repeat steps 1 through 5 until the pseudo-time problem reaches a steady state.

For each sweep, the unknowns form a tridiagonal matrix. The discretized equations at the cell center ij for the v, first ρ, u, and second ρ equations respectively are,

$$\begin{aligned}
a_{1v}\hat{v}^{k+1}_{ij-1} + a_{2v}\hat{v}^{k+1}_{ij} + a_{3v}\hat{v}^{k+1}_{ij+1} &= a_{4v},\\
a_{1r1}\hat{\rho}^{k+\frac{1}{2}}_{ij-1} + a_{2r1}\hat{\rho}^{k+\frac{1}{2}}_{ij} + a_{3r1}\hat{\rho}^{k+\frac{1}{2}}_{ij+1} &= a_{4r1},\\
a_{1u}\hat{u}^{k+1}_{i-1j} + a_{2u}\hat{u}^{k+1}_{ij} + a_{3u}\hat{u}^{k+1}_{i+1j} &= a_{4u},\\
a_{1r2}\hat{\rho}^{k+1}_{i-1j} + a_{2r2}\hat{\rho}^{k+1}_{ij} + a_{3r2}\hat{\rho}^{k+1}_{i+1j} &= a_{4r2},
\end{aligned} \quad (3.28)$$

where,

$$a_{1v} = \alpha\Delta\tau\left[-\eta'_{vj}\left(vv^{-}_{vij} - V\right) + \frac{2}{\hat{\rho}^{k}_{vij}}\left\{-\frac{\Delta\tau\eta'_{vj}\eta'_{uj}}{\beta} - \frac{1}{Re}\left(\eta'^{\,2}_{vj} - \frac{\eta''_{2vj}}{2}\right)\right\}\right],$$

$$a_{2v} = 1 + \Delta\tau + \alpha\Delta\tau\eta'_{vj}D_y v_{ij} + \frac{2\alpha\Delta\tau}{\hat{\rho}^{k}_{vij}}\left\{\frac{\Delta\tau}{\beta}\eta'_{vj}\left(\eta'_{uj+1} + \eta'_{uj}\right) + \frac{1}{Re}2\eta'^{\,2}_{vj}\right\},$$

$$a_{3v} = \alpha\Delta\tau\left[\eta'_{vj}\left(vv^{+}_{vij} - V\right) + \frac{2}{\hat{\rho}^{k}_{vij}}\left\{-\frac{\Delta\tau\eta'_{vj}\eta'_{uj+1}}{\beta} - \frac{1}{Re}\left(\eta'^{\,2}_{vj} + \frac{\eta''_{2vj}}{2}\right)\right\}\right],$$

$$a_{4v} = \hat{v}^{k}_{ij} - \frac{2\alpha\Delta\tau\eta'_{vj}}{\hat{\rho}^{k}_{vij}}\left(\hat{p}^{k}_{ij+1} - \hat{p}^{k}_{ij} - \frac{\Delta\tau}{\beta}\frac{1}{h}(\hat{u}^{k}_{ij+1} - \hat{u}^{k}_{i-1j+1} - \hat{u}^{k}_{ij} + \hat{u}^{k}_{i-1j})\right)$$
$$+ \Delta\tau H_{vij},$$

$$\hat{\rho}^{k}_{vij} = \hat{\rho}^{k}_{ij+1} + \hat{\rho}^{k}_{ij} + \rho_{ij+1} + \rho_{ij},$$

$$a_{1r1} = -\frac{\alpha\Delta\tau}{4}\left(\hat{v}^{k+1} + v - V\right)_{ijP}\eta'_{uj},$$

$$a_{2r1} = 1 + \frac{\Delta\tau}{2},$$

$$a_{3r1} = \frac{\alpha\Delta\tau}{4}\left(\hat{v}^{k+1} + v - V\right)_{ijP}\eta'_{uj},$$

$$a_{4r1} = \hat{\rho}^{k}_{ij} + \frac{\Delta\tau}{2}H_{r1ij},$$

$$a_{1u} = -\frac{\alpha\Delta\tau}{h}uu^{-}_{uij} + \frac{2\alpha\Delta\tau}{\hat{\rho}^{k+\frac{1}{2}}_{uij}}\left[-\frac{\Delta\tau}{\beta h^2} - \frac{1}{Reh^2}\right],$$

$$a_{2u} = 1 + \Delta\tau + \frac{\alpha\Delta\tau}{h}\left(\frac{u_{i+1j} - u_{i-1j}}{2}\right) + \frac{2\alpha\Delta\tau}{\hat{\rho}^{k+\frac{1}{2}}_{uij}}\left[\frac{2\Delta\tau}{\beta h^2} + \frac{2}{Reh^2}\right],$$

$$a_{3u} = \frac{\alpha\Delta\tau}{h}uu^{+}_{uij} + \frac{2\alpha\Delta\tau}{\hat{\rho}^{k+\frac{1}{2}}_{uij}}\left[-\frac{\Delta\tau}{\beta h^2} - \frac{1}{Reh^2}\right],$$

$$a_{4u} = \hat{u}^{k}_{ij} - \frac{\alpha\Delta\tau}{\hat{\rho}^{k+\frac{1}{2}}_{uij}}\frac{1}{h}\left\{\hat{p}^{k}_{i+1j} - \hat{p}^{k}_{ij} + \frac{\Delta\tau}{\beta}\eta'_{uj}\left(\hat{v}^{k+1}_{i+1j-1} - \hat{v}^{k+1}_{i+1j} + \hat{v}^{k+1}_{ij} - \hat{v}^{k+1}_{ij-1}\right)\right\}$$
$$+ \Delta\tau H_{uij},$$

$$\hat{\rho}^{k+\frac{1}{2}}_{uij} = \hat{\rho}^{k+\frac{1}{2}}_{ij} + \hat{\rho}^{k+\frac{1}{2}}_{i+1j} + \rho_{ij} + \rho_{i+1j},$$

$$a_{1r2} = -\frac{\alpha\Delta\tau}{4h}\left(\hat{u}^{k+1} + u\right)_{ijP},$$

$$a_{2r2} = 1 + \frac{\Delta\tau}{2},$$

$$a_{3r2} = \frac{\alpha\Delta\tau}{4h}\left(\hat{u}^{k+1} + u\right)_{ijP},$$

$$a_{4r2} = \hat{\rho}^{k+\frac{1}{2}}_{ij} + \frac{\Delta\tau}{2}H_{r2ij}.$$

Dirichlet boundary conditions are enforced during the sweep in the y-direction while periodic boundary conditions are enforced during the sweep in the x-direction. The iterative scheme of the pseudo-time problem has two parameters $\Delta\tau$ and β that effect the convergence rate. It should also be noted that other permutations for the order of the sweeping are possible. However, there is no apriori advantage of one over the other. In the following subsections, we will discuss the choice of $\Delta\tau$, and β used in our simulation, and nine other possible sweeping arrangements.

3.5.1 Optimal choice for β, $\Delta\tau$, and γ

For a particular order of sweeping, there is no guarantee that the overall iteration will converge. However, we can choose the pseudo-time step $\Delta\tau$, so that the tridiagonal matrix is diagonally dominant, *e.g.*,

$$|a_{2c}| > |a_{1c}| + |a_{3c}|, \tag{3.29}$$

where c stands for either $v, u, r1$, or $r2$. For the v equation, the inequality (3.29) is satisfied if

$$\begin{aligned} \Delta\tau &> \frac{\|\rho(v-V)\|_\infty \beta \Delta\eta}{\gamma}, \\ \text{and} \quad & Re\|\rho(v-V)\|_\infty \Delta\eta > 1. \end{aligned} \tag{3.30}$$

For the u equation, we have the condition,

$$\begin{aligned} \Delta\tau &> \|\rho u\|_\infty \beta \Delta x, \\ \text{and} \quad & Re\|\rho u\|_\infty \Delta x > 1. \end{aligned} \tag{3.31}$$

For the density equation, the matrix is diagonally dominant for all $\Delta\tau > 0$ if

$$\begin{aligned} \frac{\alpha\|u\|_\infty}{h} &\leq 1, \\ \text{and} \quad \frac{\alpha\gamma\|v-V\|_\infty}{\Delta\eta} &\leq 1. \end{aligned} \tag{3.32}$$

The first condition of equation (3.32) results from the first sweep of the density equation in the y-direction, and the second one corresponds to the second sweep in the x-direction.

It should be emphasized that the conditions derived here only serve as guidelines in the actual calculation. As can be seen in equations (3.30), and (3.31), the optimal value of $\Delta\tau$ depends on β, and hence a heuristic choice of the pair $(\Delta\tau, \beta)$ is necessary in order to achieve a fast convergence of the overall system (3.17) to a pseudo steady state solution.

Since the code is time dependent, an optimal choice for γ, hence β, and $\Delta\tau$ is also a function of time. Instead of updating these parameters at every time step,

which is difficult and not very practical, we chose a particular γ for a run so that the maximum residual error in the impulsive pressure calculation is as small as possible. With some experimentation, for $L = 1.0$, a good value of γ is around 0.2 for which the error is of the order 10^{-13} to 10^{-10}. With this γ, for a typical grid sizes of $h = .042$ (61 grid points), and $\Delta\eta = .0199$ (100 grid points), equations (3.30) to (3.31) suggest the values of $\Delta\tau \geq 50$ for $\Delta t = 0.02$. Using trial and error, for the first physical time step, the number of iterations of the pseudo-time problem is minimized when β and $\Delta\tau$ are chosen to be 25 and 50 respectively.

As seen from equations (3.30) to (3.31) for $\Delta\tau$, since the magnitude of the velocities and the density are the same for all cases considered, the optimal values of $\Delta\tau$ should be close to each other. Hence, we keep the same value of β and $\Delta\tau$ for every computation. It is observed that these values of $\Delta\tau$ and β indeed give a satisfactory convergence rate. For small Atwood numbers A, the number of pseudo-time iterations is around 20 to 30 in order to satisfy the divergence free condition to a level of 10^{-10}. For higher A, it increases to 100 which is the maximum number of pseudo-time iteration used for all calculations.

For a grid size of 151 by 100, and the time step of 0.02, the computing time for one physical time step (100 pseudo-time iterations) is around 3.6 minutes on a Silicon Graphics IRIS 4D/240. Hence, to simulate 4 units of physical time, it takes around 12 CPU hours (half a day). Note that since our grid is staggered, whenever we use the term 61 *by* 100 *grid*, we mean a grid system having 61 points on the u grid in the x direction, and 100 points on the v grid in the y direction.

3.5.2 Optimal order of sweeping

In the discussion of the particular scheme presented above, we have neither criteria nor the overall rate of convergence for the iteration of the pseudo-time problem. The choice of β and $\Delta\tau$ is heuristic, and depends strongly on numerical experimentation. Hence the question of a specific order of sweeping for which an

optimal rate of convergence is obtained is even harder to answer. In the following discussion, we hope to resolve this issue using some numerical experimentation.

Assume that the rate of convergence for each arrangement of the sweeping is consistent in time. Then, it is sufficient to compare the robustness of different orderings using the results of the first time step. Note that for a sweep in the y direction, the Dirichlet boundary conditions are used, and for the x sweep, the periodic conditions are used. Hence, it is convenient to denote the y sweep as D, and the x sweep as P. Using this notation, the specific ordering discussed can be presented as Dv, $D\rho$, Pu, $P\rho$. This is the case 1 listed below in Table 3.1 which includes all of the possible permutations for this 4-sweep arrangement.

Table 3.1

All permutations of the 4-sweep arrangements

Case	Order of sweeping			
1	Dv	Dρ	Pu	Pρ
2	Pv	Pρ	Du	Dρ
3	Dv	Pρ	Pu	Dρ
4	Pv	Dρ	Du	Pρ
5	Du	Dρ	Pv	Pρ
6	Du	Pρ	Pv	Dρ
7	Pu	Dρ	Dv	Pρ
8	Pu	Pρ	Dv	Dρ

Note that since we must have both x and y sweeps for the density, and alternating D, and P for u and v, the number of possible arrangements is reduced.

In the 4-sweep arrangement, u (similarly for v) can have either D or P but not both. It is possible to have both D and P for u in a single pseudo-time step by including an extra sweep. This results in what we called the 6-sweep arrangement. In Table 3.2, we present seven possible permutations of this kind.

Table 3.2

Some permutations of the 6-sweep arrangements

Case	Order of sweeping					
1	Dv	Pu	$D\rho$	Du	Pv	$P\rho$
2	Dv	Pv	$D\rho$	Du	Pu	$P\rho$
3	Du	Pu	$D\rho$	Dv	Pv	$P\rho$
4	Du	Pv	$D\rho$	Dv	Pu	$P\rho$
5	Pv	Pu	$D\rho$	Du	Dv	$P\rho$
6	Pv	Pu	$P\rho$	Du	Dv	$D\rho$
7	Pu	Pv	$P\rho$	Dv	Du	$D\rho$

To compare the robustness of the different arrangements, we consider the evolution of the maximum residual errors of equations (3.16) as functions of the iteration numbers of the pseudo-time problem. Figures 3.2 to 3.4 are the plots of the logarithms of these errors versus the iteration numbers. Figure 3.2 and 3.3 are for the arrangements tabulated in Table 3.1, and 3.2 respectively, for the case of a single scale perturbation with $A = -0.5$, $L = 1.0$, $\epsilon = 0.3$, and $\mathrm{Re} = 10^6$, on a 21 by 100 grid. Figure 3.4 is the combination of Figure 3.2, and 3.3. For all cases, among the four equations of (3.16), the residual error of the divergence free condition is always biggest as shown in part (a) of Figures 3.2 to 3.4. For the cases in Table 3.1, the convergence rates of the velocity equations approach the same limit for cases 1, 3, 7, 8. The iterations of the cases 2, 4, 5, 6 diverge for every equation. There is some spreading in the limit of the convergence rate for the density equation. As shown in Figure 3.3, this spreading is also true for all cases in Table 3.2 except for the continuity equation, which has the largest residual error.

Combining Figure 3.2 and 3.3, we see that for both kinds of arrangements, as the number of iteration increases, the limit of the largest residual error does not vary significantly from case to case as shown in Figure 3.4-a. Hence, we can conclude that whenever the scheme converges the order of the sweeping is equivalent for the overall convergence of the pseudo-time problem. Moreover, the free divergence

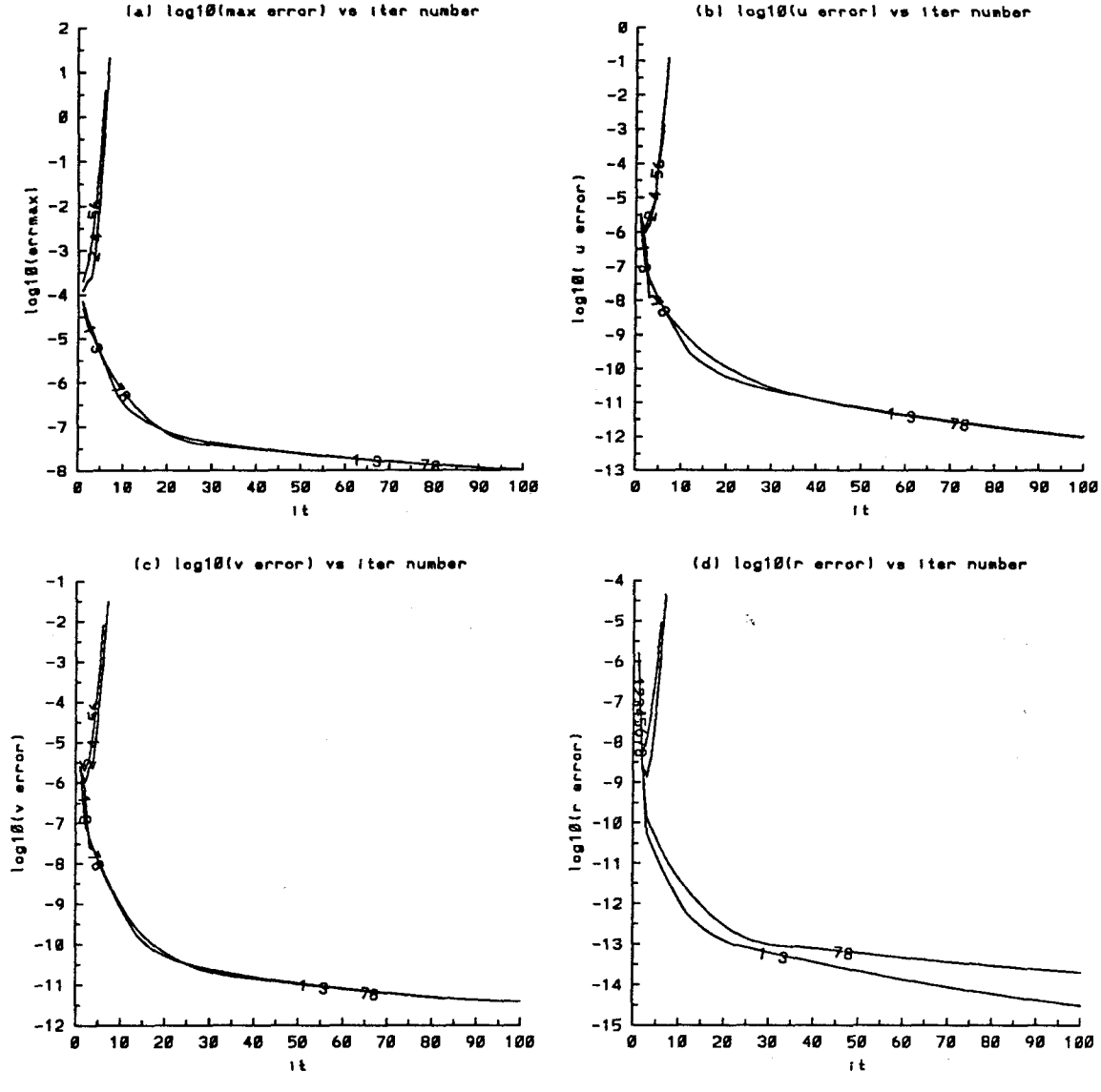

Figure 3.2 Convergence rate of the pseudo-time problem for the 4-sweep arrangements listed in Table 3.1 a) residual error of the divergence free condition b) residual error of the u equation c) residual error of the v equation d) residual error of the ρ equation

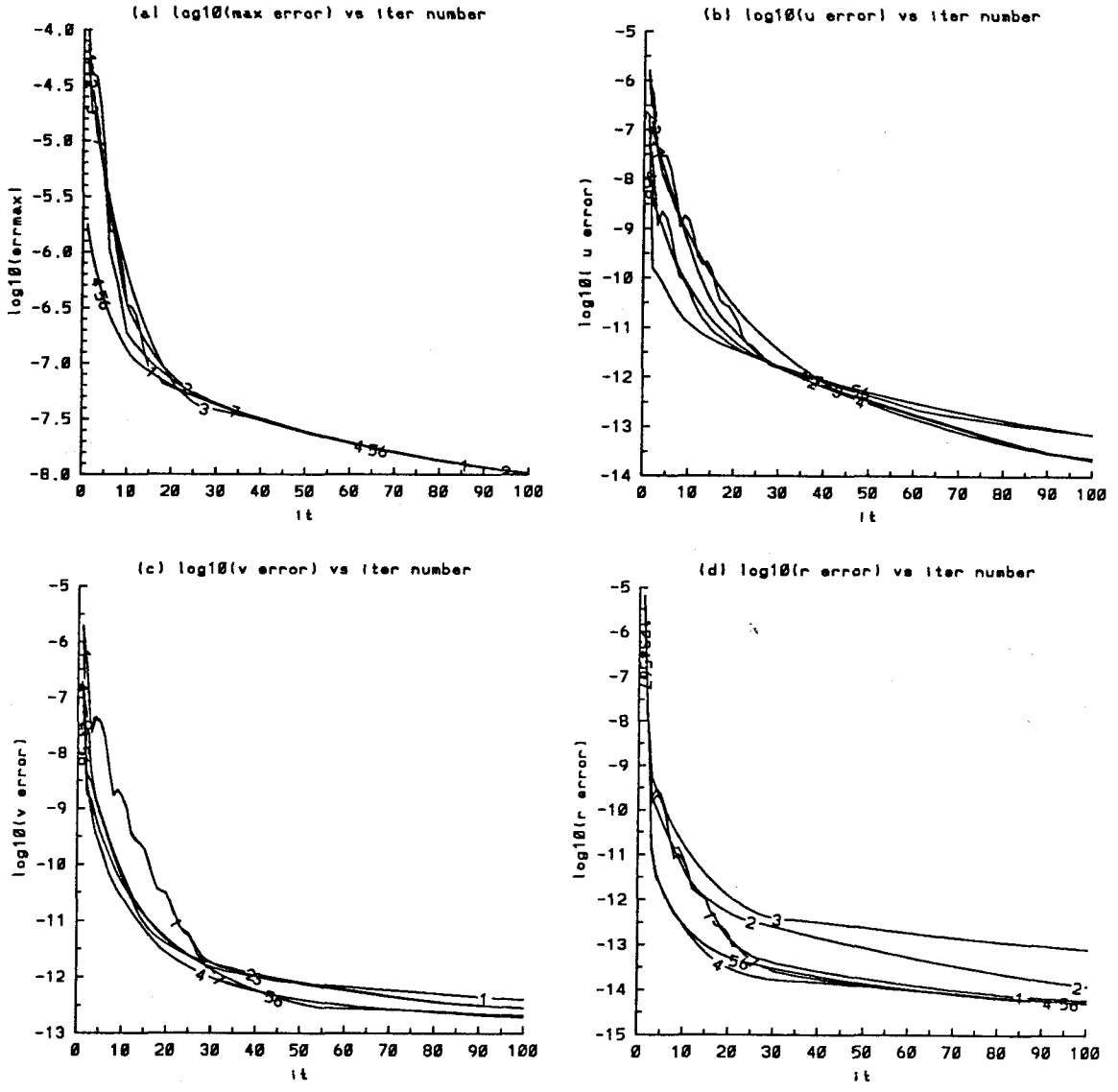

Figure 3.3 Convergence rate of the pseudo-time problem for the 6-sweep arrangements listed in Table 3.2 a) residual error of the divergence free condition b) residual error of the u equation c) residual error of the v equation d) residual error of the ρ equation

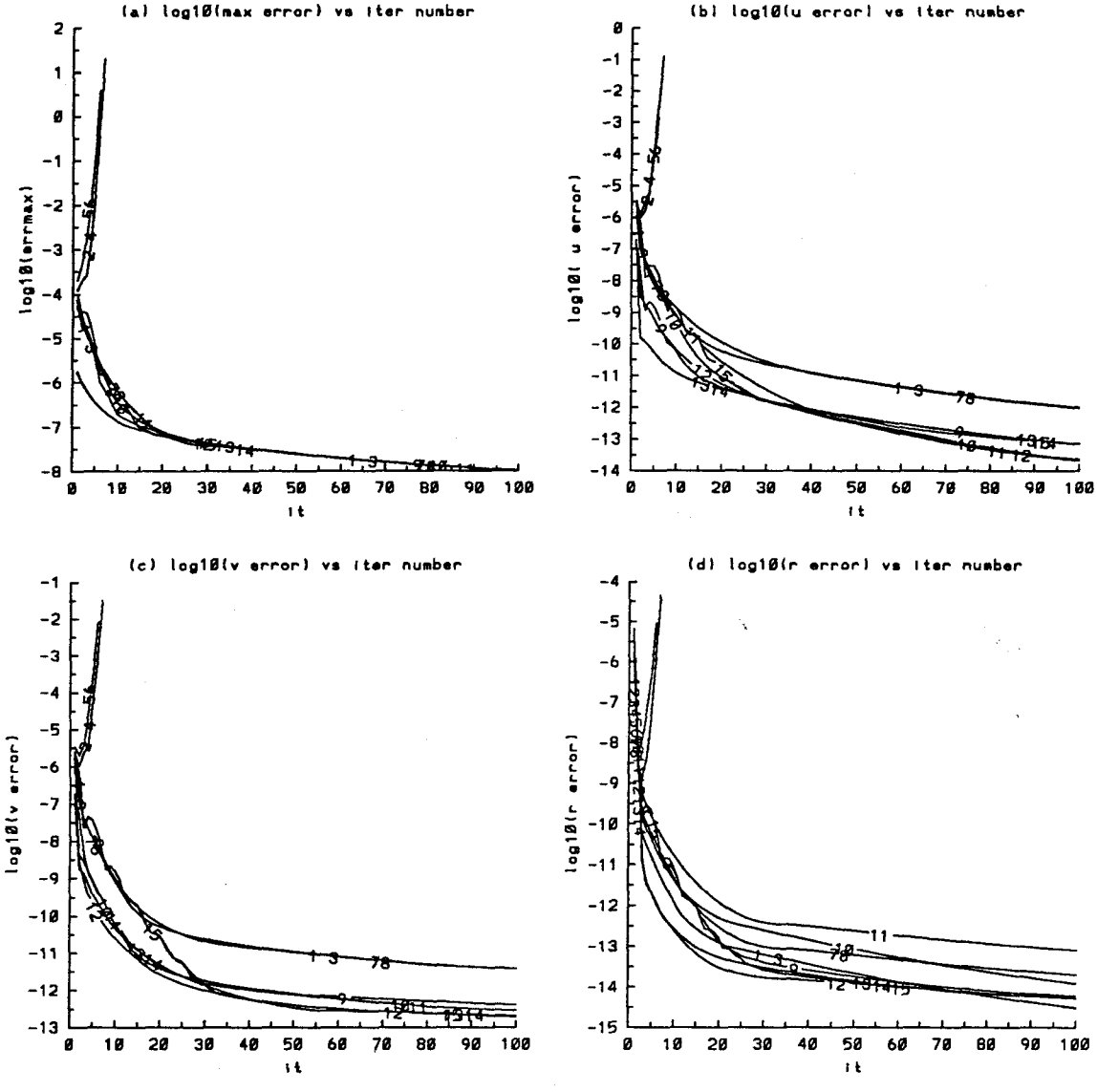

Figure 3.4 Convergence rate of the pseudo-time problem for the 4- and 6-sweep arrangements listed in Table 3.1 and 3.2 a) residual error of the divergence free condition b) residual error of the u equation c) residual error of the v equation d) residual error of the ρ equation

condition is not improved with a longer iteration of the velocity as done in the cases of Table 3.2. The particular scheme selected in this section is an acceptable as well as efficient algorithm in regard to all of the permutations discussed in this section.

In order to test the accuracy and the efficiency of our scheme, we have compared our numerical results to five different computational methods. To assure that our artificial compressibility scheme is second order in space and time, we test the code with a specific exact solution. For a short initial time interval, we test the numerical solution against the first and second order time linearized solution of the Navier-Stokes equation. To verify the efficiency of our scheme, we solve the nonlinear set of equations (3.16) by the Newton-Raphson method. The stability of our time dependent scheme can only be appreciated when the problem is solved explicitly using the MAC method devised by Harlow and Welch (1965) for the momentum equations, and the explicit Lax scheme for the density equation. Finally, there is another test for our numerical result due to the weak nature of the instability. This last check, which also serves as a model for our problem, can be regarded as the description of the flow using the Lagangian motion of the fluid particles with the initial flow field remaining fixed. A detailed discussion of this last check will be postponed until Chapter 4. In the following sections of this chapter, only the details of the first four numerical tests are described.

3.6 Verification of second order accuracy in time and space

As discussed in section 3.5, except for the time derivative, we discretize all terms of the Navier-Stokes equation using the Crank-Nicholson scheme. This results in a nontrivial set of nonlinear equations, but we gain second order accuracy in time and space. In order to verify this, we compare our numerical solutions against a known divergence free flow field. We choose the following flow field for numerical

experimentation:

$$\begin{aligned} u &= -\sin\lambda x \,\mathrm{sech}\, y \tanh y \cos t, \\ v &= -\lambda \cos\lambda x \,\mathrm{sech}\, y \cos t, \\ \rho &= \left(\xi \cos\lambda x \,\mathrm{sech}\, y + \frac{1}{2} + \frac{A}{2}\tanh y\right)(\cos t + 2), \\ p &= \cos\lambda x \sin y \cos t. \end{aligned} \tag{3.33}$$

When the density, the velocities, and the pressure of this flow are substituted into the governing equations, except for the continuity equation (3.10), equations (3.7) to (3.9) have respectively the following additional source terms when V is set to 1,

$$\begin{aligned} (3.7) \quad : \quad & \sin\lambda x \,\mathrm{sech}\, y \tanh y (\sin t - \cos t \tanh y) - \frac{\lambda}{\rho}\sin\lambda x \sin y \cos t \\ & + \sin\lambda x \cos t \mathrm{sech}^3 y (1 + \lambda \cos\lambda x \cos t \,\mathrm{sech}\, y) \\ & - \frac{1}{\rho Re}\sin\lambda x \cos t \,\mathrm{sech}\, y \tanh y \left(\lambda^2 - \tanh^2 y + 5\mathrm{sech}^2 y\right), \\ (3.8) \quad : \quad & \lambda \cos\lambda x \,\mathrm{sech}\, y (\sin t - \tanh y \cos t) \\ & - \lambda^2 \mathrm{sech}^2 y \tanh y \cos^2 t + \frac{1}{\rho}\cos\lambda x \cos y \cos t \\ & - \frac{1}{\rho Re}\lambda \cos\lambda x \,\mathrm{sech}\, y \cos t \left(\lambda^2 - 2\tanh^2 y + 1\right), \\ (3.9) \quad : \quad & -\sin t \left(\xi \cos\lambda x \,\mathrm{sech}\, y + \frac{1}{2} + \frac{A}{2}\tanh y\right) \\ & + (\cos t + 2)\left\{\xi\lambda \sin^2 \lambda x \mathrm{sech}^2 y \tanh y \cos t \right. \\ & \left. - (\lambda \cos\lambda x \,\mathrm{sech}\, y \cos t + 1)\left(-\xi \cos\lambda x \,\mathrm{sech}\, y \tanh y + \frac{A}{2}\mathrm{sech}^2 y\right)\right\}. \end{aligned}$$

We treat these new terms the same way as the other nonlinear terms of the equations. They only modify the element a_{4c}, $c = v,\ r1,\ u,\ or\ r2$ of the sweeping matrix. For the tests, we use the following set of parameters,

$$\lambda = 4, \quad \xi = 0.2, \quad A = 0.6,$$

which appear in equation (3.35). The domain of the flow is discretized uniformly over the region,

$$0 \le x \le \frac{\pi}{2}, \quad \text{and} \quad -\frac{\pi}{4} \le y \le \frac{\pi}{4}.$$

We solve the problem for two different Reynolds number, $Re = 10$, and 100. To test our scheme, we first obtain the solution on a 32 by 32 grid (*e.g.* $\Delta x = 0.051$, $\Delta y = 0.051$) with $\Delta t = 0.05$ for $Re = 10$, and $\Delta t = 0.025$ for $Re = 100$. Then, another solution on a 64 by 64 grid with half of the mentioned time step is also obtained. Since our scheme is second order accurate in space and time, we expect to have a fourfold reduction of error when the spatial and temporal step sizes reduce by a factor of one-half.

Figures 3.5 to 3.7 present the results for $Re = 10$, and those of Figures 3.8 to 3.10 for $Re = 100$ with time t ranging from 0 to 2π. For each flow variable, we use the maximum norm for the deviation from the exact solution and normalize it to the known maximum of the respective variable. There are four plots in each figure. Plots (a) and (b) show these errors for two set of grids: curve 1 is for 32 by 32 grid, and curve 2 is for 64 by 64 grid. In plots (c) and (d), we plot in curve 1 the ratio of the (64,64) error to that of (32,32), and in curve 2 the mean time average $E_{d/s}$ of this ratio using the trapezoidal integration.

For $Re = 10$, the maximum relative errors are less than 0.8% for u, 0.28% for v, 0.9% for ρ, and 4.5% for p in the solution with the 32 by 32 grid. With 64 by 64 grid, the corresponding errors are reduced to 0.2%, 0.07%, 0.25%, and 1.3%. The mean time average $E_{d/s}$ are 0.235, 0.237, 0.277, 0.246 for u, v, ρ, and p respectively. For the maximum relative errors, the corresponding values for $Re = 100$ are 2.8%, 0.6%, 2.4%, and 6.5% in the solution with a coarse grid, and 0.7%, 0.13%, 0.6%, and 1.8% in the solution with a fine grid. The mean time average $E_{d/s}$ are 0.20, 0.225, 0.24, 0.23. Figures 3.7-a, c and 3.10-a, c are the plots of the maximum errors of the four mentioned relative errors. In most of the time, the error in calculating the pressure is highest. The oscillation of the errors is due to the rough oscillation that we impose on the exact solutions. For coarse step sizes, because of the hyperbolicity of the density equation, the density errors are slowly increasing with time. However, this effect reduces significantly at higher resolution. In Figures 3.7-b, d, and 3.10-b, d, we also plot the absolute errors of the divergence free conditions. For both of the

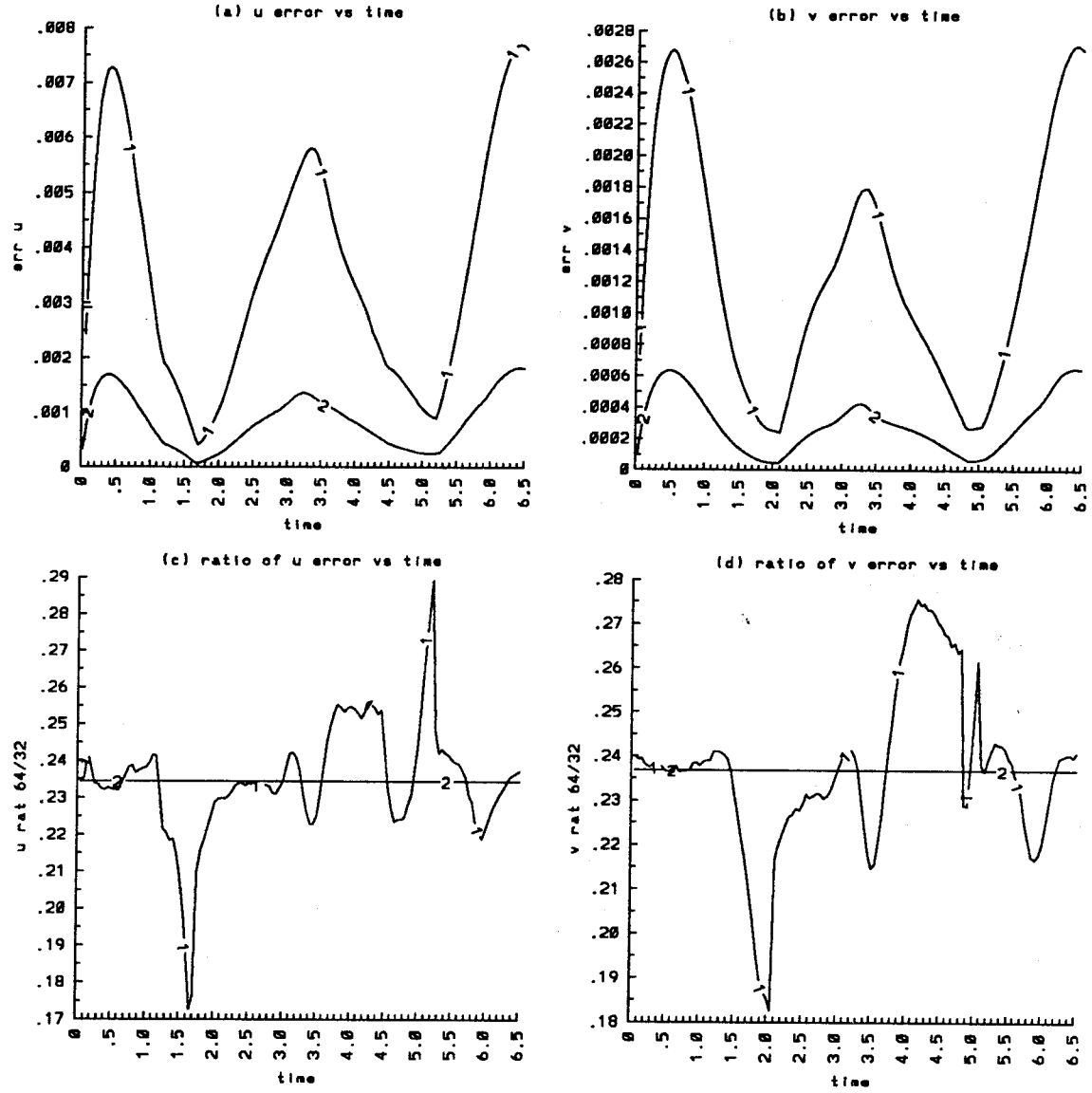

Figure 3.5 Time evolution of the velocity error $Re = 10$ a) maximum u error b) maximum v error: curve 1–32 grid points, curve 2–64 grid points c) curve 1– ratio of the u error 64/32 in (a), curve 2–time mean average of the ratio error d) same as (c) but for v in (b).

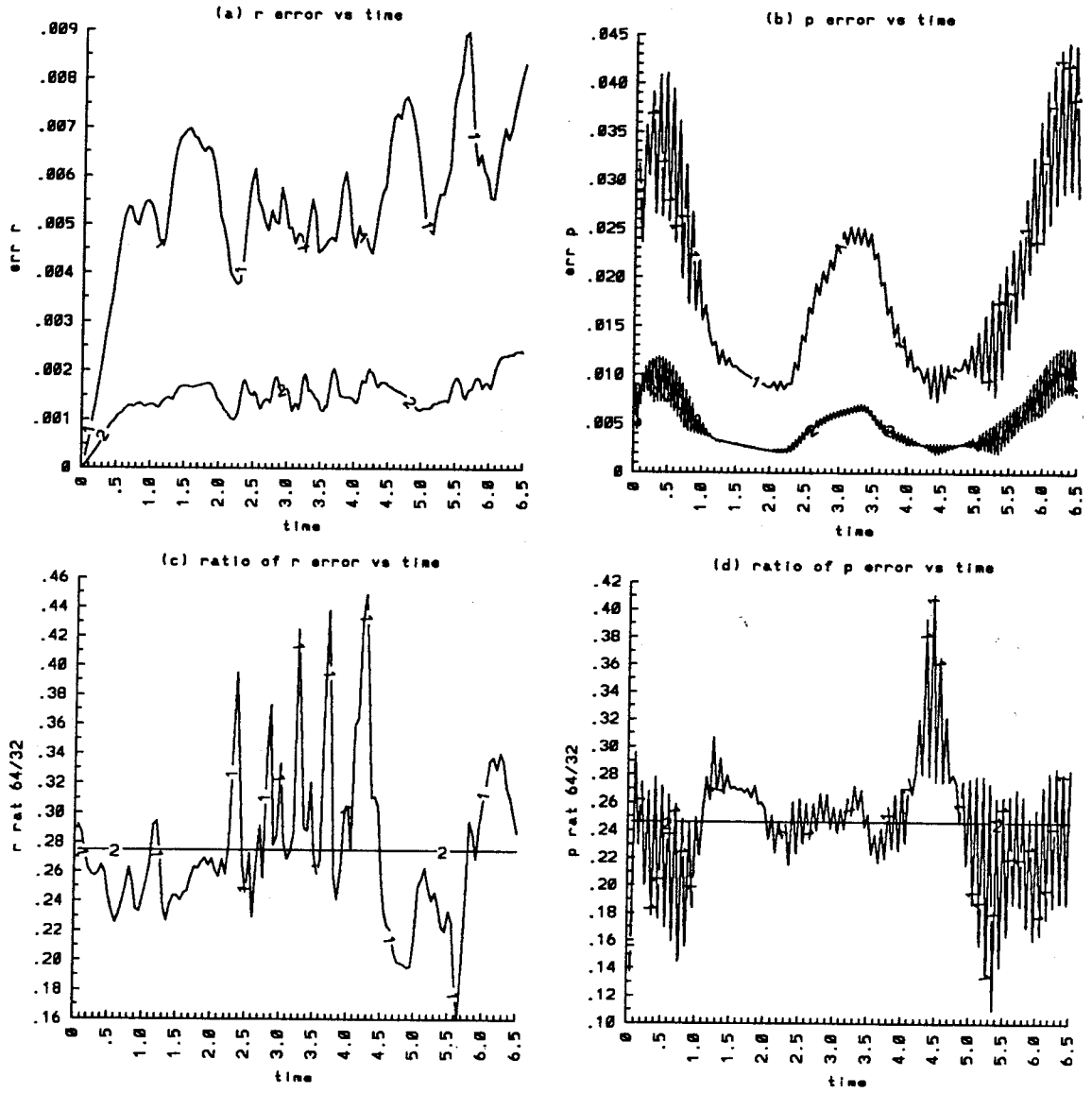

Figure 3.6 Time evolution of the density and pressure error $Re = 10$ a) maximum ρ error b) maximum p error: curve 1–32 grid points, curve 2–64 grid points c) curve 1– ratio of the ρ error 64/32 in (a), curve 2–time mean average of the ratio error d) same as (c) but for p in (b).

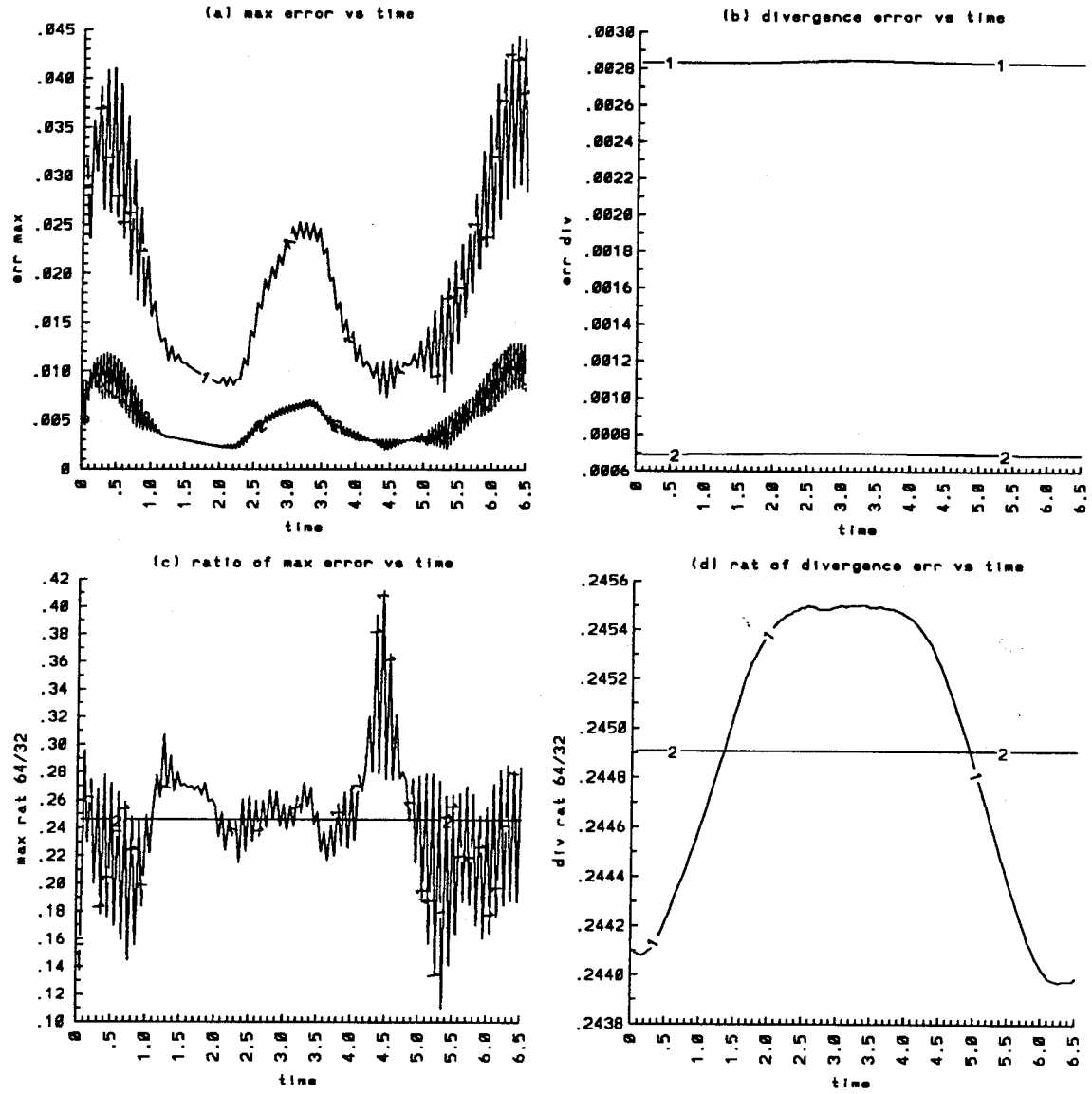

Figure 3.7 Time evolution of the maximum error and divergence free error $Re =$ 10 a) maximum error b) maximum $\nabla \cdot \mathrm{u}$ error: curve 1–32 grid points, curve 2–64 grid points c) curve 1– ratio of the maximum error 64/32 in (a), curve 2–time mean average of the ratio error d) same as (c) but for $\nabla \cdot \mathrm{u}$ in (b).

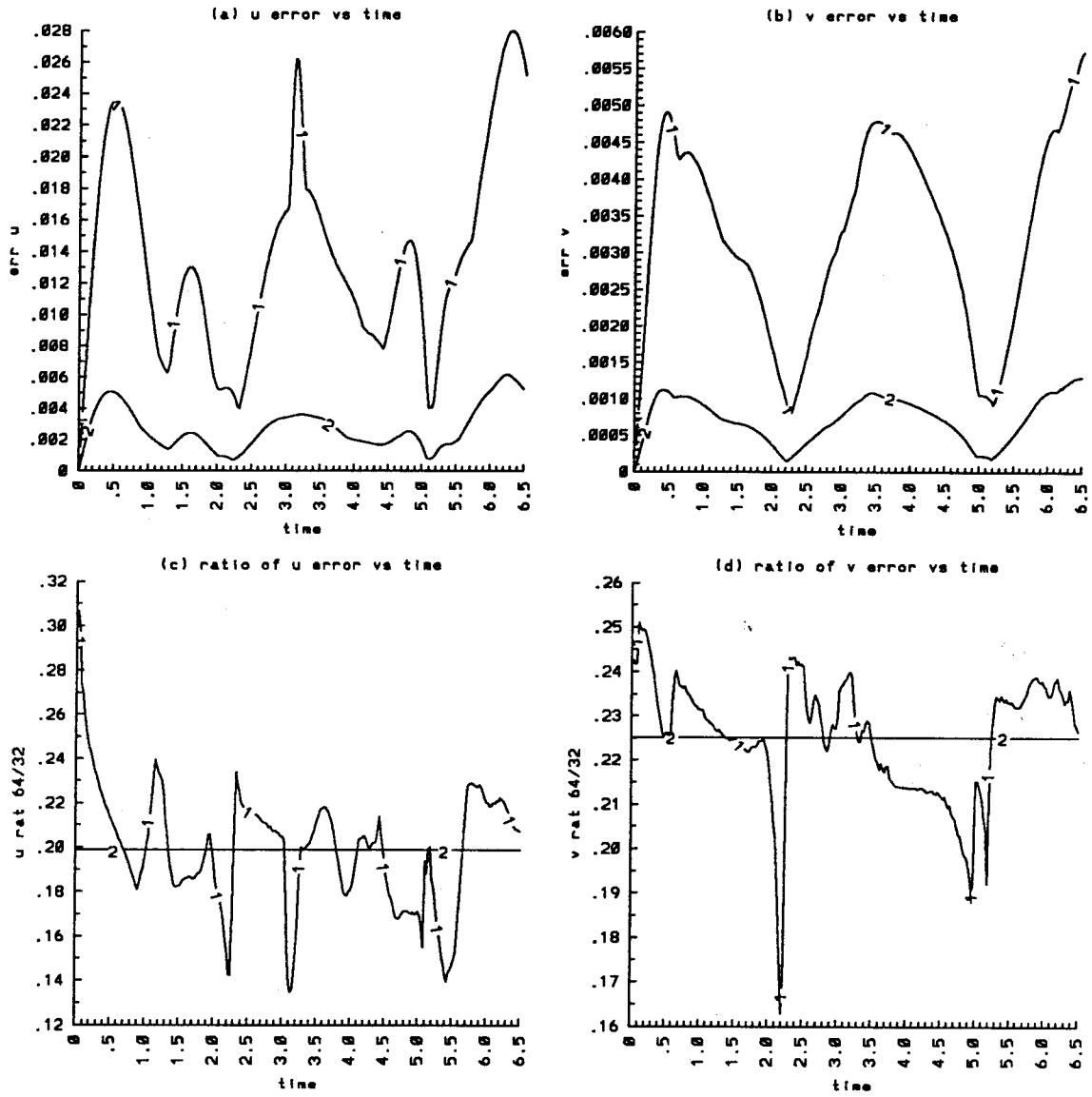

Figure 3.8 Time evolution of the velocity error $Re = 100$ a) maximum u error b) maximum v error: curve 1–32 grid points, curve 2–64 grid points c) curve 1–ratio of the u error 64/32 in (a), curve 2–time mean average of the ratio error d) same as (c) but for v in (b).

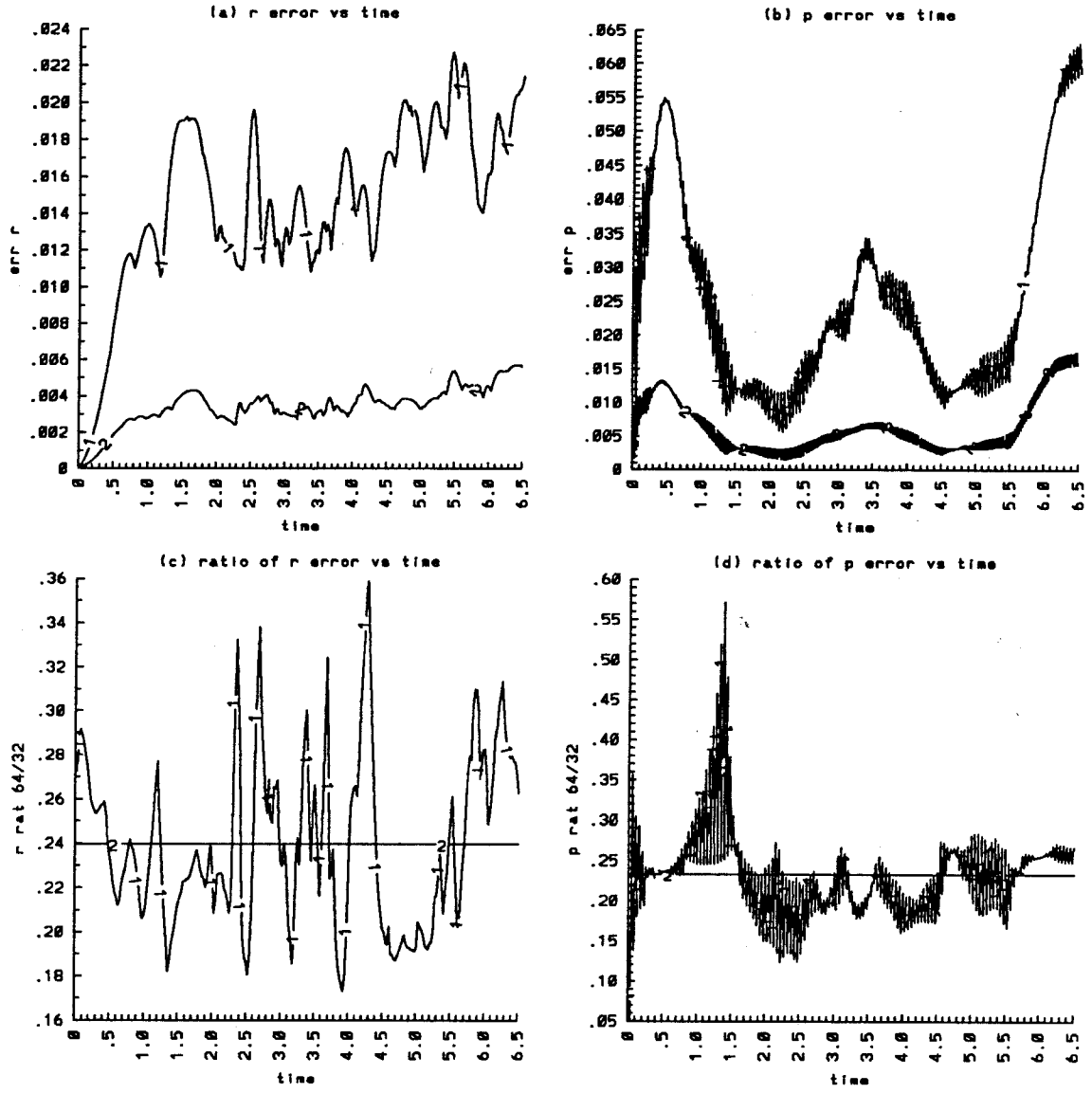

Figure 3.9 Time evolution of the density and pressure error $Re = 100$ a) maximum ρ error b) maximum p error: curve 1–32 grid points, curve 2–64 grid points c) curve 1– ratio of the ρ error 64/32 in (a), curve 2–time mean average of the ratio error d) same as (c) but for p in (b).

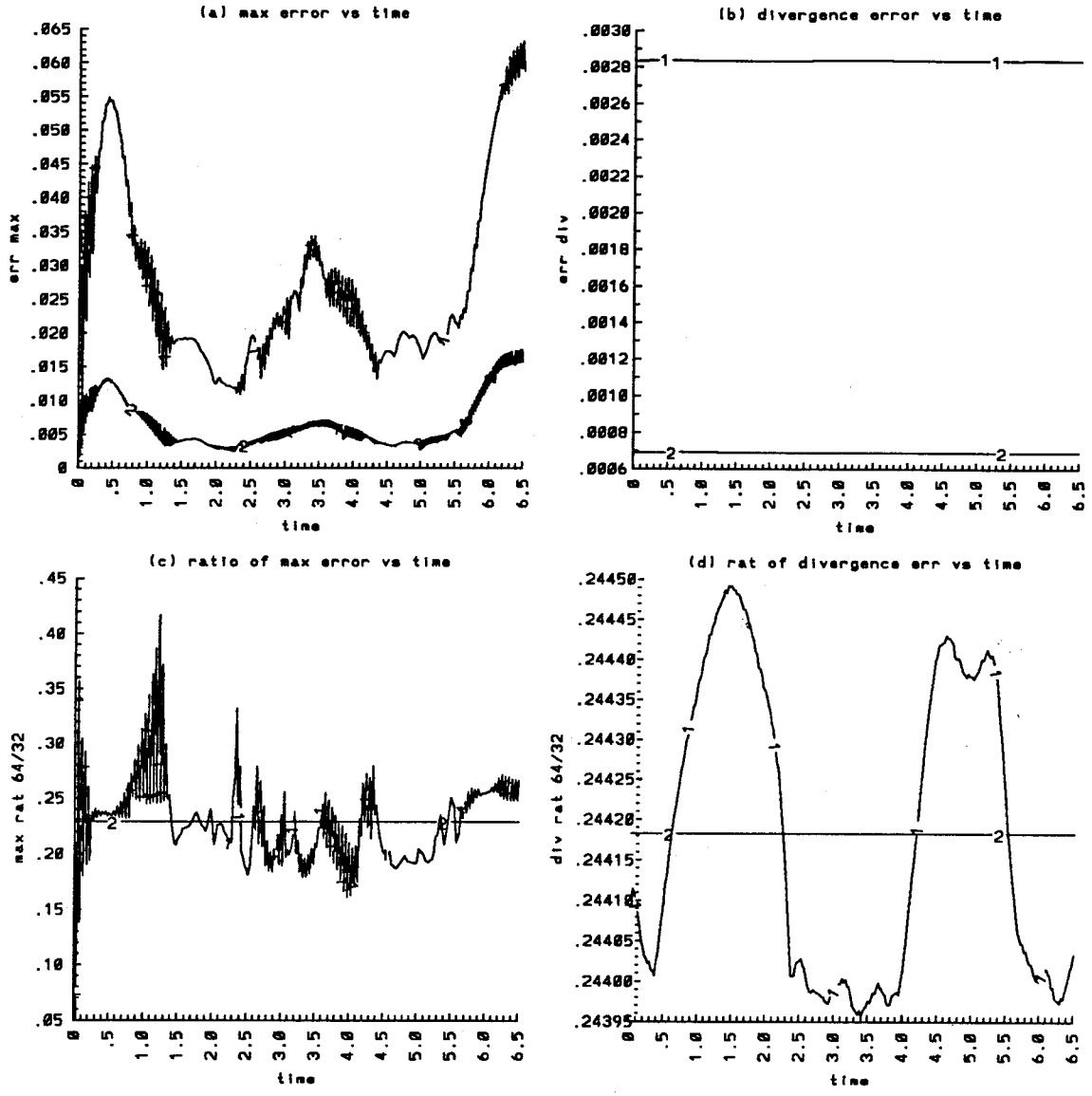

Figure 3.10 Time evolution of the maximum error and divergence free error $Re = 100$ a) maximum error b) maximum $\nabla \cdot \mathrm{u}$ error: curve 1–32 grid points, curve 2–64 grid points c) curve 1– ratio of the maximum error 64/32 in (a), curve 2–time mean average of the ratio error d) same as (c) but for $\nabla \cdot \mathrm{u}$ in (b).

Re numbers, the divergences are consistently around 28×10^{-4}, and 7×10^{-4} for 32 by 32, and 64 by 64 grid respectively. The order of these errors is consistent with the step sizes used.

In summary, we conclude that for the particular artificial problem considered, our time dependent code gives accurate solutions of errors less than 4.5% for $Re = 10$, and 6.5% for $Re = 100$ when a coarse grid is used. The corresponding errors for a grid with double resolution are reduced to less than 1.3% and 1.8%. On the mean time average, the errors reduce approximately fourfold when the spatial and temporal step sizes are reduced by one-half, and hence our code is second order accurate in time and space. Since our problem is time dependent, it is neccessary to have some justifications for the validity of the solution as time increases. In the next section, we will check our solution at initial times using the linearized Navier-Stokes equations. A discussion of the validity of the solution for long times is also included.

3.7 Accuracy of the solution in time

The short time and long time justification of our solution are discussed in this section. We first formulate the linearized Navier-Stokes equations applicable to our problem. Then, in order to illustrate the stability of our implicit scheme as opposed to an explicit one, a numerical solution using the MAC method and the explicit Lax scheme is given. Finally, in the end, we discuss the results of these calculations.

3.7.1 Linearized Navier-Stokes equations

For a short initial time interval, it is possible to check our time dependent result against the solution of the time linearized Navier-Stokes equations. Let our solution have the following expansion in time,

$$u = u_0 + tu_1 + t^2u_2 + \cdots,$$

$$v = v_0 + tv_1 + t^2 v_2 + \cdots,$$
$$p = p_0 + tp_1 + t^2 p_2 + \cdots, \tag{3.34}$$
$$\rho = \rho_0 + t\rho_1 + t^2 \rho_2 + \cdots.$$

Substitute this expansion into equations (3.7) to (3.10), we have the following set of equations:

$$O(t): \quad \rho_1 = -\Big\{u_0\rho_{ox} + (v_0 - V)\,\rho_{oy}\Big\},$$
$$u_1 + \frac{p_{ox}}{\rho_0} = -\Big\{\left(u_0^2\right)_x + \left(u_0\left(v_0 - V\right)\right)_y - \frac{1}{\rho_0 Re}\nabla^2 u_0\Big\},$$
$$v_1 + \frac{p_{oy}}{\rho_0} = -\Big\{\left(u_0\left(v_0 - V\right)\right)_x + \Big(\left(v_0 - V\right)^2\Big)_y - \frac{1}{\rho_0 Re}\nabla^2 v_0\Big\},$$
$$0 = u_{ox} + v_{oy}. \tag{3.35}$$

$$O\left(t^2\right): \quad \rho_2 = -\frac{1}{2}\Big\{u_0\rho_{1x} + u_1\rho_{ox} + (v_0 - V)\,\rho_{1y} + v_1\rho_{oy}\Big\},$$
$$u_2 + \frac{p_{1x}}{2\rho_0} = -\frac{1}{2\rho_0}\Big\{u_1\rho_1 + \left(u_0^2\right)_x\rho_1 + 2\rho_0\left(u_0u_1\right)_x + \rho_1\left(u_0\left(v_0 - V\right)\right)_y$$
$$+ \rho_0\left(u_0v_1 + \left(v_0 - V\right)u_1\right)_y - \frac{1}{Re}\nabla^2 u_1\Big\},$$
$$v_2 + \frac{p_{1y}}{2\rho_0} = -\frac{1}{2\rho_0}\Big\{v_1\rho_1 + \rho_1\left(u_0\left(v_0 - V\right)\right)_x + \rho_0\left(u_0v_1 + \left(v_0 - V\right)u_1\right)_x$$
$$+ \rho_1\Big(\left(v_0 - V\right)^2\Big)_y + 2\rho_0\left(\left(v_0 - V\right)v_1\right)_y - \frac{1}{Re}\nabla^2 v_1\Big\},$$
$$0 = u_{1x} + v_{1y}. \tag{3.36}$$

$$O\left(t^3\right): \quad \rho_3 = -\frac{1}{3}\Big\{u_0\rho_{2x} + u_1\rho_{1x} + u_2\rho_{ox} + (v_0 - V)\,\rho_{2y} + v_1\rho_{1y} + v_2\rho_{oy}\Big\},$$
$$u_3 + \frac{p_{2x}}{3\rho_0} = -\frac{1}{3\rho_0}\Big\{u_1\rho_2 + 2u_2\rho_1 + \left(u_0^2\right)_x\rho_2 + 2\rho_1\left(u_0u_1\right)_x + \rho_0\left(u_1^2 + 2u_0u_2\right)_x$$
$$+ \rho_2\left(u_0\left(v_0 - V\right)\right)_y + \rho_1\left(u_0v_1 + \left(v_0 - V\right)u_1\right)_y$$
$$+ \rho_0\left(u_0v_2 + u_1v_1 + \left(v_0 - V\right)u_2\right)_y - \frac{1}{Re}\nabla^2 u_2\Big\}, \tag{3.37}$$
$$v_3 + \frac{p_{2y}}{3\rho_0} = -\frac{1}{3\rho_0}\Big\{v_1\rho_2 + 2v_2\rho_1 + \rho_0\left(u_0v_2 + u_1v_1 + u_2\left(v_0 - V\right)\right)_x$$
$$+ \rho_2\left(u_0\left(v_0 - V\right)\right)_x + \rho_1\left(u_0v_1 + \left(v_0 - V\right)u_1\right)_x + \rho_2\Big(\left(v_0 - V\right)^2\Big)_y$$
$$+ 2\rho_1\left(\left(v_0 - V\right)v_1\right)_y + \rho_0\left(2\left(v_0 - V\right)v_2 + v_1^2\right)_y - \frac{1}{Re}\nabla^2 v_2\Big\},$$
$$0 = u_{2x} + v_{2y}.$$

Similar to the solution of the initial pressure in section 3.4, we use the MAC method to solve for p_1, and p_2. The artificial pressure boundary condition is again used. Once p_1, and p_2 are determined, the second and third order problems are completely specified.

3.7.2 Lax scheme and MAC method

A crucial property of a time dependent scheme is its stability as time increases. Due to the implicit nature of our scheme, we can obtain a stable numerical solution for a very long time. This stability is not obtained in an explicit scheme. To experiment, we use the MAC method to solve for the velocity and the pressure field, and the Lax scheme to obtain the evolution of the density. In the MAC method, we solve for the pressure field as in section 3.4, and the velocities are updated using the momentum equations. For a uniform grid with equal step size in both of the directions, stability condition of the MAC method requires,

$$\Delta t \leq \min\left(\frac{h^2 \rho Re}{4}\right). \tag{3.38}$$

The Lax scheme for the density is,

$$\begin{aligned}\rho_{ij}^{n+1} = & \frac{1}{4}\left(\rho_{i+1j}^{n} + \rho_{i-1j}^{n} + \rho_{ij+1}^{n} + \rho_{ij-1}^{n}\right) \\ & - \frac{\Delta t}{2h}\left((\rho u)_{i+1j}^{n} - (\rho u)_{i-1j}^{n}\right) \\ & - \frac{\Delta t}{2}\eta_u^{'}\left((\rho(v-V))_{ij+1}^{n} - (\rho(v-V))_{ij-1}^{n}\right).\end{aligned} \tag{3.39}$$

The Courant condition for this explicit time scheme is

$$\Delta t \leq \frac{1}{\sqrt{2}}\left(\frac{u^2}{h^2} + \frac{(v-V)^2\gamma^2}{\Delta\tau^2}\right)^{-\frac{1}{2}}. \tag{3.40}$$

A full necessary and sufficient condition for the stability of the overall scheme is not derived, but the two criteria given above provide a good guide for the choice of time step size relative to the spatial ones.

3.7.3 Comparison with perturbation and MAC method

In order to test the accuracy of our solution in a short initial time interval, we compare it to the first and second order solution of the time linearized Navier-Stokes equation. The long time accuracy of our scheme is based on a heuristic extension of the Lax's equivalence theorem for a linear operator, which states that: *given a properly posed initial-value problem and a finite difference approximation to it that satisfies the consistency condition, stability is the necessary and sufficient condition for convergence.* Since our equations are nonlinear, strictly speaking the stability criteria has no theoretical support. However, one hopes that Lax's theorem is true to some extent in the nonlinear problem, and if it is we can say that our implicit scheme provides the necessary stability condition, and hence convergence to a genuine solution. To illustrate this property, we solve the problem using an explicit algorithm which uses the MAC method for updating the velocity and the pressure field, and the Lax scheme for advancing the density.

For this test, we use the initial density profile given in equation (2.73), with A = − 0.5, $\epsilon = 0.3$, and $Re = 10^6$ on a 101 by 100 grid. In order to measure the differences between the various solutions, we define the following quantities for u,

$$E_{u1} = \frac{\|u_{MAC} - u\|_\infty}{\|u\|_\infty}$$

$$E_{u2} = \frac{\|u_0 + tu_1 - u\|_\infty}{\|u\|_\infty}$$

$$E_{u3} = \frac{\|u_0 + tu_1 + t^2u_2 - u\|_\infty}{\|u\|_\infty}$$

$$E_{u4} = \frac{\|\frac{u - u_0}{t} - u_1\|_\infty}{\|u\|_\infty}$$

$$E_{u5} = \frac{\|\frac{u - u_0}{t^2} - \frac{u_1}{t} - u_2\|_\infty}{\|u\|_\infty}$$

where u, u_{MAC}, u_0, u_1, and u_2 denote the u component of the velocity as computed by our numerical scheme, the explicit scheme, the zero, first, and second order

linearization. For v, ρ, and p, we define similar terms with the subscripts u in the above expressions for the errors E replaced accordingly.

In Figure 3.11 we plot the time evolution of E_{u1}, E_{u2}, E_{u3}, and in Figures 3.12, to 3.14 similar results for v, ρ, and p without the term E_{p3}. Our numerical results show consistency with the perturbation solution. The differences as compared to the first order problem are larger than those of the second order one. Up to time $t = 2.0$, the maximum deviation of the four variables is less than 4.4% for the first order problem, and 1.5% for the second one. The results of the explicit scheme are consistent with the implicit scheme except for the density which diverges quickly. This difference in the time behavior between the density and the other variables indicates a weak coupling between the density and the momentum equations, which is an important fact supporting our linear model discussed in the later section.

For a short initial time, the perturbation solution can be regarded as representative of the true solution. As shown in Figure 3.13, the large deviation between the explicit and the perturbation solution of the density even at short time is an illustration of the interdependency between stability and convergence in Lax's equivalence theorem. For long time simulation, since we are interested in the inviscid regime of the instability, a good measure of the stability of the scheme is its ability to conserve the input energy. Hence, in all of our simulations, we compute the time evolution of the following total kinetic energy,

$$K.E. = \frac{1}{2} \int \int \rho \left((v - V)^2 + u^2 \right) dxdy.$$

In Figures 3.15 and 3.16, we plot respectively the time evolution of the total kinetic energy of the second intial random profile for the Atwood number $A = -0.2$, and $A = -0.8$. The details of this initial density distribution will be discussed in Chapter 4. In this discussion, however, it is sufficient to note that for low Atwood number, the conservation of energy is extremely good, and the scheme is very stable as shown in Figure 3.15. The energy decreases linearly with time, and up to time $t = 90$, less than 1.23% of the initial energy has been dissipated. Note that around

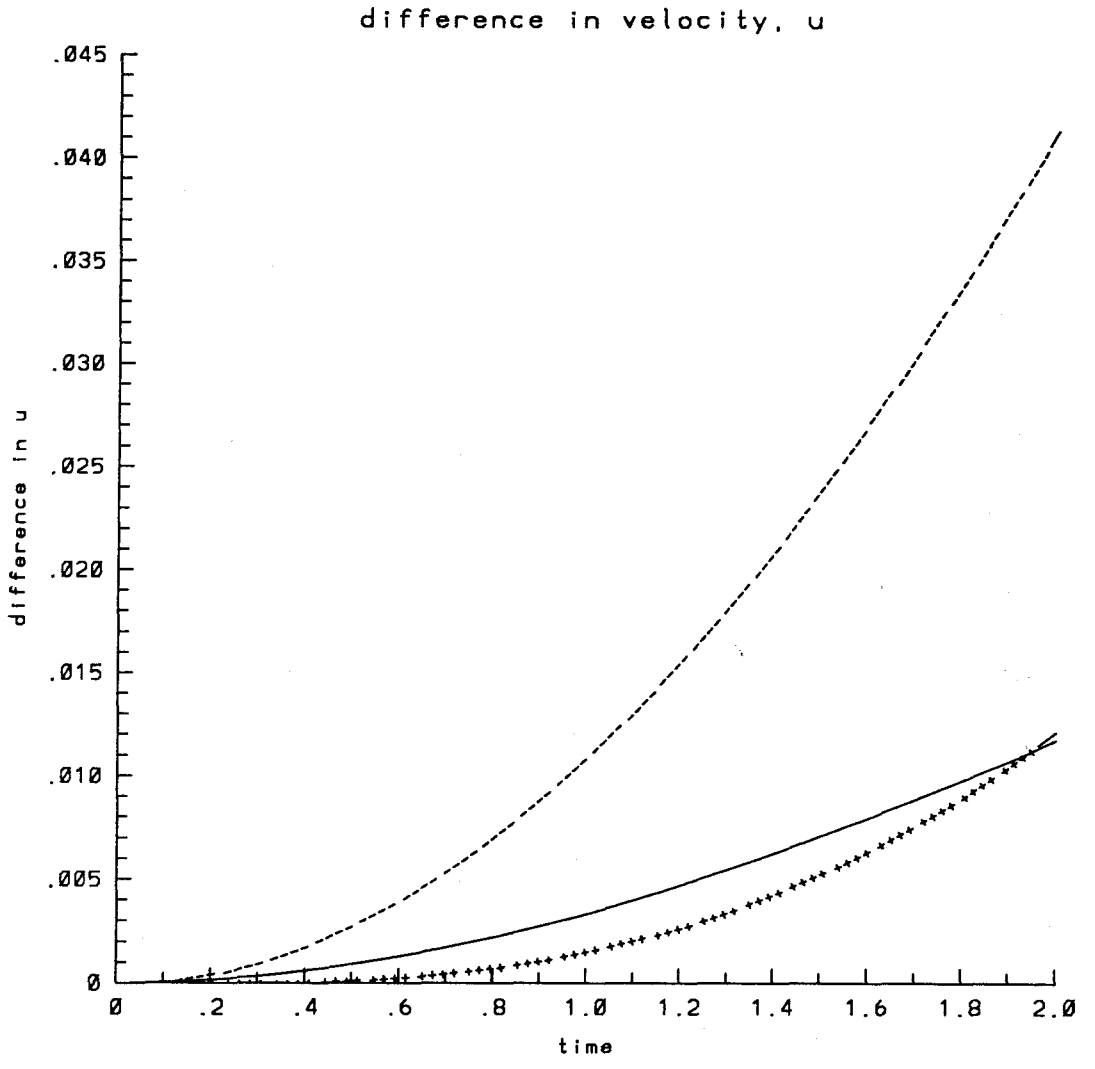

Figure 3.11 Time evolution of the difference in the velocity u as computed from the artificial compressibility method and : a) —— the MAC method b) $- - -$ the first order, and c) $+ + +$ the second order solution of the time linearized Navier-Stokes equation. The difference is normalized with the maximum value of u.

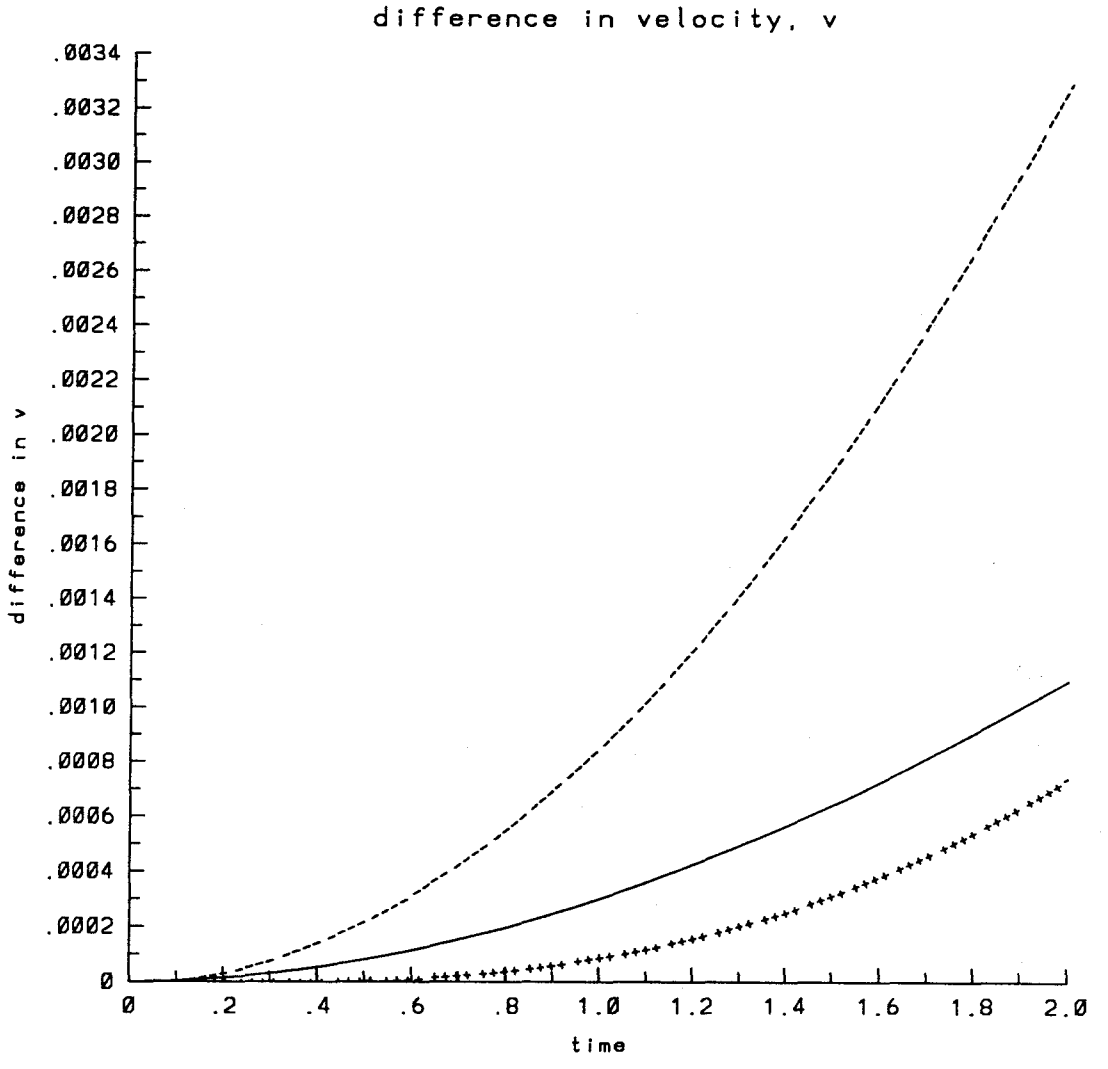

Figure 3.12 Time evolution of the difference in the velocity v as computed from the artificial compressibility method and : a) —— the MAC method b) $---$ the first order, and c) $+++$ the second order solution of the time linearized Navier-Stokes equation. The difference is normalized with the maximum value of v.

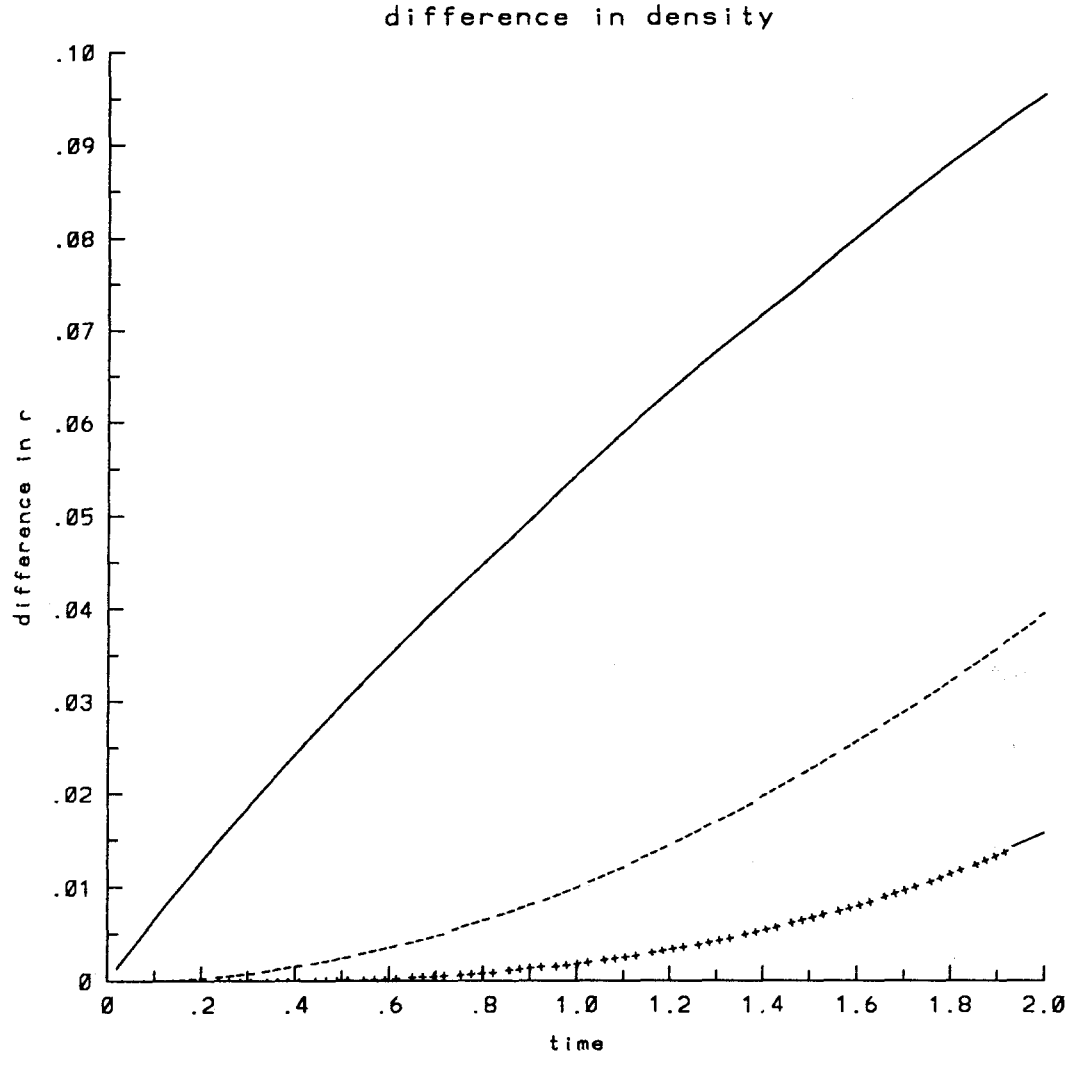

Figure 3.13 Time evolution of the difference in the density ρ as computed from the artificial compressibility method and : a) —— the MAC method b) $- - -$ the first order, and c) $+ + +$ the second order solution of the time linearized Navier-Stokes equation. The difference is normalized with the maximum value of ρ.

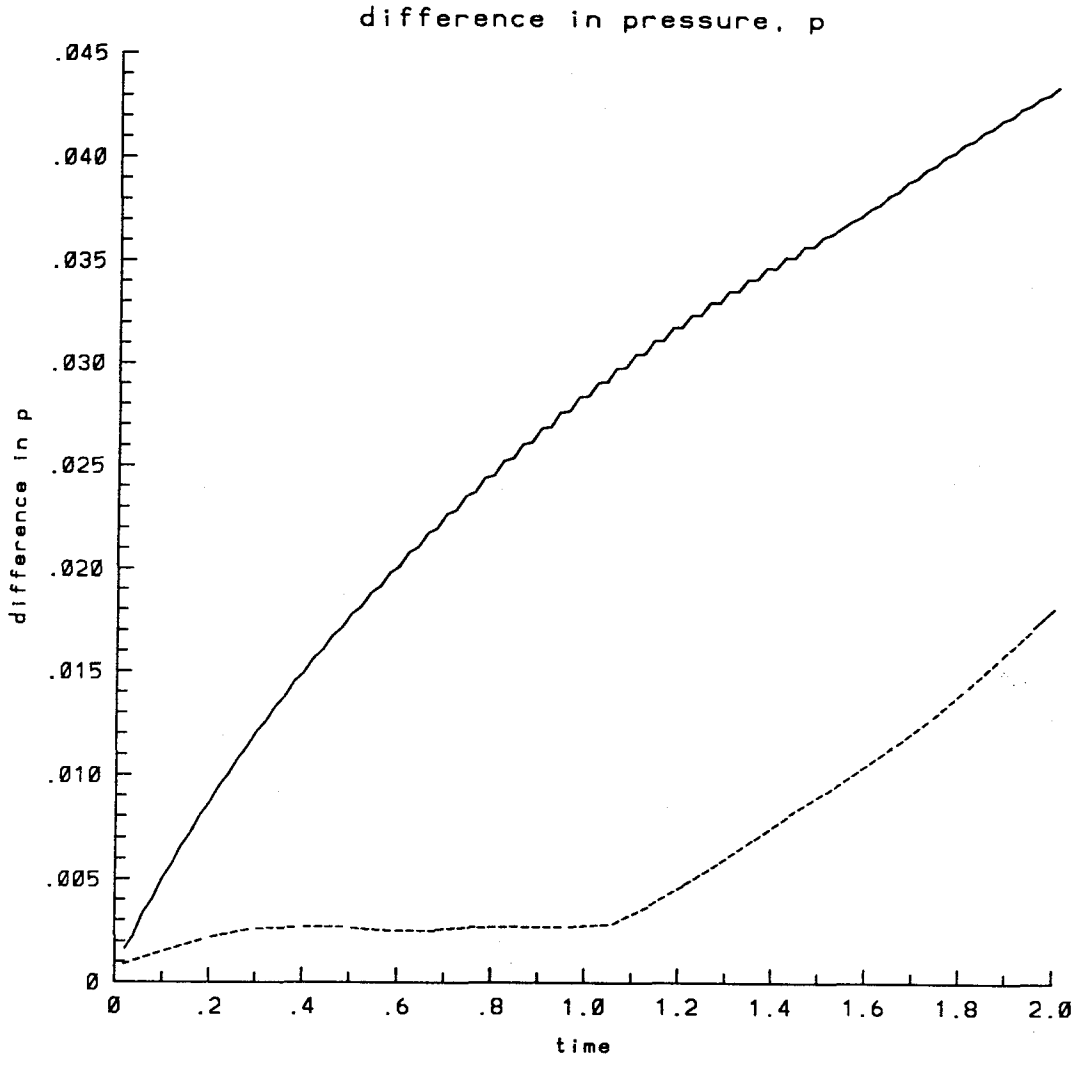

Figure 3.14 Time evolution of the difference in the pressure p as computed from the artificial compressibility method and : a) —— the MAC method, and b) – – – the first order solution of the time linearized Navier-Stokes equation. The difference is normalized with the maximum value of p.

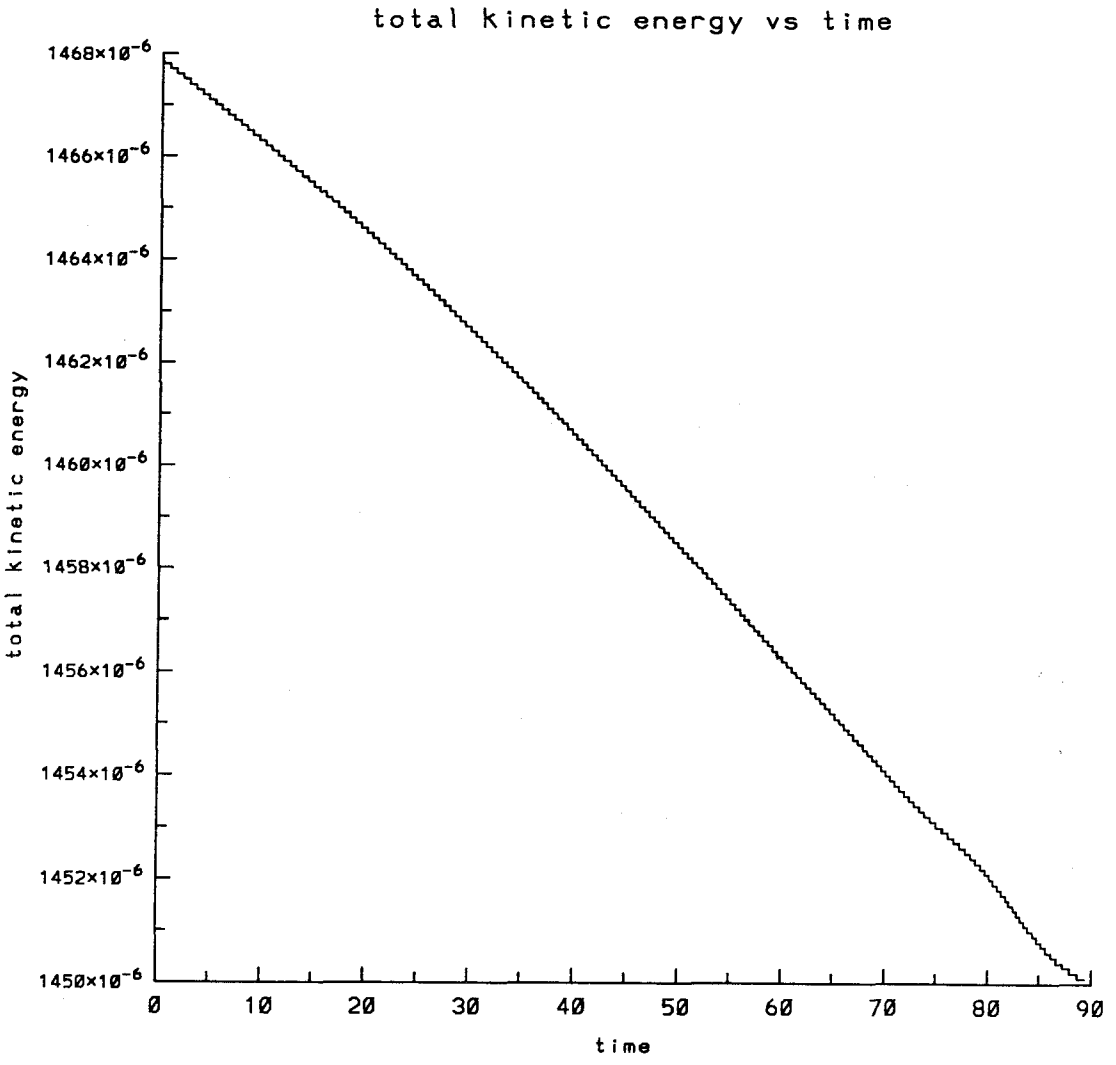

Figure 3.15 Time evolution of the total kinetic energy for the second initial random profile, A = -0.2, $t = 0$ to 89.34.

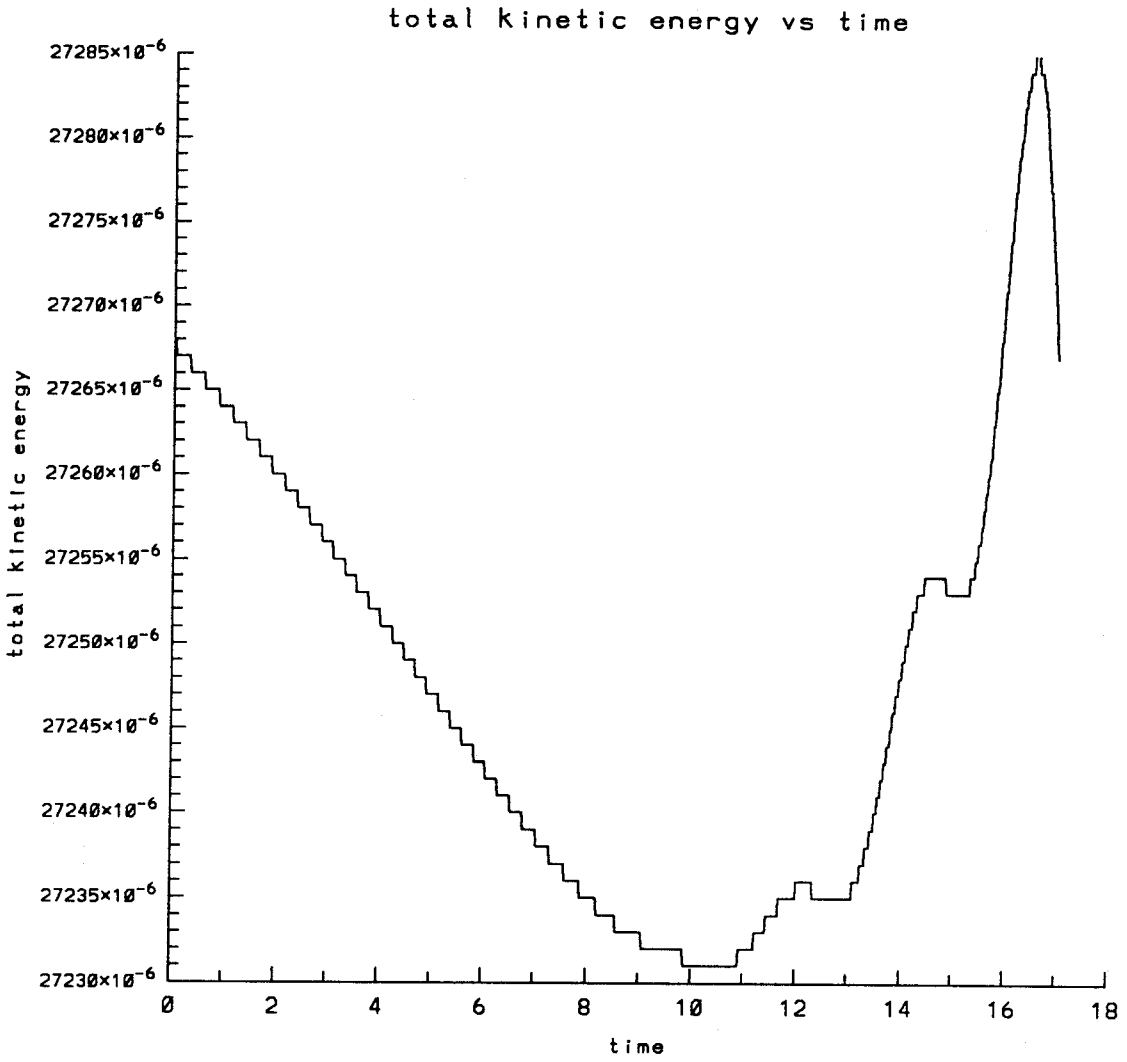

Figure 3.16 Time evolution of the total kinetic energy for the second initial random profile, A = −0.8, t = 0 to 17.

this time, there is a small oscillation in the energy curve. As the Atwood number increases, this oscillation appears at an earlier time. As shown in Figure 3.16, the oscillation starts around the time $t = 10$ for $A = -0.8$. In all calculations, the iterations do not converge after several oscillations. However, it is observed that the solution is still acceptable when the energy oscillates to around 3% higher than the initial energy. We use this condition as a criteria for stopping the calculation. With an enhanced resolution, it is possible to continue the calculation for a longer time.

Since our scheme is, in theory, second order accurate in time and space, we expect E_{u4}, E_{v4}, $E_{\rho 4}$, and E_{p4} to increase linearly in time. This linear dependency is clearly seen except for E_{p4} as shown in Figures 3.17 to 3.20. One possible reason for the deviation of E_{p4} from linearity is the lack of a time evolution equation for pressure in the governing equations. Hence, the pressure is not obtained by the Crank-Nicholson discretization as in the case of the velocity and the density. The second order in time and space of the scheme for the pressure is not guaranteed. Note that the E_{p4} decreases as t^g, where g is some negative number, initially and changes to linear behavior near $t = 1.0$. From this behavior of E_{p4} versus time, we can infer that the residual error in the pressure is of the order $O(\triangle t^q)$, where $0 < q \leq 1$. We also plot in Figures 3.17 to 3.19 the time evolution of E_{u5}, E_{v5}, and $E_{\rho 5}$. Since E_{u4}, E_{v4}, $E_{\rho 4}$, and $E_{\rho 5}$ are linear, while E_{u5}, and E_{v5} behave similarly to E_{p4}, with arguments similar to the case of E_{p4}, we can infer that the residual error of the velocity and the density are of the order $O(\triangle t^q)$, where $1 \leq q < 2$ for the velocity, and $q \geq 2$ for the density.

From the comparison with the perturbation and the explicit solution, we conclude that our numerical code gives consistent results in time with the scheme having the order $O(\triangle t^q)$, where $1 \leq q < 2$ for the velocity, $q \geq 2$ for the density, and $0 < q \leq 1$ for the pressure. The explicit scheme is highly unstable and there is a weak coupling between the density and the momentum equation. The linearity of the residual errors $E_{i4,5}$ where $i = u,\ v,\ \rho,\ p$ for time $t > 1$ indicates a weak

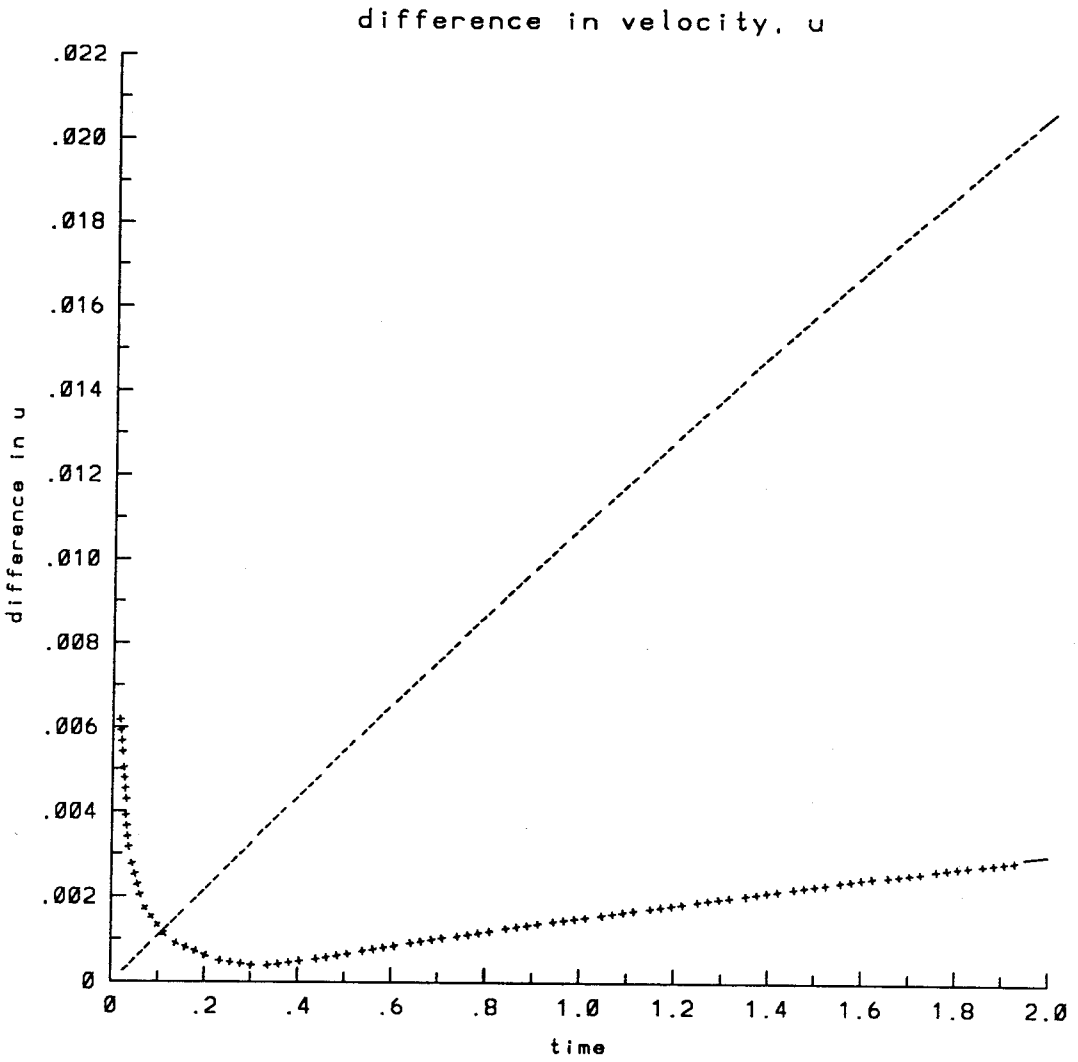

Figure 3.17 Time evolution of the difference : a) $---$ E_{u4}, and b) $+++$ E_{u5}. The difference is normalized with the maximum value of u.

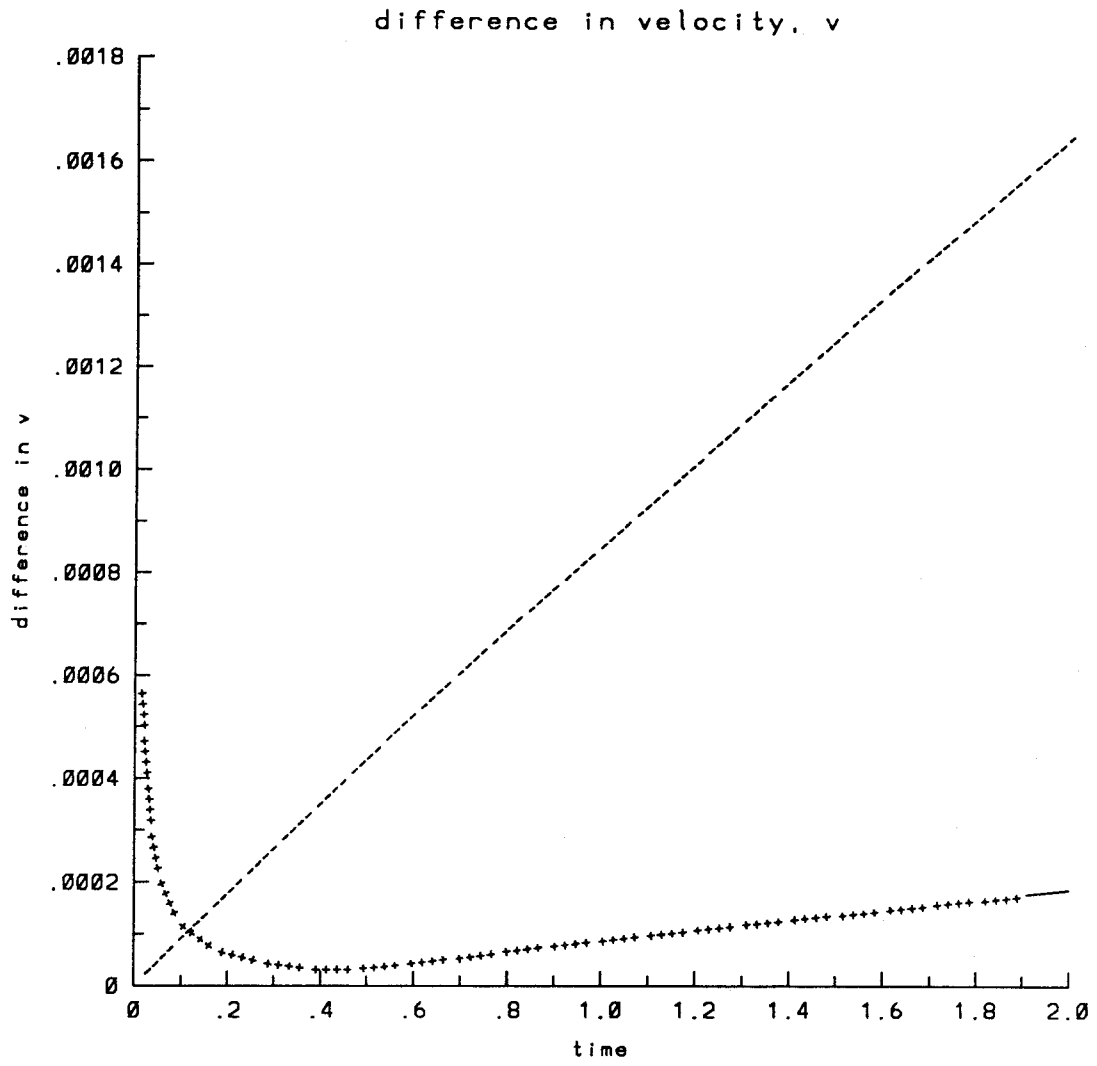

Figure 3.18 Time evolution of the difference : a) $---$ E_{v4}, and b) $+++$ E_{v5}. The difference is normalized with the maximum value of v.

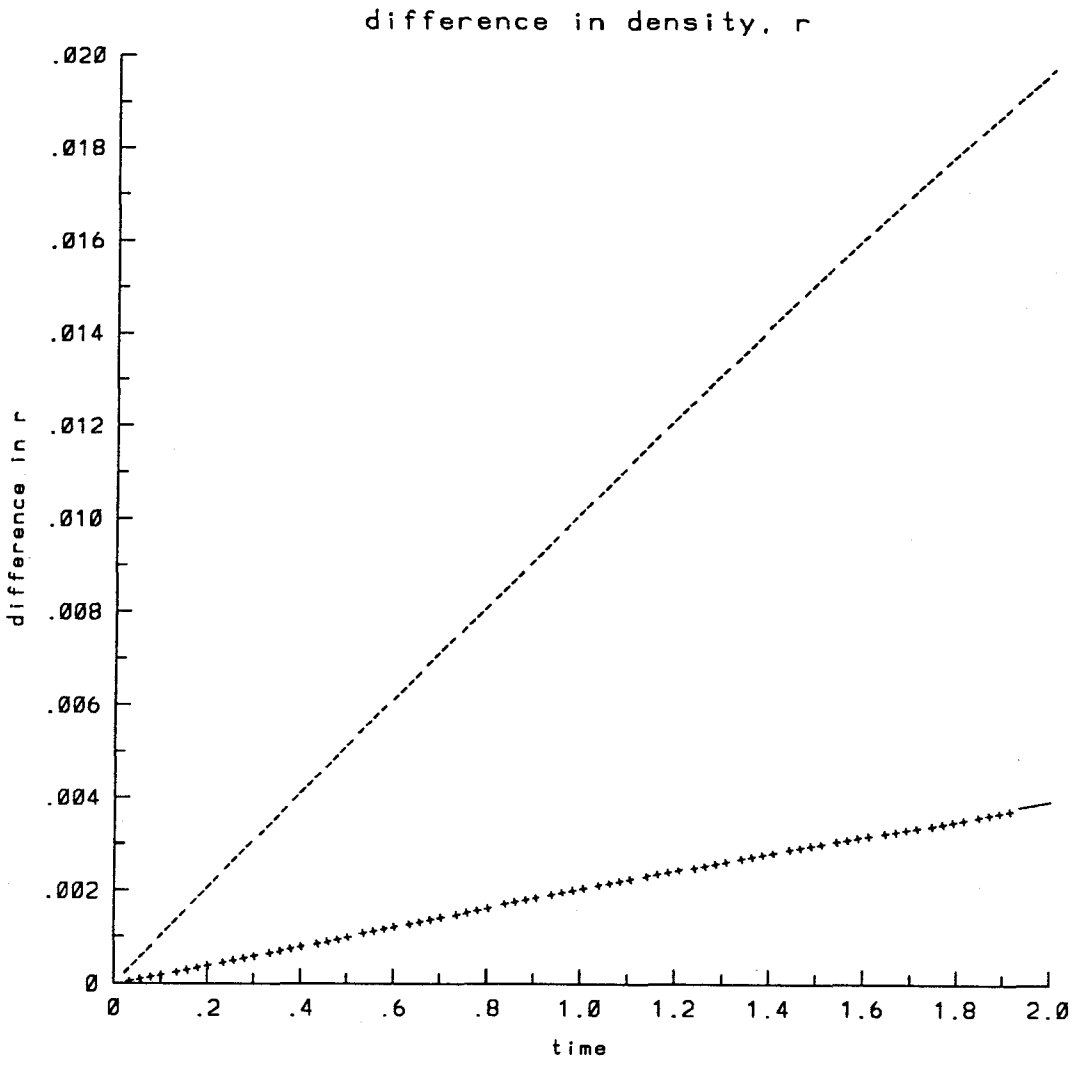

Figure 3.19 Time evolution of the difference : a) $---$ $E_{\rho 4}$, and b) $+++$ $E_{\rho 5}$. The difference is normalized with the maximum value of ρ.

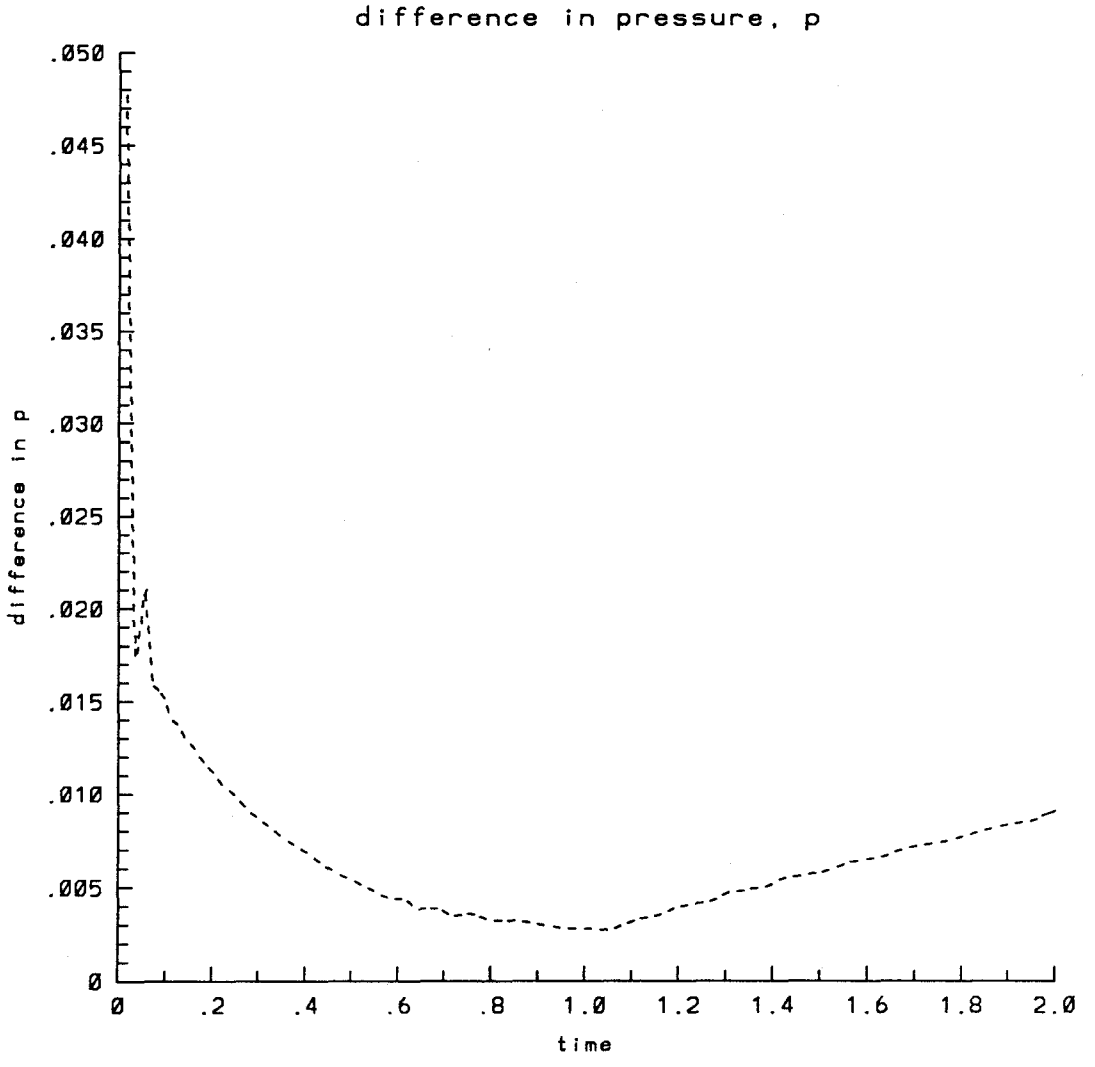

Figure 3.20 Time evolution of the difference E_{p4}. The difference is normalized with the maximum value of p.

dependence on time of the flow variables.

3.8 Newton-Raphson method

Another way to solve the nonlinear equation (3.16) is by the Newton-Raphson method. Let $\hat{u} = \hat{u}_0 + \hat{u}_1$ with similar perturbations for $\hat{v}, \hat{p}, \hat{\rho}$. The subscripts 0 and 1 respectively denote the present and the guessed values of a particular quantity in a Newton-Raphson iteration step. A linearization of the system (3.16) gives,

$$\begin{aligned}
&\hat{u}_1 + \alpha\Big\{2\left(\hat{u}_0+u\right)\hat{u}_{1x} + 2\left(\hat{u}_{ox}+u_x\right)\hat{u}_1 + \left(\hat{u}_{oy}+u_y\right)\hat{v}_1 + \hat{u}_{1y}\left(\hat{v}_0+v-V\right) \\
&\quad + \left(\hat{u}_0+u\right)\hat{v}_{1y} + \Big(\hat{v}_{oy} + \left(v-V\right)_y\Big)\hat{u}_1 - \frac{\hat{p}_{ox}+p_x}{\left(\hat{\rho}_0+\rho\right)^2}\hat{\rho}_1 + \frac{\hat{p}_{1x}}{\left(\hat{\rho}_0+\rho\right)} \\
&\quad + \frac{\nabla^2\left(\hat{u}_0+u\right)}{Re\left(\hat{\rho}_0+\rho\right)^2}\hat{\rho}_1 - \frac{\nabla^2\hat{u}_1}{Re\left(\hat{\rho}_0+\rho\right)}\Big\} = I_u, \qquad (3.41)
\end{aligned}$$

$$\begin{aligned}
&\hat{v}_1 + \alpha\Big\{\left(\hat{u}_{ox}+u_x\right)\hat{v}_1 + \left(\hat{v}_o+v-V\right)\hat{u}_{1x} + \left(\hat{u}_o+u\right)\hat{v}_{1x} + \hat{u}_1\left(\hat{v}_{ox} + \left(v-V\right)_x\right) \\
&\quad + 2\left(\hat{v}_0+v-V\right)\hat{v}_{1y} + 2\Big(\hat{v}_{oy} + \left(v-V\right)_y\Big)\hat{v}_1 - \frac{\hat{p}_{oy}+p_y}{\left(\hat{\rho}_0+\rho\right)^2}\hat{\rho}_1 + \frac{\hat{p}_{1y}}{\hat{\rho}_0+\rho} \\
&\quad + \frac{\nabla^2\left(\hat{v}_0+v\right)}{Re\left(\hat{\rho}_0+\rho\right)^2}\hat{\rho}_1 - \frac{\nabla^2\hat{v}_1}{Re\left(\hat{\rho}_0+\rho\right)}\Big\} = I_v, \qquad (3.42)
\end{aligned}$$

$$\begin{aligned}
&\hat{\rho}_1 + \alpha\Big\{\hat{u}_1\left(\hat{\rho}_{ox}+\rho_x\right) + \left(\hat{u}_0+u\right)\hat{\rho}_{1x} + \hat{v}_1\left(\hat{\rho}_{oy}+\rho_y\right) + \left(\hat{v}_0+v-V\right)\hat{\rho}_{1y}\Big\} \\
&\quad = I_r, \qquad (3.43)
\end{aligned}$$

$$\hat{u}_{1x} + \hat{v}_{1y} = I_d, \qquad (3.44)$$

where

$$\begin{aligned}
I_u = -\hat{u}_0 - \alpha\Big\{&2\left(\hat{u}_0+u\right)\hat{u}_{ox} + 2\left(\hat{u}_0+u\right)u_x + \left(\hat{u}_{oy}+u_y\right)\left(\hat{v}_0+v-V\right) \\
&+ \left(\hat{u}_0+u\right)\Big(\hat{v}_{oy} + \left(v-V\right)_y\Big) + \frac{\hat{p}_{ox}+p_x}{\hat{\rho}_0+\rho} - \frac{\nabla^2\left(\hat{u}_0+u\right)}{Re\left(\hat{\rho}_0+\rho\right)} + \left(u^2\right)_x \\
&+ \left(u\left(v-V\right)\right)_y + \frac{p_x}{\rho} - \frac{\nabla^2 u}{\rho Re}\Big\},
\end{aligned}$$

$$I_v = -\hat{v}_0 - \alpha\Big\{ (\hat{u}_{ox} + u_x)(\hat{v}_o + v - V) + (\hat{u}_0 + u)(\hat{v}_{ox} + (v-V)_x)$$
$$+ 2(\hat{v}_o + v - V)\left(\hat{v}_{oy} + (v-V)_y\right) + \frac{\hat{p}_{oy} + p_y}{\hat{\rho}_0 + \rho} - \frac{\nabla^2(\hat{v}_0 + v)}{Re(\hat{\rho}_0 + \rho)}$$
$$+ (u(v-V))_x + \left((v-V)^2\right)_y + \frac{p_y}{\rho} - \frac{\nabla^2 v}{\rho Re}\Big\},$$
$$I_r = -\hat{\rho}_0 - \alpha\Big\{ (\hat{u}_0 + u)(\hat{\rho}_{ox} + \rho_x) + (\hat{v}_0 + v - V)(\hat{\rho}_{oy} + \rho_y)$$
$$+ u\rho_x + (v-V)\rho_y\Big\},$$
$$I_d = -\hat{u}_{ox} - u_x - \hat{v}_{oy} - v_y.$$

The above four equations for the four unknowns $\hat{u}_1, \hat{v}_1, \hat{p}_1, \hat{\rho}_1$ can be discretized and solved by direct Gaussian elimination. However, due to the number of unknowns, and the constraints of computer memory, direct solution is prohibitive. Instead of solving the system directly, we use an iterative method that sweeps in the x-direction, and continuously updates the variables after each sweep. Let k denote the k^{th} iteration of a particular Newton-Raphson step. For each iteration, at the center point ij of a u, v, p cell, we have respectively the following discretizations of the u, v, ρ, and the continuity equation,

$$\left(-\frac{A_u}{2h} + \frac{H_u}{h^2}\right)\hat{u}^{k+1}_{1i-1j} + J\hat{v}^{k+1}_{1i-1j} + J\hat{\rho}^{k+1}_{1i-1j} + J\hat{p}^{k+1}_{1i-1j}$$
$$+ \left(B_u - \frac{2H_u}{h^2} - 2H_u\eta_u^{'2}\right)\hat{u}^{k+1}_{1ij} + \left(\frac{C_u}{4} + \frac{E_u\eta_u^{'}}{2}\right)\hat{v}^{k+1}_{1ij} + \frac{F_u}{2}\hat{\rho}^{k+1}_{1ij} - \frac{G_u}{h}\hat{p}^{k+1}_{1ij}$$
$$+ \left(\frac{A_u}{2h} + \frac{H_u}{h^2}\right)\hat{u}^{k+1}_{1i+1j} + \left(\frac{C_u}{4} + \frac{E_u\eta_u^{'}}{2}\right)\hat{v}^{k+1}_{1i+1j} + \frac{F_u}{2}\hat{\rho}^{k+1}_{1i+1j} + \frac{G_u}{h}\hat{p}^{k+1}_{1i+1j}$$
$$= -\frac{C_u}{4}(\hat{v}^k_{1i+1j-1} + \hat{v}^k_{1ij-1}) - D_u\eta_u^{'}D_y\hat{u}^k_{1ij} + \frac{E_u}{2}\eta_u^{'}(\hat{v}^k_{1ij-1} + \hat{v}^k_{1i+1j-1})$$
$$-H_u\left((\hat{u}^k_{1ij+1} + \hat{u}^k_{1ij-1})\eta_u^{'2} + \eta_{2u}^{''}D_y\hat{u}^k_{1ij}\right) + I_u, \tag{3.45}$$

$$\left(-\frac{B_v}{2h} + \frac{D_v}{4}\right)\hat{u}^{k+1}_{1i-1j} + \left(-\frac{C_v}{2h} + \frac{H_v}{h^2}\right)\hat{v}^{k+1}_{1i-1j} + J\hat{\rho}^{k+1}_{1i-1j} + J\hat{p}^{k+1}_{1i-1j}$$
$$+ \left(\frac{B_v}{2h} + \frac{D_v}{4}\right)\hat{u}^{k+1}_{1ij} + \left(A_v - \frac{2H_v}{h^2} - 2H_v\eta_v^{'2}\right)\hat{v}^{k+1}_{1ij} + \frac{F_v}{2}\hat{\rho}^{k+1}_{1ij} - G_v\eta_v^{'}\hat{p}^{k+1}_{1ij}$$

$$
\begin{aligned}
&+J\hat{u}_{1i+1j}^{k+1}+\left(\frac{C_v}{2h}+\frac{H_v}{h^2}\right)\hat{v}_{1i+1j}^{k+1}+J\hat{\rho}_{1i+1j}^{k+1}+J\hat{p}_{1i+1j}^{k+1}\\
&=-\frac{D_v}{4}\left(\hat{u}_{1i-1j+1}^{k}+\hat{u}_{1ij+1}^{k}\right)-\frac{B_v}{2h}\left(\hat{u}_{1ij+1}^{k}-\hat{u}_{1i-1j+1}^{k}\right)-E_v\eta_v^{'}D_y\hat{v}_{ij}^{k}\\
&-\frac{F_v}{2}\hat{\rho}_{1ij+1}^{k}-G_v\eta_v^{'}\hat{p}_{ij+1}^{k}-H_v\left(\eta_v^{'2}\left(\hat{v}_{1ij+1}^{k}+\hat{v}_{1ij-1}^{k}\right)+\eta_{2v}^{''}D_y\hat{v}_{1ij}^{k}\right)\\
&+I_v,
\end{aligned}
\tag{3.46}
$$

$$
\begin{aligned}
&\frac{A_r}{2}\hat{u}_{1i-1j}^{k+1}+J\hat{v}_{1i-1j}^{k+1}-\frac{B_r}{2h}\hat{\rho}_{1i-1j}^{k+1}+J\hat{p}_{1i-1j}^{k+1}\\
&+\frac{A_r}{2}\hat{u}_{1ij}^{k+1}+\frac{C_r}{2}\hat{v}_{1ij}^{k+1}+\hat{\rho}_{1ij}^{k+1}+J\hat{p}_{1ij}^{k+1}\\
&+J\hat{u}_{1i+1j}^{k+1}+J\hat{v}_{1i+1j}^{k+1}+\frac{B_r}{2h}\hat{\rho}_{1i+1j}^{k+1}+J\hat{p}_{1i+1j}^{k+1}\\
&=-\frac{C_r}{2}\hat{v}_{1ij-1}^{k}-D_r\eta_u^{'}D_y\hat{\rho}_{1ij}^{k}+I_r,
\end{aligned}
\tag{3.47}
$$

$$
\begin{aligned}
&-\frac{1}{h}\hat{u}_{1i-1j}^{k+1}+J\hat{v}_{1i-1j}^{k+1}+J\hat{\rho}_{1i-1j}^{k+1}+J\hat{p}_{1i-1j}^{k+1}\\
&+\frac{1}{h}\hat{u}_{1ij}^{k+1}+\eta_u^{'}\hat{v}_{1ij}^{k+1}+J\hat{\rho}_{1ij}^{k+1}+J\hat{p}_{1ij}^{k+1}\\
&+J\hat{u}_{1i+1j}^{k+1}+J\hat{v}_{1i+1j}^{k+1}+J\hat{\rho}_{1i+1j}^{k+1}+J\hat{p}_{1i+1j}^{k+1}\\
&=\eta_u^{'}\hat{v}_{1ij-1}^{k}+I_d,
\end{aligned}
\tag{3.48}
$$

where

$$A_u=2\alpha\left(\hat{u}_0+u\right)$$

$$B_u=1+\alpha\left(2\left(\hat{u}_{ox}+u_x\right)+\hat{v}_{oy}+\left(v-V\right)_y\right)$$

$$C_u=\alpha\left(\hat{u}_{oy}+u_y\right)$$

$$D_u=\alpha\left(\hat{v}_0+v-V\right)$$

$$E_u=\alpha\left(\hat{u}_0+u\right)$$

$$F_u=\alpha\left(-\frac{\hat{p}_{ox}+p_x}{\left(\hat{\rho}_0+\rho\right)^2}+\frac{\nabla^2\left(\hat{u}_0+u\right)}{Re\left(\hat{\rho}_0+\rho\right)^2}\right)$$

$$G_u = \frac{\alpha}{\hat{\rho}_0 + \rho}$$

$$H_u = -\frac{\alpha}{Re\,(\hat{\rho}_0 + \rho)}$$

$$A_v = 1 + \alpha\,(\hat{u}_{ox} + u_x + 2\,(\hat{v}_{oy} + (v - V)_y))$$

$$B_v = \alpha\,(\hat{v}_o + v - V)$$

$$C_v = \alpha\,(\hat{u}_o + u)$$

$$D_v = \alpha\,(\hat{v}_{ox} + (v - V)_x)$$

$$E_v = 2\alpha\,(\hat{v}_0 + v - V)$$

$$F_v = \alpha\left(-\frac{\hat{p}_{oy} + p_y}{(\hat{\rho}_0 + \rho)^2} + \frac{\nabla^2\,(\hat{v}_0 + v)}{Re\,(\hat{\rho}_0 + \rho)^2}\right)$$

$$G_v = \frac{\alpha}{\hat{\rho}_0 + \rho}$$

$$H_v = -\frac{\alpha}{Re\,(\hat{\rho}_0 + \rho)}$$

$$A_r = \alpha\,(\hat{\rho}_{ox} + \rho_x)$$

$$B_r = \alpha\,(\hat{u}_o + u)$$

$$C_r = \alpha\,(\hat{\rho}_{oy} + \rho_y)$$

$$D_r = \alpha\,(\hat{v}_o + v - V)$$

$$J = 0.$$

The unknowns are arranged in the following order,

$$\hat{u}^k_{i-1,j}, \hat{v}^k_{i-1,j}, \hat{\rho}^k_{i-1,j}, \hat{p}^k_{i-1,j}, \hat{u}^k_{i,j}, \hat{v}^k_{i,j}, \hat{\rho}^k_{i,j}, \hat{p}^k_{i,j}, \hat{u}^k_{i+1,j}, \hat{v}^k_{i+1,j}, \hat{\rho}^k_{i+1,j}, \hat{p}^k_{i+1,j}.$$

This results in a doubly-bordered band diagonal matrix with a bandwidth of 15 elements. The bordering is due to the periodic boundary condition in the x-direction. After convergence of quantities at iteration $k+1$, the guess for the Newton-Raphson iteration is updated and the procedure continues.

Figure 3.21 shows the differences of the flow variables in using these two methods for the case of A = -0.5, $\lambda = 1.0$, $\epsilon = 0.3$, Re = 10^4 with the initial density (2.73) on a 21 by 100 grid. The differences are taken at time t = 0, 4, 8, 12, 16, and

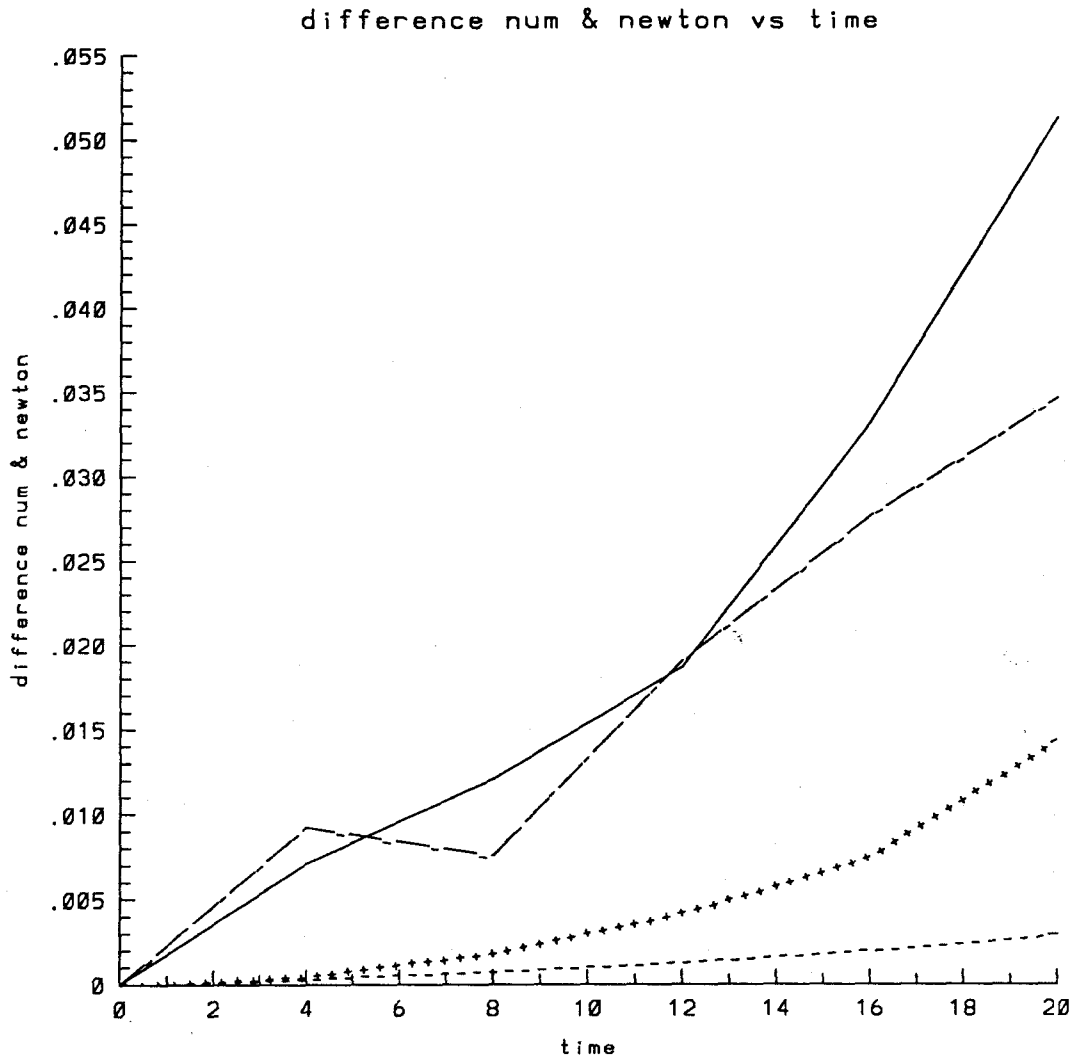

Figure 3.21 Time evolution of the differences in the flow variables obtained by the artificial compressibility method and the Newton-Raphson method for the pseudo-time problem. a) — u b) $- - -$ v c) $+ + +$ ρ d) — · — p.

20. The velocity and the density are normalized to their maximum values obtained from the artificial compressibility code. At the end of the time $t = 20$, the differences are respectively 5.1%, 0.29%, 1.4%, and 3.5% for the velocity u, v, the density ρ, and the pressure p. The differences in v between the two solutions are smallest for all time. The large difference in u and p are due to the magnitudes of maximum u and p being of order $O(10^{-2} - 10^{-3})$. Up to time $t = 4$, the difference between the two solutions are less than 1%. As the time for the simulation increases, the Newton scheme converges very slowly. This effect is due to the iteration of the resulting matrix in the Newton scheme instead of a direct inversion. Hence, the two solutions are slowly separating from each other as time increases. The total computing time for the Newton scheme is around four and one-half times more than the artificial compressibility method. Since we are interested in the multiple scale problem, the required fine grid resolution makes the direct inversion very difficult to implement, and the computing time too large for the time dependent study.

In conclusion, the above comparison with a solution obtained from Newton-Raphson method provides another accuracy check to our solution. However, the most important feature of this calculation is to show the robustness of our scheme, which is essential for the unsteady problem under consideration.

In this chapter, we have formulated a numerical scheme for solving the unsteady two-dimensional incompressible Richtmyer-Meshkov problem. We have also discussed several numerical tests to check its accuracy, stability, and efficiency. In the next chapter, simulation results on the growth of the Richtmyer-Meshkov instability will be presented.

CHAPTER 4

RESULTS

The numerical results of the simulation of Richtmyer-Meshkov instability are included in this chapter. In the first section, we define the average quantities which characterize the results of our numerical simulations. Section 2 describes the two kinds of initial density distribution considered. Since the instability is weak, a model for its initial development based solely on the action of the vorticity field imposed by the impulsive acceleration is developed. We call this the *' linear model'*, and its details are discussed in Section 3. In Section 4, we present the growth rates of a continuously stratified fluid layer as compared to those predicted by Richtmyer for a sharp fluid interface with an equivalent jump in density. The next two sections include the results of the simulation for both the single scale and random multiple scale perturbations of a stratified fluid.

4.1 Characteristic average quantities of the flow

In order to characterize our results, we consider two kinds of average quantitites for the density, one in the y-direction, and the other in the x-direction. The average in the y-direction is a function of x and is defined as follows,

$$\bar{\rho}_y(x) = \frac{2Y\rho_+ - \int_{-Y}^{Y} \rho(x,y)dy}{\rho_+ - \rho_-} - Y, \tag{4.1}$$

where Y is the maximum value of y in the region composed of the v cells, ρ_+, ρ_- is the uniform density as $y \to \pm\infty$ respectively.

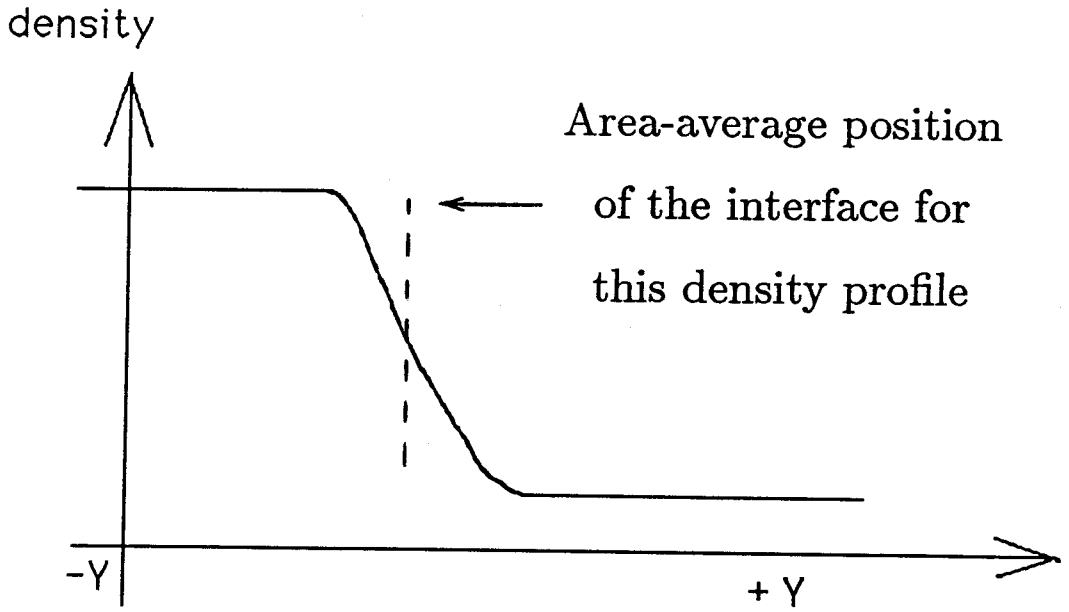

Figure 4.1 Dependence of the density on y for a fixed x.

For a given x, the density ρ is a function of y as shown in Figure 4.1, and equation (4.1) is a kind of area average of the density. The definition for $\bar{\rho}_y(x)$ defines an average interface for the stratified layer. It gives the exact functional form of a sharp interface $y = f(x)$ which separates two regions of uniform density ρ_+, and ρ_-. Hence, this definition is convenient for the comparision of the numerical results to those predicted by the Richtmyer theory (1960), since an average amplitude based on $\bar{\rho}_y(x)$ can be defined as,

$$a = \frac{\max\left(\bar{\rho}_y\left(x\right)\right) - \min\left(\bar{\rho}_y\left(x\right)\right)}{2}. \tag{4.2}$$

The growth of the instability is characterized by the time derivative of a. In our numerical code, we interpolate $\bar{\rho}_y(x)$ using cubic splines before a is computed so that a smooth growth rate da/dt as a function of time is obtained.

The second density average is defined as follows,

$$\bar{\rho}_x(y) = \frac{1}{2\pi}\int_0^{2\pi} \rho(x,y)dx, \tag{4.3}$$

which is the standard area average. From $\bar{\rho}_x(y)$, we can define a width δ of the stratified layer. Let y_+ be the position of $\bar{\rho}_x(y)$ such that,

$$y_+ = \min\left(\|\bar{\rho}_x(y) - \rho_+\| \leq d\|\rho_+ - \rho_-\|\right),$$

where d is some specified percentage for the cut off. Similarly, let y_- be such that,

$$y_- = \max\left(\|\bar{\rho}_x(y) - \rho_-\| \leq d\|\rho_+ - \rho_-\|\right).$$

Then the width of the density layer is defined as,

$$\delta = y_+ - y_-. \tag{4.4}$$

In searching for y_+, and y_-, we use linear interpolation with d taken to be 2%, *i.e.*, the width δ covers a distance over which the variation of the density within the layer is 98% of the maximum density jump.

4.2 Initial density distributions

In order to understand the growth of the instability, we consider two different kinds of initial density distributions. The first one which is also known as the single scale perturbation is of the form,

$$\rho(x,y) = \frac{1}{2}\left(1 + A\tanh\left(\frac{1}{L}\left(y - \epsilon\cos(x)\right)\right)\right), \tag{4.5}$$

where A is the Atwood number, and L is the characteristic thickness of the density layer. The factor $1/2$ normalizes the density to the interval from 0 to 1 for the maximum possible Atwood number of 1. For $L > 0$, equation (4.5) describes a continuously stratified interface. As L approaches zero, the layer reduces to a sharp

interface with ϵ as the amplitude of the perturbation. In his theory, Richtmyer (1960) considered the instability of a sharp interface with an infinitesimal perturbation subjected to an impulsive acceleration. With the density profile (4.5), we can justify our numerical results when L, and ϵ are taken to zero, in that order, for a sharp interface with infinitesimal perturbations. Besides this consistency check, this profile is convenient for the study of the nonlinear effects in the growth of the instability of a highly perturbed interface.

In view of a more realistic perturbation which occurs in experimental studies, we would like to have some randomness as well as multiple wave numbers presented in our initial distribution. To accomplish this effect, we replace $\cos(x)$ in equation (4.5) by the sum,

$$\sum_{k=1}^{N} e^{-\varsigma(k-1)^2} \left(\frac{1}{2} - r_{k1}\right) \cos(kx), \tag{4.6}$$

or

$$\sum_{k=1}^{N} e^{-\varsigma(k-1)^2} \left\{ \left(\frac{1}{2} - r_{k1}\right) \cos(kx) + \left(\frac{1}{2} - r_{k2}\right) \sin(kx) \right\}, \tag{4.7}$$

where k is the wave number, r_{k1}, r_{k2} are random numbers with $0 \leq r_{k1}, r_{k2} \leq 1$, and ς is a controlling parameter for the spread of the wave number distribution. For $N = 1$, $r_{k1} = -0.5$, and $r_{k2} = 0.5$, equations (4.6), and (4.7) reduce to $\cos(x)$.

For the single scale perturbation, we study the effects of the Atwood number (A), the perturbed amplitude (ϵ), and the characteristic length (L) on the development of the instability. For the multiple scale calculations, we only consider the role of the Atwood number on six different random intial profiles. The first four profiles are computed from equation (4.6), and the fifth and sixth random profiles from equation (4.7). Before the numerical results of these problems are presented, we discuss below a model for the initial growth of the instability.

4.3 'Linear' theory model

Due to the weak nature of the instability, we can assume that the initial flow

field caused by the passage of the shock, which is modeled by the action of an impulsive motion, is not altered significantly afterward. The role of the energy deposited at the initial instant in the subsequent growth of the instability is mainly to increase the mixing of the layer by moving the fluid particles in a Lagrangian fashion. We call this model of the instability, the 'linear' theory model. The linearity of the model is due to the fact that we have approximated the shock as an impulsive motion, and only the action of this flow field controls the later development.

Consider the distribution $\rho_0(x,\eta)$ of the density at a particular time t_0. At a later time $t = t_0 + \Delta t$, the distribution of the density is $\rho(x,\eta)$. The density at a node point ij, at time t, is the density of a fluid particle which has arrived at the point ij from a point having the coordinate (x_0,η_0), at a time Δt earlier (see Figure 4.2). Assume that the velocity of the fluid particle during this motion from the time t_0 to t is constant and equals to the velocity at the node point ij, (*i.e.*, the redistribution of the density does not affect the flow field significantly,) then the overall algorithm to obtain $\rho(x,\eta)$ from $\rho_0(x,\eta)$ is as follows.

1. Compute the velocity at center ij of the p cells,

$$\begin{aligned} u_c &= \frac{1}{2}\left(u_{ij} + u_{i-1,j}\right) \\ v_c &= \frac{1}{2}\left(v_{ij} + v_{i,j-1}\right) - V. \end{aligned} \tag{3.8}$$

2. Use this velocity to obtain the position (x_0,η_0) of the fluid particle at time t_0,

$$\begin{aligned} x_0 &= x_{ij} - u_c\Delta t \\ \eta_0 &= \eta_{ij} - v_c\Delta t \end{aligned} \tag{3.9}$$

3. Search for the square grid which contains the point (x_0,η_0). Due to our assumption of constancy of the velocity, we choose the time step so that (x_0,η_0) will lie very close to the point ij in one of its four adjacent squares.
4. The final step is to interpolate the density at (x_0,η_0) using ρ_0, and assign this value to the point ij. Let the coordinates of the corners of the square be

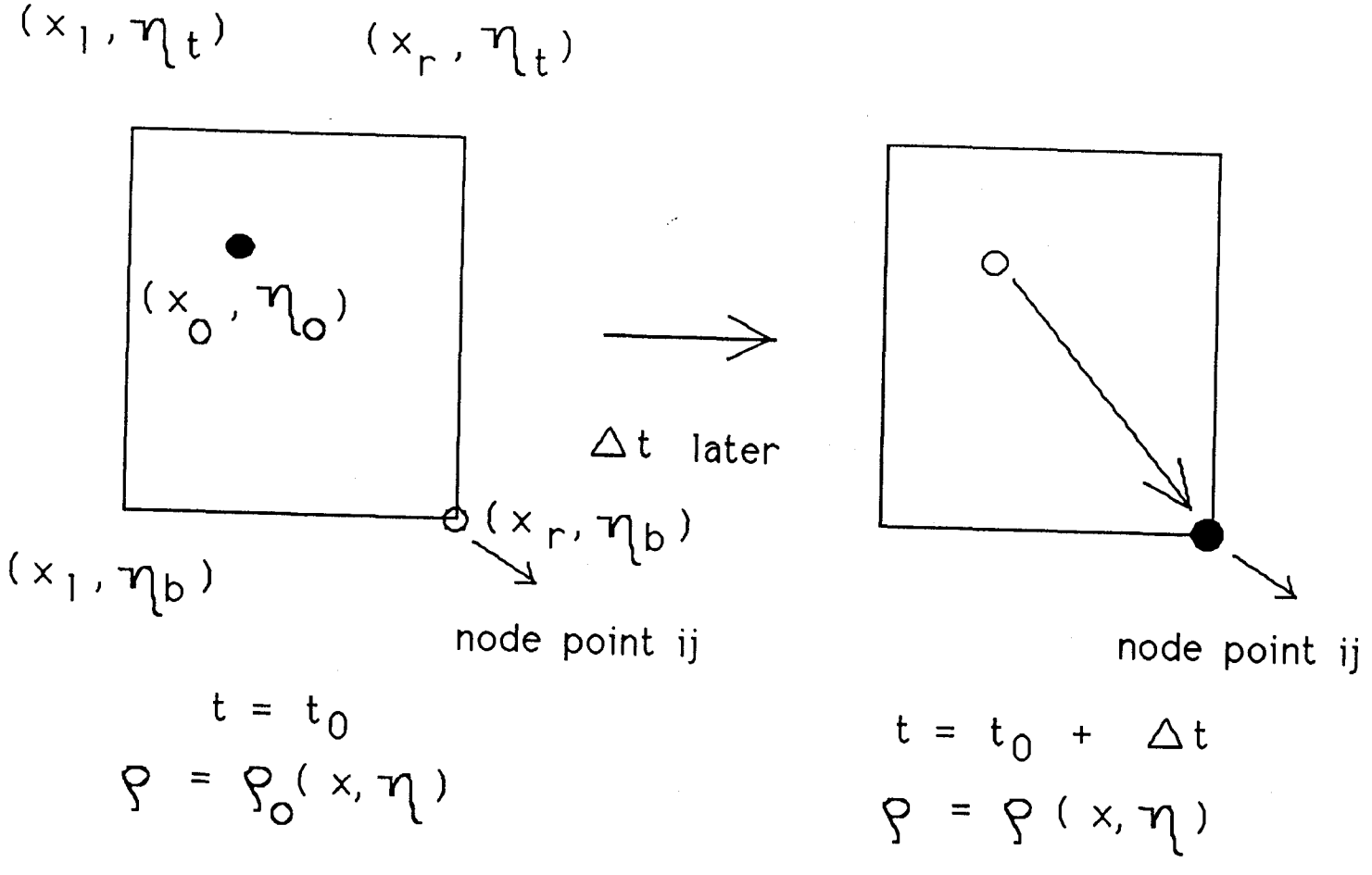

Figure 4.2 Motion of a fluid particle in the linear theory model.

(x_l, η_b), (x_r, η_b), (x_r, η_t), (x_l, η_t), where the subscripts l, r, b, t denote left, right, bottom, top respectively. Then (x_0, η_0) is normalized to

$$\begin{aligned} x_{on} &= \frac{x_0 - x_l}{x_r - x_l}, \\ \eta_{on} &= \frac{\eta_0 - \eta_b}{\eta_t - \eta_b}. \end{aligned} \tag{3.10}$$

The density at (x_0, η_0) is calculated from the density at the corners of the square using bilinear interpolation,

$$\begin{aligned} \rho_0(x_0, \eta_0) = (1 - x_{on})(1 - \eta_{on})\,\rho_0(x_l, \eta_b) + x_{on}(1 - \eta_{on})\,\rho_0(x_r, \eta_b) \\ + x_{on}\eta_{on}\rho_0(x_r, \eta_t) + (1 - x_{on})\,\eta_{on}\rho_0(x_l, \eta_t). \end{aligned} \tag{3.11}$$

The validity of this model for short time is expected to be very good. Hence, it can also be used as the fifth check on our numerical results.

4.4 Single scale initial growth rate

The initial density distribution in equation (4.5) for the single scale problem has three parameters. The Atwood number A is a measure of the density jump across the stratified layer; similarly L is a measure of the characteristic length of the width of the density layer, and ϵ is the amplitude of the perturbation. The density profile considered is convenient because it includes the sharp interface as a special case, *i.e.*, L $\to$ 0. In this section, we would like to study the dependence of the initial growth rate of the perturbation as a function of the three mentioned parameters.

The problem is solved on a 21 by 200 grid, with $\mu = 10^{-6}$, and $\Delta t = 0.002$. We consider three Atwood numbers A = -0.2, -0.5, and -0.8, five different characteristic lengths L = 0.001, 0.01, 0.1, 1.0, and 10.0, with four values of the perturbation amplitude ϵ = 0.01, 0.1, 1.0, and 10.0. In Table 4.1, we present the results of this study.

Table 4.1

Ratio of the initial Richtmyer growth rate over that of numerical simulation

A	$\epsilon \Downarrow$ L $\Rightarrow$	10.0	1.0	0.1	0.01	0.001
± 0.2	0.01	15.026	2.1280	1.1023	1.0283	1.0187
		0.02	0.2	0.8	0.85	0.93
	0.1	15.027	2.1304	1.1052	1.0163	1.0125
		0.02	0.2	0.8	0.8	0.8
	1.0	15.118	2.3657	1.3626	1.1503	1.0971
		0.008	0.2	0.2	0.2	0.2
	10.0	19.359	10.519	7.5656	7.5863	7.6016
		0.008	0.05	0.05	0.05	0.08
± 0.5	0.01	14.363	2.0371	1.0886	1.0266	1.0187
		0.02	0.2	0.8	0.85	0.93
	0.1	14.364	2.0365	1.0915	1.0147	1.0127
		0.02	0.2	0.8	0.8	0.8
	1.0	15.066	2.2155	1.3451	1.3329	1.3326
		0.008	0.2	0.2	0.2	0.2
	10.0	18.505	9.9856	6.9315	6.9807	6.9815
		0.008	0.05	0.05	0.05	0.05
± 0.8	0.01	12.776	1.8298	1.0580	1.0228	1.0187
		0.02	0.2	0.8	0.85	0.93
	0.1	12.776	1.8294	1.0608	1.0153	1.0590
		0.02	0.2	0.8	0.85	0.9
	1.0	12.842	2.0520	1.3040	1.2310	1.1956
		0.008	0.2	0.2	0.4	0.4
	10.0	16.554	8.8304	5.6359	6.0836	6.0445
		0.008	0.05	0.08	0.1	0.1

There are two numbers in each entry of the table. The first number is the ratio of the initial growth rate of the average amplitude as predicted by the Richtmyer theory over that of numerical simulation. In calculating the equivalent Richtmyer growth rate given in equation (2.18) for a continuous interface, we use the initial average amplitude defined in equation (4.2) as a_0, the velocity V of the flow at infinity as the jump velocity v_0 of the interface after the impulsive acceleration, and $k = 1$. The numerical growth rate is computed using forward differences in time. Since the growth rate is an odd function of A, the ratios of the growth rates for $\pm A$

are the same. Hence, the results reported here are also those for positive Atwood numbers. Due to the large variation in the density gradient for the various cases, we have to use different values of γ for the grid distribution. It should be recalled that γ is the controlling parameter for the grid distribution about the origin. The second entry in the table is the value of γ used.

The results in Table 4.1 are plotted in three sets of Figures 4.3-6, 4.7-10, 4.11-14. The first, second, and third set present respectively the ratios of the growth rates as functions of the characteristic length L, the perturbation amplitude ϵ, and the Atwood number A.

4.4.1 Effect of thickness on initial growth rate

As shown in Figures 4.3-6, for a given A, as L approaches zero, *i.e.*, a sharp interface, the ratios approaches finite limits which appear to be the lower bounds except for the cases of A = -0.8, and $\epsilon = 10.0$, in which there is a minimum around L = 0.1. For small perturbation amplitude ϵ, the limit approaches 1.0 from above, which seems to happen as early as L = 0.1. For L = 0.1 to L = 0.001, the ratios of the growth rate do not vary significantly. The ratios increase from L = 0.1 to L = 1.0. For a thicker interface L = 1.0 to L = 10.0, the ratios continue to grow to $O(10)$. For $\epsilon = 10.0$, L = 10.0, and A = 0.2, the ratio can be as high as 19.4. The corresponding values for A = 0.5 and 0.8 are respectively 18.5 and 16.6. Thus our numerical results are consistent with the predictions of the Richtmyer theory for a sharp interface. They also confirm the fact that by decreasing the density gradient, one can reduce the growth of the Richtmyer-Meshkov instability as predicted by the linear theory of Saffman and Meiron (1989). The results also agree qualitatively with the experiments of Brouillette (1989) in which he observes a tenfold reduction in the growth rate for a ratio of thickness to wavelength around 3. Thus, for a continuous interface, Richtmyer formula (2.18) overpredicts the growth rate.

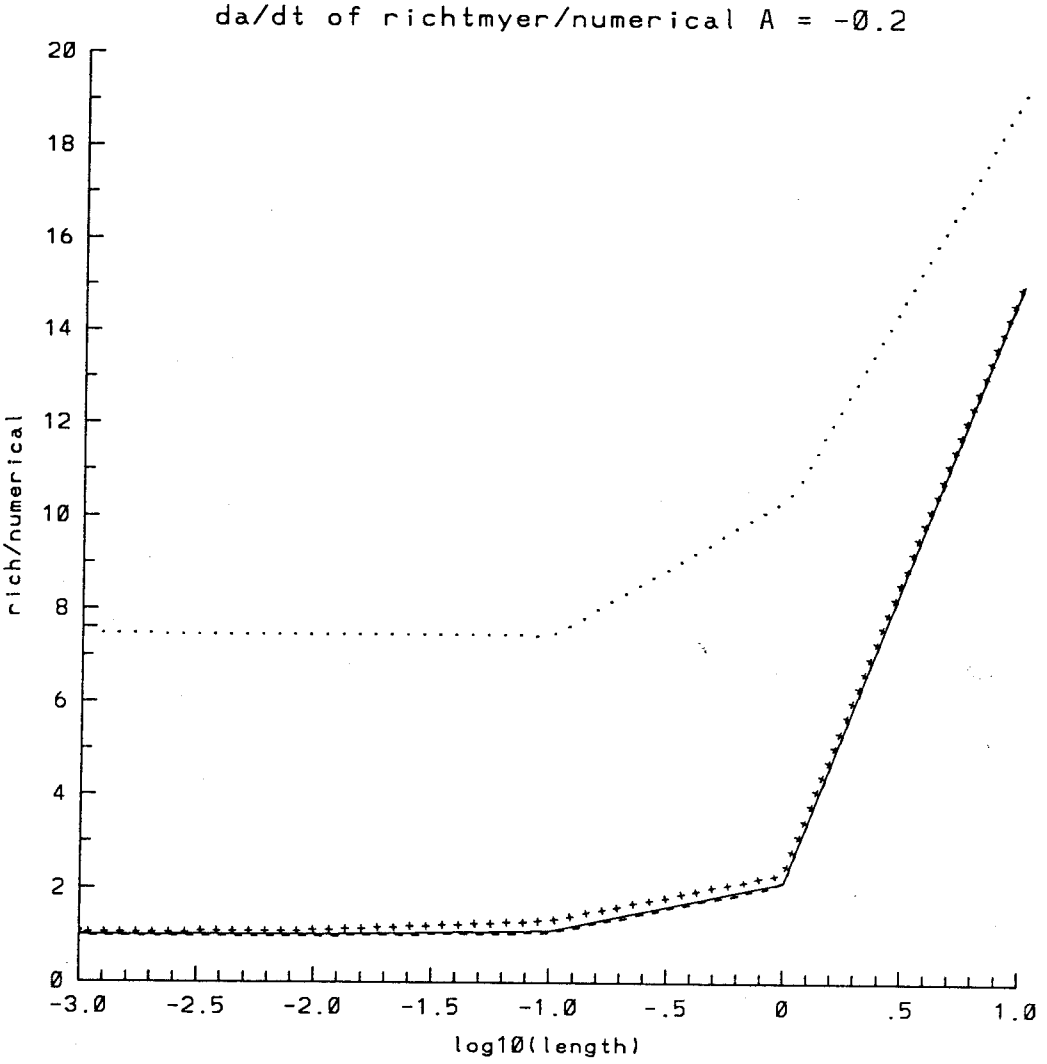

Figure 4.3 The ratio of the Richtmyer average amplitude growth rate (da/dt) over that of numerical simulation at $t = 0$ versus $\log_{10} L$ for A $= -0.2$: a) $---$ $\epsilon =$ 0.01 b) — $\epsilon = 0.1$ c) $+++$ $\epsilon = 1.0$ d) $\cdots$ $\epsilon = 10.0$. Note that the actual data points are given in Table 4.1, and just for the purpose of illustration, they are connected by curves of different styles as shown above.

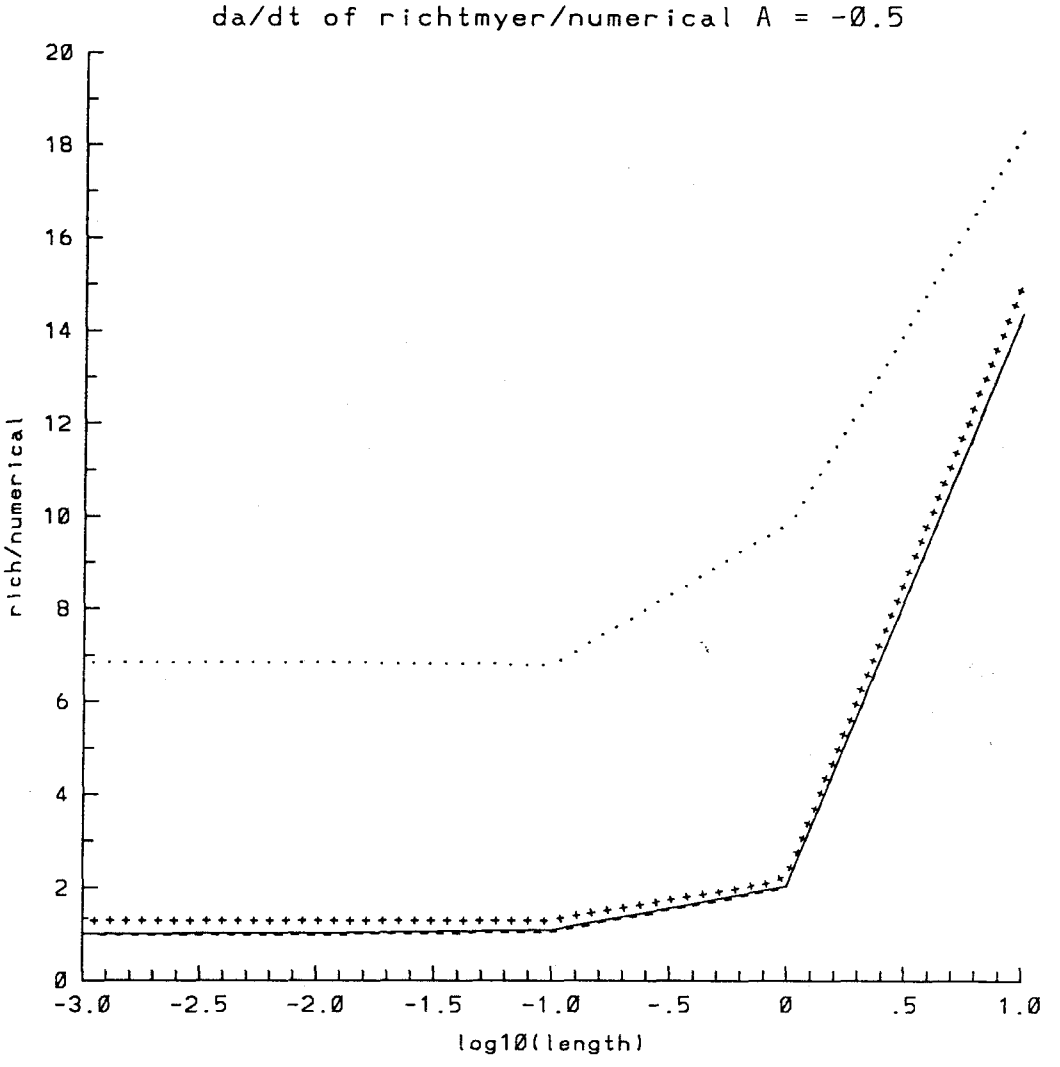

Figure 4.4 The ratio of the Richtmyer average amplitude growth rate (da/dt) over that of numerical simulation at $t = 0$ versus $\log_{10} L$ for A $= -0.5$: a) $---$ $\epsilon =$ 0.01 b) — $\epsilon = 0.1$ c) $+++$ $\epsilon = 1.0$ d) $\cdots$ $\epsilon = 10.0$. Note that the actual data points are given in Table 4.1, and just for the purpose of illustration, they are connected by curves of different styles as shown above.

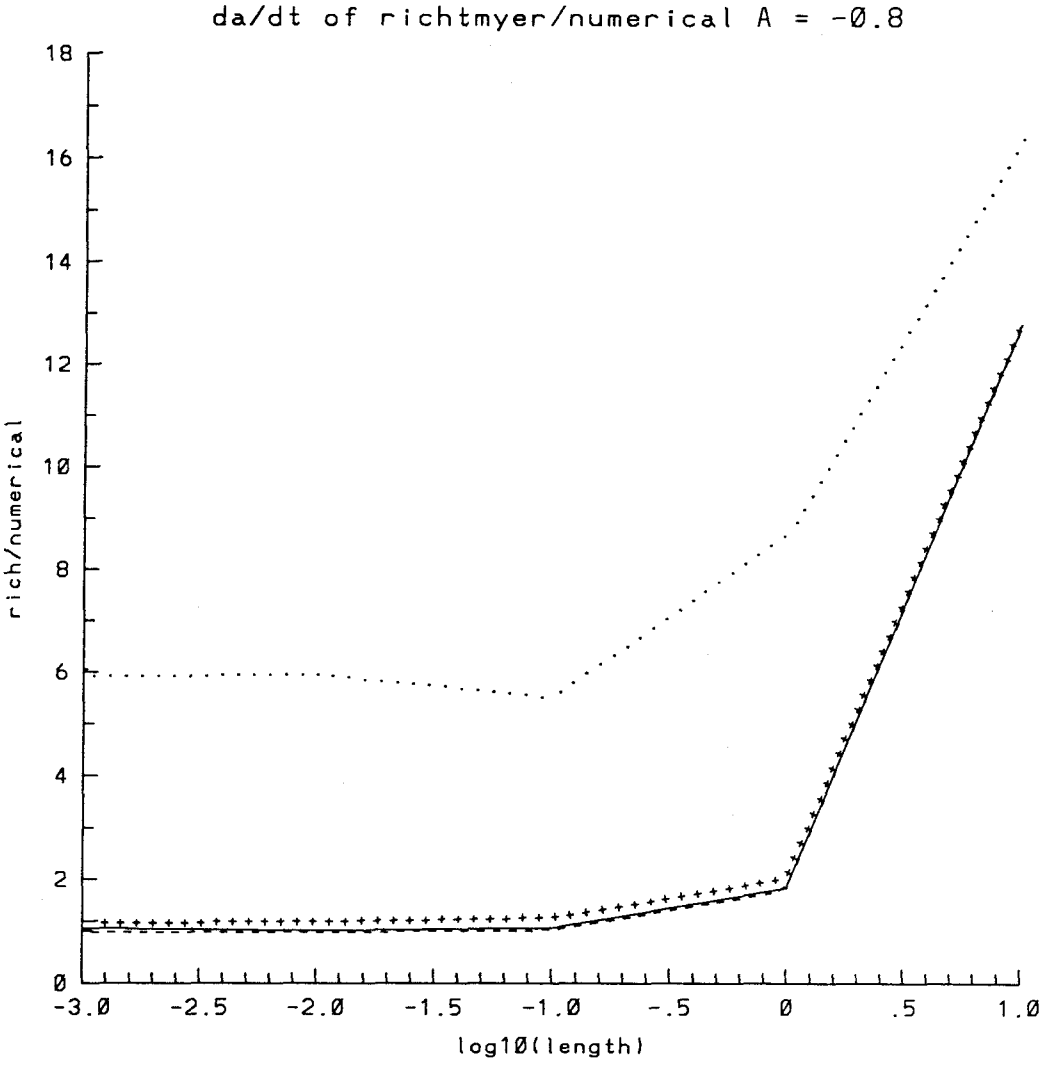

Figure 4.5 The ratio of the Richtmyer average amplitude growth rate (da/dt) over that of numerical simulation at $t = 0$ versus $\log_{10} L$ for A $= -0.8$: a) $---$ $\epsilon =$ 0.01 b) — $\epsilon = 0.1$ c) $+++$ $\epsilon = 1.0$ d) $\cdots$ $\epsilon = 10.0$. Note that the actual data points are given in Table 4.1, and just for the purpose of illustration, they are connected by curves of different styles as shown above.

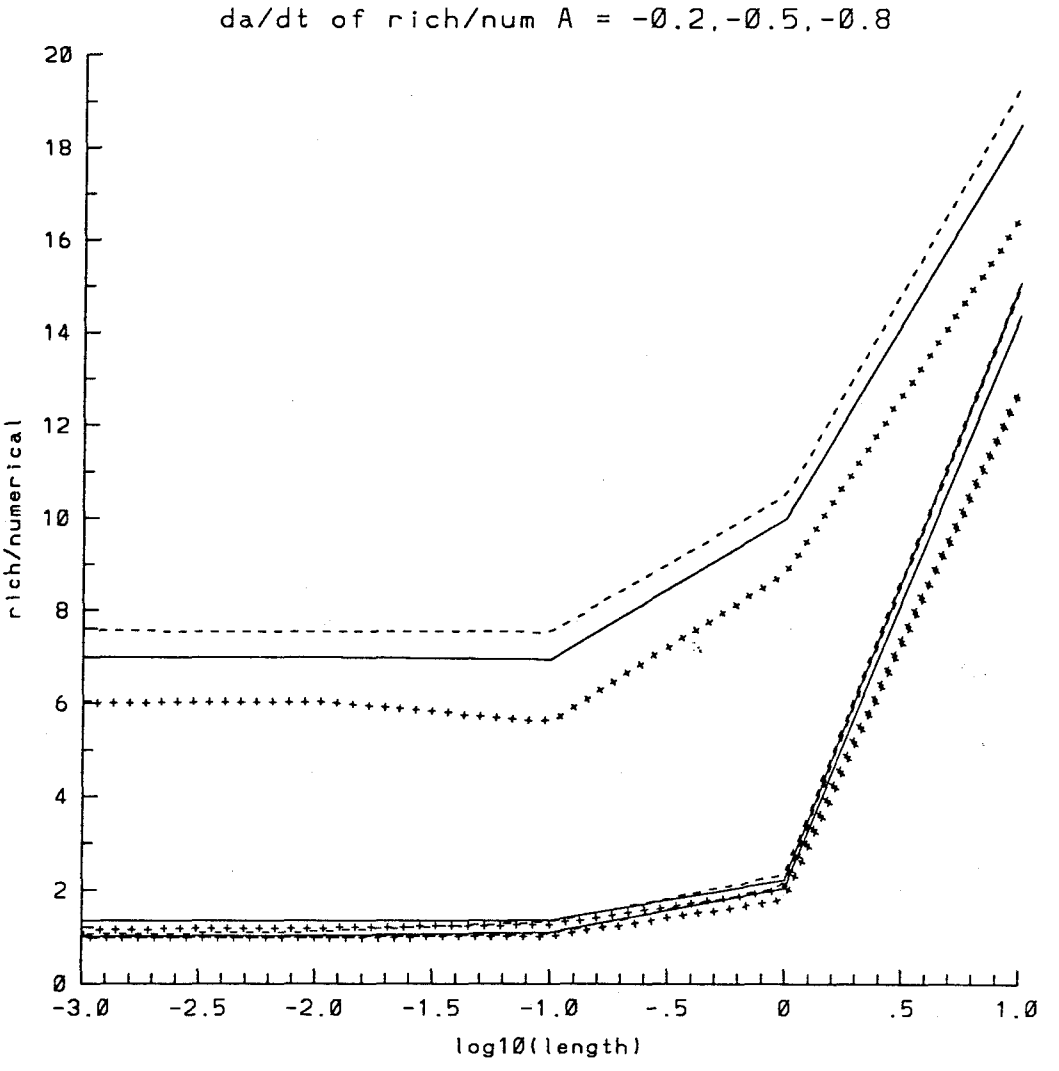

Figure 4.6 The ratio of the Richtmyer average amplitude growth rate (da/dt) over that of numerical simulation at $t = 0$ versus $\log_{10} L$ for : a) − − − A = −0.2, b) — A = −0.5 c) +++ A = −0.8, each with four values of $\epsilon = 0.01$, 0.1, 1.0, and 10.0. Note that the actual data points are given in Table 4.1, and just for the purpose of illustration, they are connected by curves of different styles as shown above.

4.4.2 Effect of perturbed amplitude on initial growth rate

The behavior of the ratios of the growth rates as a function of the perturbation amplitude ϵ is similar to that of L. As shown in Figures 4.7-10, the ratios attain a limit from above when ϵ is less than 1.0. Again the Richtmyer limits are confirmed. For $\epsilon = 0.01$ to 1.0, the ratios do not vary significantly. The ratios of the growth rates increase monotonically with the perturbation amplitude. The rate of the overprediction of the growth rate as a function of the perturbation amplitude is less than that as a function of the characteristic length. Therefore the effect of increasing the nonlinearity due to the perturbation amplitude is less important than the effect of increasing the width of the stratified layer.

4.4.3 Effect of density difference on initial growth rate

Figures 4.11-14 show the variation of the ratios of the growth rates with A. As ϵ or L increases, the overprediction is greater for the small density differences. Up to $\epsilon = 1.0$, and $L = 1.0$, the amount of overprediction is independent of the Atwood number, and the actual growth rates are half that predicted from Richtmyer theory when $\epsilon = 1.0$, and $L = 1.0$. For higher ϵ and L, the ratios have a maximum at $A = 0$. For the particular density profile under consideration, the effect of density difference as characterized by A on the growth rates is smallest among the three parameters: A, ϵ, and L.

In summary, for the initial development of the single scale instability, the results in this section have confirmed the reduction of the growth rates as compared to those predicted from the Richtmyer theory as L, and ϵ are increased. The effect of increasing ϵ on the growth rate is smaller than that of increasing L, and that of A is smallest among the three parameters. The actual growth rate is half the Richtmyer value for $\epsilon = 1.0$, and $L = 1.0$ independent of the Atwood number. In the next section, we will study the time evolution of the instability for the single

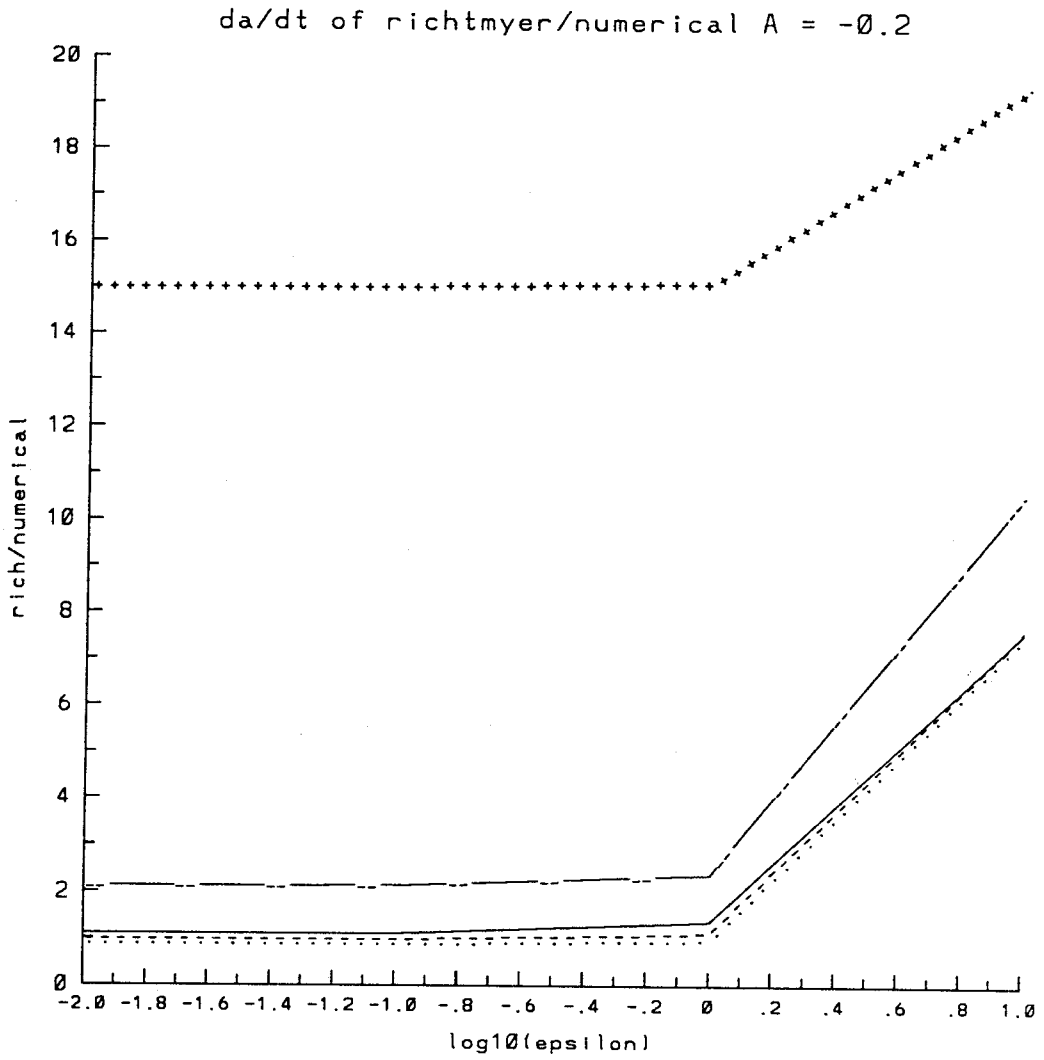

Figure 4.7 The ratio of the Richtmyer average amplitude growth rate (da/dt) over that of numerical simulation at $t = 0$ versus $\log_{10} \epsilon$ for A $= -0.2$: +++ L $=$ 10.0, — - - — L $= 1.0$, — L $= 0.1$, – – – L $= 0.01$, $\cdots$ L $= 0.001$. Note that the actual data points are given in Table 4.1, and just for the purpose of illustration, they are connected by curves of different styles as shown above.

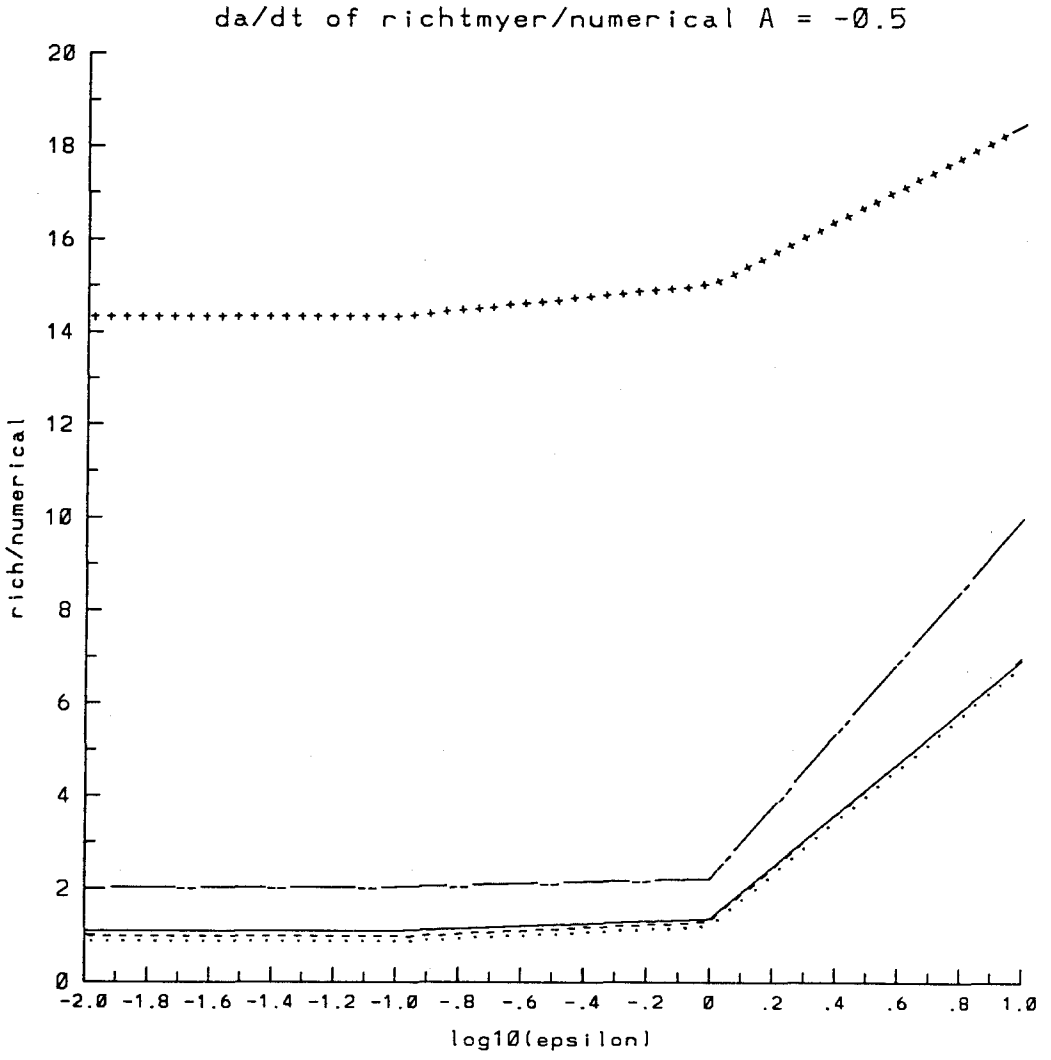

Figure 4.8 The ratio of the Richtmyer average amplitude growth rate (da/dt) over that of numerical simulation at $t = 0$ versus $\log_{10} \epsilon$ for A $= -0.5$: +++ L $=$ 10.0, — - - — L $= 1.0$, — L $= 0.1$, – – – L $= 0.01$, $\cdots$ L $= 0.001$. Note that the actual data points are given in Table 4.1, and just for the purpose of illustration, they are connected by curves of different styles as shown above.

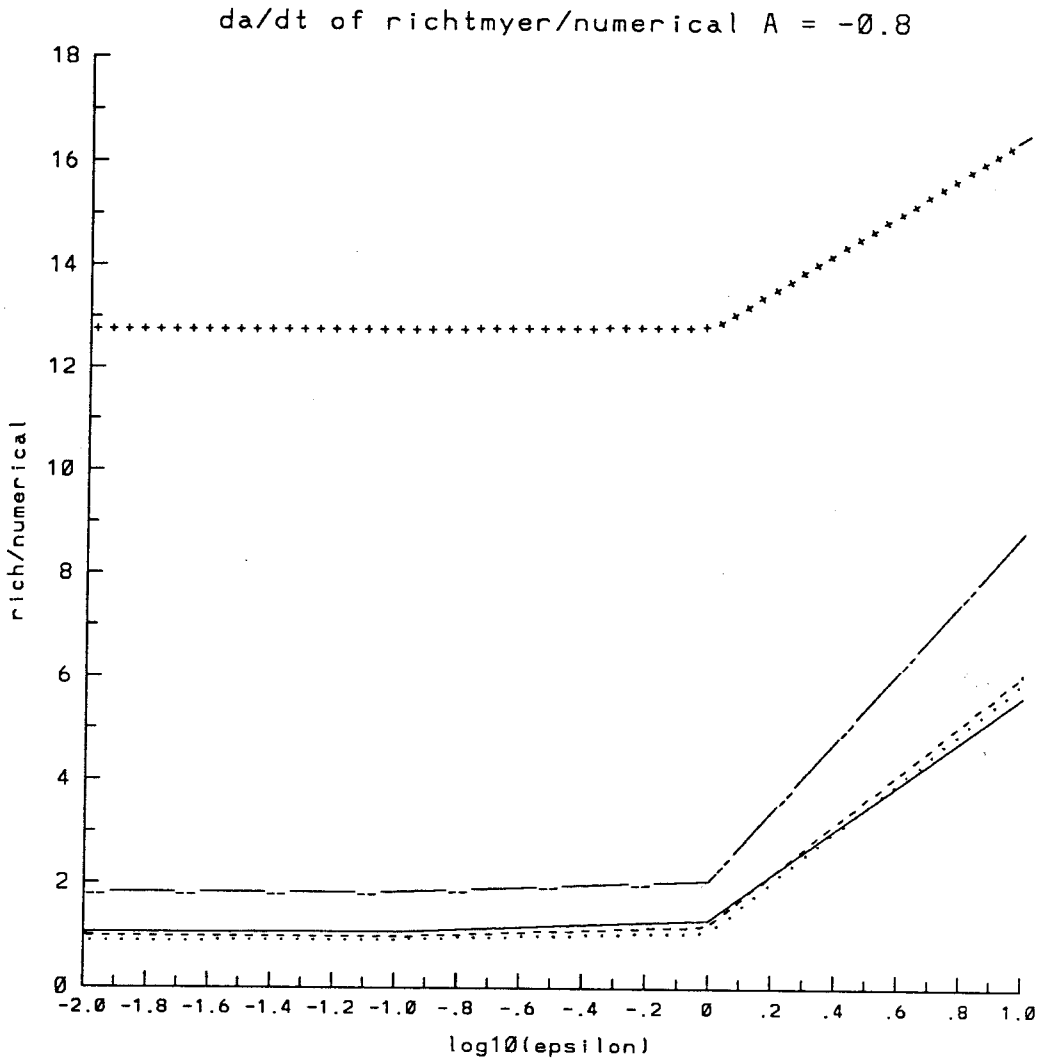

Figure 4.9 The ratio of the Richtmyer average amplitude growth rate (da/dt) over that of numerical simulation at $t = 0$ versus $\log_{10} \epsilon$ for A $= -0.8$: +++ L $=$ 10.0, — - - — L $= 1.0$, — L $= 0.1$, – – – L $= 0.01$, $\cdots$ L $= 0.001$. Note that the actual data points are given in Table 4.1, and just for the purpose of illustration, they are connected by curves of different styles as shown above.

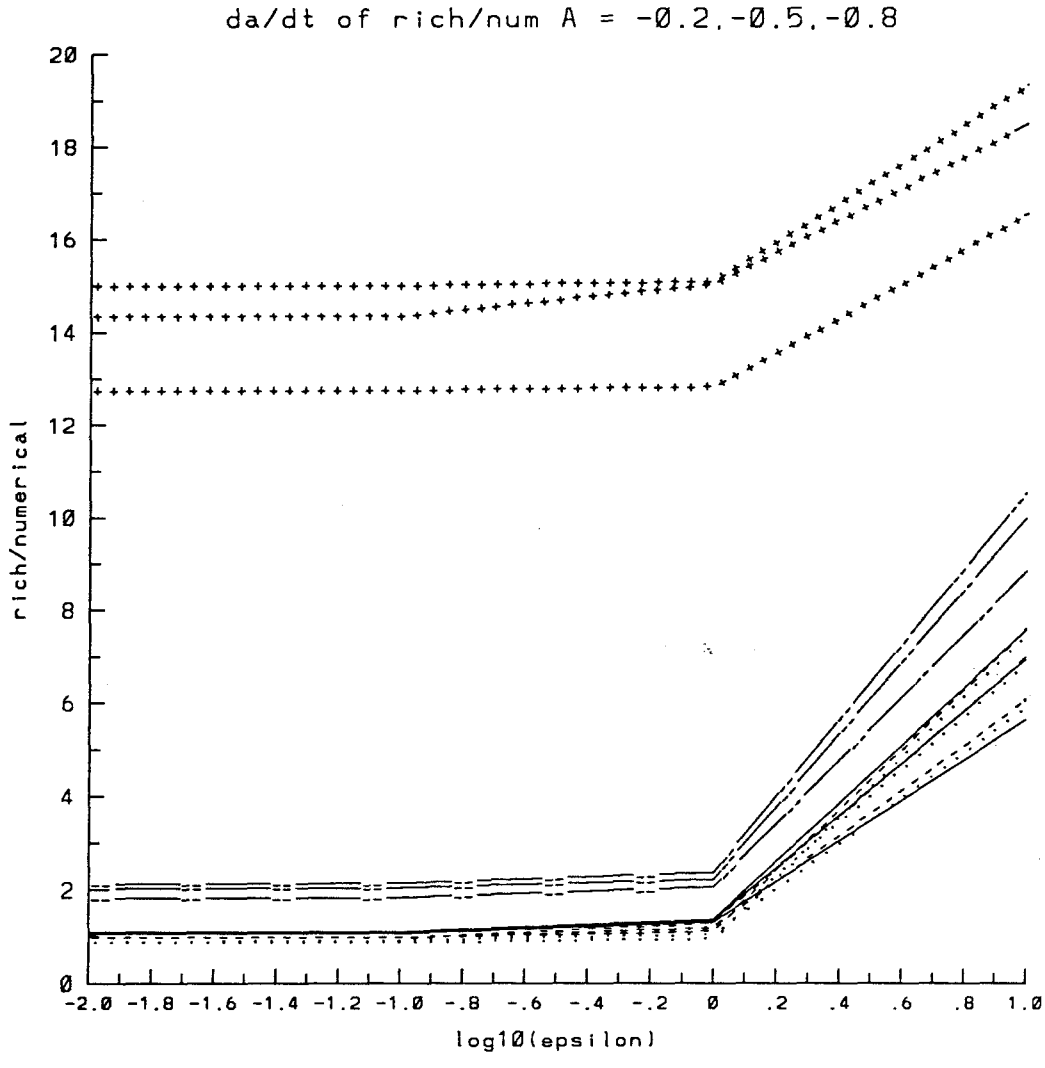

Figure 4.10 The ratio of the Richtmyer average amplitude growth rate (da/dt) over that of numerical simulation at $t = 0$ versus $\log_{10} \epsilon$ for A $= -0.2, -0.5, -0.8$: +++ L = 10.0, — - - — L = 1.0, — L = 0.1, – – – L = 0.01, $\cdots$ L = 0.001. Note that the actual data points are given in Table 4.1, and just for the purpose of illustration, they are connected by curves of different styles as shown above.

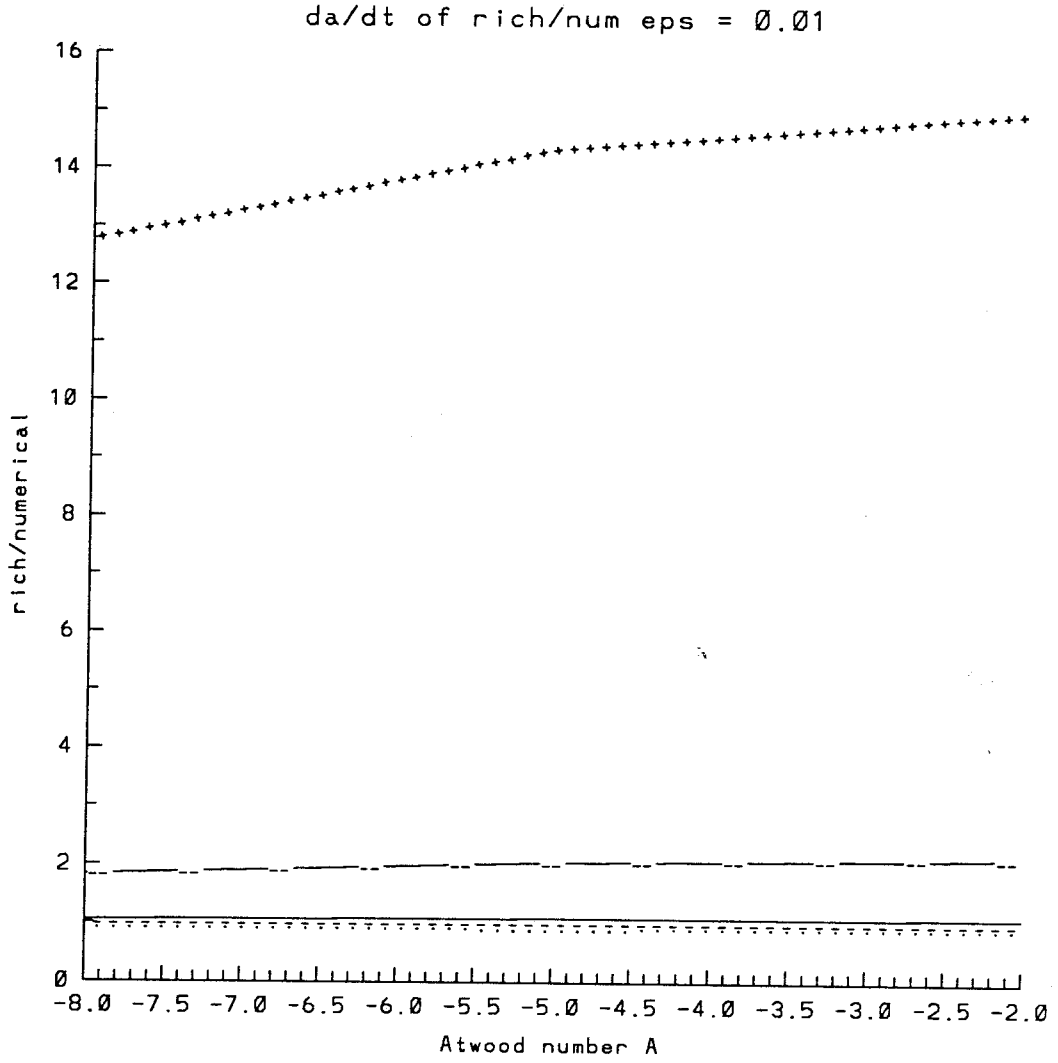

Figure 4.11 The ratio of the Richtmyer average amplitude growth rate (da/dt) over that of numerical simulation at $t = 0$ versus the Atwood number A for $\epsilon = 0.01$: +++ L = 10.0, — - - — L = 1.0, — L = 0.1, – – – L = 0.01, $\cdots$ L = 0.001. Note that the actual data points are given in Table 4.1, and just for the purpose of illustration, they are connected by curves of different styles as shown above.

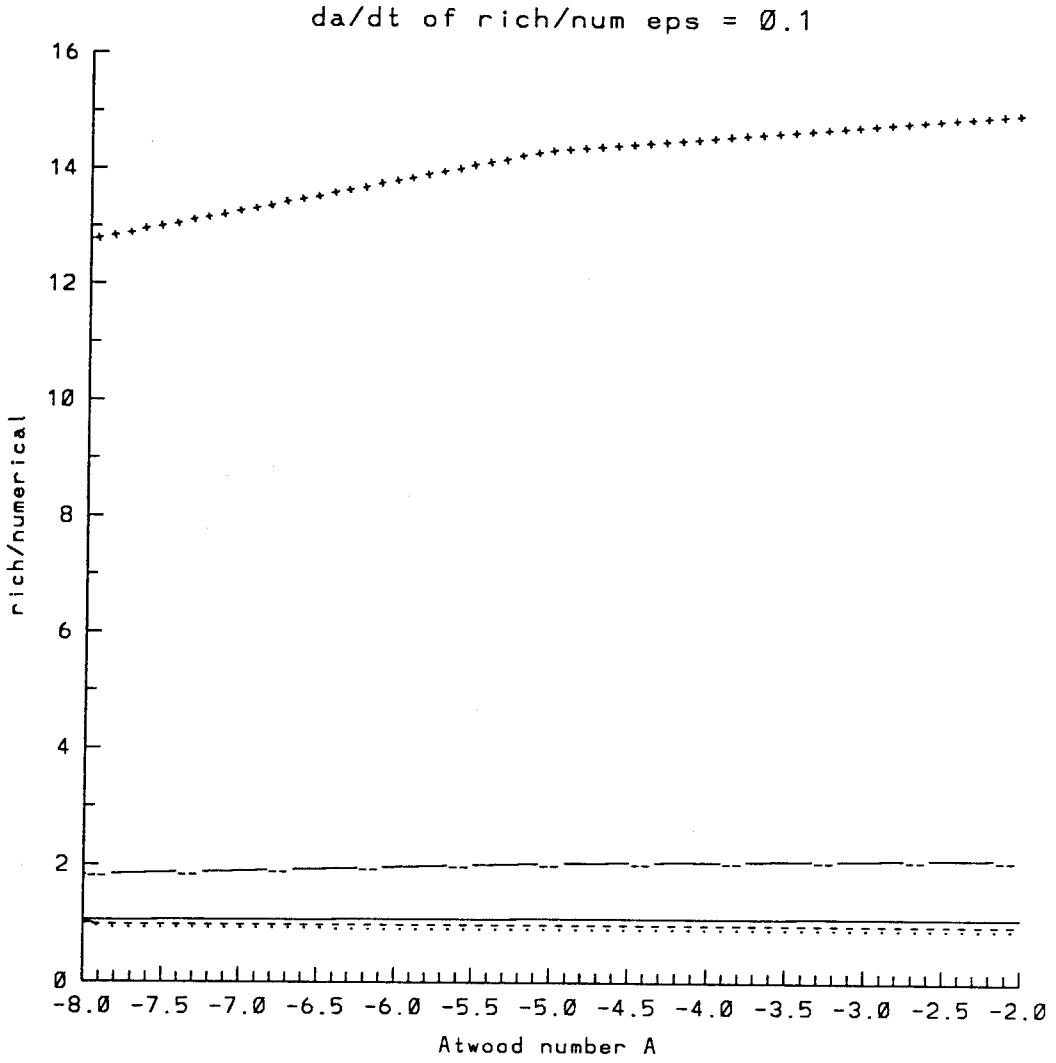

Figure 4.12 The ratio of the Richtmyer average amplitude growth rate (da/dt) over that of numerical simulation at $t = 0$ versus the Atwood number A for $\epsilon = 0.1$: +++ L = 10.0, — - - — L = 1.0, — L = 0.1, − − − L = 0.01, $\cdots$ L = 0.001. Note that the actual data points are given in Table 4.1, and just for the purpose of illustration, they are connected by curves of different styles as shown above.

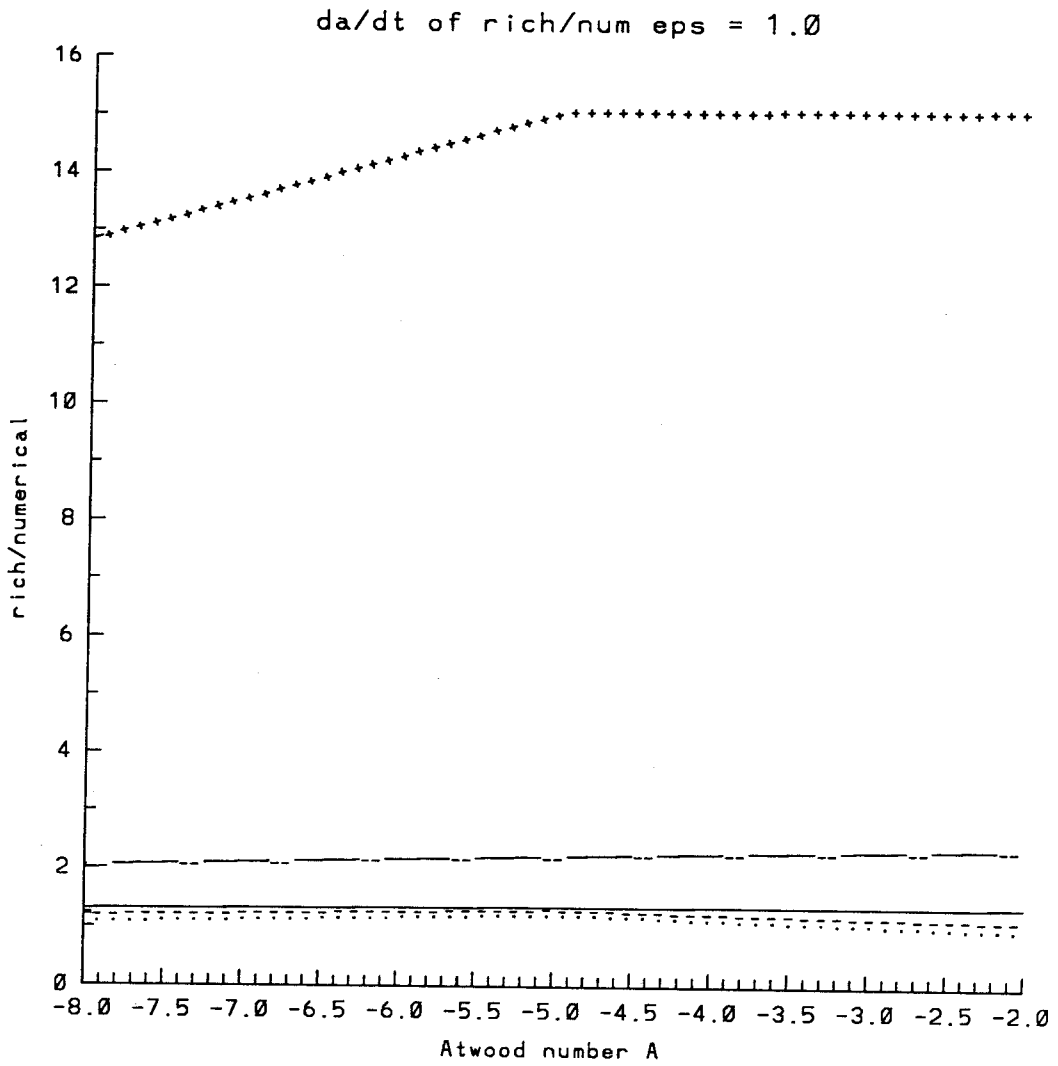

Figure 4.13 The ratio of the Richtmyer average amplitude growth rate (da/dt) over that of numerical simulation at $t = 0$ versus the Atwood number A for $\epsilon = 1.0$: +++ L = 10.0, — - - — L = 1.0, — L = 0.1, – – – L = 0.01, $\cdots$ L = 0.001. Note that the actual data points are given in Table 4.1, and just for the purpose of illustration, they are connected by curves of different styles as shown above.

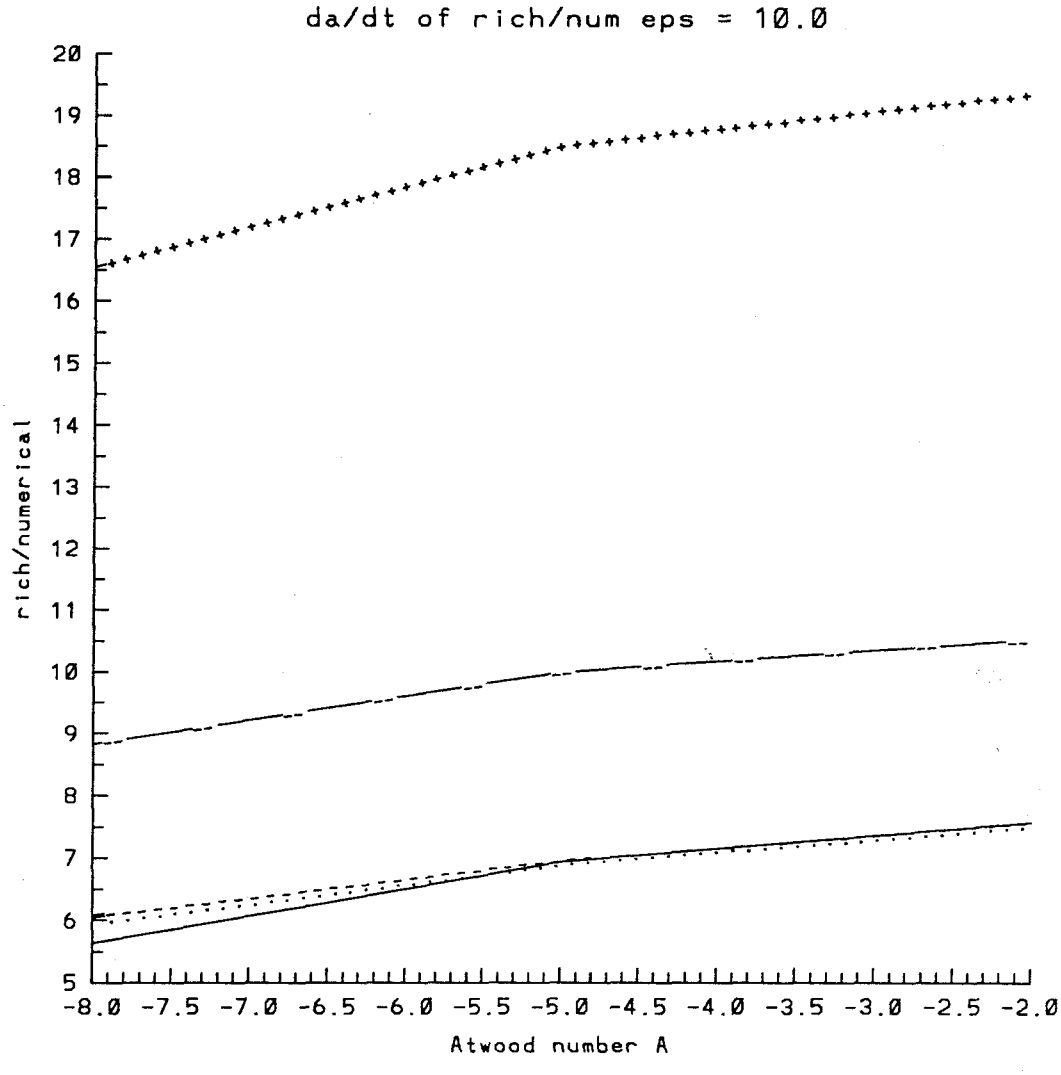

Figure 4.14 The ratio of the Richtmyer average amplitude growth rate (da/dt) over that of numerical simulation at $t = 0$ versus the Atwood number A for $\epsilon = 10.0$: +++ L = 10.0, — - - — L = 1.0, — L = 0.1, – – – L = 0.01, $\cdots$ L = 0.001. Note that the actual data points are given in Table 4.1, and just for the purpose of illustration, they are connected by curves of different styles as shown above.

scale problem.

4.5 Instability of the single scale problem

In this section, we consider the temporal development of the incompressible Richtmyer-Meshkov instability at a continuous interface having an initial single scale perturbation as given in equation (4.5). For L = 1.0, we have studied the cases with combinations from five Atwood numbers A = -0.05, -0.2, -0.5, ± 0.8, and three perturbation amplitudes $\epsilon = 0.2$, 0.5, and 1.0. For L = 0.5, we consider only one case with A = -0.5, and $\epsilon = 0.2$. In Table 4.2, we summarize the general information about the cases considered.

The first row in an entry of the table indicates the grid resolution used. Since we are interested in the long time behavior of the instability, whenever possible, we will let the simulation proceed up to a time t around 80. In the second row of the table's entries, we record the time around which there is numerical oscillation if the time t equals to 80 is not yet reached. The oscillation occurs due to the appearance of small scales which our grid can not resolve properly. With an increase in the number of grid points, the calculation can be extended to a longer time. The next two numbers of the entries are respectively the maximum norms of the pseudo-time derivatives of the unsteady problem in equations (3.18), (3.21), (3.23), and (3.25) and the residual errors of the nonlinear system of equation (3.16) at the recorded time in the second row. The fifth number is the Figure number which has the results for that particular case. The letters l, ω, and 3-D indicate respectively the cases displaying results using the linear theory model, and those cases for which vorticity contours and three-dimensional surfaces of $\bar{\rho}_y(x)$, and $\bar{\rho}_x(y)$ are provided.

For each case, we summarize the results in a set of Figures in which are plotted the time evolution of the average quantities, the position of the peaks of $\bar{\rho}_y(x)$, and the density contours. For the average quantities, we have the results for $\bar{\rho}_y(x)$, $\bar{\rho}_x(y)$, average amplitude a, width of the density layer δ, the growth rate da/dt, as

Table 4.2

Parameters for single scale problem.

L	A ⇓ ϵ ⇒	0.2	0.5	1.0
1.0	−0.05	61, 100 80 8.99×10^{-11} 9.76×10^{-5} 4.15	61, 100 80 9.46×10^{-11} 2.38×10^{-6} 4.16	101, 100 80 9.27×10^{-11} 1.78×10^{-6} 4.17
	−0.2	61, 100 80 9.97×10^{-11} 9.39×10^{-5} 4.18	61, 100 80 9.50×10^{-10} 3.58×10^{-6} 4.19	151, 100 53 6.44×10^{-10} 1.60×10^{-4} 4.20
	−0.5	61, 100 80 2.28×10^{-10} 1.56×10^{-6} 4.21 3-D	141, 100 53 1.46×10^{-9} 1.21×10^{-5} 4.22 l, ω, 3-D	151, 100 40 1.04×10^{-7} 1.18×10^{-4} 4.23 3-D
	−0.8		141, 100 32 3.47×10^{-7} 1.28×10^{-4} 4.24	151, 100 16 1.26×10^{-7} 1.91×10^{-4} 4.25
	0.8			151, 100 13 5.18×10^{-7} 1.76×10^{-4} 4.27 l, ω, 3-D
0.5	−0.5	61, 100 80 7.56×10^{-10} 9.93×10^{-5} 4.28		

well as its magnitude relative to that predicted by Richtmyer theory, $\ln(a)$ *vs* $\ln(t)$, and $\ln(\delta)$ *vs* $\ln(t)$. The combined results for the single scale problem are presented in the set of Figures 4.29. In the following discussion, we will focus our attention on the general structure of the instability, the overall growth of the stratified layer, and the intial development of the instability as predicted by the linear theory model.

4.5.1 General structure of the instability

For a given A, as ϵ increases, the middle peak of $\bar{\rho}_y(x)$ flattens. This effect becomes more pronounced as seen in Figures 4.15.1a–4.17.1a for A $= -0.05$, and Figures 4.18.1a–4.20.1a for A $= -0.2$. For higher Atwood numbers, after a maximal flattening, $\bar{\rho}_y(x)$ reduces in width and develops additional symmetry peaks as seen in Figures 4.21.1a–4.23.1a for A $= -0.5$, and 4.24.1a–4.25.1a for A $= -0.8$. A similar development of the asymmetry in $\bar{\rho}_x(y)$ around $\rho = 0.5$, and $y = 0.0$ is also seen in part (b) of the mentioned set of Figures for $\bar{\rho}_y(x)$. As ϵ increases, $\bar{\rho}_x(y)$ tends to change from a monotonic function into one having a relative maximum and minimum. As A increases, the asymmetry of $\bar{\rho}_x(y)$ moves toward the front of the stratified layer indicating that on the average the entrainment of the globule of heavy fluid into the lighter one is faster than the entrainment of lighter one into the heavy fluid. This asymmetry in the structures of the spikes of heavy fluid, and the bubbles of light fluid is also observed in the full compressible simulation by Mikaelian (1988), and Youngs (1984).

Detailed information on the average speed of the spike and the bubble is obtained from Figures 4.15.3 to 4.25.3 in which we plot the time evolution of the position of the peaks in the average density profile $\bar{\rho}_y(x)$ along with their time derivative. In general, for small A, and ϵ, the speeds of the bubble and the spike are equal and opposite. The light fluid penetrates the heavier fluid at the same speed as the heavy fluid falls into the lighter one. As time increases, the speeds decrease at the same rate. For higher A, and ϵ, initially, the spikes and the bubbles have

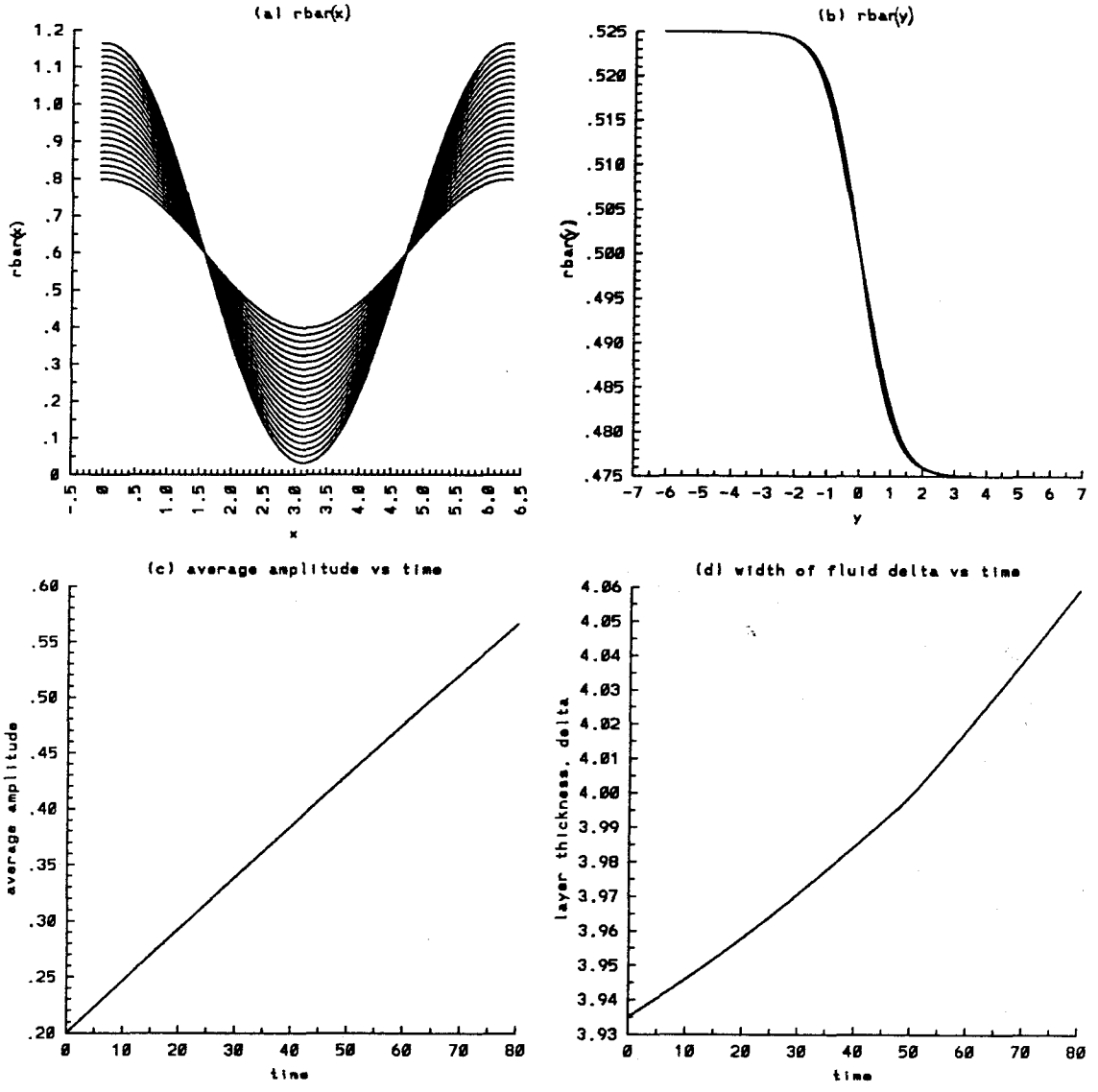

Figure 4.15.1 Time evolution of the average quantities for the single scale profile L = 1.0, A = −0.05, $\epsilon = 0.2$, $t = 0$ to 80 : a) $\bar{\rho}_y(x)$, b) $\bar{\rho}_x(y)$, c) average amplitude, and d) width of the density layer.

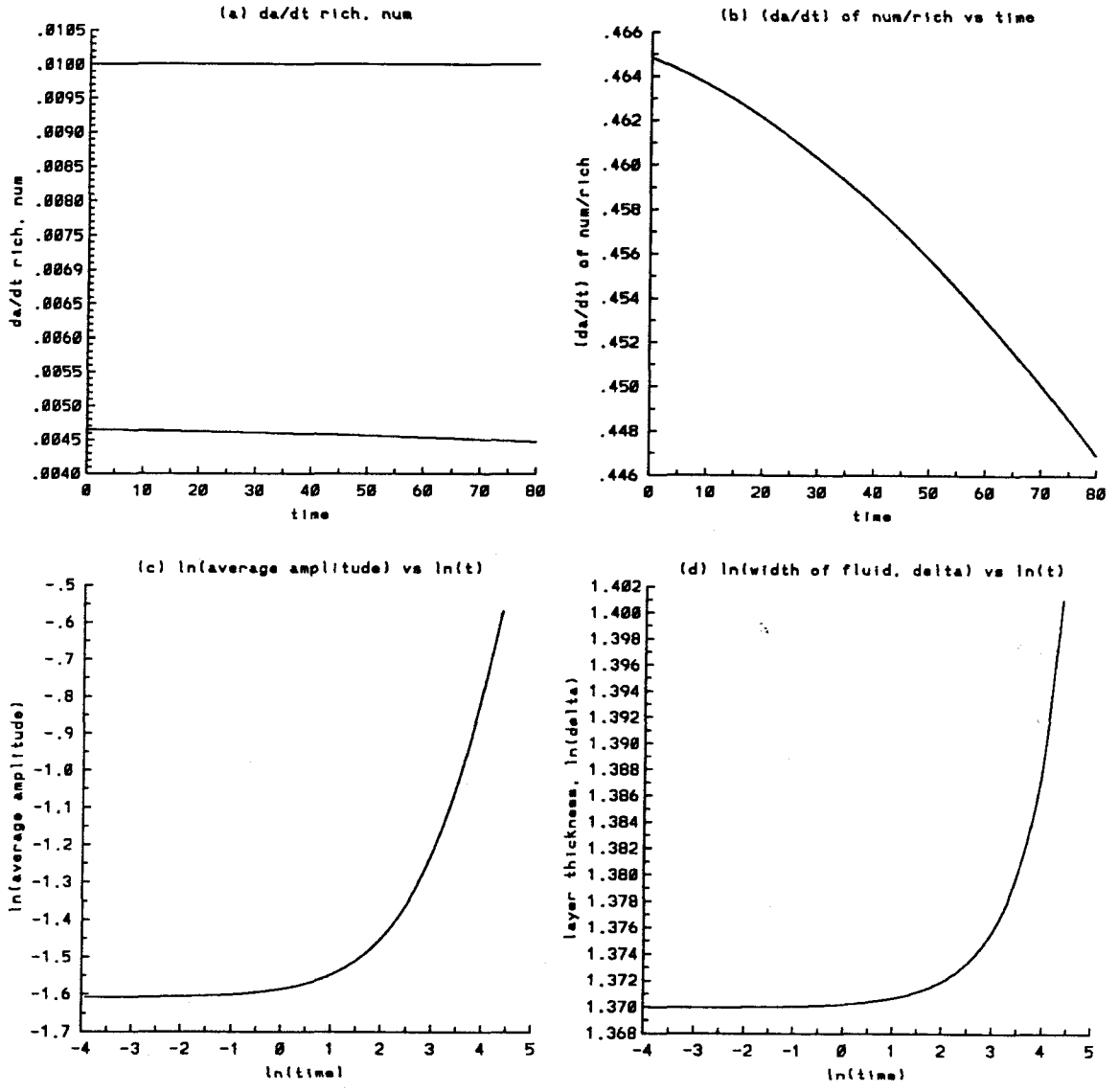

Figure 4.15.2 Time evolution of the average quantities for the single scale profile $\lambda = 1.0$, A $= -0.05$, $\epsilon = 0.2$, $t = 0$ to 80 : a) growth rate da/dt of the average amplitude, numerical and Richtmyer theory (straight line), b) the ratio of the numerical growth rate da/dt over that predicted by Richtmyer theory, c) $\ln(a)$ *vs* $\ln(t)$, d) $\ln(\delta)$ *vs* $\ln(t)$.

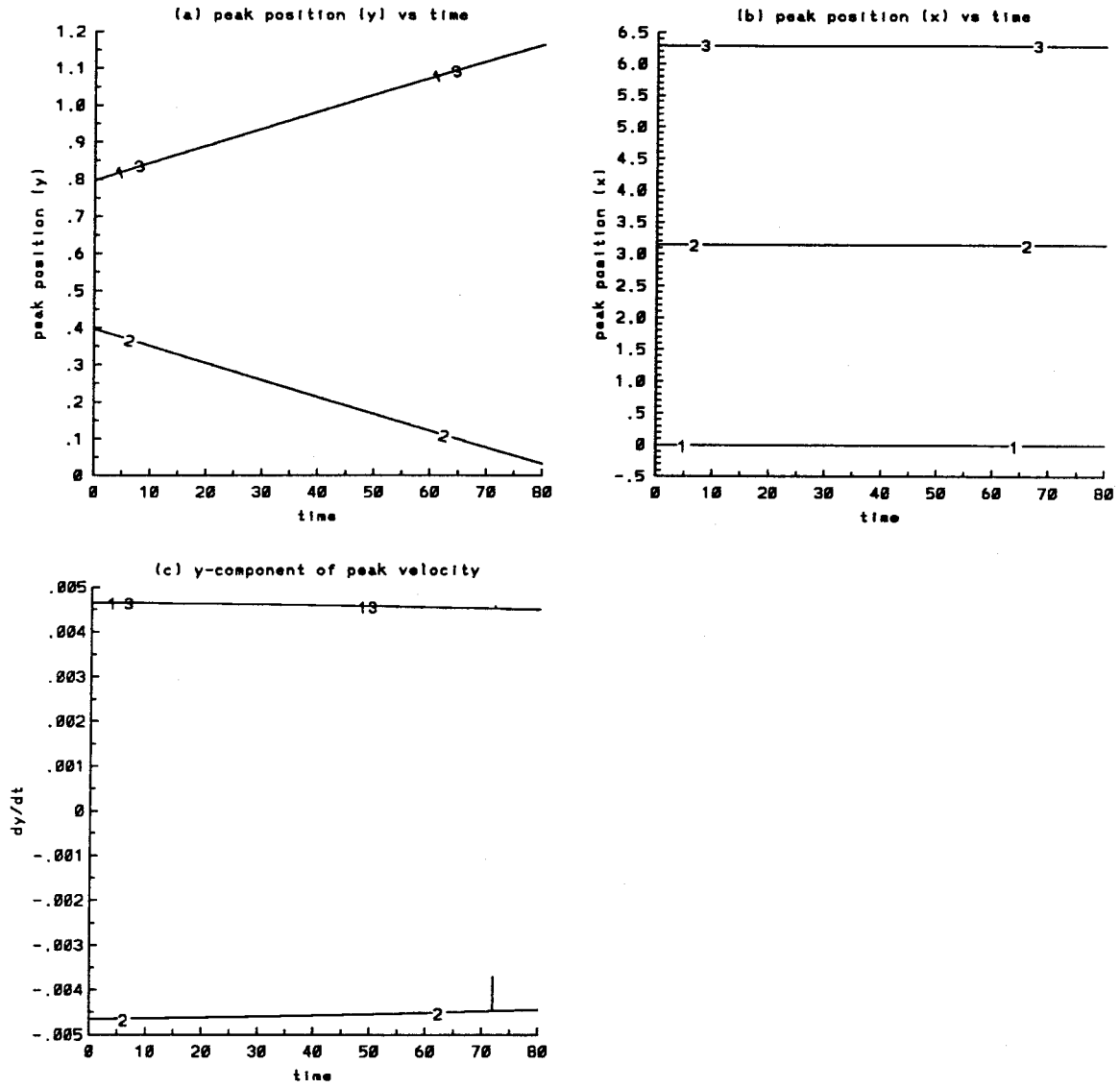

Figure 4.15.3 Time evolution of the positions and velocities of the average peaks in the single scale profile L = 1.0, A = −0.05, $\epsilon = 0.2$, $t = 0$ to 80 a) y b) x c) dy/dt. The numbers on the curves refer to the peaks on the curves $\bar{\rho}_y(x)$ versus x.

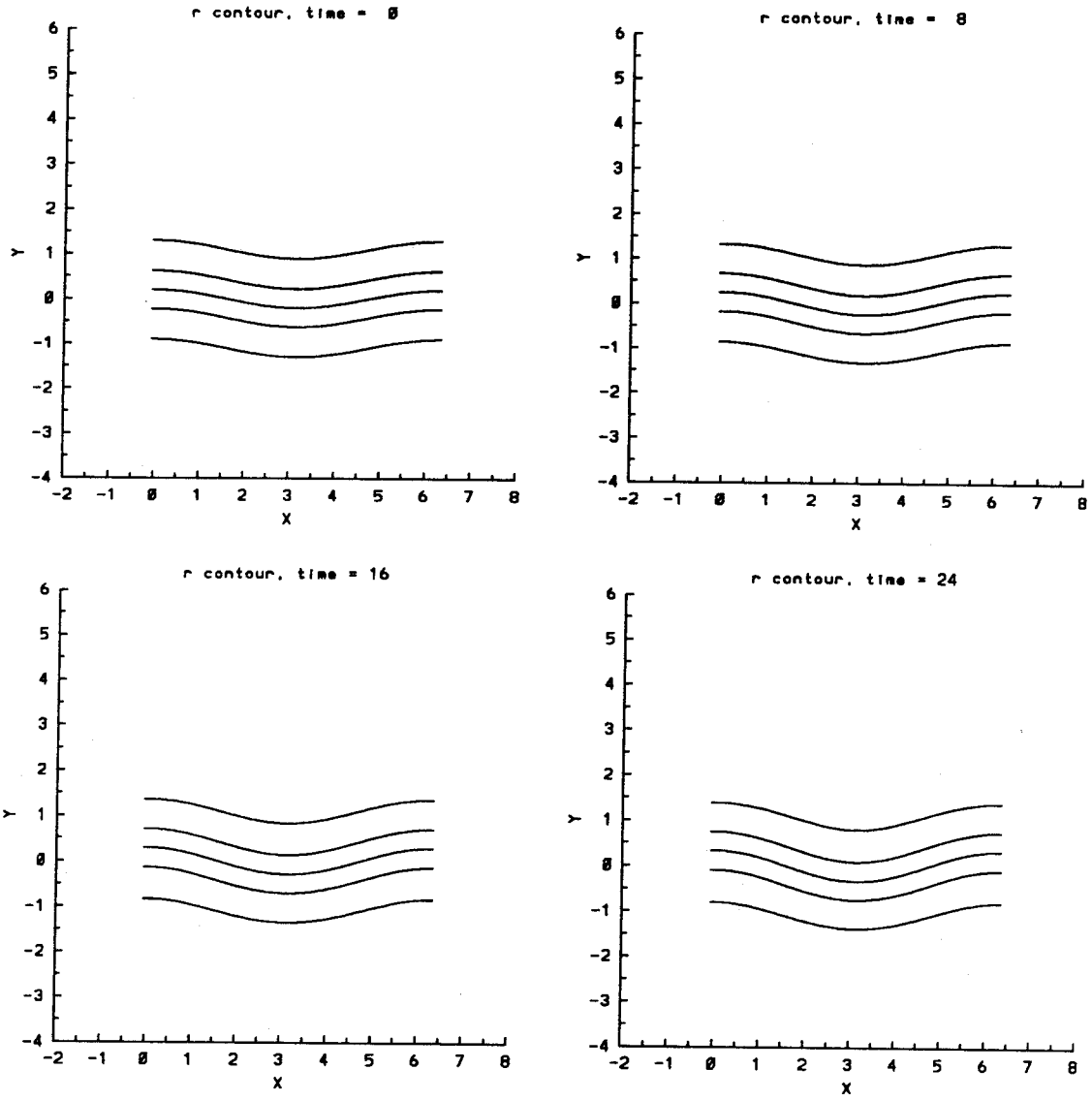

Figure 4.15.4 Time evolution of the density contours for the single scale profile L = 1.0, A = −0.05, $\epsilon = 0.2$, $t = 0$, 8, 16, 24. The contours are at $\rho = 0.48$, 0.49, 0.50, 0.51, 0.52 in that order from top to bottom of each figure.

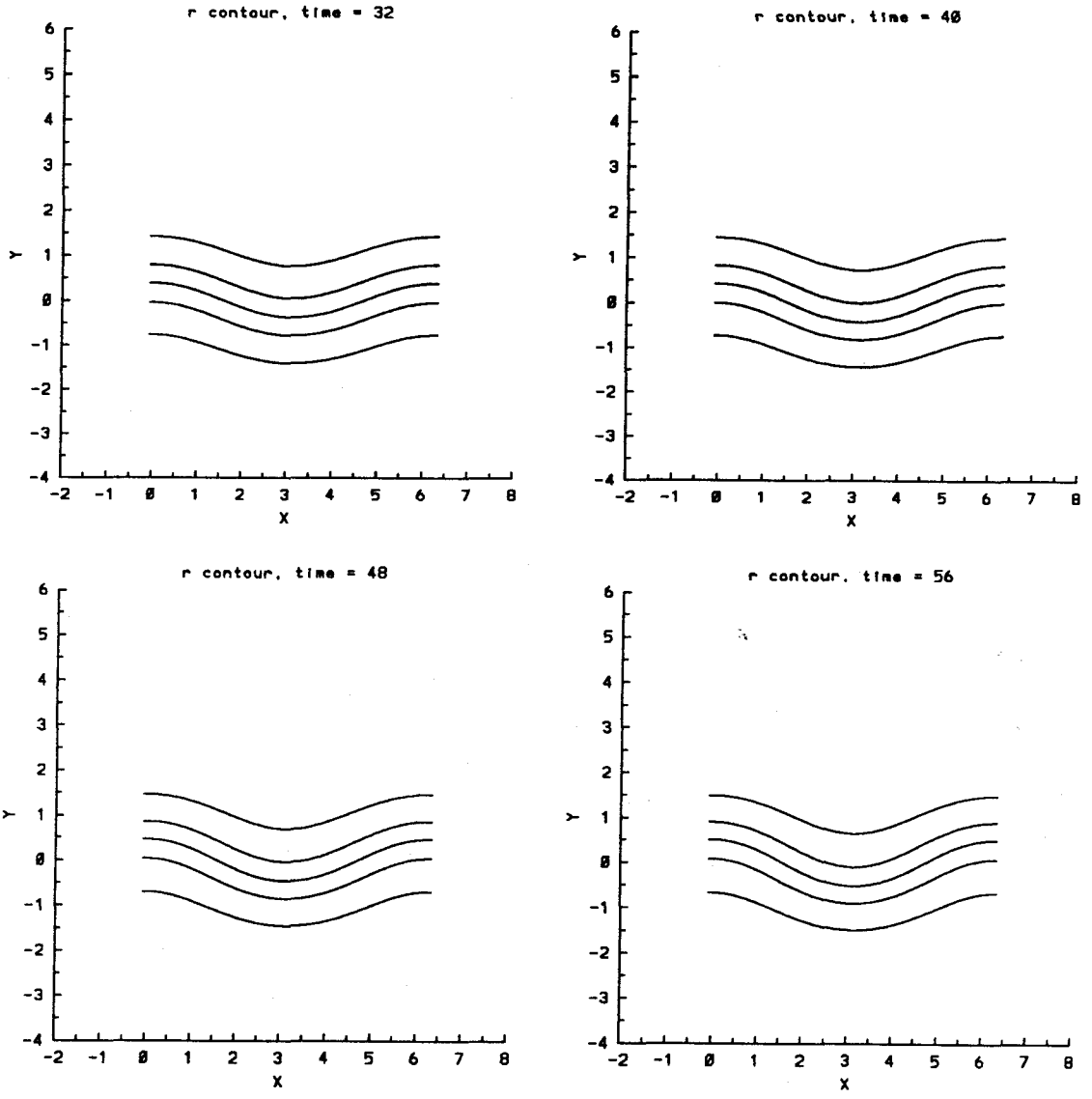

Figure 4.15.5 Time evolution of the density contours for the single scale profile L = 1.0, A = −0.05, $\epsilon = 0.2$, $t = 32, 40, 48, 56$. The contours are at $\rho = 0.48, 0.49, 0.50, 0.51, 0.52$ in that order from top to bottom of each figure.

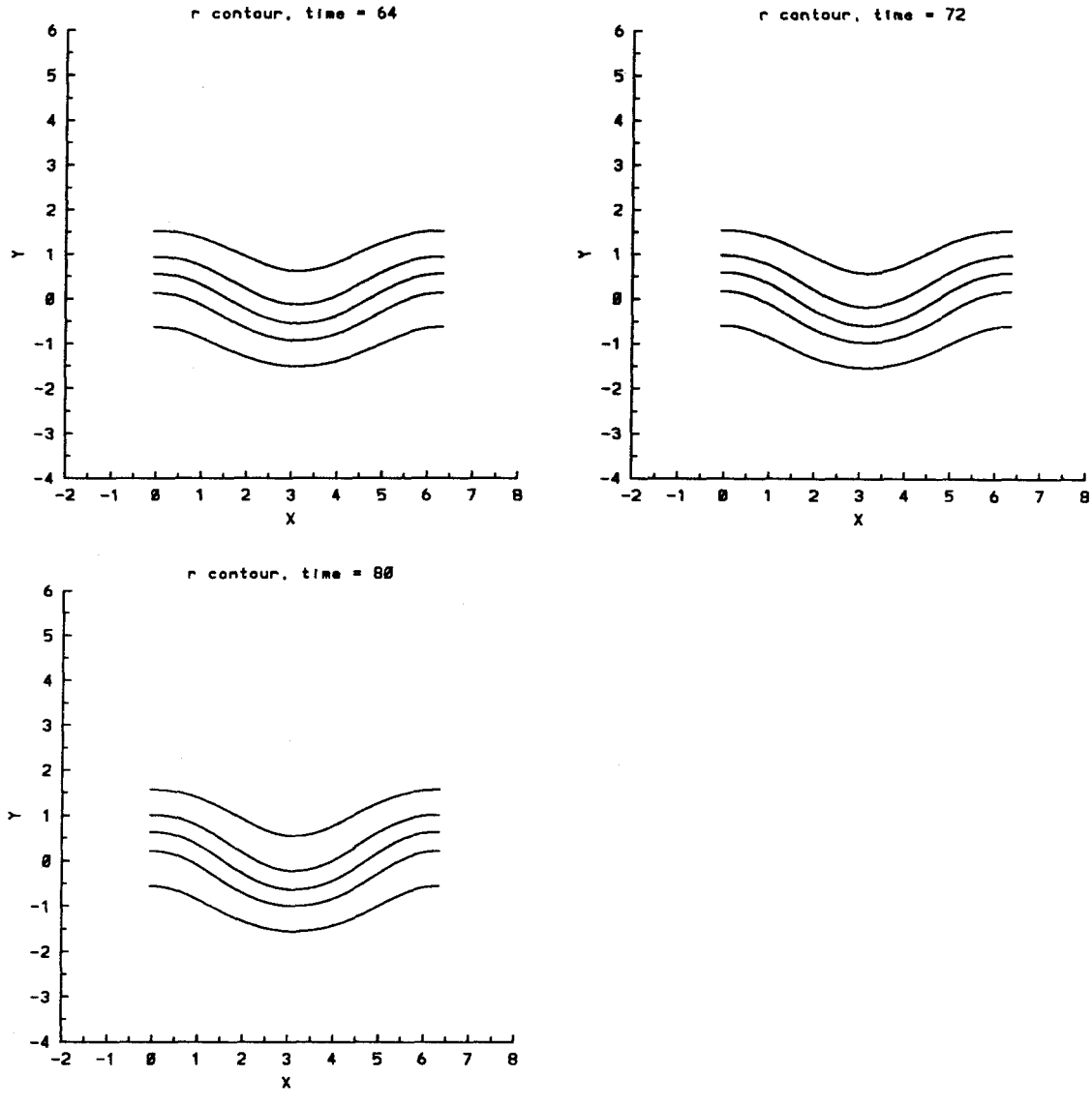

Figure 4.15.6 Time evolution of the density contours for the single scale profile L = 1.0, A = −0.05, $\epsilon = 0.2$, $t = 64$, 72, 80. The contours are at $\rho = 0.48$, 0.49, 0.50, 0.51, 0.52 in that order from top to bottom of each figure.

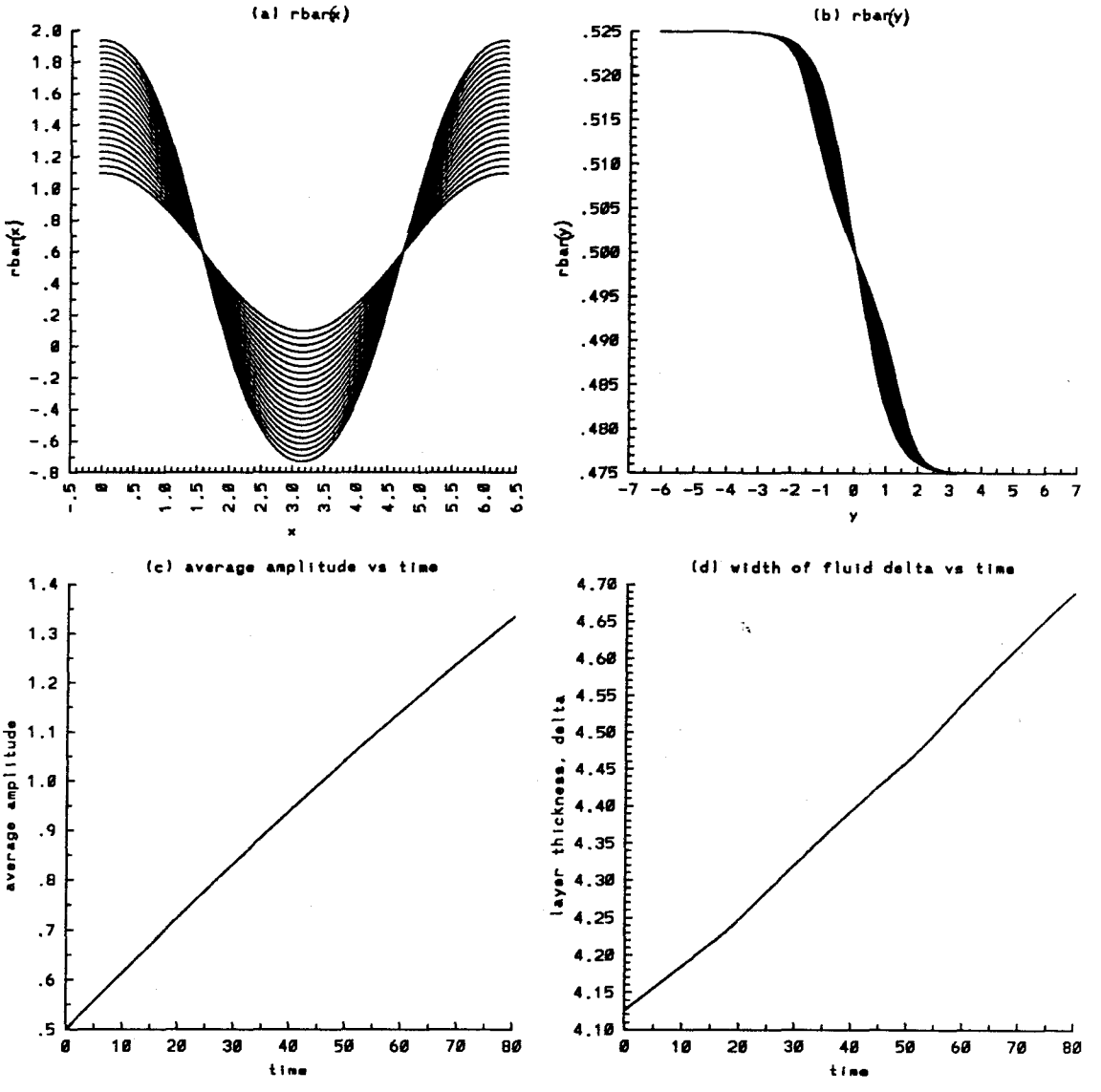

Figure 4.16.1 Time evolution of the average quantities for the single scale profile L = 1.0, A = −0.05, $\epsilon = 0.5$, $t = 0$ to 80 : a) $\bar{\rho}_y(x)$, b) $\bar{\rho}_x(y)$, c) average amplitude, and d) width of the density layer.

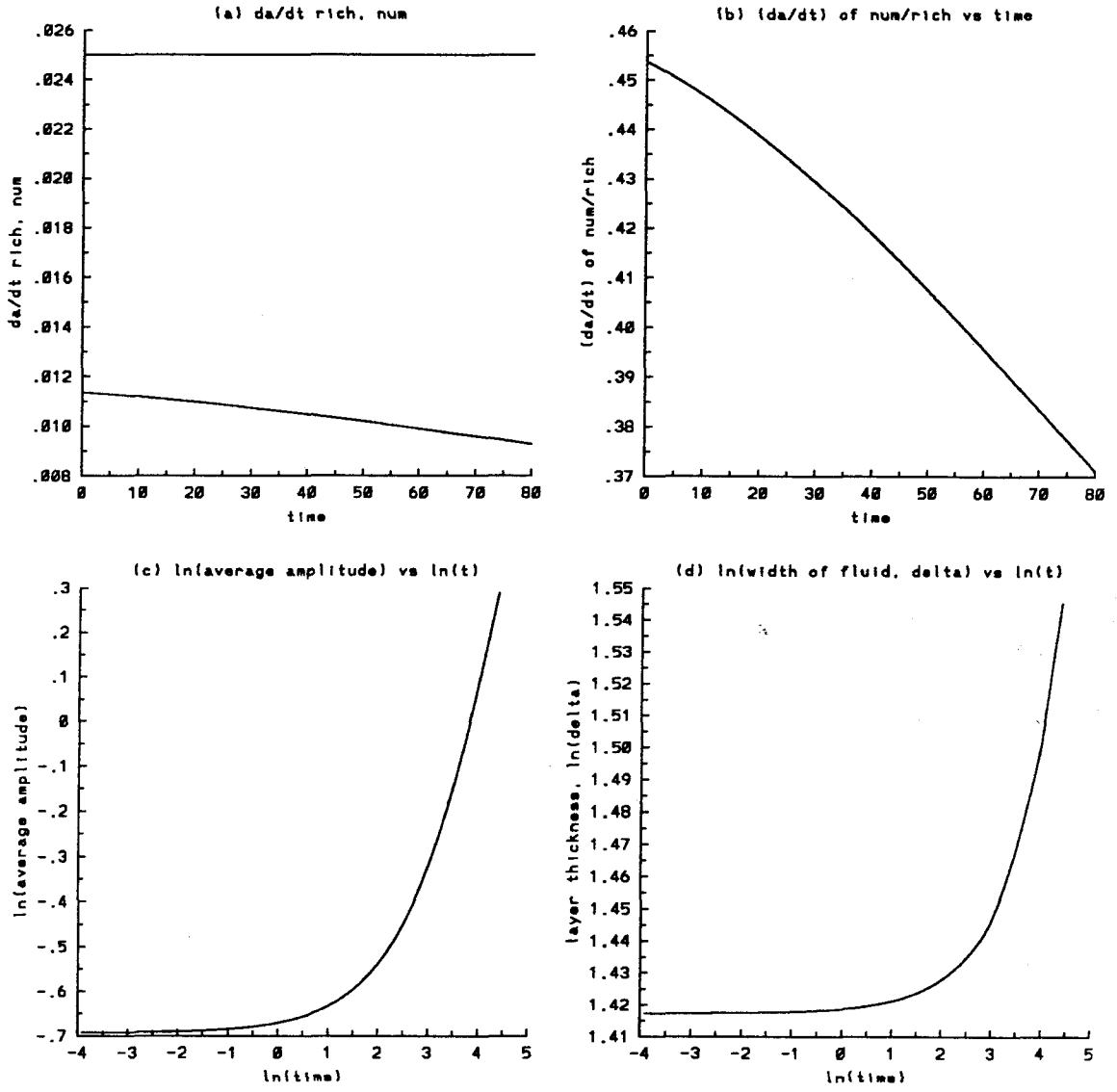

Figure 4.16.2 Time evolution of the average quantities for the single scale profile $L = 1.0$, $A = -0.05$, $\epsilon = 0.5$, $t = 0$ to 80 : a) growth rate da/dt of the average amplitude, numerical and Richtmyer theory (straight line), b) the ratio of the numerical growth rate da/dt over that predicted by Richtmyer theory, c) $\ln(a)$ *vs* $\ln(t)$, d) $\ln(\delta)$ *vs* $\ln(t)$.

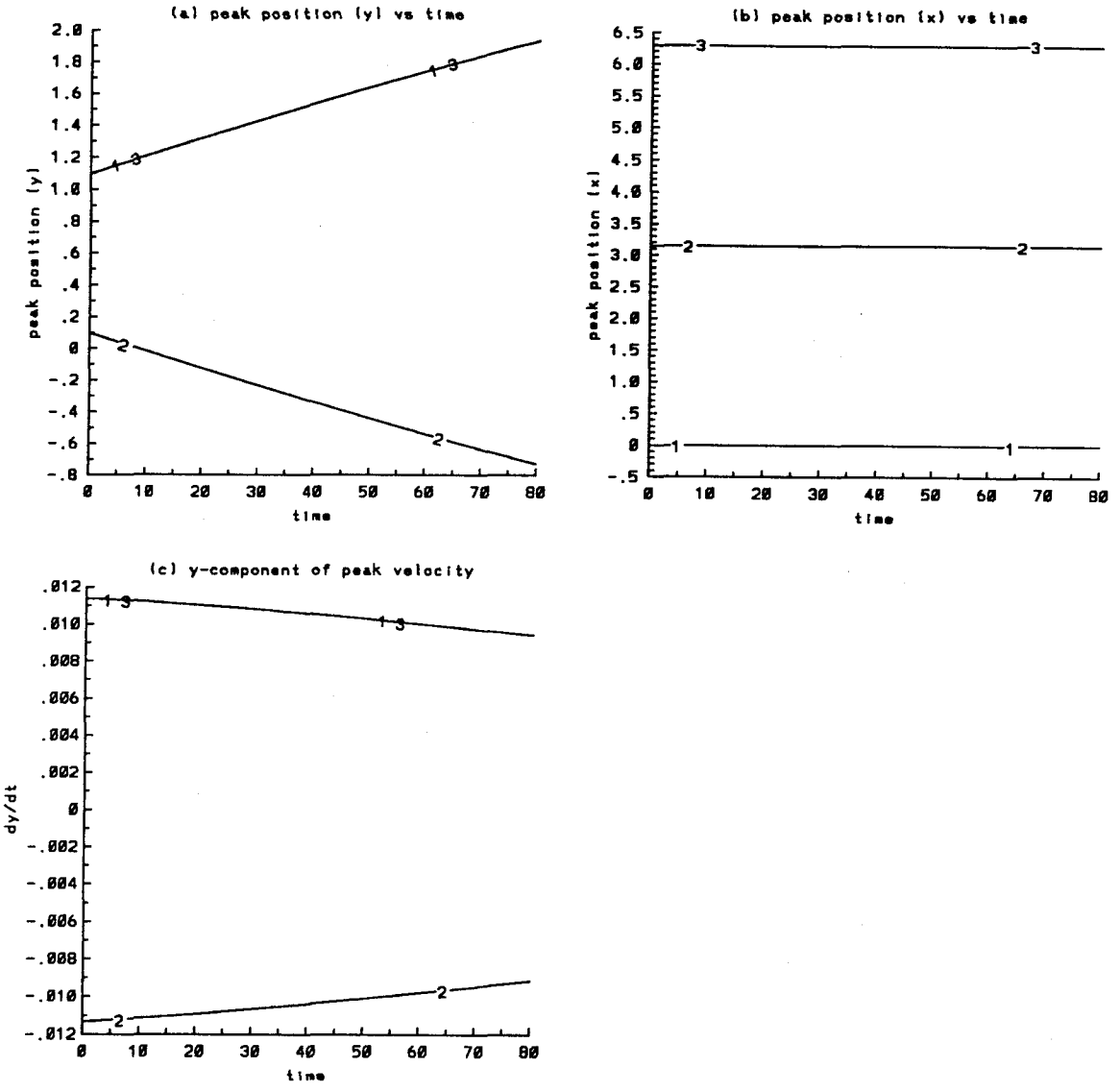

Figure 4.16.3 Time evolution of the positions and velocities of the average peaks in the single scale profile L = 1.0, A = −0.05, $\epsilon = 0.5$, $t = 0$ to 80 a) y b) x c) dy/dt. The numbers on the curves refer to the peaks on the curves $\bar{\rho}_y(x)$ versus x.

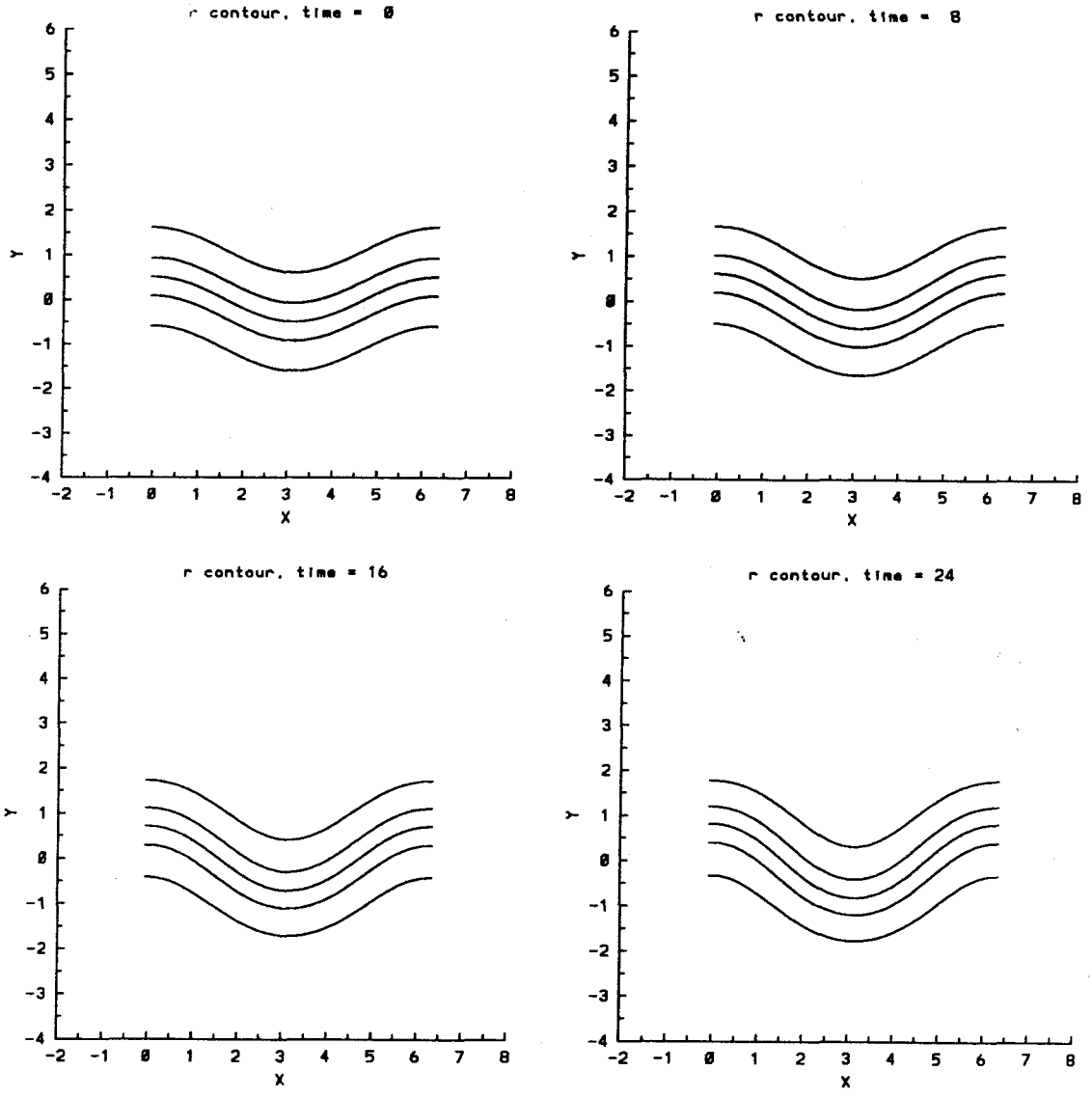

Figure 4.16.4 Time evolution of the density contours for the single scale profile L = 1.0, A = −0.05, $\epsilon = 0.5$, $t = 0$, 8, 16, 24. The contours are at $\rho = 0.48$, 0.49, 0.50, 0.51, 0.52 in that order from top to bottom of each figure.

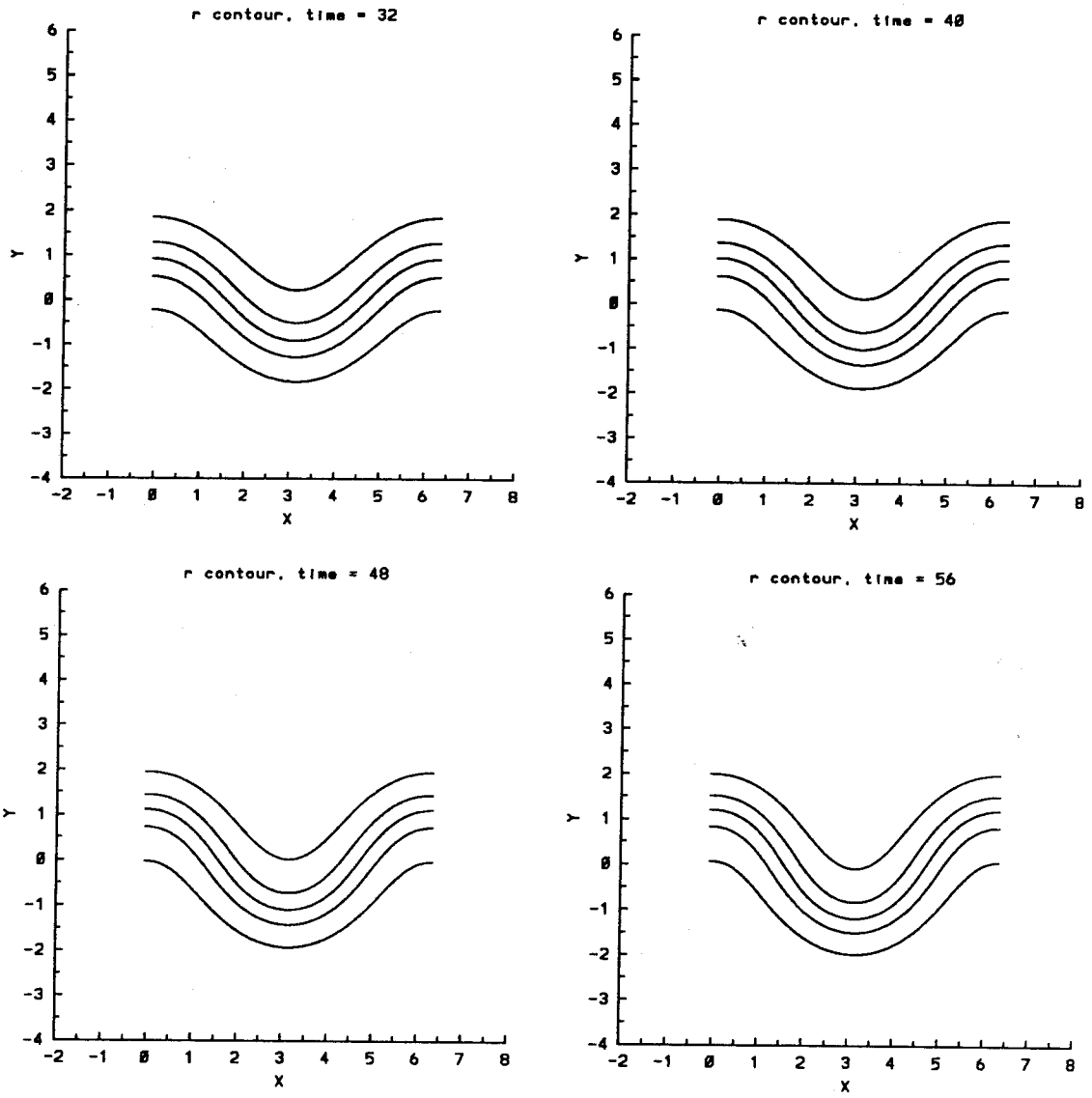

Figure 4.16.5 Time evolution of the density contours for the single scale profile $\mathrm{L} = 1.0$, $\mathrm{A} = -0.05$, $\epsilon = 0.5$, $t = 32$, 40, 48, 56. The contours are at $\rho = 0.48$, 0.49, 0.50, 0.51, 0.52 in that order from top to bottom of each figure.

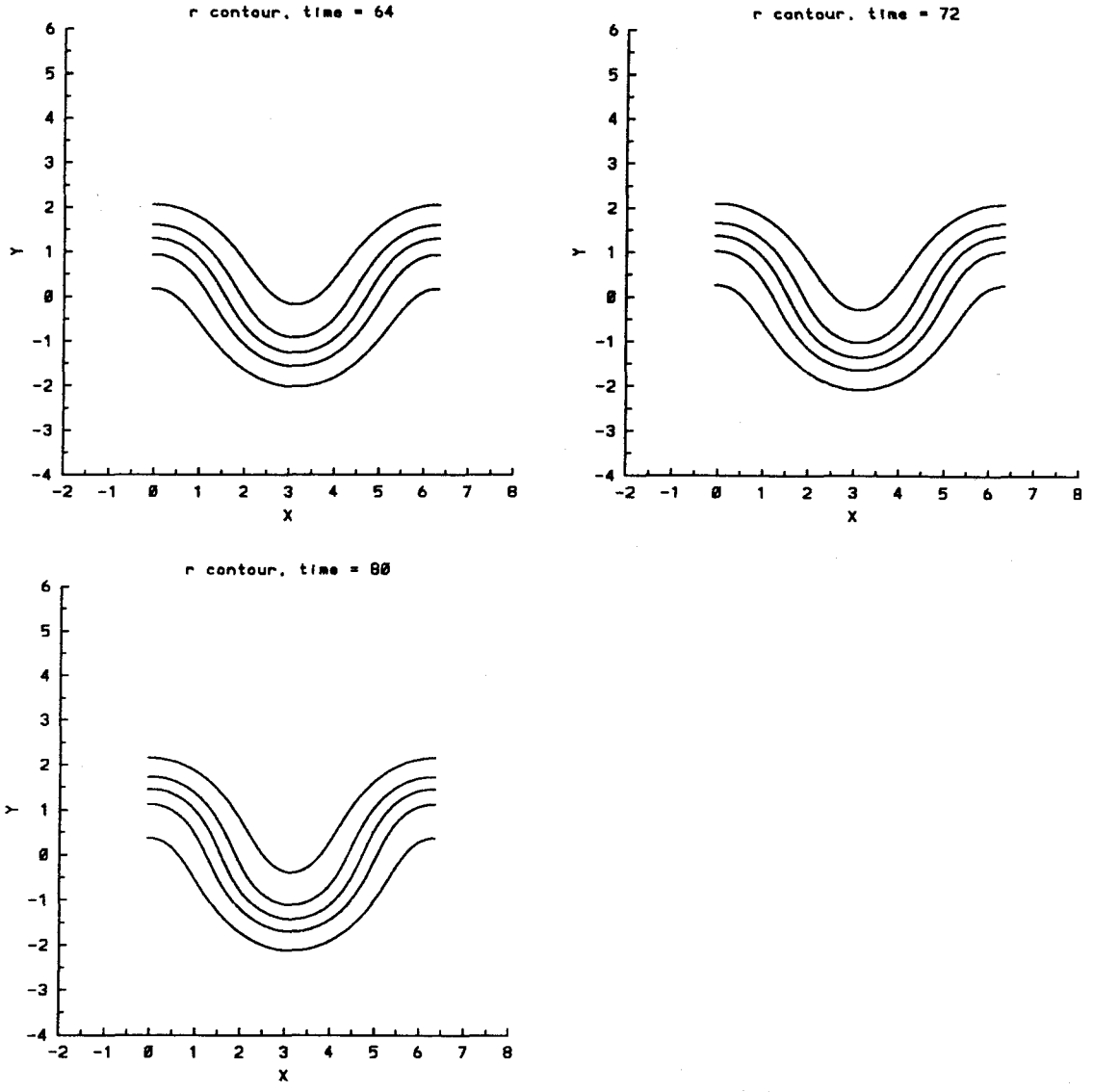

Figure 4.16.6 Time evolution of the density contours for the single scale profile $\lambda = 1.0$, A $= -0.05$, $\epsilon = 0.5$, $t = 64$, 72, 80. The contours are at $\rho = 0.48$, 0.49, 0.50, 0.51, 0.52 in that order from top to bottom of each figure.

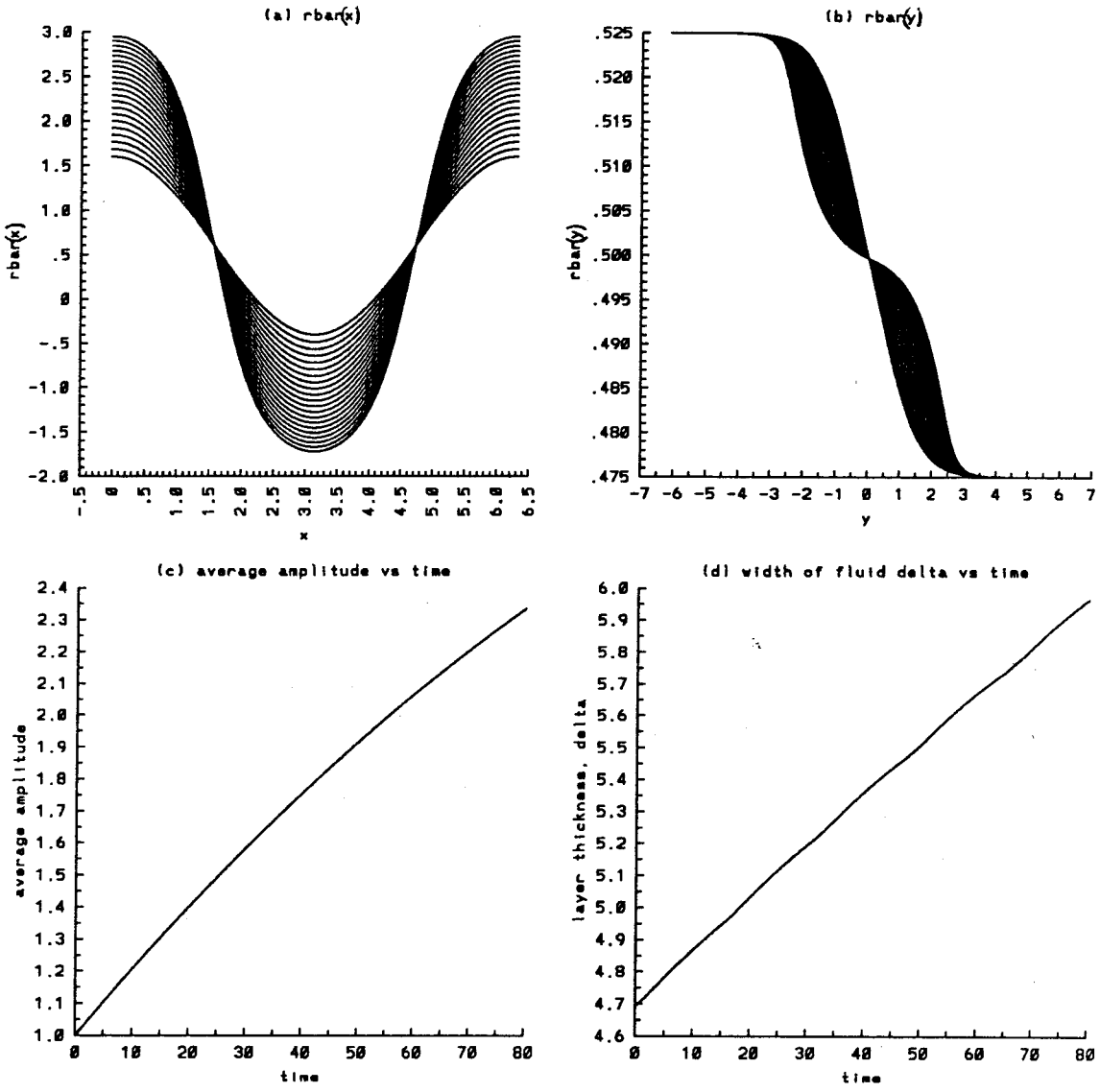

Figure 4.17.1 Time evolution of the average quantities for the single scale profile L = 1.0, A = −0.05, $\epsilon = 1.0$, $t = 0$ to 80 : a) $\bar{\rho}_y(x)$, b) $\bar{\rho}_x(y)$, c) average amplitude, and d) width of the density layer.

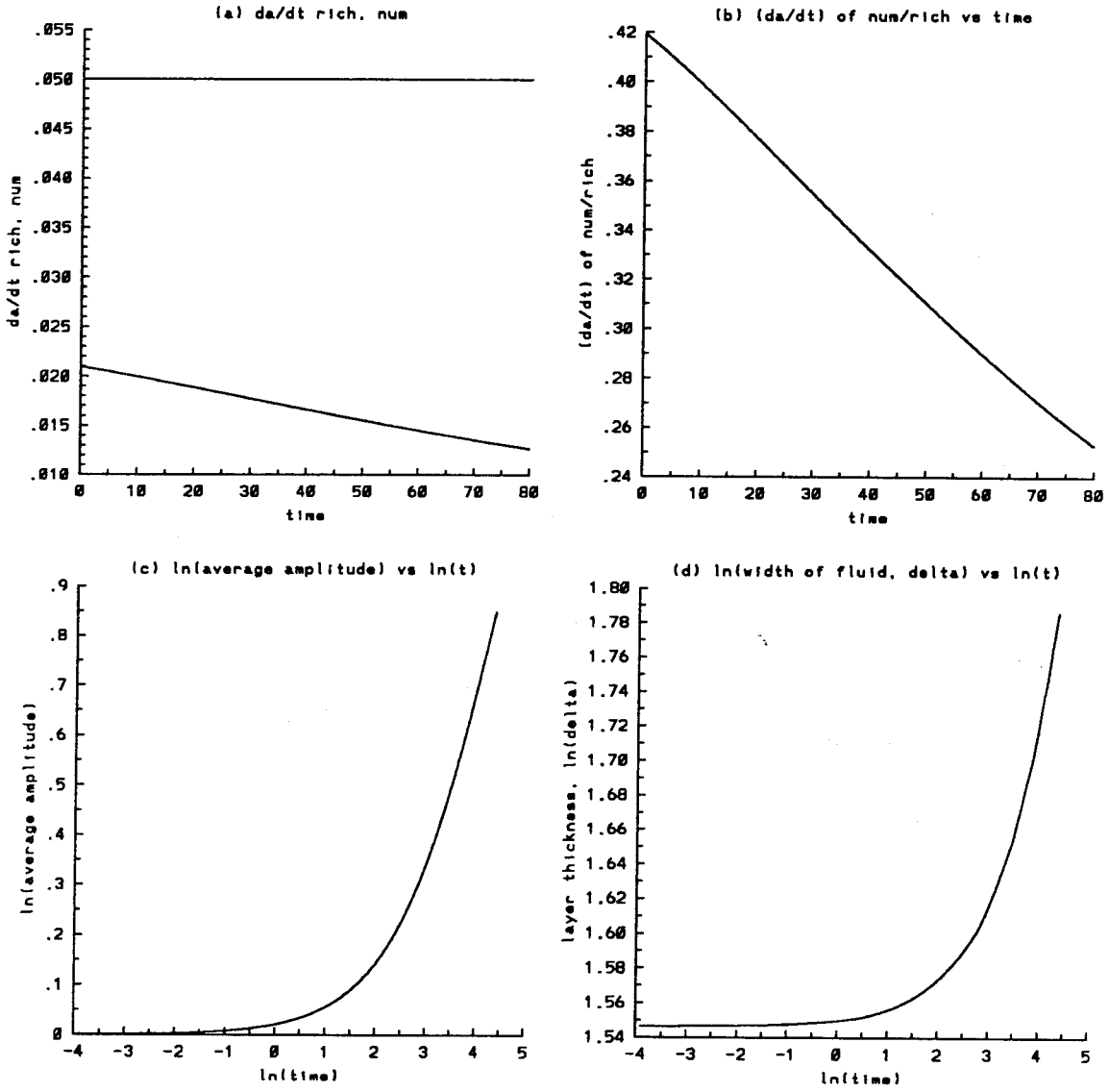

Figure 4.17.2 Time evolution of the average quantities for the single scale profile $\lambda = 1.0$, A $= -0.05$, $\epsilon = 1.0$, $t = 0$ to 80 : a) growth rate da/dt of the average amplitude, numerical and Richtmyer theory (straight line), b) the ratio of the numerical growth rate da/dt over that predicted by Richtmyer theory, c) $\ln(a)$ *vs* $\ln(t)$, d) $\ln(\delta)$ *vs* $\ln(t)$.

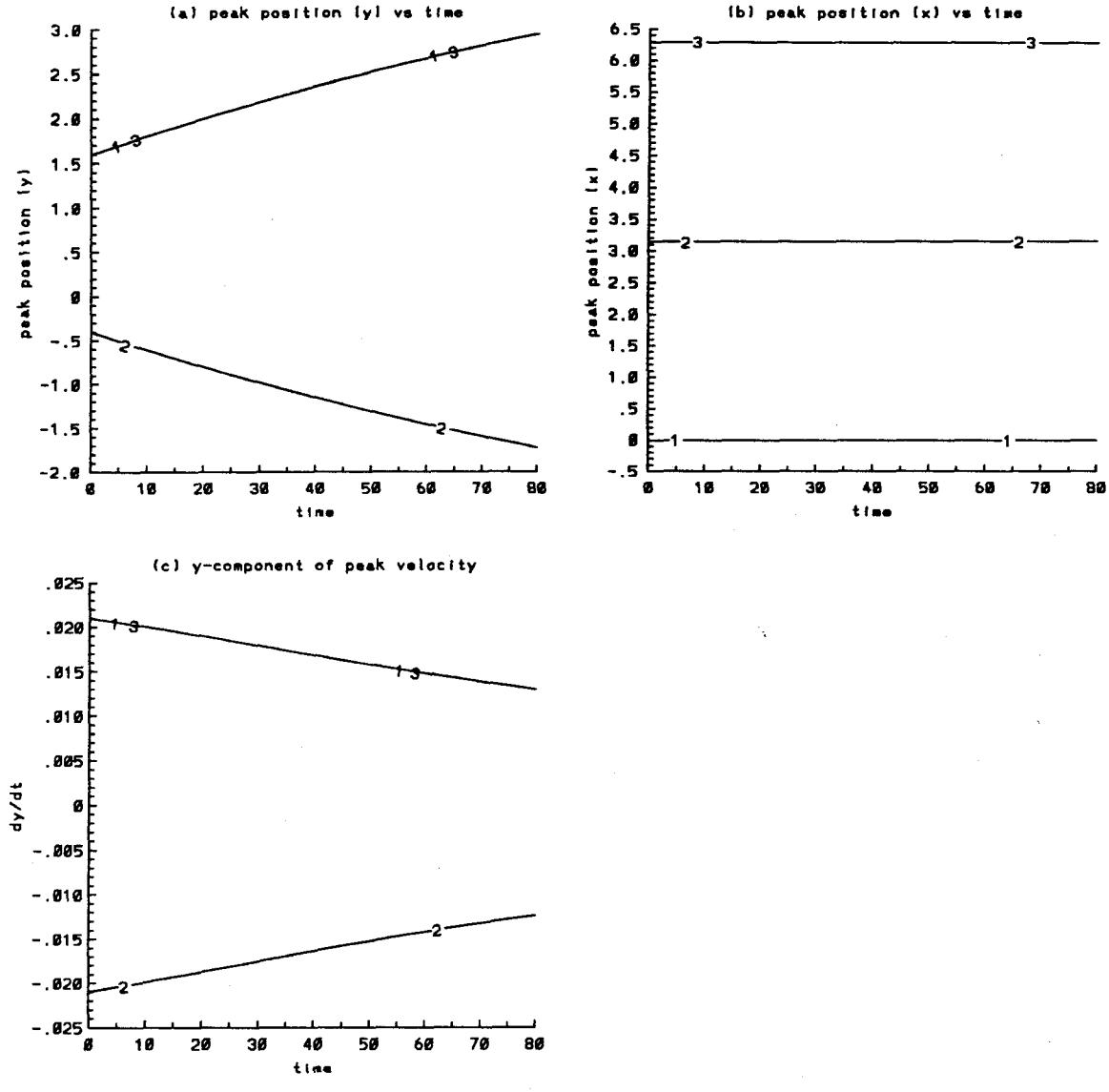

Figure 4.17.3 Time evolution of the positions and velocities of the average peaks in the single scale profile L = 1.0, A = −0.05, $\epsilon = 1.0$, $t = 0$ to 80 a) y b) x c) dy/dt. The numbers on the curves refer to the peaks on the curves $\bar{\rho}_y(x)$ versus x.

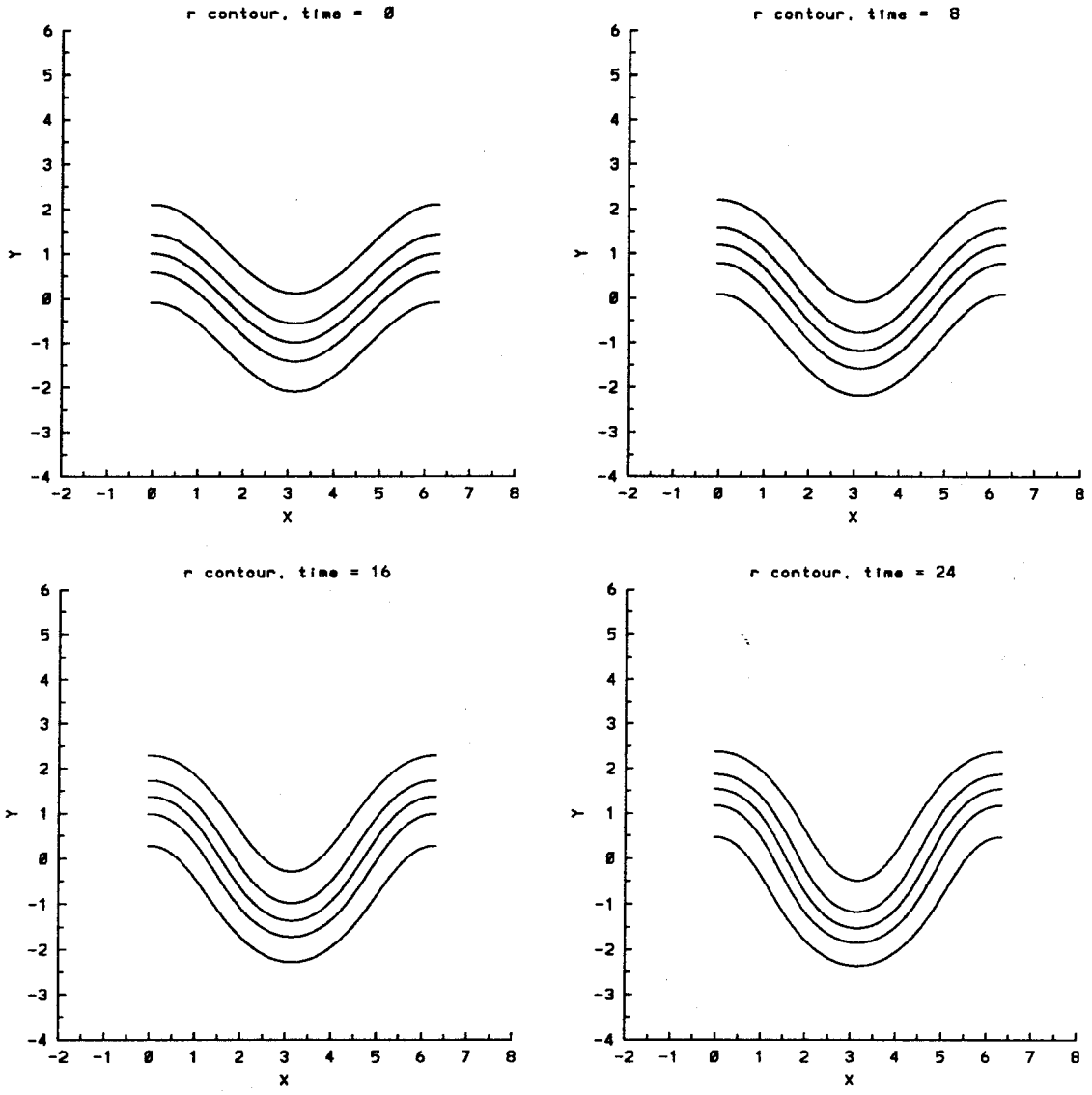

Figure 4.17.4 Time evolution of the density contours for the single scale profile L = 1.0, A = −0.05, $\epsilon = 1.0$, $t = 0$, 8, 16, 24. The contours are at $\rho = 0.48$, 0.49, 0.50, 0.51, 0.52 in that order from top to bottom of each figure.

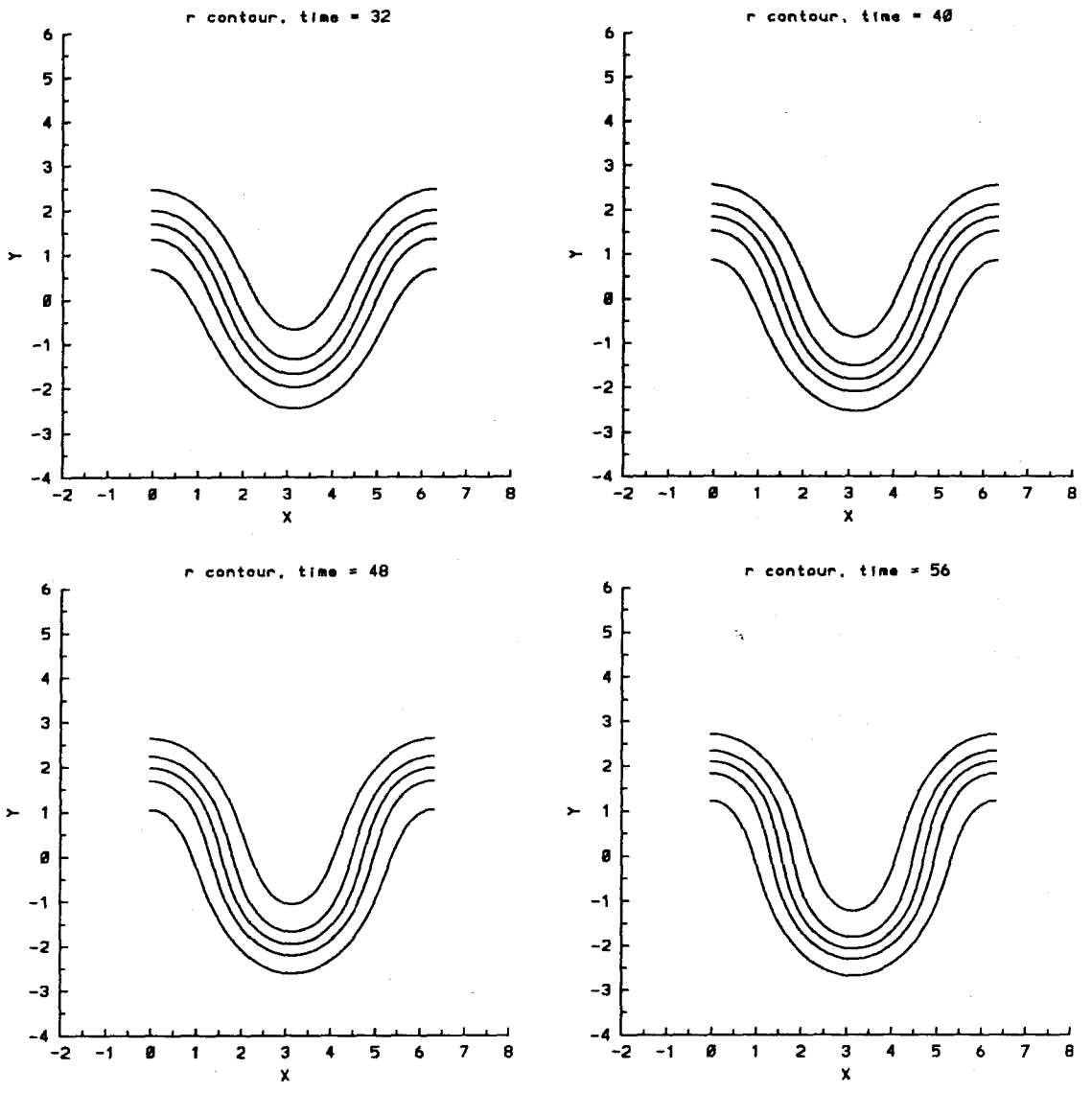

Figure 4.17.5 Time evolution of the density contours for the single scale profile L = 1.0, A = −0.05, $\epsilon = 1.0$, $t = 32, 40, 48, 56$. The contours are at $\rho = 0.48, 0.49, 0.50, 0.51, 0.52$ in that order from top to bottom of each figure.

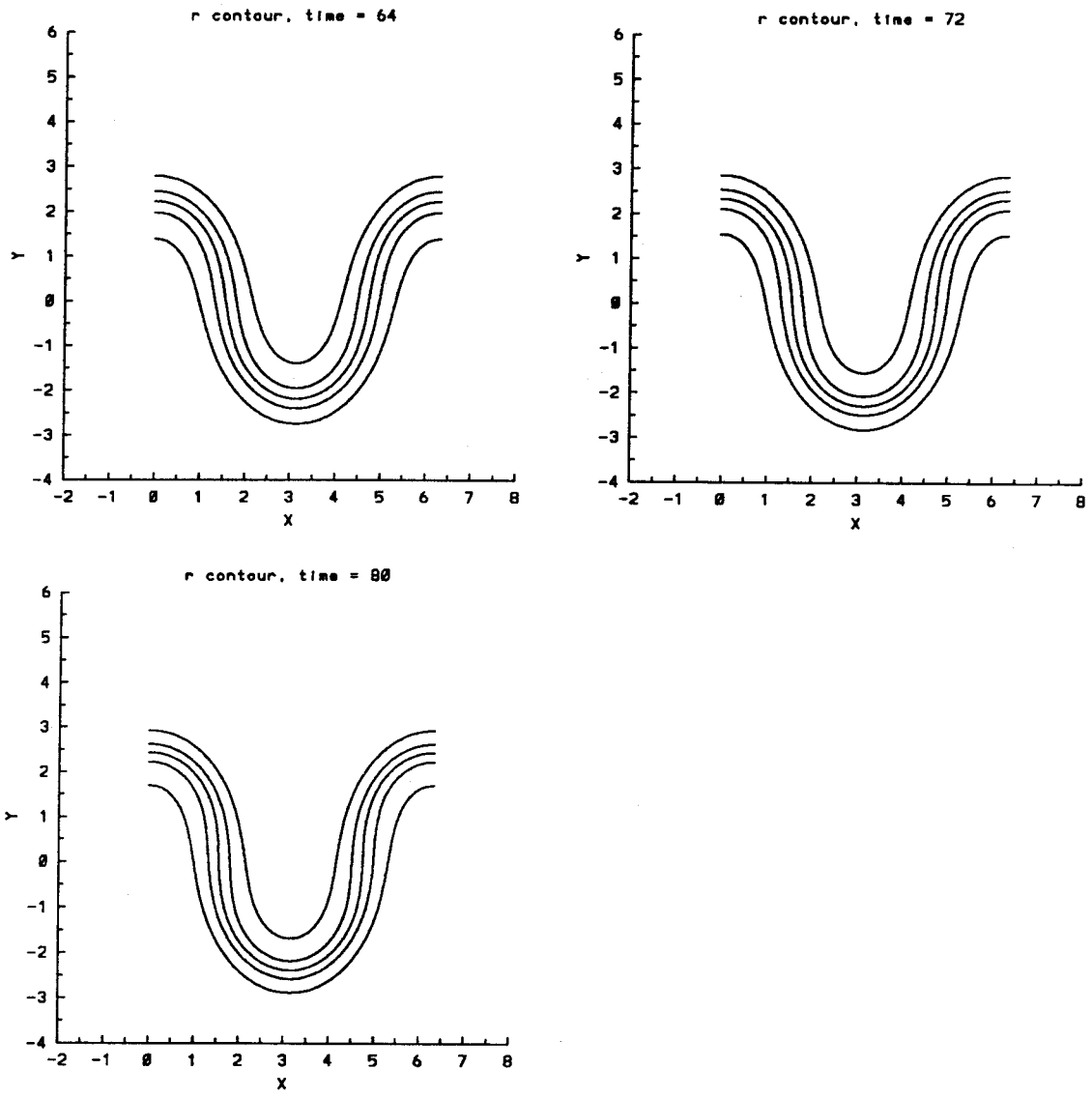

Figure 4.17.6 Time evolution of the density contours for the single scale profile L = 1.0, A = −0.05, $\epsilon = 1.0$, $t = 64$, 72, 80. The contours are at $\rho = 0.48$, 0.49, 0.50, 0.51, 0.52 in that order from top to bottom of each figure.

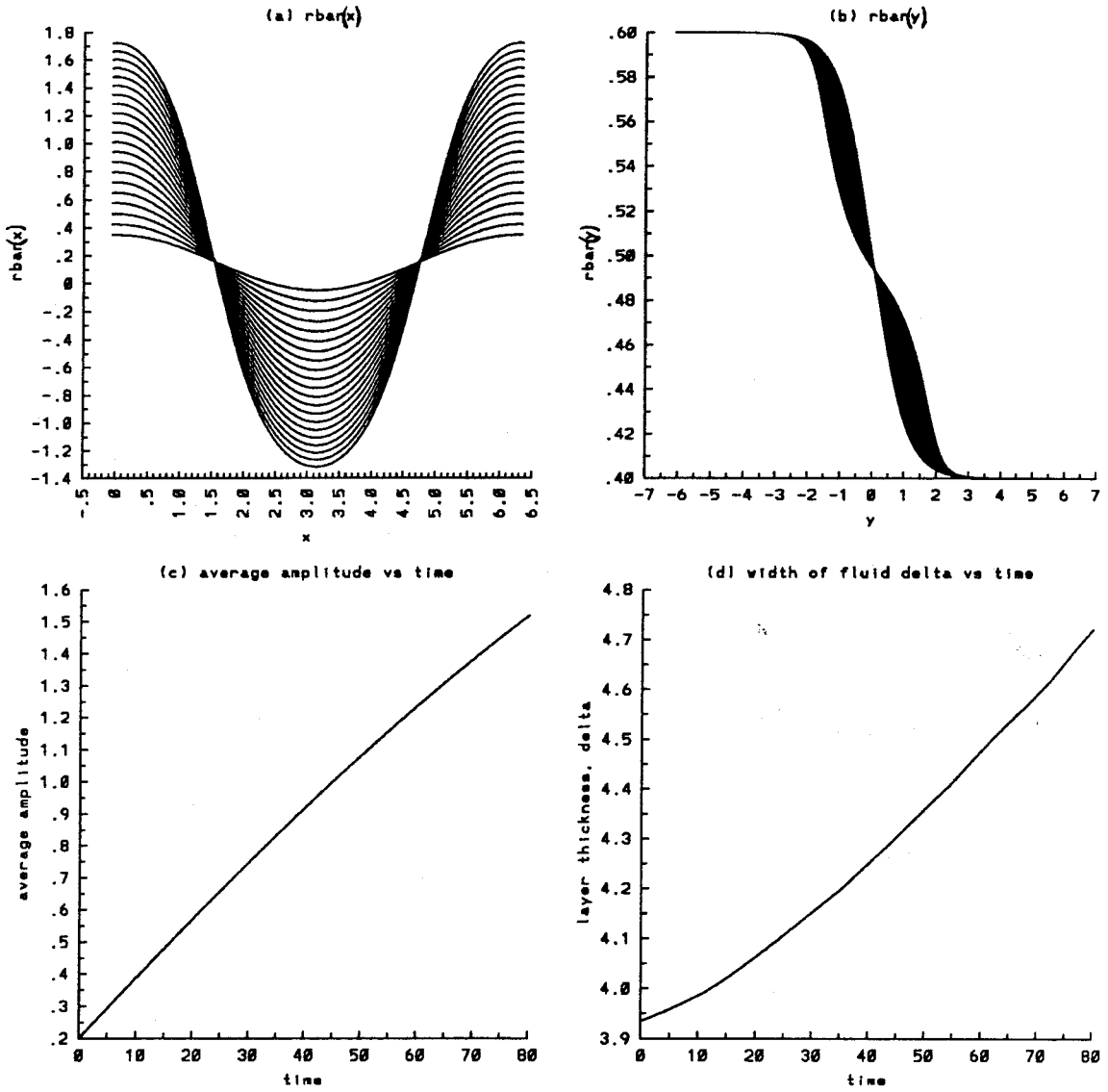

Figure 4.18.1 Time evolution of the average quantities for the single scale profile L = 1.0, A = −0.2, $\epsilon = 0.2$, $t = 0$ to 80 : a) $\bar{\rho}_y(x)$, b) $\bar{\rho}_x(y)$, c) average amplitude, and d) width of the density layer.

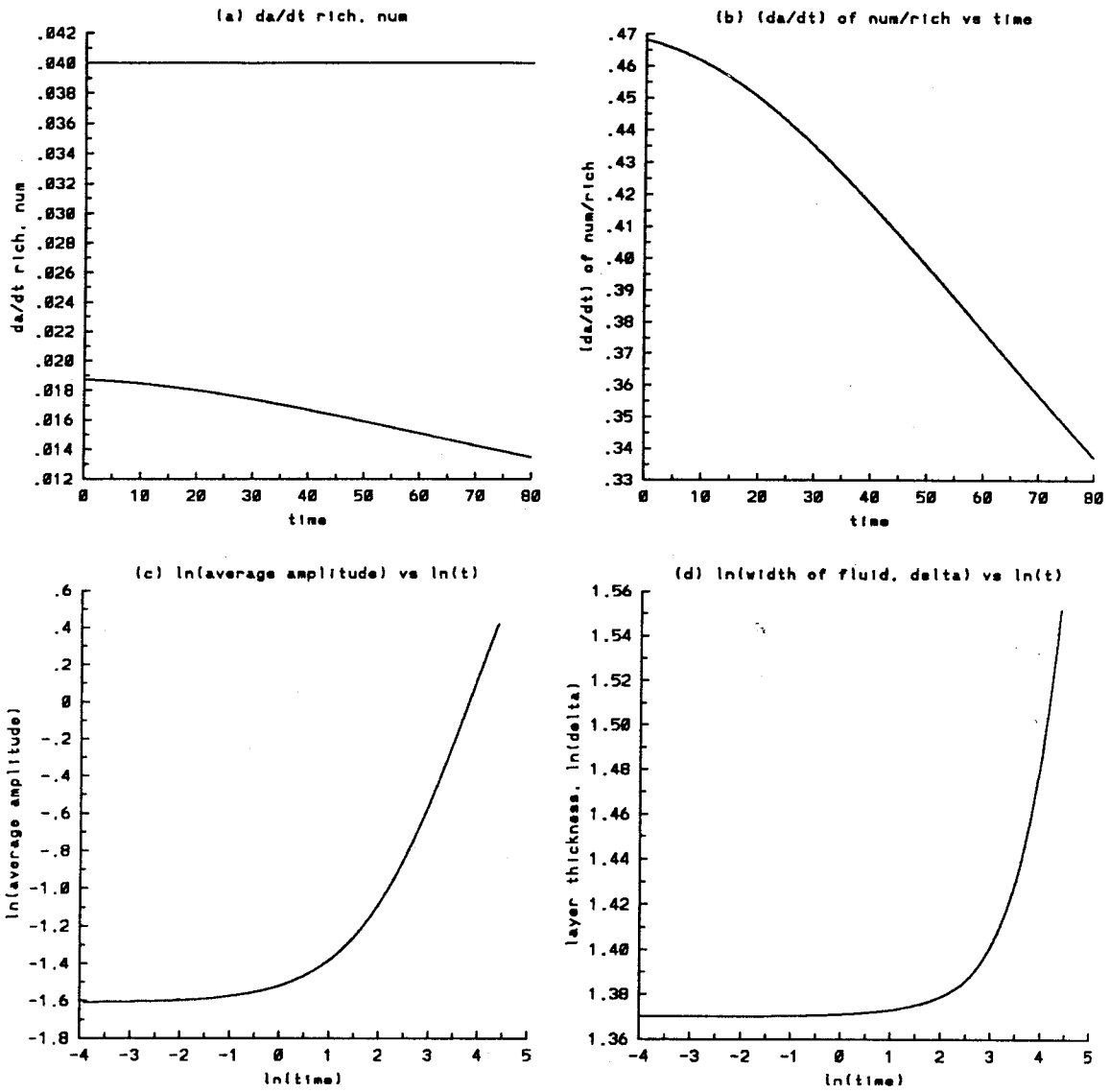

Figure 4.18.2 Time evolution of the average quantities for the single scale profile $L = 1.0$, A $= -0.2$, $\epsilon = 0.2$, $t = 0$ to 80 : a) growth rate da/dt of the average amplitude, numerical and Richtmyer theory (straight line), b) the ratio of the numerical growth rate da/dt over that predicted by Richtmyer theory, c) $\ln(a)$ *vs* $\ln(t)$, d) $\ln(\delta)$ *vs* $\ln(t)$.

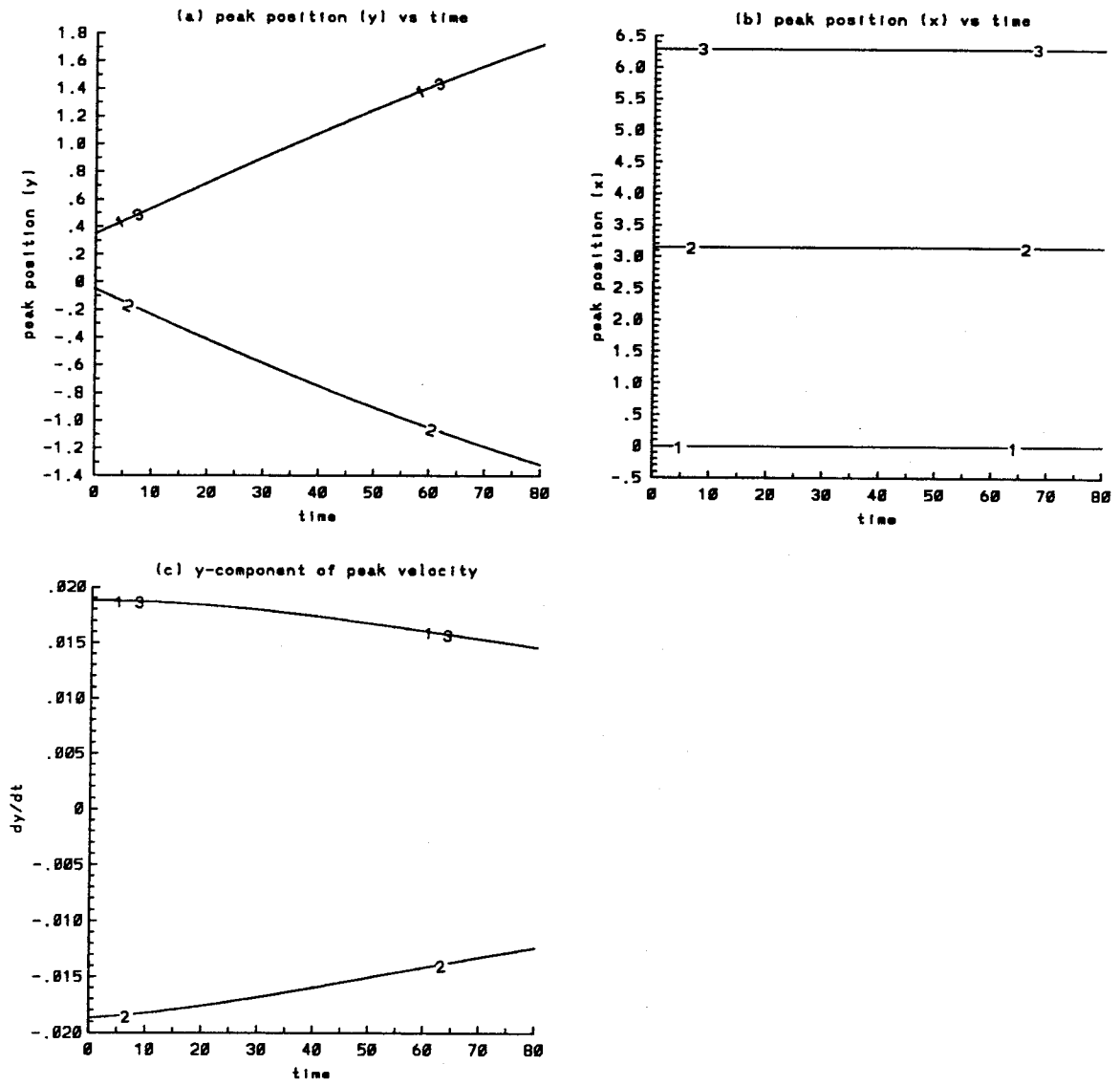

Figure 4.18.3 Time evolution of the positions and velocities of the average peaks in the single scale profile L = 1.0, A = −0.2, $\epsilon = 0.2$, $t = 0$ to 80 a) y b) x c) dy/dt. The numbers on the curves refer to the peaks on the curves $\bar{\rho}_y(x)$ versus x.

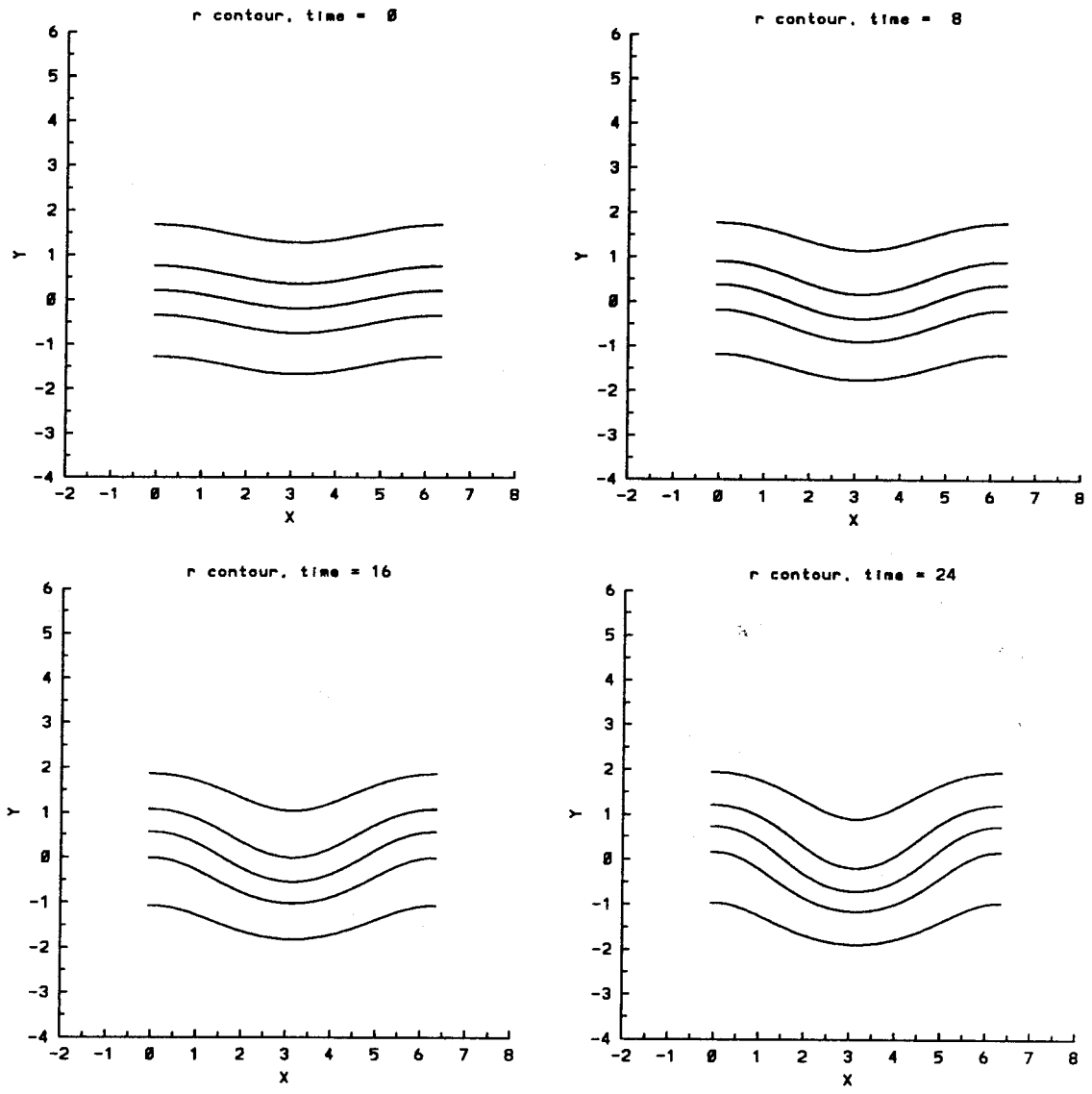

Figure 4.18.4 Time evolution of the density contours for the single scale profile L = 1.0, A = −0.2, $\epsilon = 0.2$, $t = 0$, 8, 16, 24. The contours are at $\rho = 0.41$, 0.45, 0.50, 0.55, 0.59 in that order from top to bottom of each figure.

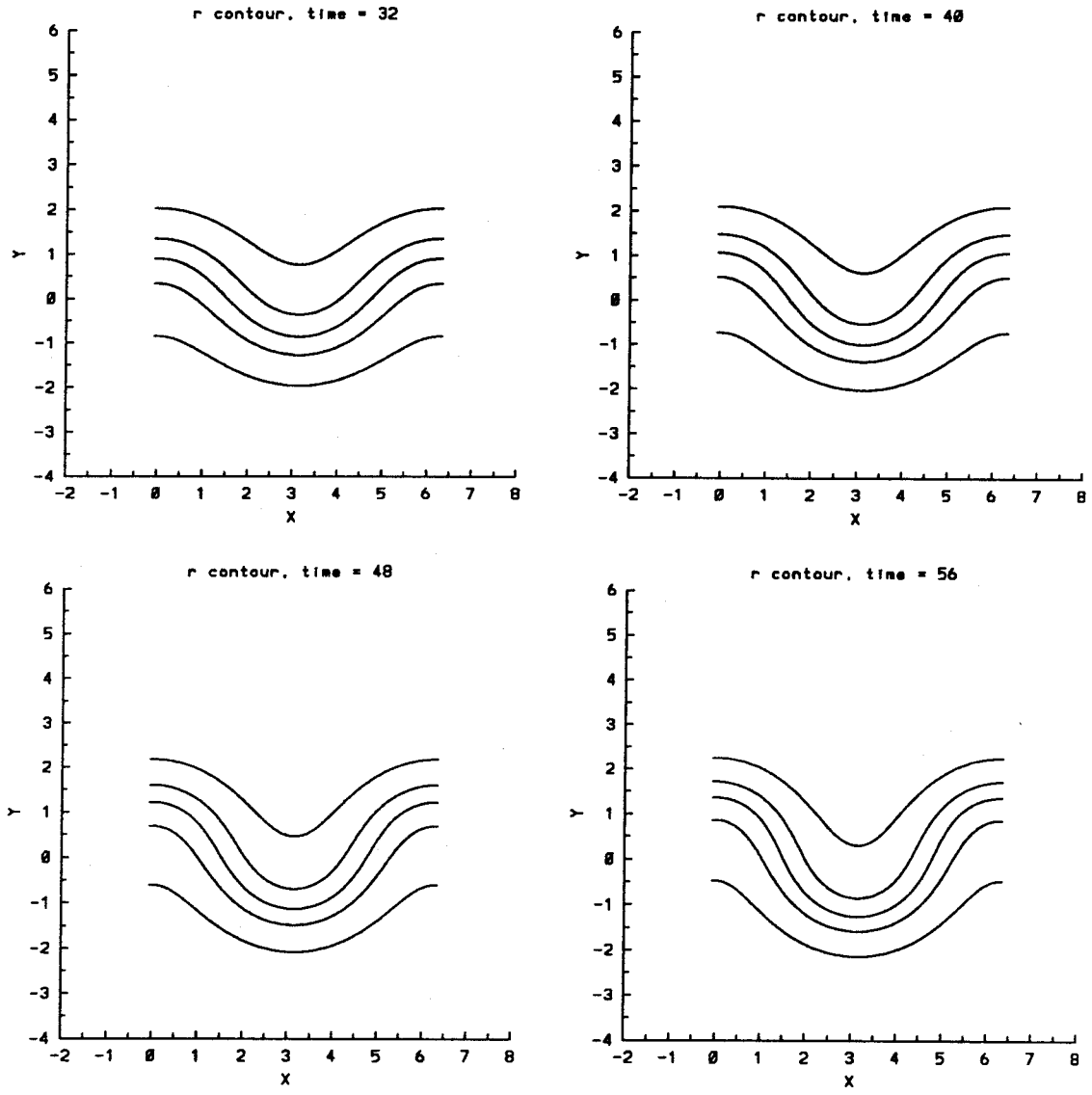

Figure 4.18.5 Time evolution of the density contours for the single scale profile L = 1.0, A = −0.2, $\epsilon = 0.2$, t = 32, 40, 48, 56. The contours are at ρ = 0.41, 0.45, 0.50, 0.55, 0.59 in that order from top to bottom of each figure.

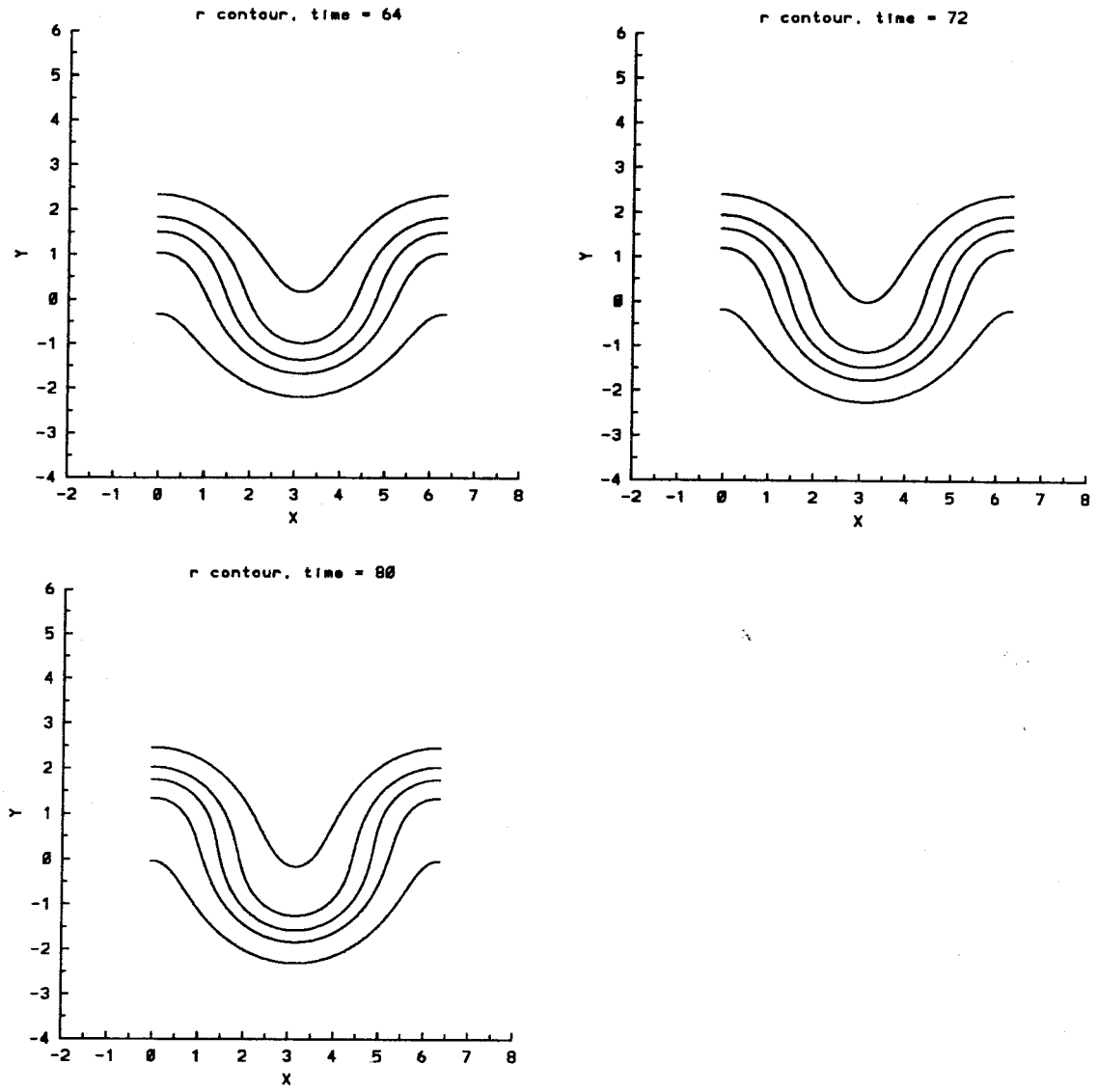

Figure 4.18.6 Time evolution of the density contours for the single scale profile L = 1.0, A = −0.2, ϵ = 0.2, t = 64, 72, 80. The contours are at ρ = 0.41, 0.45, 0.50, 0.55, 0.59 in that order from top to bottom of each figure.

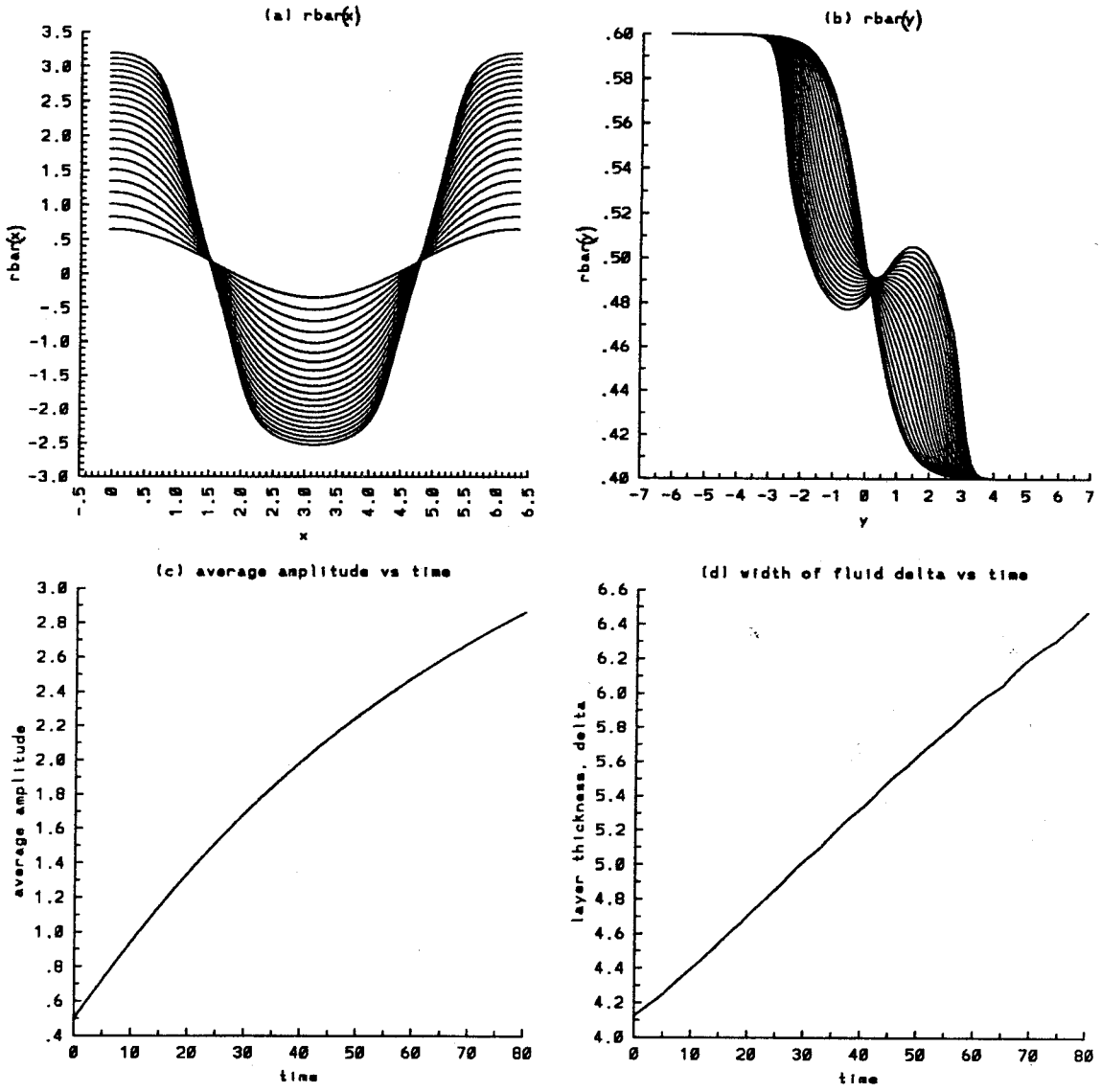

Figure 4.19.1 Time evolution of the average quantities for the single scale profile L = 1.0, A = −0.2, $\epsilon = 0.5$, $t = 0$ to 80 : a) $\bar{\rho}_y(x)$, b) $\bar{\rho}_x(y)$, c) average amplitude, and d) width of the density layer.

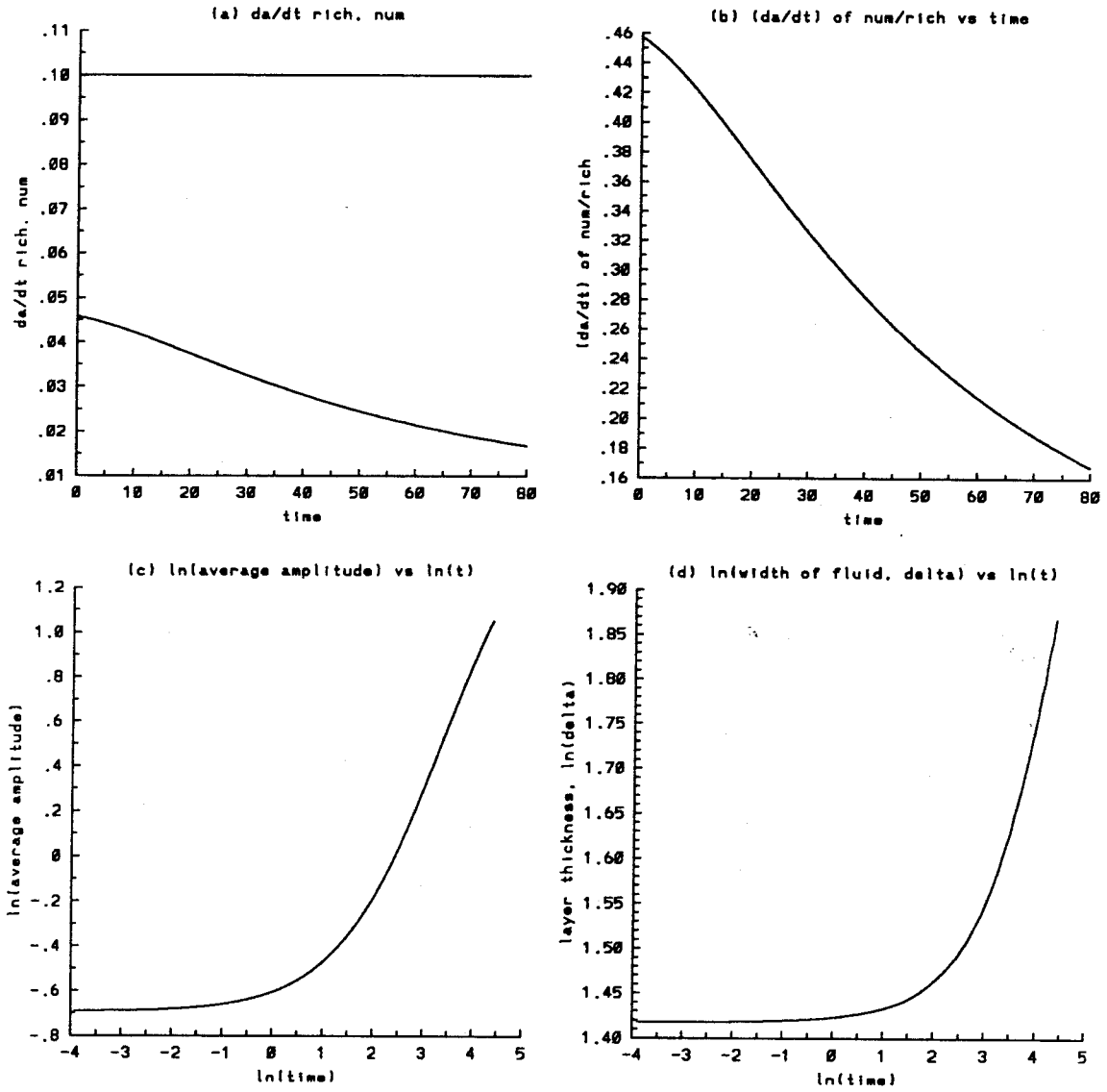

Figure 4.19.2 Time evolution of the average quantities for the single scale profile L = 1.0, A = −0.2, $\epsilon = 0.5$, $t = 0$ to 80 : a) growth rate da/dt of the average amplitude, numerical and Richtmyer theory (straight line), b) the ratio of the numerical growth rate da/dt over that predicted by Richtmyer theory, c) $\ln(a)$ *vs* $\ln(t)$, d) $\ln(\delta)$ *vs* $\ln(t)$.

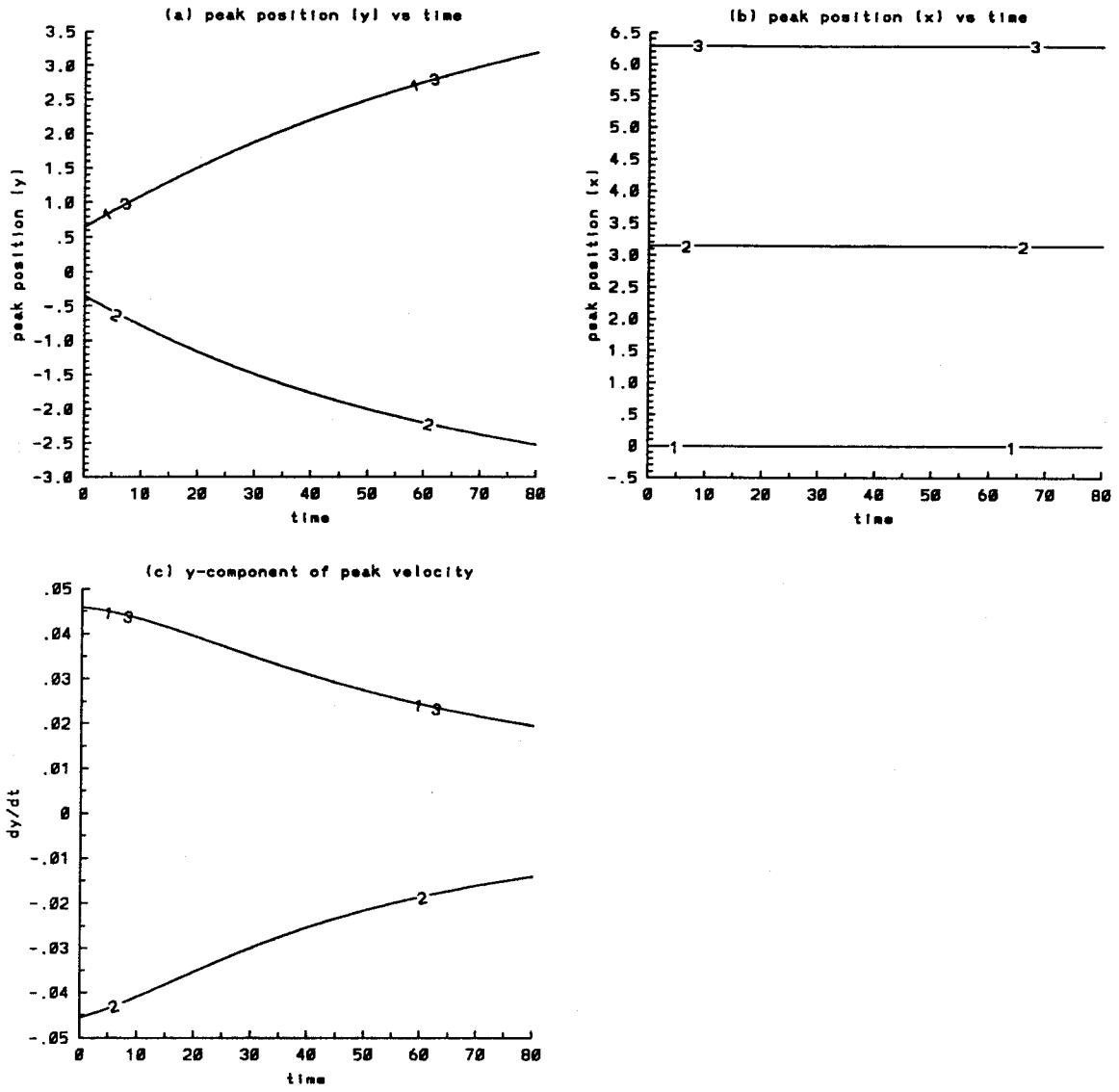

Figure 4.19.3 Time evolution of the positions and velocities of the average peaks in the single scale profile L = 1.0, A = −0.2, $\epsilon = 0.5$, $t = 0$ to 80 a) y b) x c) dy/dt. The numbers on the curves refer to the peaks on the curves $\bar{\rho}_y(x)$ versus x.

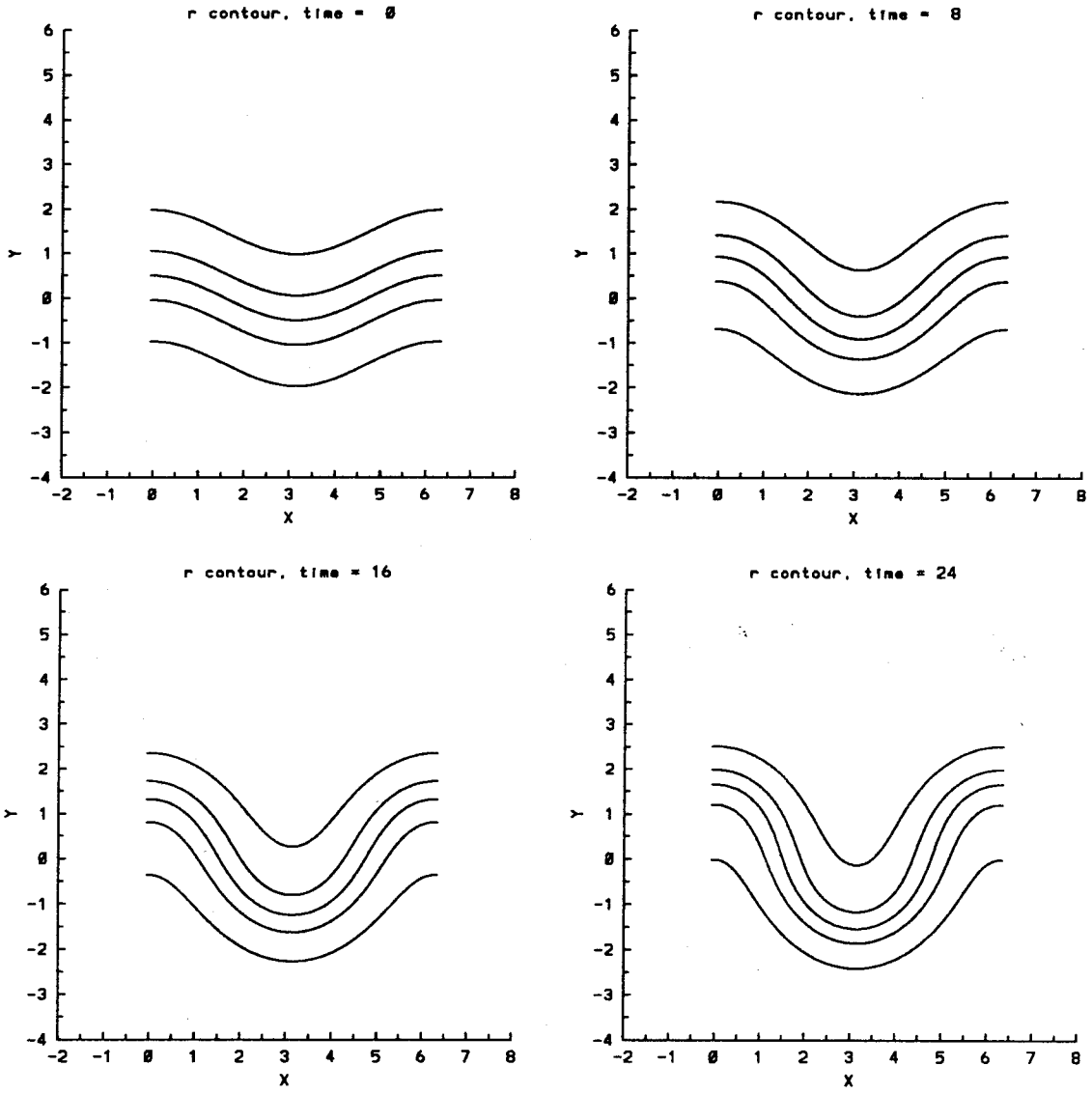

Figure 4.19.4 Time evolution of the density contours for the single scale profile $\mathrm{L} = 1.0$, $\mathrm{A} = -0.2$, $\epsilon = 0.5$, $t = 0$, 8, 16, 24. The contours are at $\rho = 0.41$, 0.45, 0.50, 0.55, 0.59 in that order from top to bottom of each figure.

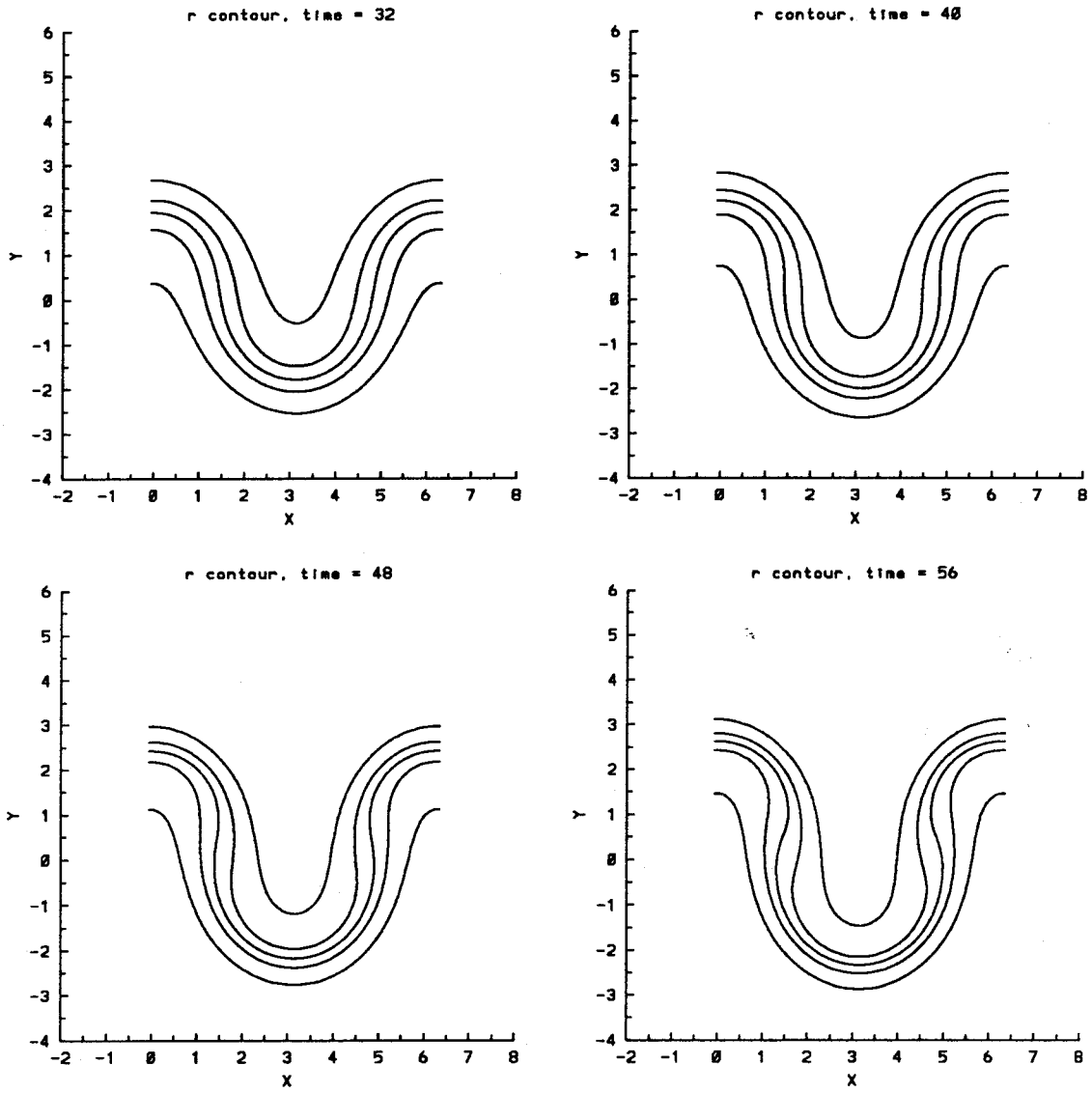

Figure 4.19.5 Time evolution of the density contours for the single scale profile L = 1.0, A = −0.2, $\epsilon = 0.5$, $t = 32, 40, 48, 56$. The contours are at $\rho = 0.41, 0.45, 0.50, 0.55, 0.59$ in that order from top to bottom of each figure.

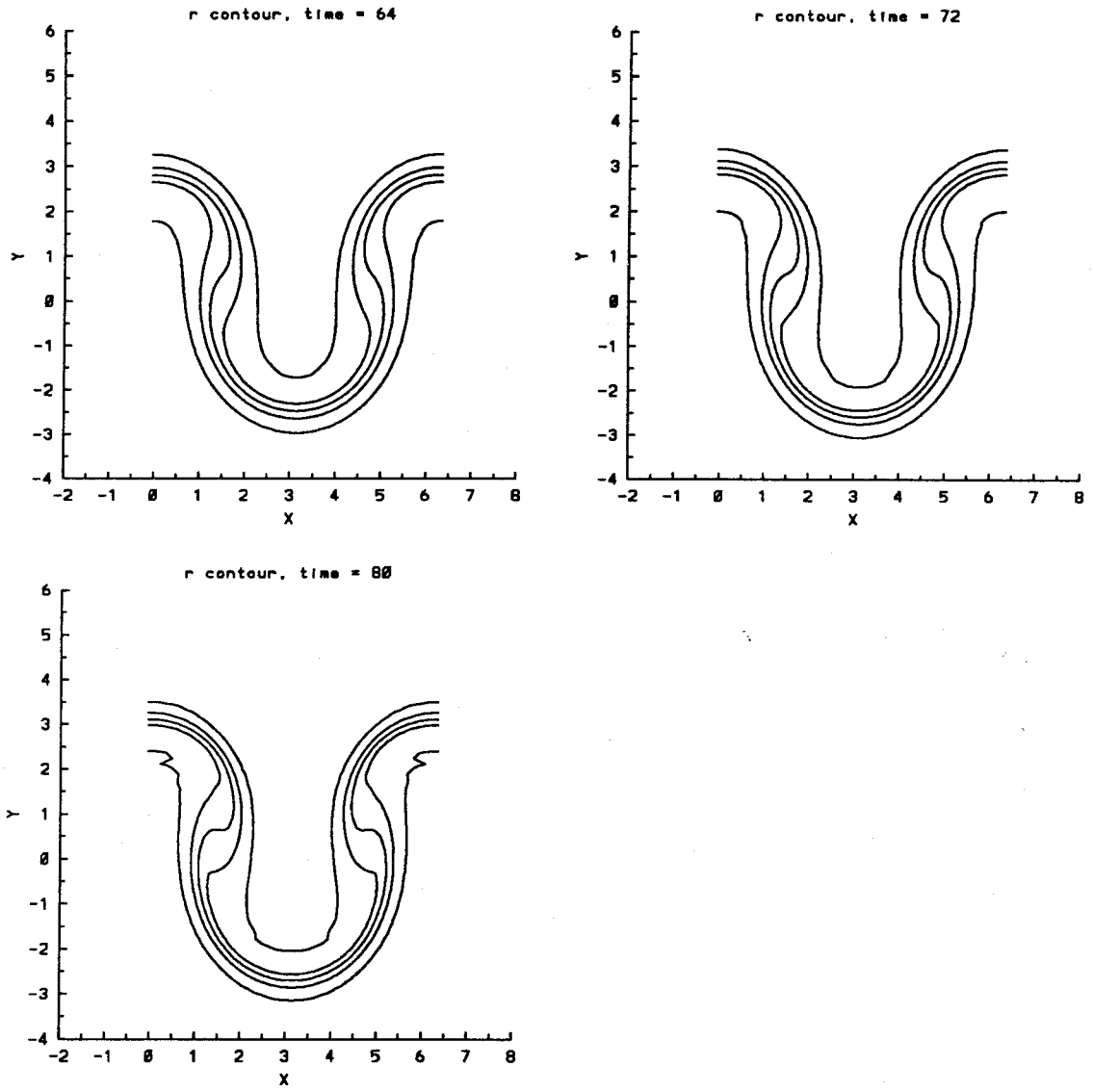

Figure 4.19.6 Time evolution of the density contours for the single scale profile L = 1.0, A = −0.2, $\epsilon = 0.5$, $t = 64$, 72, 80. The contours are at $\rho = 0.41$, 0.45, 0.50, 0.55, 0.59 in that order from top to bottom of each figure.

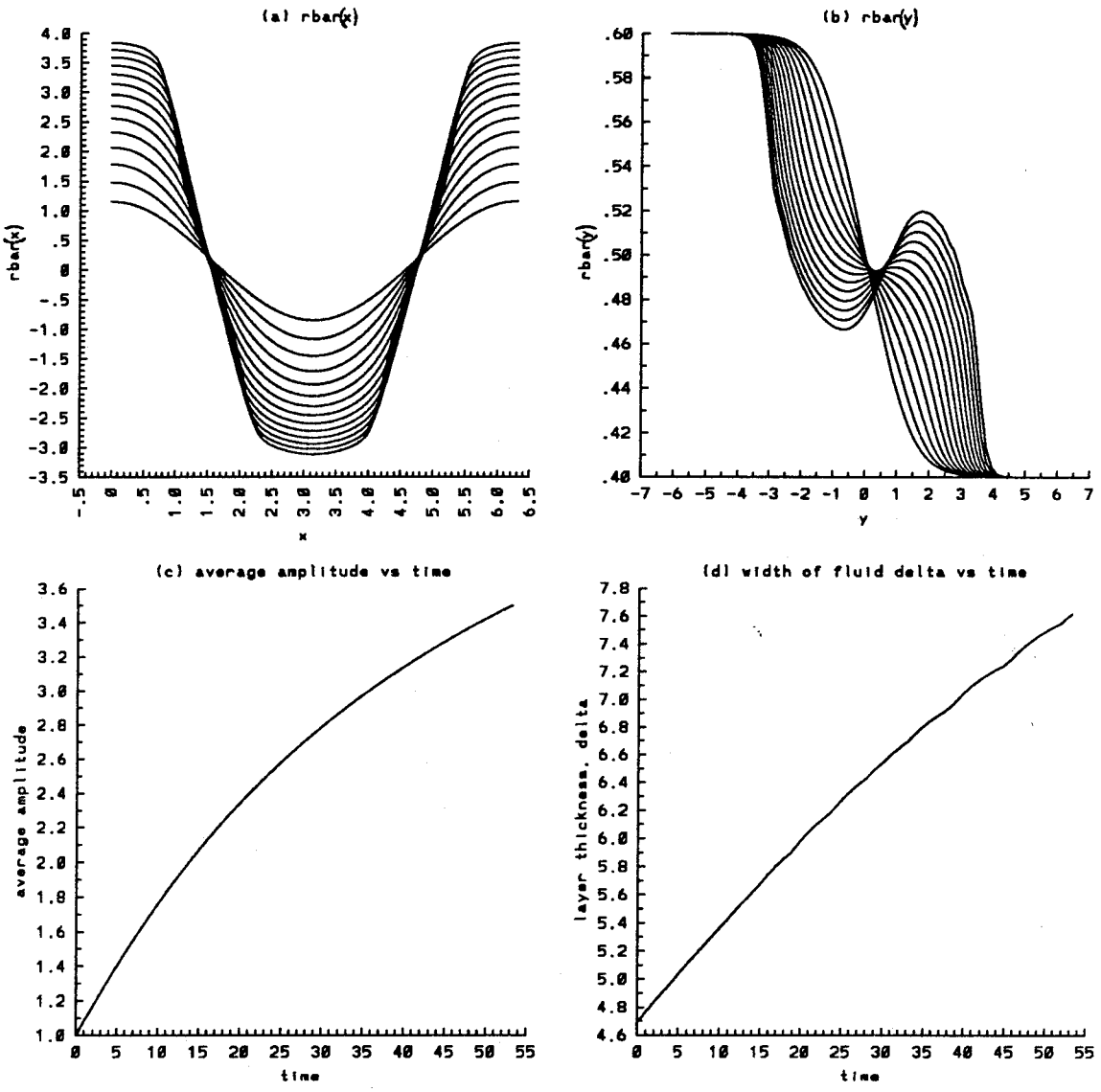

Figure 4.20.1 Time evolution of the average quantities for the single scale profile L = 1.0, A = −0.2, $\epsilon = 1.0$, $t = 0$ to 53 : a) $\bar{\rho}_y(x)$, b) $\bar{\rho}_x(y)$, c) average amplitude, and d) width of the density layer.

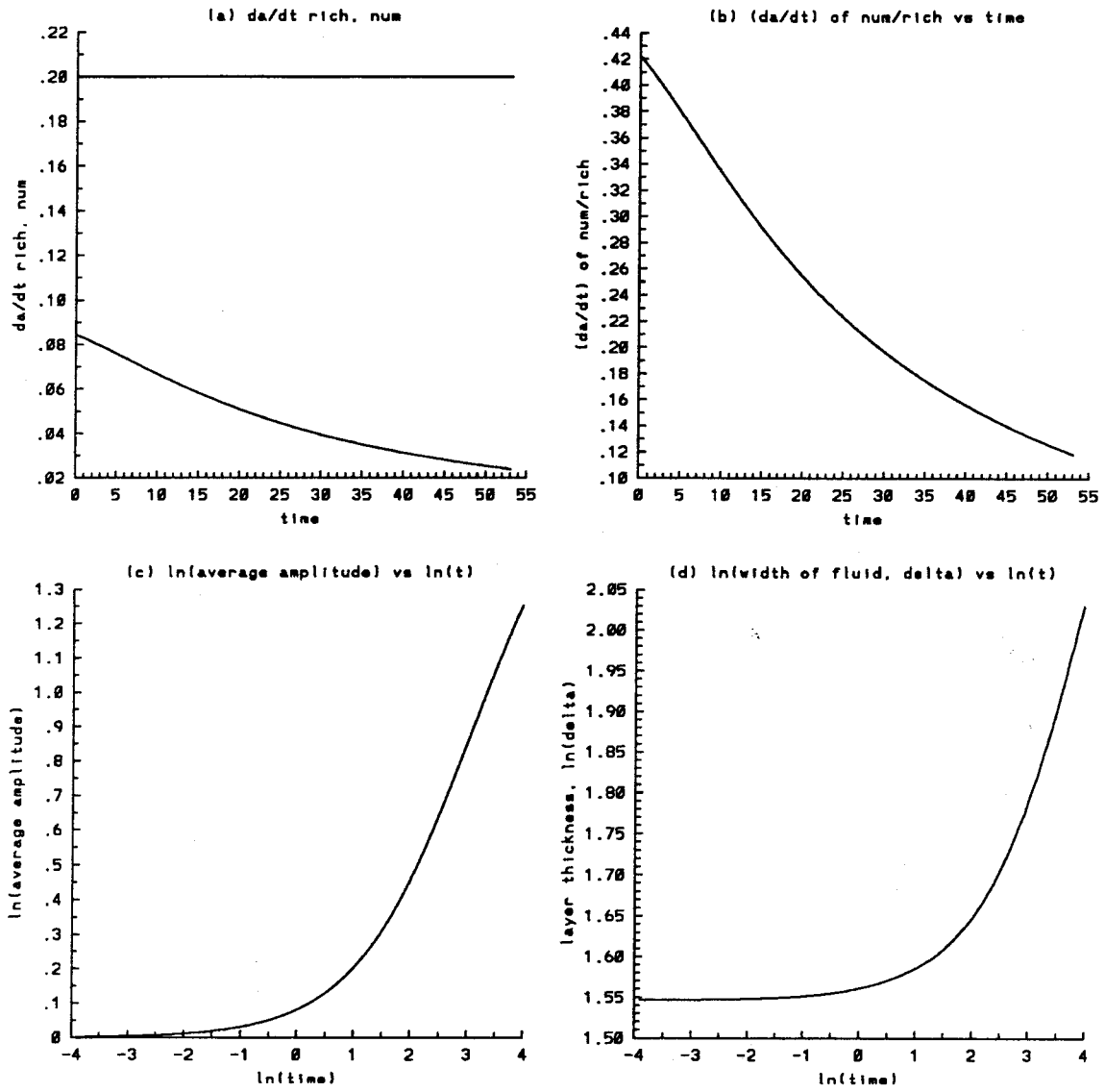

Figure 4.20.2 Time evolution of the average quantities for the single scale profile L = 1.0, A = −0.2, $\epsilon = 1.0$, $t = 0$ to 53 : a) growth rate da/dt of the average amplitude, numerical and Richtmyer theory (straight line), b) the ratio of the numerical growth rate da/dt over that predicted by Richtmyer theory, c) $\ln(a)$ *vs* $\ln(t)$, d) $\ln(\delta)$ *vs* $\ln(t)$.

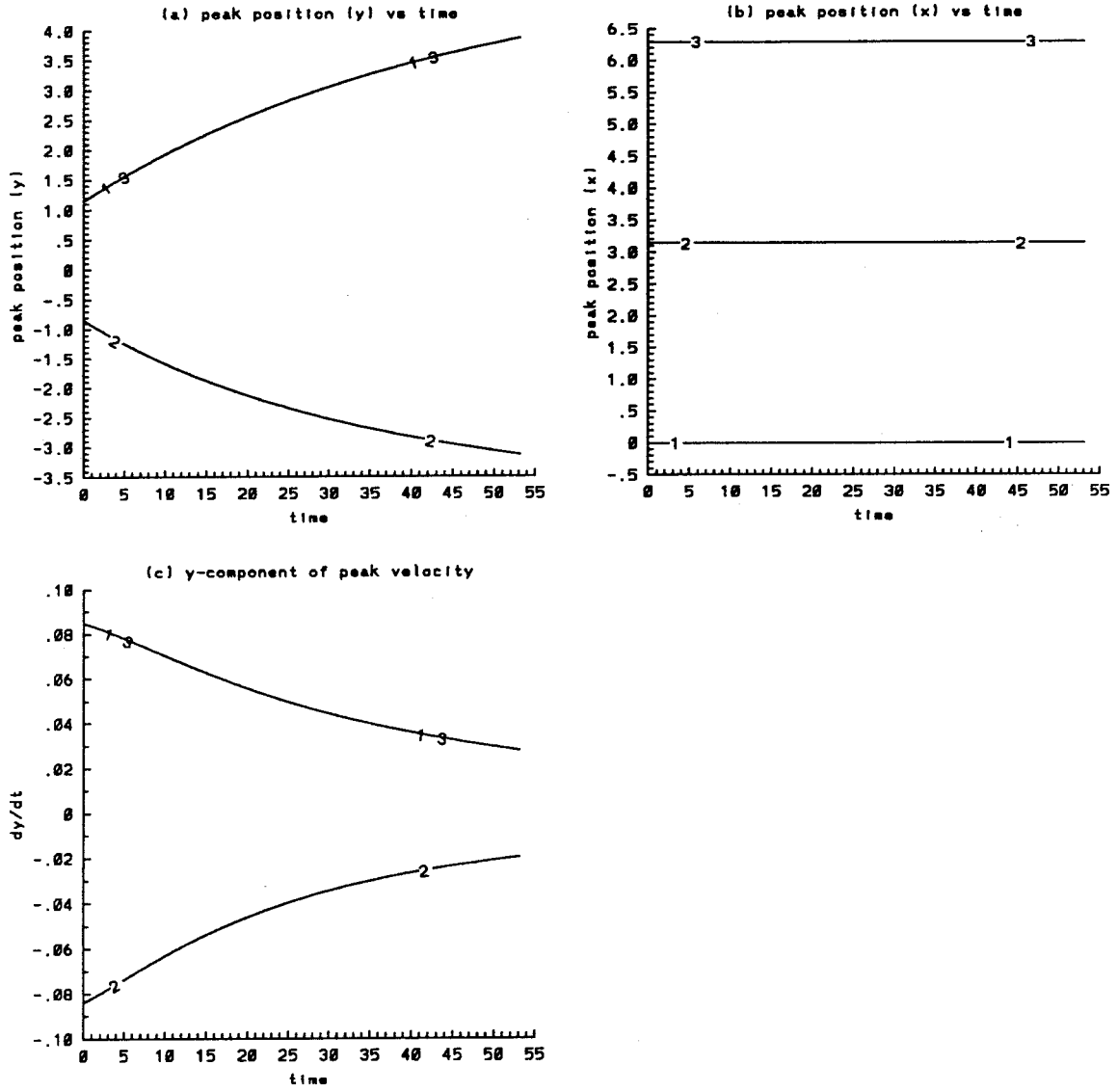

Figure 4.20.3 Time evolution of the positions and velocities of the average peaks in the single scale profile L = 1.0, A = −0.2, $\epsilon = 1.0$, $t = 0$ to 53 a) y b) x c) dy/dt. The numbers on the curves refer to the peaks on the curves $\bar{\rho}_y(x)$ versus x.

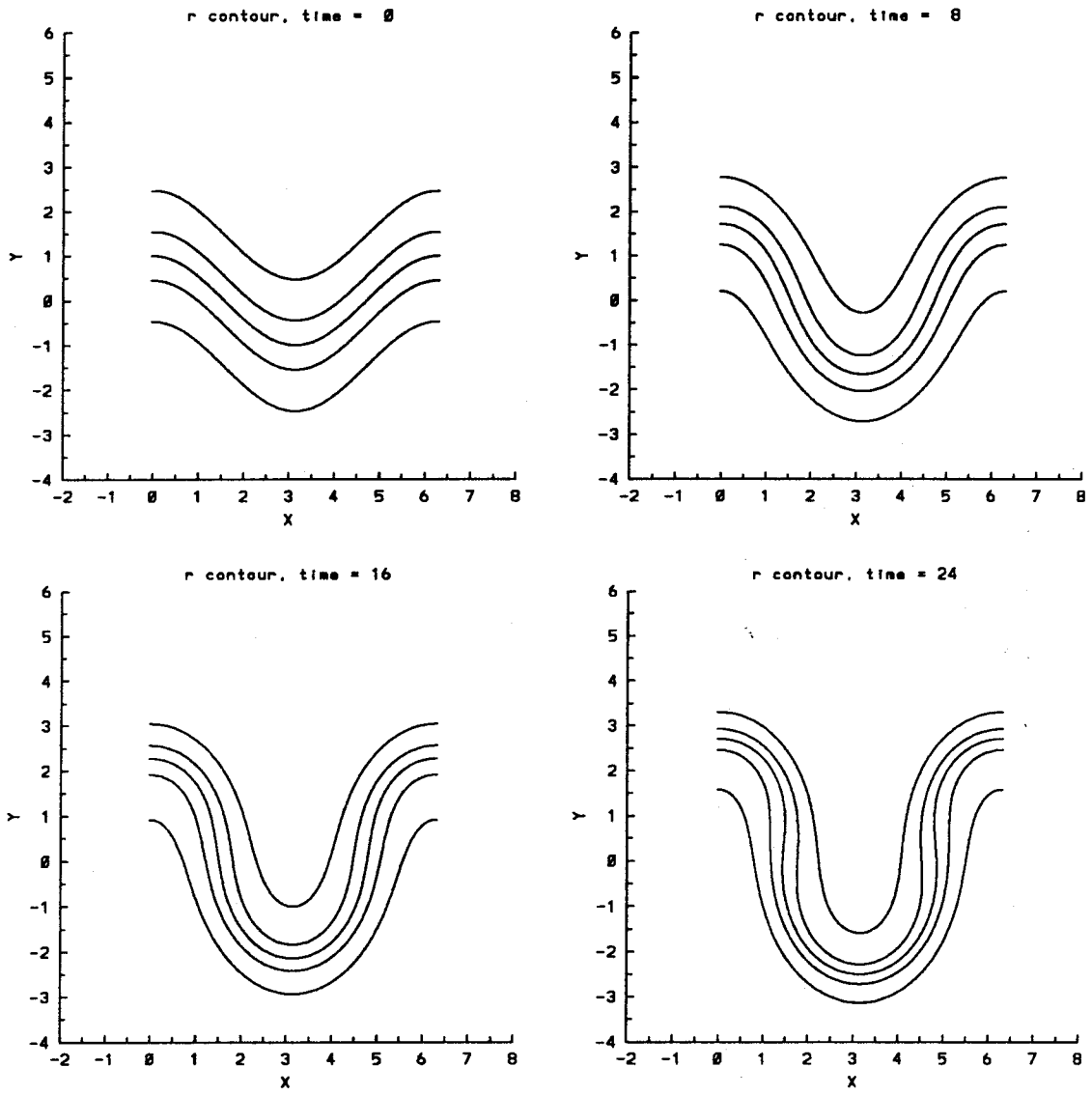

Figure 4.20.4 Time evolution of the density contours for the single scale profile L = 1.0, A = −0.2, $\epsilon = 1.0$, $t = 0$, 8, 16, 24. The contours are at $\rho = 0.41$, 0.45, 0.50, 0.55, 0.59 in that order from top to bottom of each figure.

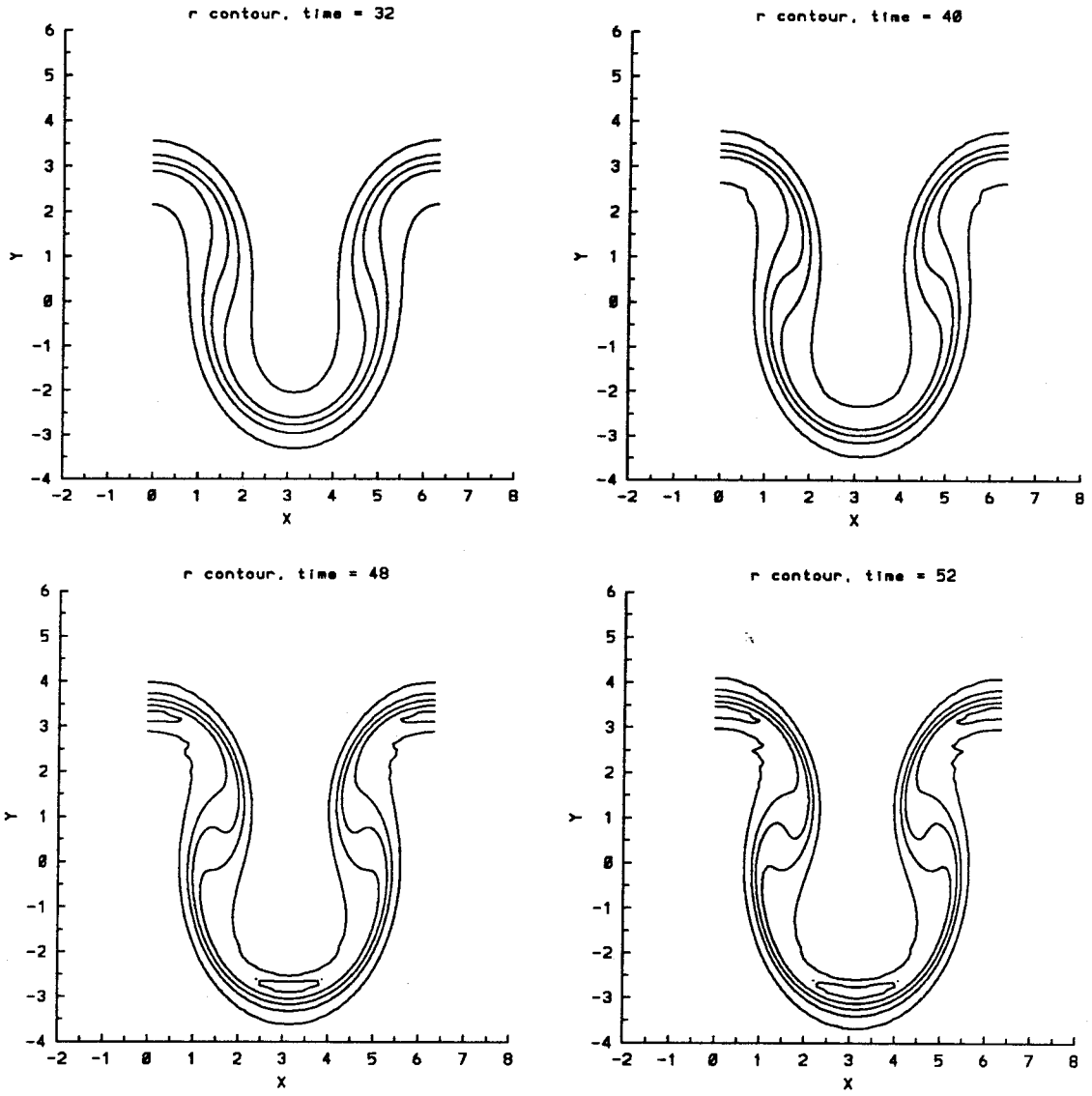

Figure 4.20.5 Time evolution of the density contours for the single scale profile L = 1.0, A = −0.2, $\epsilon = 1.0$, $t = 32$, 40, 48, 52. The contours are at $\rho = 0.41$, 0.45, 0.50, 0.55, 0.59 in that order from top to bottom of each figure.

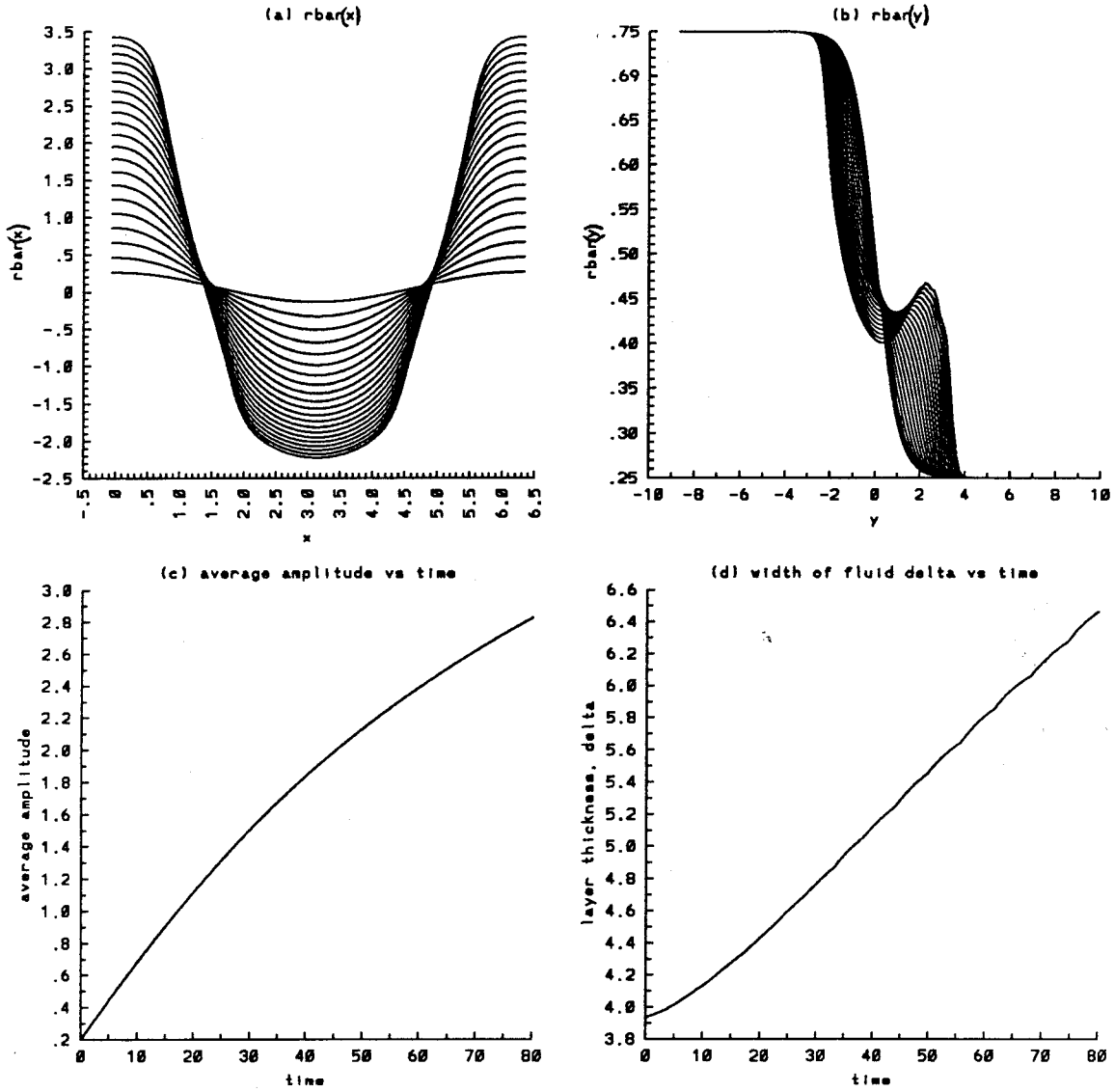

Figure 4.21.1 Time evolution of the average quantities for the single scale profile L = 1.0, A = −0.5, $\epsilon = 0.2$, $t = 0$ to 80 : a) $\bar{\rho}_y(x)$, b) $\bar{\rho}_x(y)$, c) average amplitude, and d) width of the density layer.

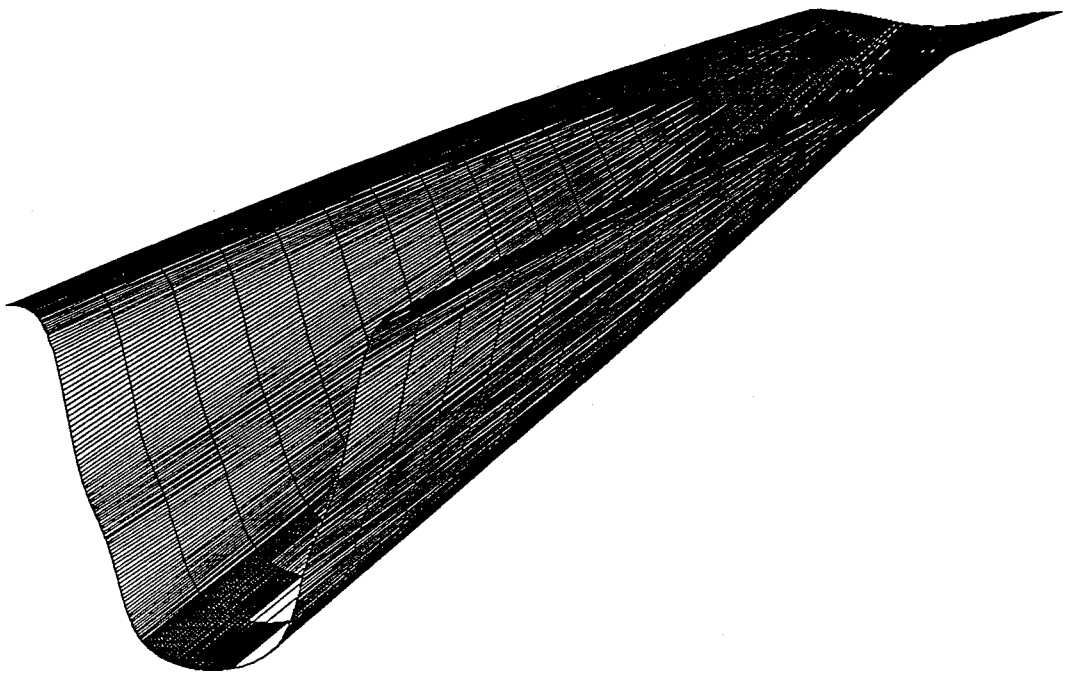

Figure 4.21.1a Three-dimensional surface of $\bar{\rho}_y(x,t)$ for the single scale profile L = 1.0, A = −0.5, $\epsilon = 0.2$, and t = 0, 80.

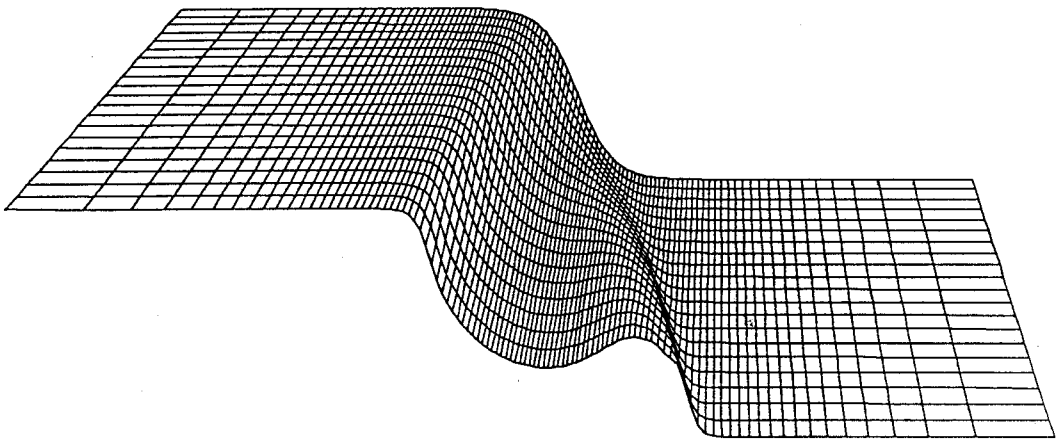

Figure 4.21.1b Three-dimensional surface of $\bar{\rho}_x(y,t)$ for the single scale profile L = 1.0, A = −0.5, $\epsilon = 0.2$, and $t = 0$, 80.

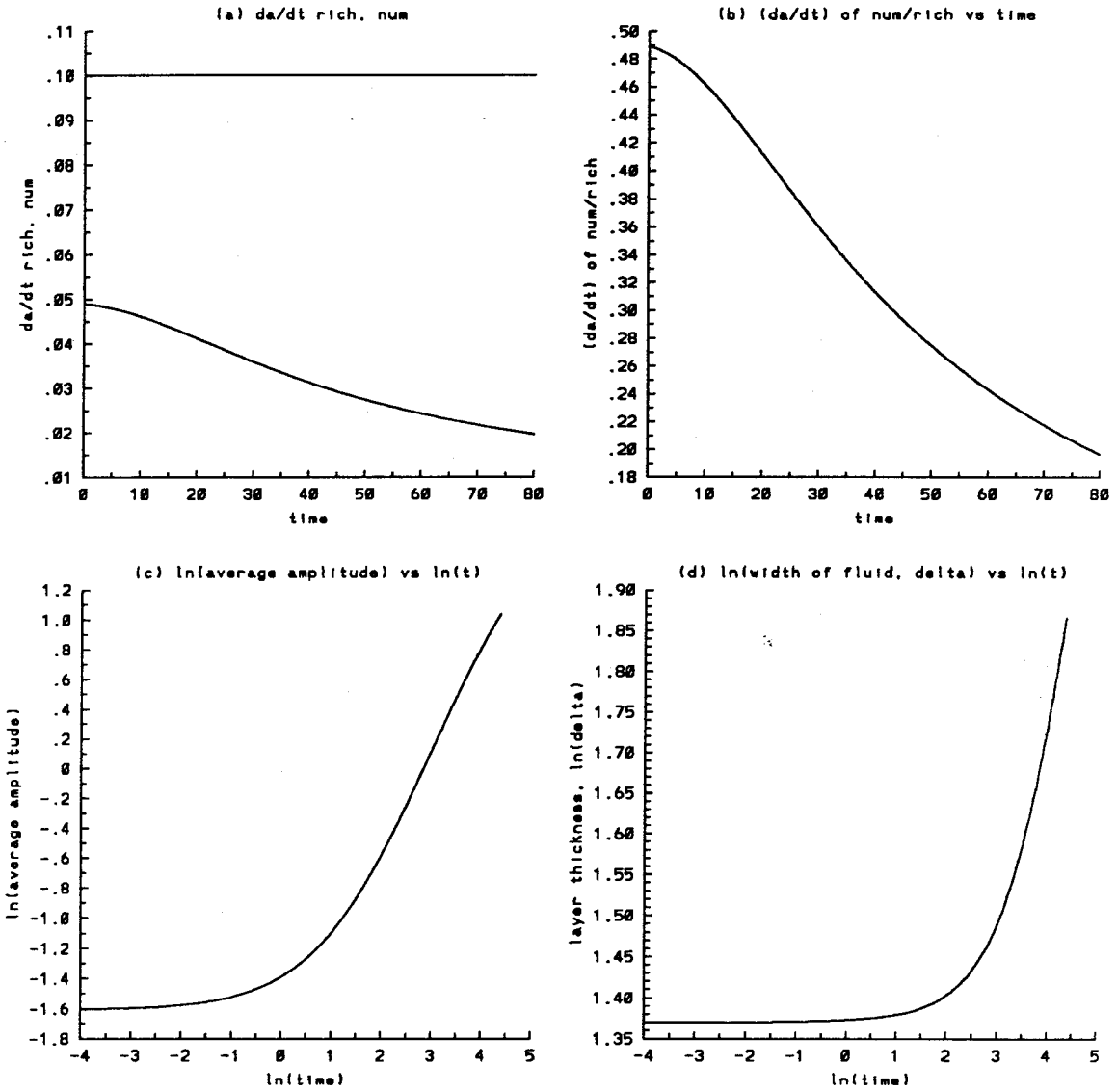

Figure 4.21.2 Time evolution of the average quantities for the single scale profile $L = 1.0$, $A = -0.5$, $\epsilon = 0.2$, $t = 0$ to 80 : a) growth rate da/dt of the average amplitude, numerical and Richtmyer theory (straight line), b) the ratio of the numerical growth rate da/dt over that predicted by Richtmyer theory, c) $\ln(a)$ *vs* $\ln(t)$, d) $\ln(\delta)$ *vs* $\ln(t)$.

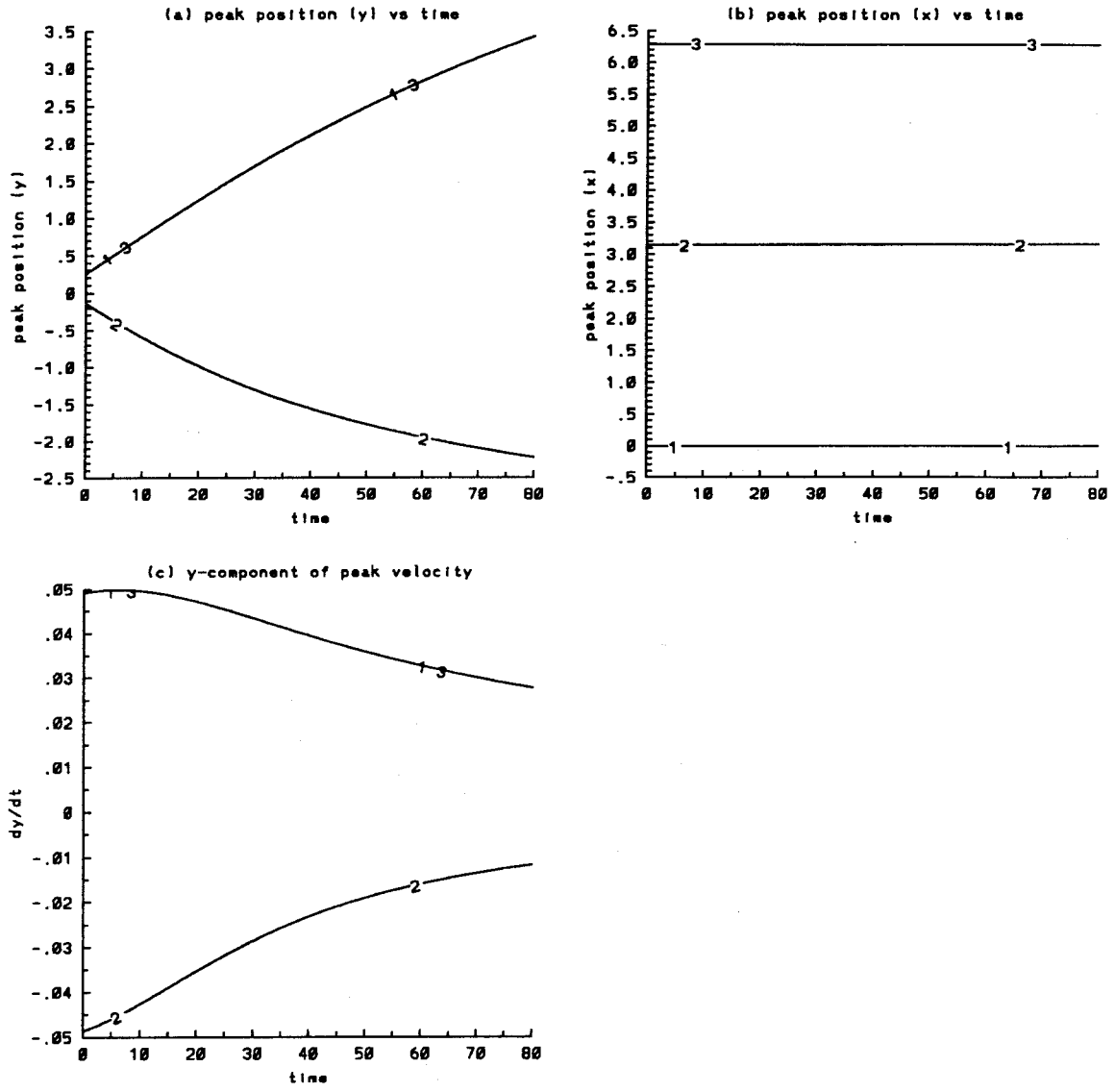

Figure 4.21.3 Time evolution of the positions and velocities of the average peaks in the single scale profile L = 1.0, A = −0.5, $\epsilon = 0.2$, $t = 0$ to 80 a) y b) x c) dy/dt. The numbers on the curves refer to the peaks on the curves $\bar{\rho}_y(x)$ versus x.

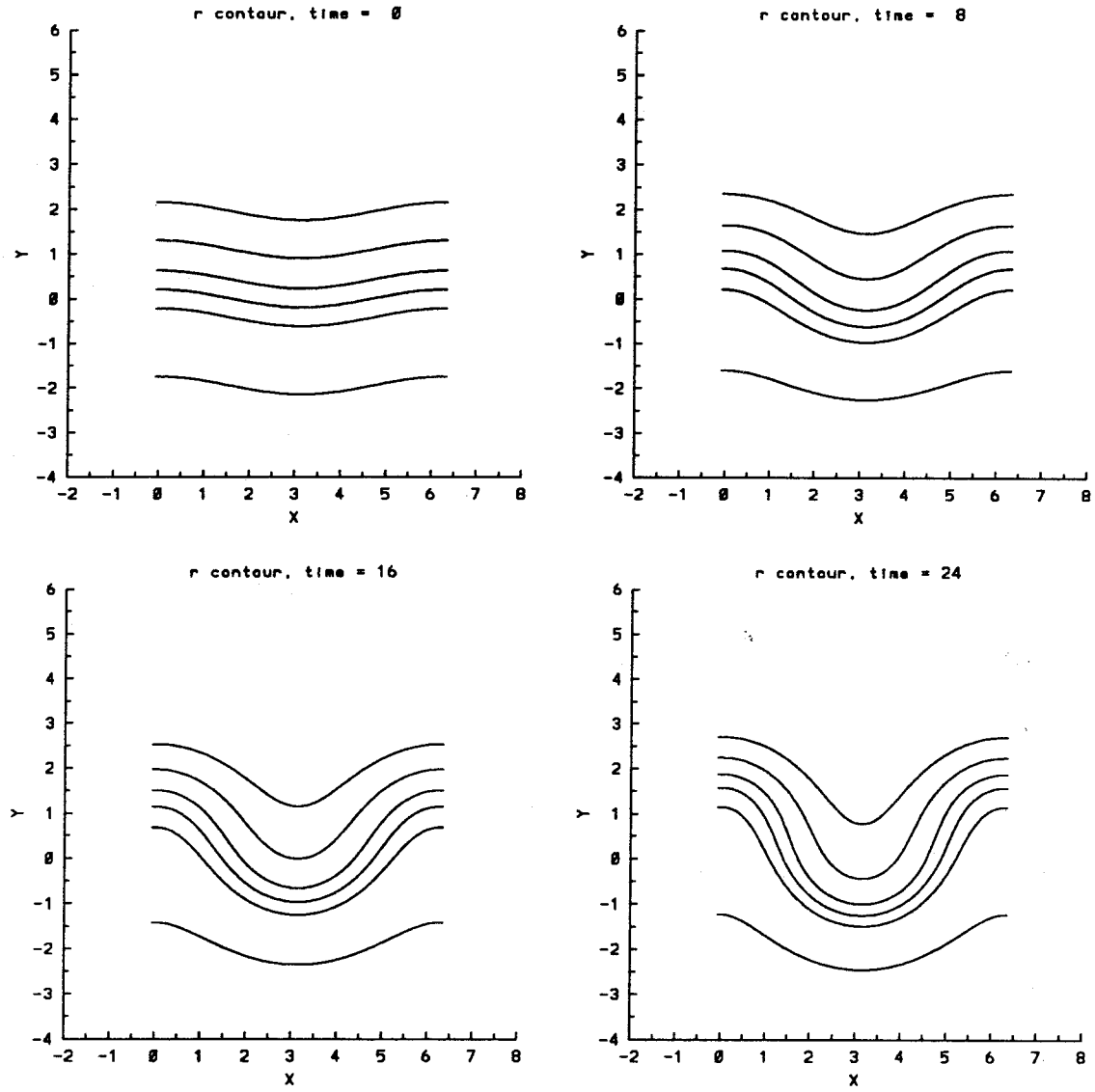

Figure 4.21.4 Time evolution of the density contours for the single scale profile $L = 1.0$, $A = -0.5$, $\epsilon = 0.2$, $t = 0$, 8, 16, 24. The contours are at $\rho = 0.26$, 0.3, 0.4, 0.5, 0.6, 0.74 in that order from top to bottom of each figure.

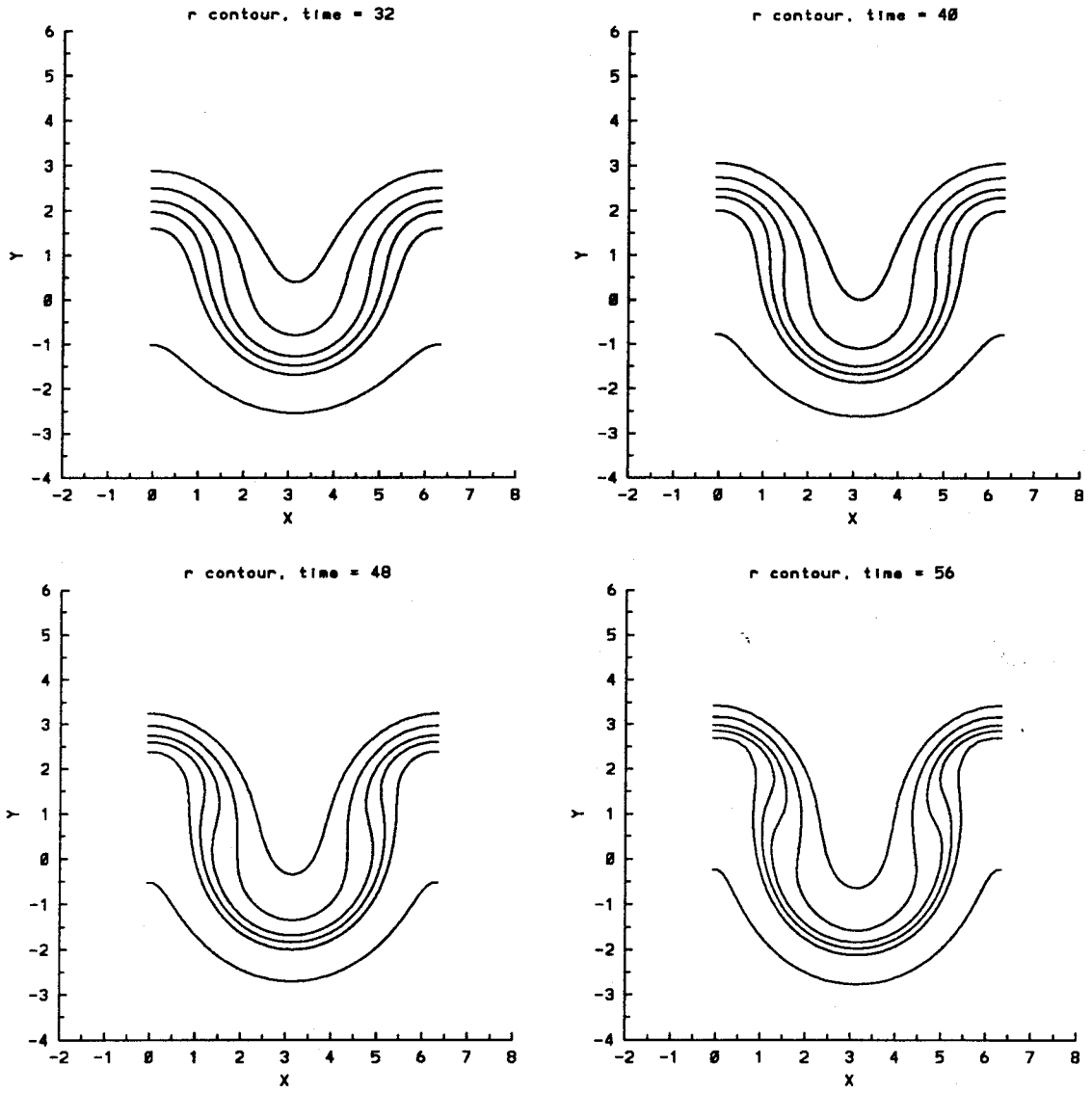

Figure 4.21.5 Time evolution of the density contours for the single scale profile L= 1.0, A = −0.5, $\epsilon = 0.2$, t = 32, 40, 48, 56. The contours are at ρ = 0.26, 0.3, 0.4, 0.5, 0.6, 0.74 in that order from top to bottom of each figure.

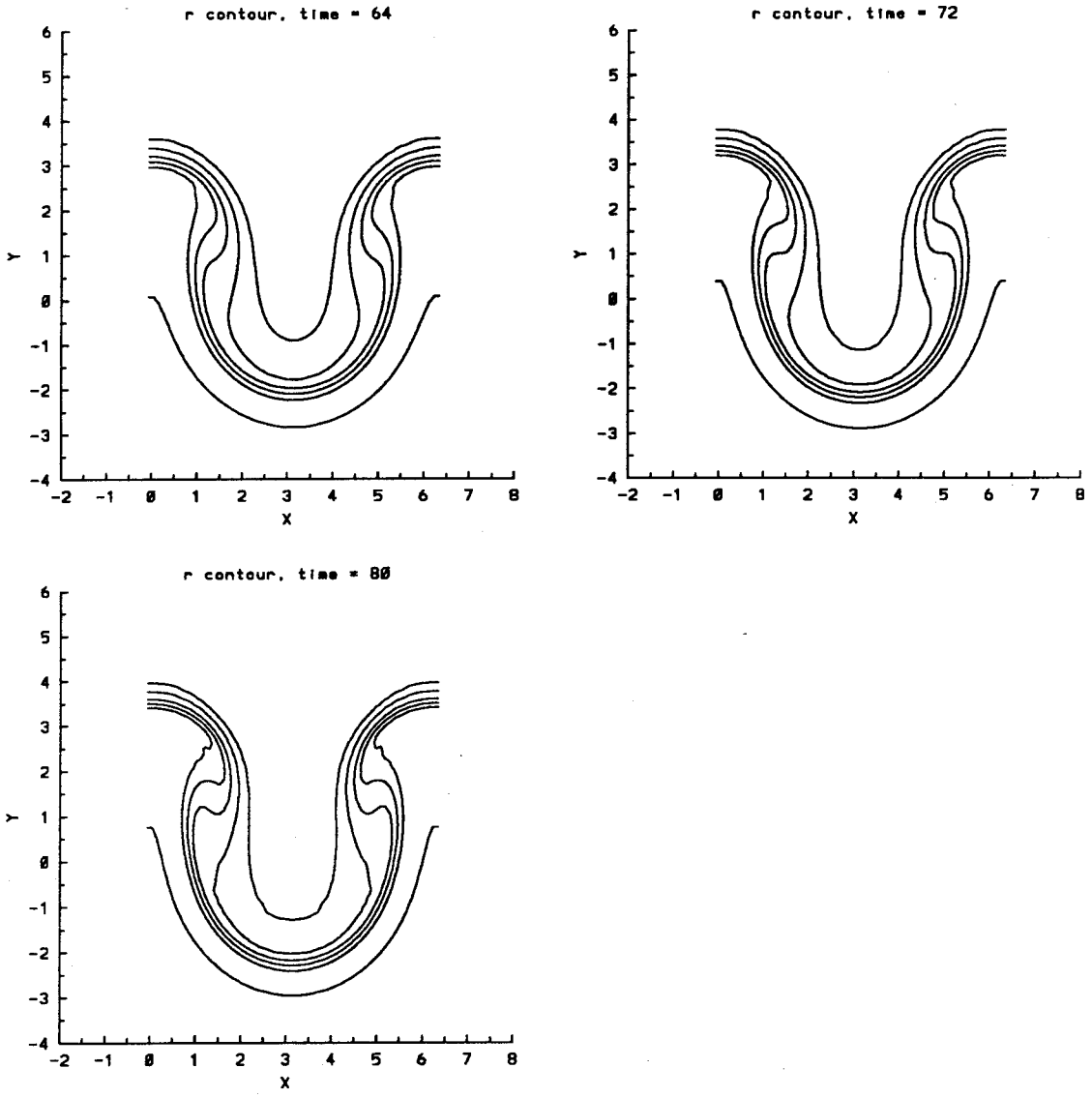

Figure 4.21.6 Time evolution of the density contours for the single scale profile L = 1.0, A = −0.5, $\epsilon = 0.2$, $t = 64, 72, 80$. The contours are at $\rho = 0.26, 0.3, 0.4, 0.5, 0.6, 0.74$ in that order from top to bottom of each figure.

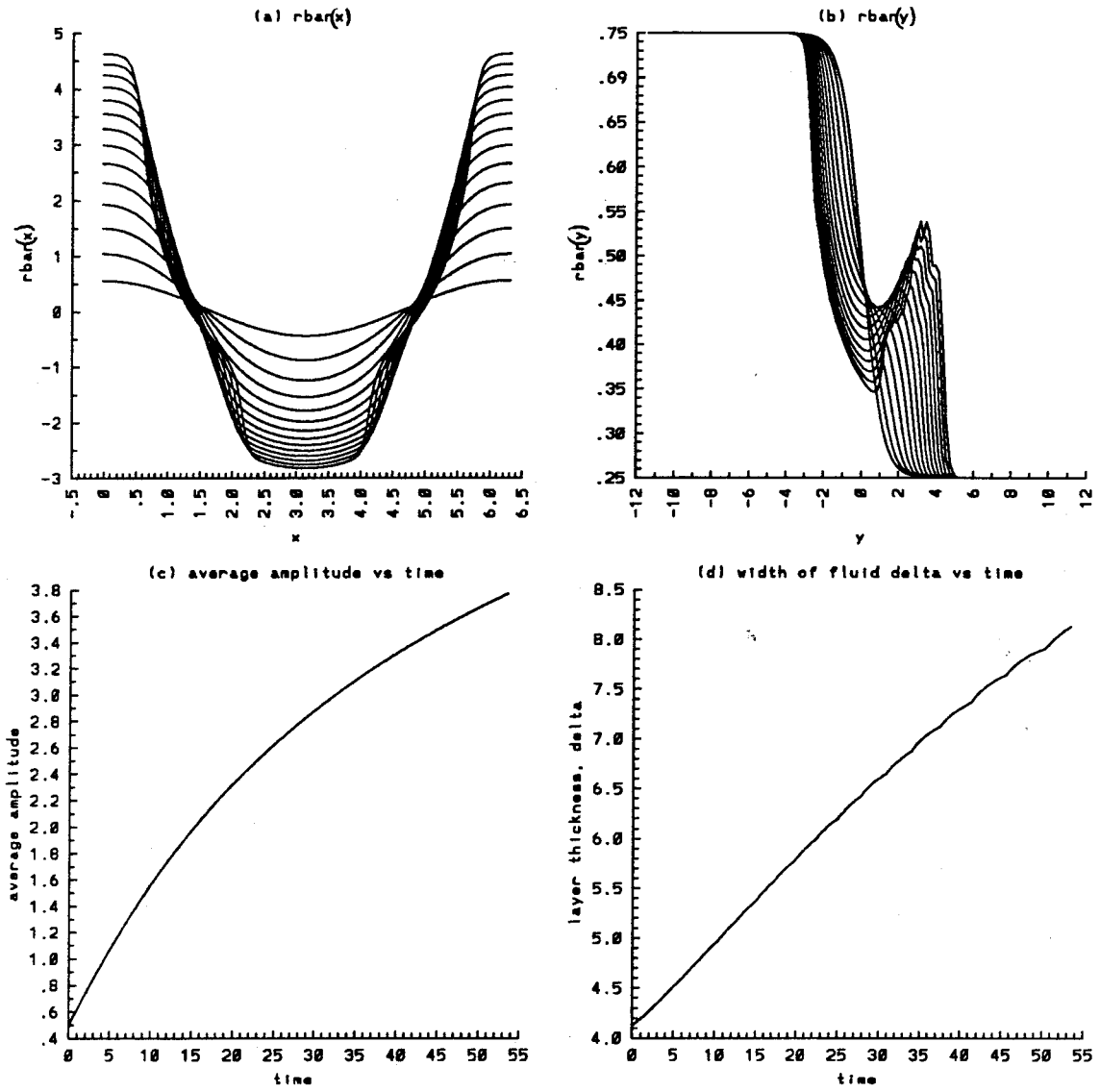

Figure 4.22.1 Time evolution of the average quantities for the single scale profile L = 1.0, A = −0.5, $\epsilon = 0.5$, $t = 0$ to 53 : a) $\bar{\rho}_y(x)$, b) $\bar{\rho}_x(y)$, c) average amplitude, and d) width of the density layer.

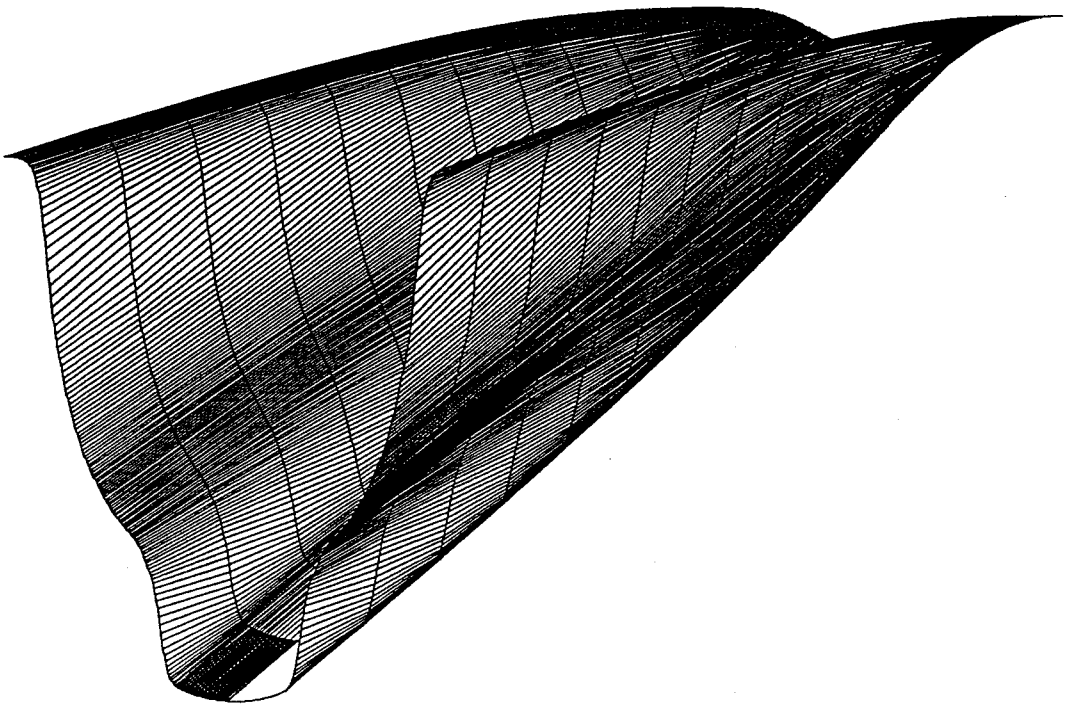

Figure 4.22.1a Three-dimensional surface of $\bar{\rho}_y(x,t)$ for the single scale profile L = 1.0, A = −0.5, $\epsilon = 0.5$, and $t = 0$, 53.

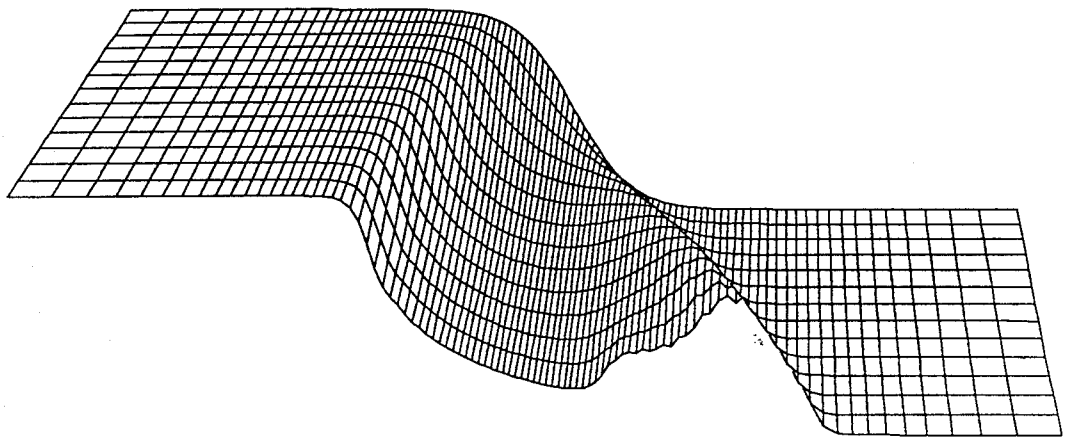

Figure 4.22.1b Three-dimensional surface of $\bar{\rho}_x(y,t)$ for the single scale profile L = 1.0, A = -0.5, $\epsilon = 0.5$, and $t = 0$, 53.

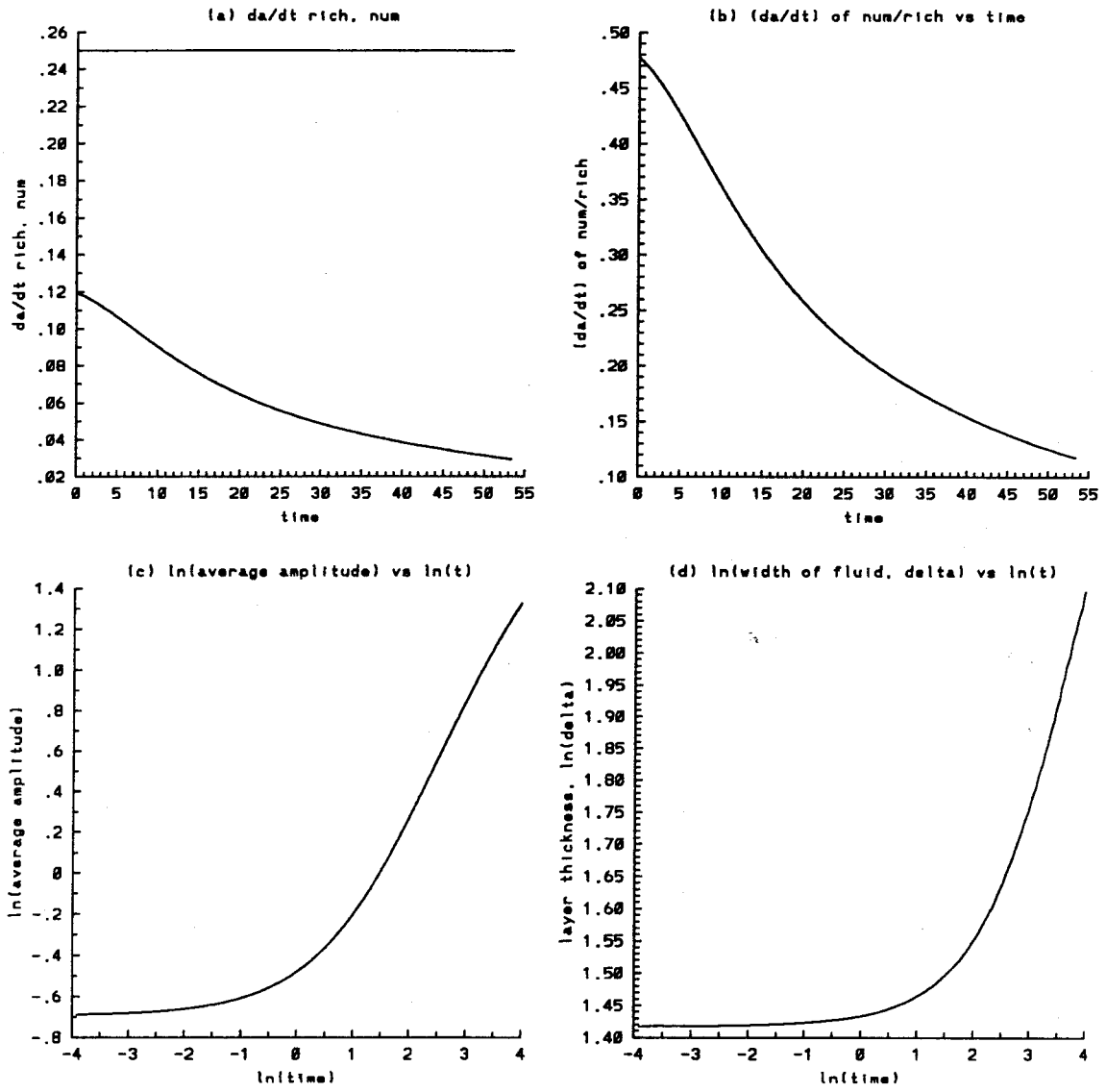

Figure 4.22.2 Time evolution of the average quantities for the single scale profile L = 1.0, A = −0.5, $\epsilon = 0.5$, $t = 0$ to 53 : a) growth rate da/dt of the average amplitude, numerical and Richtmyer theory (straight line), b) the ratio of the numerical growth rate da/dt over that predicted by Richtmyer theory, c) $\ln(a)$ *vs* $\ln(t)$, d) $\ln(\delta)$ *vs* $\ln(t)$.

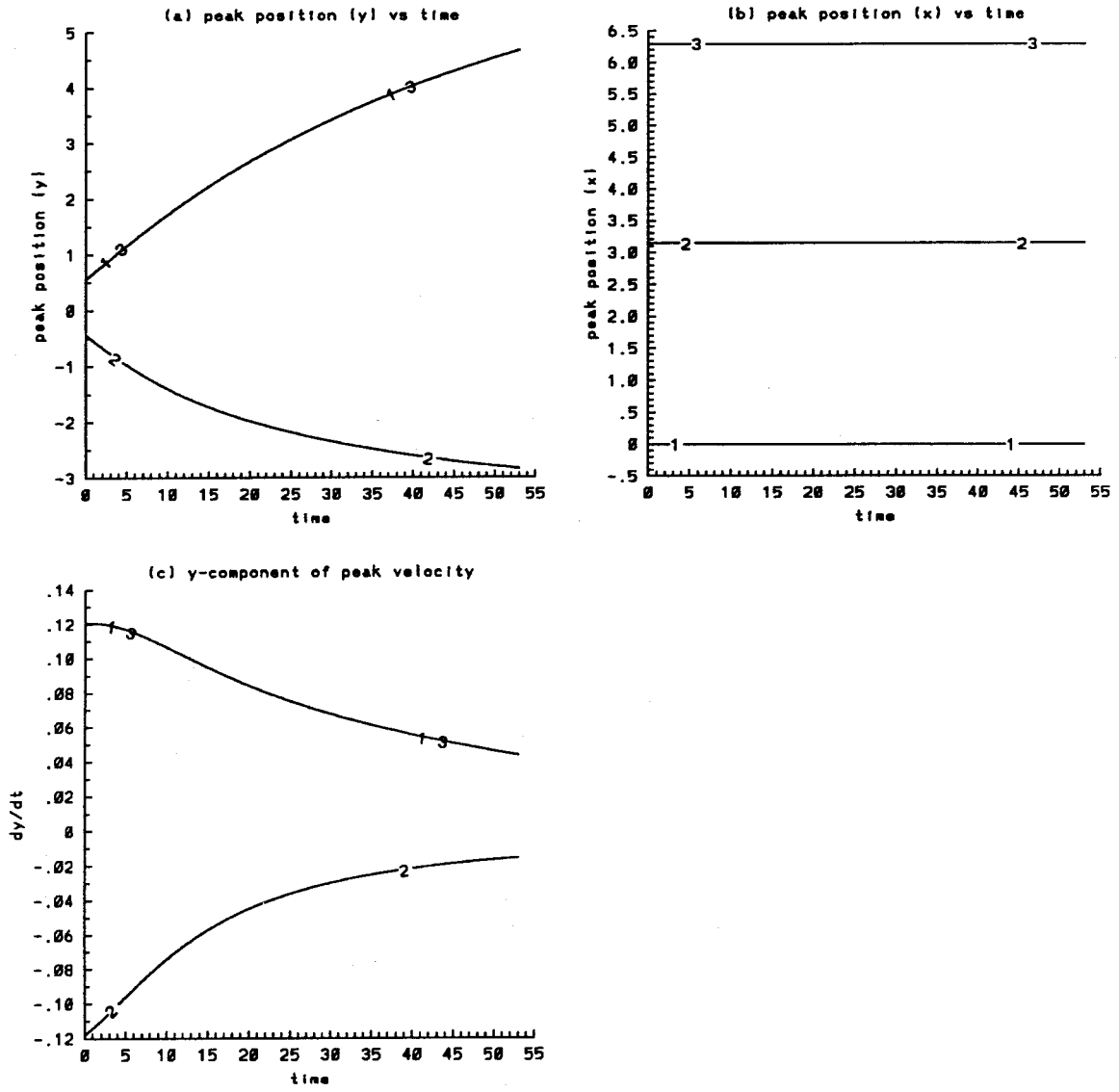

Figure 4.22.3 Time evolution of the positions and velocities of the average peaks in the single scale profile L = 1.0, A = −0.5, $\epsilon = 0.5$, $t = 0$ to 53 a) y b) x c) dy/dt. The numbers on the curves refer to the peaks on the curves $\bar{\rho}_y(x)$ versus x.

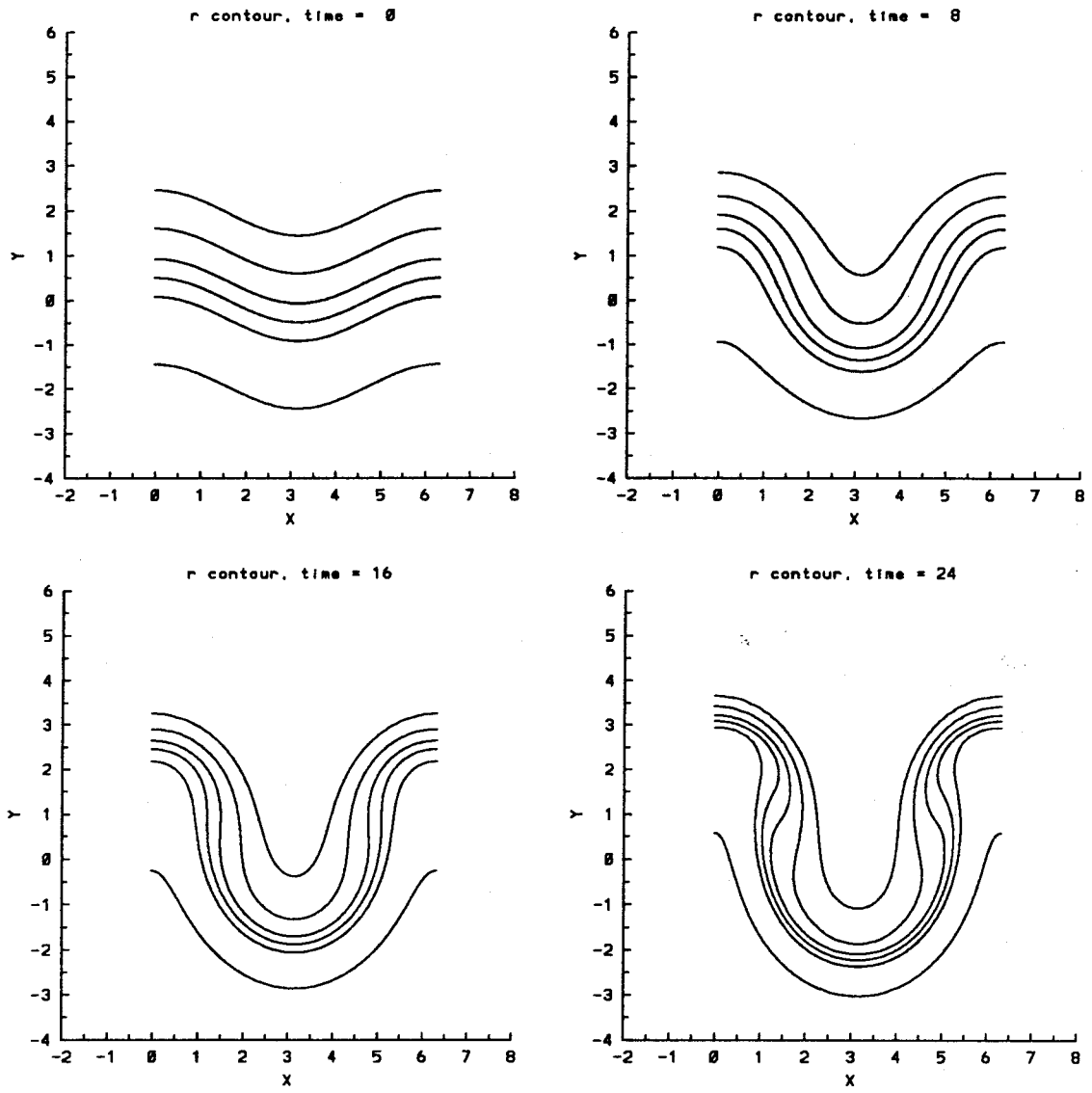

Figure 4.22.4 Time evolution of the density contours for the single scale profile L = 1.0, A = −0.5, $\epsilon = 0.5$, $t = 0$, 8, 16, 24. The contours are at $\rho = 0.26$, 0.3, 0.4, 0.5, 0.6, 0.74 in that order from top to bottom of each figure.

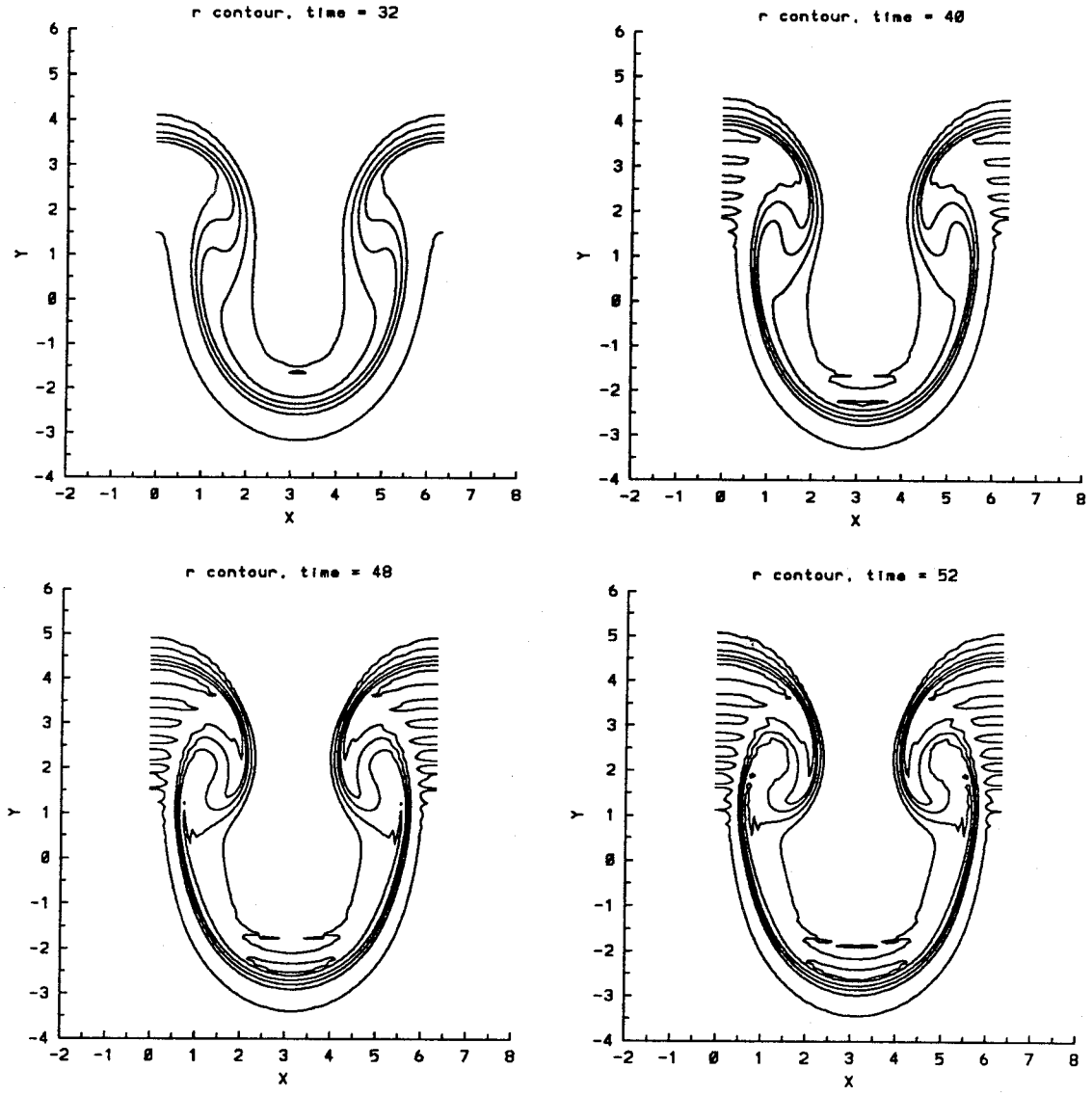

Figure 4.22.5 Time evolution of the density contours for the single scale profile L = 1.0, A = −0.5, $\epsilon = 0.5$, t = 32, 40, 48, 52. The contours are at $\rho = 0.26$, 0.3, 0.4, 0.5, 0.6, 0.74 in that order from top to bottom of each figure.

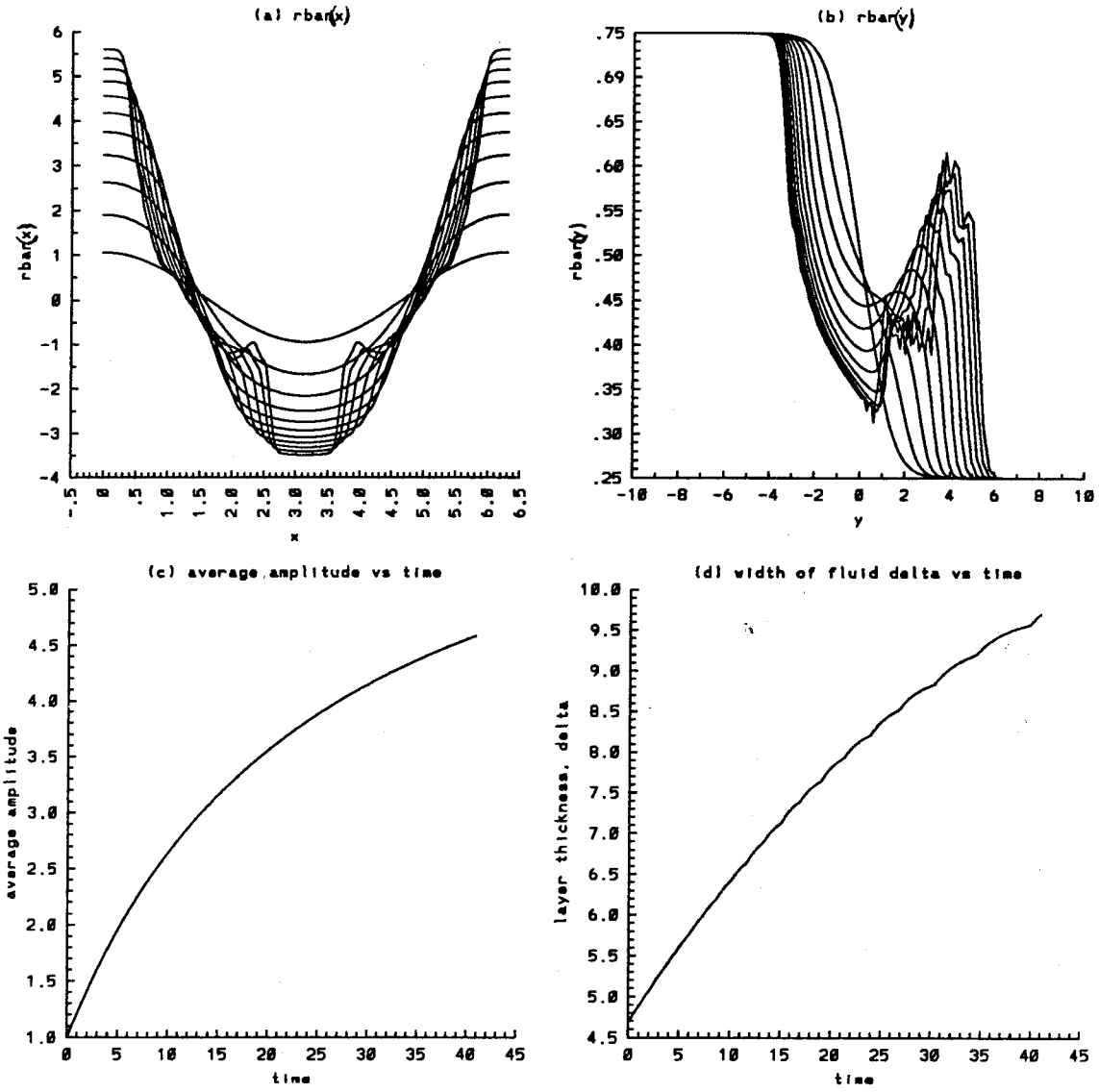

Figure 4.23.1 Time evolution of the average quantities for the single scale profile L = 1.0, A = −0.5, $\epsilon = 1.0$, $t = 0$ to 40 : a) $\bar{\rho}_y(x)$, b) $\bar{\rho}_x(y)$, c) average amplitude, and d) width of the density layer.

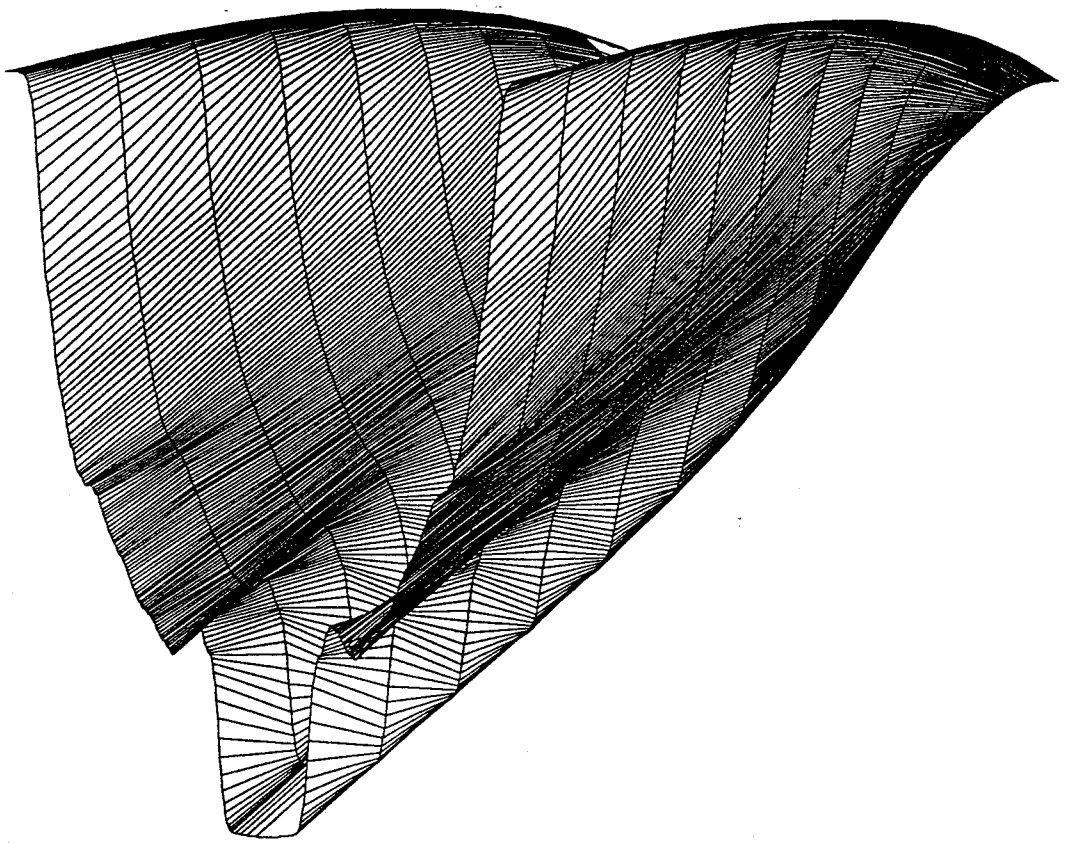

Figure 4.23.1a Three-dimensional surface of $\bar{\rho}_y(x,t)$ for the single scale profile L = 1.0, A = −0.5, $\epsilon = 1.0$, and $t = 0$, 40.

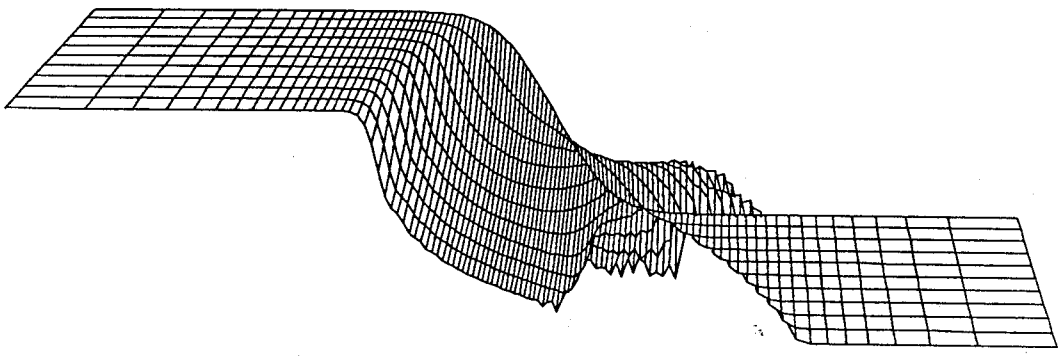

Figure 4.23.1b Three-dimensional surface of $\bar{\rho}_x(y,t)$ for the single scale profile L = 1.0, A = −0.5, $\epsilon = 1.0$, and $t = 0$, 40.

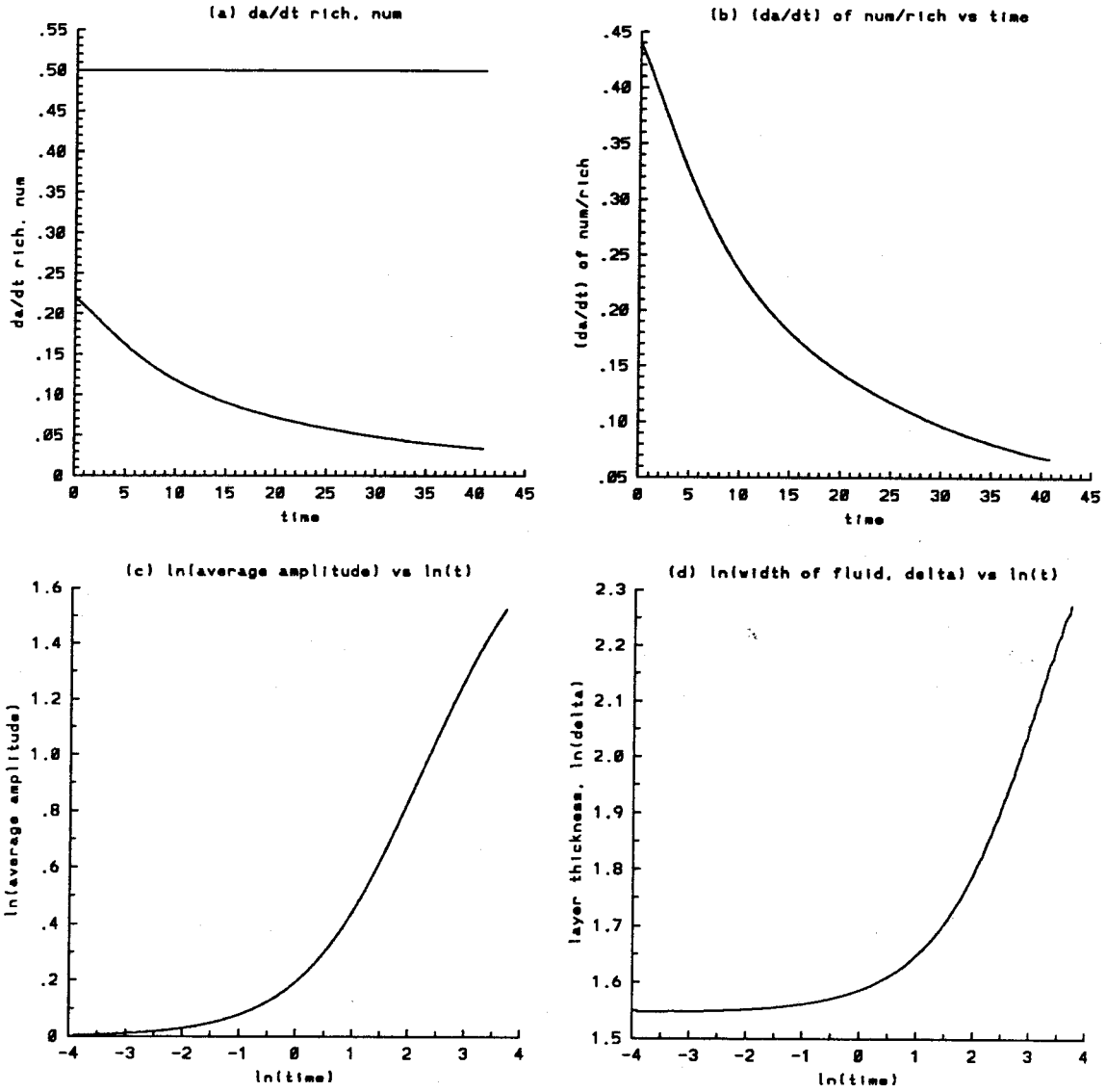

Figure 4.23.2 Time evolution of the average quantities for the single scale profile $L = 1.0$, $A = -0.5$, $\epsilon = 1.0$, $t = 0$ to 40 : a) growth rate da/dt of the average amplitude, numerical and Richtmyer theory (straight line), b) the ratio of the numerical growth rate da/dt over that predicted by Richtmyer theory, c) $\ln(a)$ *vs* $\ln(t)$, d) $\ln(\delta)$ *vs* $\ln(t)$.

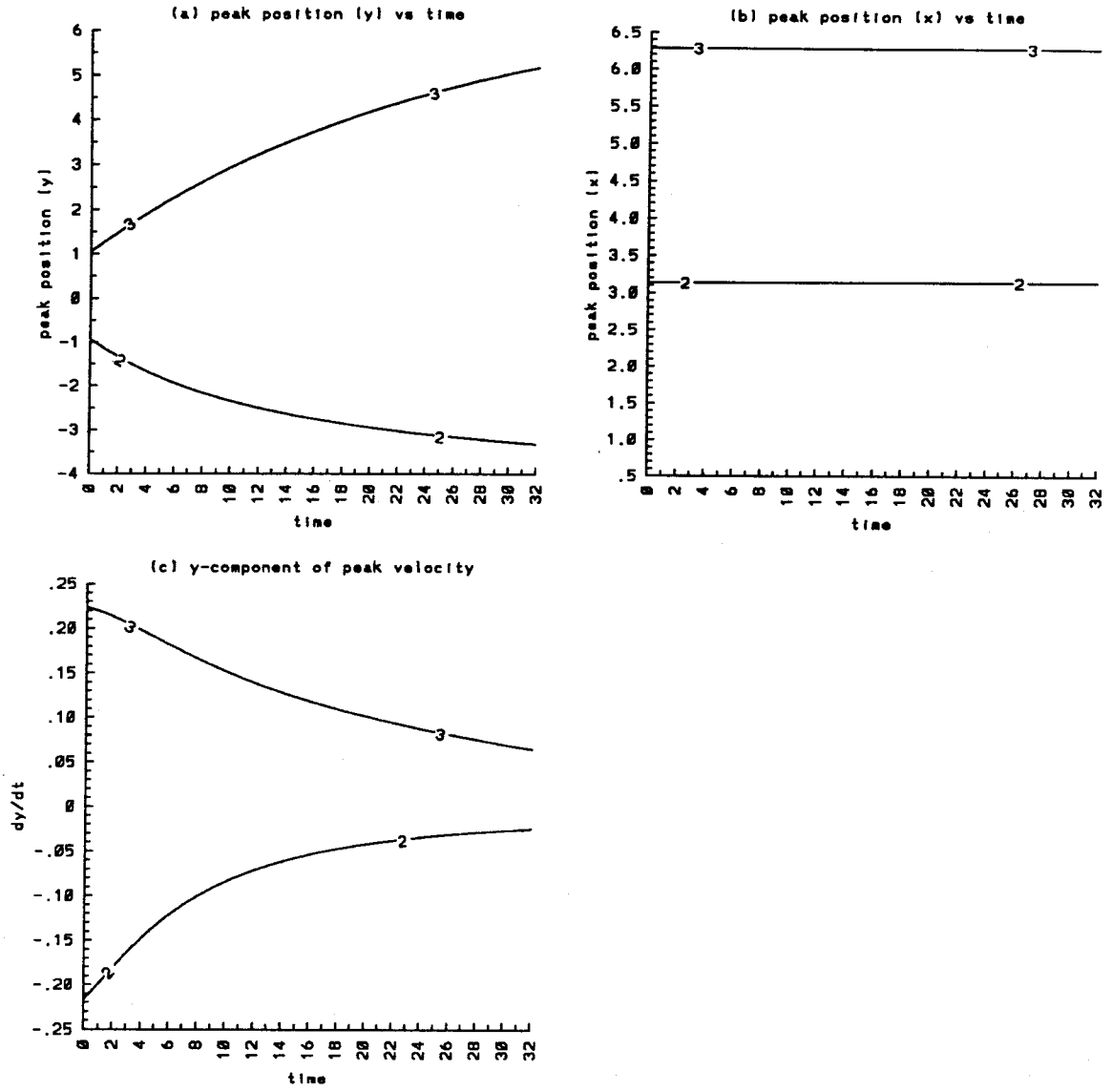

Figure 4.23.3 Time evolution of the positions and velocities of the average peaks in the single scale profile L = 1.0, A = −0.5, $\epsilon = 1.0$, $t = 0$ to 40 a) y b) x c) dy/dt. The numbers on the curves refer to the peaks on the curves $\bar{\rho}_y(x)$ versus x.

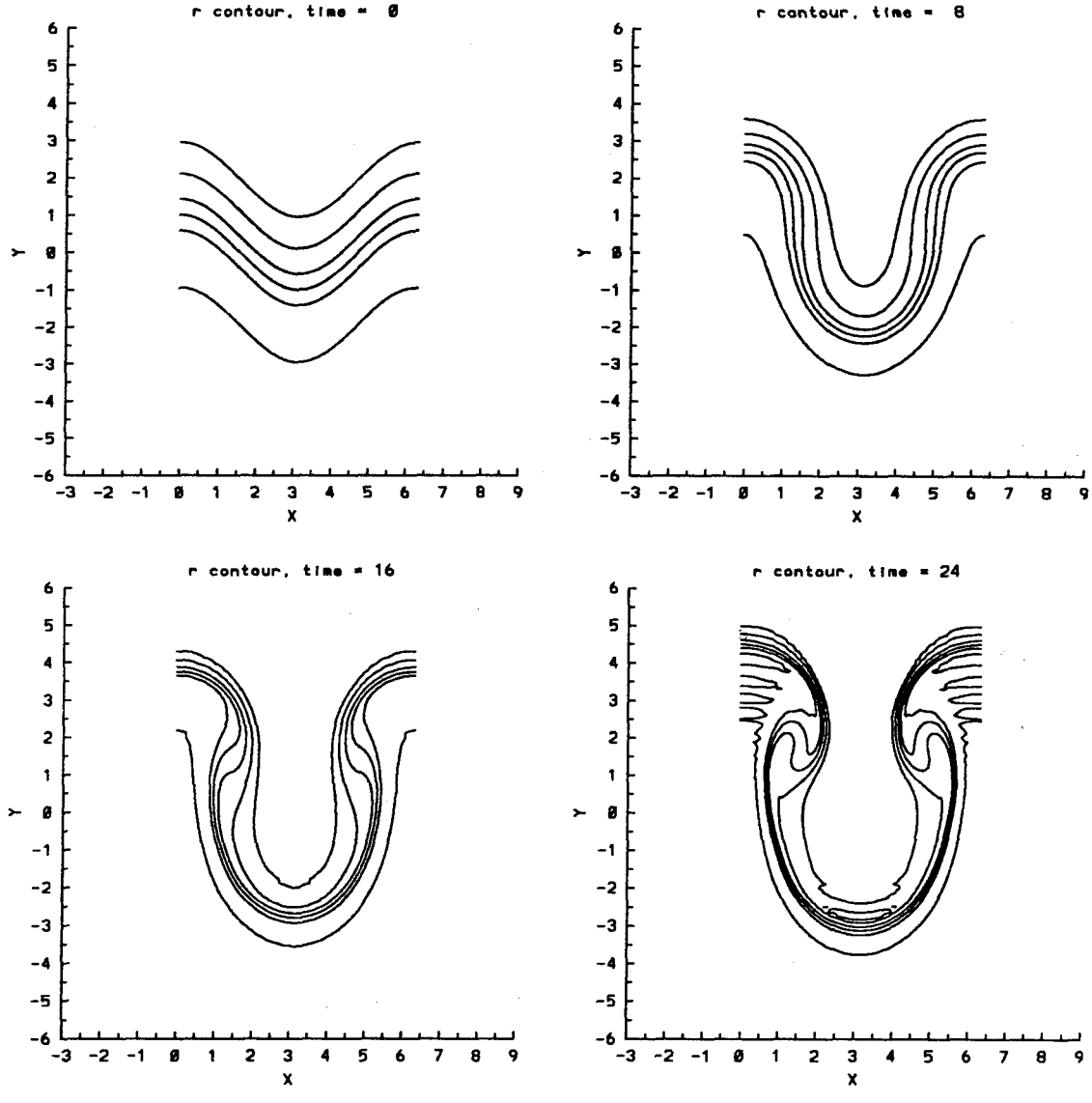

Figure 4.23.4 Time evolution of the density contours for the single scale profile L = 1.0, A = −0.5, $\epsilon = 1.0$, $t = 0$, 8, 16, 24. The contours are at $\rho = 0.26$, 0.3, 0.4, 0.5, 0.6, 0.74 in that order from top to bottom of each figure.

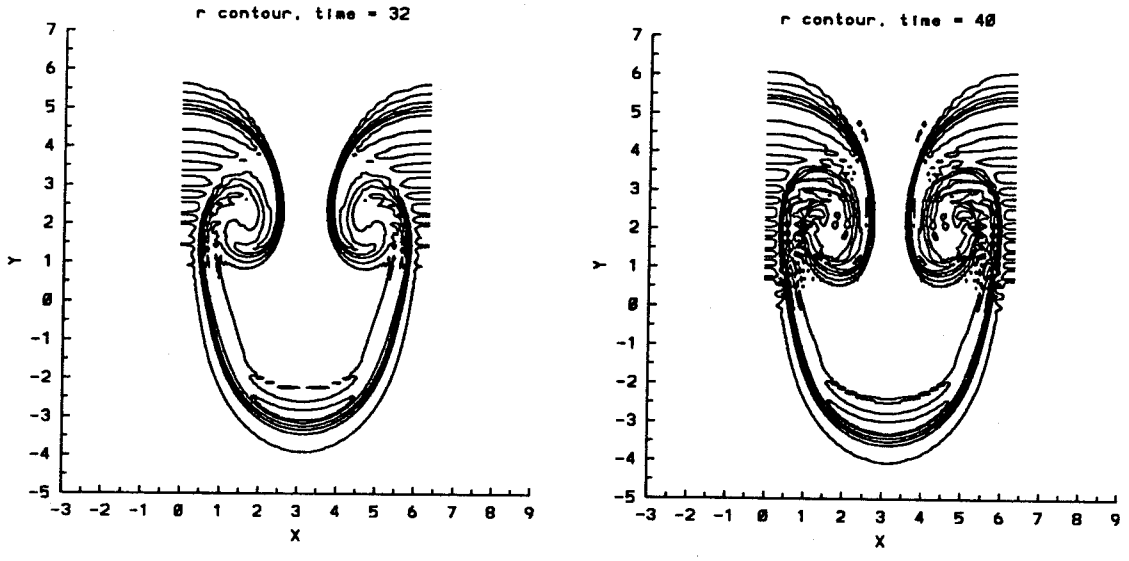

Figure 4.23.5 Time evolution of the density contours for the single scale profile L = 1.0, A = −0.5, $\epsilon = 1.0$, $t = 32$, 40. The contours are at $\rho = 0.26$, 0.3, 0.4, 0.5, 0.6, 0.74 in that order from top to bottom of each figure.

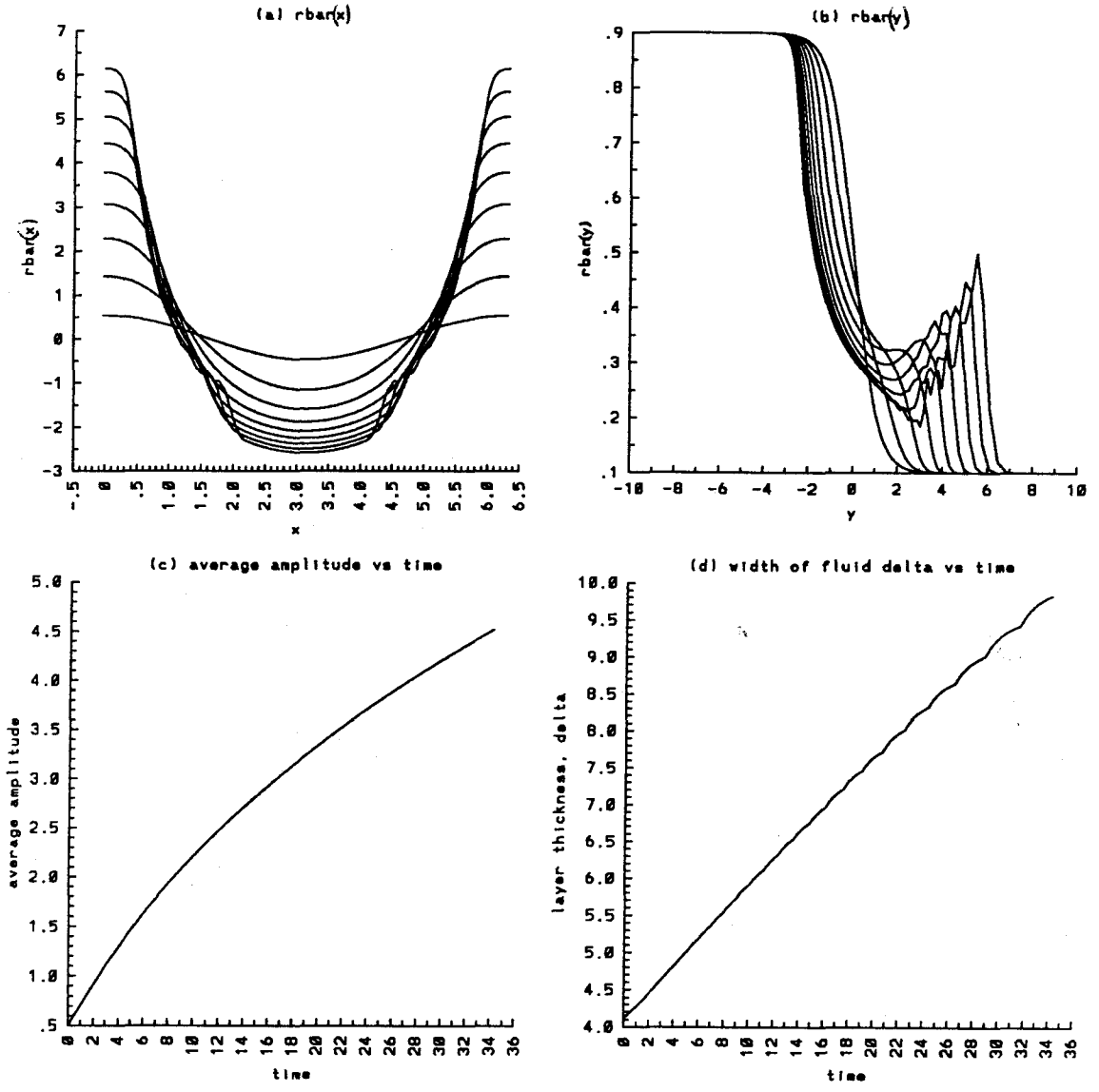

Figure 4.24.1 Time evolution of the average quantities for the single scale profile L = 1.0, A = −0.8, $\epsilon = 0.5$, $t = 0$ to 32 : a) $\bar{\rho}_y(x)$, b) $\bar{\rho}_x(y)$, c) average amplitude, and d) width of the density layer.

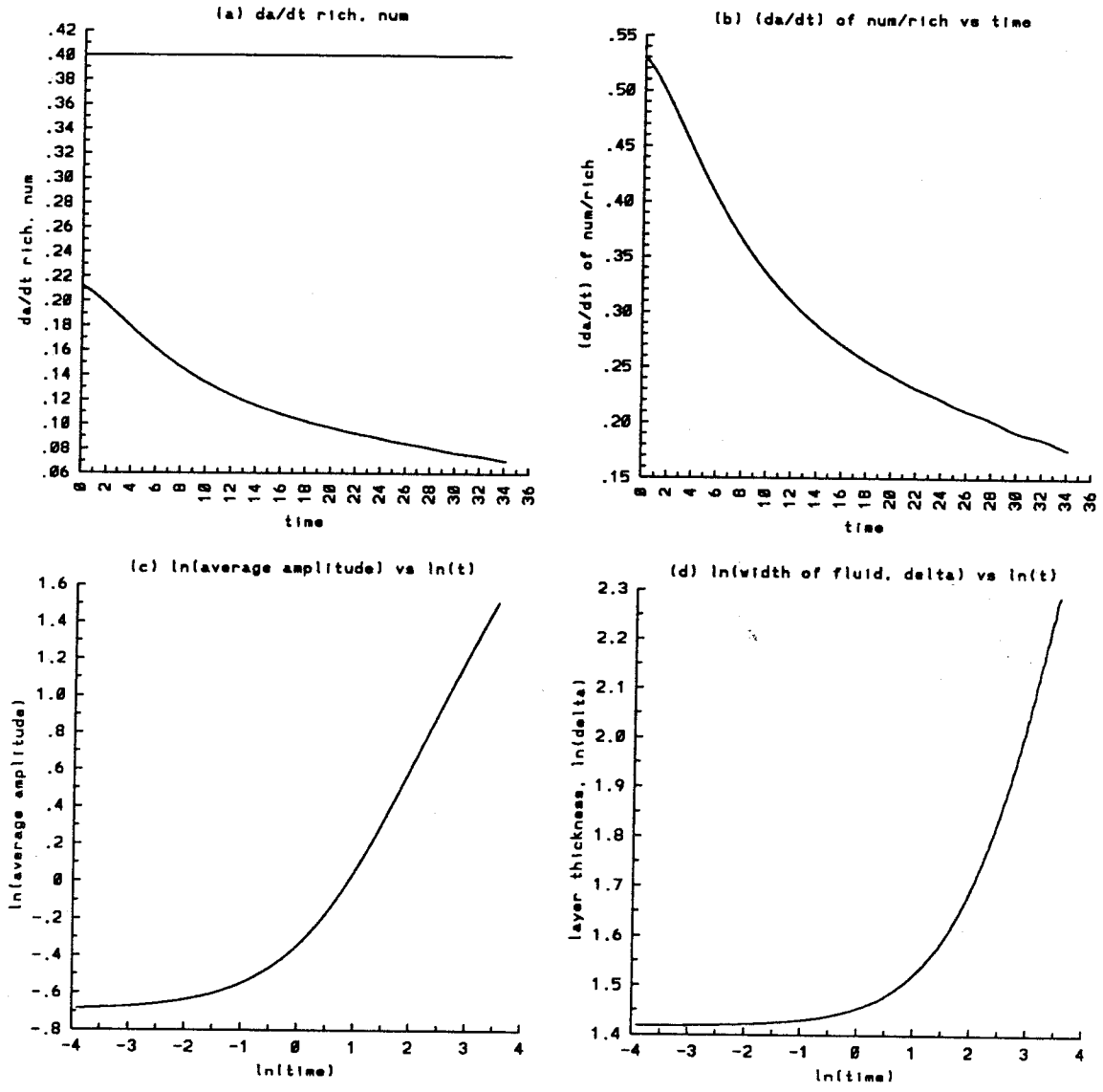

Figure 4.24.2 Time evolution of the average quantities for the single scale profile L = 1.0, A = −0.8, $\epsilon = 0.5$, $t = 0$ to 34 : a) growth rate da/dt of the average amplitude, numerical and Richtmyer theory (straight line), b) the ratio of the numerical growth rate da/dt over that predicted by Richtmyer theory, c) $\ln(a)$ *vs* $\ln(t)$, d) $\ln(\delta)$ *vs* $\ln(t)$.

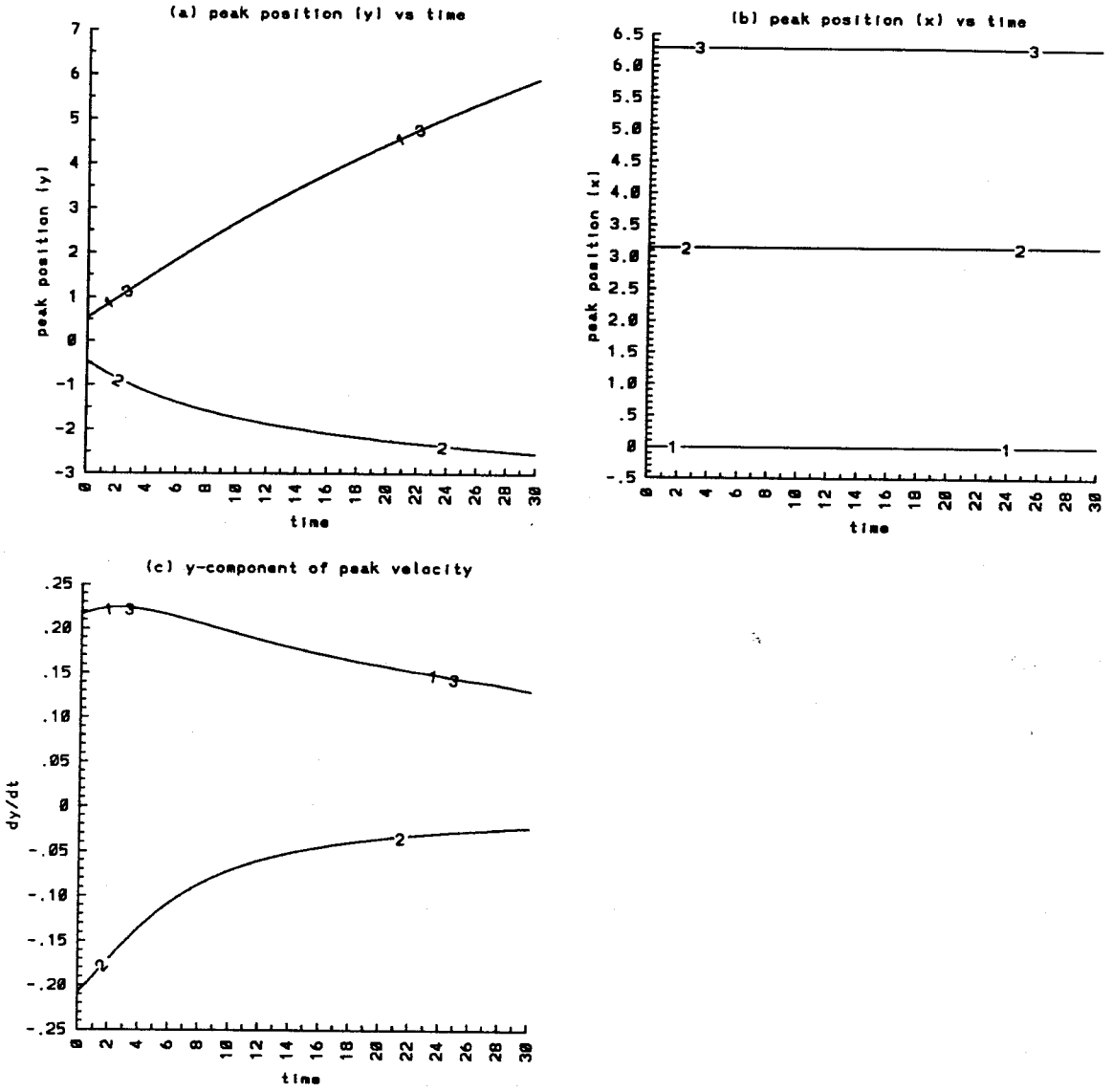

Figure 4.24.3 Time evolution of the positions and velocities of the average peaks in the single scale profile L = 1.0, A = −0.8, $\epsilon = 0.5$, $t = 0$ to 32 a) y b) x c) dy/dt. The numbers on the curves refer to the peaks on the curves $\bar{\rho}_y(x)$ versus x.

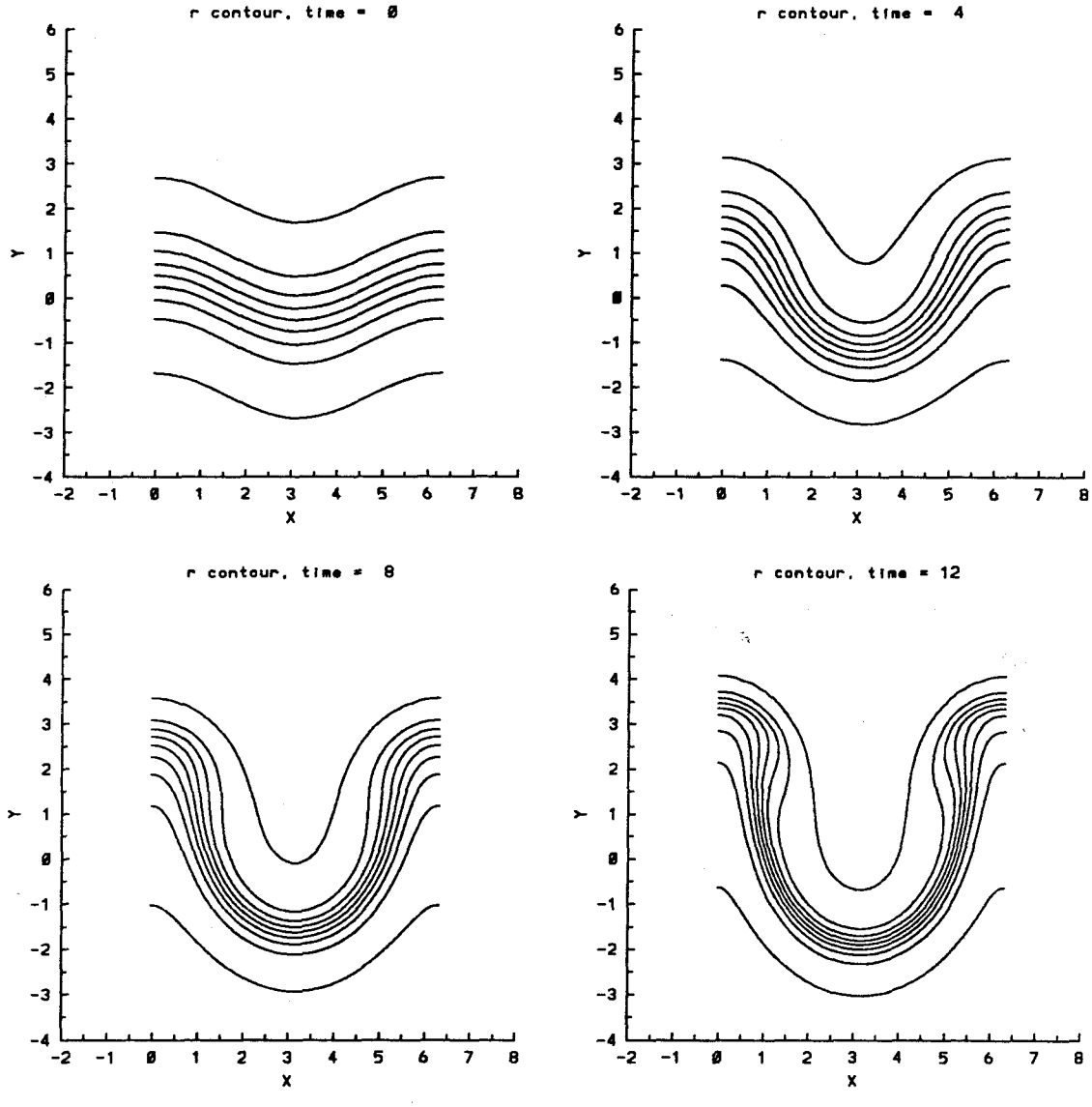

Figure 4.24.4 Time evolution of the density contours for the single scale profile L = 1.0, A = −0.8, $\epsilon = 0.5$, $t = 0$, 4, 8, 12. The contours are at $\rho = 0.11$, 0.2, 0.3, 0.4, 0.5, 0.6, 0.7, 0.8, 0.89 in that order from top to bottom of each figure.

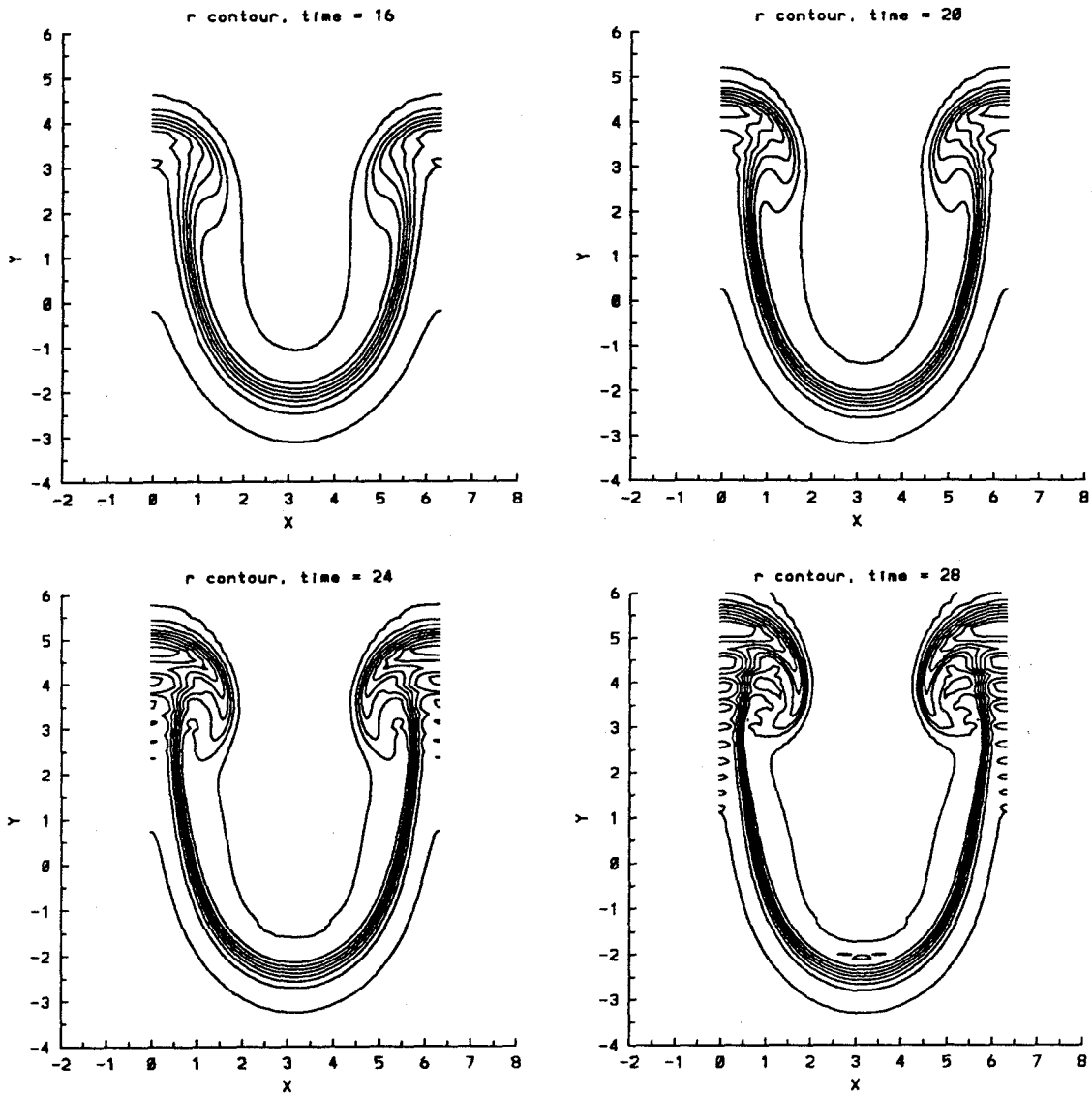

Figure 4.24.5 Time evolution of the density contours for the single scale profile L = 1.0, A = −0.8, $\epsilon = 0.5$, t = 16, 20, 24, 28. The contours are at $\rho = 0.11$, 0.2, 0.3, 0.4, 0.5, 0.6, 0.7, 0.8, 0.89 in that order from top to bottom of each figure.

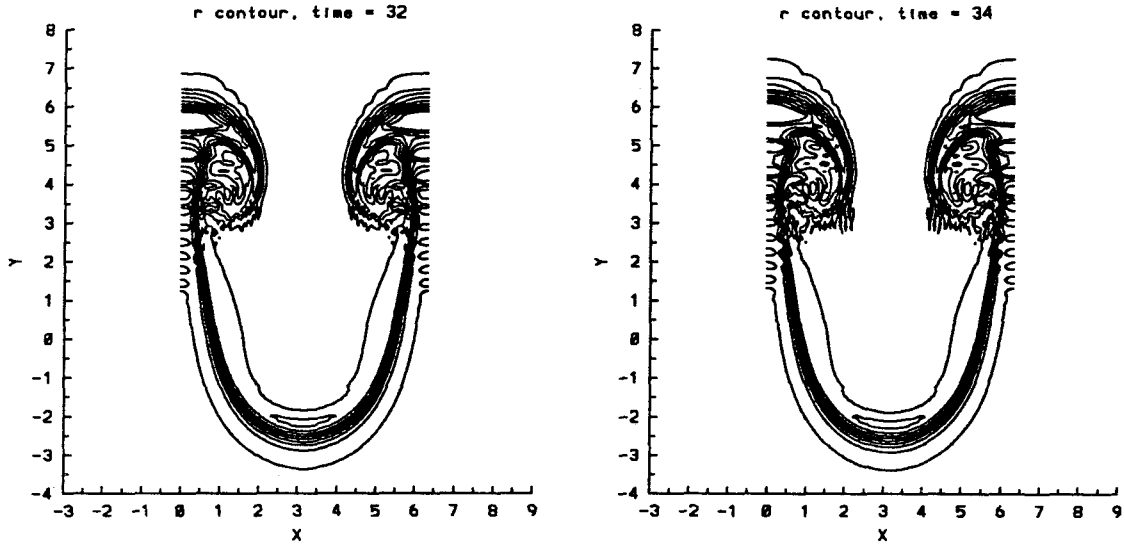

Figure 4.24.6 Time evolution of the density contours for the single scale profile L = 1.0, A = −0.8, $\epsilon = 0.5$, $t = 32, 34$. The contours are at $\rho = 0.11, 0.2, 0.3, 0.4, 0.5, 0.6, 0.7, 0.8, 0.89$ in that order from top to bottom of each figure.

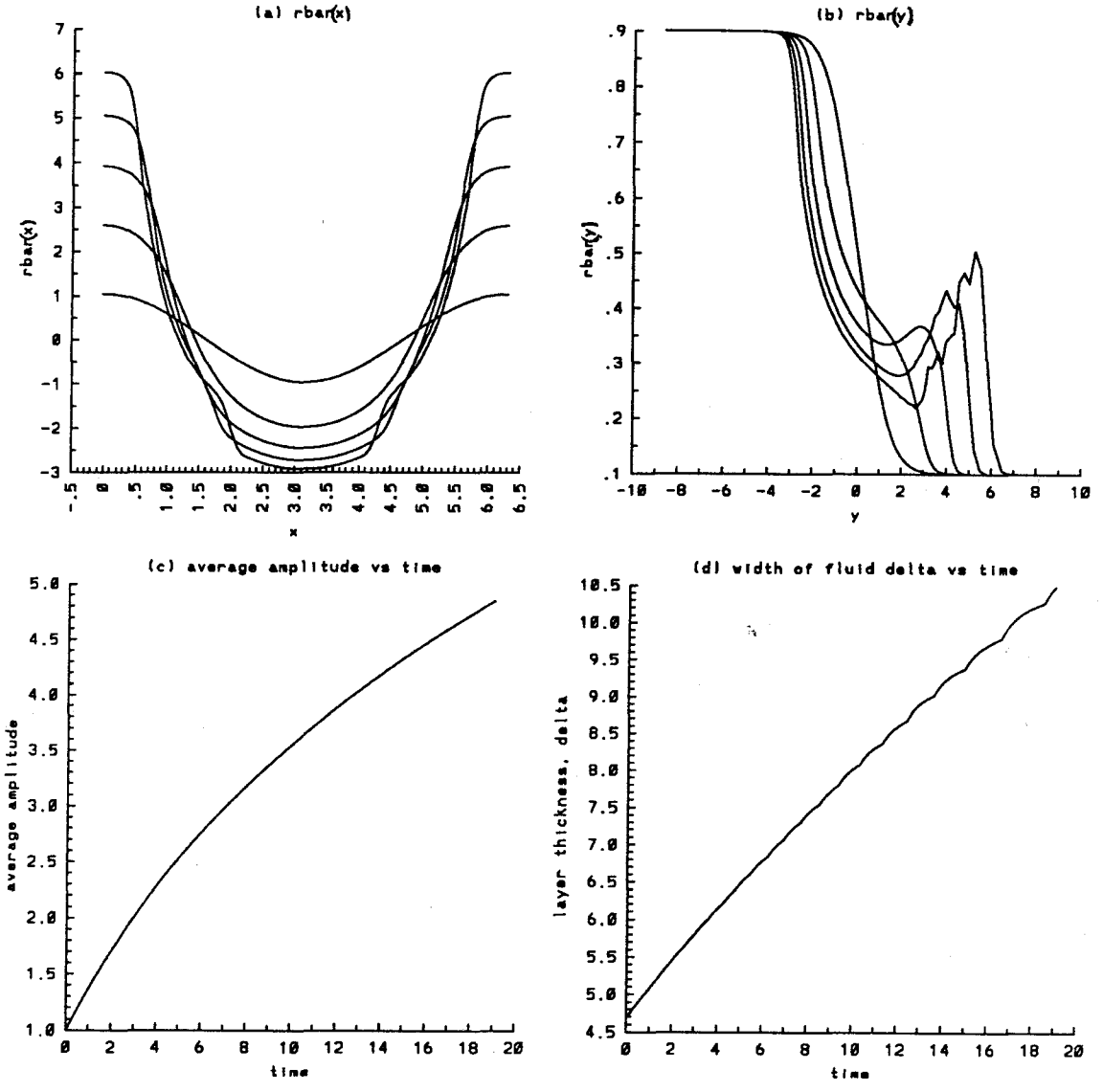

Figure 4.25.1 Time evolution of the average quantities for the single scale profile L = 1.0, A = −0.8, $\epsilon = 1.0$, $t = 0$ to 16 : a) $\bar{\rho}_y(x)$, b) $\bar{\rho}_x(y)$, c) average amplitude, and d) width of the density layer.

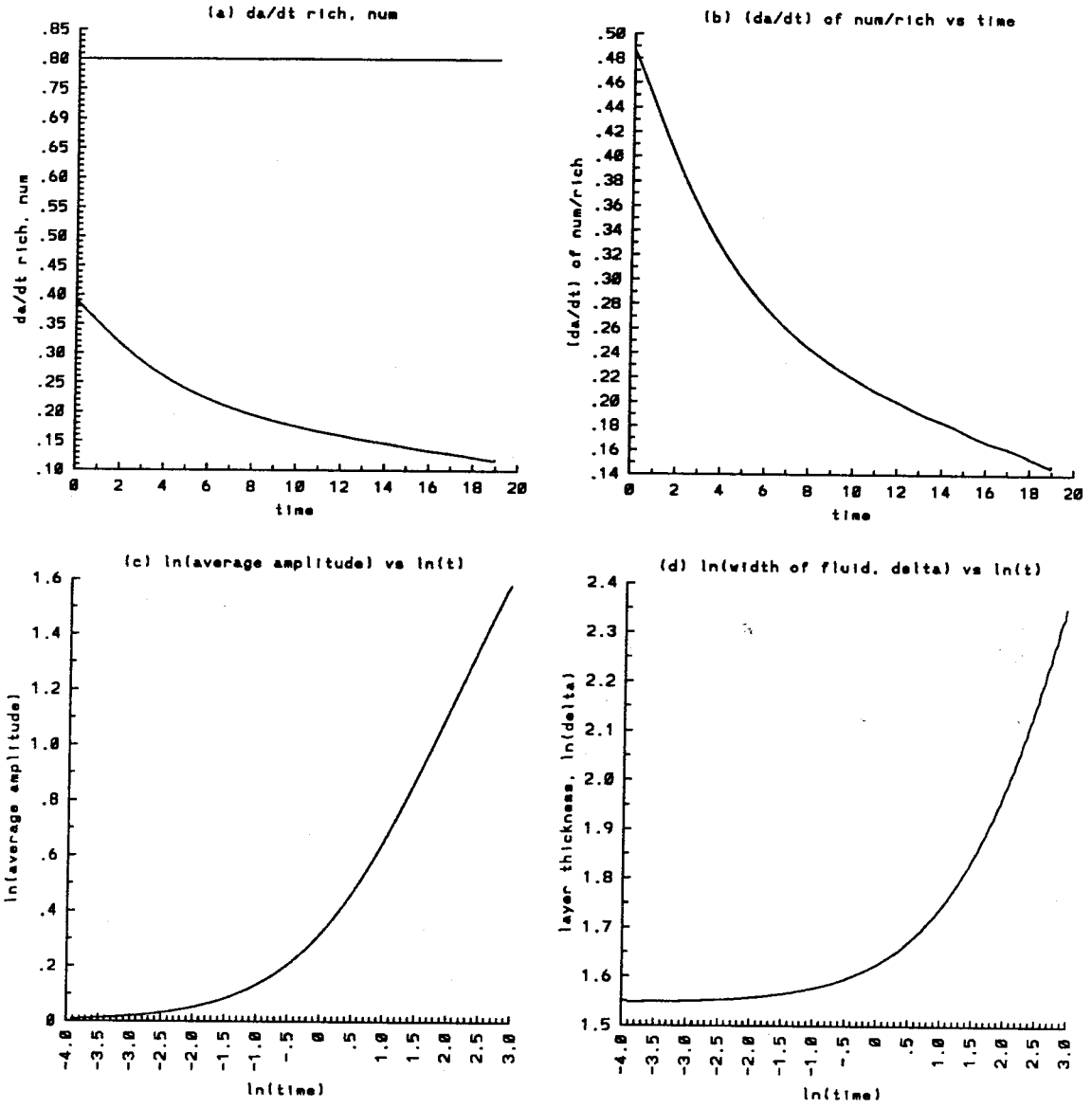

Figure 4.25.2 Time evolution of the average quantities for the single scale profile L = 1.0, A = −0.8, $\epsilon = 1.0$, $t = 0$ to 16 : a) growth rate da/dt of the average amplitude, numerical and Richtmyer theory (straight line), b) the ratio of the numerical growth rate da/dt over that predicted by Richtmyer theory, c) $\ln(a)$ *vs* $\ln(t)$, d) $\ln(\delta)$ *vs* $\ln(t)$.

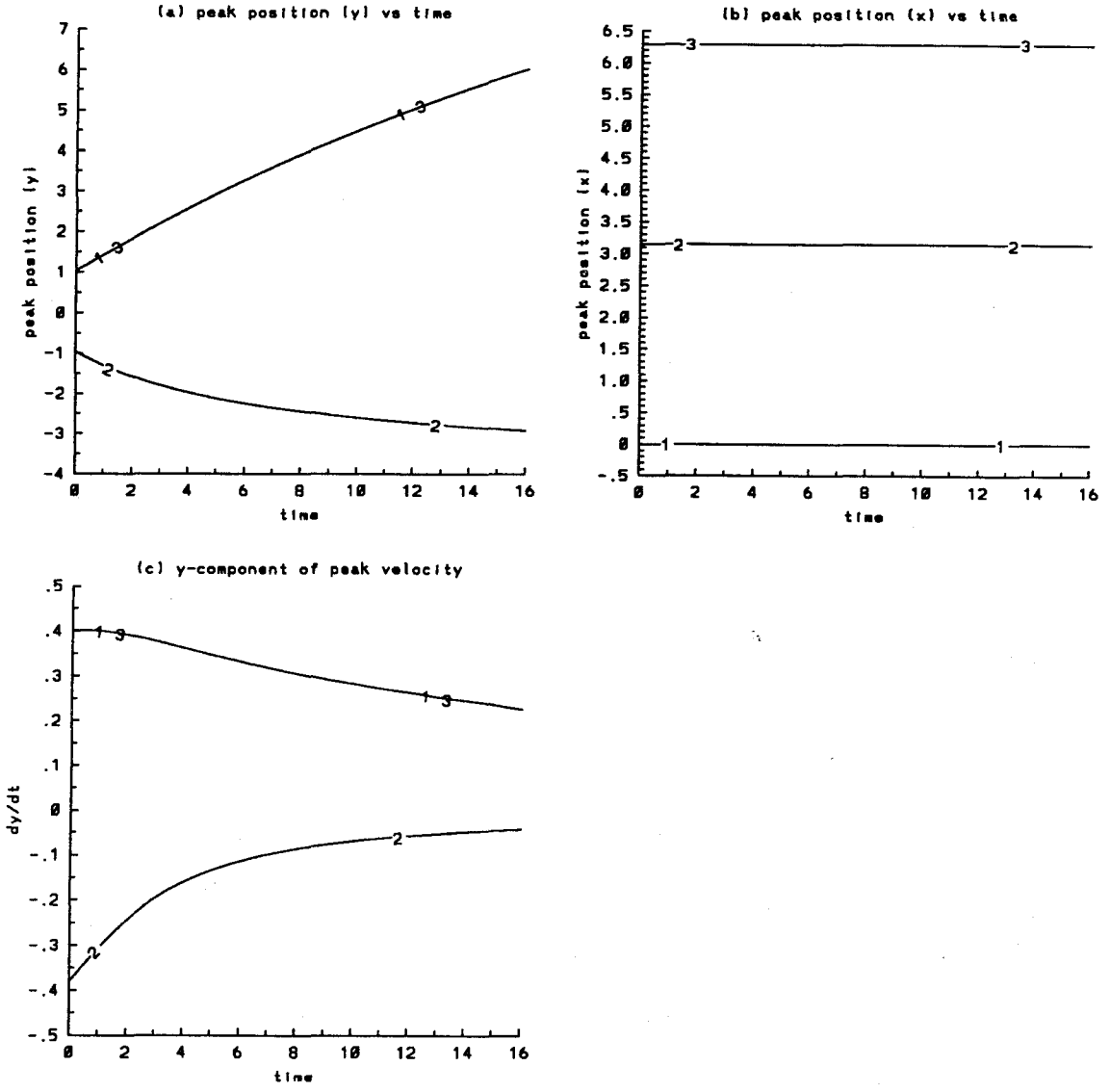

Figure 4.25.3 Time evolution of the positions and velocities of the average peaks in the single scale profile L = 1.0, A = −0.8, $\epsilon = 1.0$, $t = 0$ to 16 a) y b) x c) dy/dt. The numbers on the curves refer to the peaks on the curves $\bar{\rho}_y(x)$ versus x.

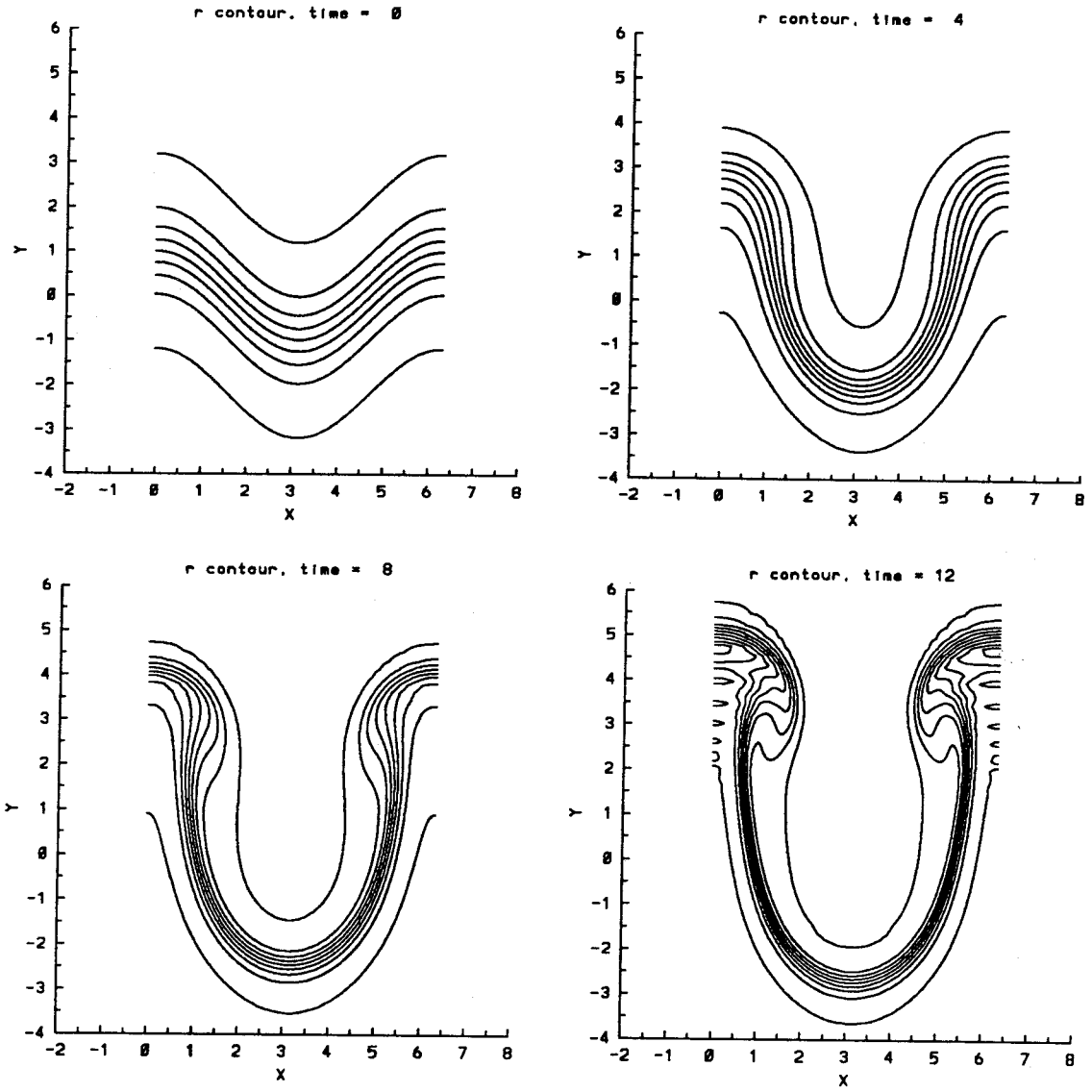

Figure 4.25.4 Time evolution of the density contours for the single scale profile L = 1.0, A = −0.8, $\epsilon = 1.0$, $t = 0$, 4, 8, 12. The contours are at $\rho = 0.11$, 0.2, 0.3, 0.4, 0.5, 0.6, 0.7, 0.8, 0.89 in that order from top to bottom of each figure.

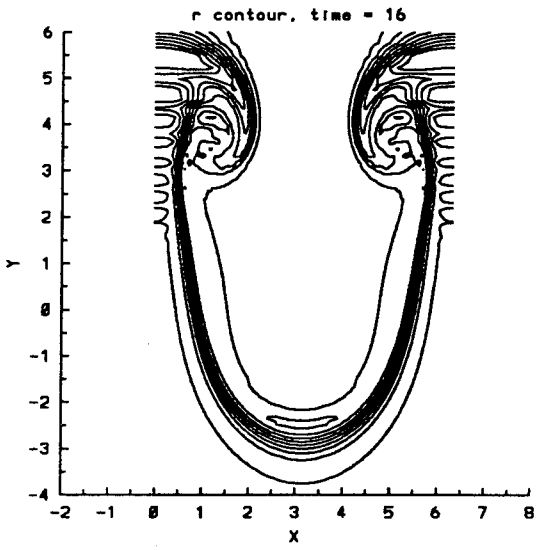

Figure 4.25.5 Time evolution of the density contours for the single scale profile L = 1.0, A = −0.8, $\epsilon = 1.0$, $t = 16$. The contours are at $\rho = 0.11$, 0.2, 0.3, 0.4, 0.5, 0.6, 0.7, 0.8, 0.89 in that order from top to bottom of each figure.

approximately the same speeds. The nonlinearity, however, causes the bubbles to decelerate much faster than the deceleration of the spikes.

The characteristic behaviors of $\bar{\rho}_y(x)$ and $\bar{\rho}_x(y)$ are consistent with the roll-up phenomena of the stratified layers as shown in the time evolution plots of the density contours in Figures 4.15.4–6 to 4.25.4–5. For small ϵ, the roll-up is delayed in time. For larger ϵ, the nonlinearity sets in faster, and the rolling up of the heavy fluid globule causes the pocket of the light fluid to widen horizontally instead of forming an elongated bubble of light fluid.

In Figures 4.26.1–2 for the case of L = 1.0, A = −0.5, and $\epsilon = 0.5$, we plot the time evolution of the vorticity contours. The dynamics of the vorticity contours is parallel to the development of the roll-up. Two pairs of vorticity with opposite signs are deposited initially in the stratified layer due to the impulsive acceleration. As time increases, they elongate. Around the time $t = 24$, the beginning of roll-up of the vorticity contours is seen. It becomes more pronounced at late times as shown in Figure 4.26.2.

In contrast to Rayleigh-Taylor instability, the Richtmyer-Meshkov instability occurs independently of the direction of the acceleration. As shown in the set of Figure 4.27 for L = 1.0, A = 0.8, and $\epsilon = 1.0$, when the acceleration is directed from a heavy fluid to a lighter one, the interface undergoes a phase reversal, then continues to grow. The growth of the average amplitude is linear in time and symmetric around the time t_0 where $da(t_0)/dt = 0$. The bubbles in this case are much wider than in those with negative A, *i.e.*, equivalently, the spike is narrower. In Figures 4.27.7-10, we show plots of the evolution of the vorticity field in this case. The roll-up of the vorticity contour is also seen, although it is not as pronounced as in the case of the negative Atwood number. The reason is that the interface has to reverse direction before fully developed growth is observed. Other than this difference, the general asymmetry of the spikes and the bubbles is also observed with the characteristic mushroom head of the spikes and rounded front of the bubbles.

To conclude the discussion in this section on the general structures of the

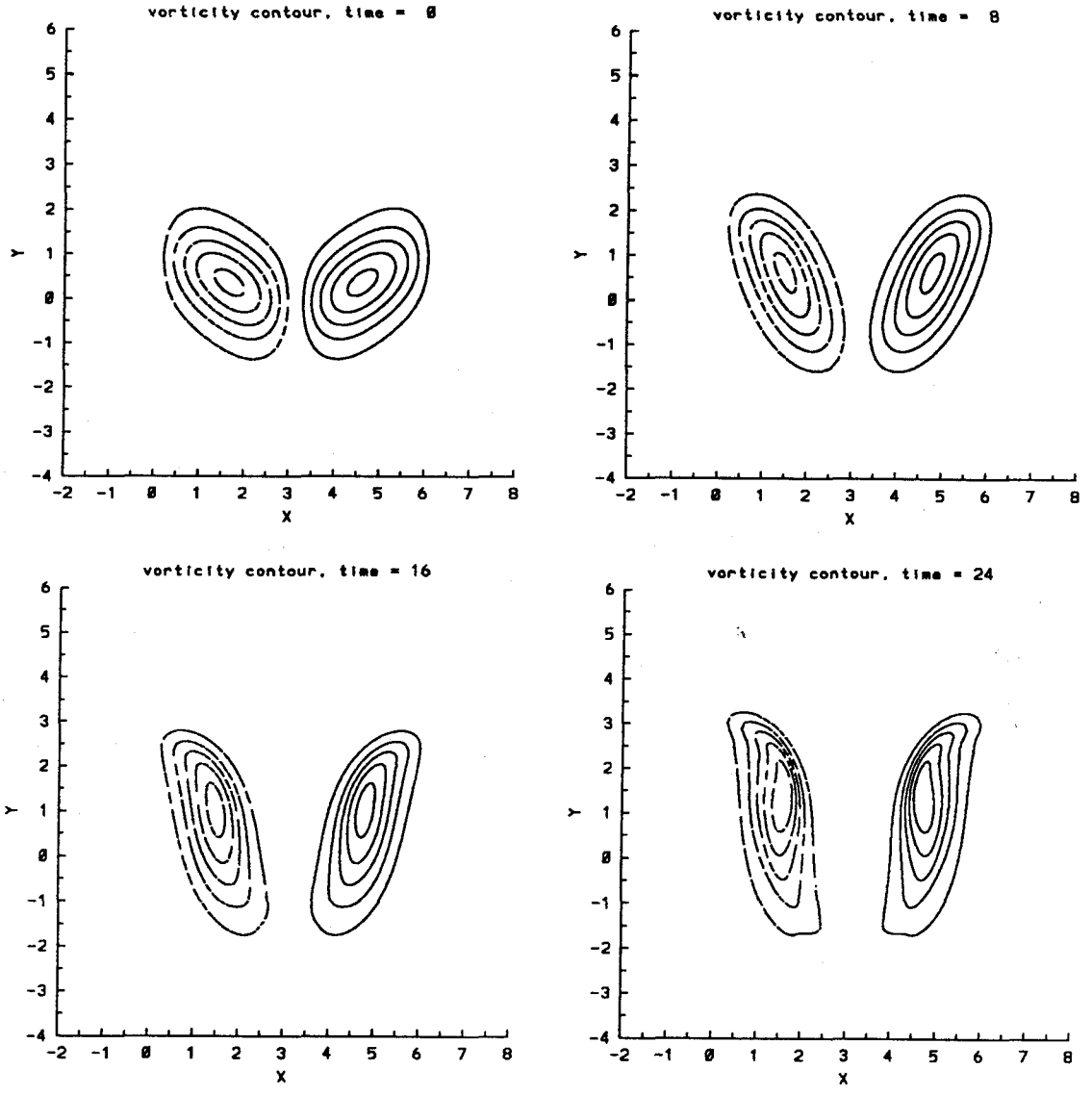

Figure 4.26.1 Time evolution of the vorticity contours for the single scale profile L = 1.0, A = −0.5, $\epsilon = 0.5$, $t = 0$, 8, 16, 24. The contours are at — · — −0.25, −0.20, −0.15, −0.10, −0.05, and — 0.25, 0.20, 0.15, 0.10, 0.05 in that order from the innermost contour line.

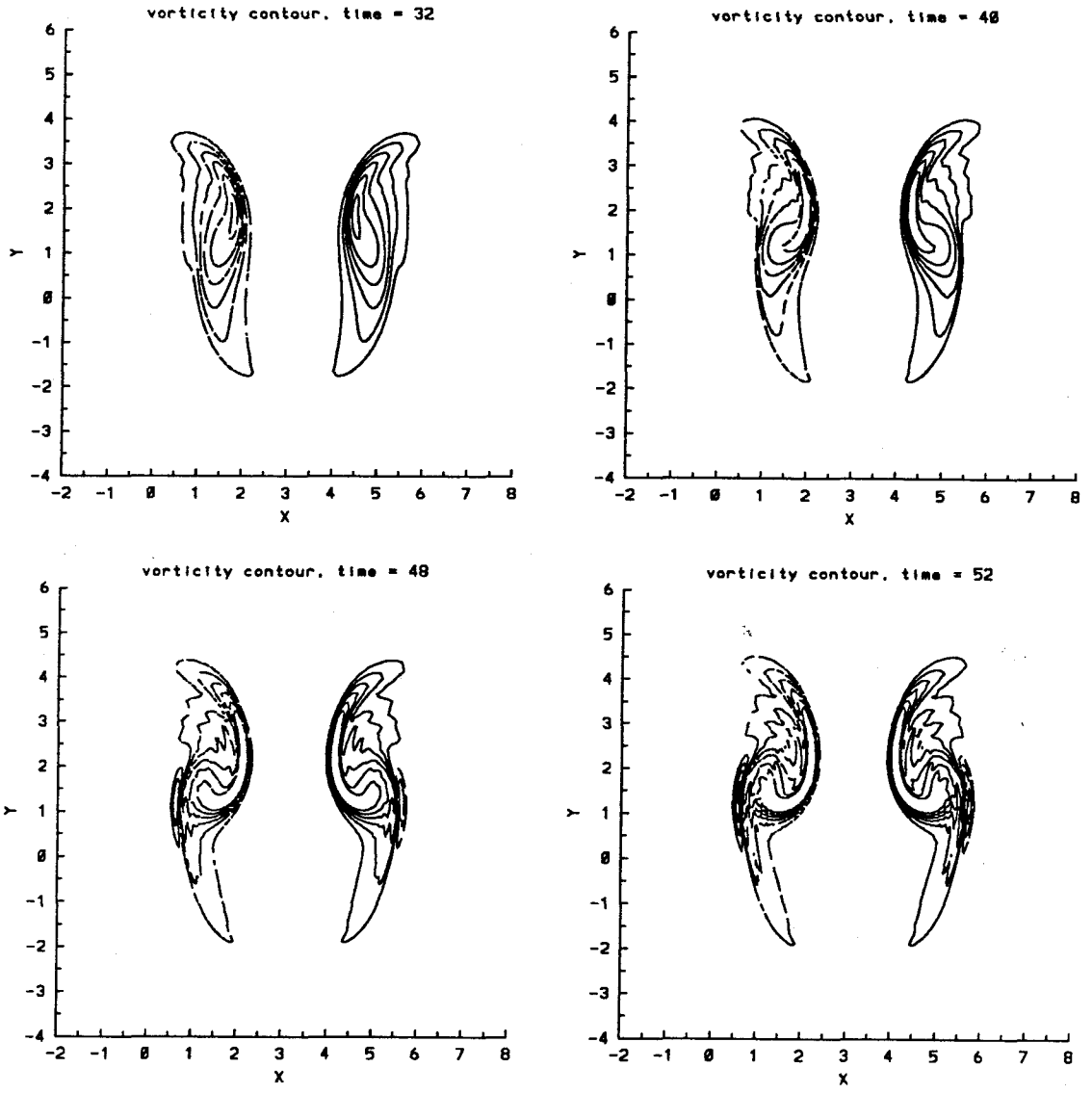

Figure 4.26.2 Time evolution of the vorticity contours for the single scale profile L = 1.0, A = −0.5, $\epsilon = 0.5$, $t = 32, 40, 48, 52$. The contours are at — · — −0.30, −0.25, −0.20, −0.15, −0.10, −0.05, and — 0.30, 0.25, 0.20, 0.15, 0.10, 0.05 in that order from the innermost contour line.

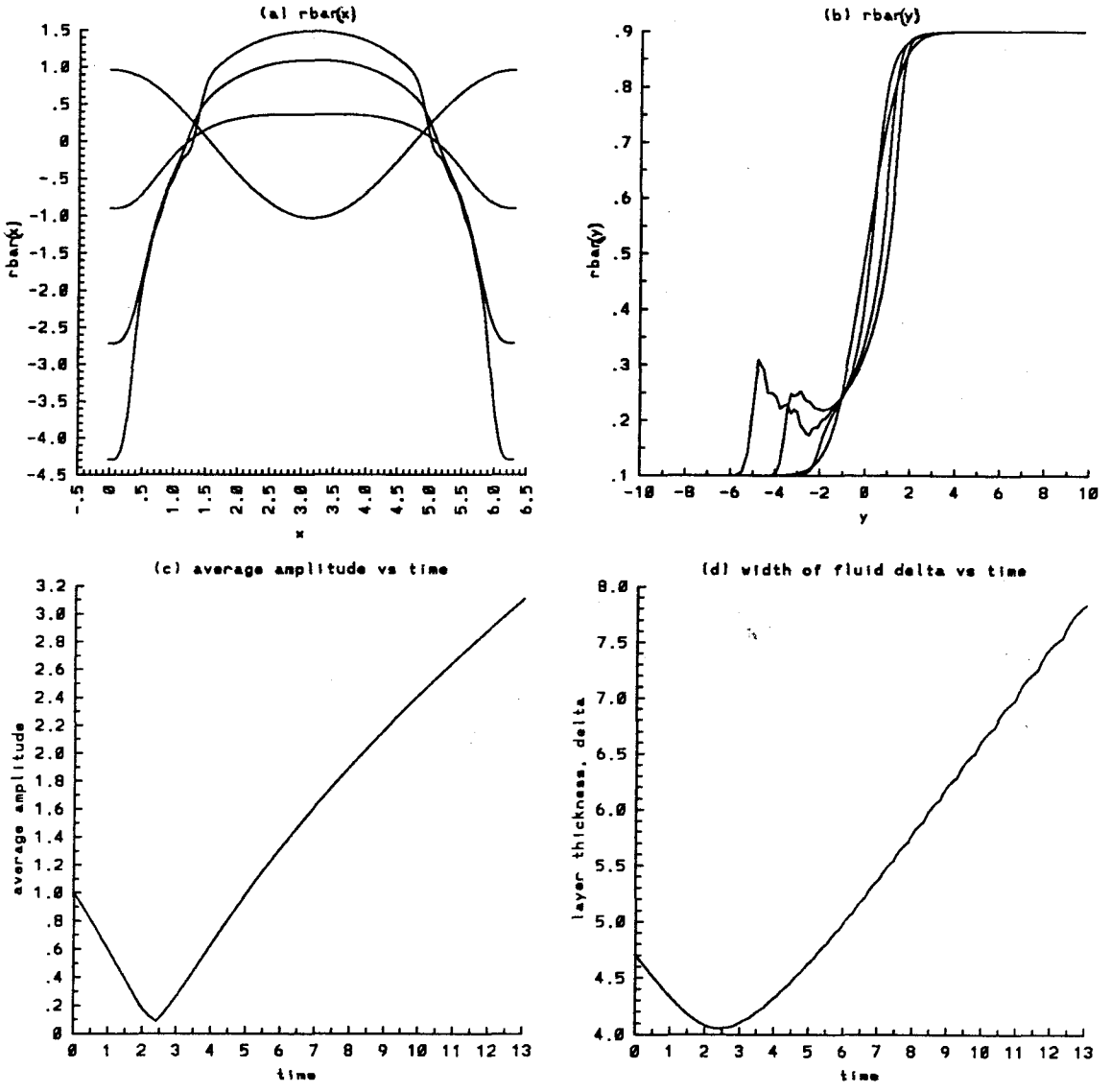

Figure 4.27.1 Time evolution of the average quantities for the single scale profile L = 1.0, A = 0.8, $\epsilon = 0.1$, $t = 0$ to 13 : a) $\bar{\rho}_y(x)$, b) $\bar{\rho}_x(y)$, c) average amplitude, and d) width of the density layer.

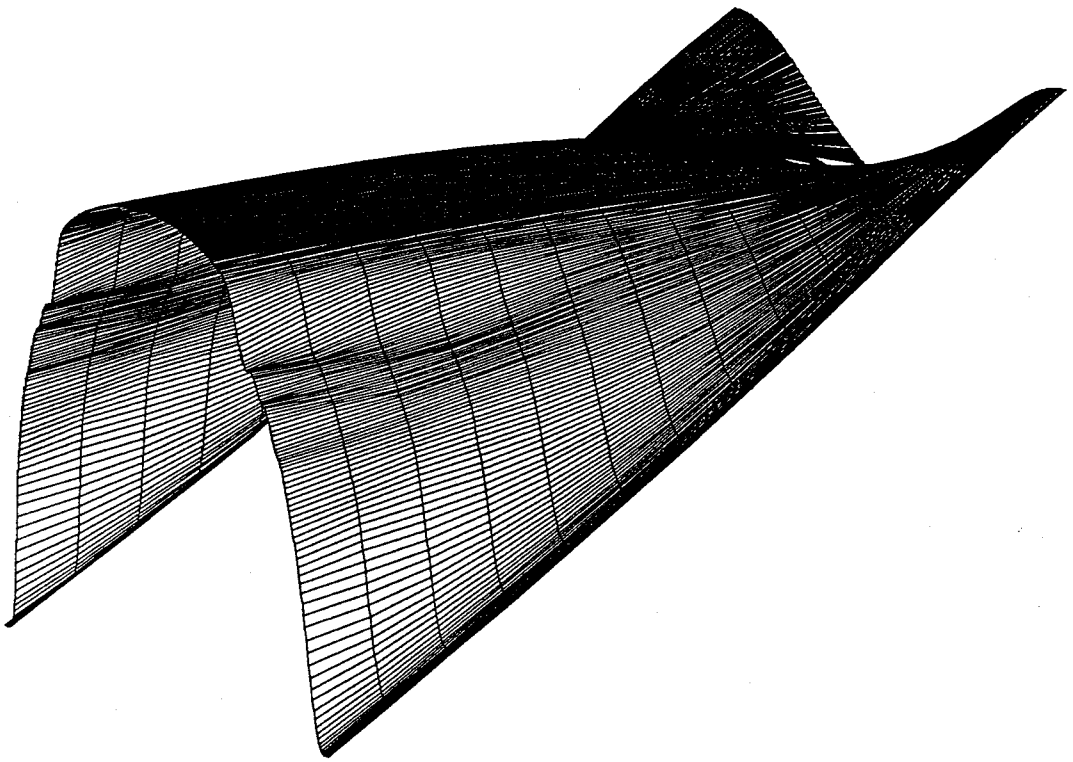

Figure 4.27.1a Three-dimensional surface of $\bar{\rho}_y(x,t)$ for the single scale profile L = 1.0, A = 0.8, $\epsilon = 1.0$, and $t = 0$, 13.

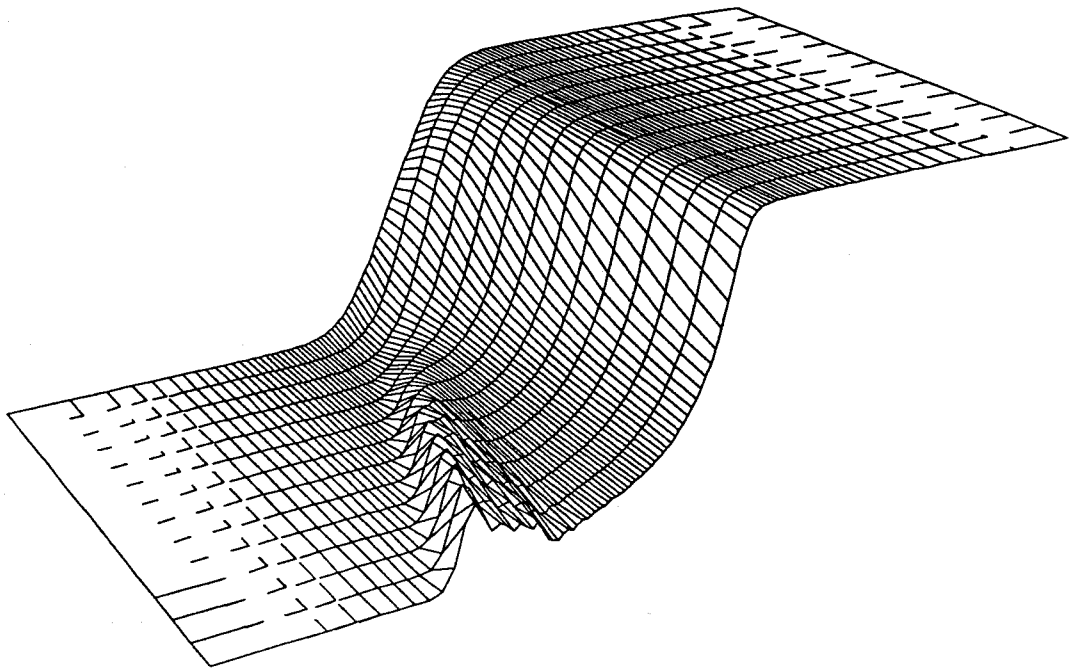

Figure 4.27.1b Three-dimensional surface of $\bar{\rho}_x(y,t)$ for the single scale profile L = 1.0, A = 0.8, $\epsilon = 1.0$, and $t = 0$, 13.

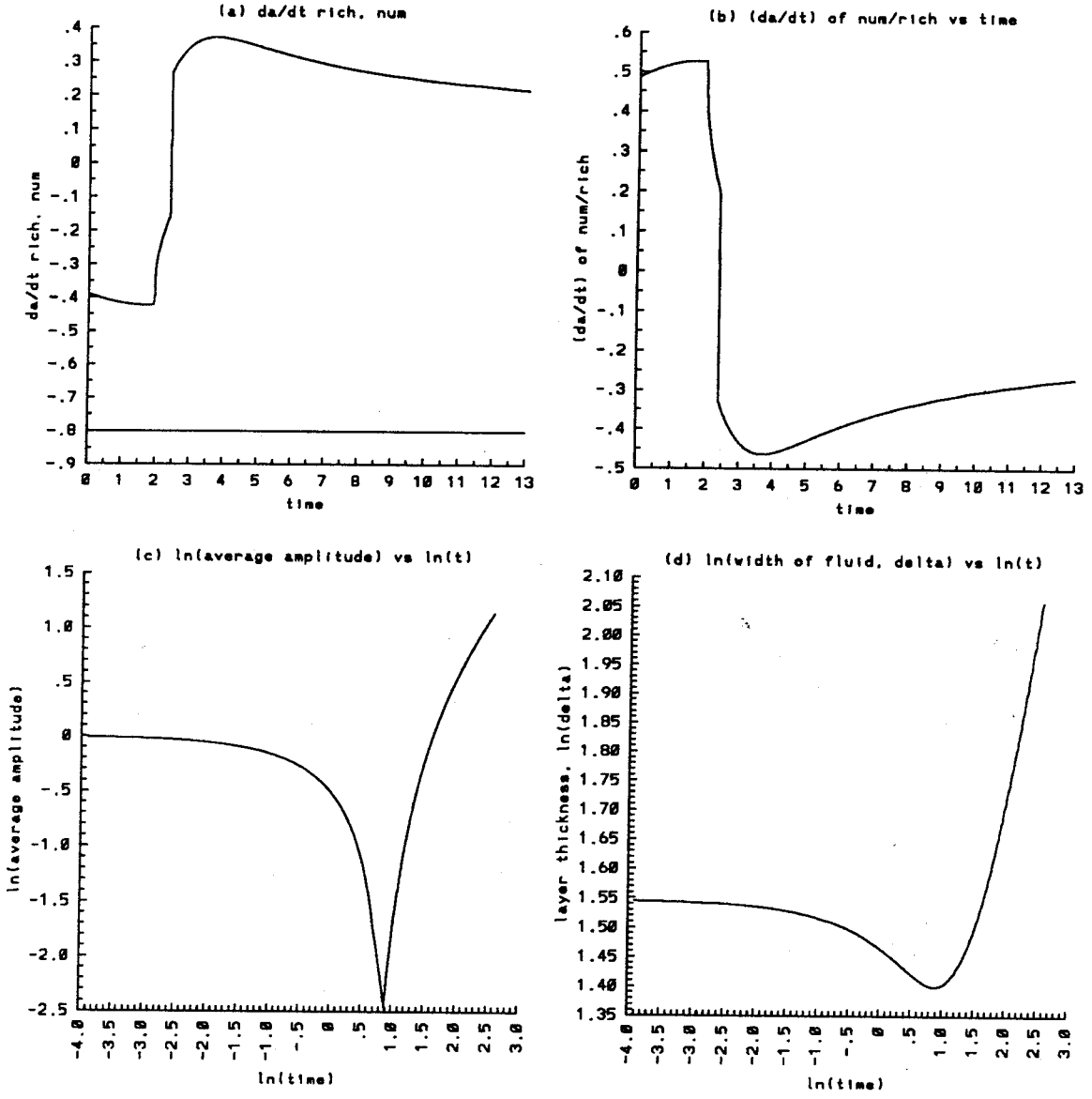

Figure 4.27.2 Time evolution of the average quantities for the single scale profile L = 1.0, A = 0.8, $\epsilon = 1.0$, $t = 0$ to 13 : a) growth rate da/dt of the average amplitude, numerical and Richtmyer theory (straight line), b) the ratio of the numerical growth rate da/dt over that predicted by Richtmyer theory, c) $\ln(a)$ *vs* $\ln(t)$, d) $\ln(\delta)$ *vs* $\ln(t)$.

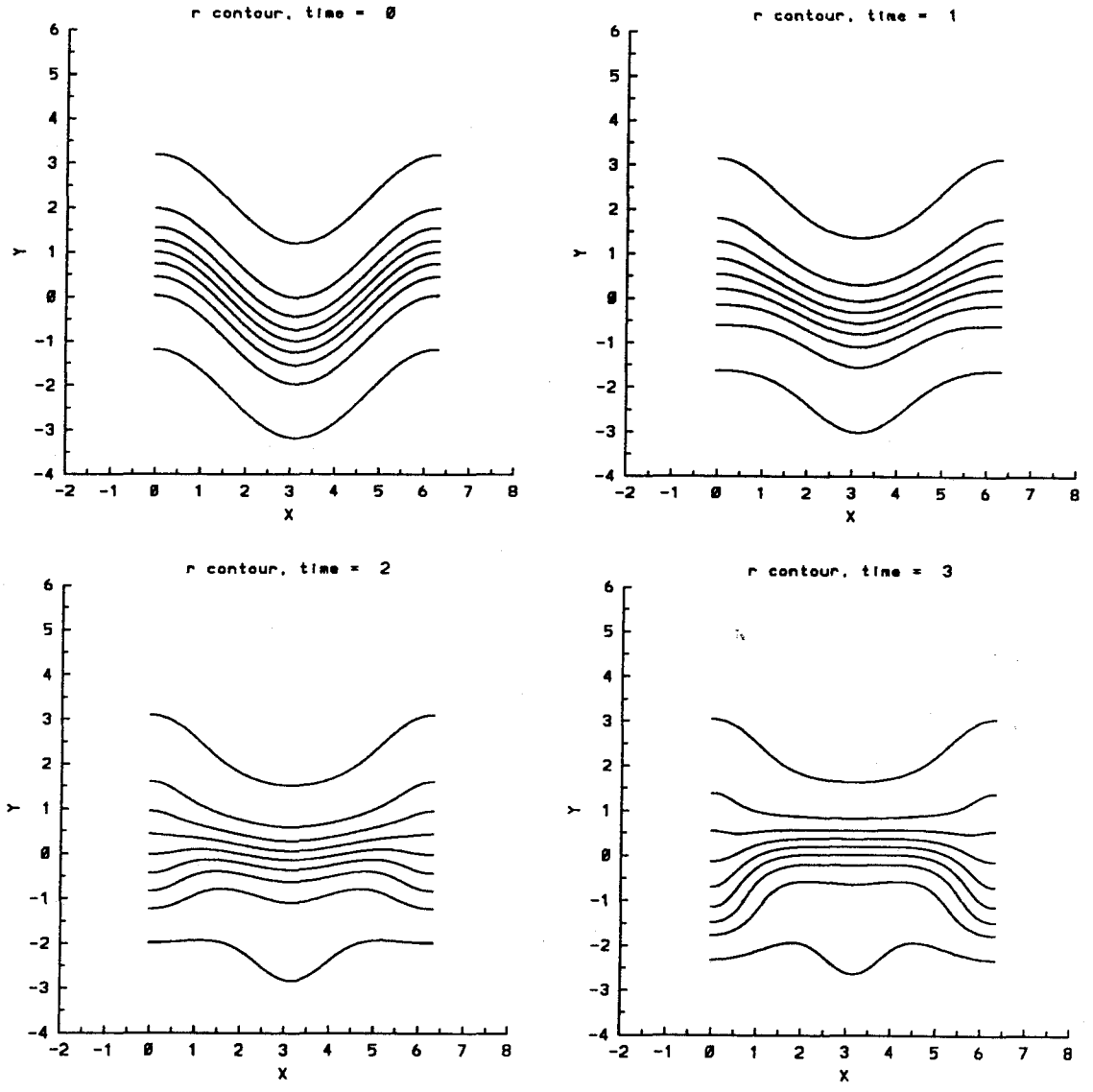

Figure 4.27.3 Time evolution of the density contours for the single scale profile L = 1.0, A = 0.8, $\epsilon = 1.0$, $t = 0$, 1, 2, 3. The contours are at $\rho = 0.11$, 0.2, 0.3, 0.4, 0.5, 0.6, 0.7, 0.8, 0.89 in that order from bottom to top of each figure.

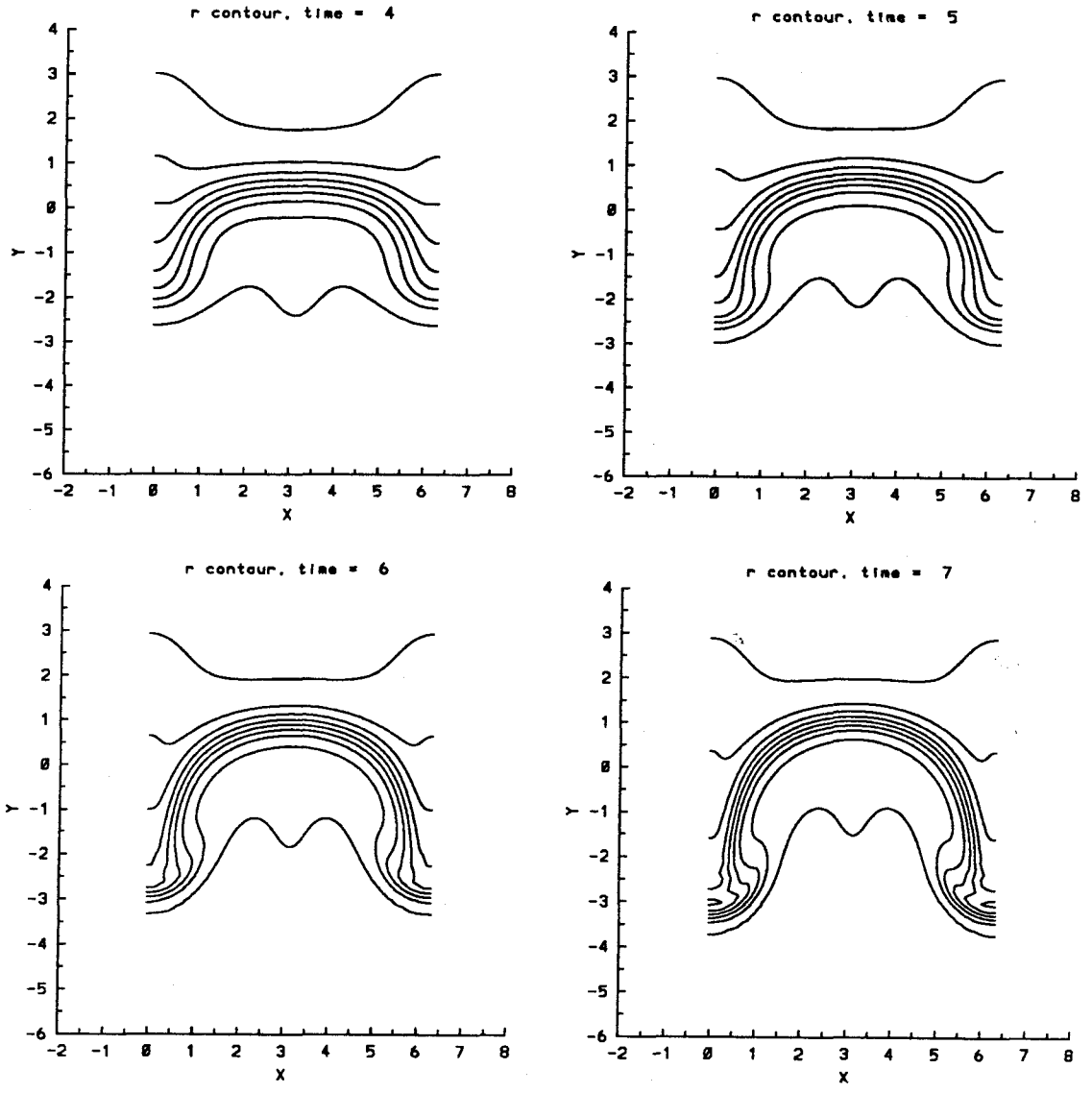

Figure 4.27.4 Time evolution of the density contours for the single scale profile L = 1.0, A = 0.8, $\epsilon = 1.0$, t = 4, 5, 6, 7. The contours are at ρ = 0.11, 0.2, 0.3, 0.4, 0.5, 0.6, 0.7, 0.8, 0.89 in that order from bottom to top of each figure.

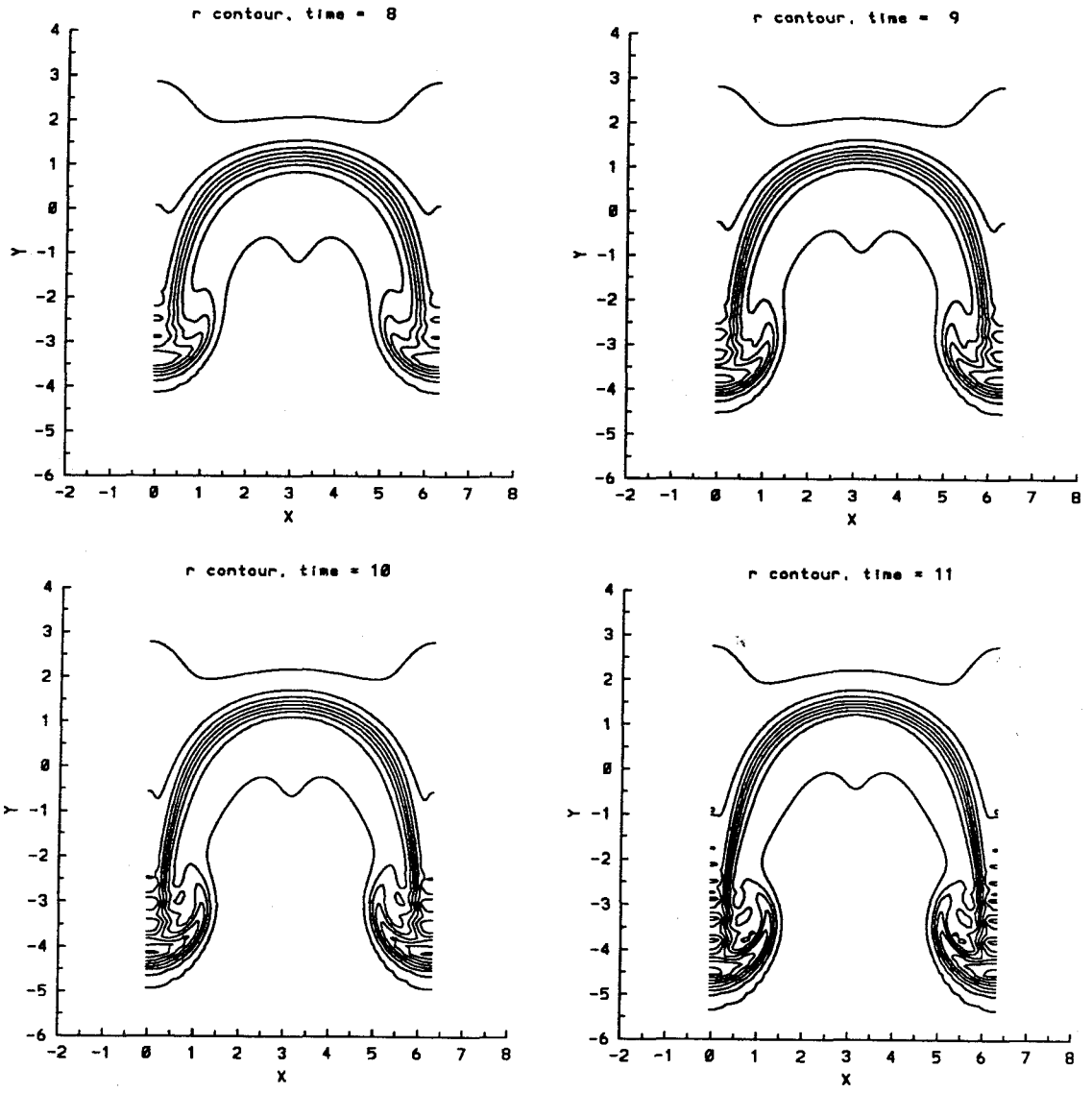

Figure 4.27.5 Time evolution of the density contours for the single scale profile L = 1.0, A = 0.8, $\epsilon = 1.0$, t = 8, 9, 10, 11. The contours are at ρ = 0.11, 0.2, 0.3, 0.4, 0.5, 0.6, 0.7, 0.8, 0.89 in that order from bottom to top of each figure.

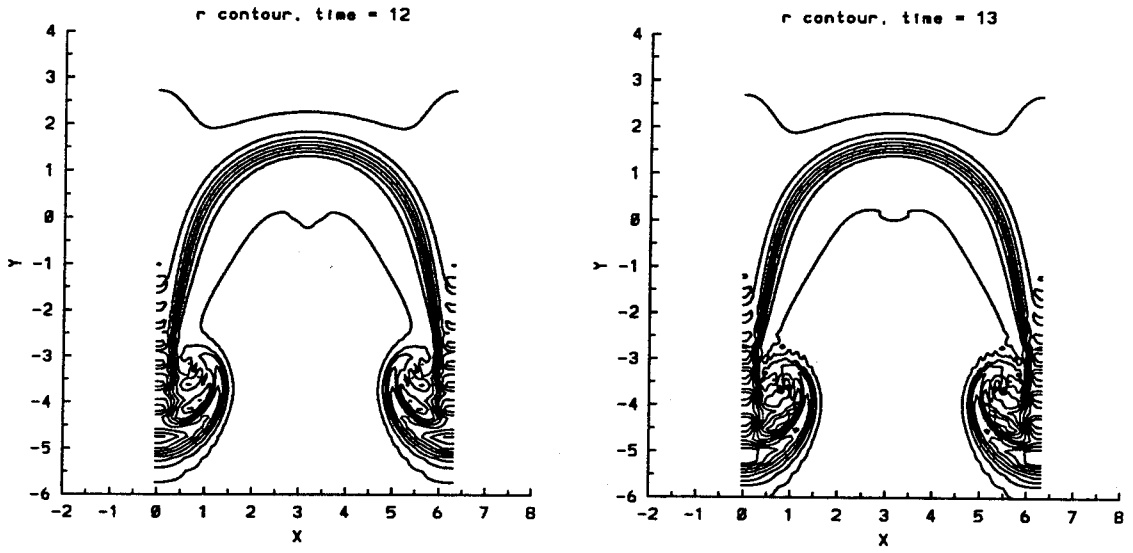

Figure 4.27.6 Time evolution of the density contours for the single scale profile L = 1.0, A = 0.8, $\epsilon = 1.0$, t = 12, 13. The contours are at ρ = 0.11, 0.2, 0.3, 0.4, 0.5, 0.6, 0.7, 0.8, 0.89 in that order from bottom to top of each figure.

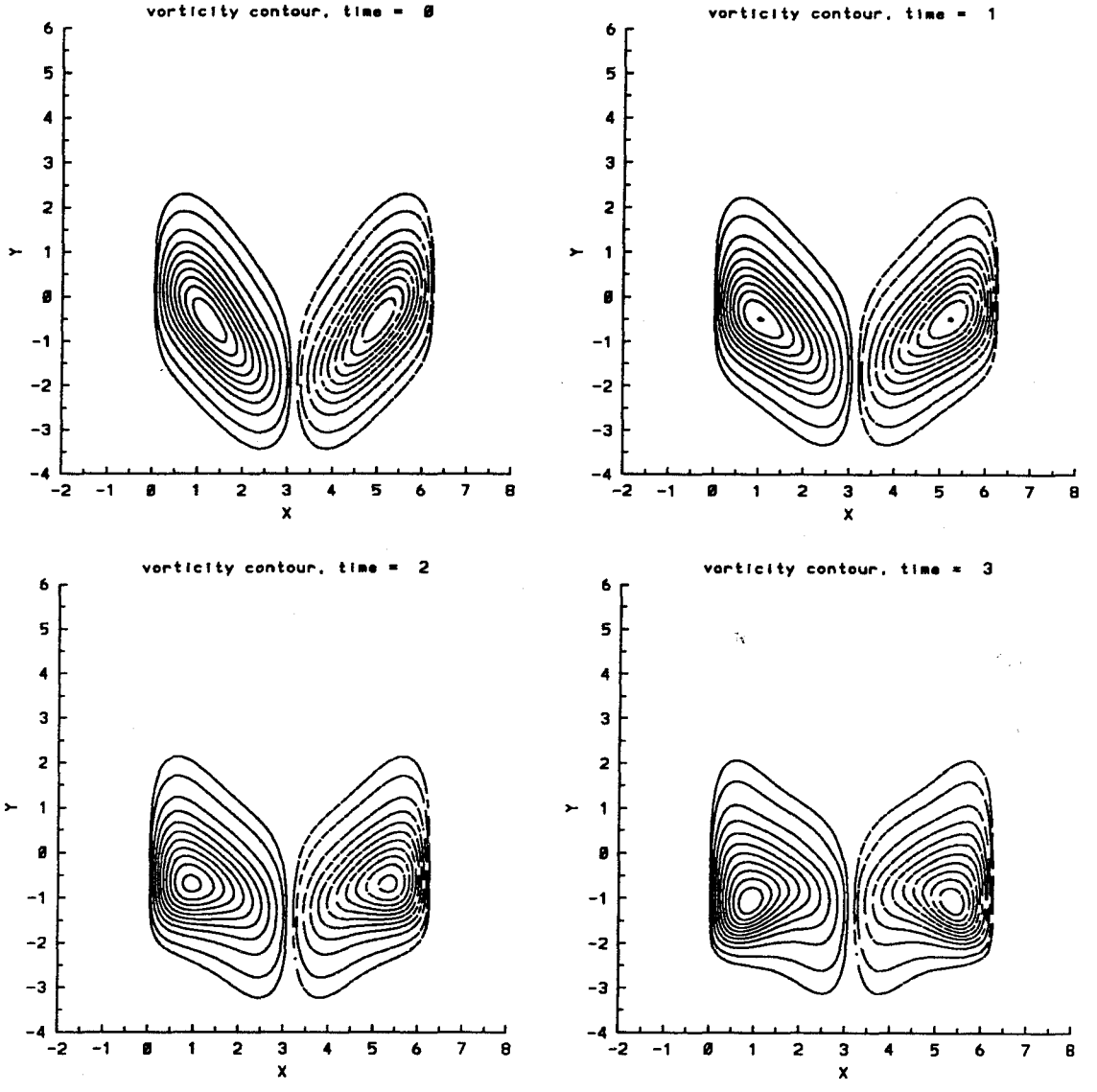

Figure 4.27.7 Time evolution of the vorticity contours for the single scale profile, L = 1.0, A = 0.8, $\epsilon = 1.0$, $t = 0, 1, 2, 3$. The contours are from -0.9 to 0.9 for $t = 0$, -1.0 to 1.0 for $t = 1, 2, 3$, with incremental step size of 0.05 from vorticity -0.1 to 0.1, and of 0.1 for bigger vorticity $|w|$. The negative contours are indicated by — · — and positive ones by —.

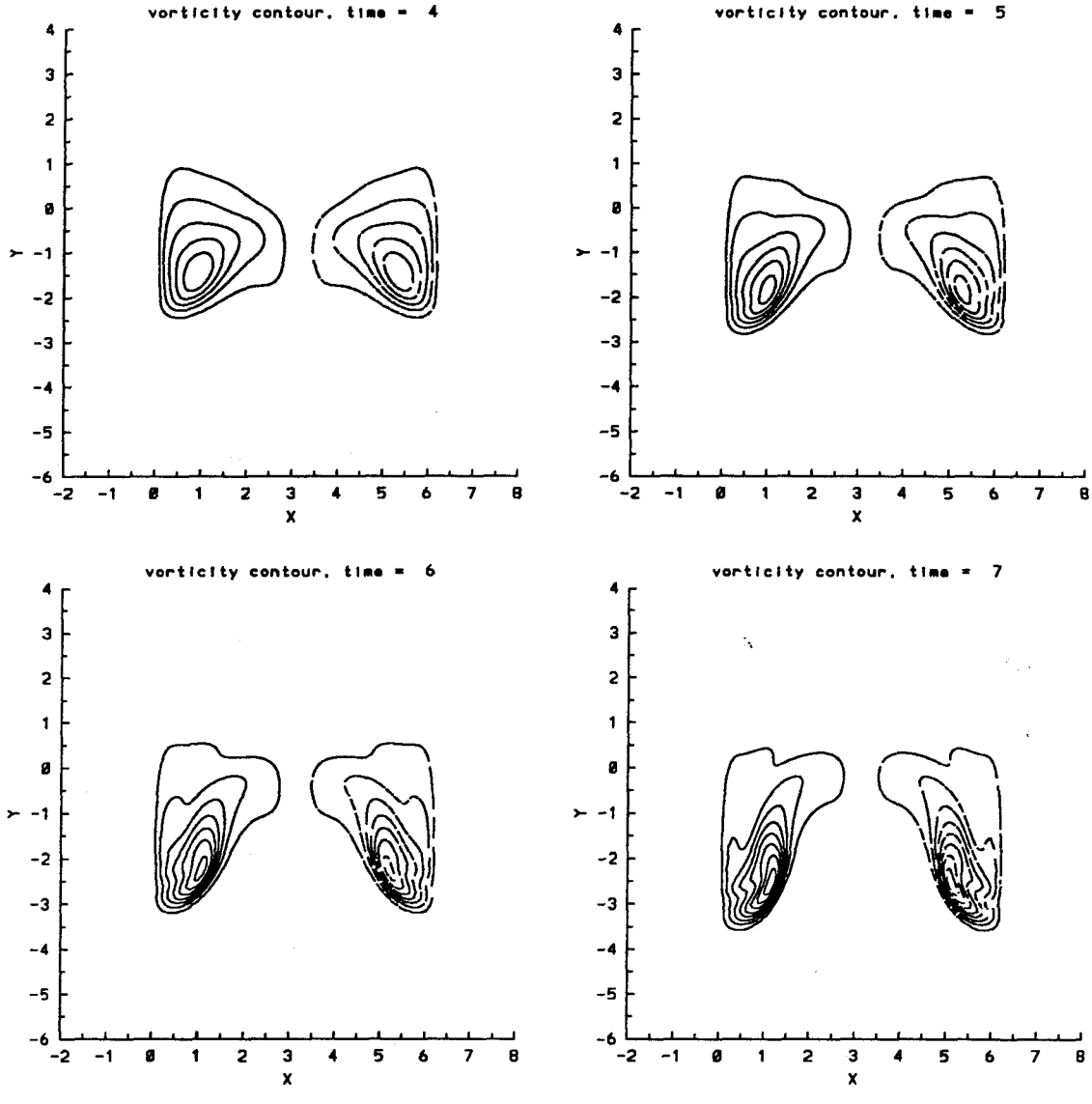

Figure 4.27.8 Time evolution of the vorticity contours for the single scale profile, L = 1.0, A = 0.8, $\epsilon = 1.0$, $t = 4, 5, 6, 7$. The contours are from -1.0 to 1.0 $t = 4$, -1.2 to 1.2 $t = 5$, -1.4 to 1.4 $t = 6$, -1.6 to 1.6 $t = 7$, with incremental step size of 0.2. The negative contours are indicated by — · — and positive ones by —.

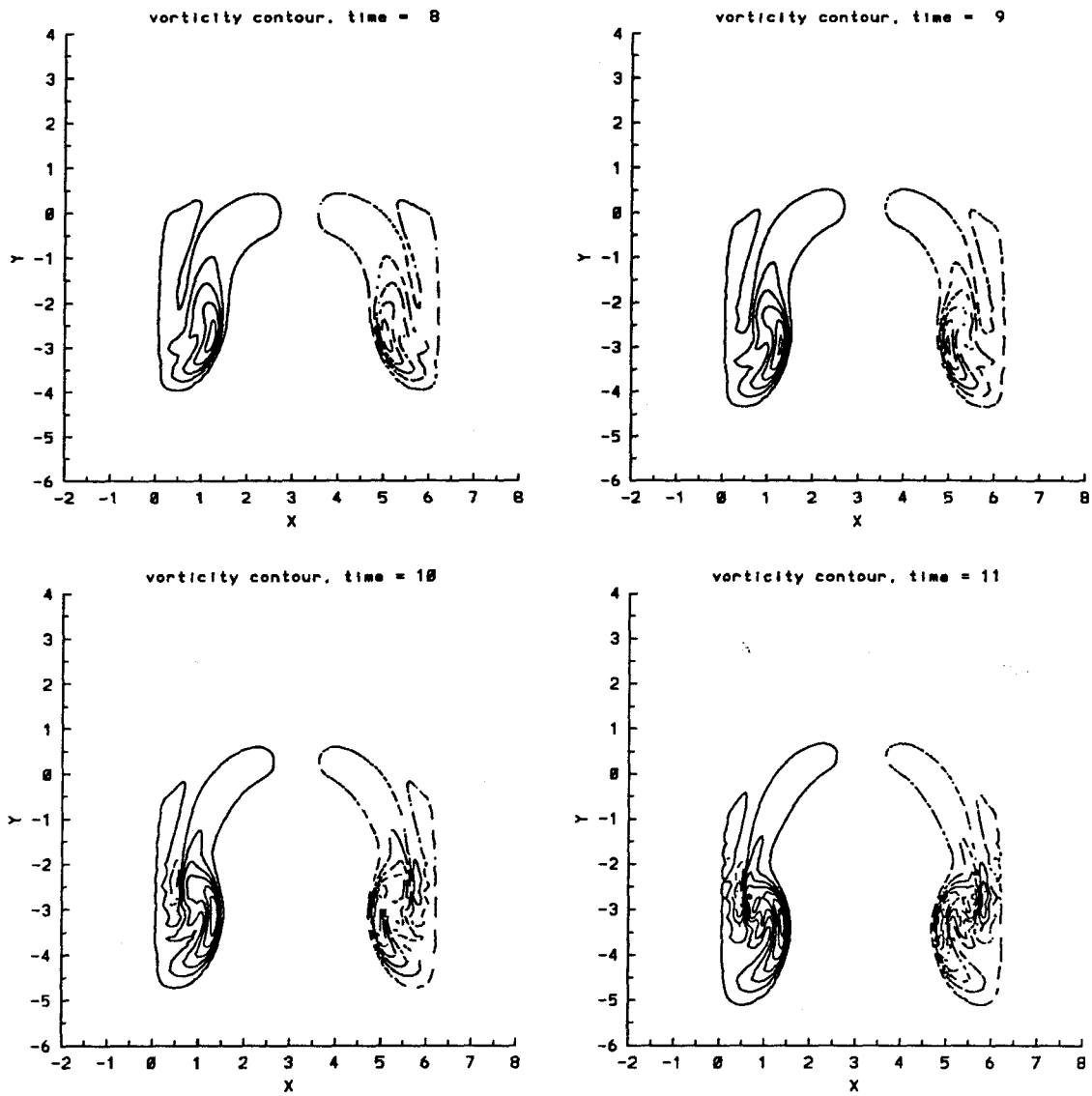

Figure 4.27.9 Time evolution of the vorticity contours for the single scale profile, L = 1.0, A = 0.8, $\epsilon = 1.0$, $t = 8, 9, 10, 11$. The contours are from -1.8 to 1.8 $t = 8$, -2.2 to 2.2 $t = 9, 10$, -2.6 to 2.6 $t = 11$, with incremental step size of 0.4. The negative contours are indicated by — · — and positive ones by —.

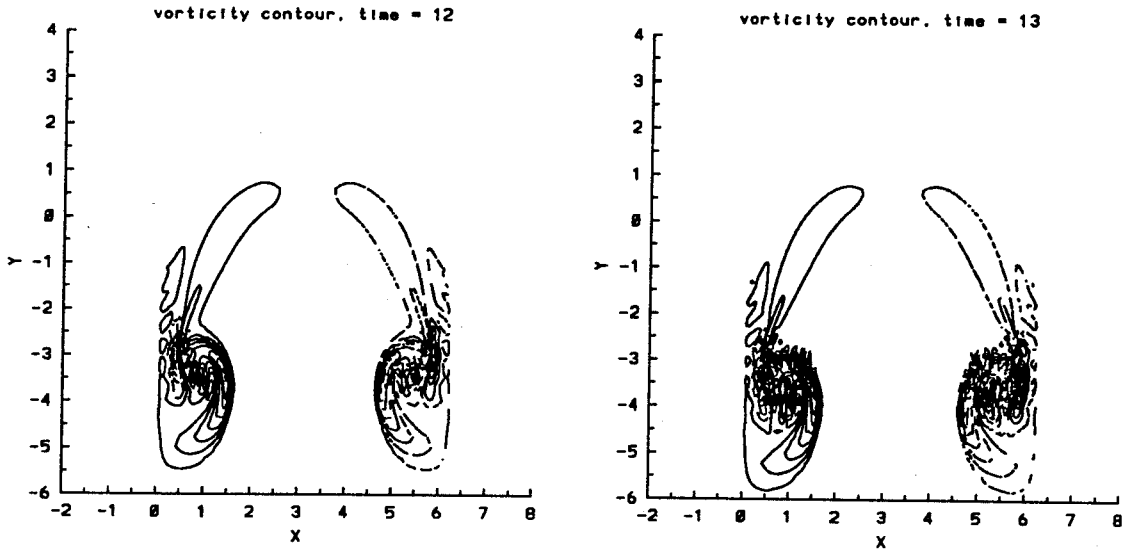

Figure 4.27.10 Time evolution of the vorticity contours for the single scale profile, L = 1.0, A = 0.8, $\epsilon = 1.0$, $t = 12$, 13. The contours are from -3.0 to 3.0 $t = 12$, 13, with incremental step size of 0.4. The negative contours are indicated by — · — and positive ones by —.

instability, for the purpose of completeness, in the set of Figure 4.28, we have the plots for the case of L = 0.5, A = −0.5, and $\epsilon = 0.2$. The overall features of the instability are similar to the case of L = 1.0, A = −0.5, and $\epsilon = 0.2$ as shown in Figures 4.21.1-6 except that the roll-up of the spikes seem to be weaker in the latter case.

4.5.2 Overall growth of the layer

For the cases with L = 1.0, the average amplitude a and the width of the density layer δ are monotonically increasing funtions of time as shown in Figures 4.29.1−2. For a given ϵ, the instability grows faster for higher A. For a given A, increasing ϵ leads to an increase in the growth. Due to the roll-up, the growth rate of the average amplitude da/dt, and the width of the density layer $d\delta/dt$ decreases in time as shown in Figures 4.29.1−2, 7. The higher the Atwood number A and the perturbation amplitude ϵ, the faster is the decay of the growth rates due to the nonlinear effect, even though they are large initially. To study the effect of the continuous density gradient on the growth rate, we plot the time evolution of the ratio of the numerical growth rate over that of Richtmyer theory in Figures 4.15.2b− 4.25.2b, and 4.29.6. For all A, and ϵ considered, the numerical growth rate is about half that predicted by Richtmyer theory. This conclusion is consistent with the result of the previous section 4.4.

As mentioned earlier, the only energy deposited into the layer is due to the initial impulsive acceleration, and since we have a small kinematic viscosity $\nu = 10^{-6}$ in the simulation, energy is approximately conserved. This constraint is satisfied in our calculation as shown in Figure 4.29.5 for the time evolution of the total kinetic energies which has been discussed carefully in section 3.7.3. Due to this constancy of the total kinetic energy, and its dependence on the initial wavelength in the case of a sharp interface, it has been argued by Brouillette and Sturtevant (1989) that the Richtmyer-Meshkov instability will not approach a self-similar asymptotic limit.

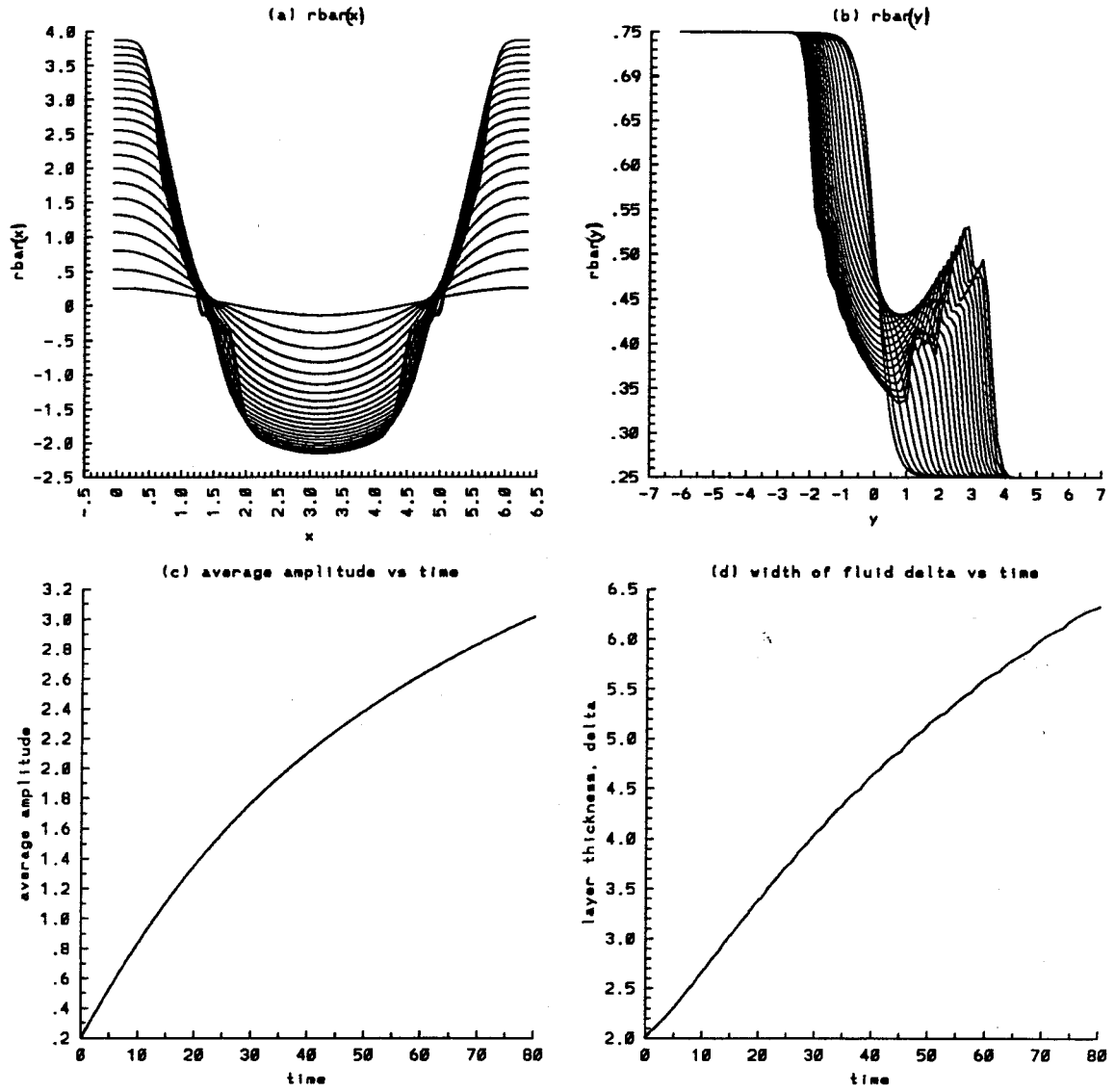

Figure 4.28.1 Time evolution of the average quantities for the single scale profile L = 0.5, A = −0.5, $\epsilon = 0.2$, $t = 0$ to 80 : a) $\bar{\rho}_y(x)$, b) $\bar{\rho}_x(y)$, c) average amplitude, and d) width of the density layer.

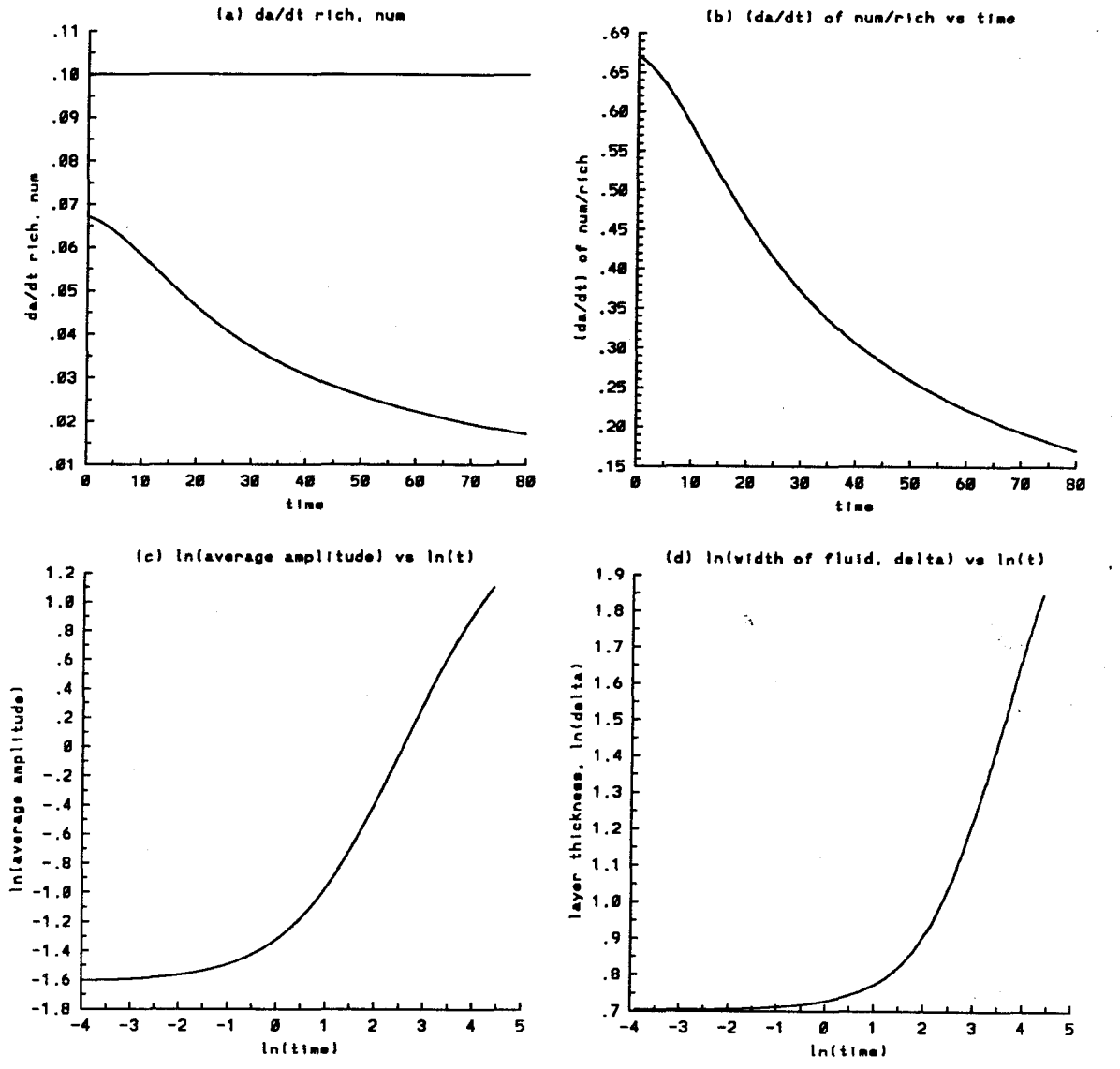

Figure 4.28.2 Time evolution of the average quantities for the single scale profile L = 0.5, A = −0.5, $\epsilon = 0.2$, $t = 0$ to 80 : a) growth rate da/dt of the average amplitude, numerical and Richtmyer theory (straight line), b) the ratio of the numerical growth rate da/dt over that predicted by Richtmyer theory, c) $\ln(a)$ *vs* $\ln(t)$, d) $\ln(\delta)$ *vs* $\ln(t)$.

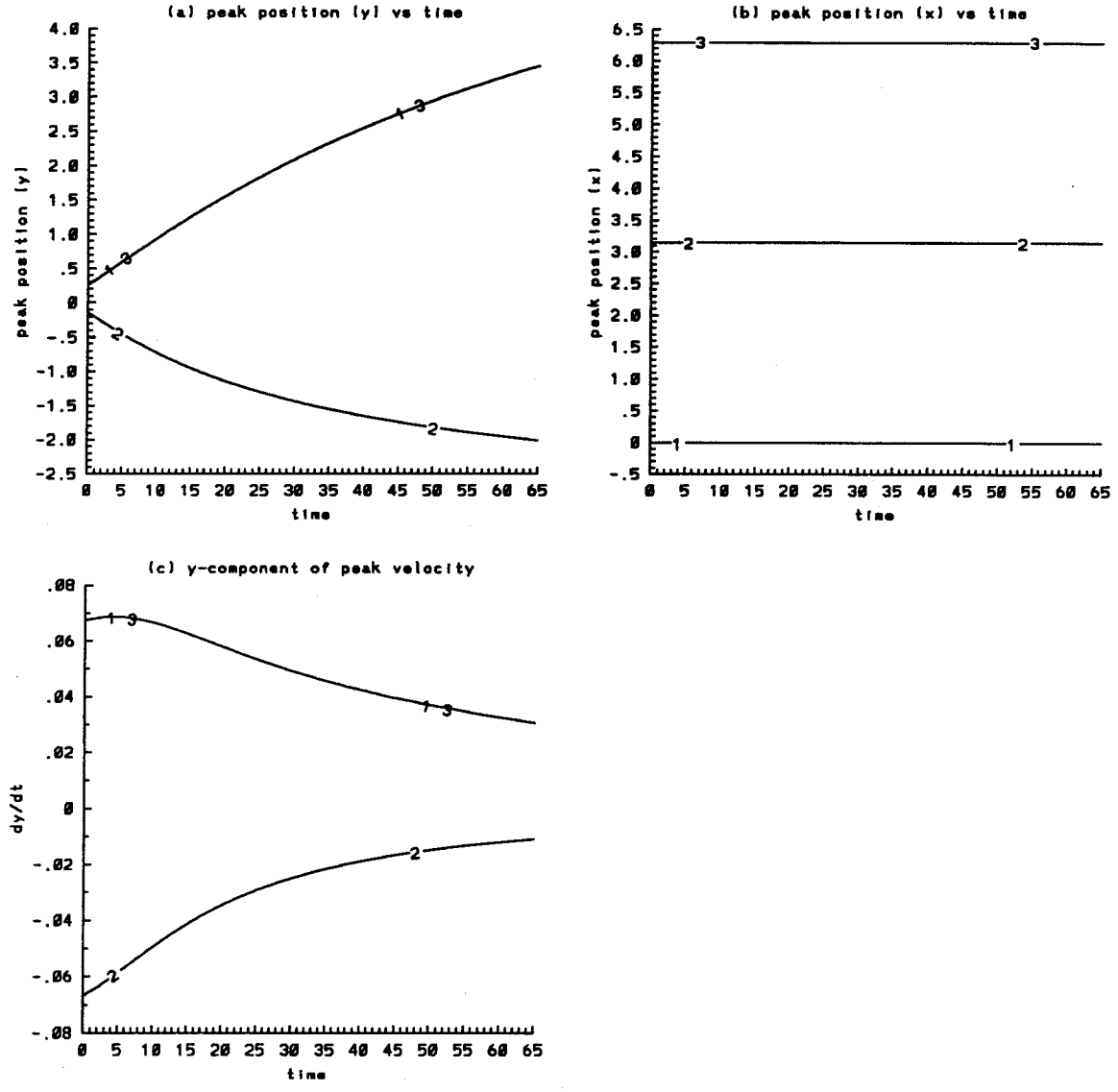

Figure 4.28.3 Time evolution of the positions and velocities of the average peaks in the single scale profile L = 0.5, A = −0.5, $\epsilon = 0.2$, $t = 0$ to 80 a) y b) x c) dy/dt. The numbers on the curves refer to the peaks on the curves $\bar{\rho}_y(x)$ versus x.

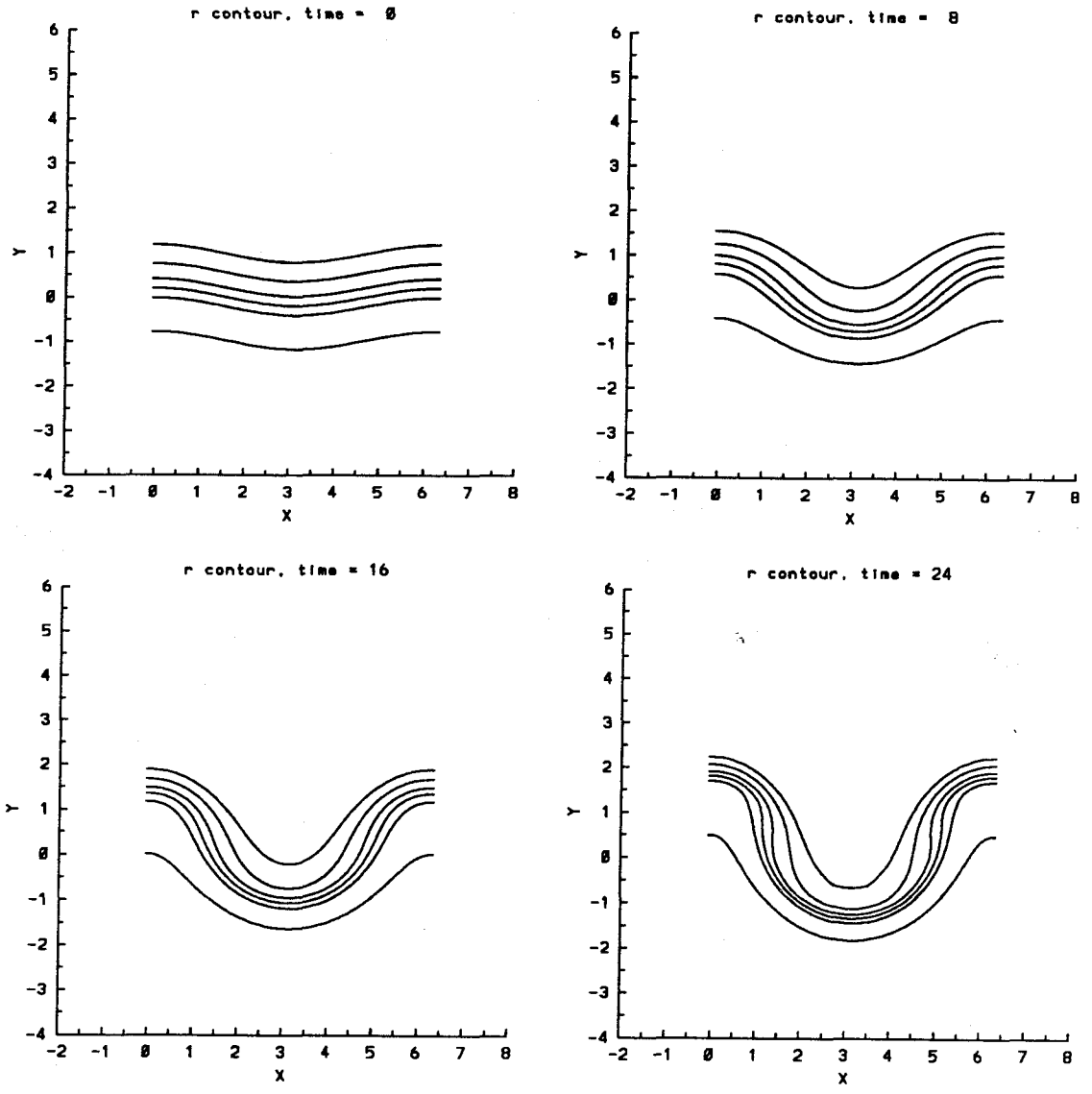

Figure 4.28.4 Time evolution of the density contours for the single scale profile L = 0.5, A = −0.5, $\epsilon = 0.2$, $t = 0$, 8, 16, 24. The contours are at $\rho = 0.26$, 0.3, 0.4, 0.5, 0.6, 0.74 in that order from top to bottom of each figure.

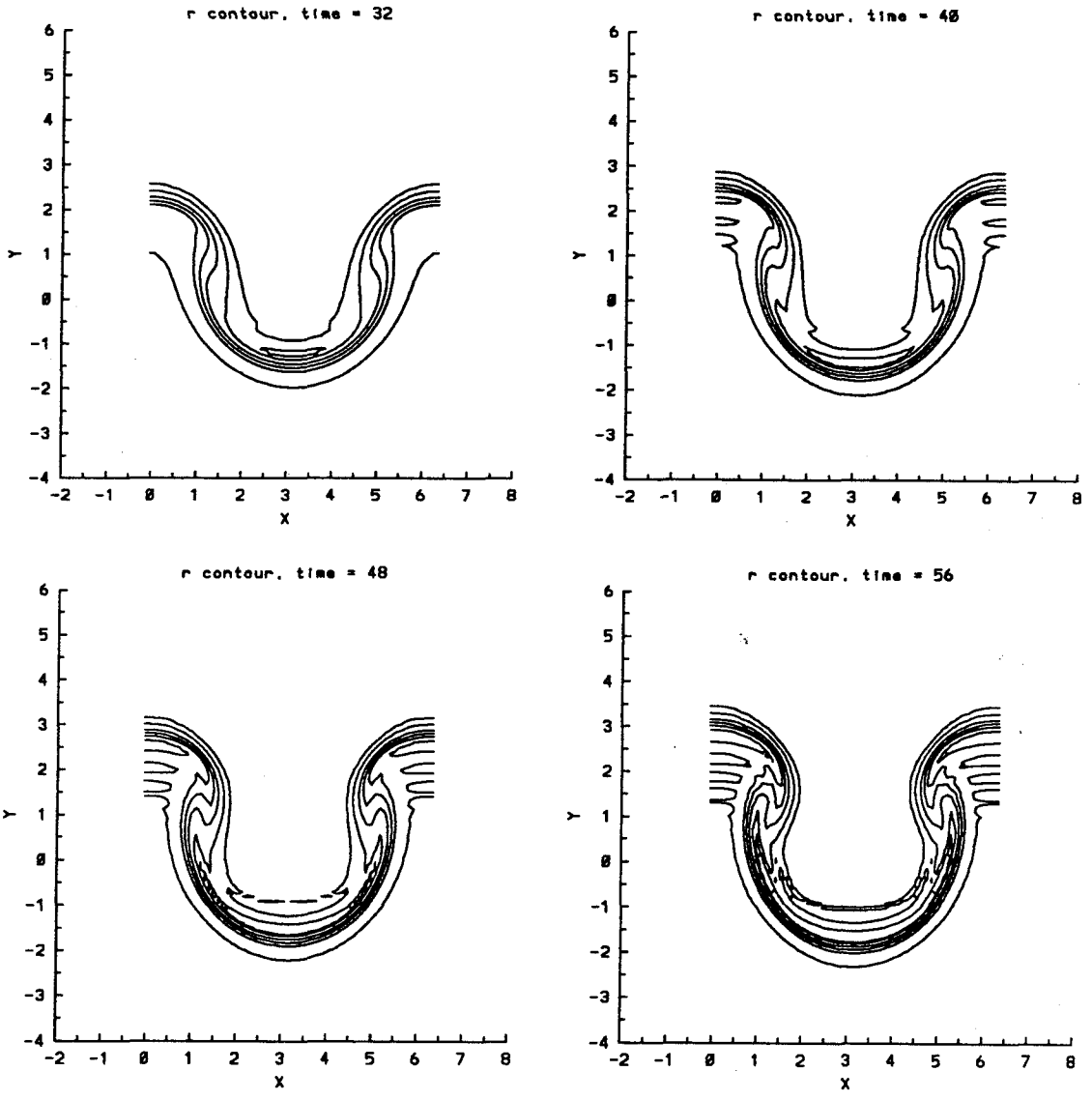

Figure 4.28.5 Time evolution of the density contours for the single scale profile L = 0.5, A = −0.5, $\epsilon = 0.2$, t = 32, 40, 48, 56. The contours are at $\rho = 0.26$, 0.3, 0.4, 0.5, 0.6, 0.74 in that order from top to bottom of each figure.

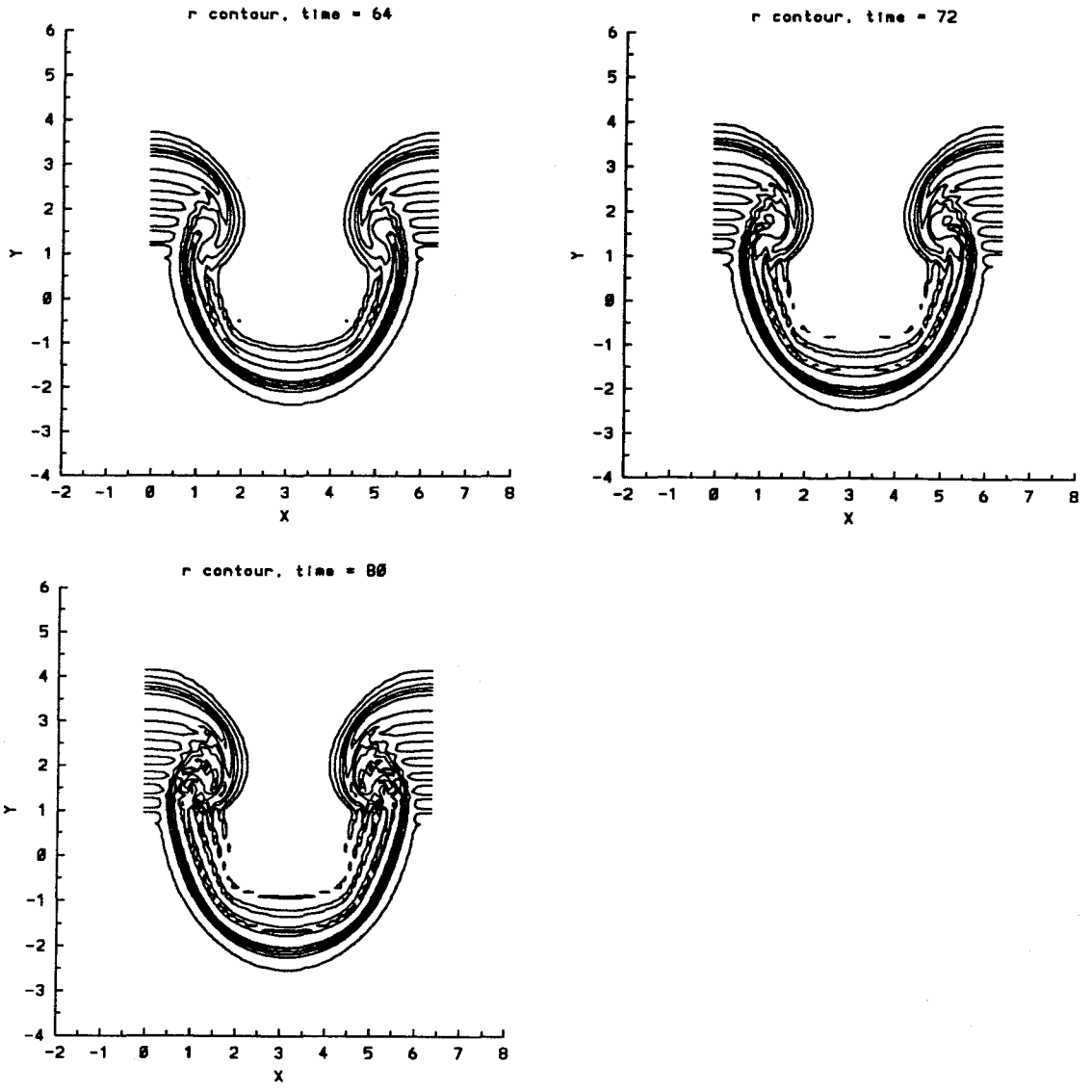

Figure 4.28.6 Time evolution of the density contours for the single scale profile L = 0.5, A = −0.5, $\epsilon = 0.2$, $t = 64, 72, 80$. The contours are at $\rho = 0.26, 0.3, 0.4, 0.5, 0.6, 0.74$ in that order from top to bottom of each figure.

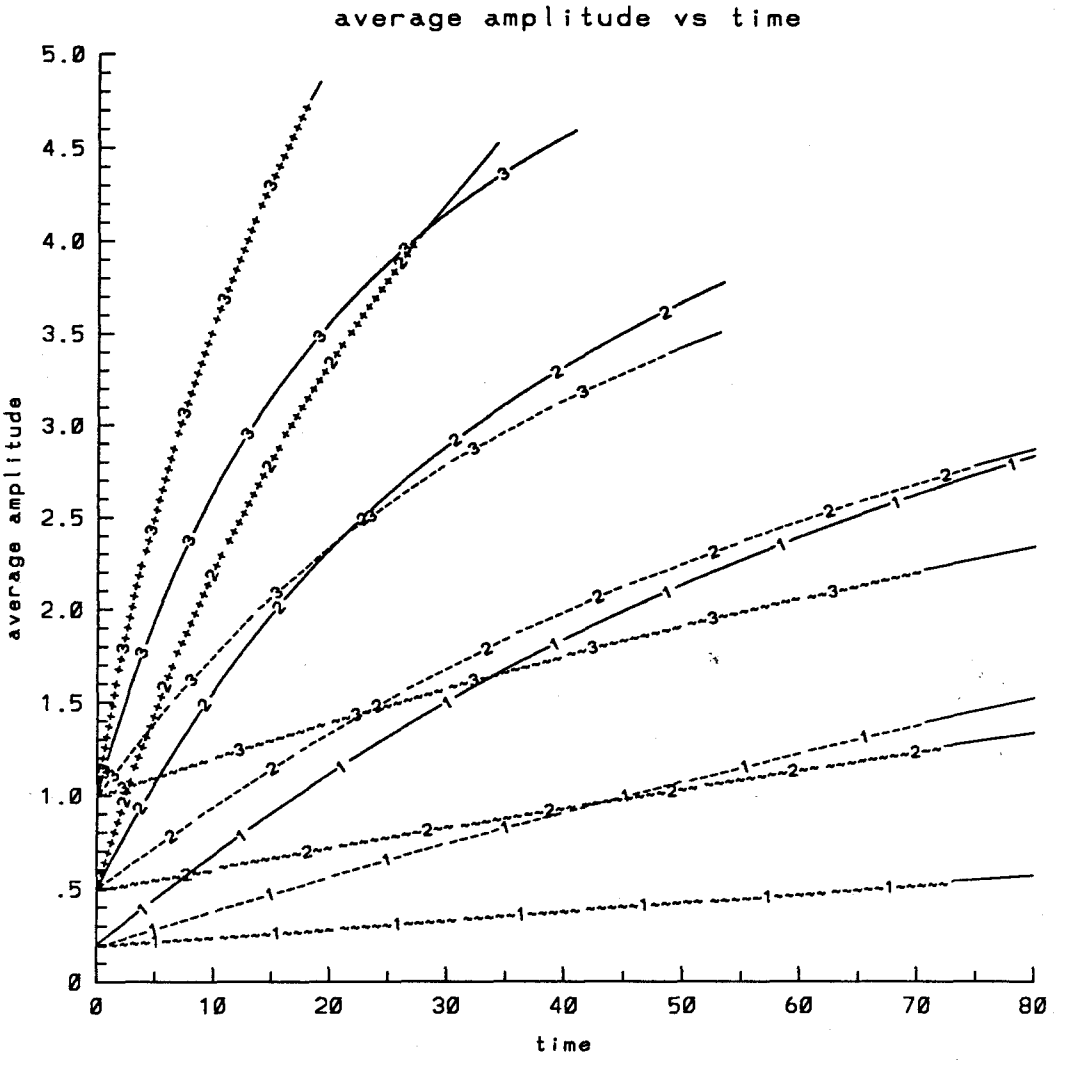

Figure 4.29.1 Combined time evolution of the average amplitude for the single scale problem L = 1.0: ~~~ A = − 0.05, − − − A = − 0.2, — A = − 0.5, +++ A = − 0.8. The numbers 1, 2, 3 on the curves refer to the values of $\epsilon = 0.2$, 0.5, and 1.0 respectively.

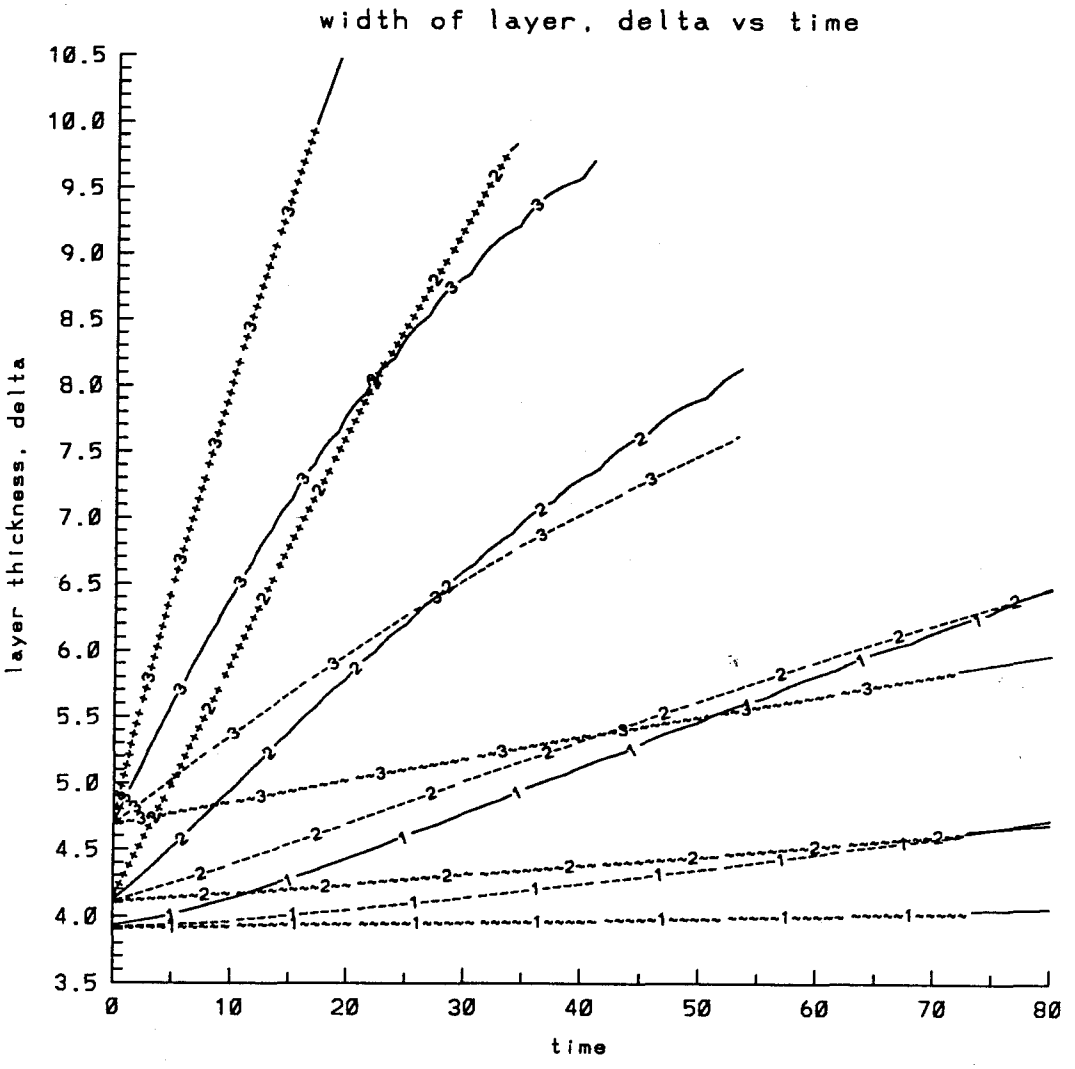

Figure 4.29.2 Time evolution of the width δ of the stratified layer for the single scale problem L = 1: ~~~ A = − 0.05, − − − A = − 0.2, — A = − 0.5, +++ A = − 0.8. The numbers 1, 2, 3 on the curves refer to the values of $\epsilon = 0.2$, 0.5, and 1.0 respectively.

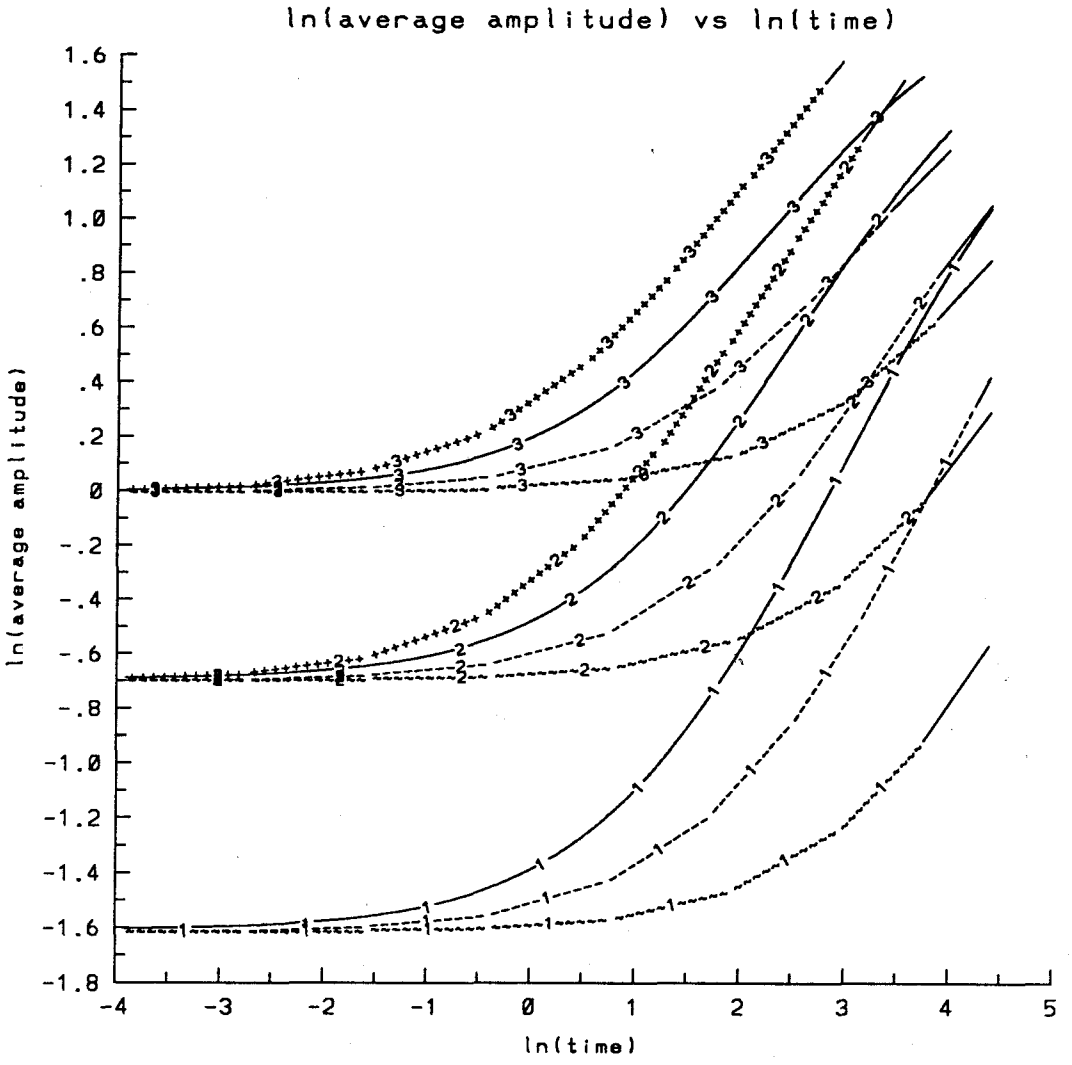

Figure 4.29.3 Combined results of ln(average amplitude) versus ln(time) for the single scale problem L = 1: ~~~ A = – 0.05, – – – A = – 0.2, — A = – 0.5, +++ A = – 0.8. The numbers 1, 2, 3 on the curves refer to the values of $\epsilon = 0.2$, 0.5, and 1.0 respectively.

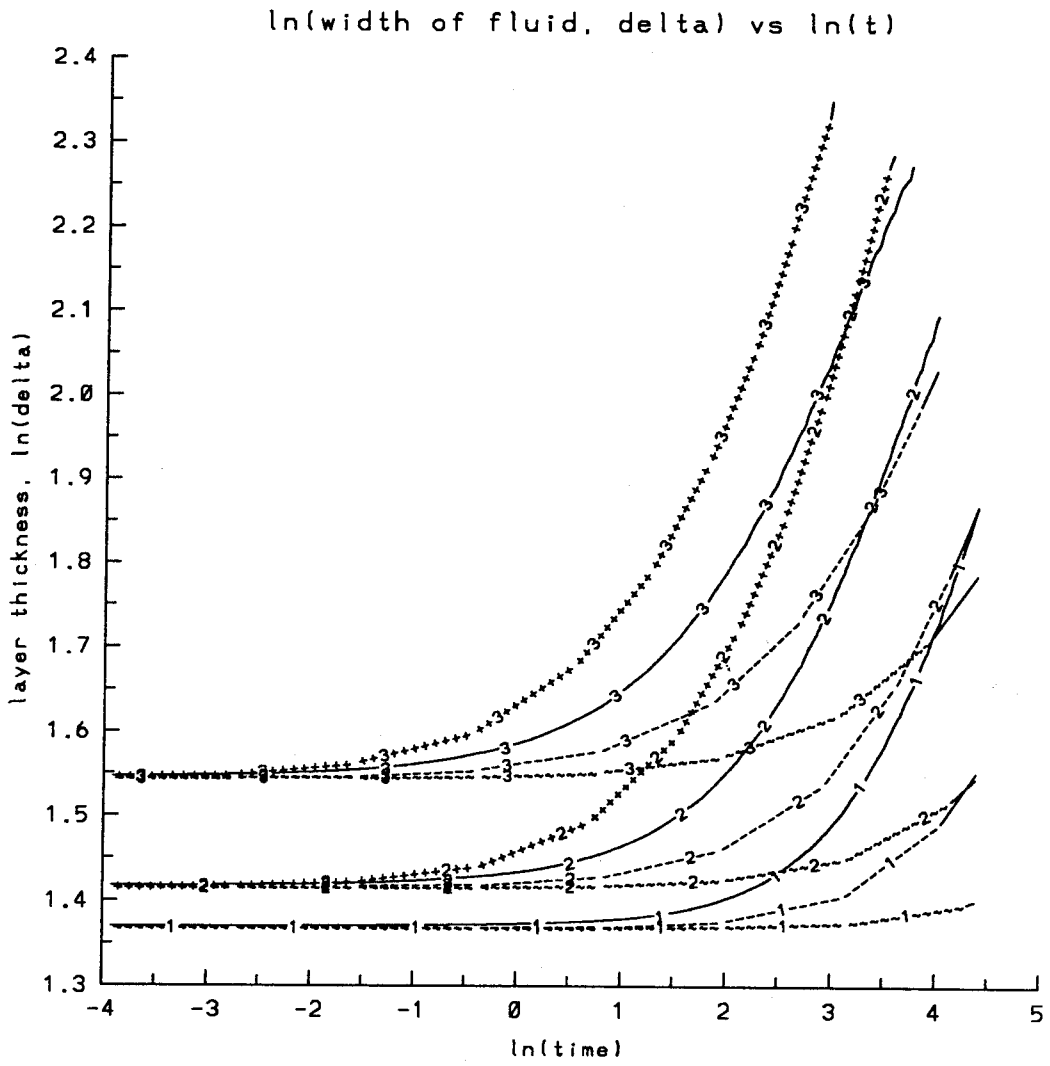

Figure 4.29.4 Combined results of ln(width of stratified layer δ) versus ln(time) for the single scale problem L = 1: ~~~ A = − 0.05, − − − A = − 0.2, — A = − 0.5, +++ A = − 0.8. The numbers 1, 2, 3 on the curves refer to the values of ϵ = 0.2, 0.5, and 1.0 respectively.

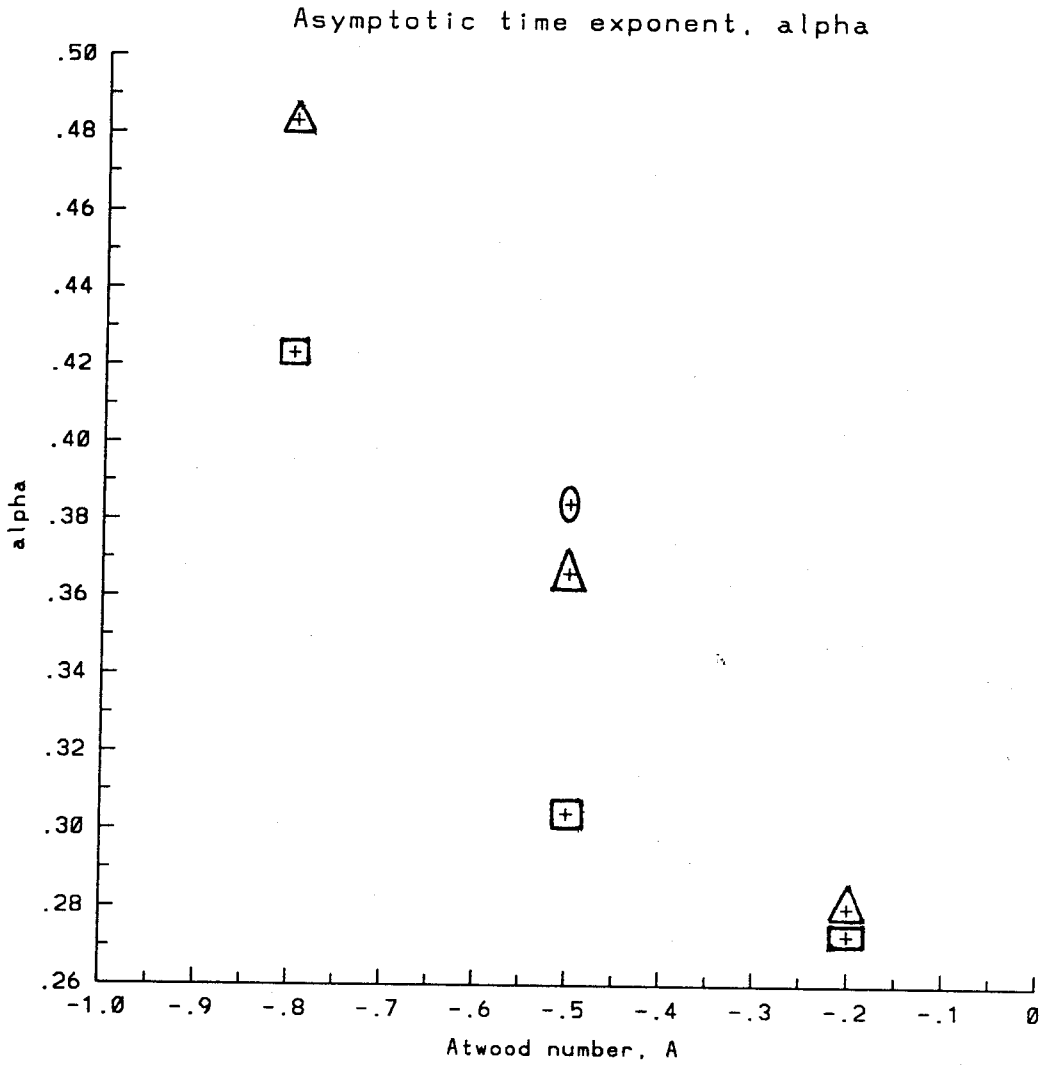

Figure 4.29.4a Asymptotic time exponent α for the growth of the width δ of the stratified layer in the single scale problem. The circles, the triangles, and the squares refer to the values of $\epsilon = 0.2$, 0.5, and 1.0 respectively.

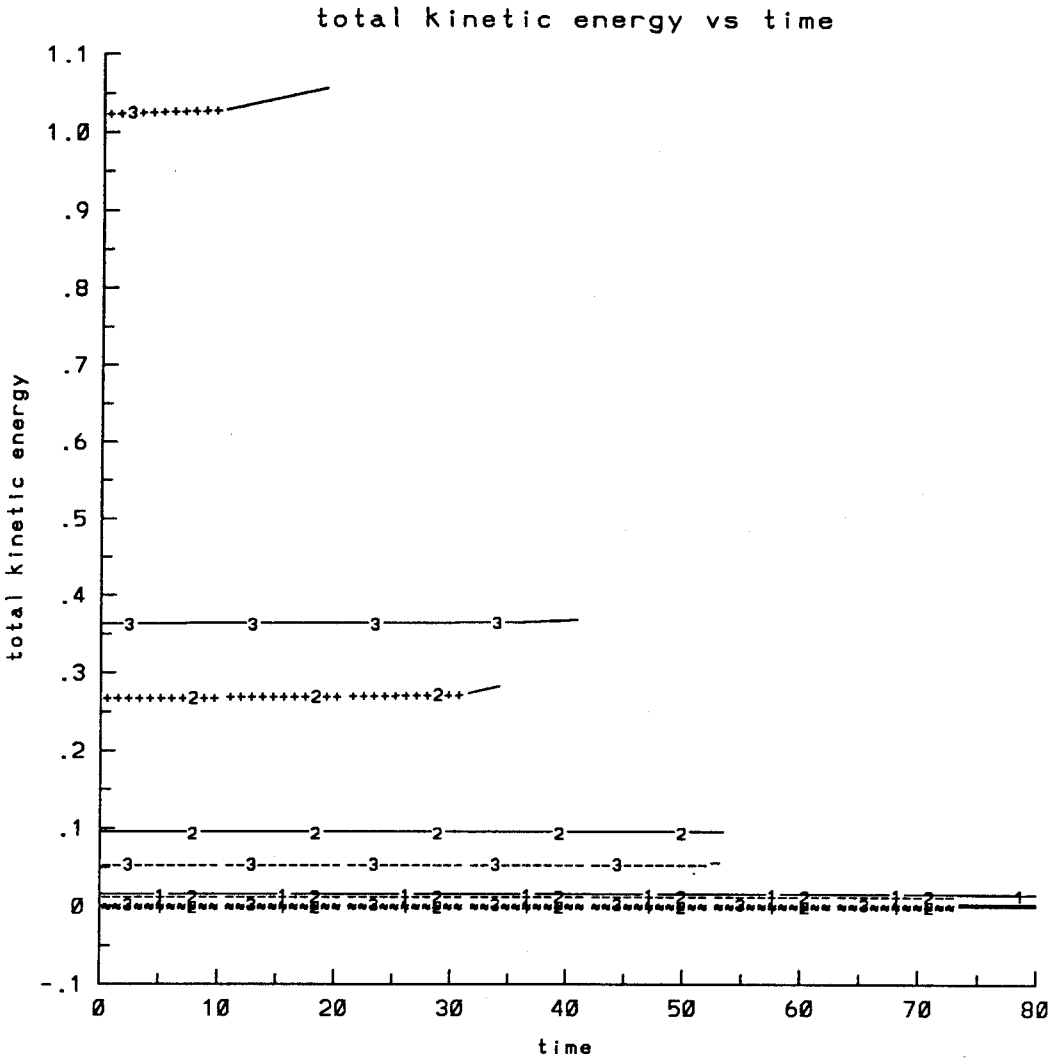

Figure 4.29.5 Time evolution of the total kinetic energy for the single scale problem L = 1: ~~~ A = − 0.05, − − − A = − 0.2, — A = − 0.5, +++ A = − 0.8. The numbers 1, 2, 3 on the curves refer to the values of $\epsilon = 0.2$, 0.5, and 1.0 respectively.

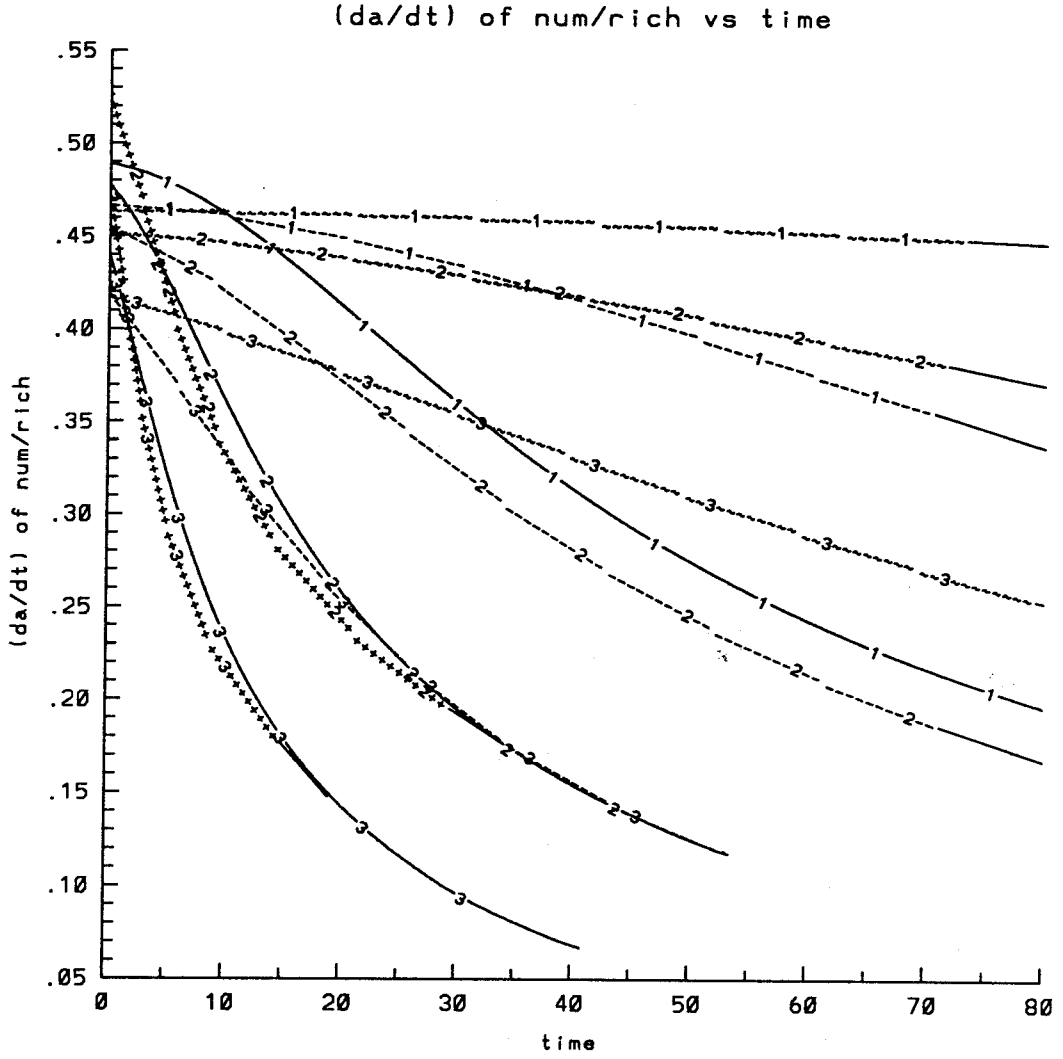

Figure 4.29.6 Time evolution of the ratio of the numerical growth rate over that of Richtmyer theory for the single scale problem L = 1: ~~~ A = – 0.05, – – – A = – 0.2, — A = – 0.5, +++ A = – 0.8. The numbers 1, 2, 3 on the curves refer to the values of $\epsilon = 0.2$, 0.5, and 1.0 respectively.

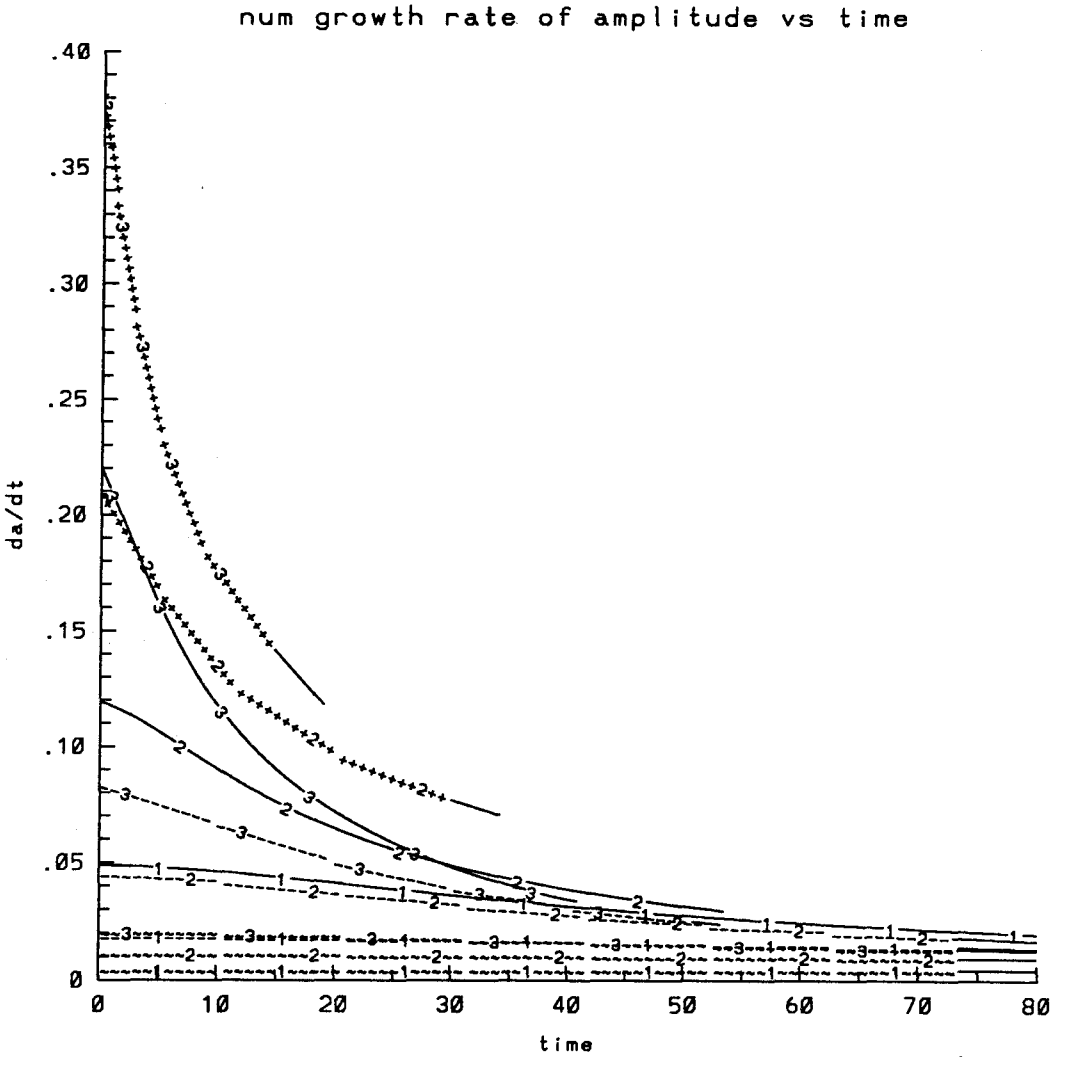

Figure 4.29.7 Time evolution of the numerical growth rate of the average amplitude (da/dt) for the single scale problem L = 1: ~~~ A = − 0.05, − − − A = − 0.2, — A = − 0.5, +++ A = − 0.8. The numbers 1, 2, 3 on the curves refer to the values of $\epsilon = 0.2$, 0.5, and 1.0 respectively.

To determine whether a universal power law in time exists for the average amplitude a and the width layer δ, we plot in Figures 4.15.2c,d–4.25c,d, and 4.29.3–4 $\ln(a)$, and $\ln(\delta)$ versus $\ln(t)$. From these Figures, we can conclude that there is no simple power law for the single scale problem. The time asymptotic limits of a and δ depend on both A and ϵ in some complicated way. In Figure 4.29.4a, we plot the asymptotic time exponent α in the asymptotic expression: $\delta \sim t^{\alpha}$ for the growth of the width δ of the stratified layer. Their values are given in Table 4.3. For a given ϵ, α is a decreasing function in the Atwood number. Similarly, for a given A, α decreases with the increase in ϵ.

Table 4.3

Asymptotic time exponent α in $\delta \sim t^{\alpha}$.

A $\Downarrow$ $\epsilon \Rightarrow$	0.2	0.5	1.0
−0.05			0.170
−0.2		0.280	0.273
−0.5	0.384	0.366	0.304
−0.8		0.483	0.423

4.5.3 Initial growth predicted by linear model

Since the instability is weak, it can be modeled by fixing the initial flow field after the impulsive acceleration, and let the flow evolve as discussed in section 4.3. Using this model, we obtain the solution for case 1 of L = 1.0, A = −0.5, ϵ = 0.5, and case 2 of L = 1.0, A = 0.8, ϵ = 1.0 as shown respectively in Figures 4.30 and 4.31. The model accurately describes the growth of the layer at early times. For example, up to time t = 15 for case 1, the differences in the average amplitude a, and the width layer δ relative to the actual calculation are small, 4.43%, and 0.62% respectively. This agreement corresponds to travel of the layer over a distance comparable to $2\frac{1}{2}$ to 3 layer widths. At lower Atwood ratio, this agreement extends for even longer times. For case 2, the reversal of phase is in very good agreement

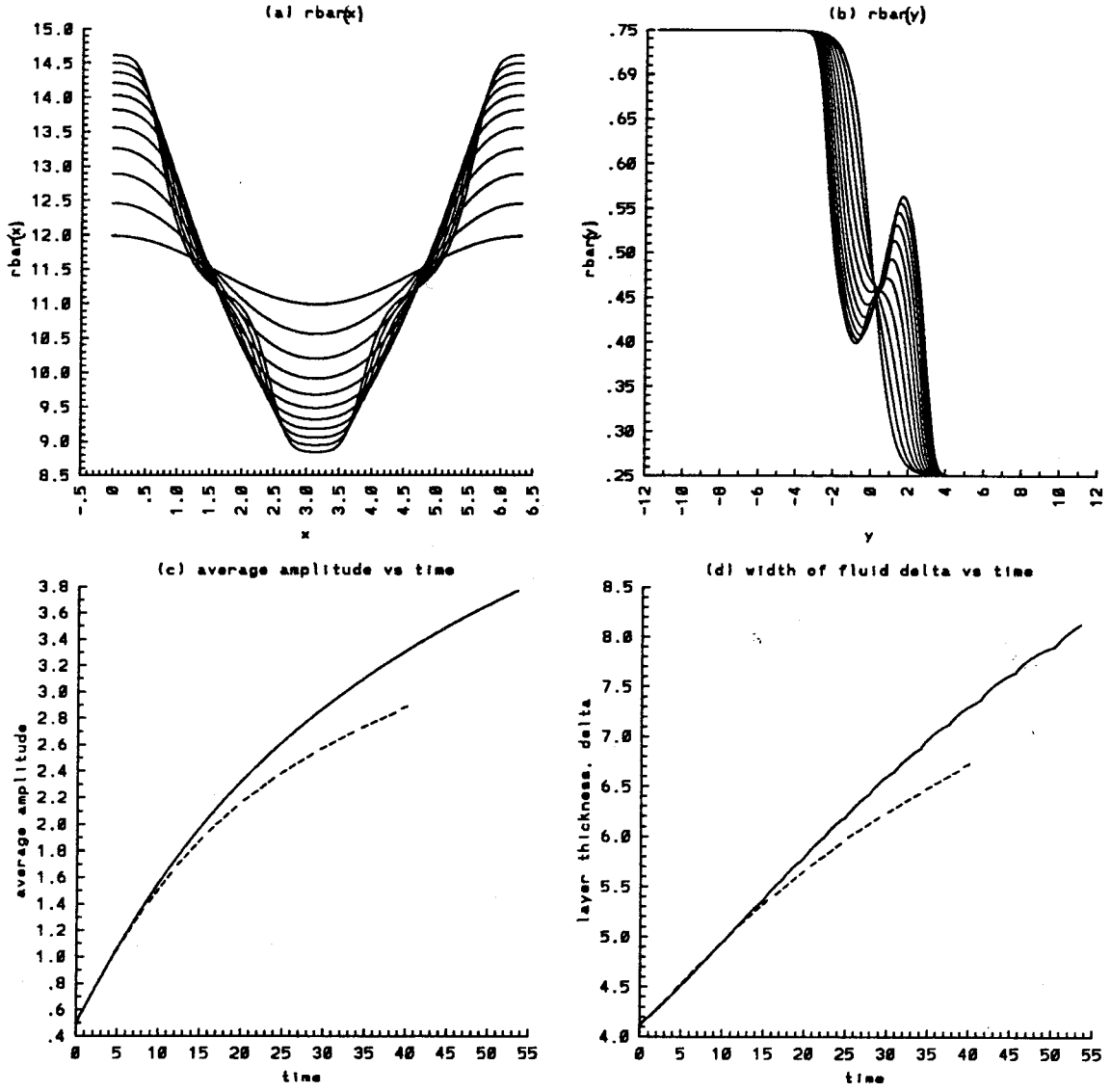

Figure 4.30.1 Time evolution of the average quantities for the single scale profile L = 1.0, A = −0.5, $\epsilon = 0.5$, $t = 0$ to 40 using the linear model : a) $\bar{\rho}_y(x)$, b) $\bar{\rho}_x(y)$. Combined results — numerical simulation, – – – linear model c) average amplitude, and d) width of the density layer.

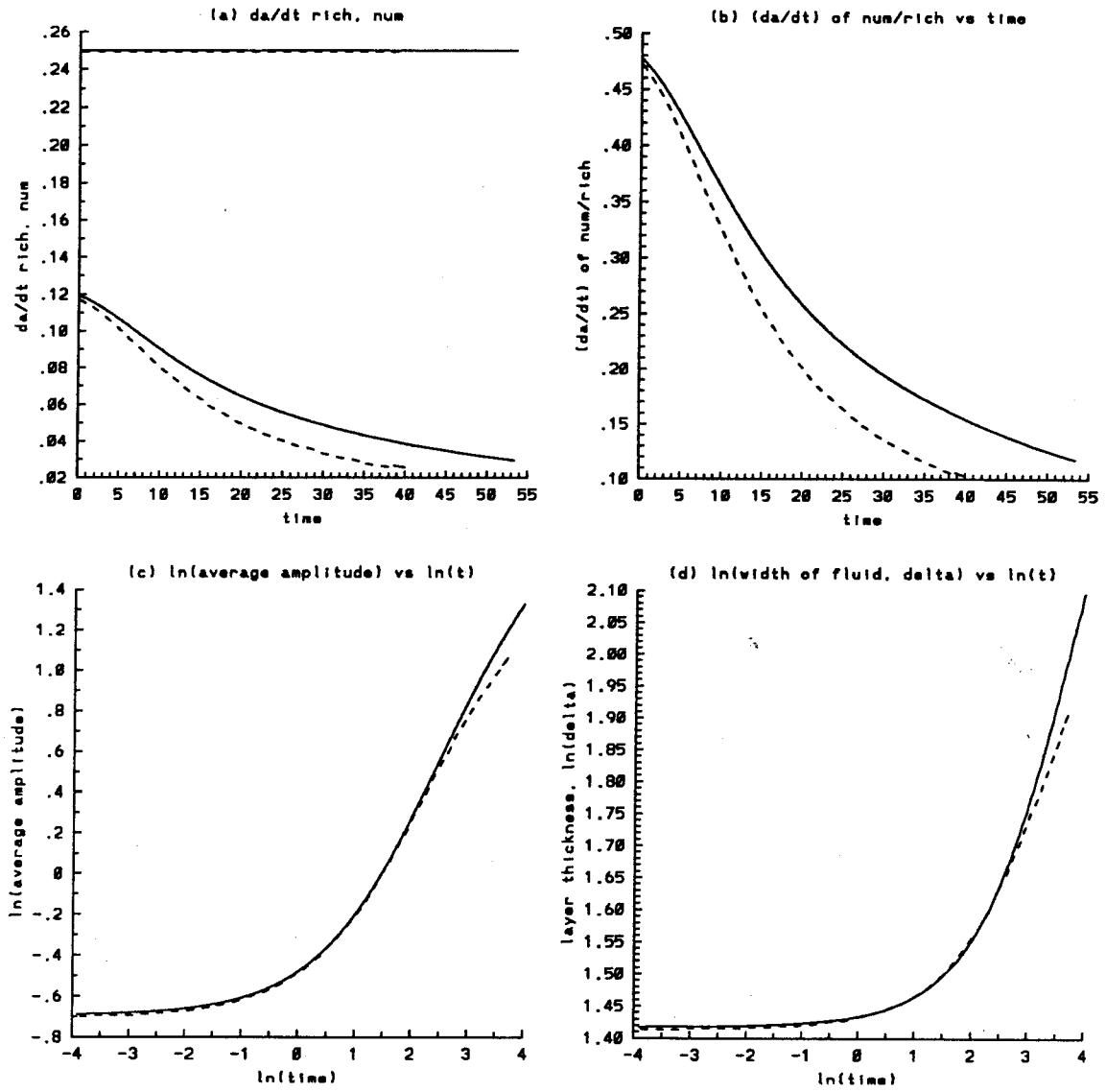

Figure 4.30.2 Time evolution of the average quantities for the single scale profile L = 1.0, A = −0.5, $\epsilon = 0.5$, $t = 0$ to 40. Combined results — numerical simulation, – – – linear model : a) growth rate da/dt of the average amplitude, numerical and Richtmyer theory (straight line), b) the ratio of the numerical growth rate da/dt over that predicted by Richtmyer theory, c) $\ln(a)$ *vs* $\ln(t)$, d) $\ln(\delta)$ *vs* $\ln(t)$.

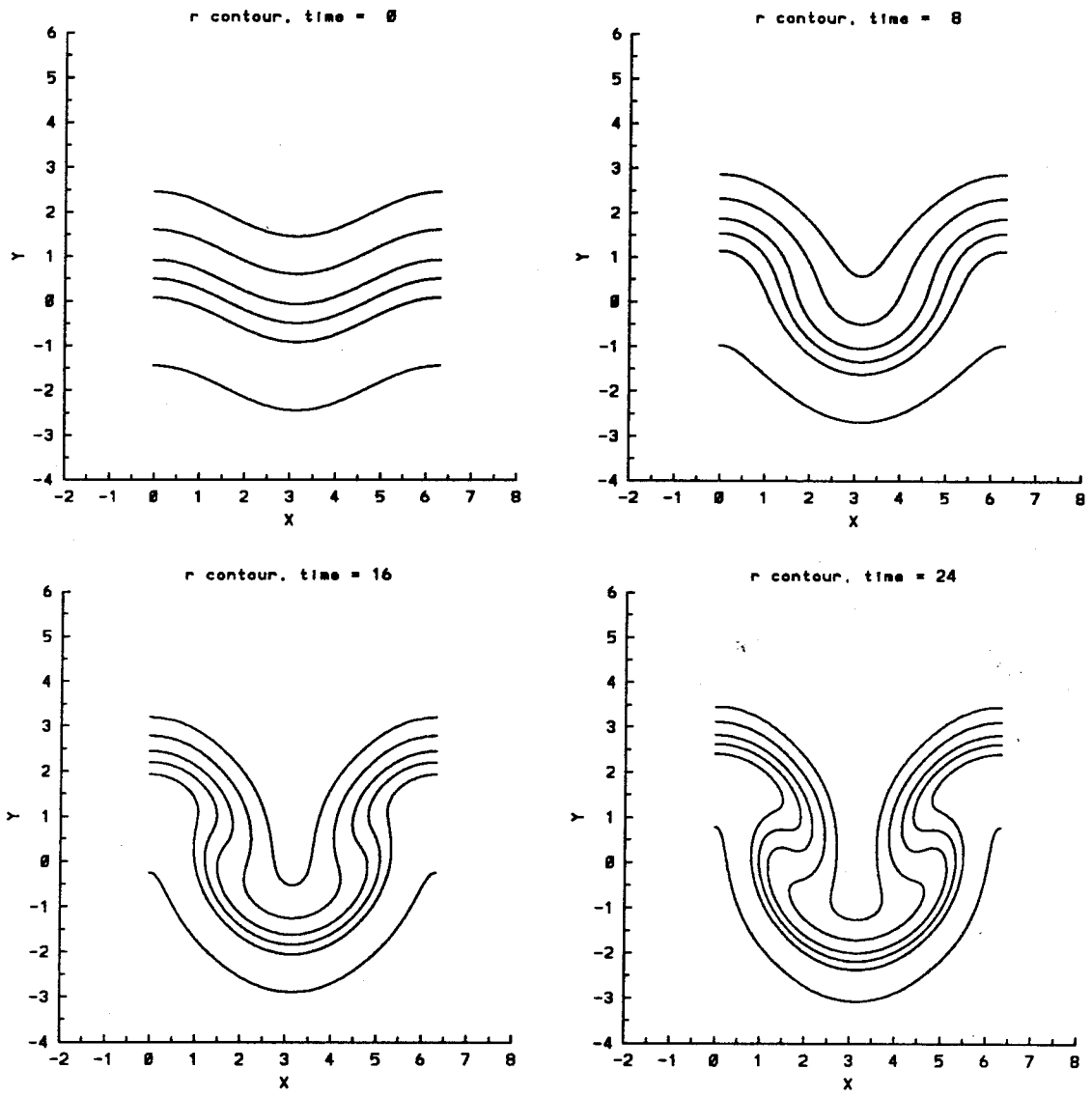

Figure 4.30.3 Time evolution of the density contours for the single scale profile L = 1.0, A = −0.5, $\epsilon = 0.5$, $t = 0$, 8, 16, 24 using the linear model. The contours are at $\rho = 0.26$, 0.3, 0.4, 0.5, 0.6, 0.74 in that order from top to bottom of each figure.

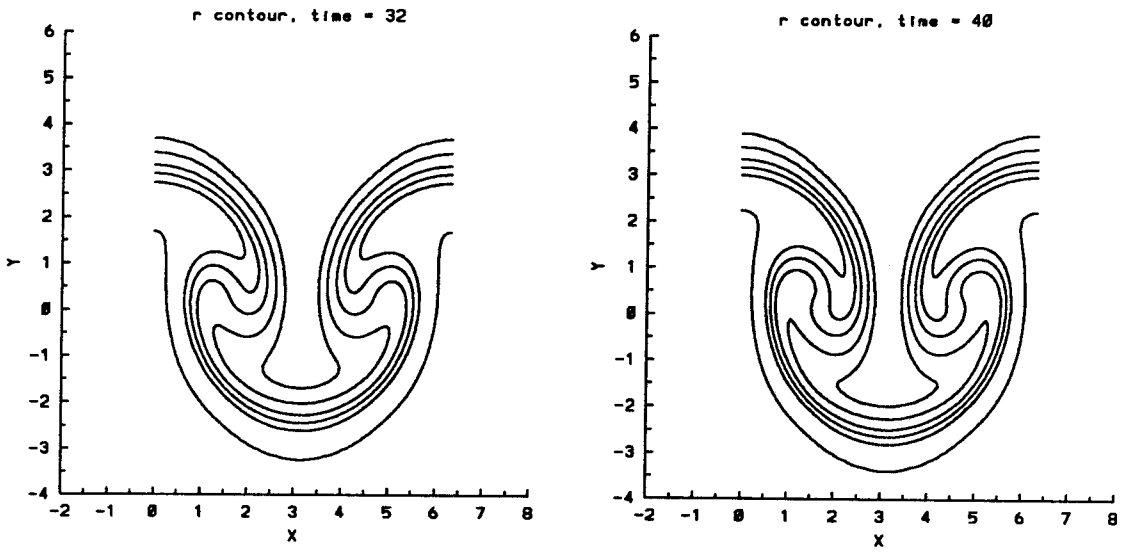

Figure 4.30.4 Time evolution of the density contours for the single scale profile L = 1.0, A = −0.5, $\epsilon = 0.5$, $t = 32$, 40 using the linear model. The contours are at $\rho = 0.26$, 0.3, 0.4, 0.5, 0.6, 0.74 in that order from top to bottom of each figure.

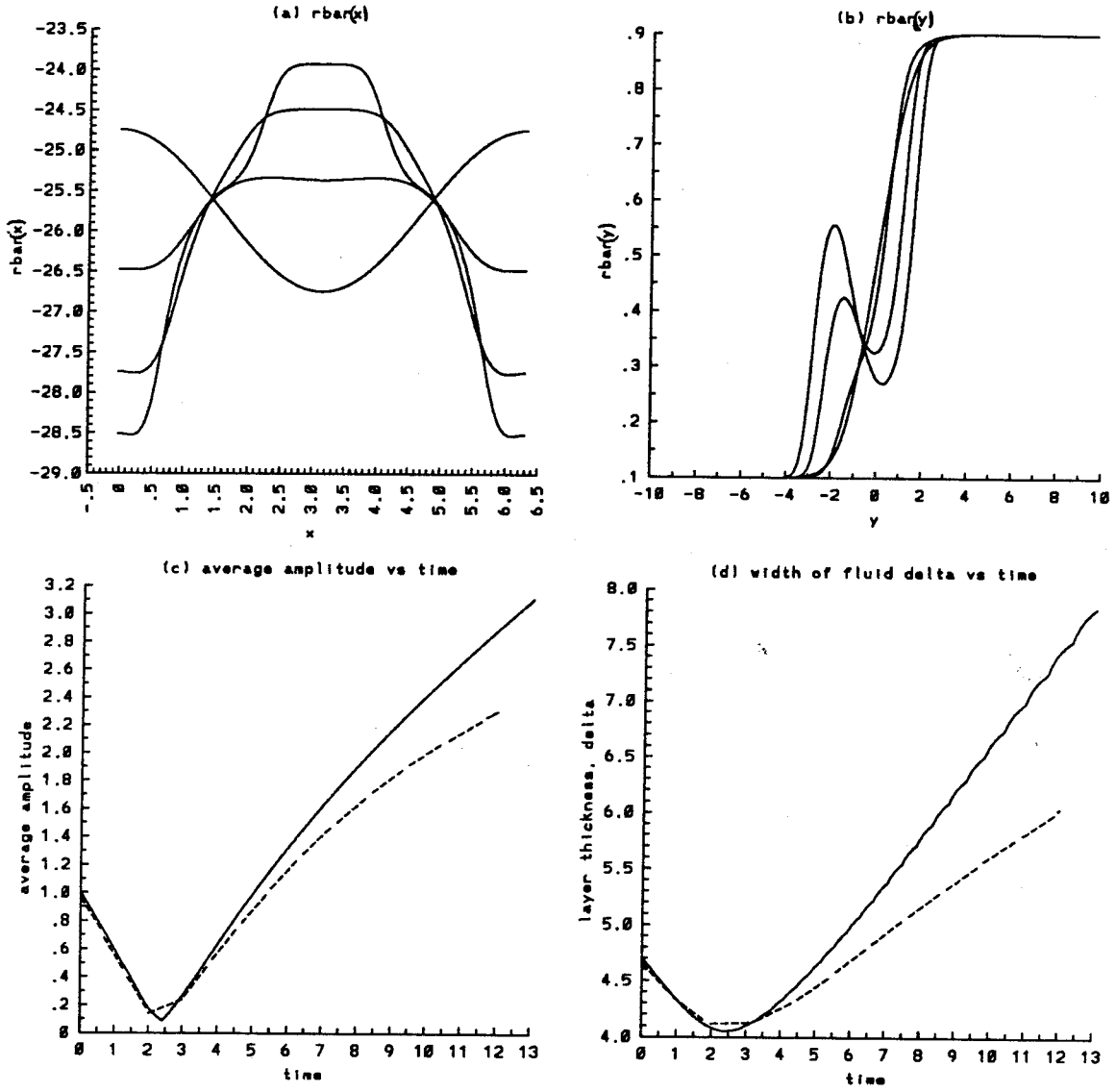

Figure 4.31.1 Time evolution of the average quantities for the single scale profile L = 1.0, A = 0.8, ϵ = 1.0, t = 0 to 12 using the linear model : a) $\bar{\rho}_y(x)$, b) $\bar{\rho}_x(y)$. Combined results — numerical simulation, – – – linear model c) average amplitude, and d) width of the density layer.

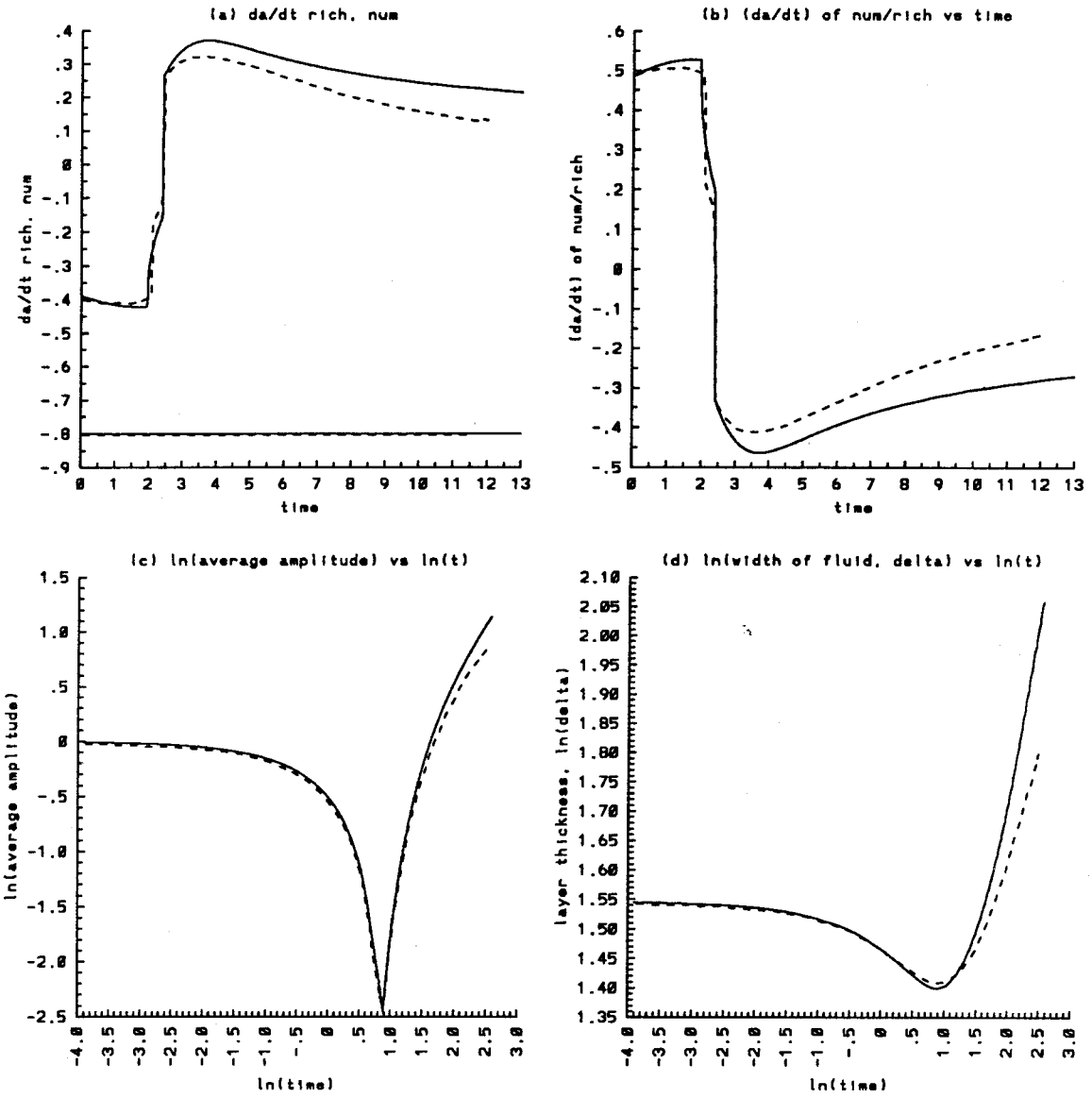

Figure 4.31.2 Time evolution of the average quantities for the single scale profile L = 1.0, A = 0.8, $\epsilon = 1.0$, $t = 0$ to 12. Combined results — numerical simulation, – – – linear model : a) growth rate da/dt of the average amplitude, numerical and Richtmyer theory (straight line), b) the ratio of the numerical growth rate da/dt over that predicted by Richtmyer theory, c) $\ln(a)$ *vs* $\ln(t)$, d) $\ln(\delta)$ *vs* $\ln(t)$.

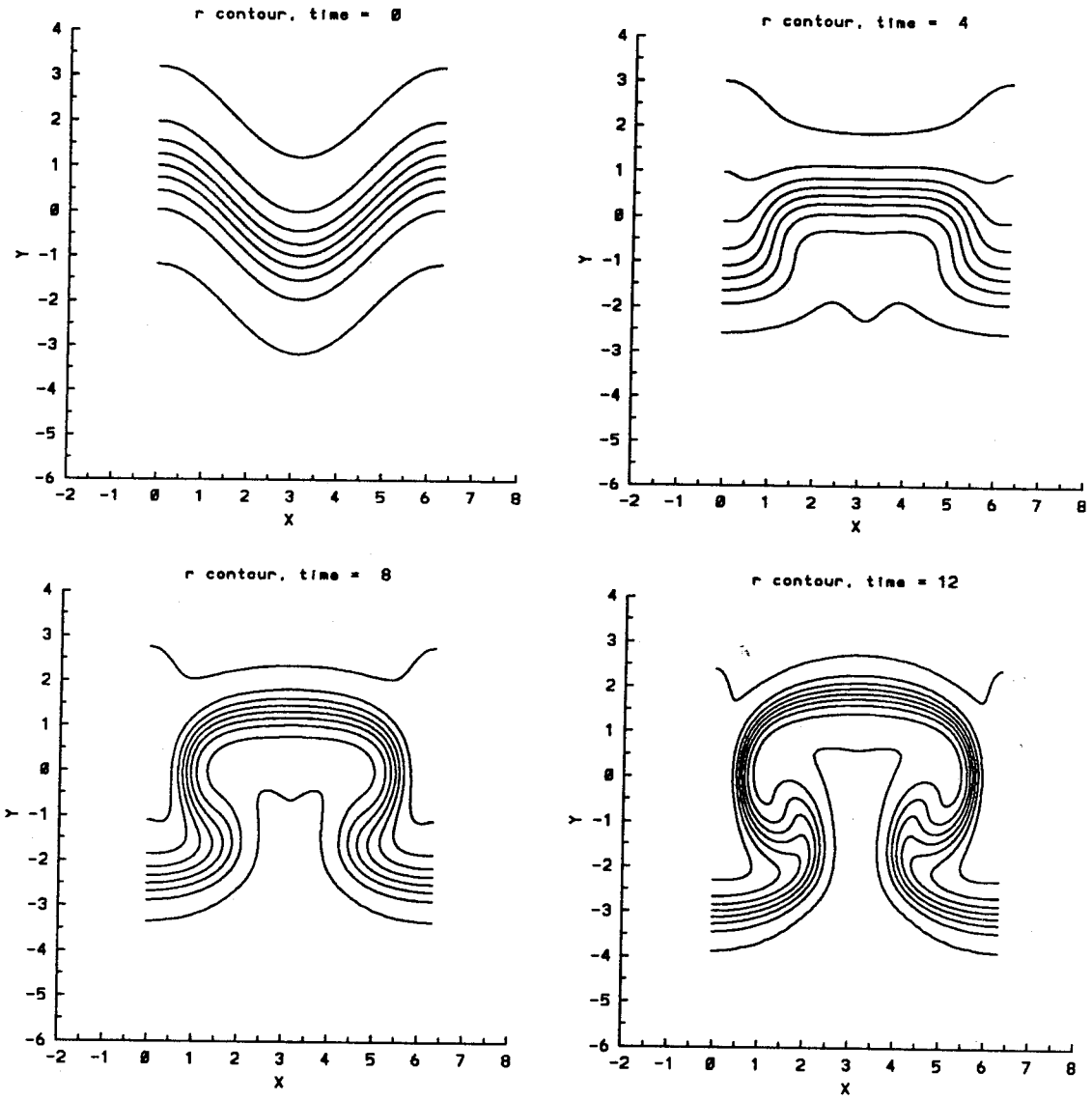

Figure 4.31.3 Time evolution of the density contours for the single scale profile L = 1.0, A = 0.8, $\epsilon = 1.0$, $t = 0$, 4, 8, 12 using the linear model. The contours are at $\rho = 0.11$, 0.2, 0.3, 0.4, 0.5, 0.6, 0.7, 0.8, 0.89 in that order from bottom to top of each figure.

with the actual flow as seen in the plots of a and δ shown in Figures 4.31.1c,d. For both cases, at late times, the model predicts a growth slower than the actual calculation. The roll-up is more compact and symmetric for the linear case. This results in a more symmetric form for the average quantities $\bar{\rho}_x(y)$. The widening of the light fluid globule is not seen and thus a sharper lower peak of $\bar{\rho}_y(x)$ is observed.

In conclusion, the single scale problem has been studied for a wide range of the Atwood numbers A, and the perturbation amplitudes ϵ. We have learned that the nonlinear effect causes a roll-up of the interface which reduces the growth of the whole layer, and increases the internal mixing. The instability is driven by the induced flow due to the interaction of the two initially imposed vortex rolls, and grows faster as A and ϵ increase. For all cases considered in this section, the initial growth rates are around half of that predicted by Richtmyer theory. In addition, there is no simple power law governing the long time asymptotic limit of the average amplitude a, and the width of the stratified layer δ.

4.6 Instability of the multiple scale problem

The simplicity of the single scale problem offers us an understanding of the basic physical mechanism underlying the instability. In most experimental studies, and realistic applications, however, the interface is composed of many random modes of perturbation. In this section, we study the instability of a continuous interface having a random initial density distribution as given in equations (4.5) to (4.7) with L = 1.0, and $\epsilon = 0.2$. We consider six different initial profiles. The first four profiles are based on equations (4.5) and (4.6), and the fifth and the sixth are based on equations (4.5) and (4.7). In Table A-1 (see Appendix), we list four sets of random numbers r_{k1} used for the first four initial profiles. For the fifth profile, we use r_{k1} listed in the second column of Table A-1 as our r_{k2}. Similarly, for the sixth profile, r_{k2} is the same as r_{k1} listed in the third column of Table A-1. We use up to 120 modes, *i.e.*, N = 120, and choose ς to be 0.01. It should be noted

that ς is a controlling parameter for the distribution of the wavenumbers. Since the calculations are carried out using double precision, *i.e.*, 16 significant digits, with this value of ς, the wavenumbers bigger than 61 will only effect the last significant figures. For all cases in this study, we use a 151 by 100 grid. Hence, up to mode 61 which already has very small amplitude $O(10^{-16})$, we have at least two grid points per wavelength. The flow field is therefore reasonably resolved.

Table 4.4

Parameters for the first four multiple scale problem.

A	1*st* profile	2*nd* profile	3*rd* profile	4*th* profile
−0.05	80 8.67×10^{-11} 3.20×10^{-6} 4.32	80 9.07×10^{-11} 2.38×10^{-6} 4.33	80 9.09×10^{-11} 2.15×10^{-6} 4.34	80 9.28×10^{-11} 2.15×10^{-6} 4.35
−0.2	71.46 1.01×10^{-10} 3.44×10^{-7} 4.36 1	89.34 9.98×10^{-11} 3.92×10^{-7} 4.37	80 3.98×10^{-10} 3.44×10^{-7} 4.38	80 1.35×10^{-10} 3.61×10^{-7} 4.39
−0.5	40 2.06×10^{-7} 9.57×10^{-5} 4.40 1	56 7.64×10^{-8} 1.79×10^{-4} 4.41 3-D	41 4.46×10^{-6} 8.52×10^{-4} 4.42	44 4.88×10^{-7} 4.06×10^{-4} 4.43
−0.8	14 1.07×10^{-6} 3.27×10^{-3} 4.44 1, ω	17 2.07×10^{-6} 2.10×10^{-3} 4.45	16 1.16×10^{-6} 6.42×10^{-3} 4.46	17 2.00×10^{-6} 2.97×10^{-3} 4.47

In Table 4.4, and 4.5, we summarize some general information regarding the multiple scale problem. The arrangement of the table is similar to that described in Table 4.2 for the single scale problem except for the information concerning the grid size. In the following sections, we will consider the general structure of

Table 4.5

Parameters for the fifth and sixth initial profiles.

A	$5th$ profile	$6th$ profile
−0.2	75.4 3.98×10^{-10} 2.52×10^{-6} 4.48 ω, 3-D	
−0.8	9 4.08×10^{-7} 3.43×10^{-4} 4.49 ω	9 1.54×10^{-7} 6.68×10^{-5} 4.50 ω

the instability, the overall growth of the stratified layer, and the initial growth of instability as predicted from linear theory model.

4.6.1 General structure of the instability

For A = −0.05, as shown in Figures 4.32 to 4.35, the growth of the peaks of the density layer is weakly dependent on each other, as seen in the average $\bar{\rho}_y(x)$ and the density contours. The speed of each peak on average as shown in plot for $\bar{\rho}_y(x)$ depends on the initial amplitude. The larger the amplitudes, the faster the peaks grow. The growth seems to be strongest in the middle of the layer, and decreases in the strength as the upper and lower boundaries of the layer are approached. A possible explanation for this behavior is that since on average, the density varies as a hyperbolic tangent in the y-direction, the density gradient is maximum in the middle of the layer. From these observations, we can possibly conclude that the instability is in the linear regime, and there is little interaction between the different peaks. There is essentially no change in the average $\bar{\rho}_x(y)$. The growth rates da/dt decrease slowly, and there is very small change in the width δ of the stratified layer as shown in the combined plot 4.52.2. A discontinuity in the plot of da/dt for the

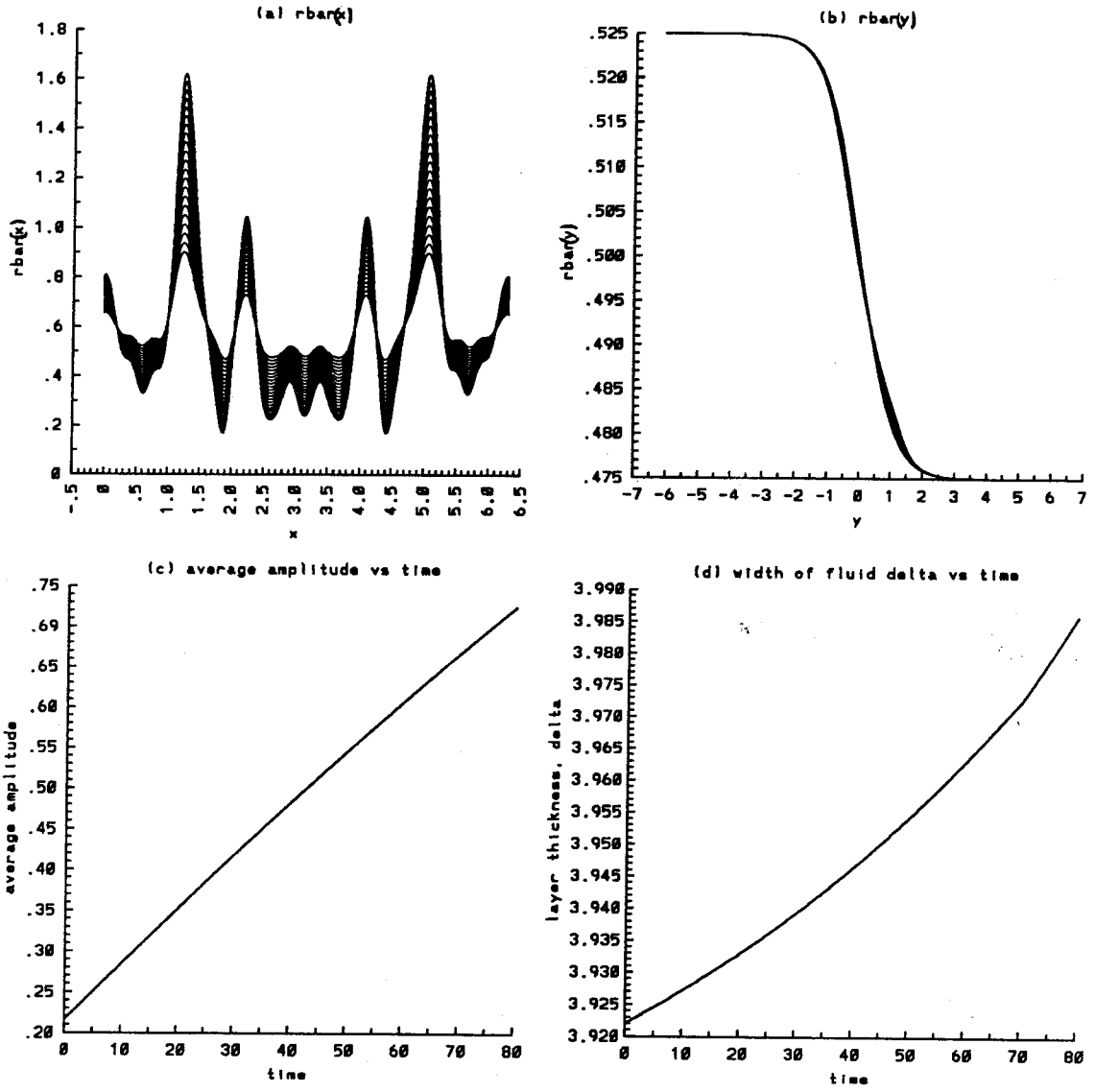

Figure 4.32.1 Time evolution of the average quantities for the first initial random profile, A = -0.05, $t = 0$ to 80 : a) $\bar{\rho}_y(x)$, b) $\bar{\rho}_x(y)$, c) average amplitude, and d) width of the density layer.

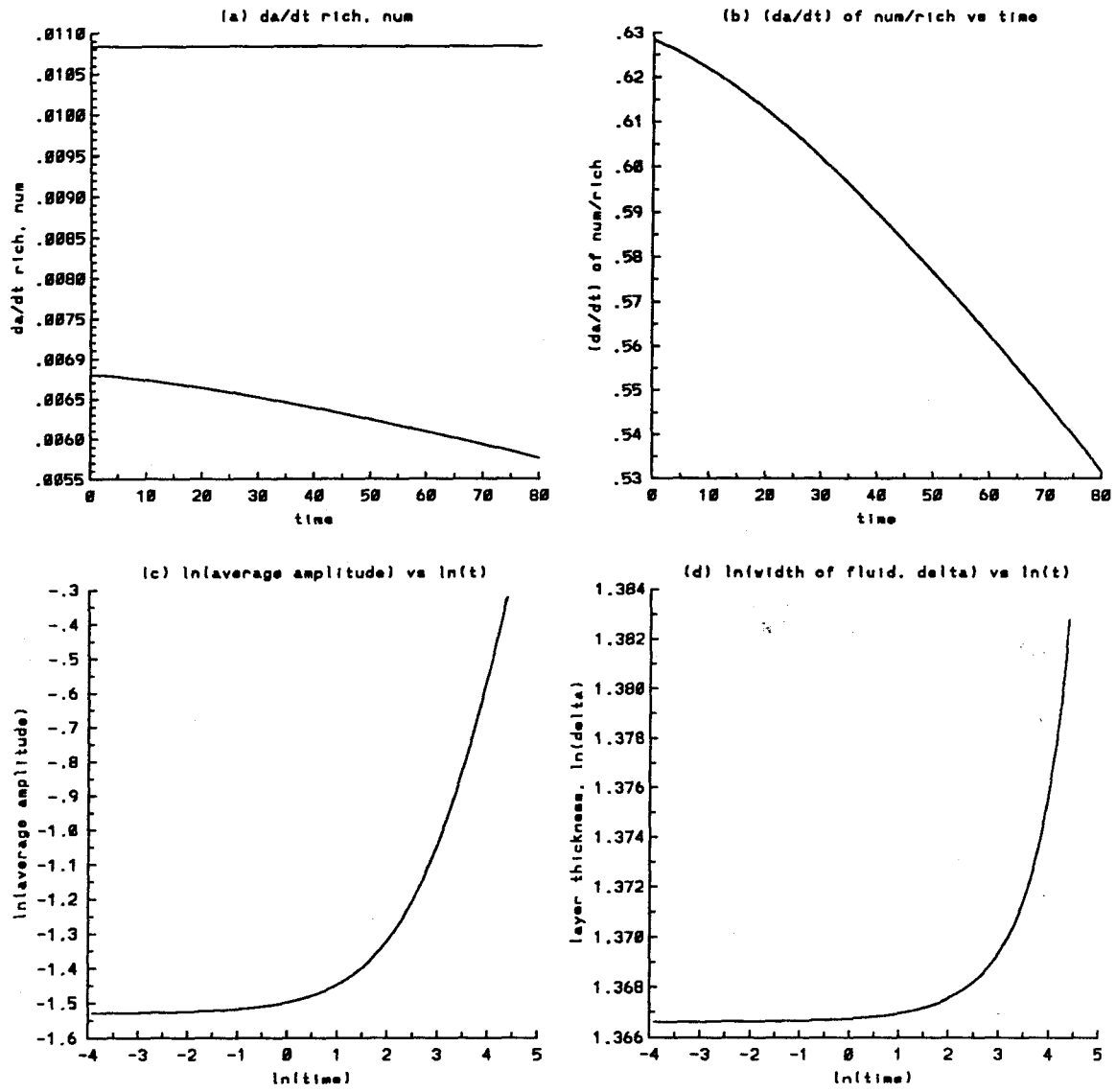

Figure 4.32.2 Time evolution of the average quantities for the first initial random profile, A = −0.05, t = 0 to 80 : a) growth rate da/dt of the average amplitude, numerical and Richtmyer theory (straight line), b) the ratio of the numerical growth rate da/dt over that predicted by Richtmyer theory, c) $\ln(a)$ *vs* $\ln(t)$, d) $\ln(\delta)$ *vs* $\ln(t)$.

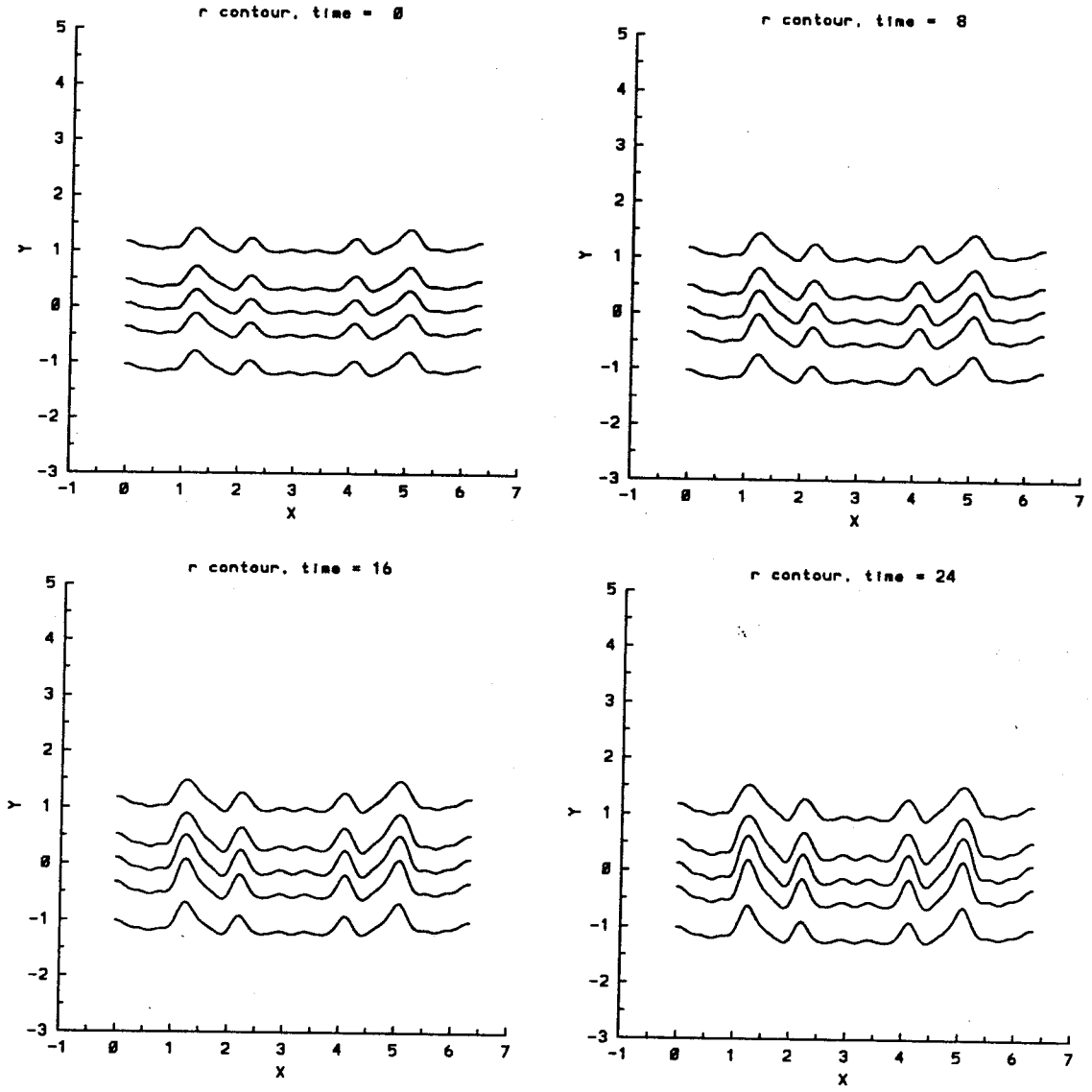

Figure 4.32.3 Time evolution of the density contours for the first initial random profile, A = −0.05, t = 0, 8, 16, 24. The contours are at ρ = 0.48, 0.49, 0.50, 0.51, 0.52.

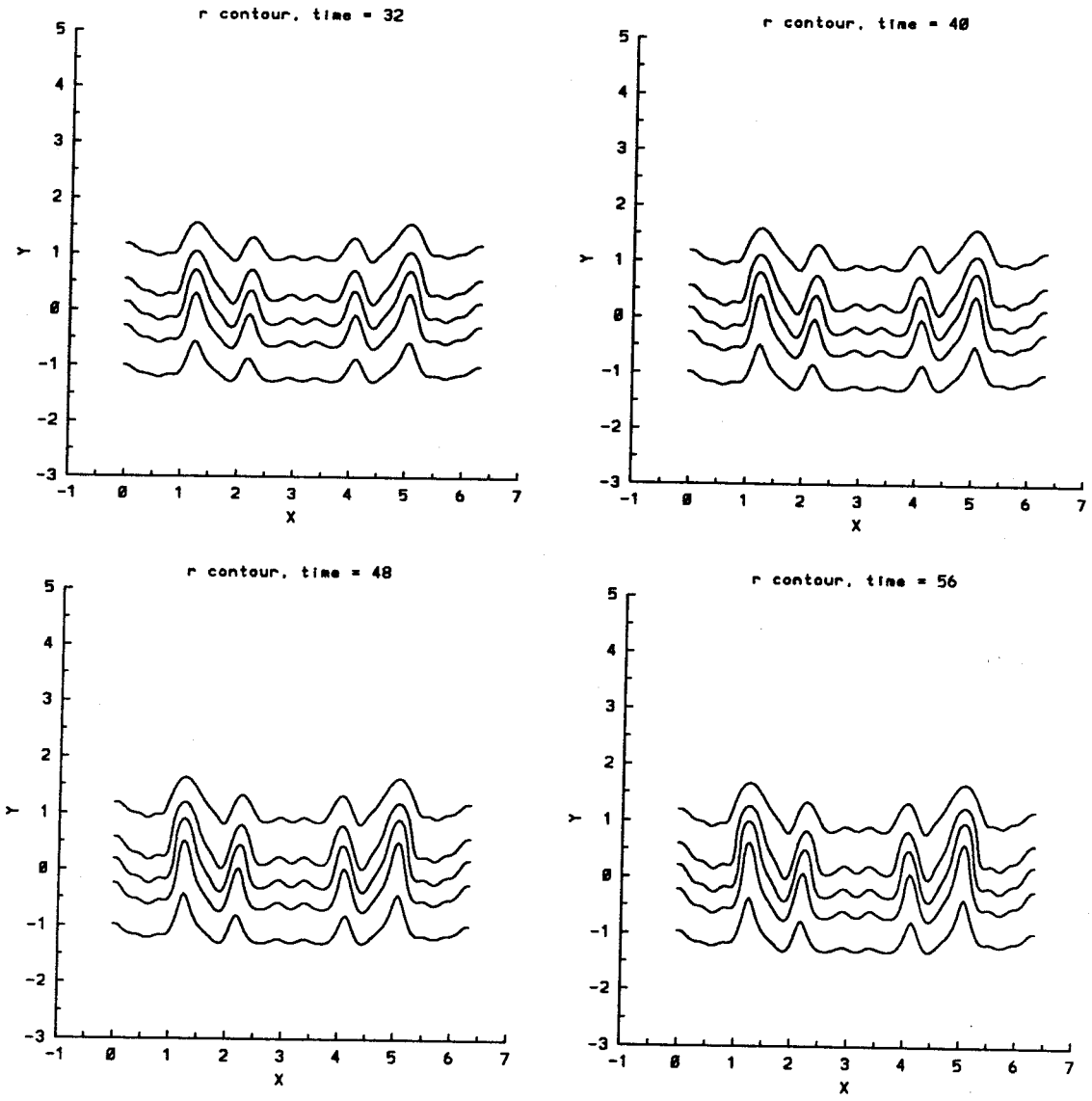

Figure 4.32.4 Time evolution of the density contours for the first initial random profile, A = −0.05, t = 32, 40, 48, 56. The contours are at ρ = 0.48, 0.49, 0.50, 0.51, 0.52.

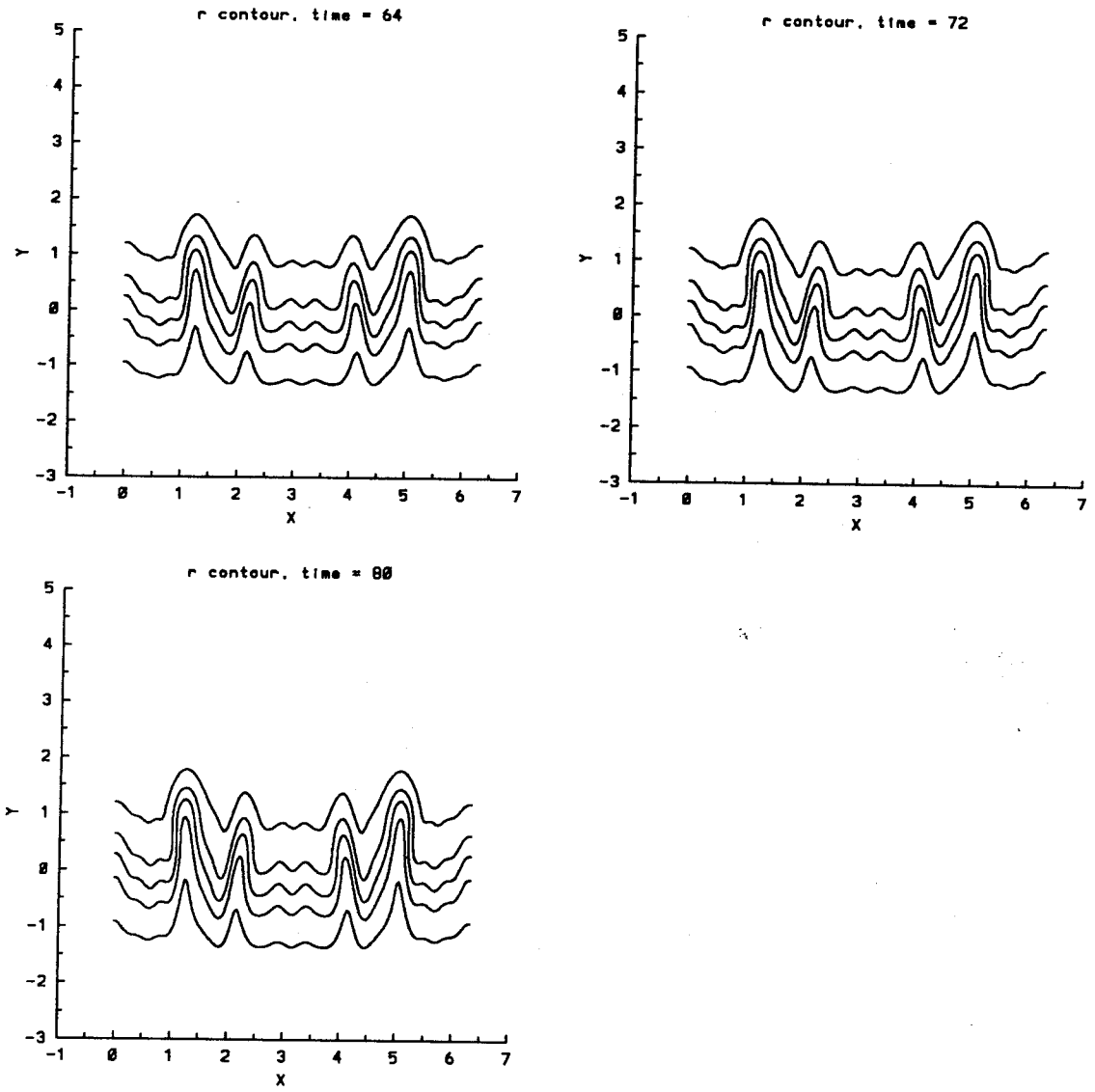

Figure 4.32.5 Time evolution of the density contours for the first initial random profile, A = -0.05, t = 64, 72, 80. The contours are at ρ = 0.48, 0.49, 0.50, 0.51, 0.52.

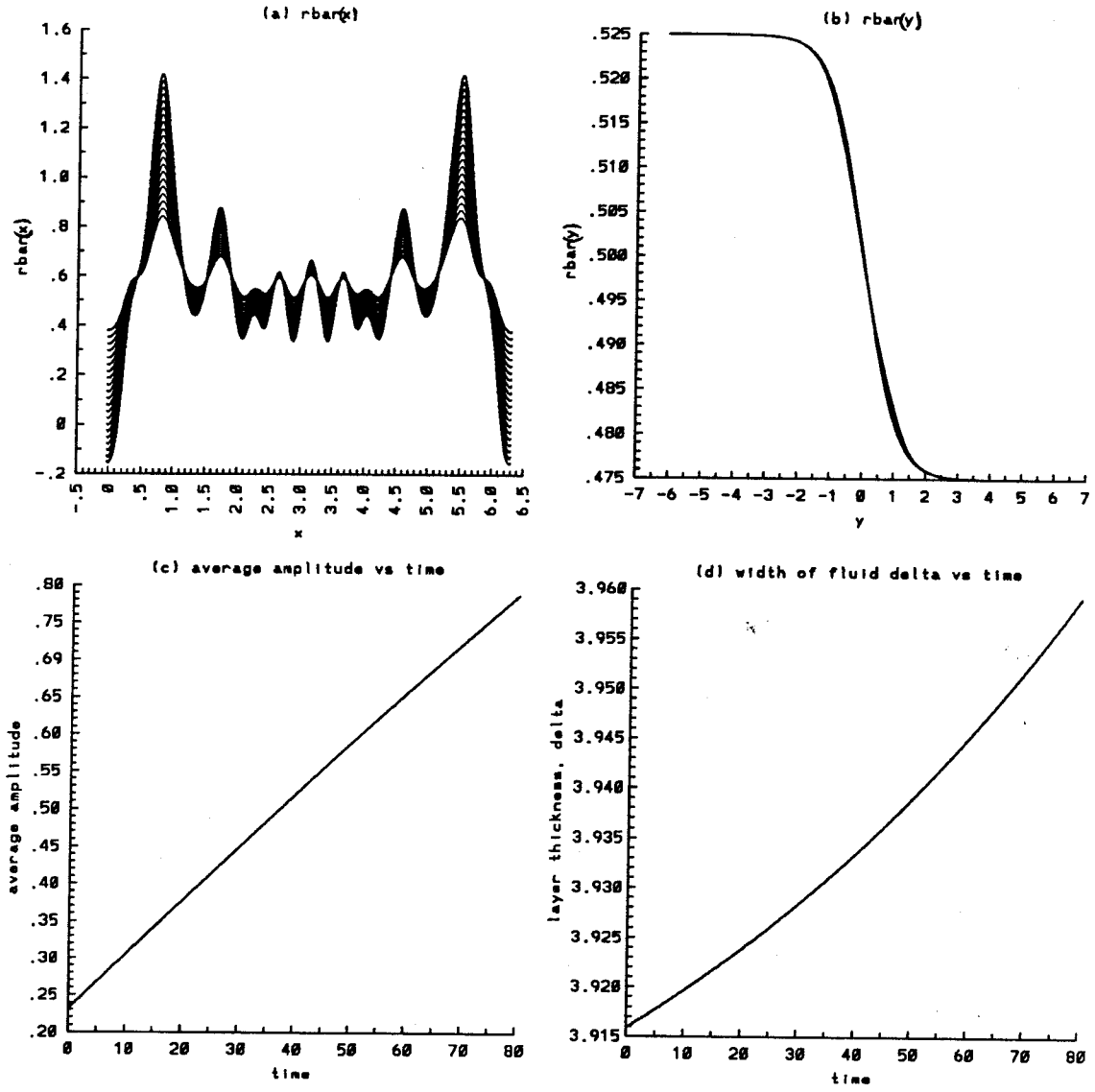

Figure 4.33.1 Time evolution of the average quantities for the second initial random profile, A = -0.05, $t = 0$ to 80 : a) $\bar{\rho}_y(x)$, b) $\bar{\rho}_x(y)$, c) average amplitude, and d) width of the density layer.

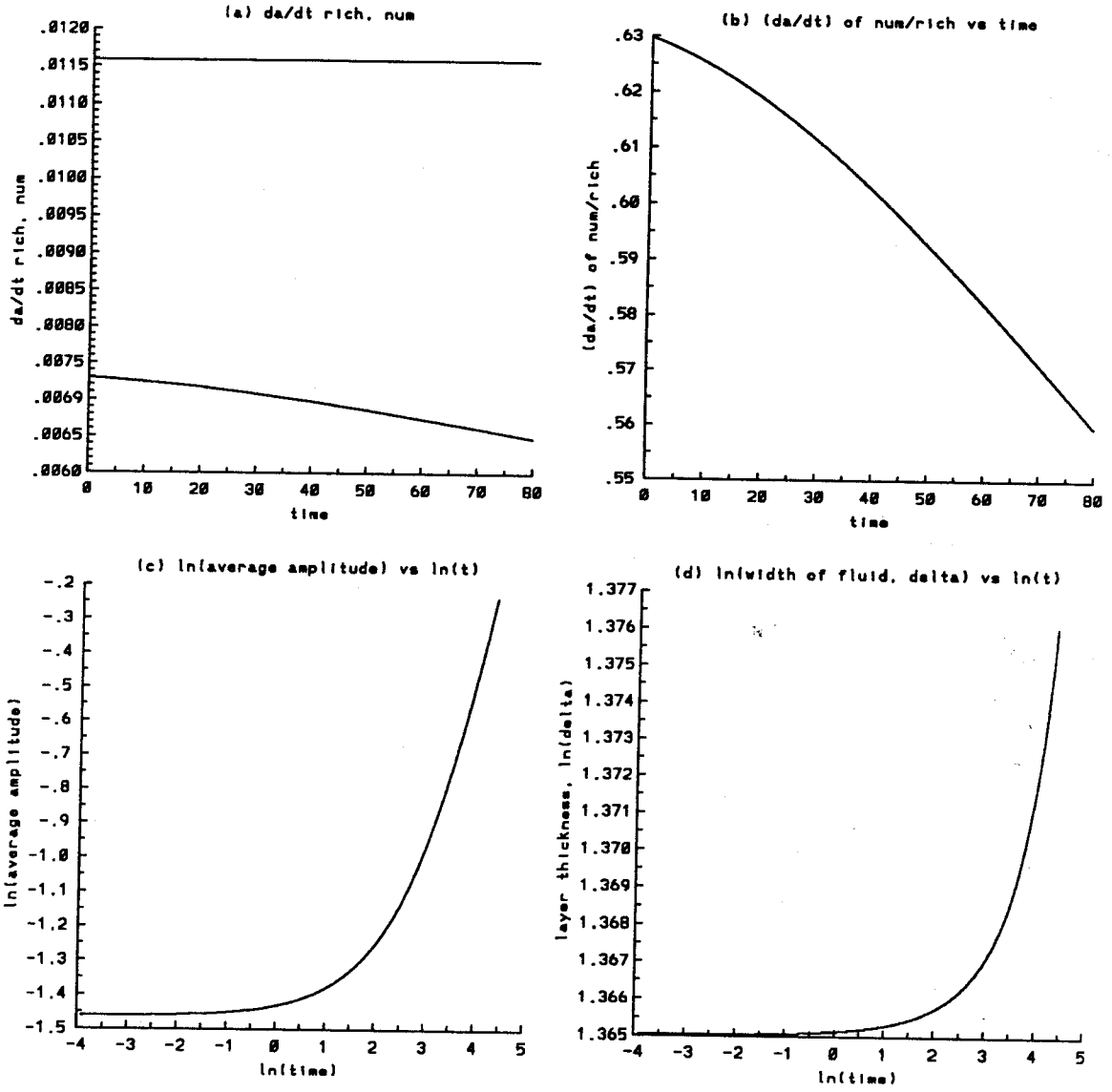

Figure 4.33.2 Time evolution of the average quantities for the second initial random profile, A = -0.05, $t = 0$ to 80 : a) growth rate da/dt of the average amplitude, numerical and Richtmyer theory (straight line), b) the ratio of the numerical growth rate da/dt over that predicted by Richtmyer theory, c) $\ln(a)$ *vs* $\ln(t)$, d) $\ln(\delta)$ *vs* $\ln(t)$.

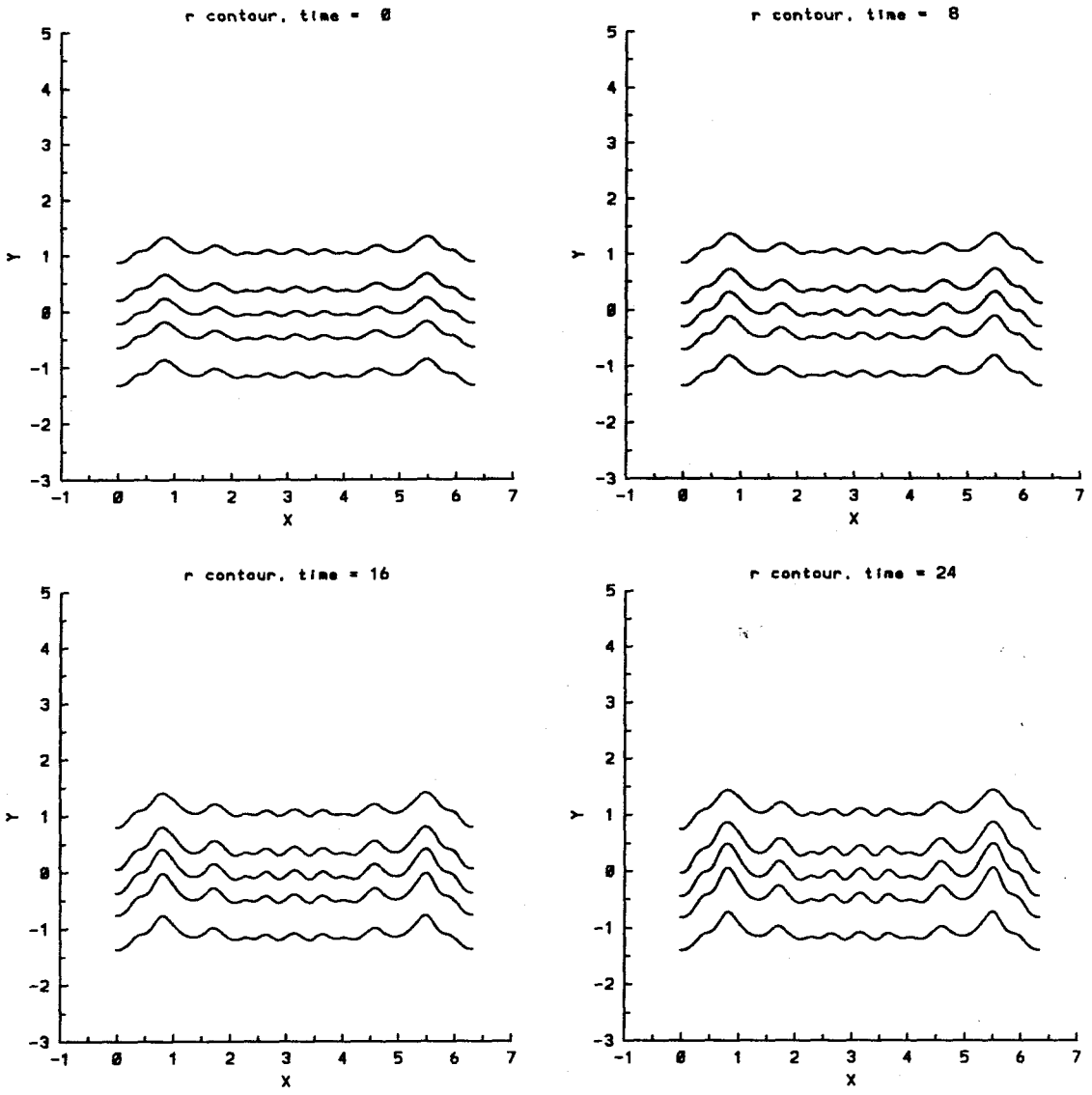

Figure 4.33.3 Time evolution of the density contours for the second initial random profile, A = −0.05, t = 0, 8, 16, 24. The contours are at ρ = 0.48, 0.49, 0.50, 0.51, 0.52.

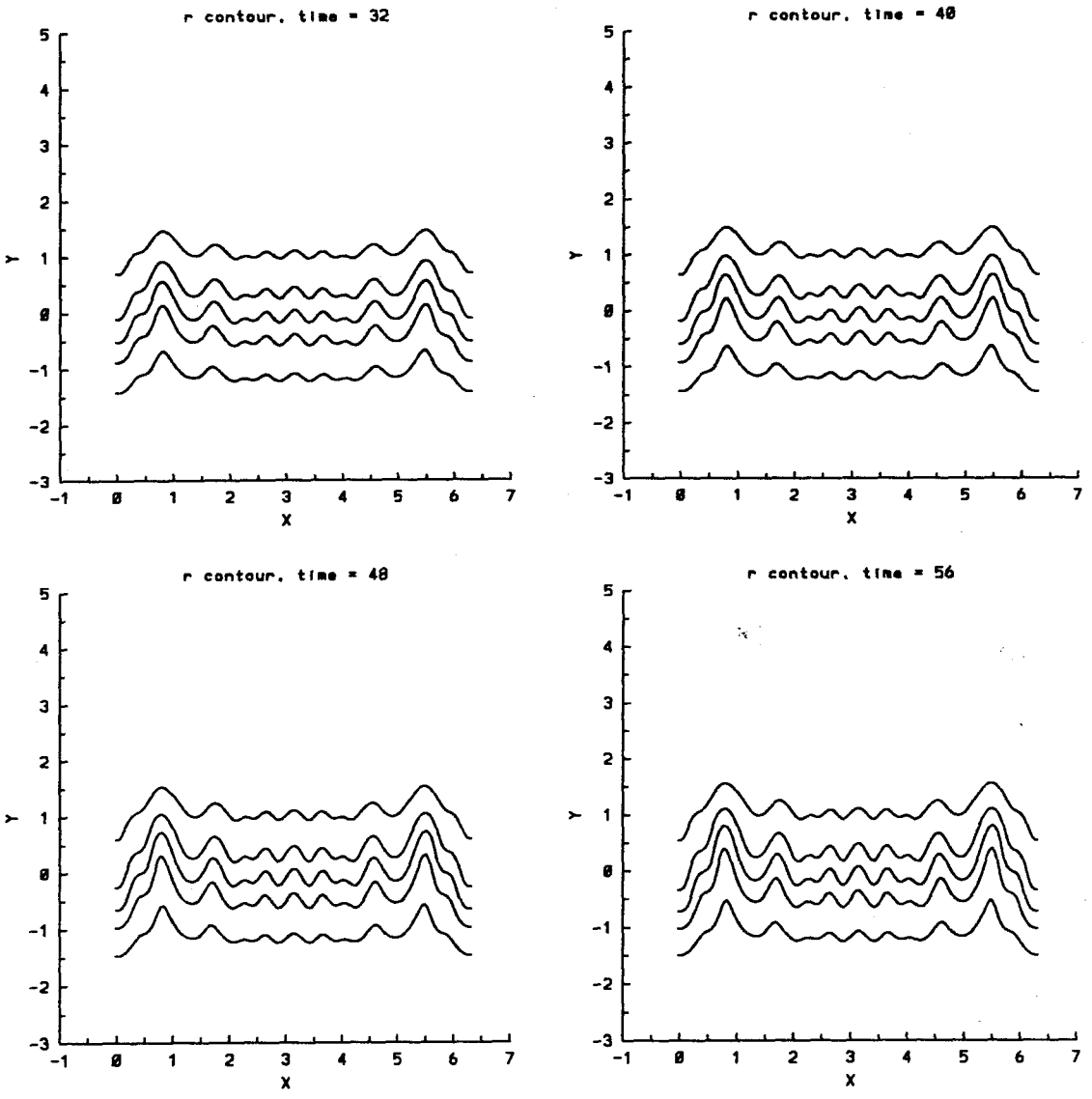

Figure 4.33.4 Time evolution of the density contours for the second initial random profile, A = -0.05, t = 32, 40, 48, 56. The contours are at ρ = 0.48, 0.49, 0.50, 0.51, 0.52.

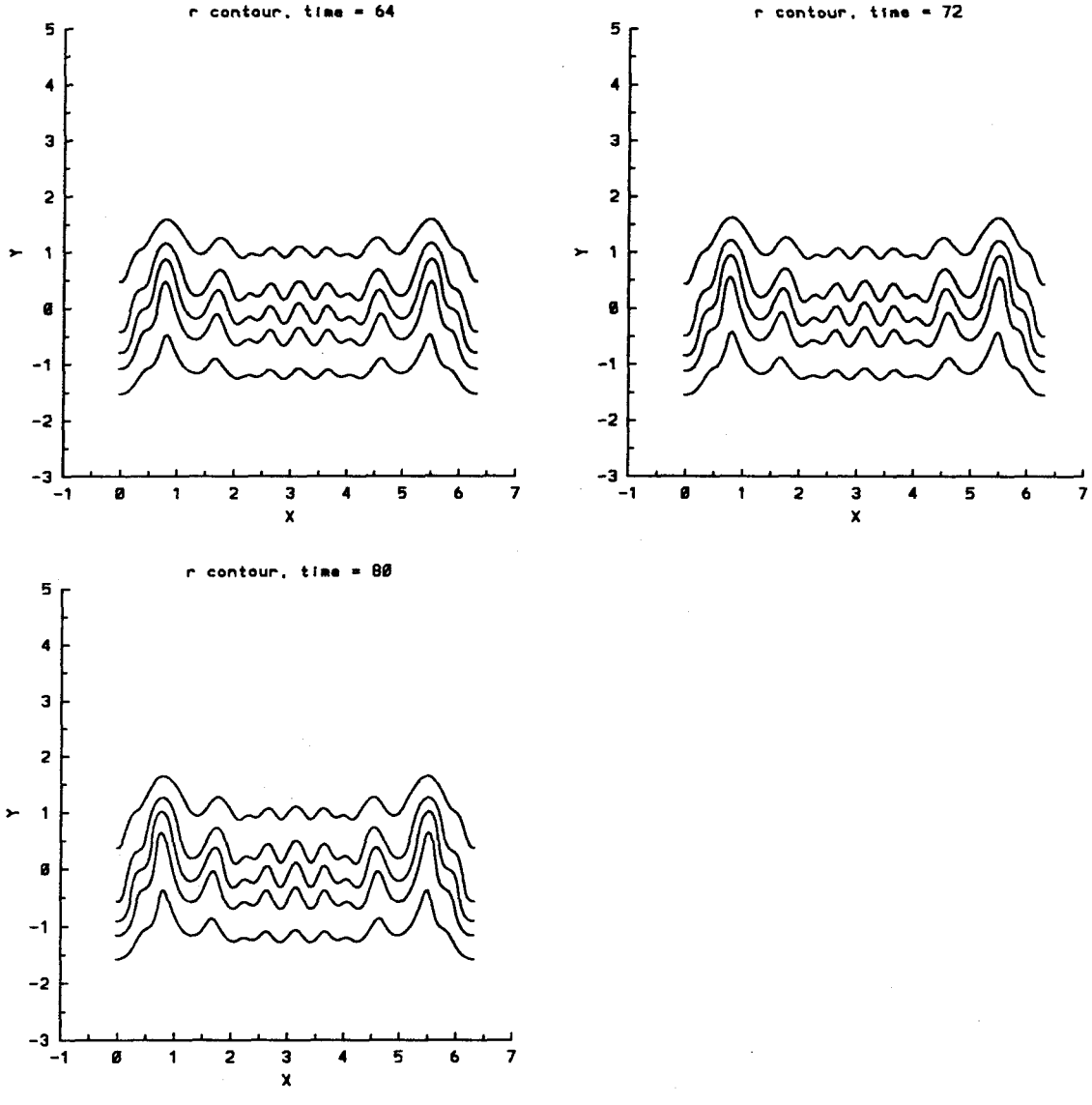

Figure 4.33.5 Time evolution of the density contours for the second initial random profile, A = -0.05, t = 64, 72, 80. The contours are at ρ = 0.48, 0.49, 0.50, 0.51, 0.52.

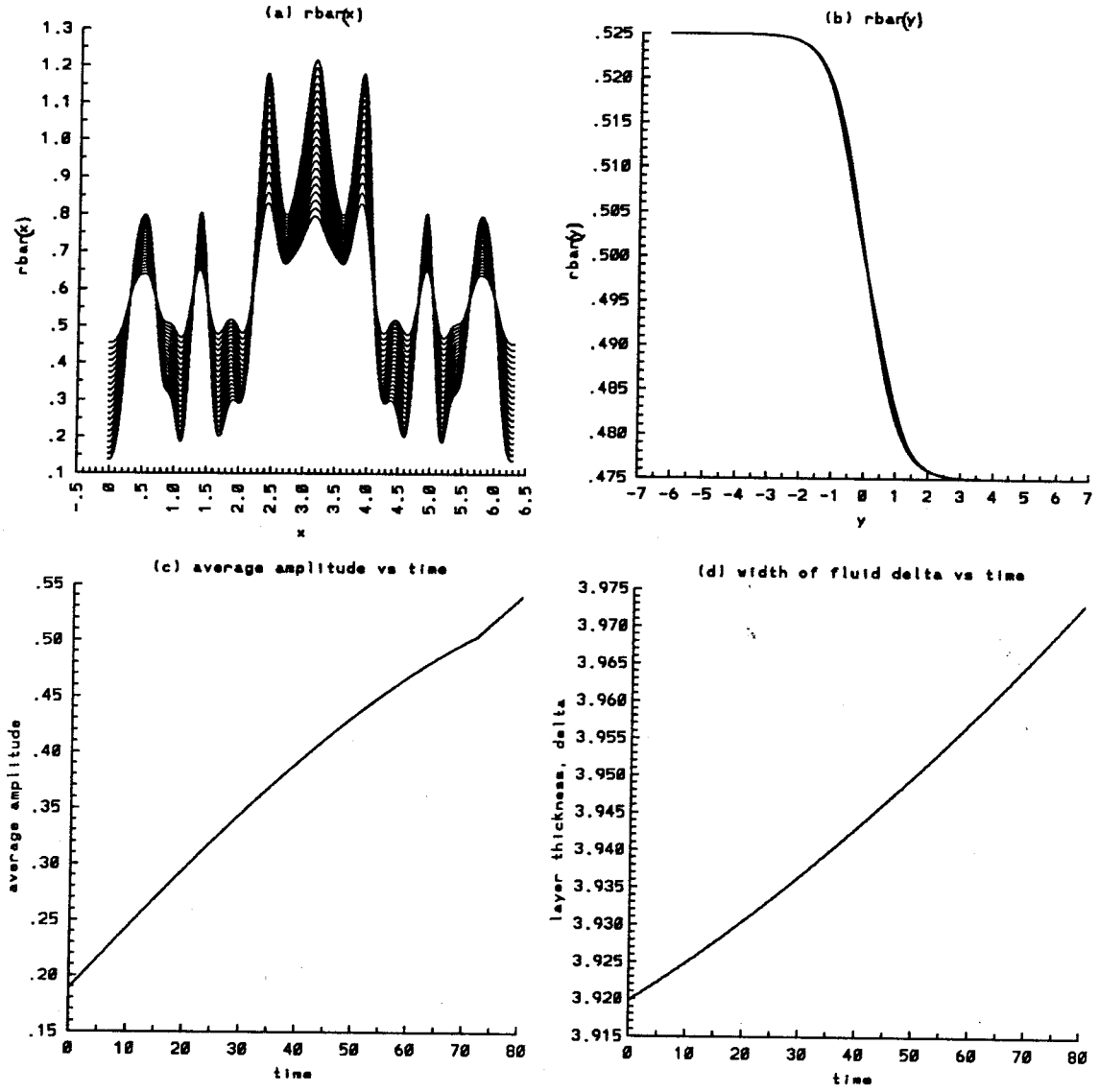

Figure 4.34.1 Time evolution of the average quantities for the third initial random profile, A = -0.05, $t = 0$ to 80 : a) $\bar{\rho}_y(x)$, b) $\bar{\rho}_x(y)$, c) average amplitude, and d) width of the density layer.

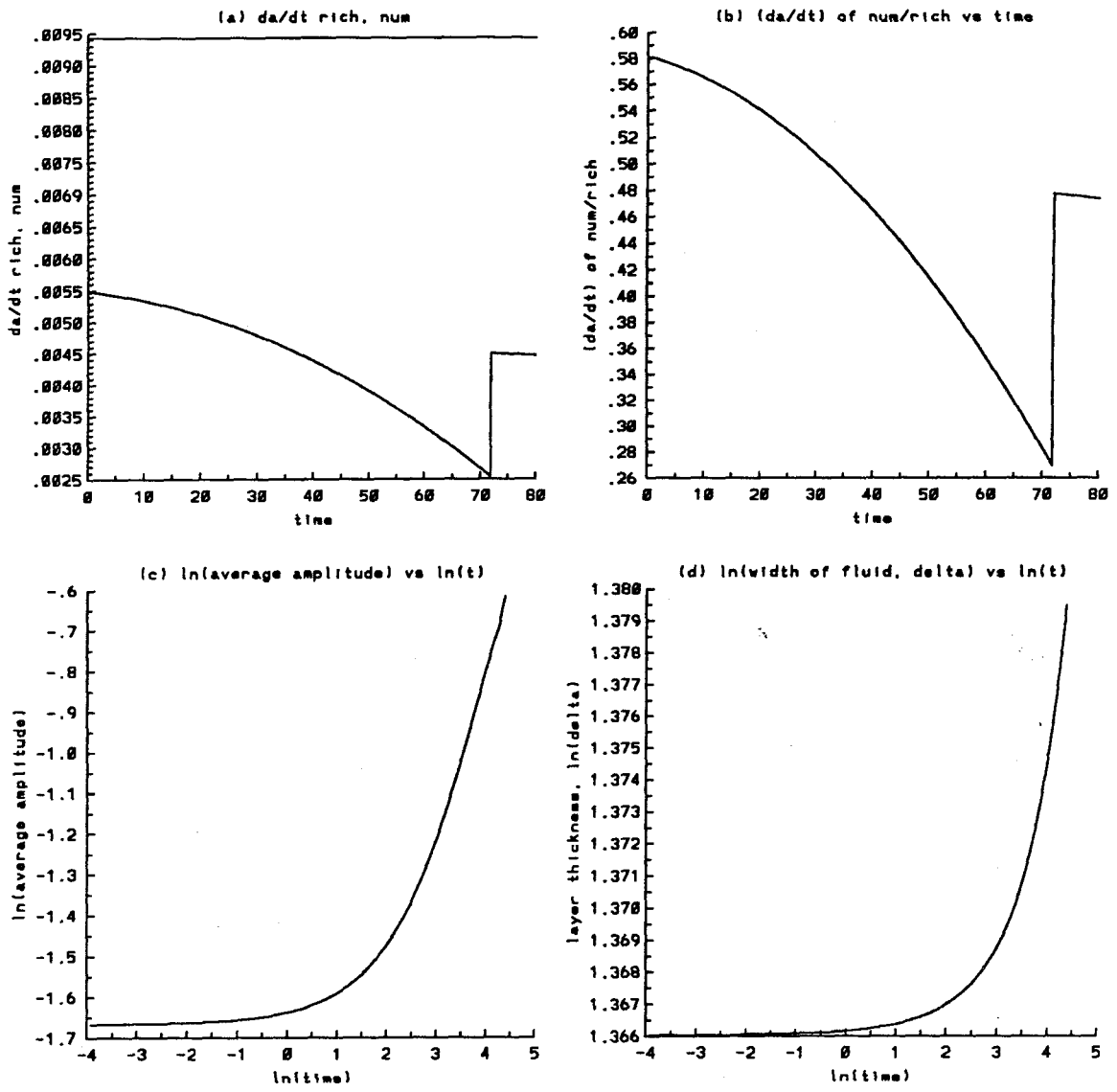

Figure 4.34.2 Time evolution of the average quantities for the third initial random profile, A = -0.05, $t = 0$ to 80 : a) growth rate da/dt of the average amplitude, numerical and Richtmyer theory (straight line), b) the ratio of the numerical growth rate da/dt over that predicted by Richtmyer theory, c) $\ln(a)$ *vs* $\ln(t)$, d) $\ln(\delta)$ *vs* $\ln(t)$.

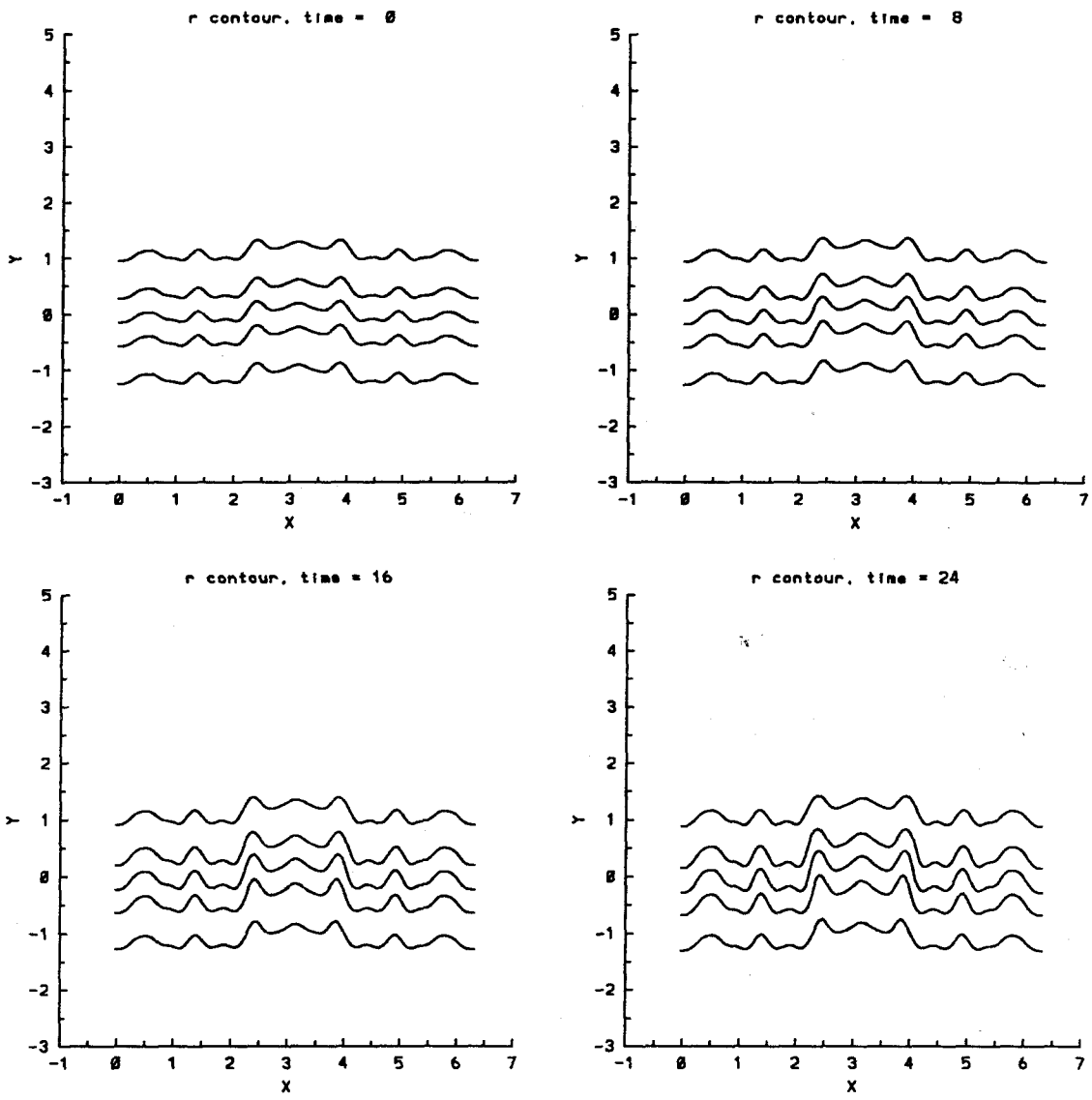

Figure 4.34.3 Time evolution of the density contours for the third initial random profile, A = -0.05, $t = 0$, 8, 16, 24. The contours are at $\rho = 0.48$, 0.49, 0.50, 0.51, 0.52.

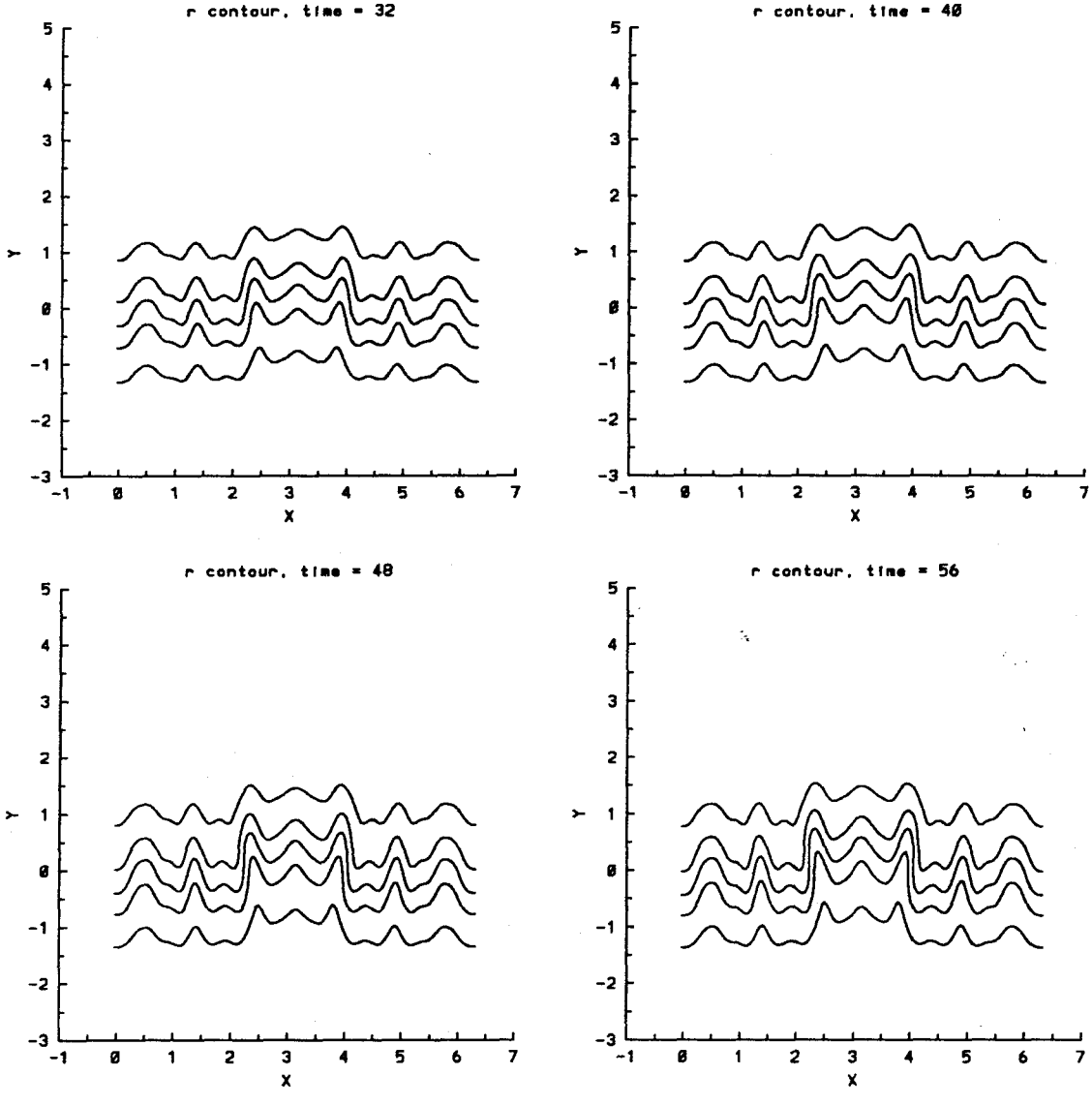

Figure 4.34.4 Time evolution of the density contours for the third initial random profile, A = −0.05, t = 32, 40, 48, 56. The contours are at ρ = 0.48, 0.49, 0.50, 0.51, 0.52.

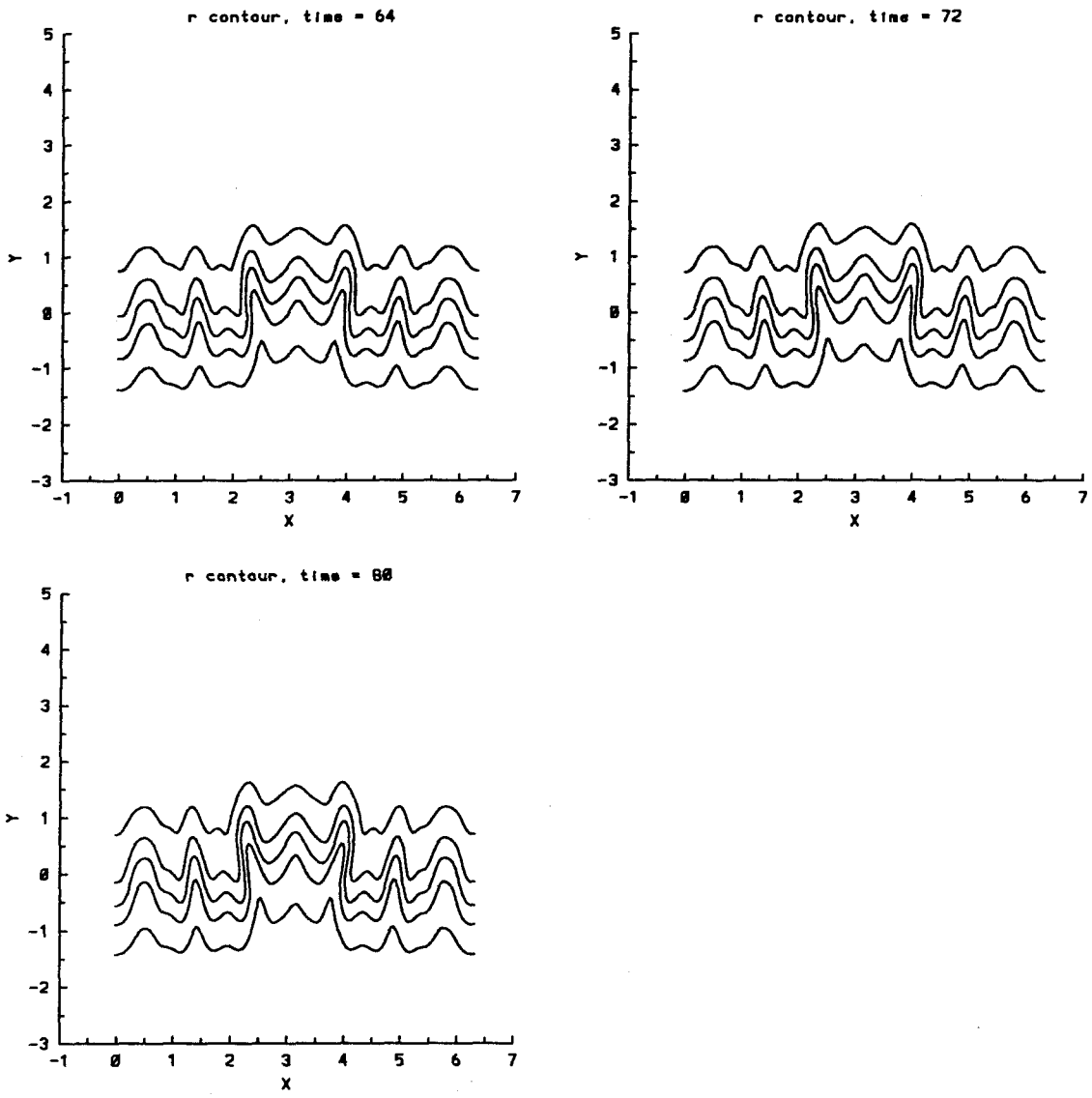

Figure 4.34.5 Time evolution of the density contours for the third initial random profile, A = −0.05, t = 64, 72, 80. The contours are at ρ = 0.48, 0.49, 0.50, 0.51, 0.52.

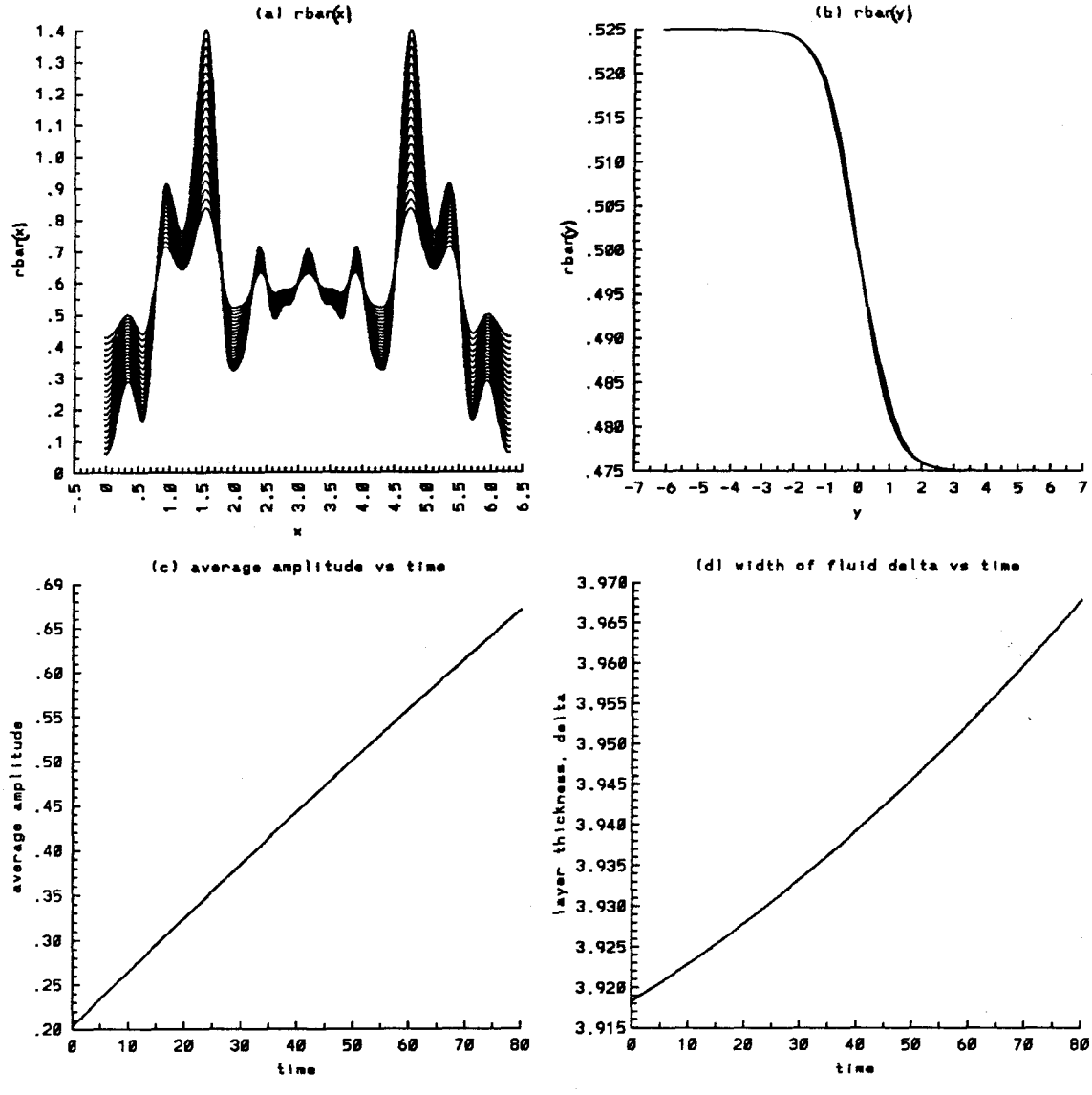

Figure 4.35.1 Time evolution of the average quantities for the fourth initial random profile, A = -0.05, $t = 0$ to 80 : a) $\bar{\rho}_y(x)$, b) $\bar{\rho}_x(y)$, c) average amplitude, and d) width of the density layer.

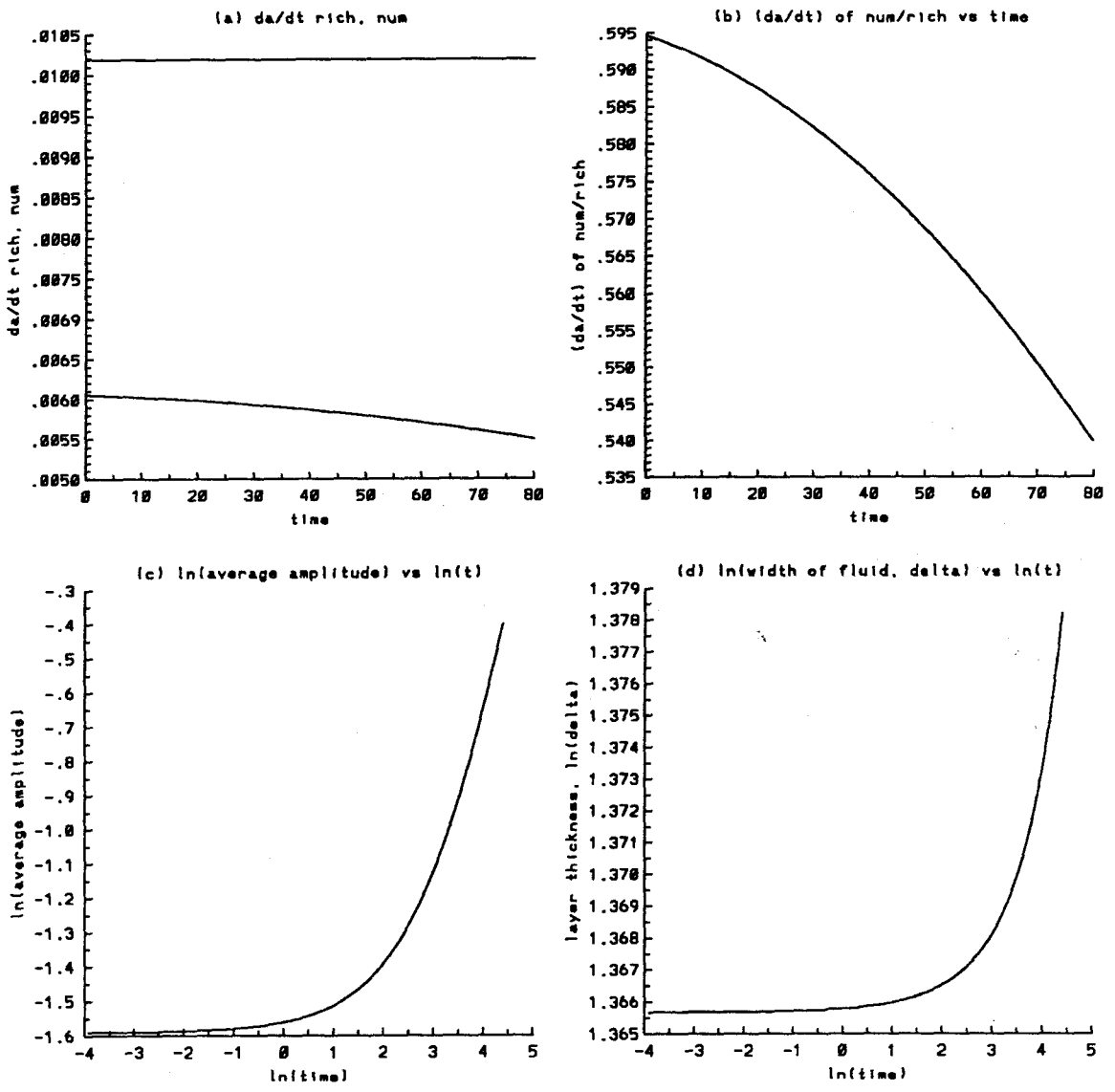

Figure 4.35.2 Time evolution of the average quantities for the fourth initial random profile, A = -0.05, $t = 0$ to 80 : a) growth rate da/dt of the average amplitude, numerical and Richtmyer theory (straight line), b) the ratio of the numerical growth rate da/dt over that predicted by Richtmyer theory, c) $\ln(a)$ *vs* $\ln(t)$, d) $\ln(\delta)$ *vs* $\ln(t)$.

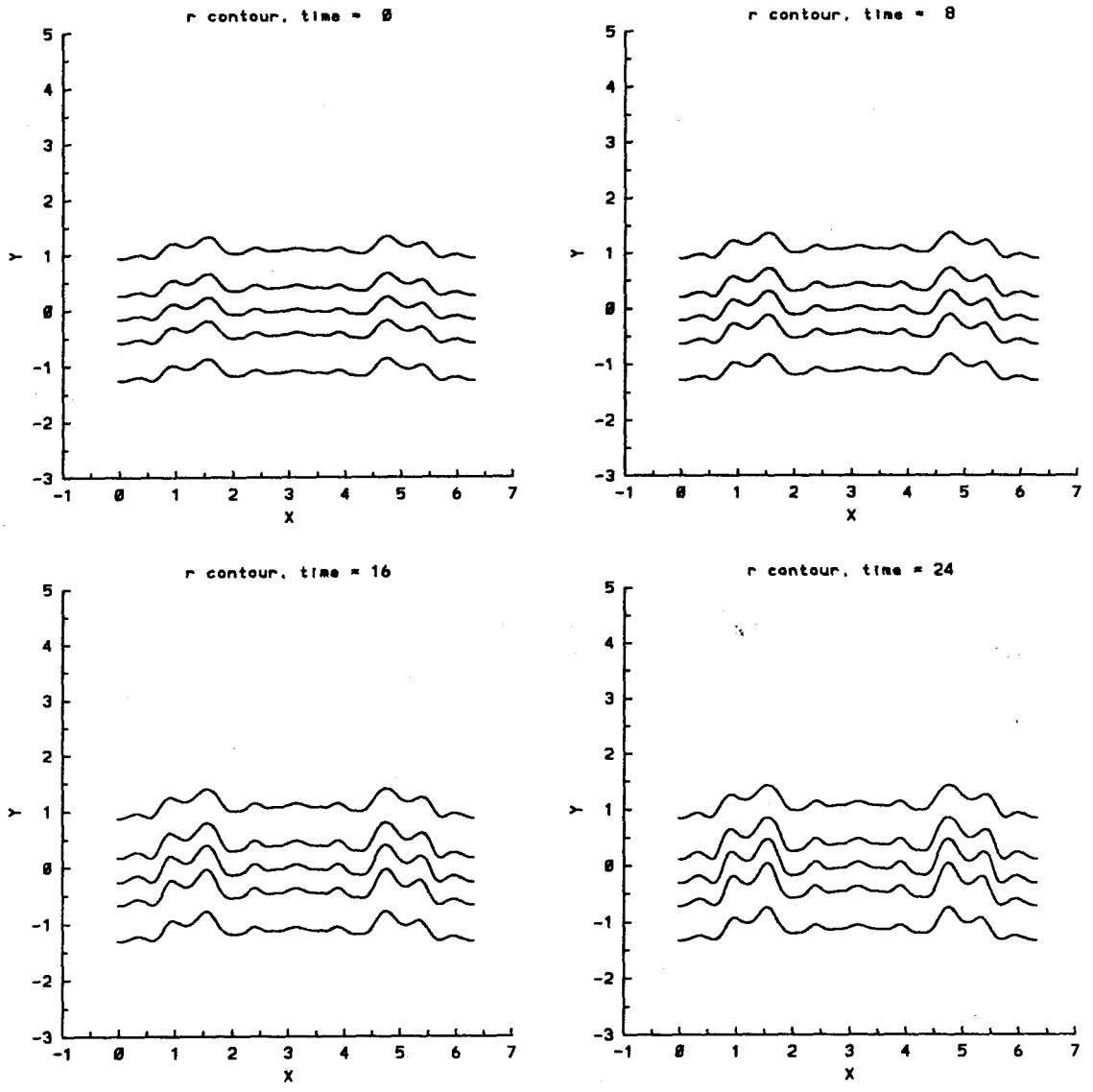

Figure 4.35.3 Time evolution of the density contours for the fourth initial random profile, A = -0.05, $t = 0$, 8, 16, 24. The contours are at $\rho = 0.48$, 0.49, 0.50, 0.51, 0.52.

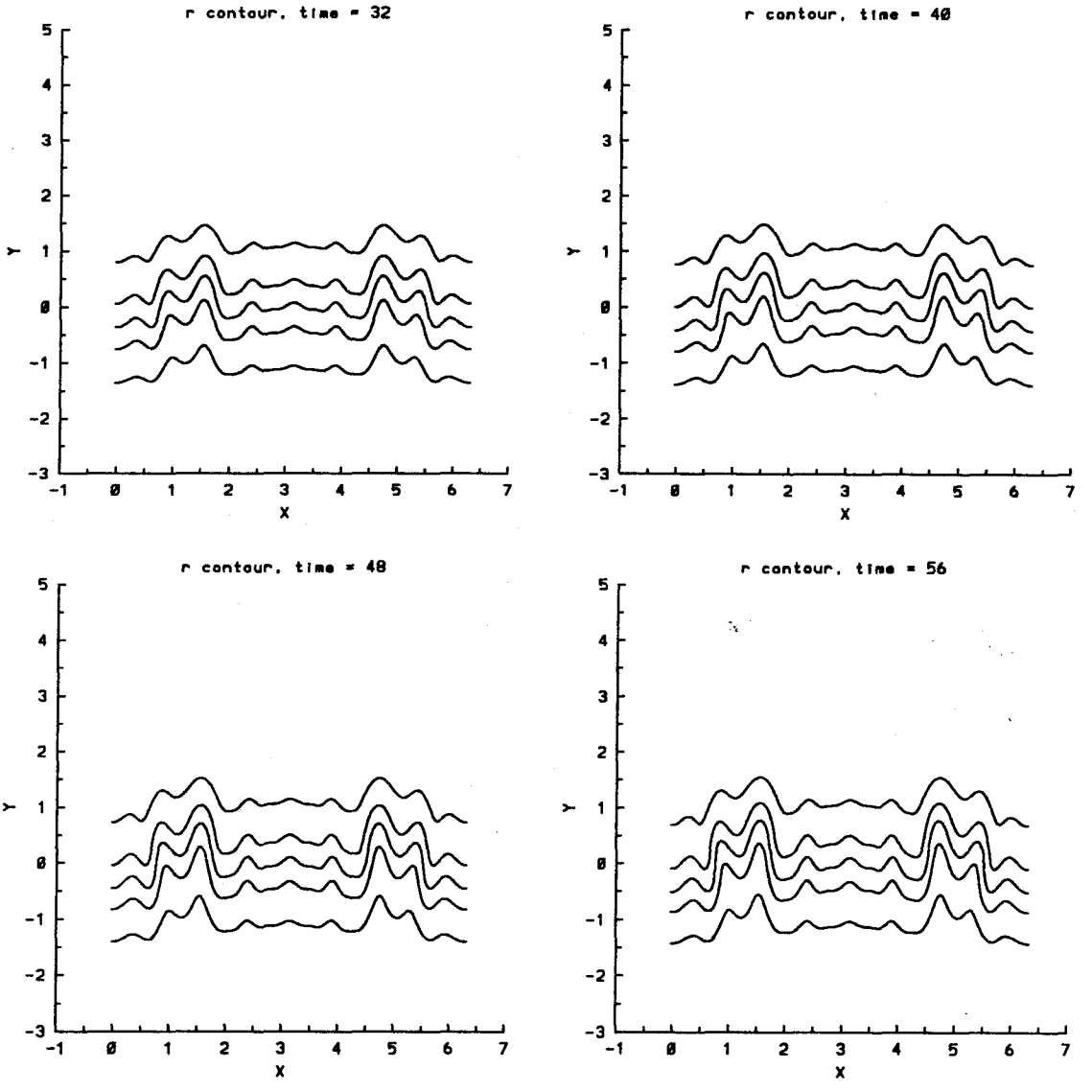

Figure 4.35.4 Time evolution of the density contours for the fourth initial random profile, A = −0.05, t = 32, 40, 48, 56. The contours are at ρ = 0.48, 0.49, 0.50, 0.51, 0.52.

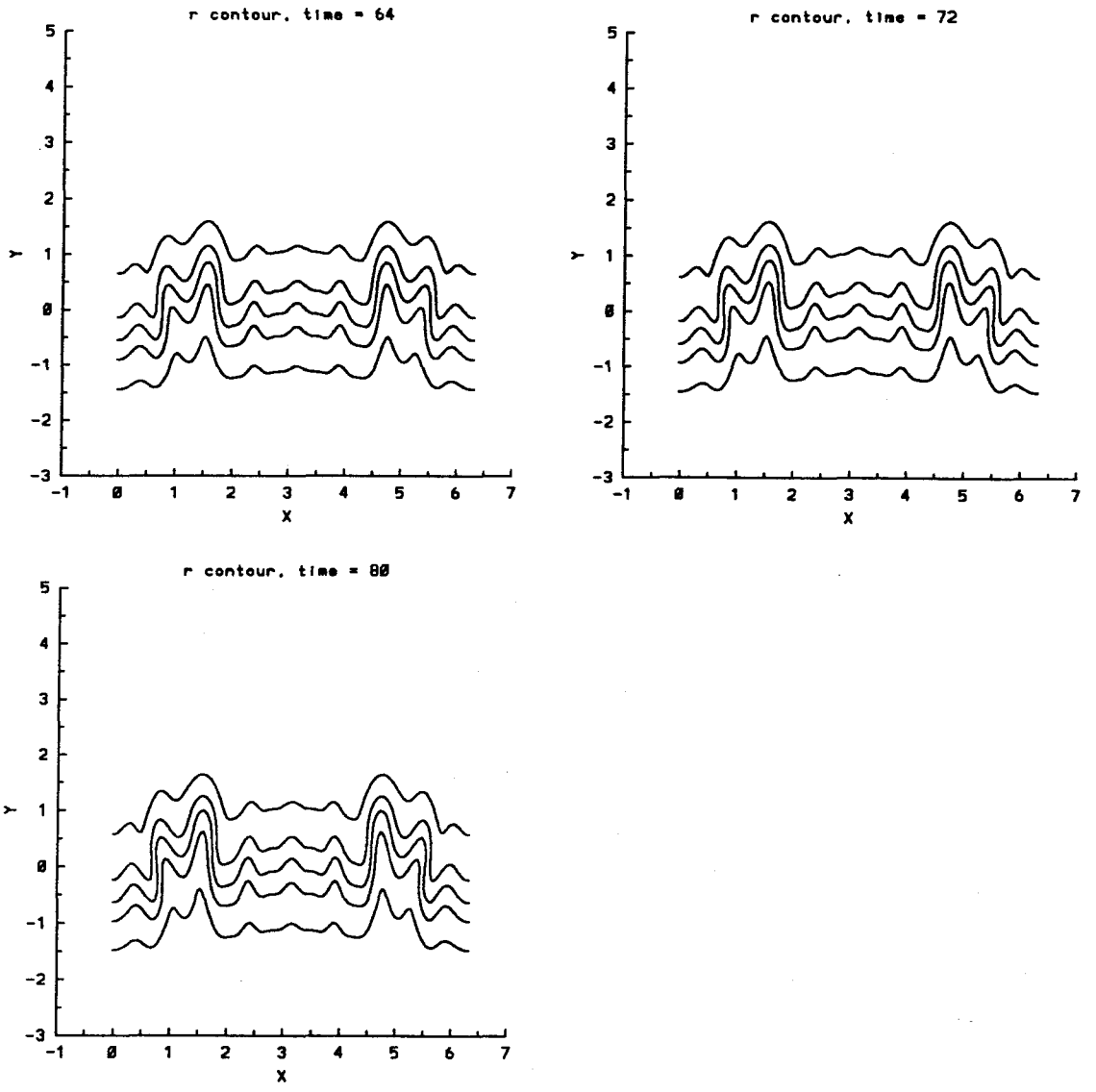

Figure 4.35.5 Time evolution of the density contours for the fourth initial random profile, A = -0.05, t = 64, 72, 80. The contours are at ρ = 0.48, 0.49, 0.50, 0.51, 0.52.

third initial random profile is observed in Figure 4.34.2. This arises from the shift in the peak from which the average amplitude a is computed.

For A = −0.2, the instability grows faster. As the internal peaks reach the boundaries of the density layer the nonlinear effects become strong and we see the emergence of globules of fluid as in the cases of the single scale perturbations. As the instability develops, the appearance of roll-up of these globules is observed as is clearly shown in Figures 4.36.4–5 to 4.39.4–5. We also plot the position of the peaks of the average density $\bar{\rho}_y(x)$ of this random profile as shown in Figure 4.51. Clearly, at initial time, the growth rates of the peaks are proportional to their initial amplitudes. Peaks with higher amplitude grow at greater speeds. As seen in Figures 4.36.2a, 4.39.2a, and 4.48.2a of the first, fourth, and fifth random profile, the growth rates of the average amplitude da/dt decrease rapidly to zero and oscillate afterward. This results from the mixing action of the roll-up in reducing the local density gradient. The consistent growth of the average amplitude a in the second and third profile is due to the symmetric mixing in the second profile while for the third profile its tallest peak has not yet developed into a globule. These behaviors can also be deduced from the shifts in the highest peaks of $\bar{\rho}_y(x)$ and the asymmetrical development of $\bar{\rho}_x(y)$ as shown in Figures 4.36.1b, 4.39.1b, and 4.48.1b. The delay in the formation of the globules until the peaks have reached the boundaries is clearly seen in Figures 4.48 for the fifth profile. As the instability grows, the formation of vortical pair structures of opposite signs interacting in a very complicated nonlinear fashion is also seen clearly in these Figures.

For higher A, A = −0.5, and A = −0.8, the characteristics of the flow discussed for A = −0.2 and A = −0.05 are greatly amplified and occur much earlier in time. In Figure 4.44.3V–4V, we plot the evolution of the vorticity contours for the first random profile with A = −0.8. Similar plots are shown in Figures 4.48.3V–5V, 4.49.3V for A = −0.2, −0.8 of the fifth profiles, and Figures 4.50.3V for A = −0.8 of the sixth profile. As in the single scale peturbation, there exist dipolar regions of vorticity consisting of elongated vortices of equal and opposite strength. Until

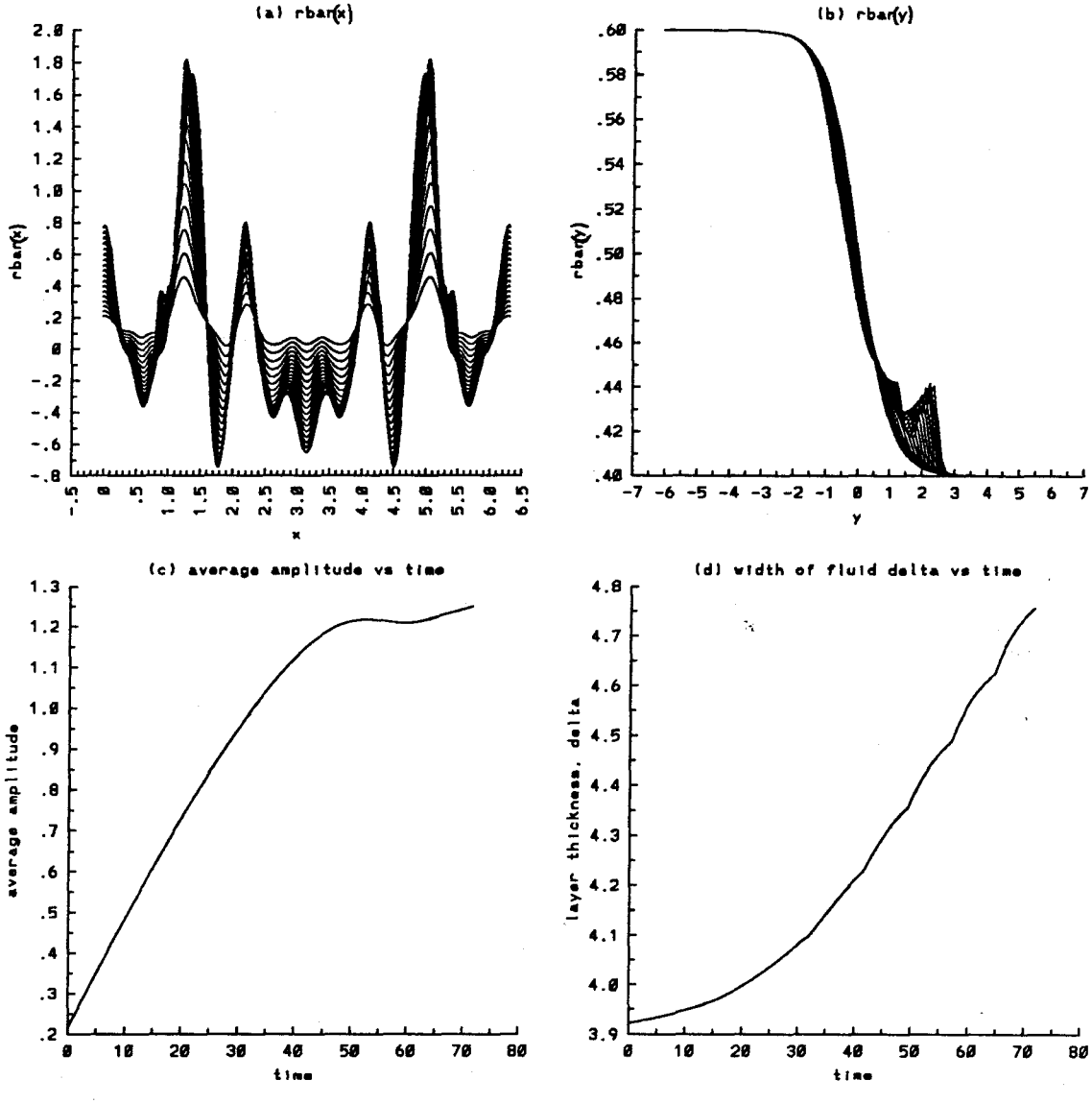

Figure 4.36.1 Time evolution of the average quantities for the first initial random profile, A = -0.2, $t = 0$ to 71.46 : a) $\bar{\rho}_y(x)$, b) $\bar{\rho}_x(y)$, c) average amplitude, and d) width of the density layer.

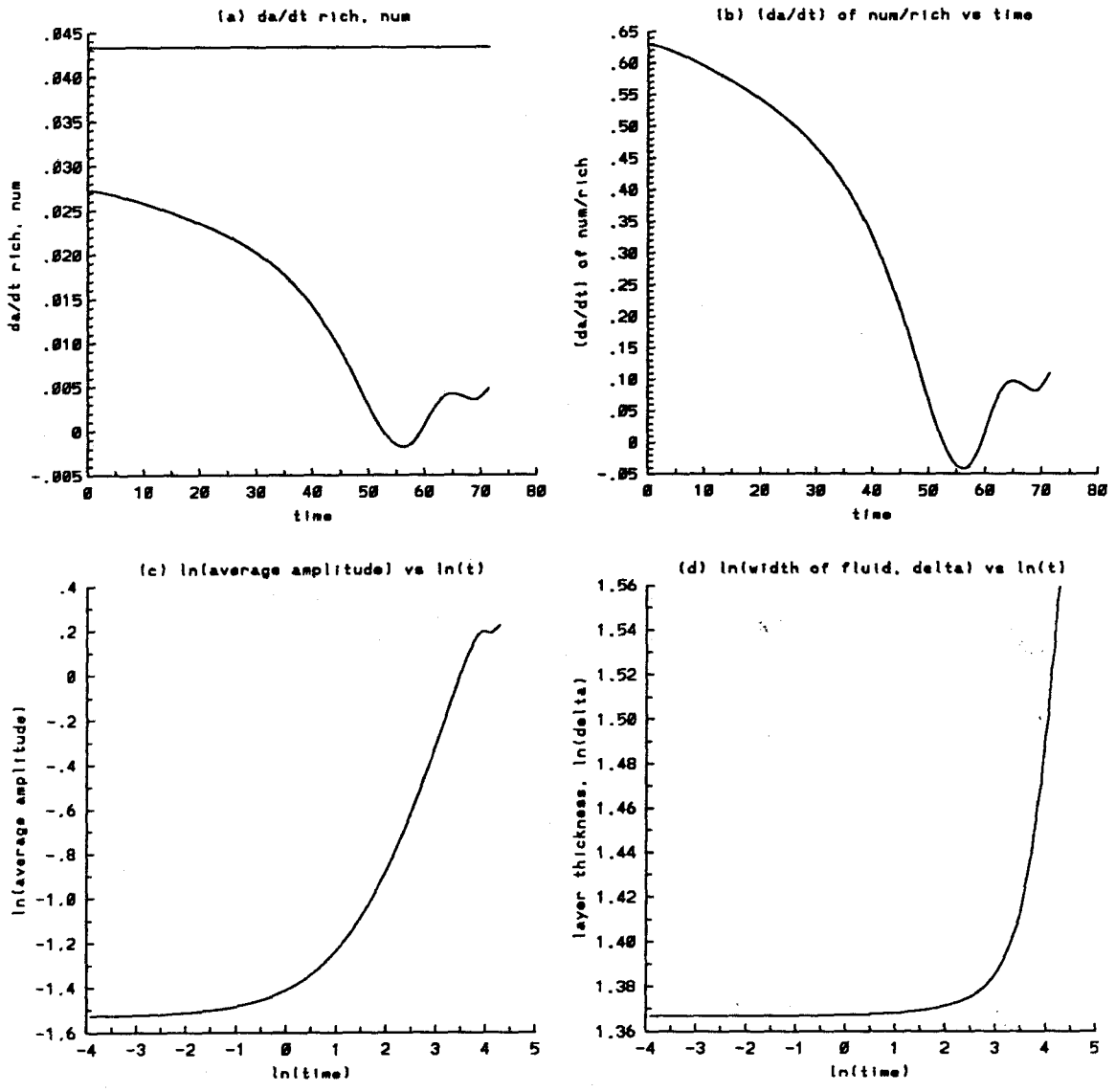

Figure 4.36.2 Time evolution of the average quantities for the first initial random profile, A = -0.2, $t = 0$ to 71.46 : a) growth rate da/dt of the average amplitude, numerical and Richtmyer theory (straight line), b) the ratio of the numerical growth rate da/dt over that predicted by Richtmyer theory, c) $\ln(a)$ *vs* $\ln(t)$, d) $\ln(\delta)$ *vs* $\ln(t)$.

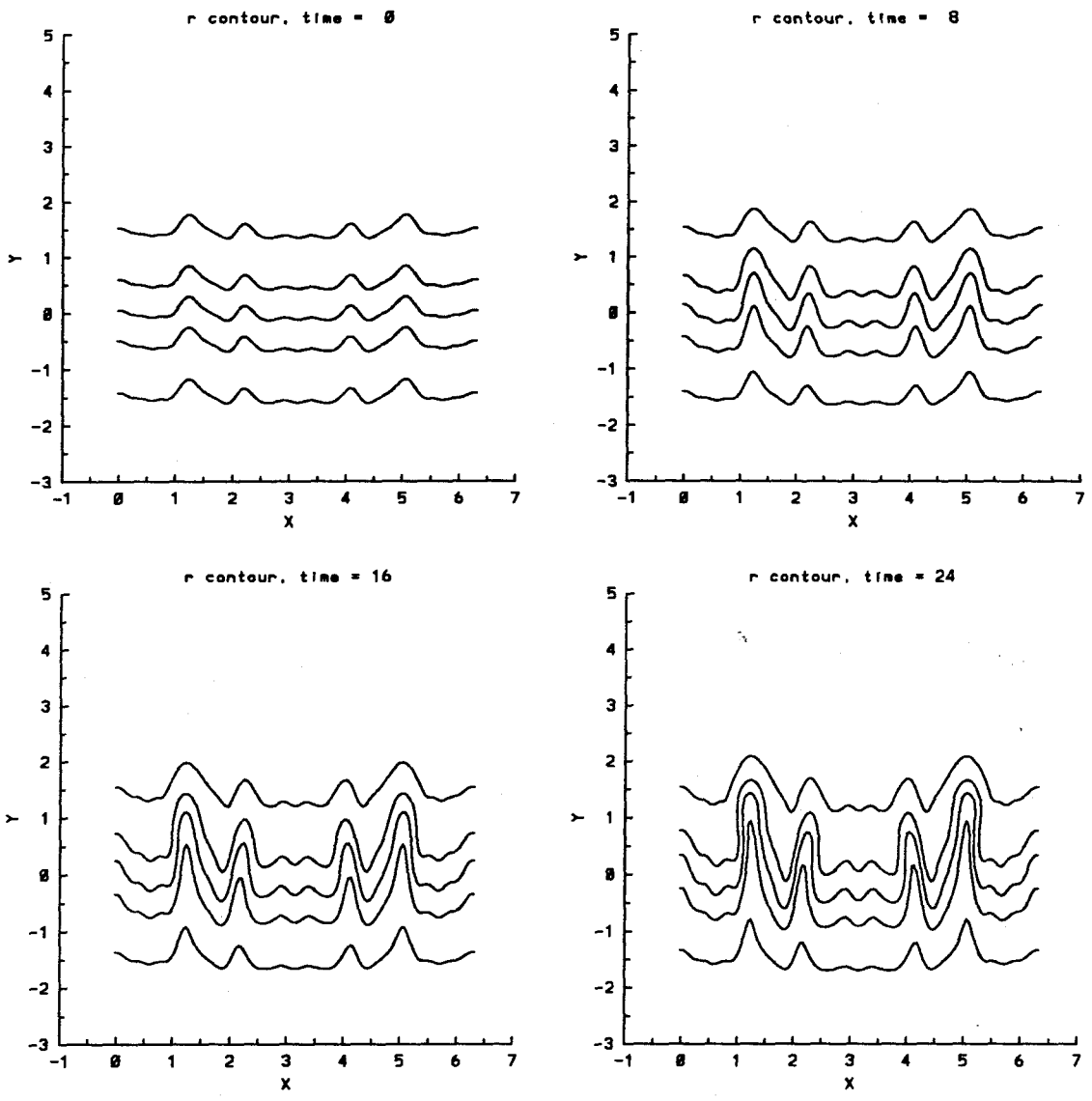

Figure 4.36.3 Time evolution of the density contours for the first initial random profile, A = −0.2, t = 0, 8, 16, 24. The contours are at ρ = 0.41, 0.45, 0.50, 0.55, 0.59.

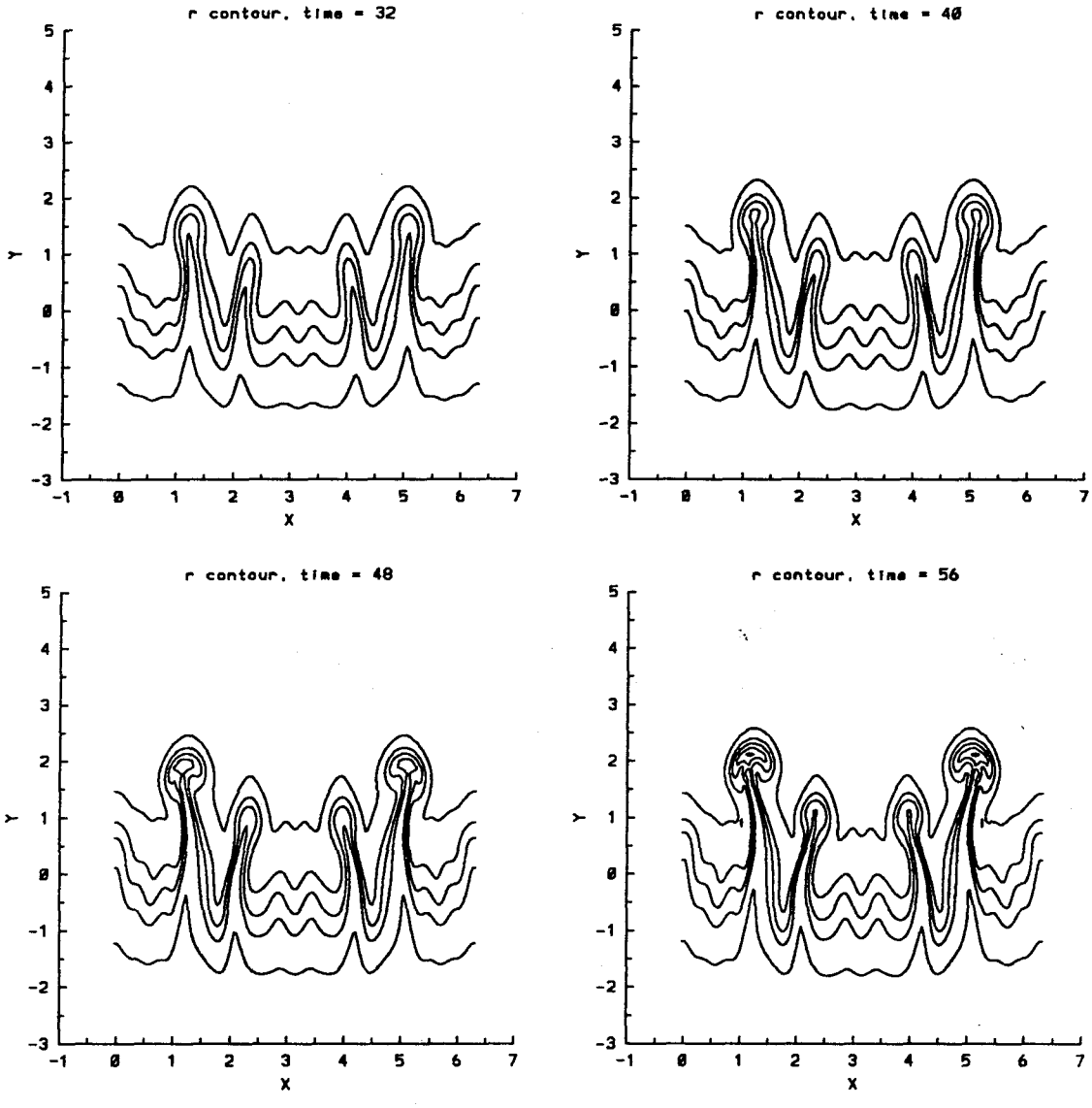

Figure 4.36.4 Time evolution of the density contours for the first initial random profile, A = -0.2, $t = 32$, 40, 48, 56. The contours are at $\rho = 0.41$, 0.45, 0.50, 0.55, 0.59.

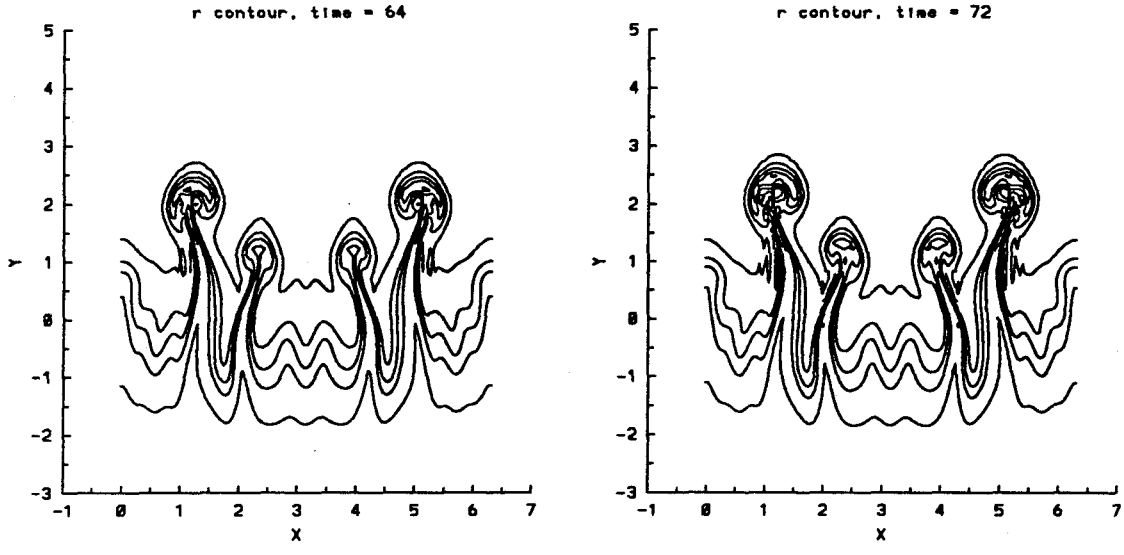

Figure 4.36.5 Time evolution of the density contours for the first initial random profile, A = -0.2, $t = 64$, 72. The contours are at $\rho = 0.41$, 0.45, 0.50, 0.55, 0.59.

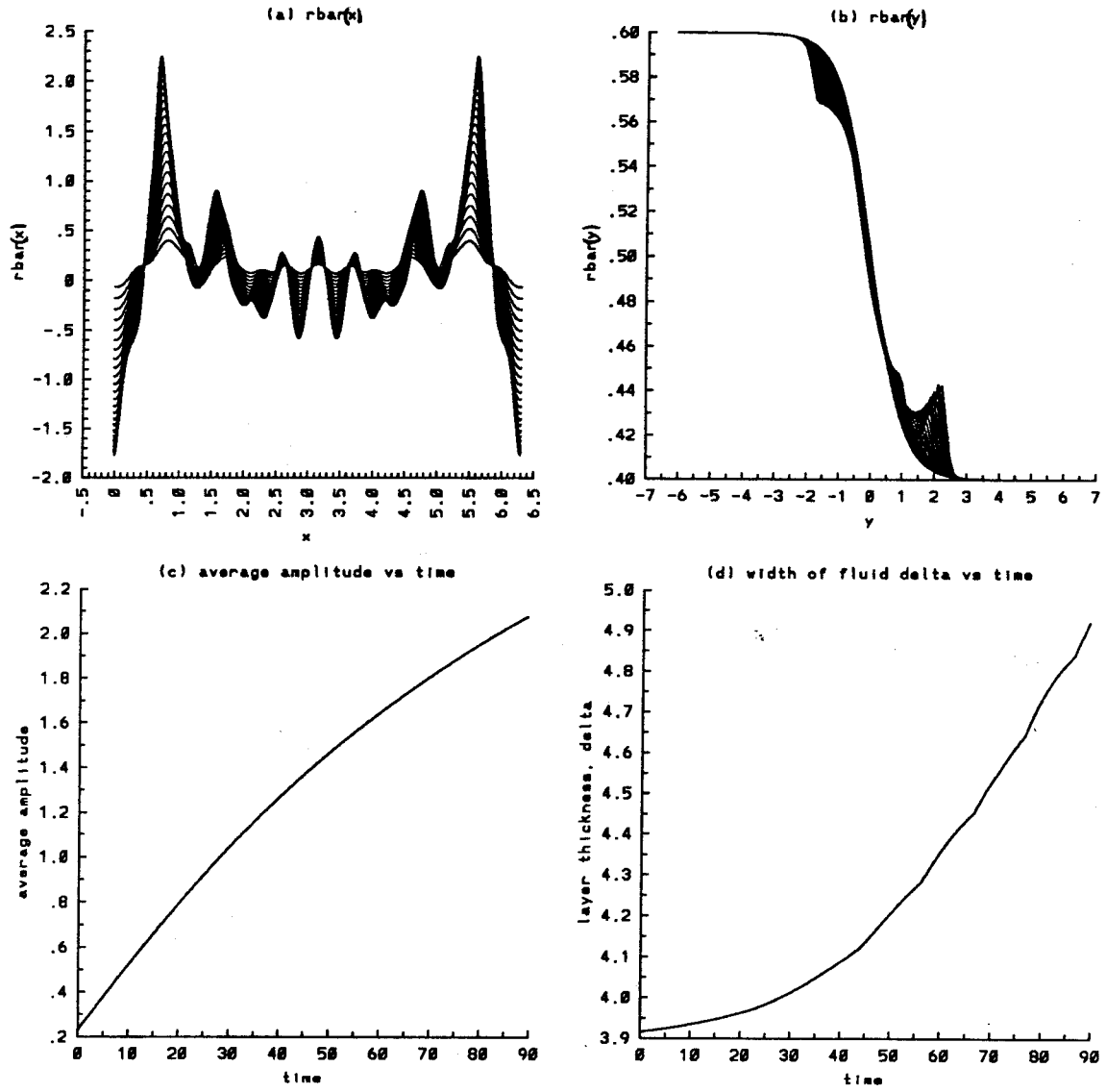

Figure 4.37.1 Time evolution of the average quantities for the second initial random profile, A = −0.2, $t = 0$ to 89.34 : a) $\bar{\rho}_y(x)$, b) $\bar{\rho}_x(y)$, c) average amplitude, and d) width of the density layer.

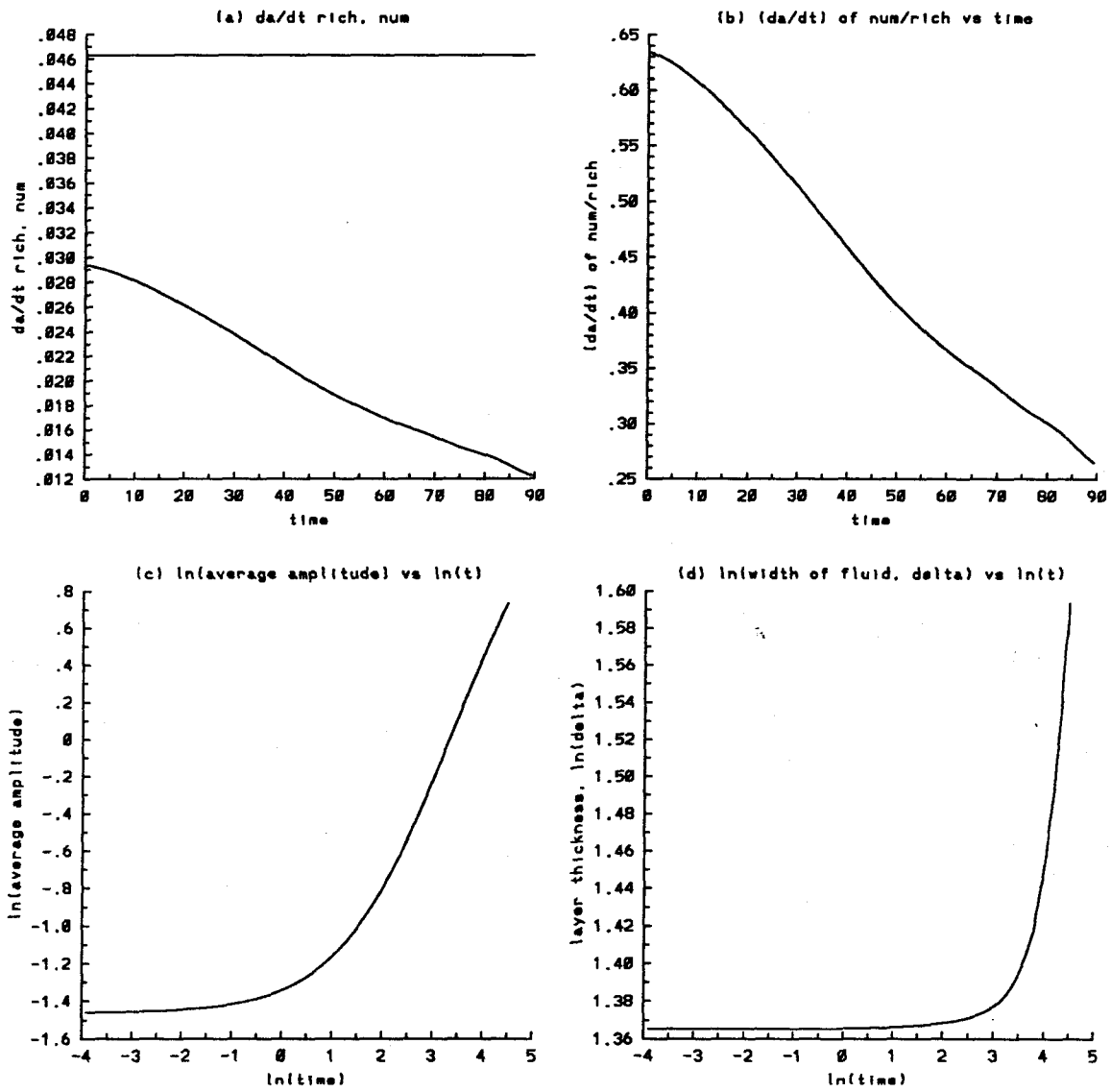

Figure 4.37.2 Time evolution of the average quantities for the second initial random profile, A = −0.2, $t = 0$ to 89.34: a) growth rate da/dt of the average amplitude, numerical and Richtmyer theory (straight line), b) the ratio of the numerical growth rate da/dt over that predicted by Richtmyer theory, c) $\ln(a)$ *vs* $\ln(t)$, d) $\ln(\delta)$ *vs* $\ln(t)$.

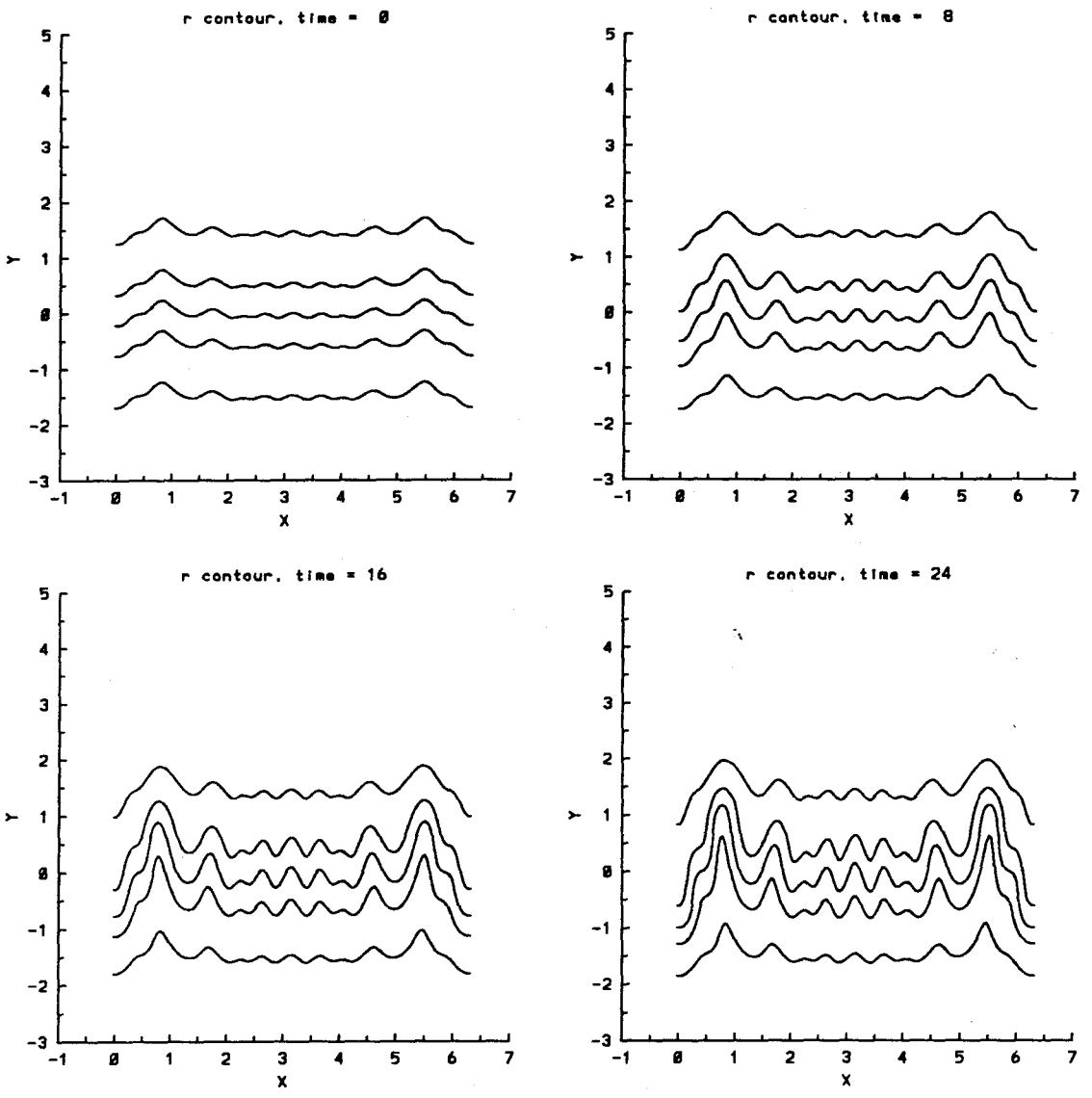

Figure 4.37.3 Time evolution of the density contours for the second initial random profile, A = −0.2, t = 0, 8, 16, 24. The contours are at ρ = 0.41, 0.45, 0.50, 0.55, 0.59.

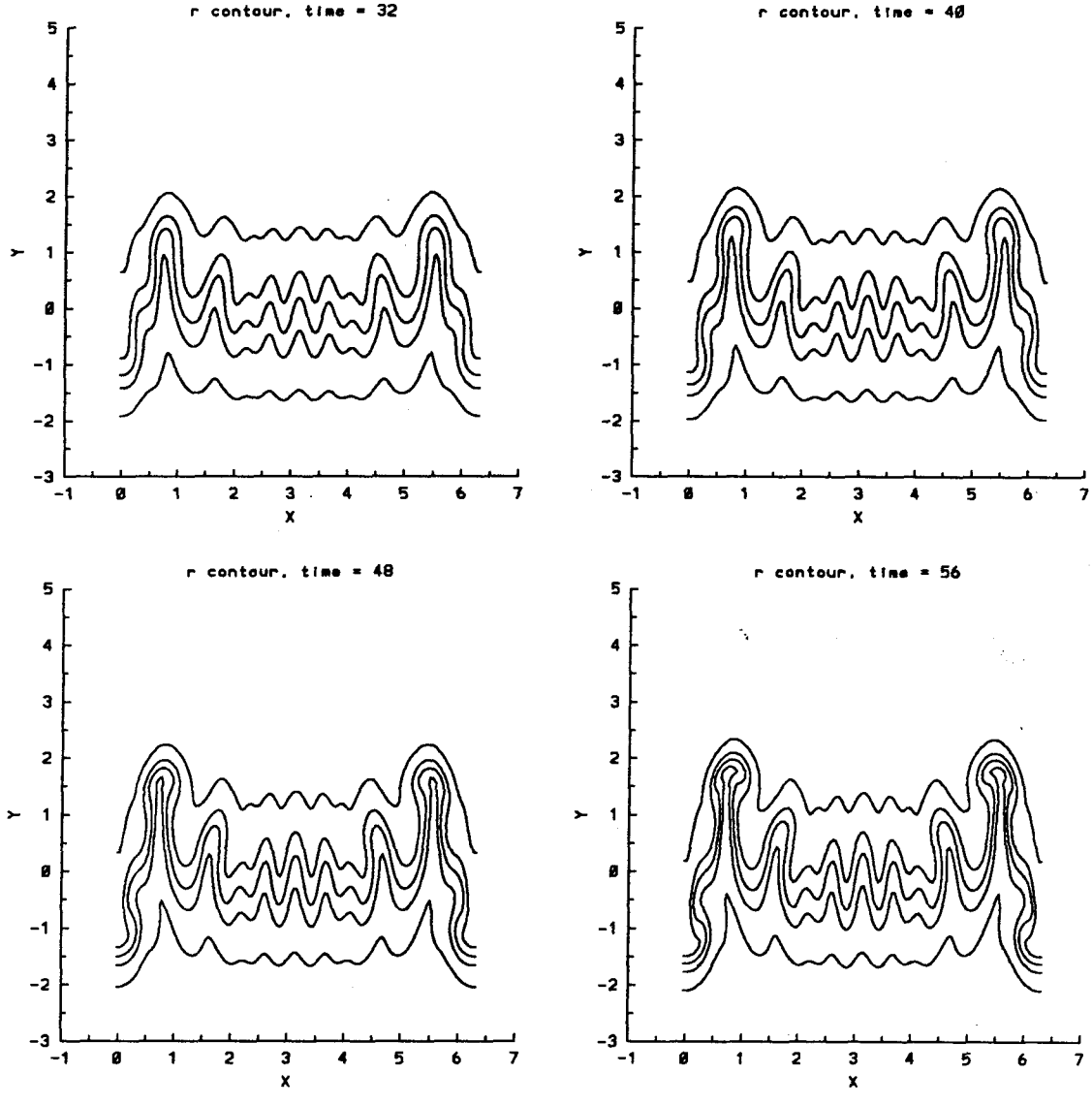

Figure 4.37.4 Time evolution of the density contours for the second initial random profile, A = -0.2, $t = 32, 40, 48, 56$. The contours are at $\rho = 0.41, 0.45, 0.50, 0.55, 0.59$.

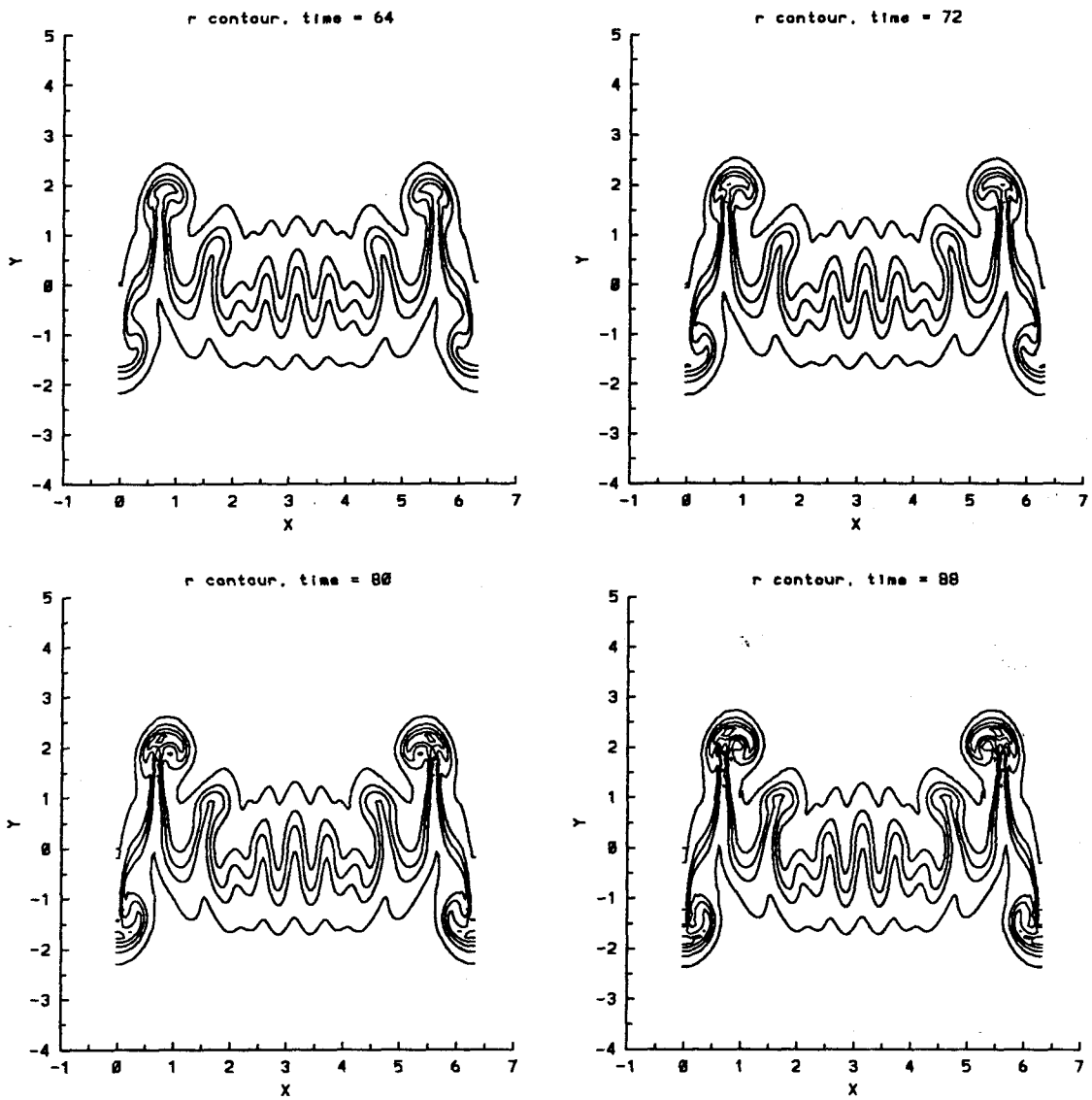

Figure 4.37.5 Time evolution of the density contours for the second initial random profile, A = −0.2, t = 64, 72, 80, 88. The contours are at ρ = 0.41, 0.45, 0.50, 0.55, 0.59.

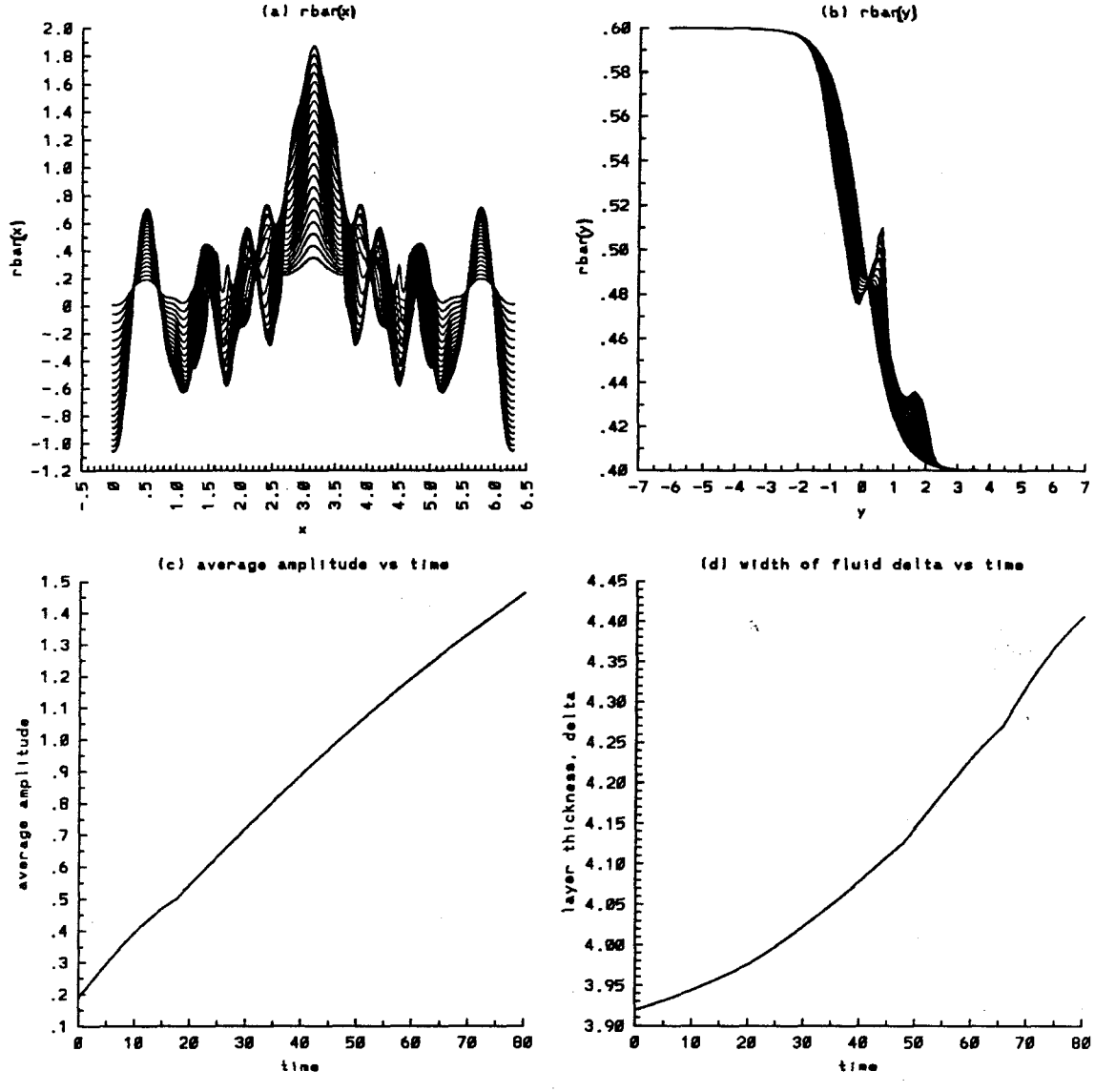

Figure 4.38.1 Time evolution of the average quantities for the third initial random profile, A $= -0.2$, $t = 0$ to 80 : a) $\bar{\rho}_y(x)$, b) $\bar{\rho}_x(y)$, c) average amplitude, and d) width of the density layer.

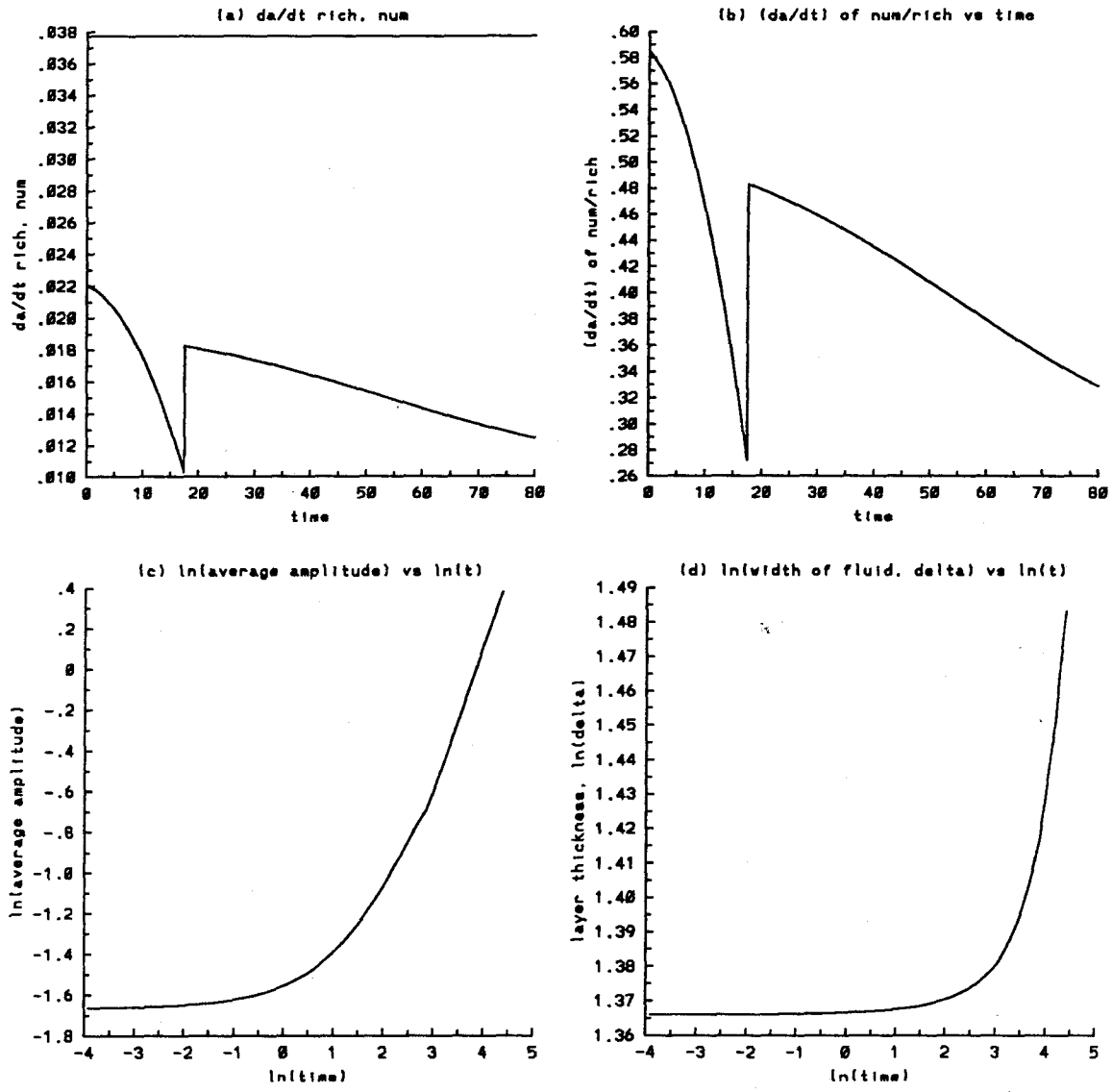

Figure 4.38.2 Time evolution of the average quantities for the third initial random profile, A = -0.2, $t = 0$ to 80 : a) growth rate da/dt of the average amplitude, numerical and Richtmyer theory (straight line), b) the ratio of the numerical growth rate da/dt over that predicted by Richtmyer theory, c) $\ln(a)$ *vs* $\ln(t)$, d) $\ln(\delta)$ *vs* $\ln(t)$.

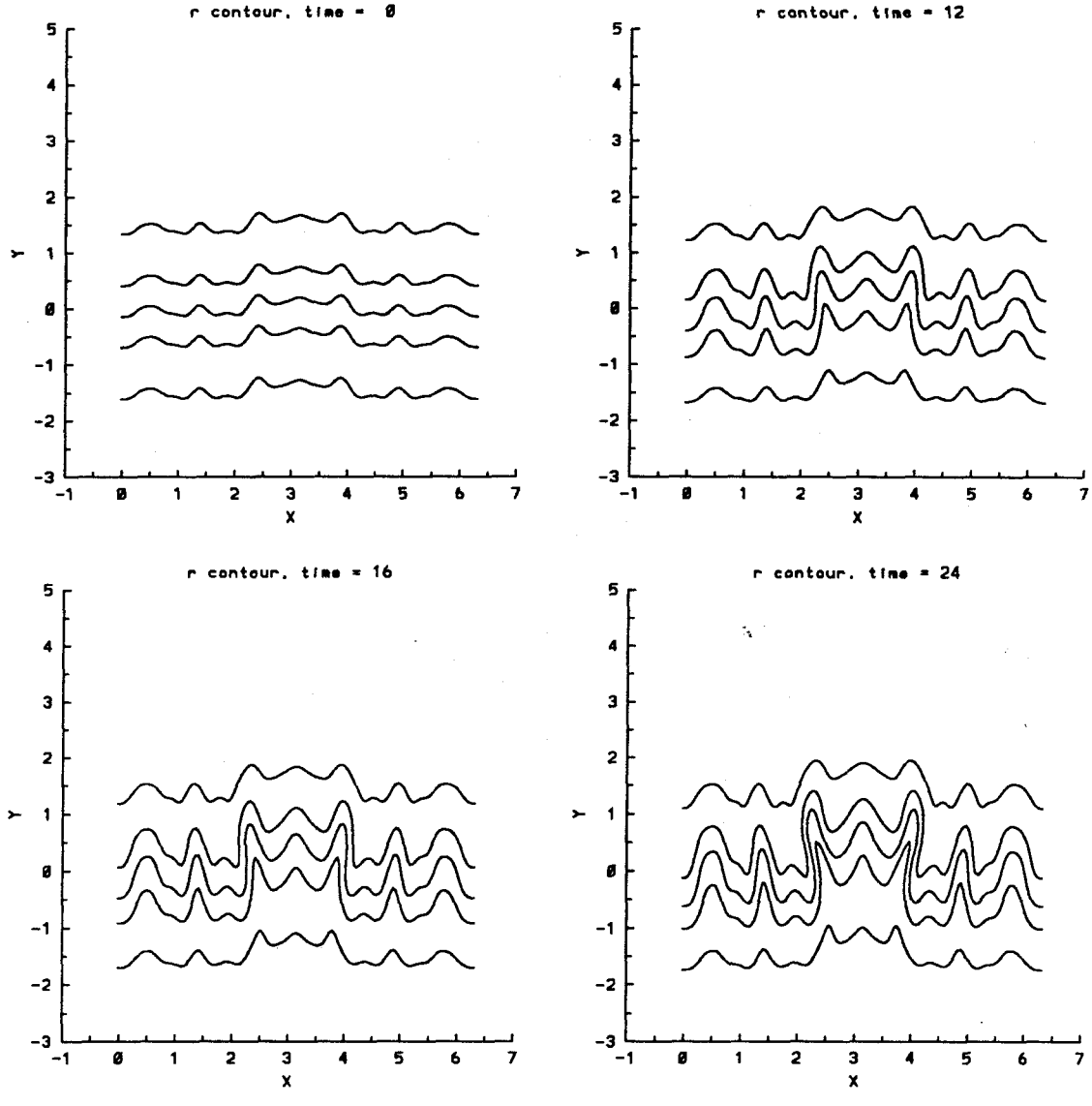

Figure 4.38.3 Time evolution of the density contours for the third initial random profile, A = -0.2, t = 0, 12, 16, 24. The contours are at ρ = 0.41, 0.45, 0.50, 0.55, 0.59.

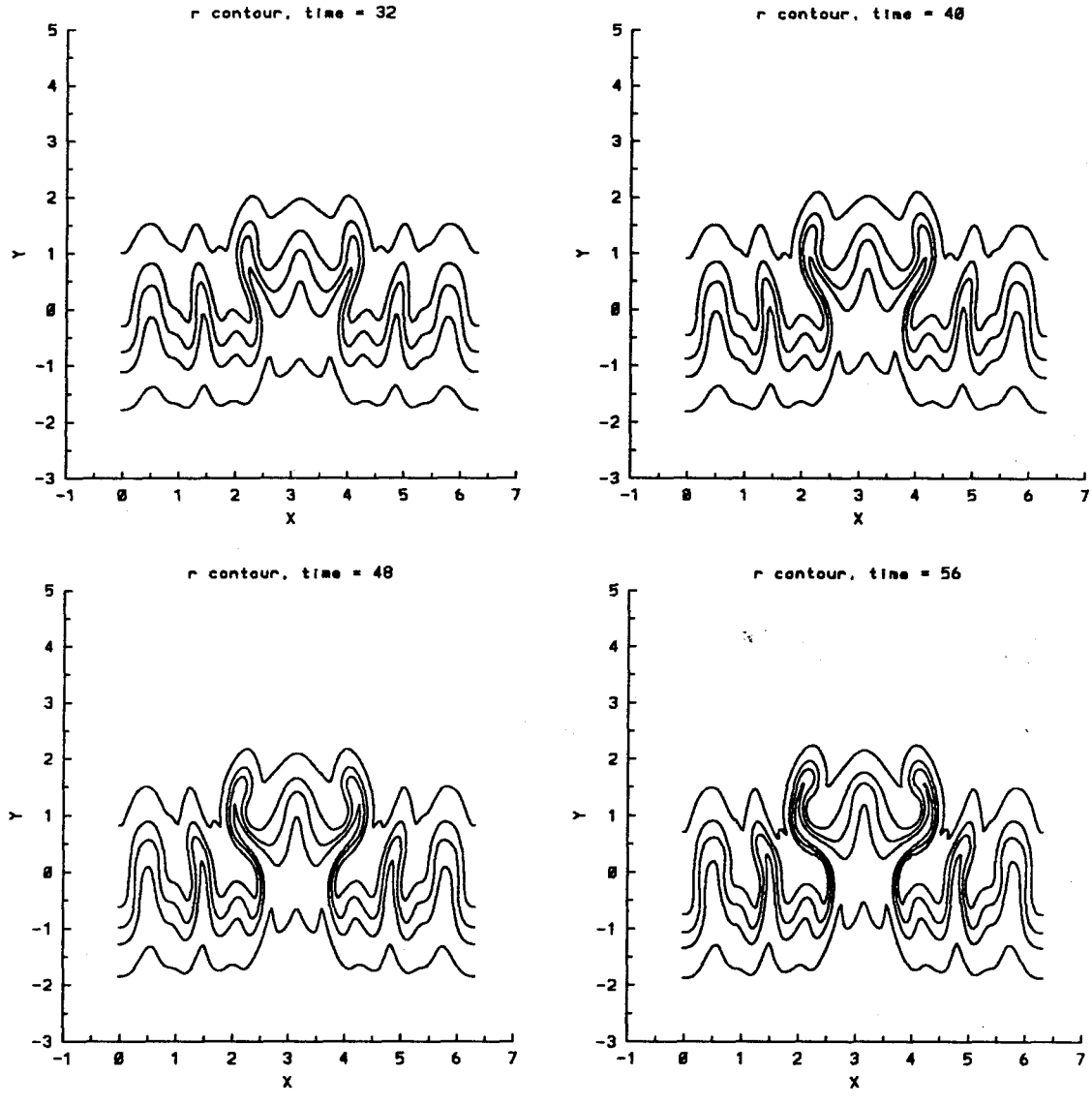

Figure 4.38.4 Time evolution of the density contours for the third initial random profile, A = -0.2, $t = 32, 40, 48, 56$. The contours are at $\rho = 0.41, 0.45, 0.50, 0.55, 0.59$.

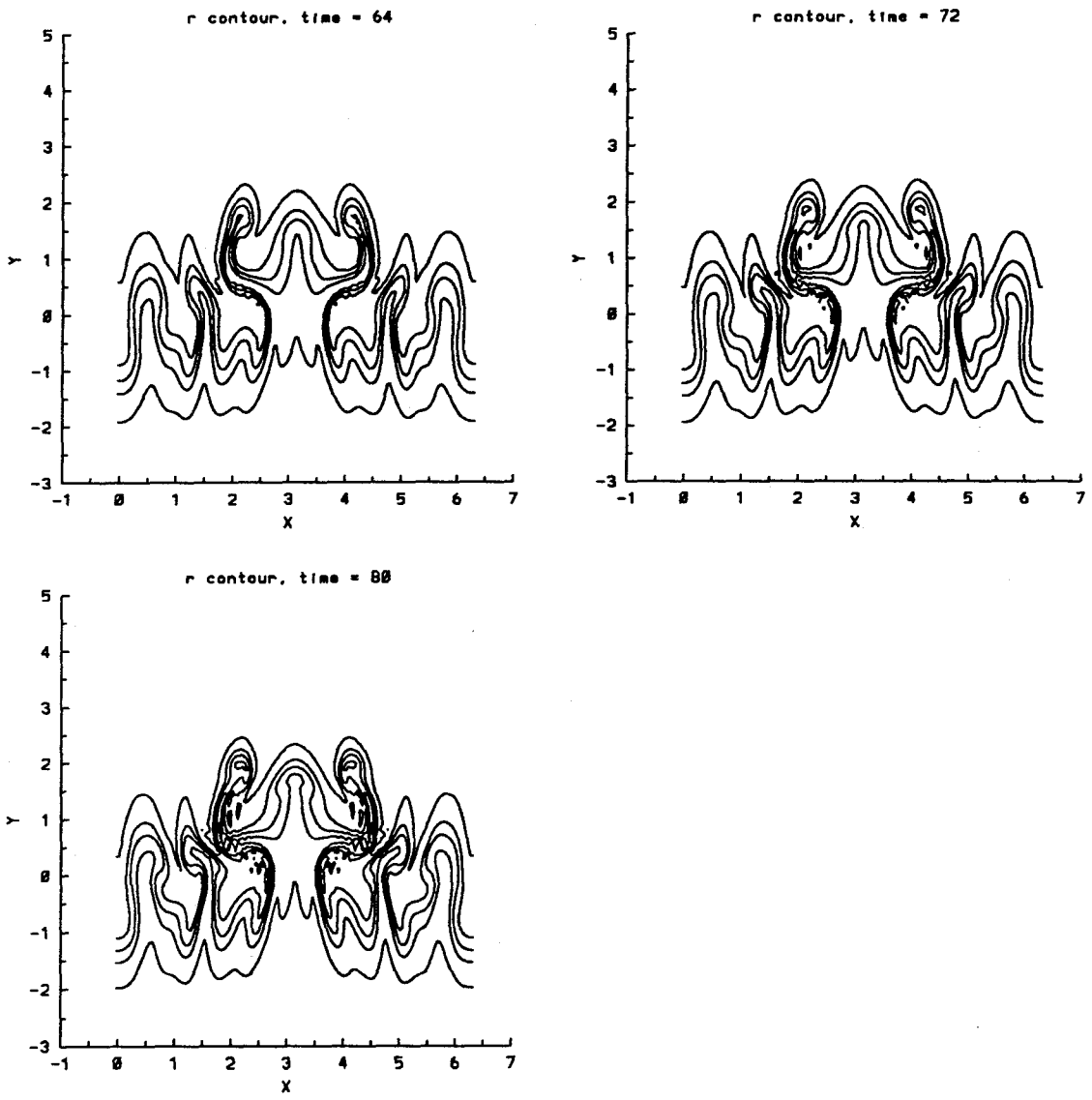

Figure 4.38.5 Time evolution of the density contours for the third initial random profile, A = −0.2, t = 64, 72, 80. The contours are at ρ = 0.41, 0.45, 0.50, 0.55, 0.59.

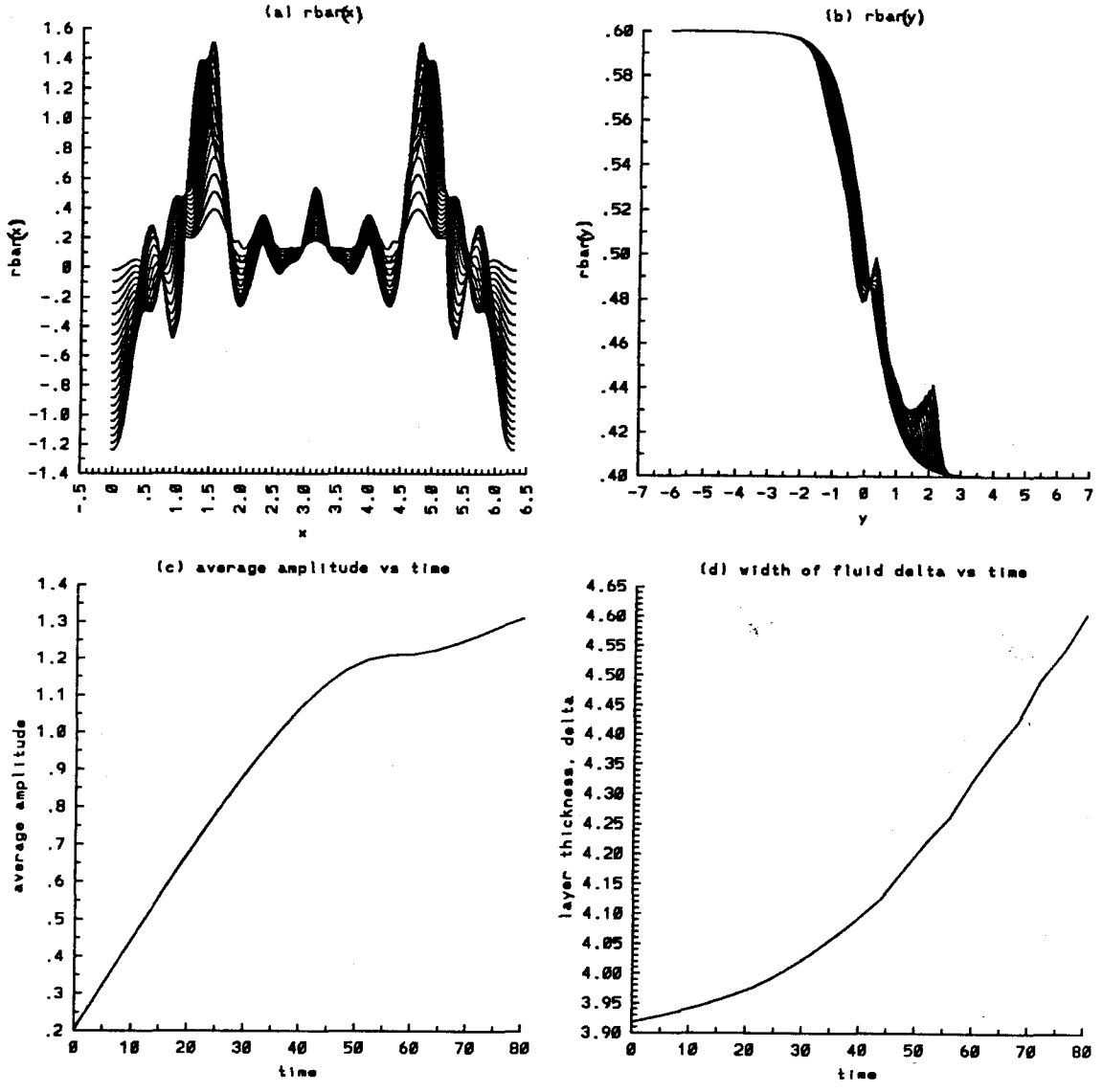

Figure 4.39.1 Time evolution of the average quantities for the fourth initial random profile, A = -0.2, $t = 0$ to 80 : a) $\bar{\rho}_y(x)$, b) $\bar{\rho}_x(y)$, c) average amplitude, and d) width of the density layer.

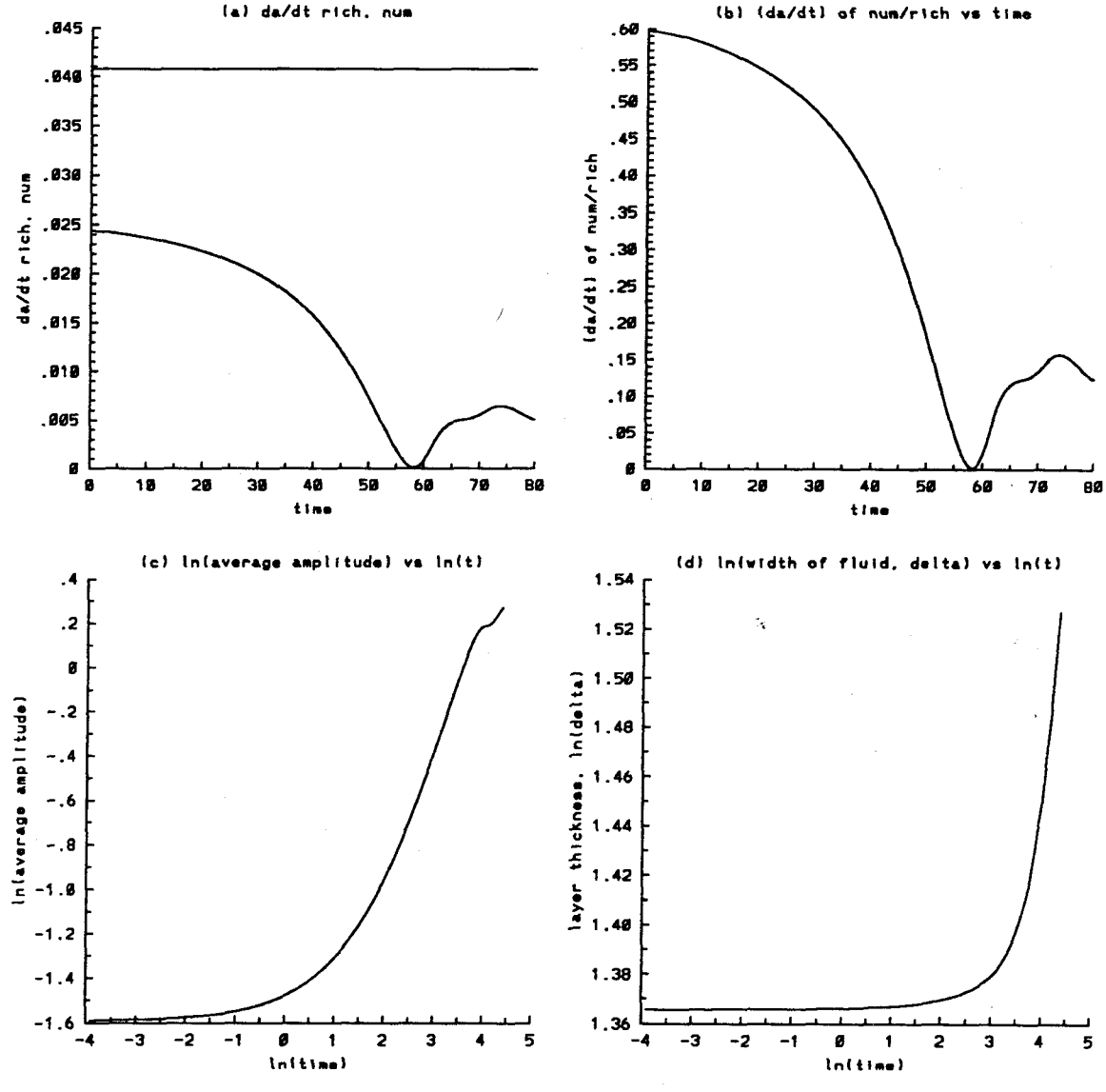

Figure 4.39.2 Time evolution of the average quantities for the fourth initial random profile, A = -0.2, $t = 0$ to 80 : a) growth rate da/dt of the average amplitude, numerical and Richtmyer theory (straight line), b) the ratio of the numerical growth rate da/dt over that predicted by Richtmyer theory, c) $\ln(a)$ *vs* $\ln(t)$, d) $\ln(\delta)$ *vs* $\ln(t)$.

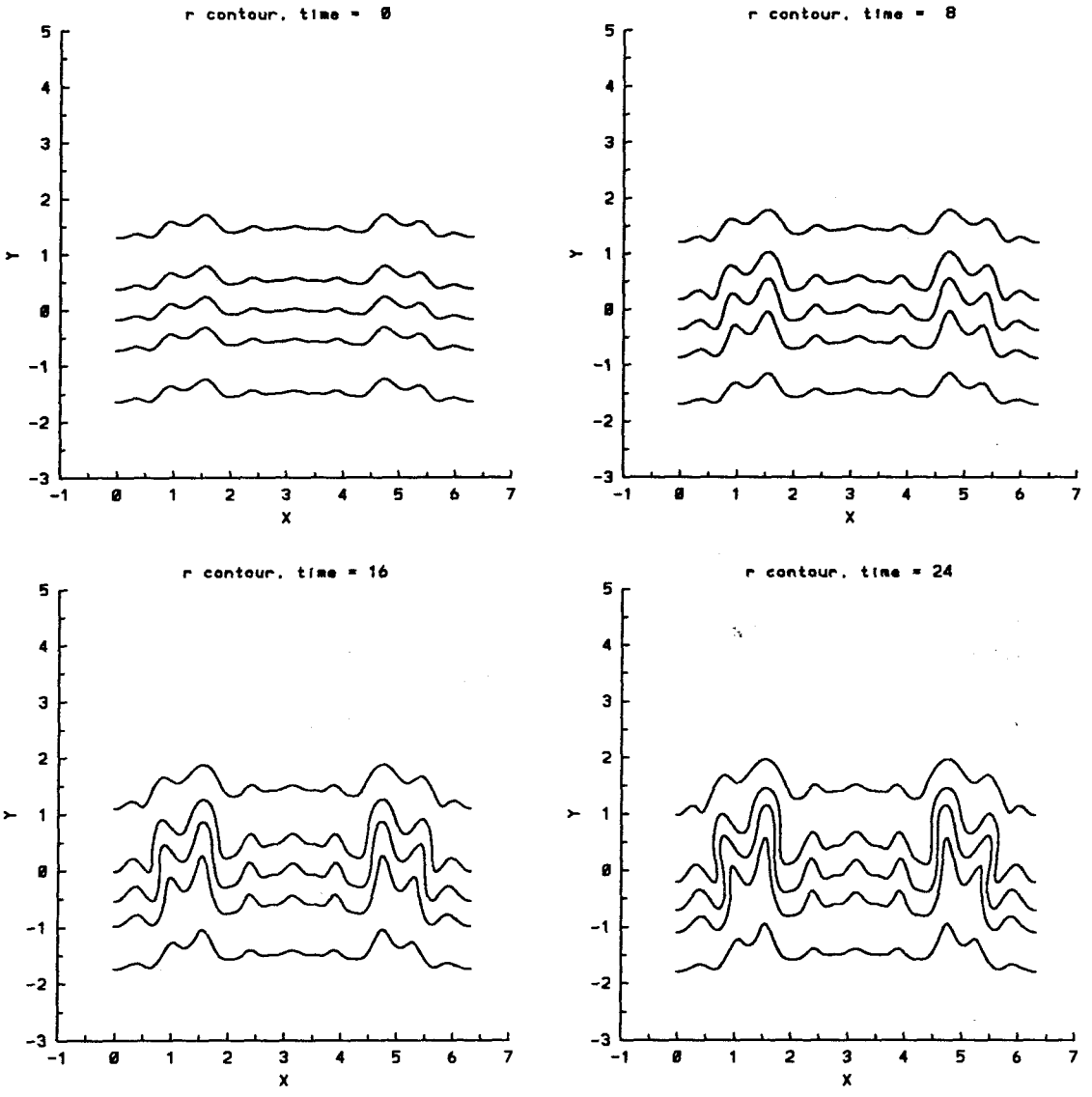

Figure 4.39.3 Time evolution of the density contours for the fourth initial random profile, A = −0.2, t = 0, 8, 16, 24. The contours are at ρ = 0.41, 0.45, 0.50, 0.55, 0.59.

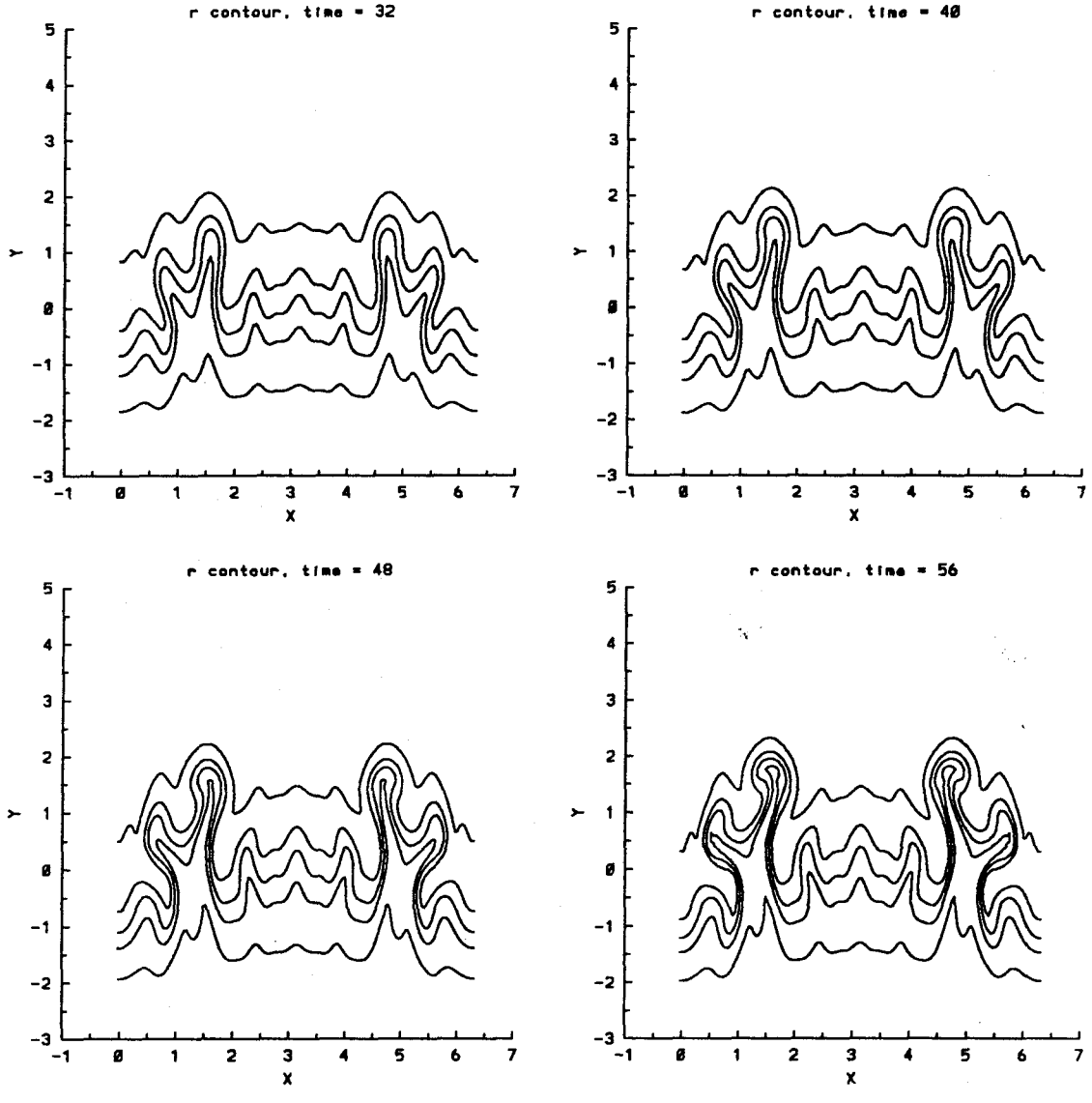

Figure 4.39.4 Time evolution of the density contours for the fourth initial random profile, A = -0.2, $t = 32, 40, 48, 56$. The contours are at $\rho = 0.41, 0.45, 0.50, 0.55, 0.59$.

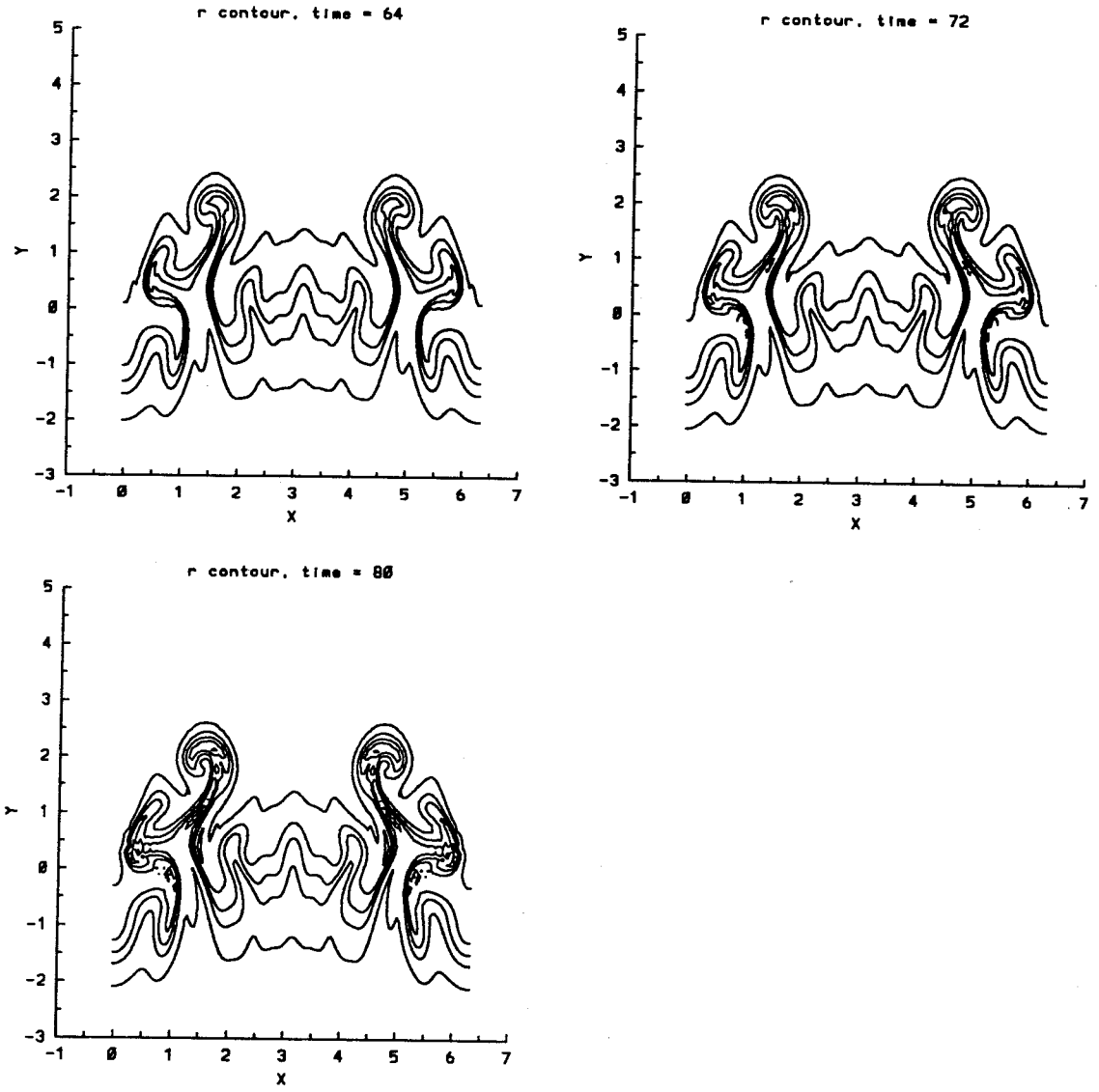

Figure 4.39.5 Time evolution of the density contours for the fourth initial random profile, A = −0.2, t = 64, 72, 80. The contours are at ρ = 0.41, 0.45, 0.50, 0.55, 0.59.

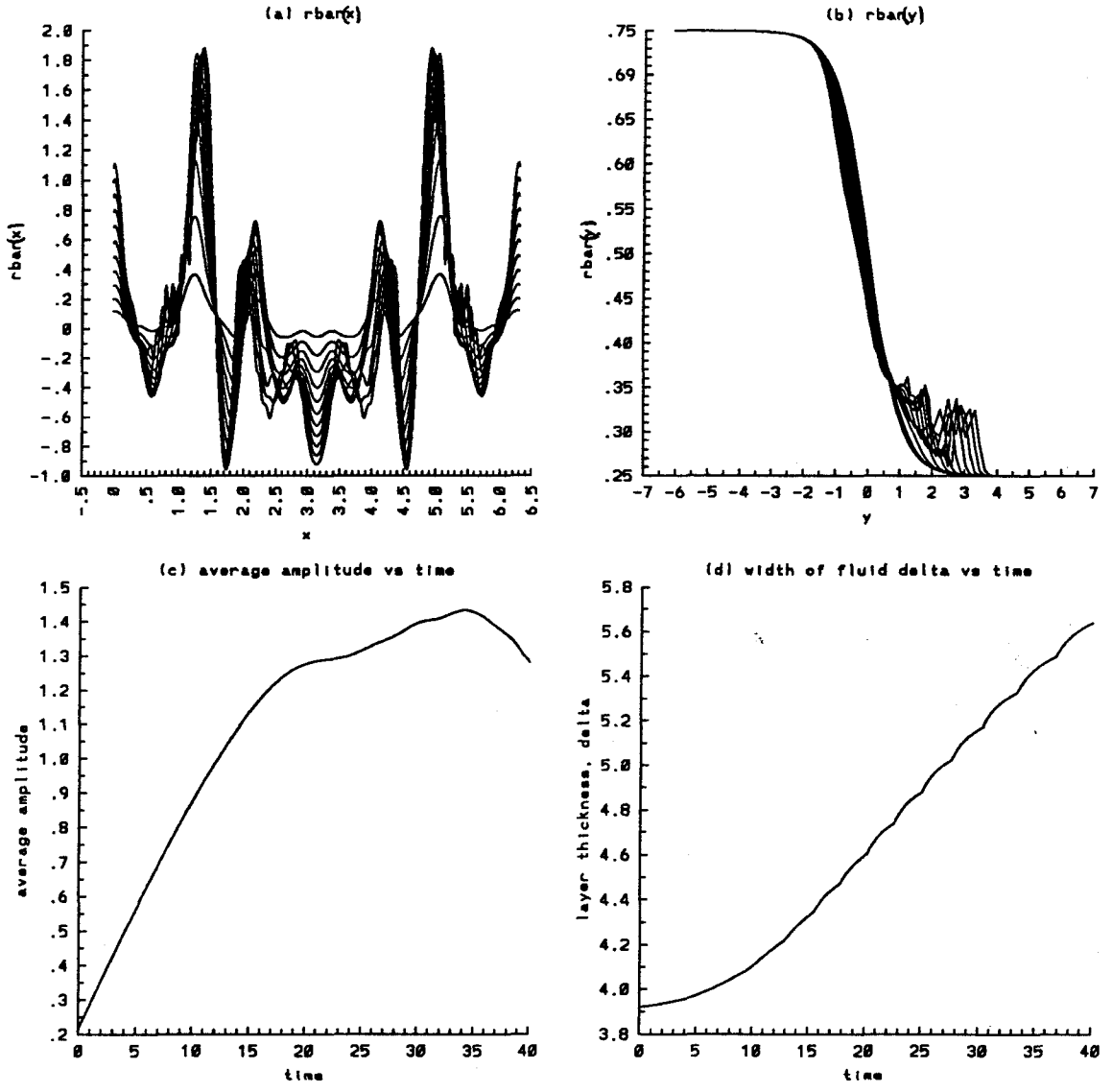

Figure 4.40.1 Time evolution of the average quantities for the first initial random profile, A = −0.5, t = 0 to 40 : a) $\bar{\rho}_y(x)$, b) $\bar{\rho}_x(y)$, c) average amplitude, and d) width of the density layer.

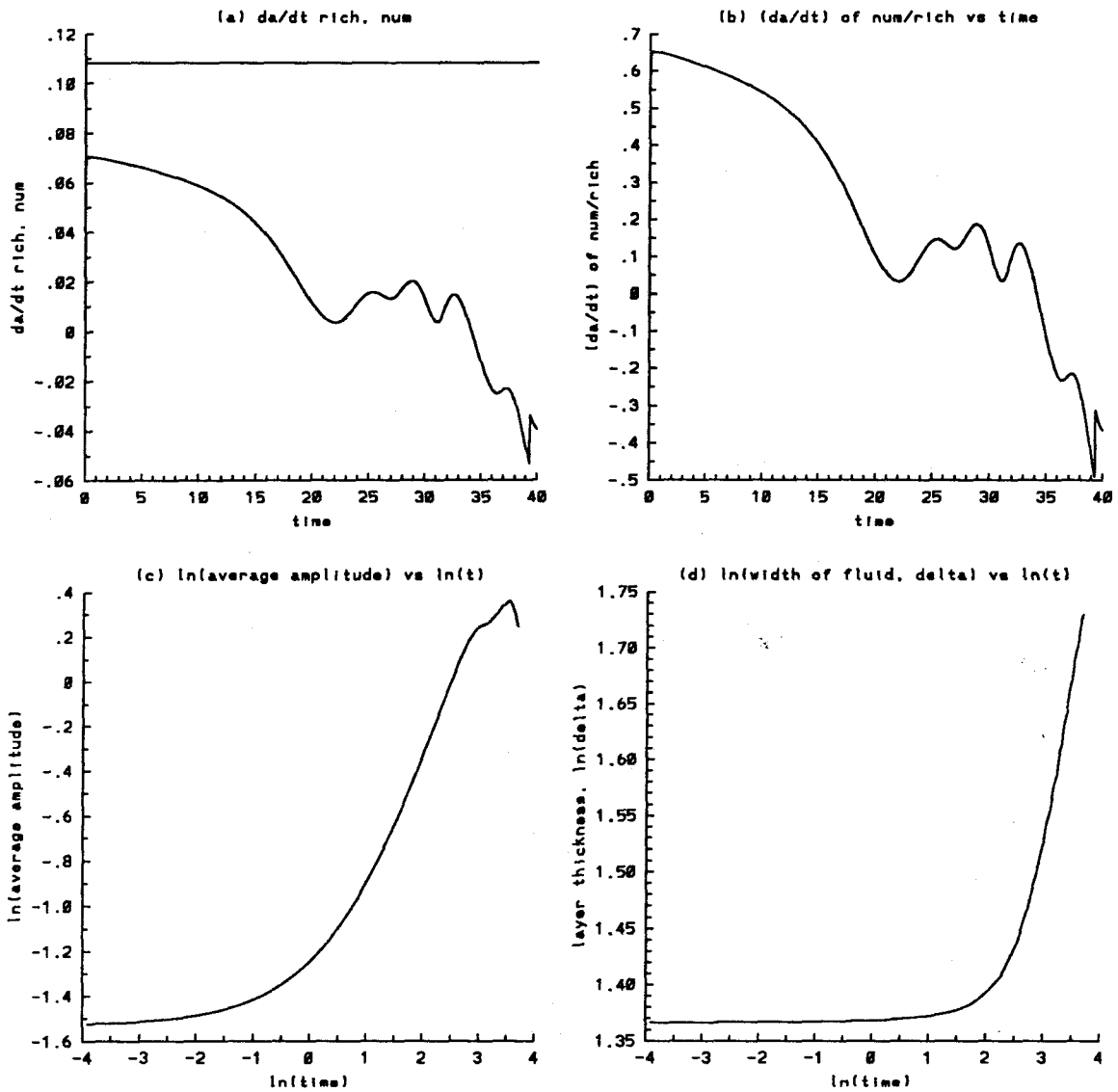

Figure 4.40.2 Time evolution of the average quantities for the first initial random profile, A = -0.5, $t = 0$ to 40 : a) growth rate da/dt of the average amplitude, numerical and Richtmyer theory (straight line), b) the ratio of the numerical growth rate da/dt over that predicted by Richtmyer theory, c) $\ln(a)$ *vs* $\ln(t)$, d) $\ln(\delta)$ *vs* $\ln(t)$.

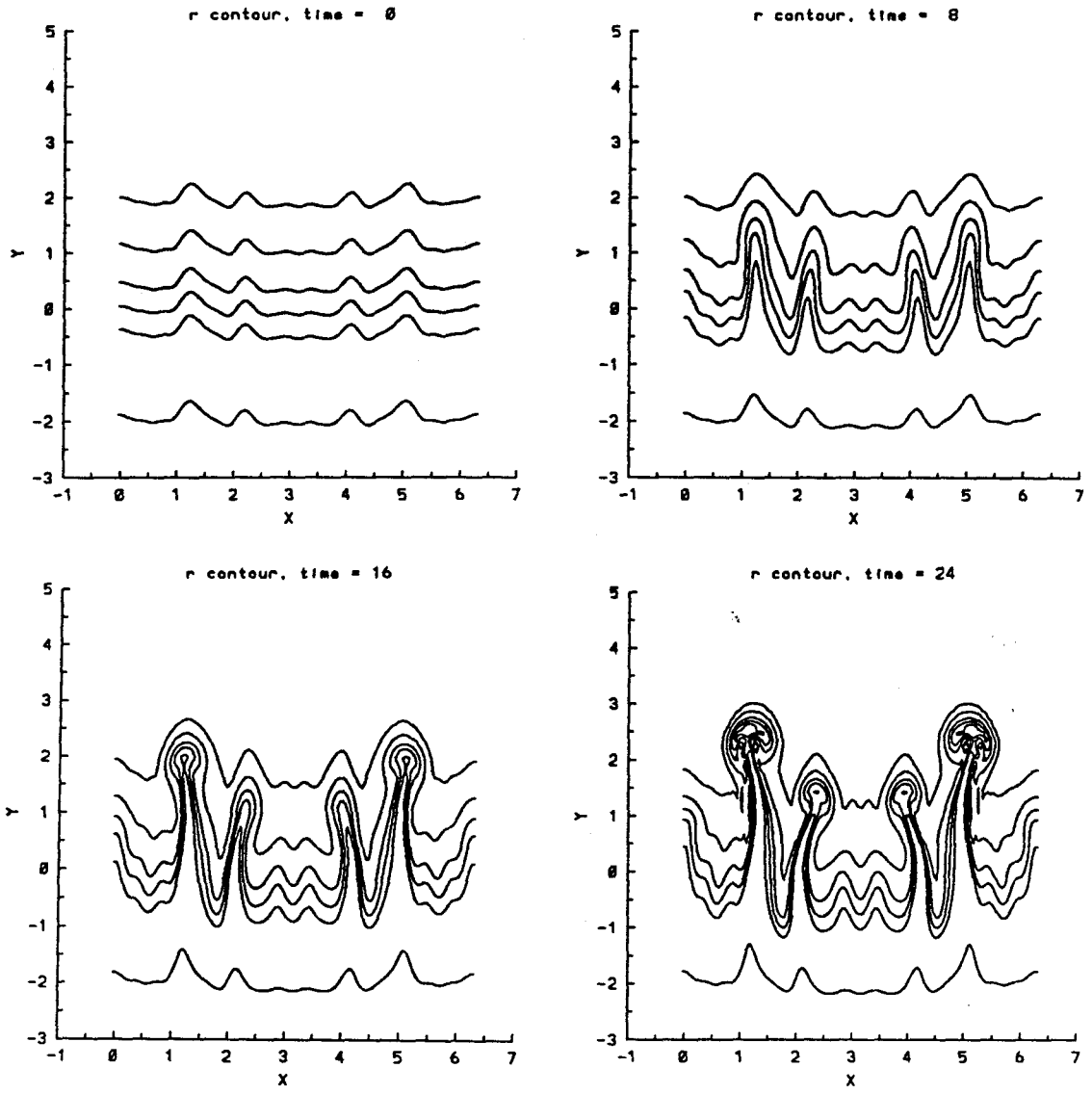

Figure 4.40.3 Time evolution of the density contours for the first initial random profile, A = −0.5, t = 0, 8, 16, 24. The contours are at ρ = 0.26, 0.3, 0.4, 0.5, 0.6, 0.74.

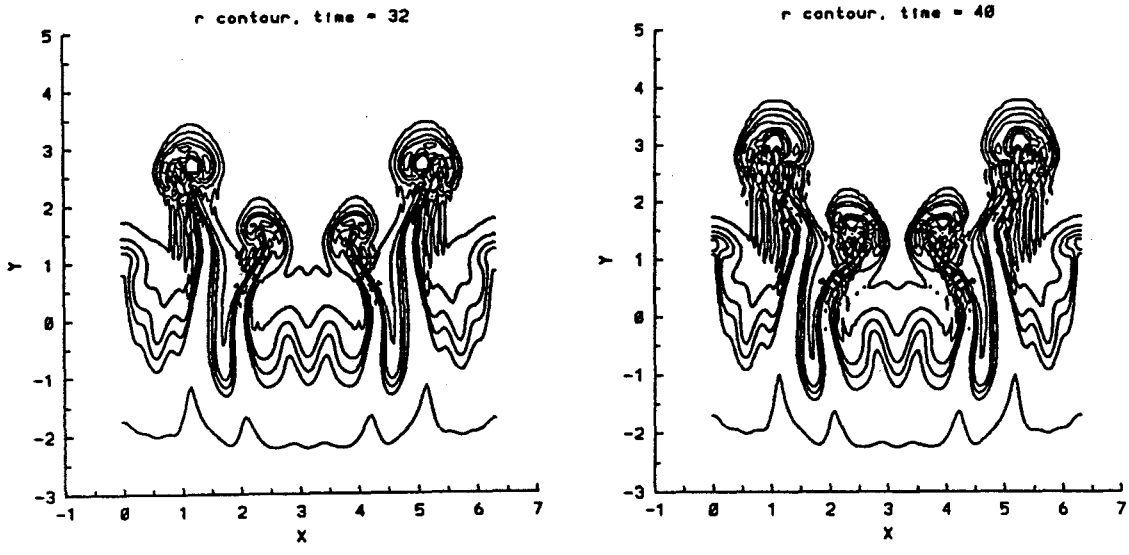

Figure 4.40.4 Time evolution of the density contours for the first initial random profile, A = -0.5, $t = 32$, 40. The contours are at $\rho = 0.26$, 0.3, 0.4, 0.5, 0.6, 0.74.

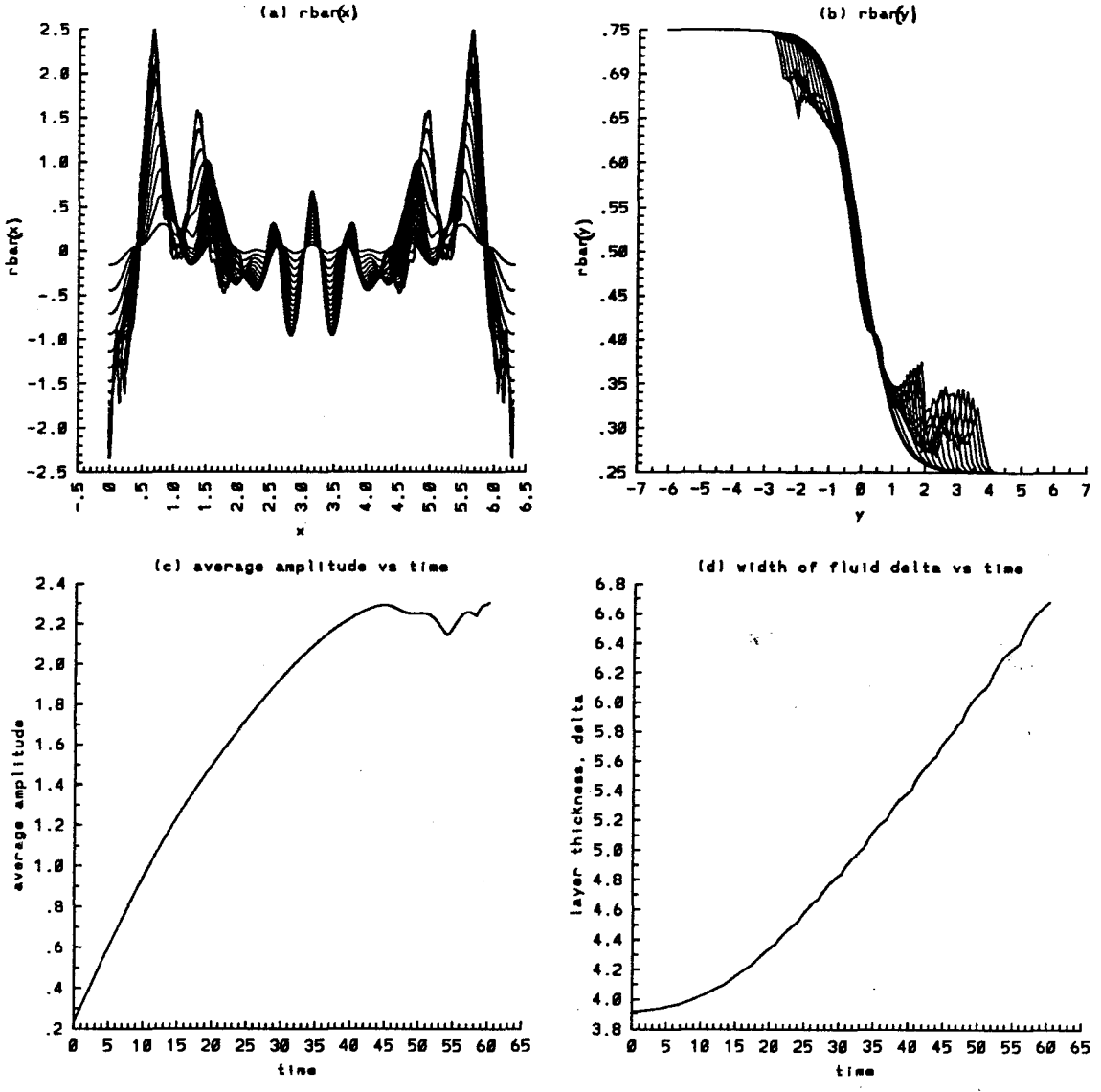

Figure 4.41.1 Time evolution of the average quantities for the second initial random profile, A = −0.5, t = 0 to 56 : a) $\bar{\rho}_y(x)$, b) $\bar{\rho}_x(y)$, c) average amplitude, and d) width of the density layer.

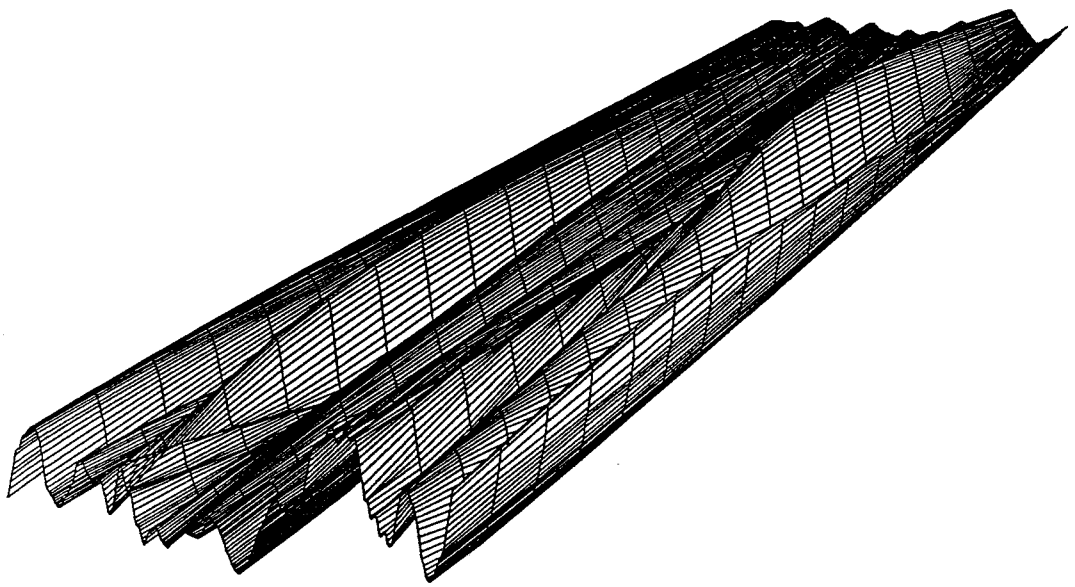

Figure 4.41.1a Three-dimensional surface of $\bar{\rho}_y(x,t)$ for the second initial random profile, A $= -0.5$ and $t = 0$, 60.

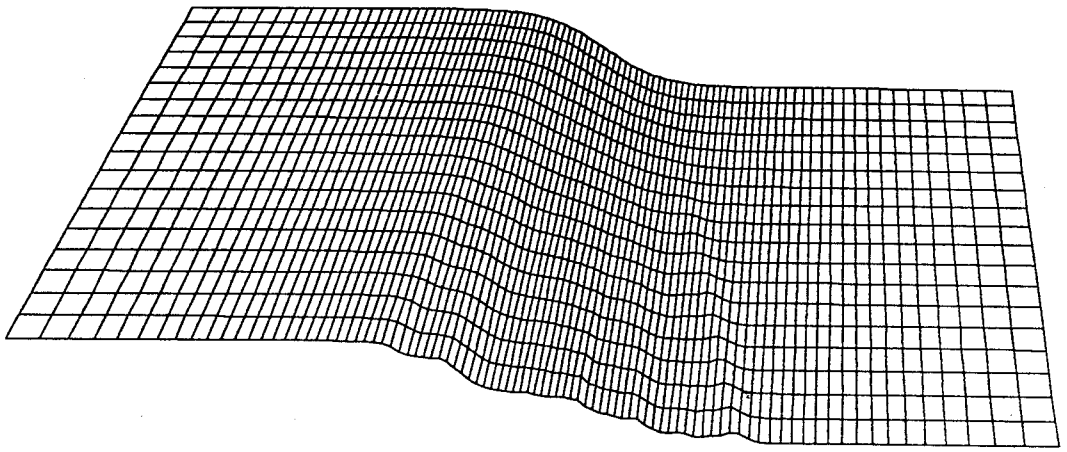

Figure 4.41.1b Three-dimensional surface of $\bar{\rho}_x(y,t)$ for the second initial random profile, A $= -0.5$ and $t = 0$, 60.

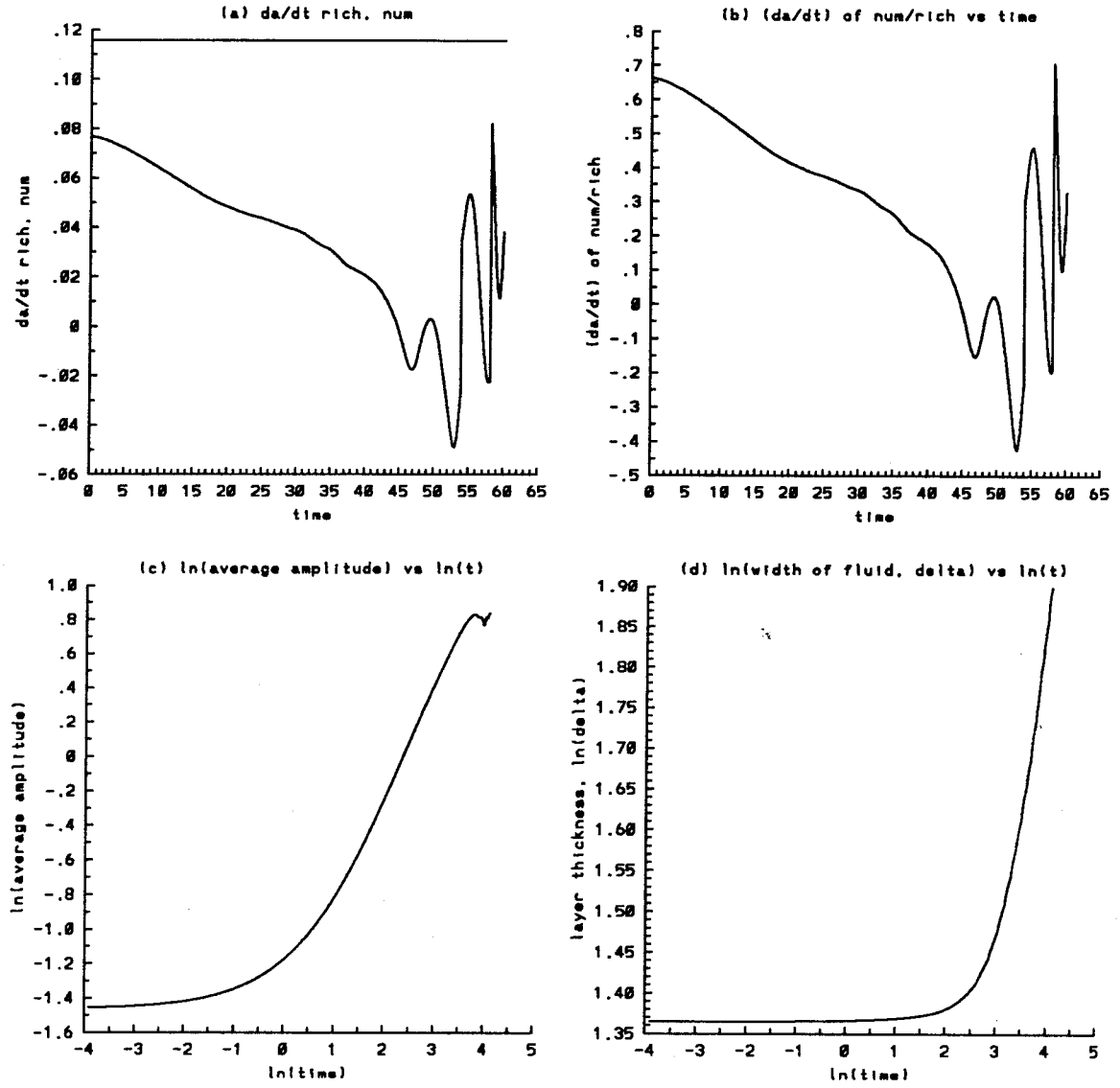

Figure 4.41.2 Time evolution of the average quantities for the second initial random profile, A = -0.5, $t = 0$ to 60 : a) growth rate da/dt of the average amplitude, numerical and Richtmyer theory (straight line), b) the ratio of the numerical growth rate da/dt over that predicted by Richtmyer theory, c) $\ln(a)$ *vs* $\ln(t)$, d) $\ln(\delta)$ *vs* $\ln(t)$.

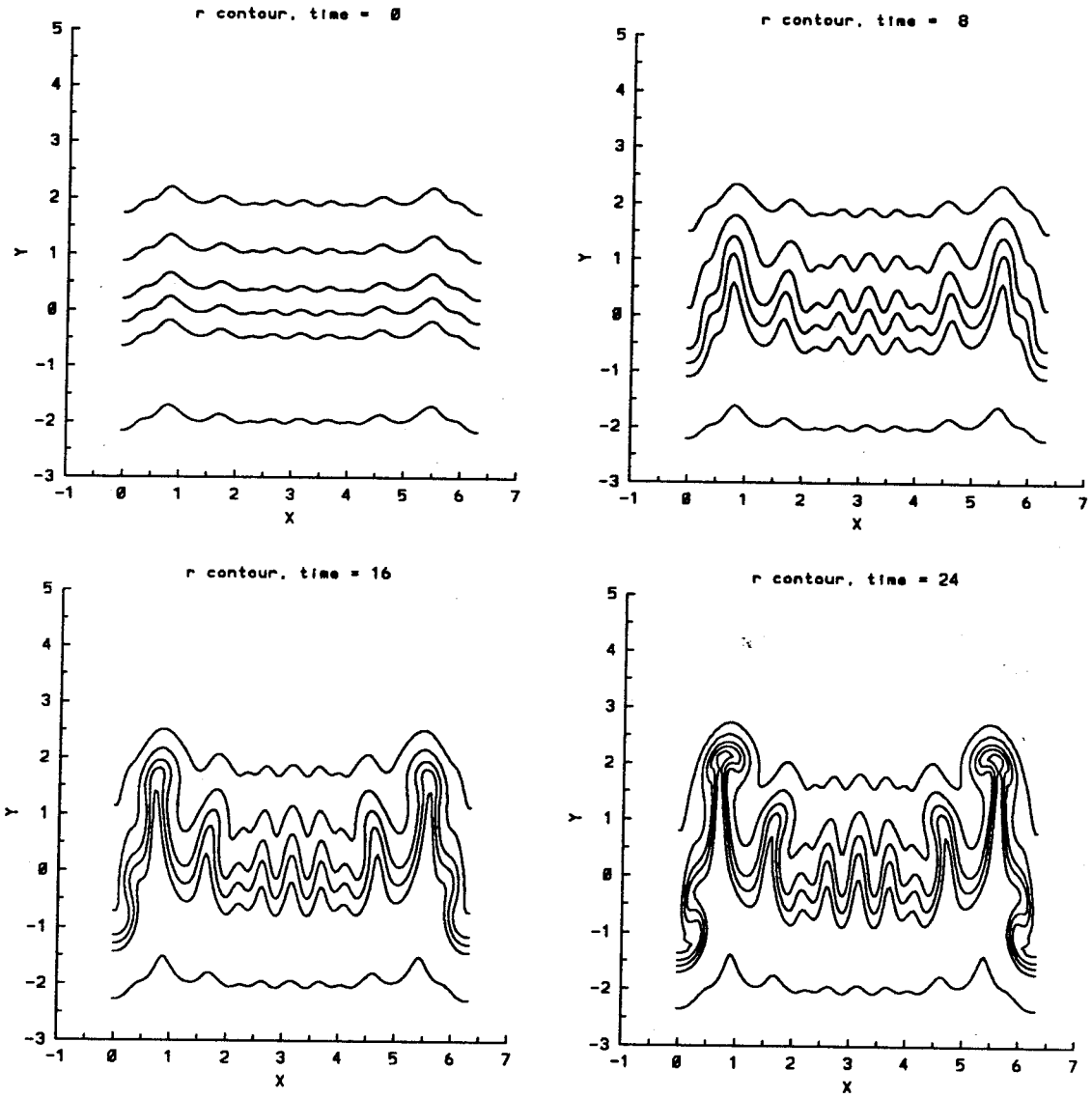

Figure 4.41.3 Time evolution of the density contours for the second initial random profile, A = −0.5, t = 0, 8, 16, 24. The contours are at ρ = 0.26, 0.3, 0.4, 0.5, 0.6, 0.74.

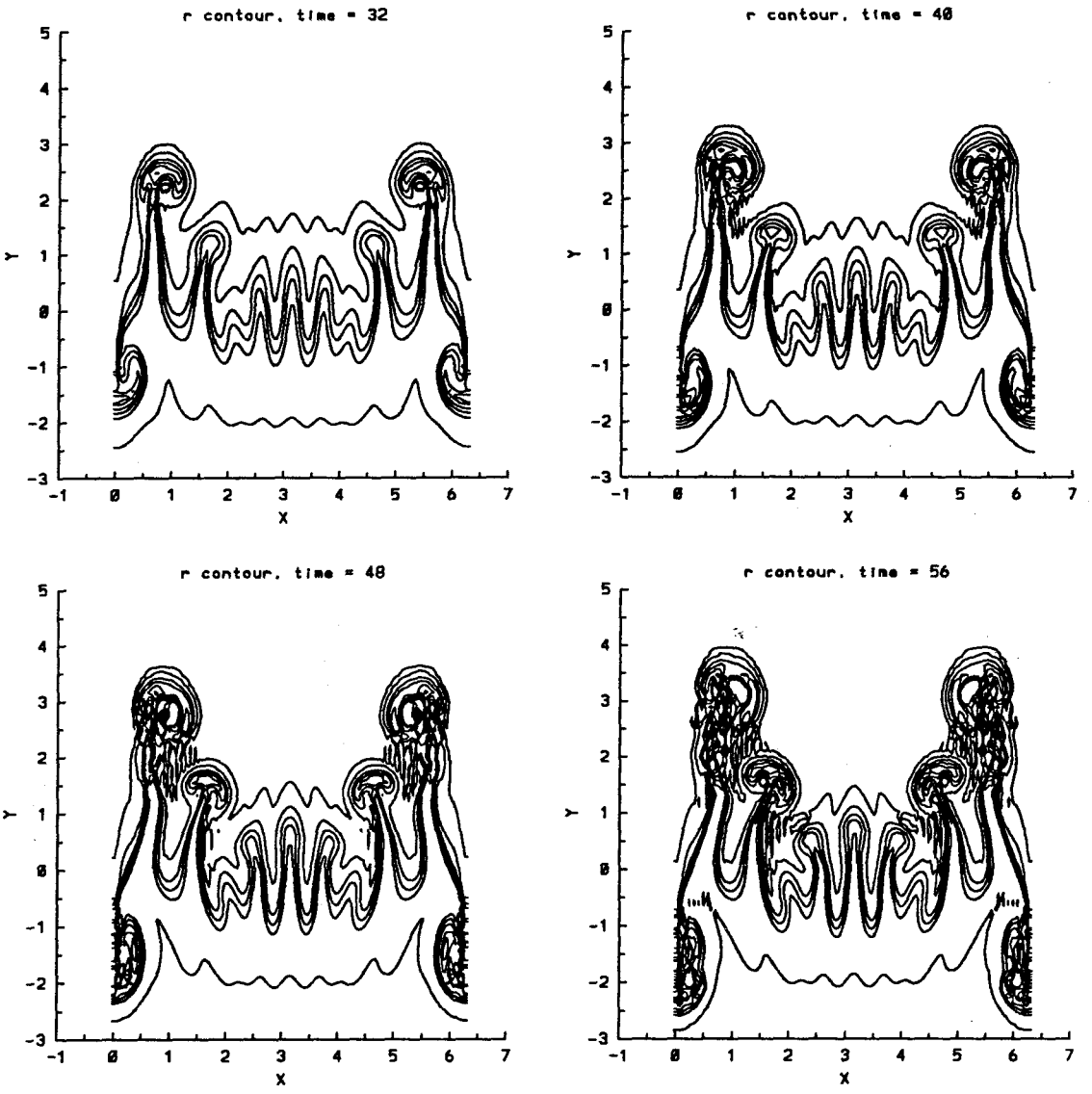

Figure 4.41.4 Time evolution of the density contours for the second initial random profile, A = −0.5, t = 32, 40, 48, 56. The contours are at ρ = 0.26, 0.3, 0.4, 0.5, 0.6, 0.74.

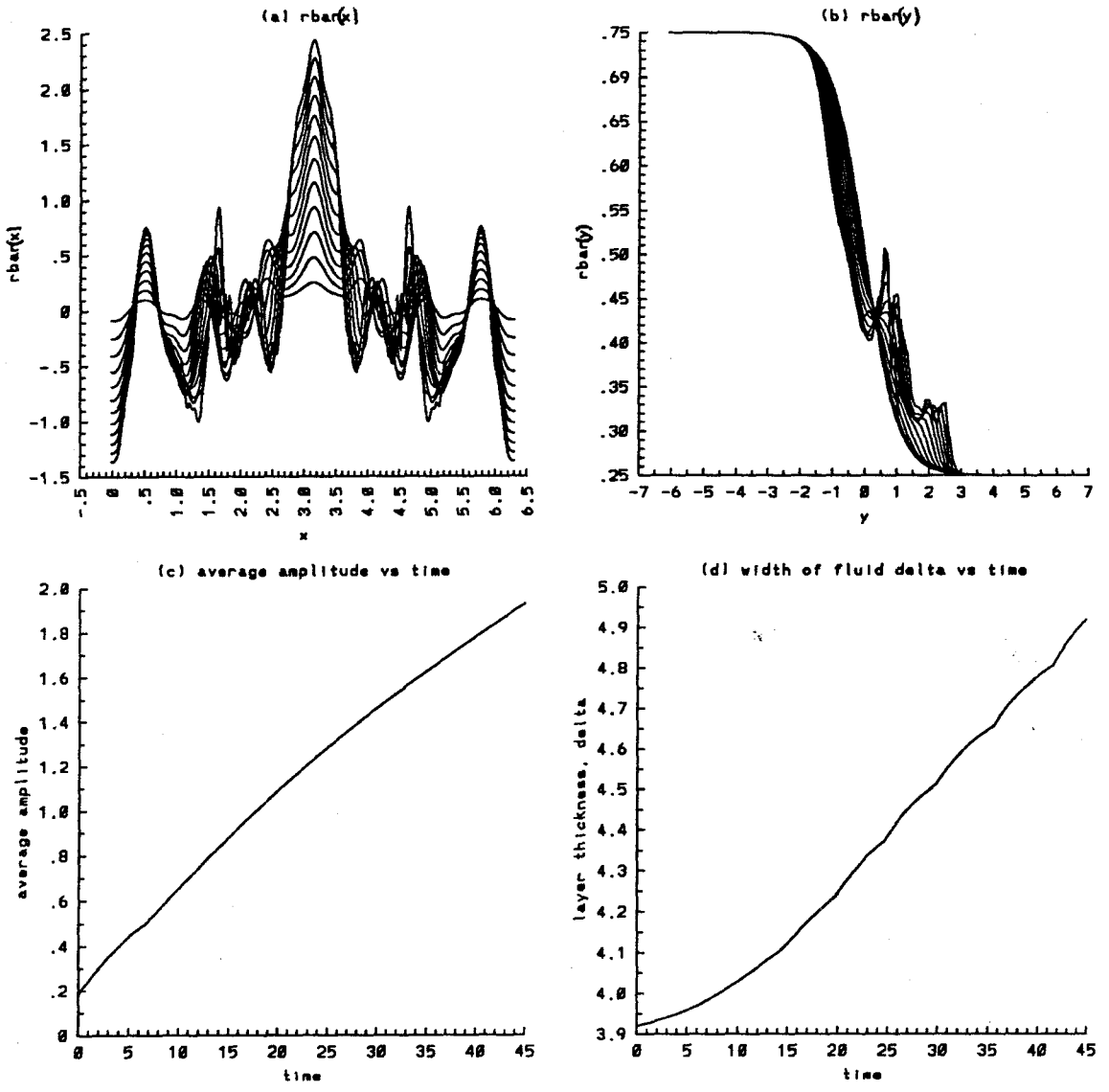

Figure 4.42.1 Time evolution of the average quantities for the third initial random profile, A = −0.5, t = 0 to 41 : a) $\bar{\rho}_y(x)$, b) $\bar{\rho}_x(y)$, c) average amplitude, and d) width of the density layer.

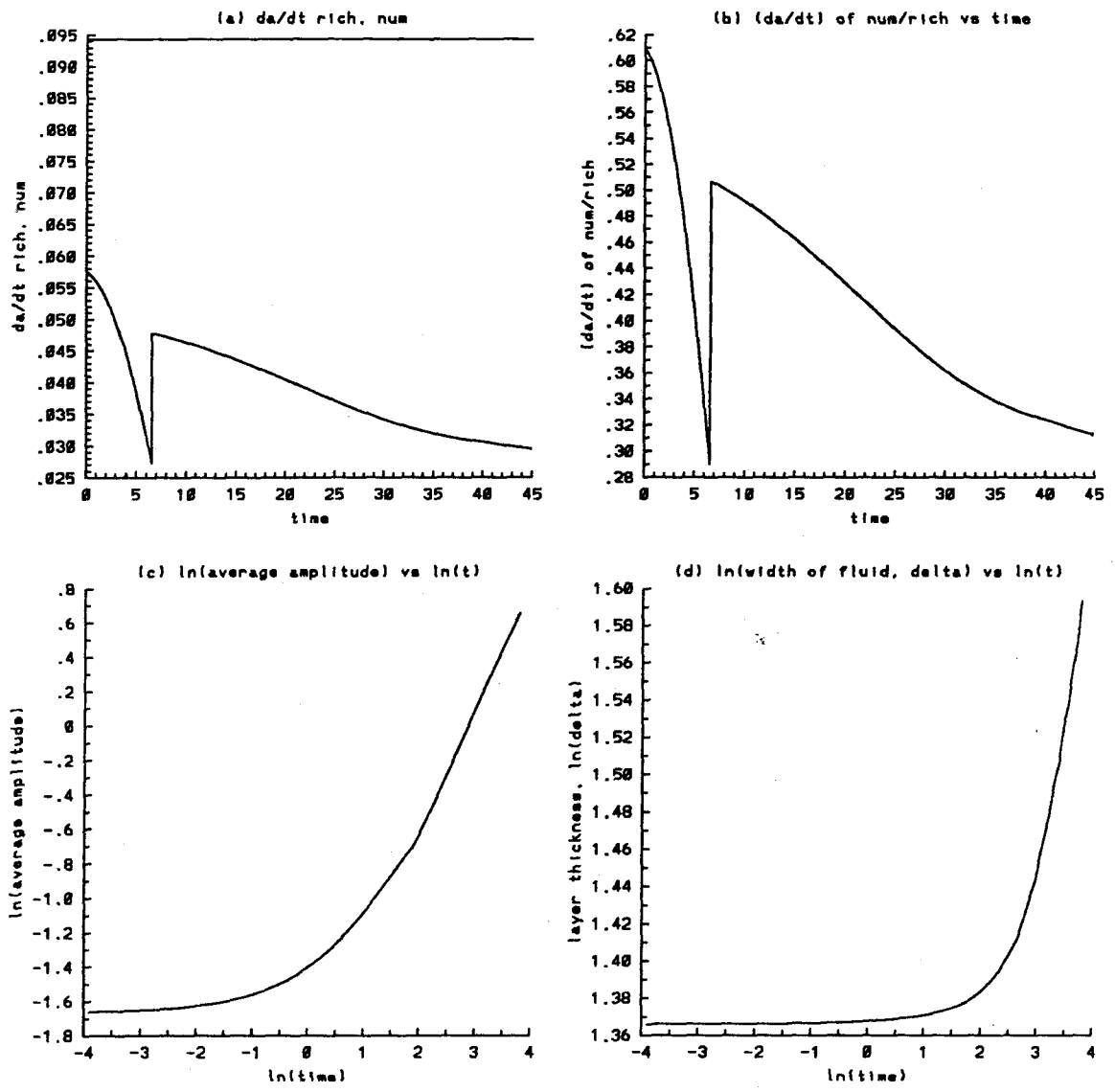

Figure 4.42.2 Time evolution of the average quantities for the third initial random profile, A = −0.5, t = 0 to 42 : a) growth rate da/dt of the average amplitude, numerical and Richtmyer theory (straight line), b) the ratio of the numerical growth rate da/dt over that predicted by Richtmyer theory, c) $\ln(a)$ *vs* $\ln(t)$, d) $\ln(\delta)$ *vs* $\ln(t)$.

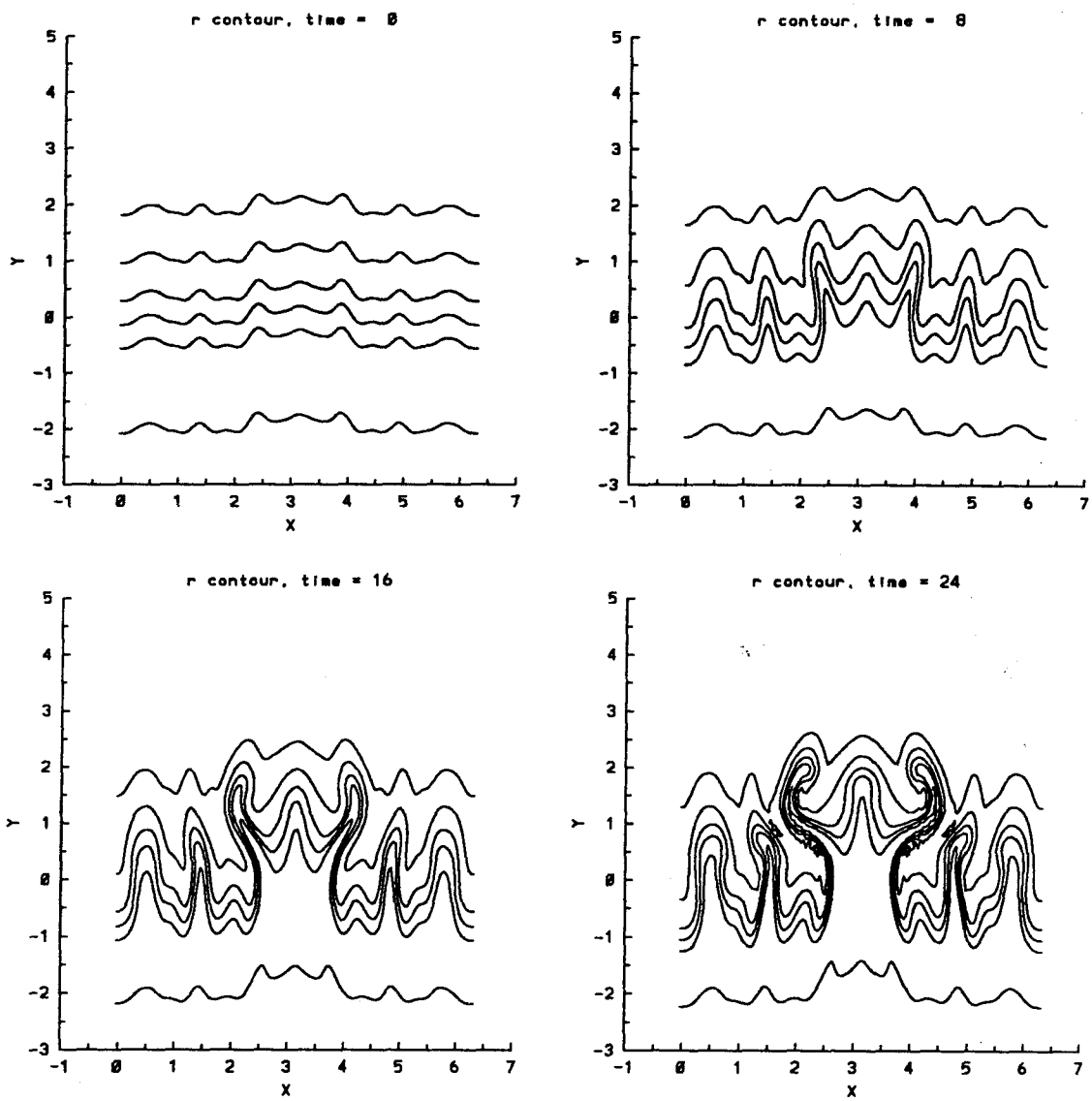

Figure 4.42.3 Time evolution of the density contours for the third initial random profile, A = -0.5, $t = 0$, 12, 16, 24. The contours are at $\rho = 0.26$, 0.3, 0.4, 0.5, 0.6, 0.74.

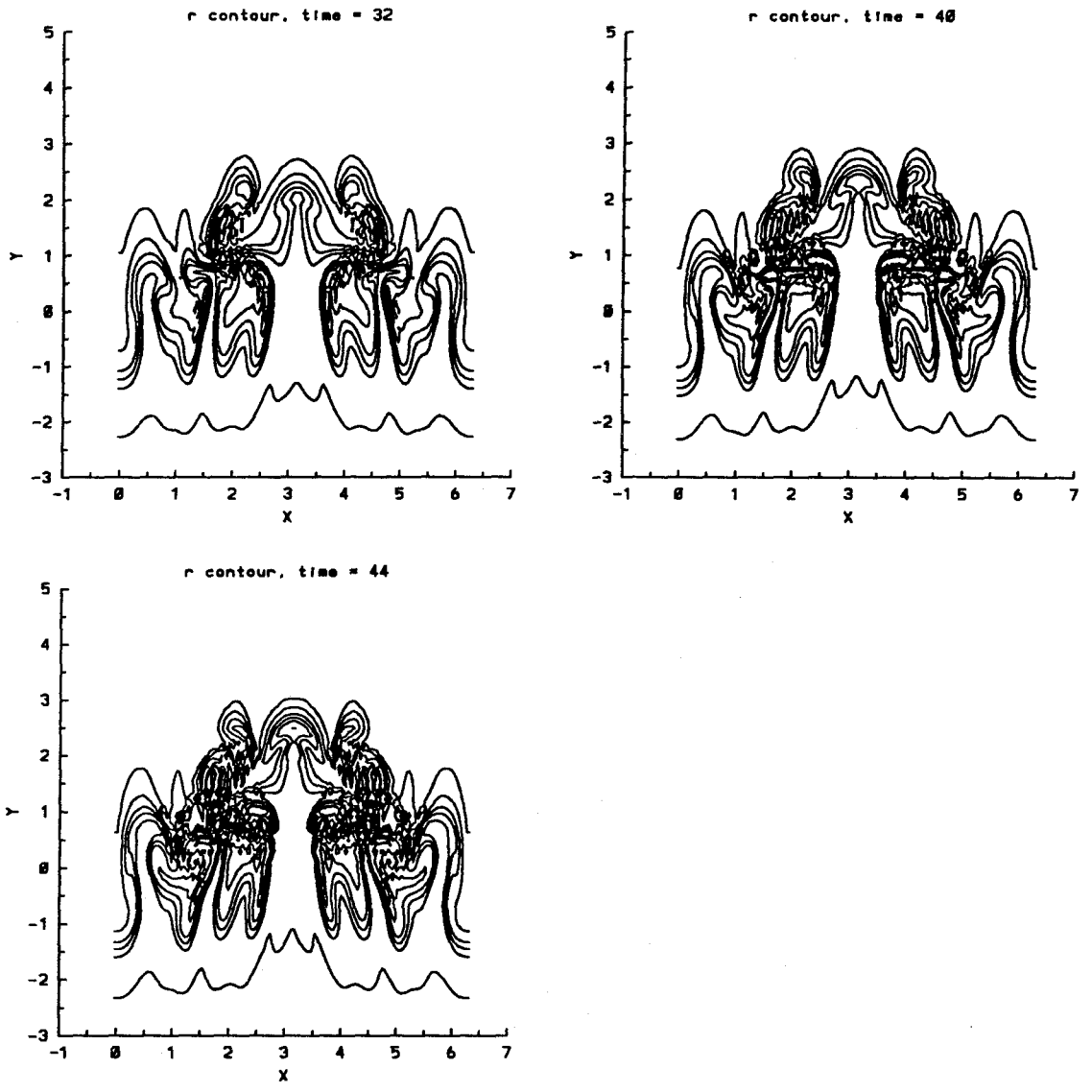

Figure 4.42.4 Time evolution of the density contours for the third initial random profile, A = −0.5, t = 32, 40, 44. The contours are at ρ = 0.26, 0.3, 0.4, 0.5, 0.6, 0.74.

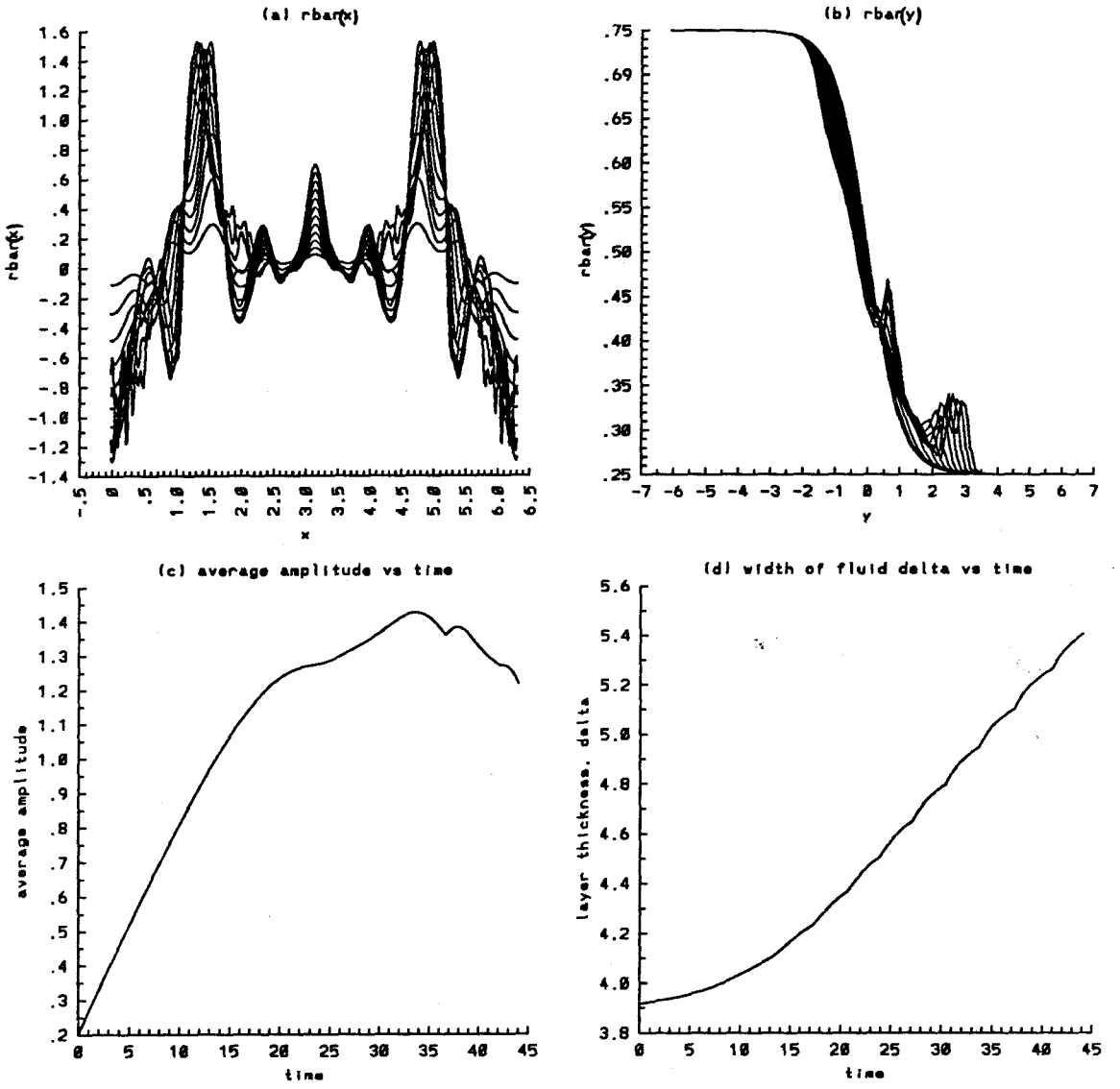

Figure 4.43.1 Time evolution of the average quantities for the fourth initial random profile, A = −0.5, t = 0 to 44 : a) $\bar{\rho}_y(x)$, b) $\bar{\rho}_x(y)$, c) average amplitude, and d) width of the density layer.

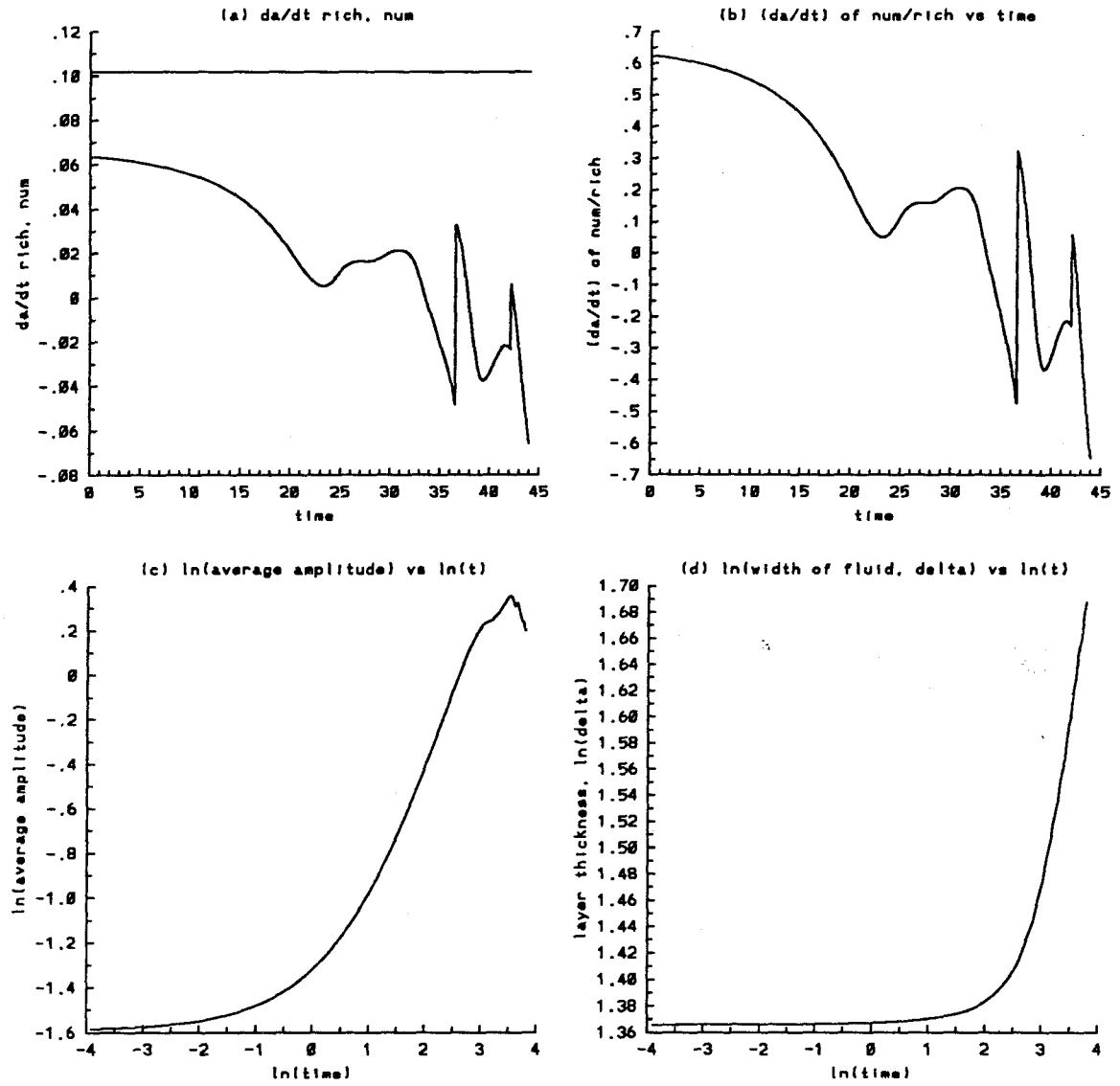

Figure 4.43.2 Time evolution of the average quantities for the fourth initial random profile, A = -0.5, $t = 0$ to 44 : a) growth rate da/dt of the average amplitude, numerical and Richtmyer theory (straight line), b) the ratio of the numerical growth rate da/dt over that predicted by Richtmyer theory, c) $\ln(a)$ *vs* $\ln(t)$, d) $\ln(\delta)$ *vs* $\ln(t)$.

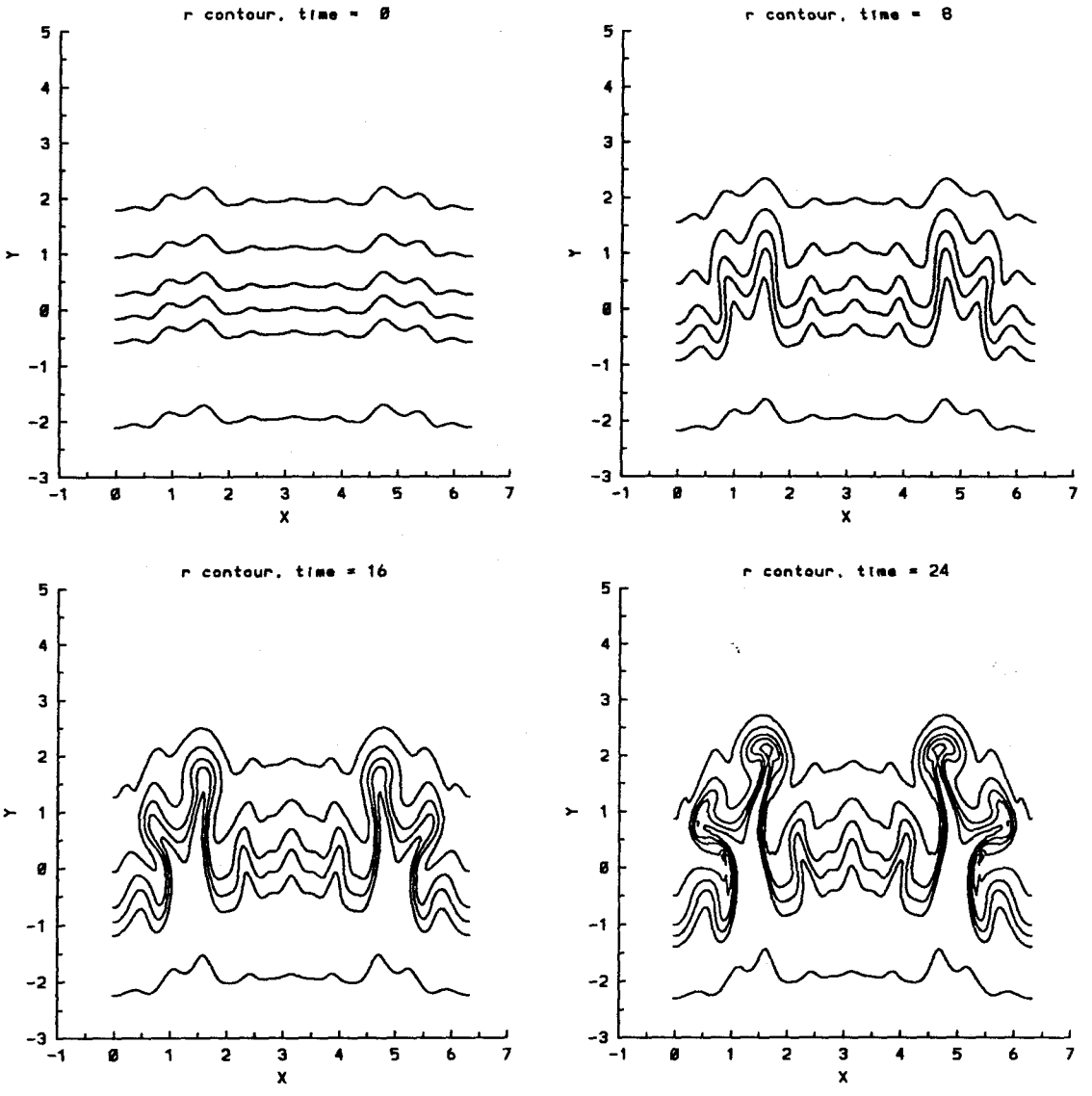

Figure 4.43.3 Time evolution of the density contours for the fourth initial random profile, A = −0.5, t = 0, 8, 16, 24. The contours are at ρ = 0.26, 0.3, 0.4, 0.5, 0.6, 0.74.

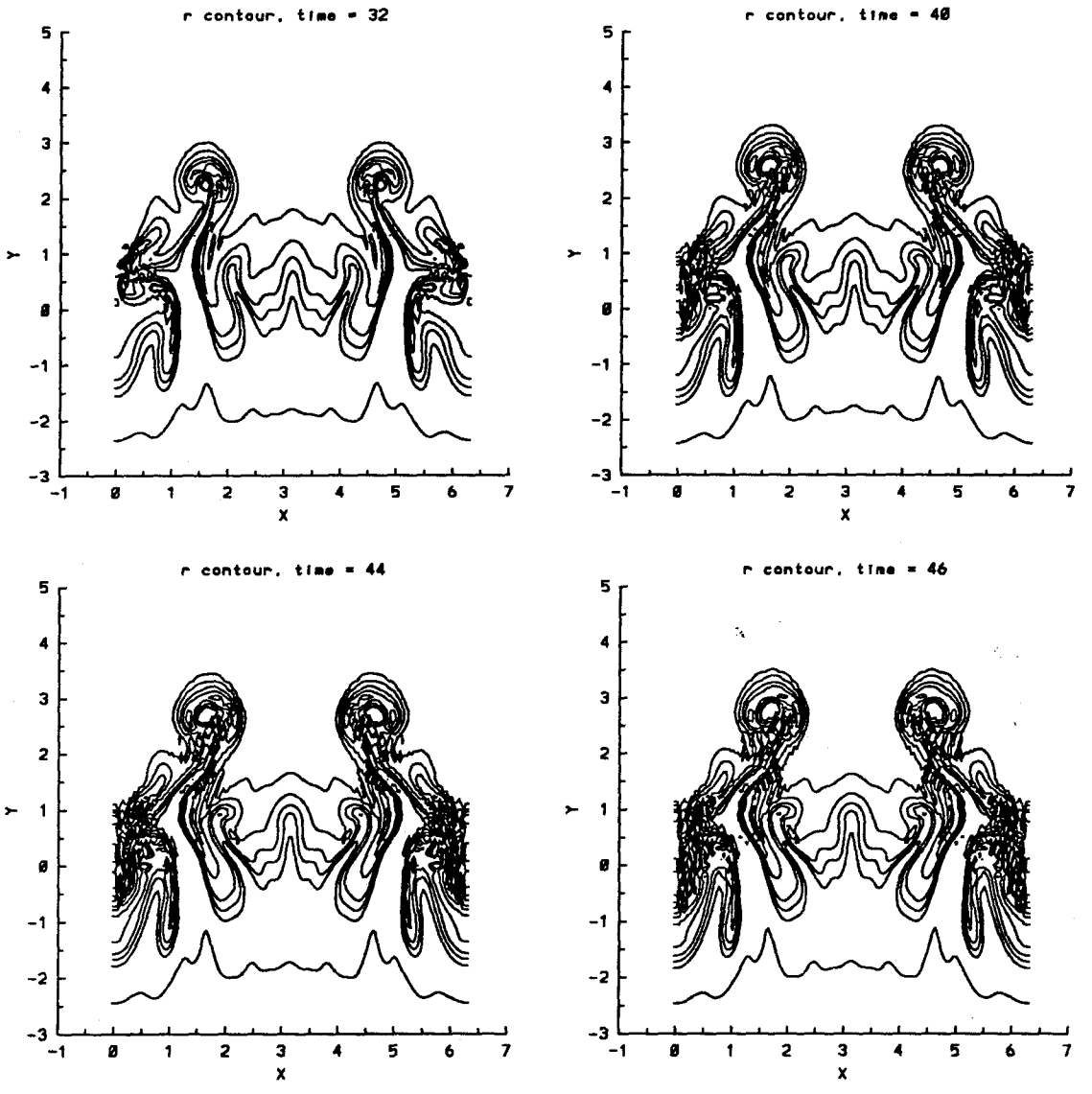

Figure 4.43.4 Time evolution of the density contours for the fourth initial random profile, A = −0.5, t = 32, 40, 44, 46. The contours are at ρ = 0.26, 0.3, 0.4, 0.5, 0.6, 0.74.

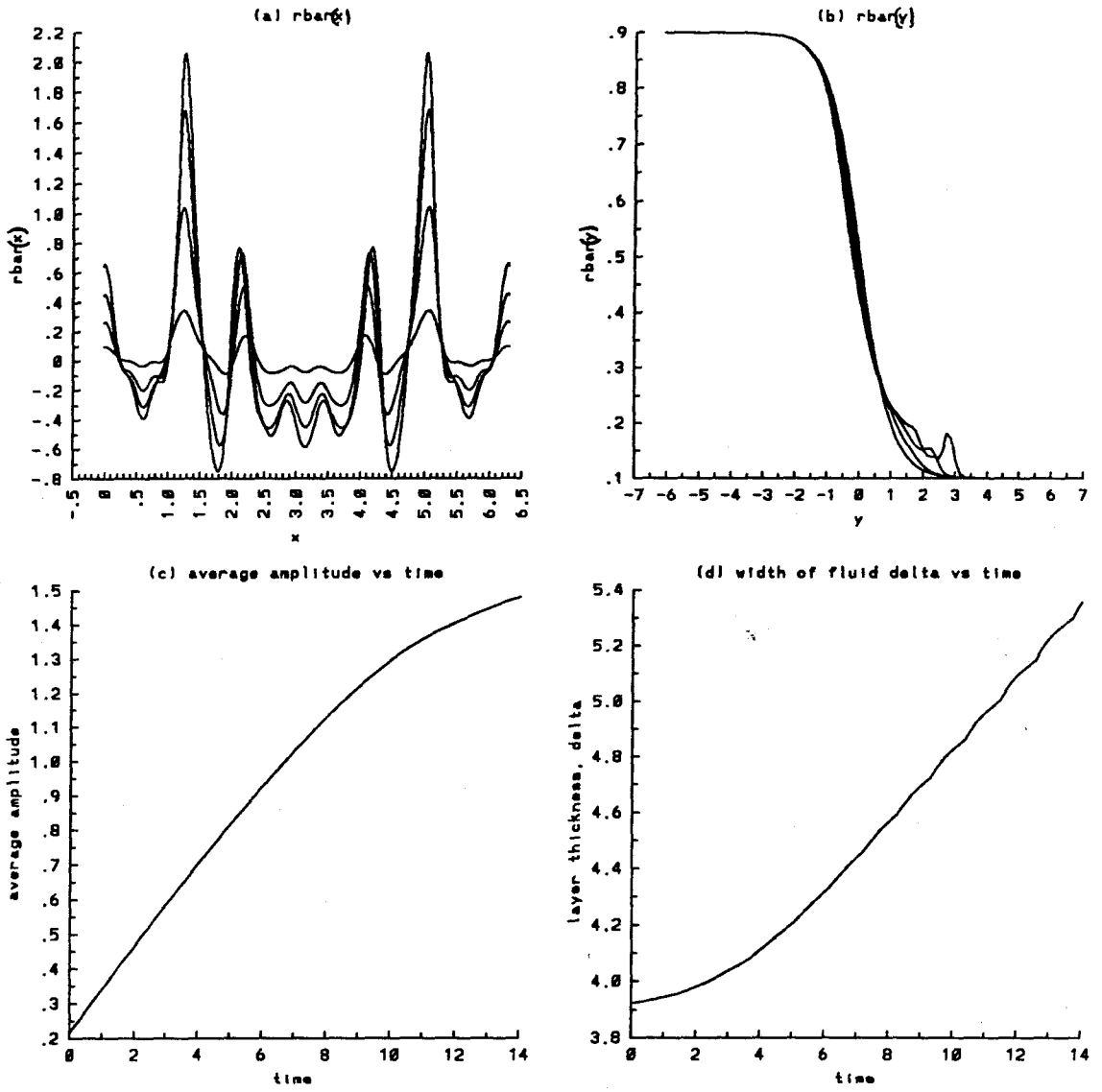

Figure 4.44.1 Time evolution of the average quantities for the first initial random profile, A = -0.8, $t = 0$ to 14 : a) $\bar{\rho}_y(x)$, b) $\bar{\rho}_x(y)$, c) average amplitude, and d) width of the density layer.

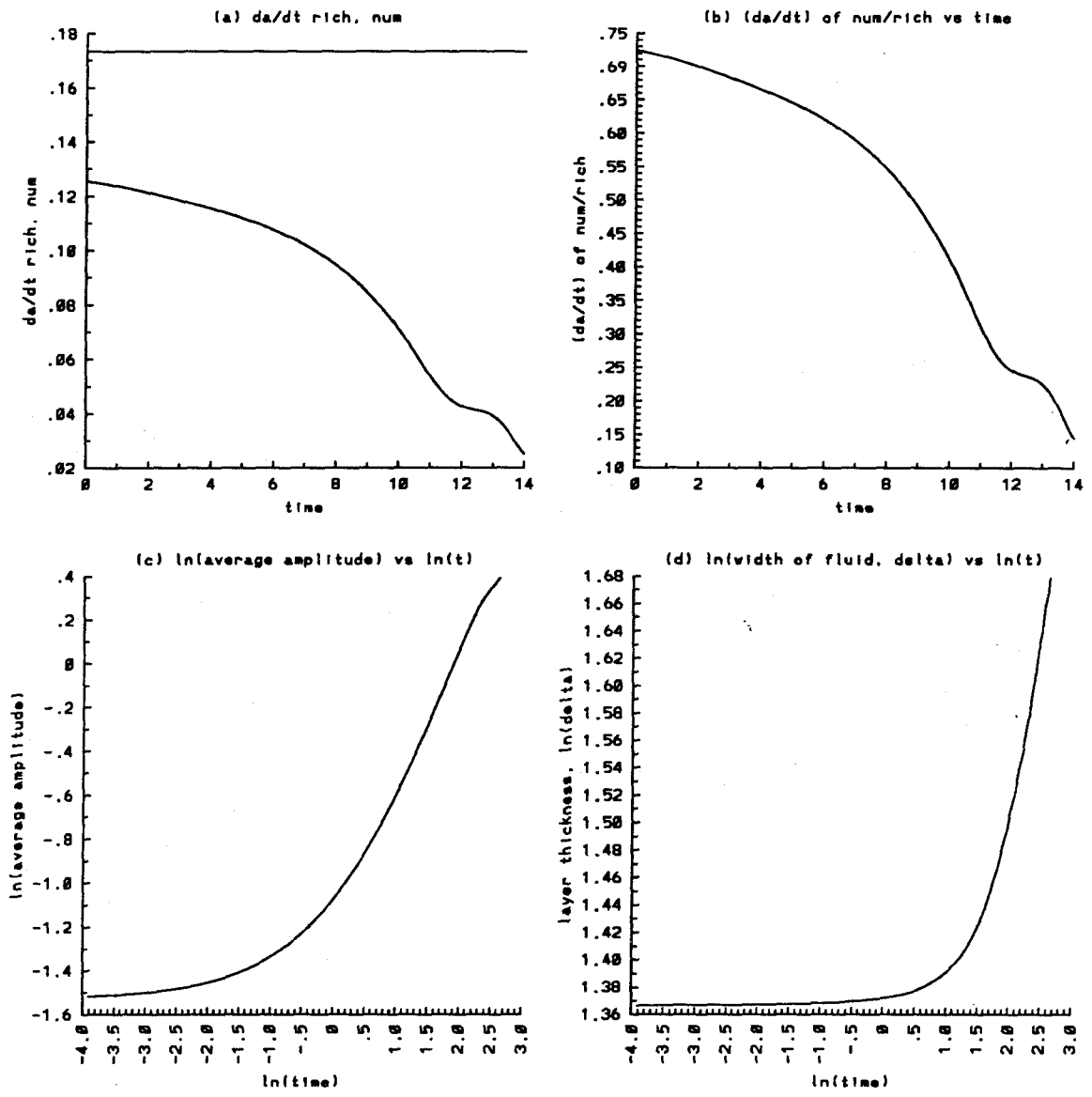

Figure 4.44.2 Time evolution of the average quantities for the first initial random profile, A = −0.8, t = 0 to 14 : a) growth rate da/dt of the average amplitude, numerical and Richtmyer theory (straight line), b) the ratio of the numerical growth rate da/dt over that predicted by Richtmyer theory, c) $\ln(a)$ *vs* $\ln(t)$, d) $\ln(\delta)$ *vs* $\ln(t)$.

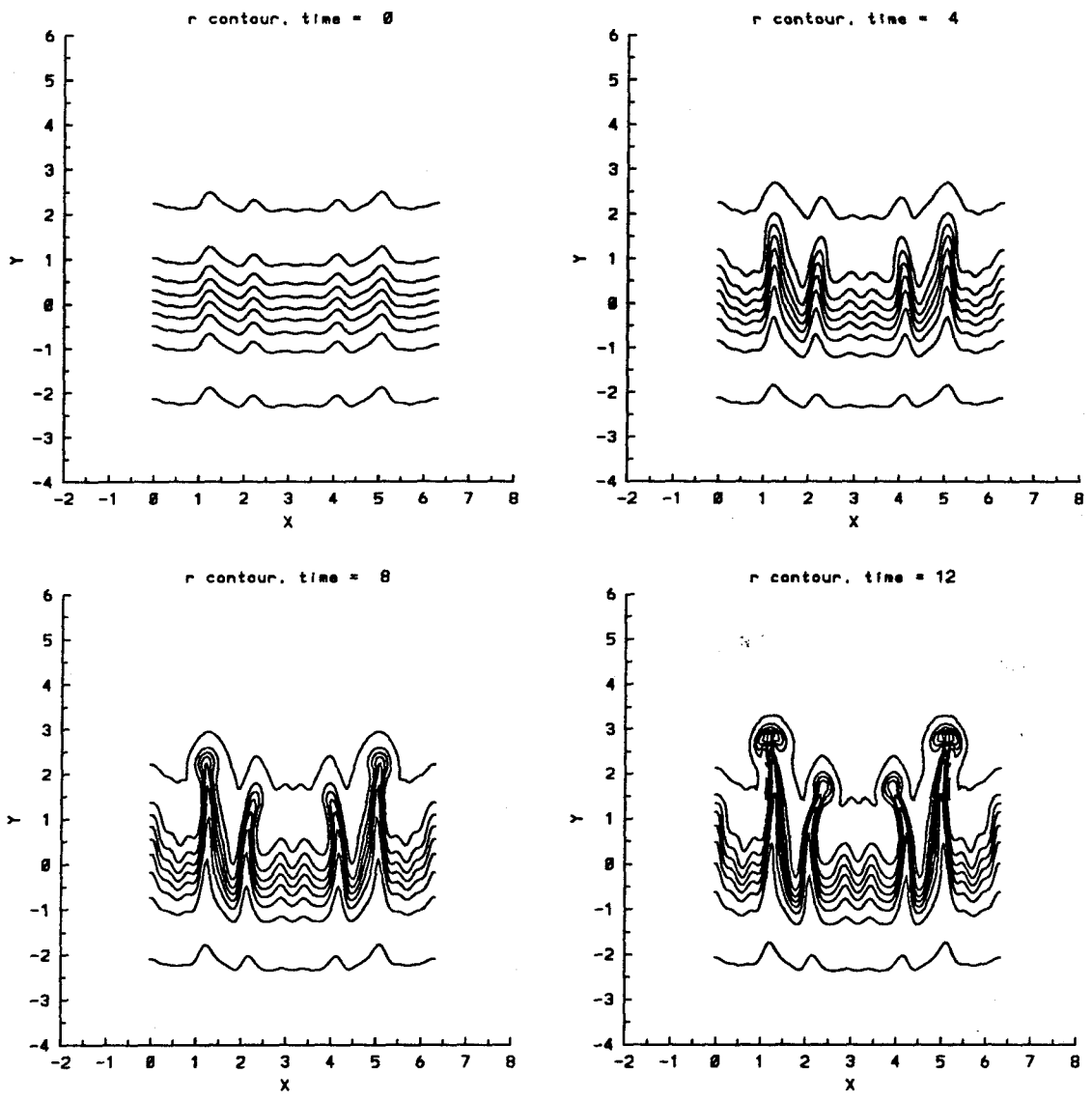

Figure 4.44.3 Time evolution of the density contours for the first initial random profile, A = −0.8, t = 0, 4, 8, 12. The contours are at ρ = 0.11, 0.2, 0.3, 0.4, 0.5, 0.6, 0.7, 0.8, 0.89.

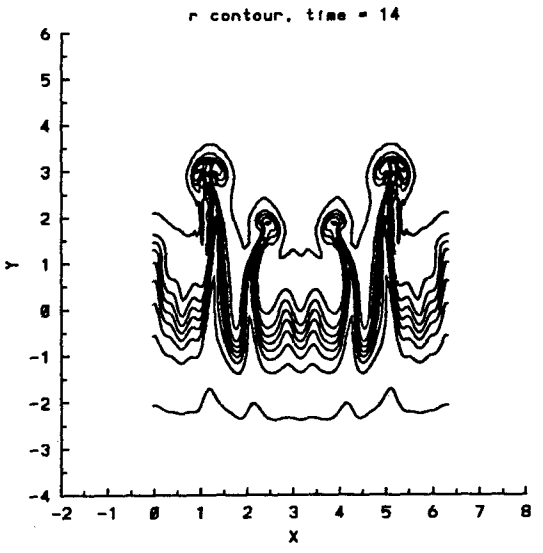

Figure 4.44.4 Time evolution of the density contours for the first initial random profile, A = −0.8, $t = 14$. The contours are at $\rho = 0.11$, 0.2, 0.3, 0.4, 0.5, 0.6, 0.7, 0.8, 0.89.

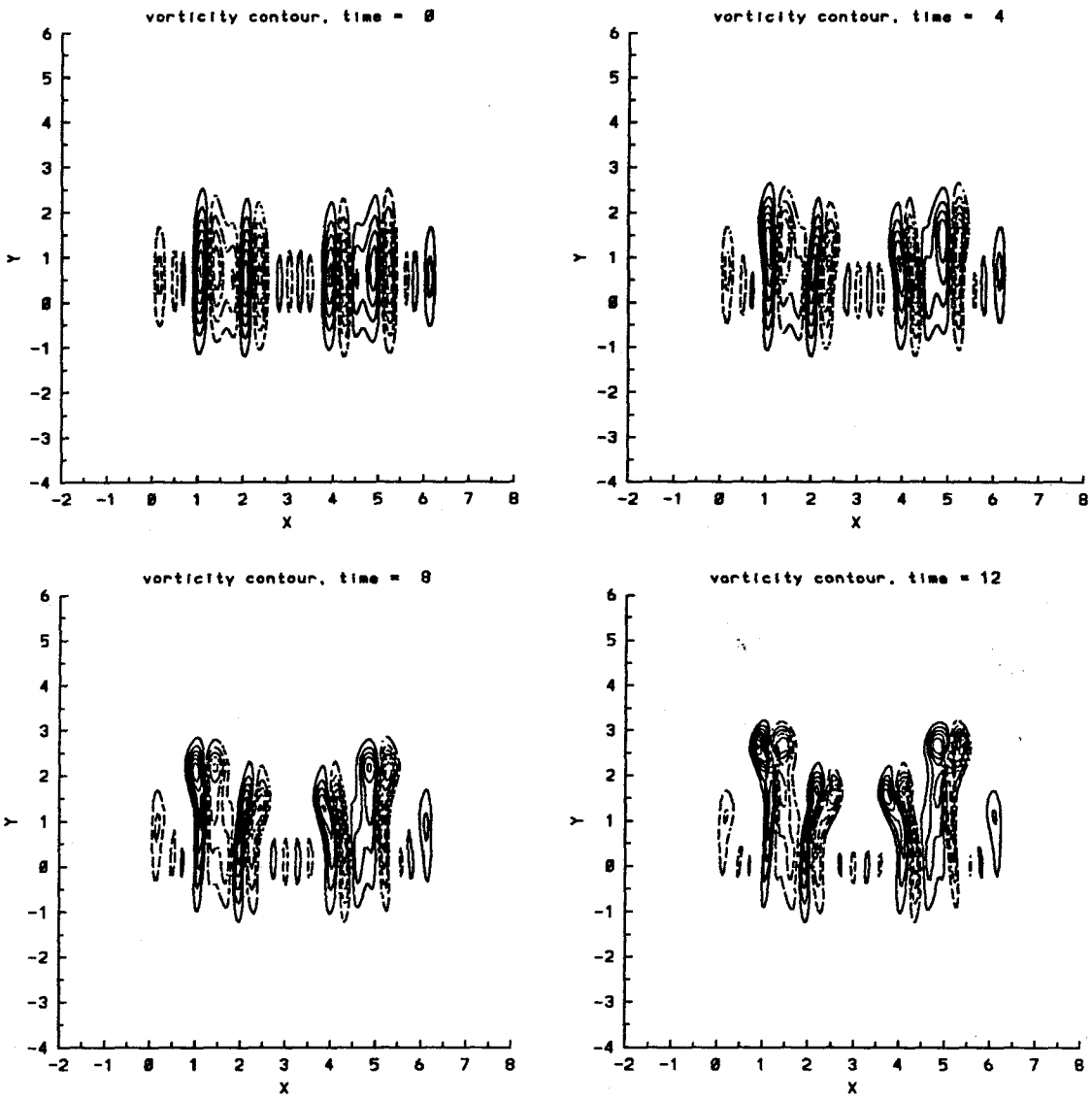

Figure 4.44.3V Time evolution of the vorticity contours for the first initial random profile, A = −0.8, t = 0, 4, 8, 12. The contours are at — · — −1.6, −1.4, −1.2, −1.0, −0.8, −0.6, −0.4, −0.2, and — 0.2, 0.4, 0.6, 0.8, 1.0, 1.2, 1.4, 1.6 in that order from the innermost contour line. There are no ±1.6 contours at t = 0, 4, 8, and no ±1.4 at t = 4, 8.

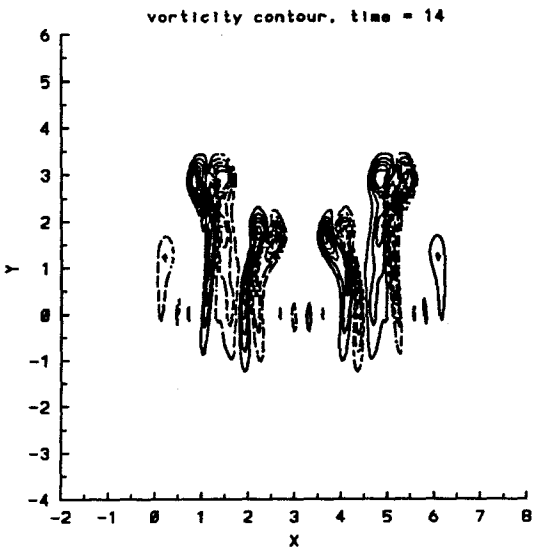

Figure 4.44.4V Time evolution of the vorticity contours for the first initial random profile, A = −0.8, t = 14. The contours are at — · — −1.6, −1.4, −1.2, −1.0, −0.8, −0.6, −0.4, −0.2, and — 0.2, 0.4, 0.6, 0.8, 1.0, 1.2, 1.4, 1.6 in that order from the innermost contour line.

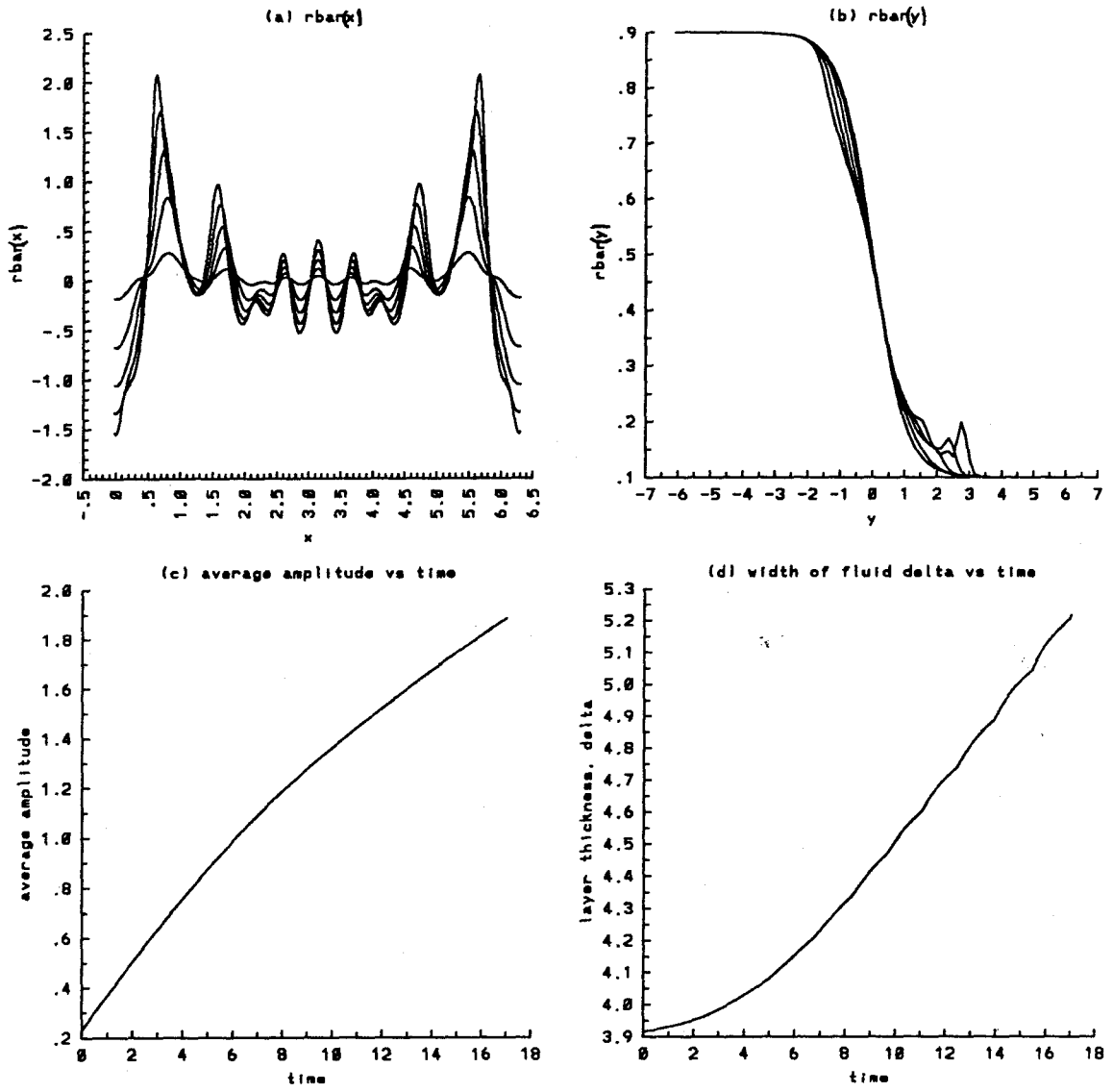

Figure 4.45.1 Time evolution of the average quantities for the second initial random profile, A = −0.8, $t = 0$ to 17 : a) $\bar{\rho}_y(x)$, b) $\bar{\rho}_x(y)$, c) average amplitude, and d) width of the density layer.

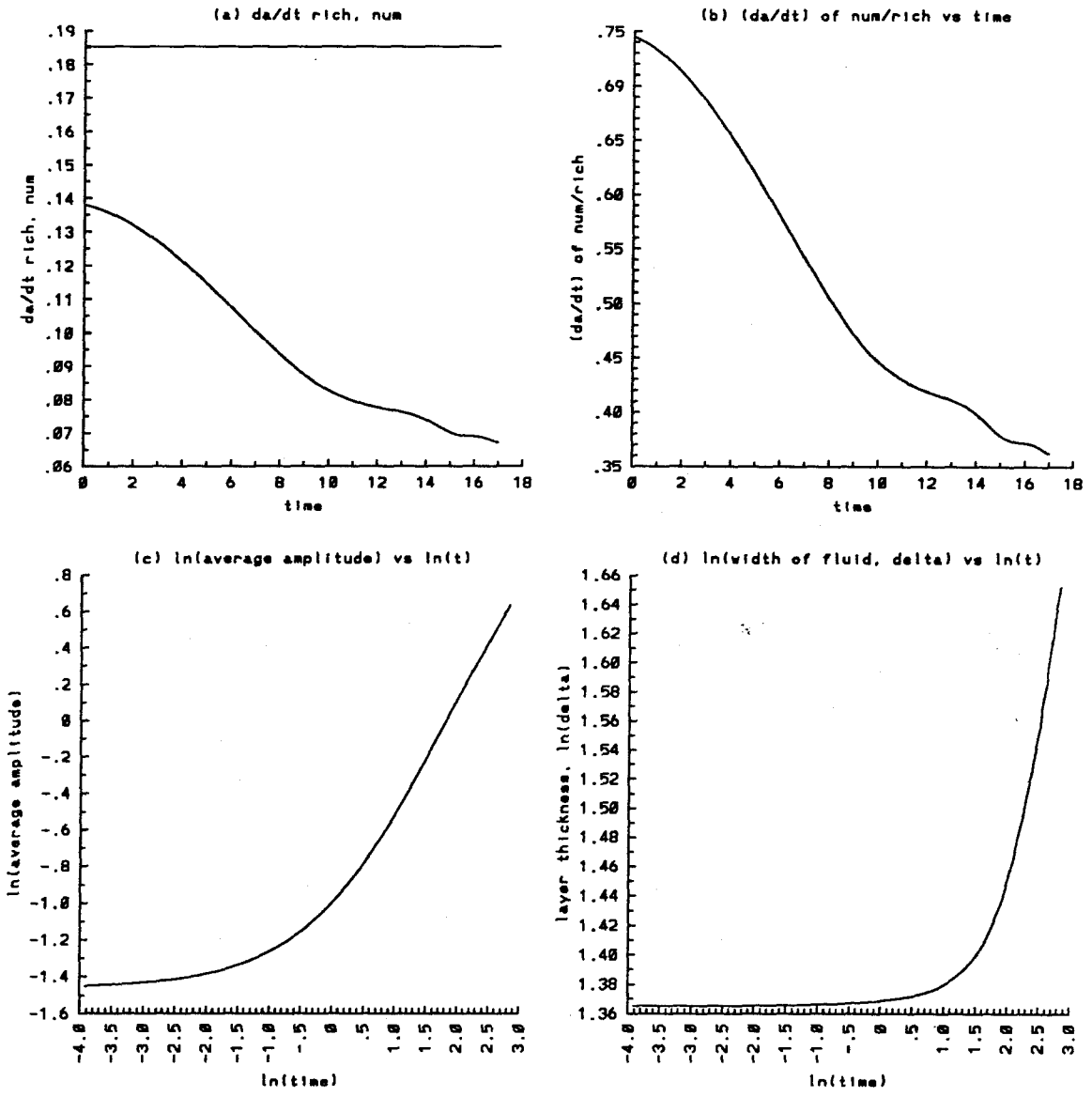

Figure 4.45.2 Time evolution of the average quantities for the second initial random profile, A = −0.8, $t = 0$ to 17 : a) growth rate da/dt of the average amplitude, numerical and Richtmyer theory (straight line), b) the ratio of the numerical growth rate da/dt over that predicted by Richtmyer theory, c) $\ln(a)$ *vs* $\ln(t)$, d) $\ln(\delta)$ *vs* $\ln(t)$.

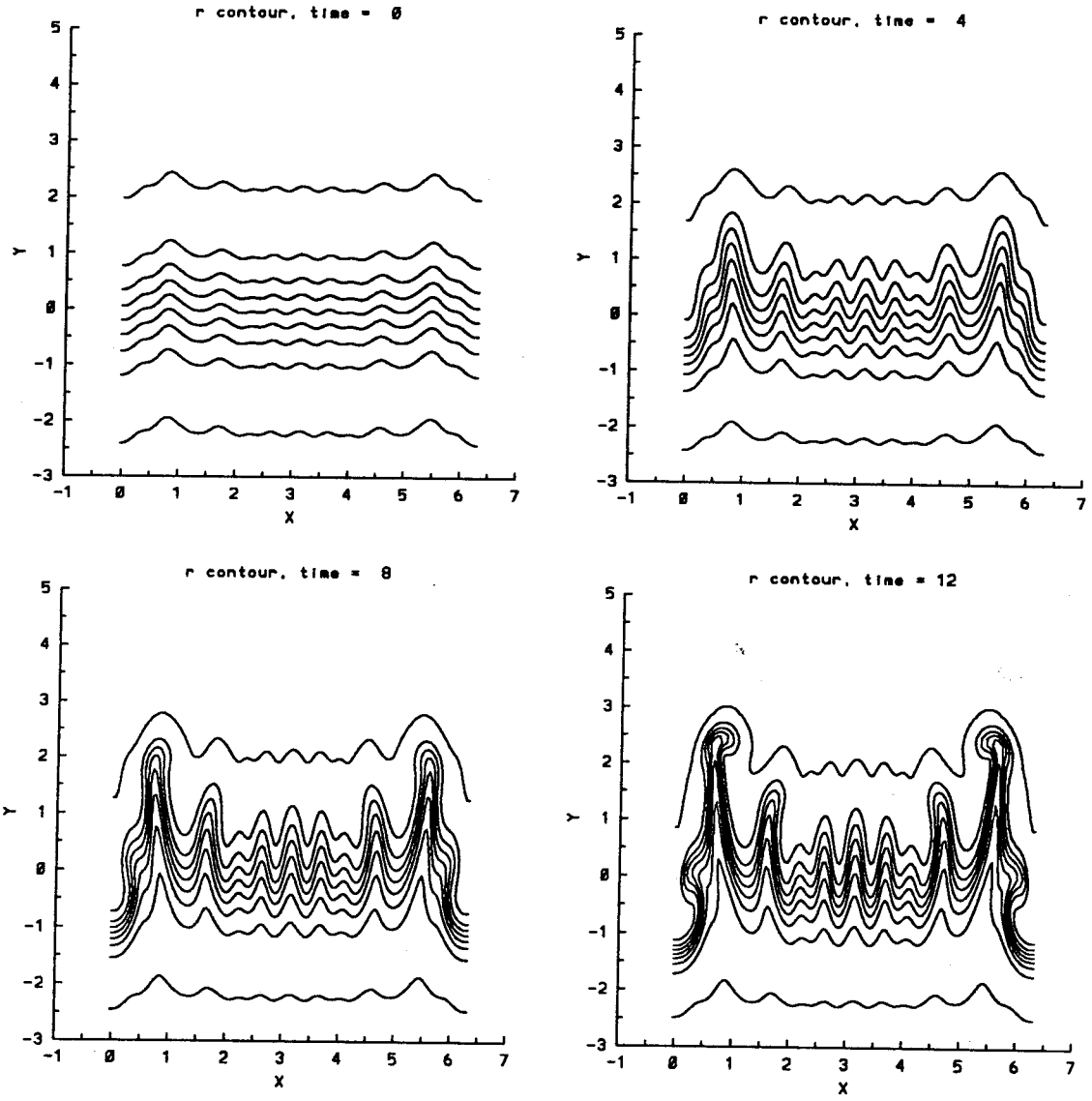

Figure 4.45.3 Time evolution of the density contours for the second initial random profile, A = −0.8, t = 0, 4, 8, 12. The contours are at ρ = 0.11, 0.2, 0.3, 0.4, 0.5, 0.6, 0.7, 0.8, 0.89.

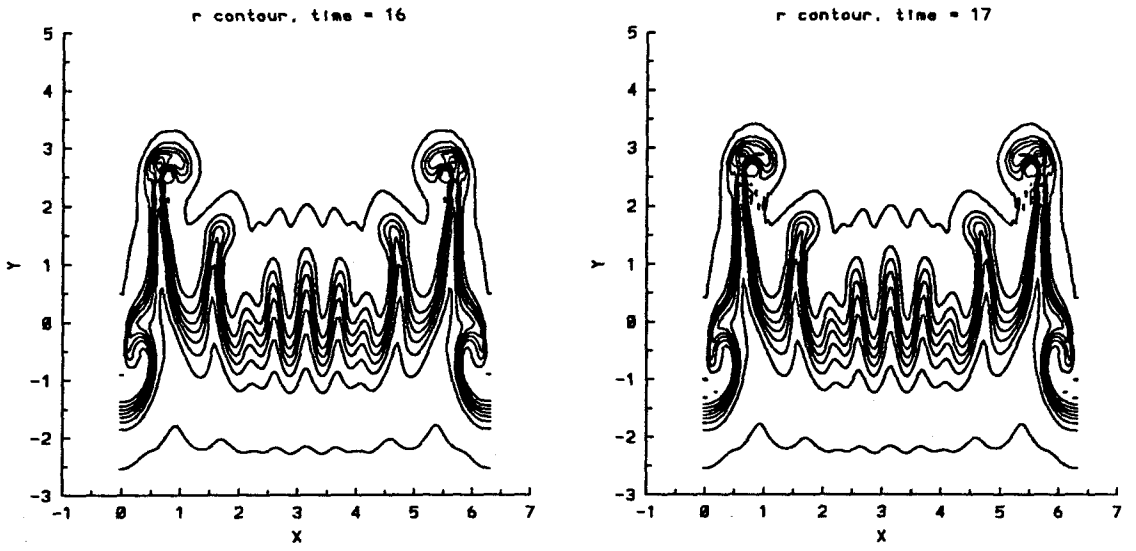

Figure 4.45.4 Time evolution of the density contours for the second initial random profile, A = −0.8, t = 16, 17. The contours are at ρ = 0.11, 0.2, 0.3, 0.4, 0.5, 0.6, 0.7, 0.8, 0.89.

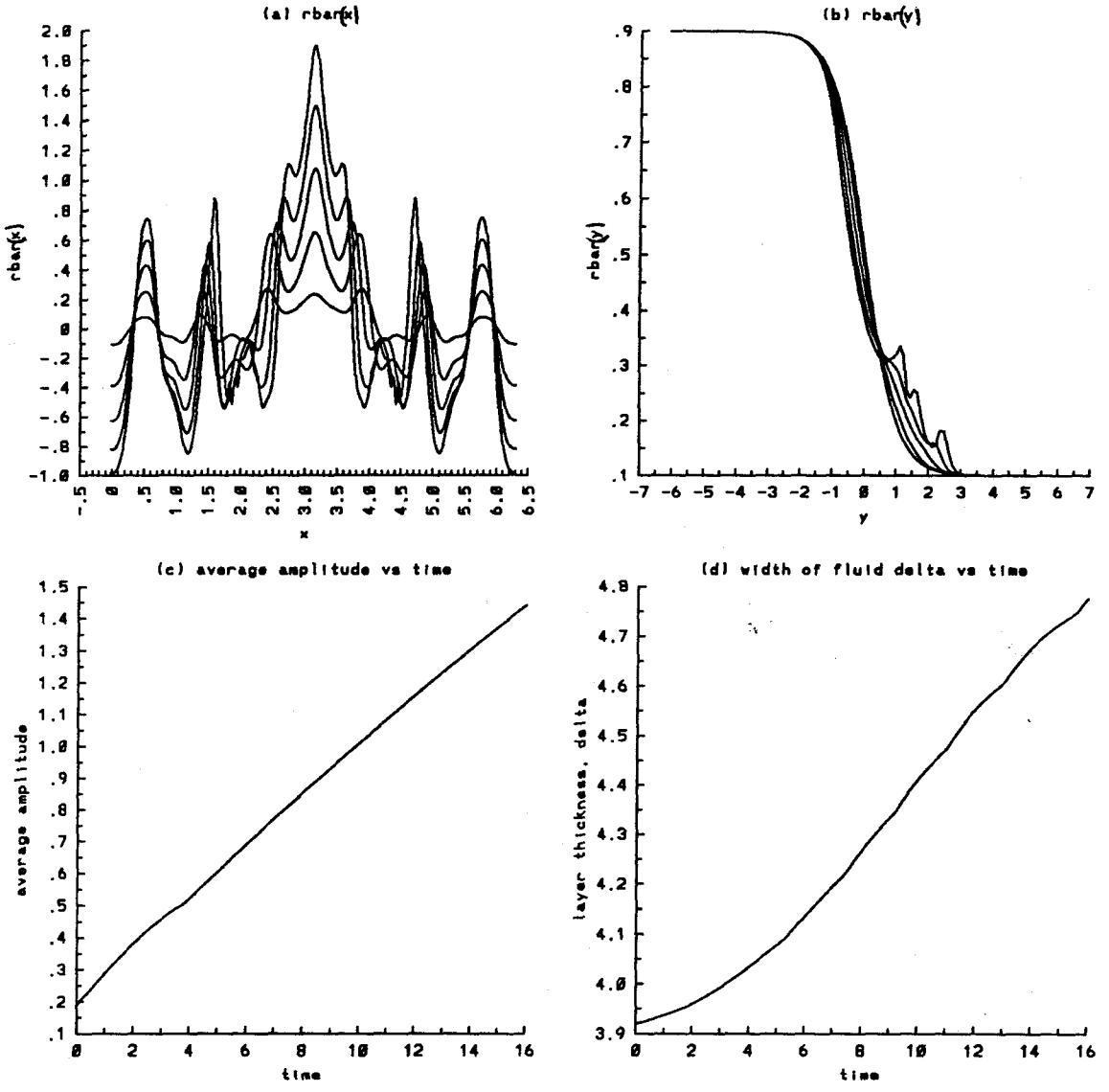

Figure 4.46.1 Time evolution of the average quantities for the third initial random profile, A $= -0.8$, $t = 0$ to 16 : a) $\bar{\rho}_y(x)$, b) $\bar{\rho}_x(y)$, c) average amplitude, and d) width of the density layer.

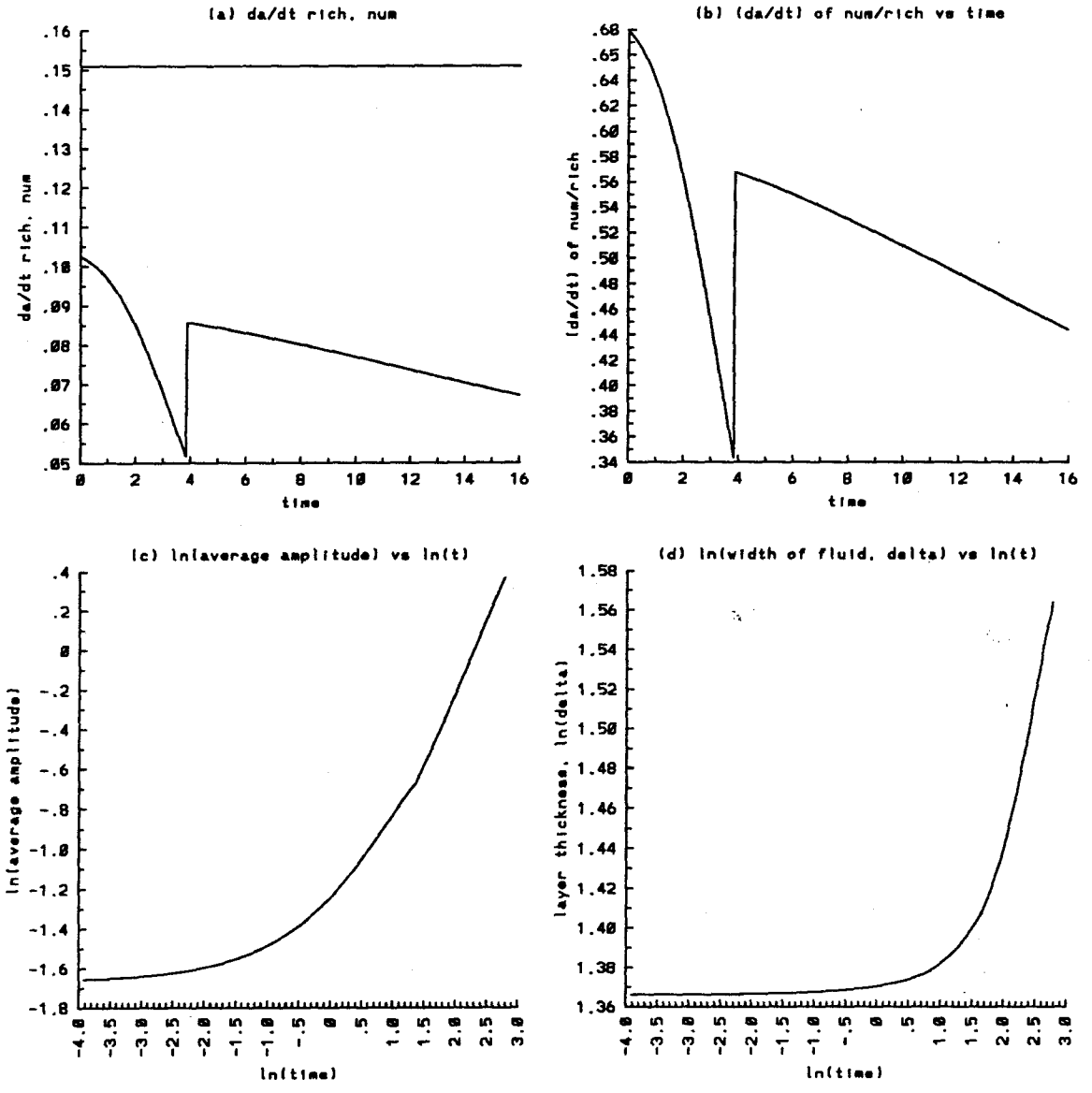

Figure 4.46.2 Time evolution of the average quantities for the third initial random profile, A = -0.8, $t = 0$ to 16 : a) growth rate da/dt of the average amplitude, numerical and Richtmyer theory (straight line), b) the ratio of the numerical growth rate da/dt over that predicted by Richtmyer theory, c) $\ln(a)$ *vs* $\ln(t)$, d) $\ln(\delta)$ *vs* $\ln(t)$.

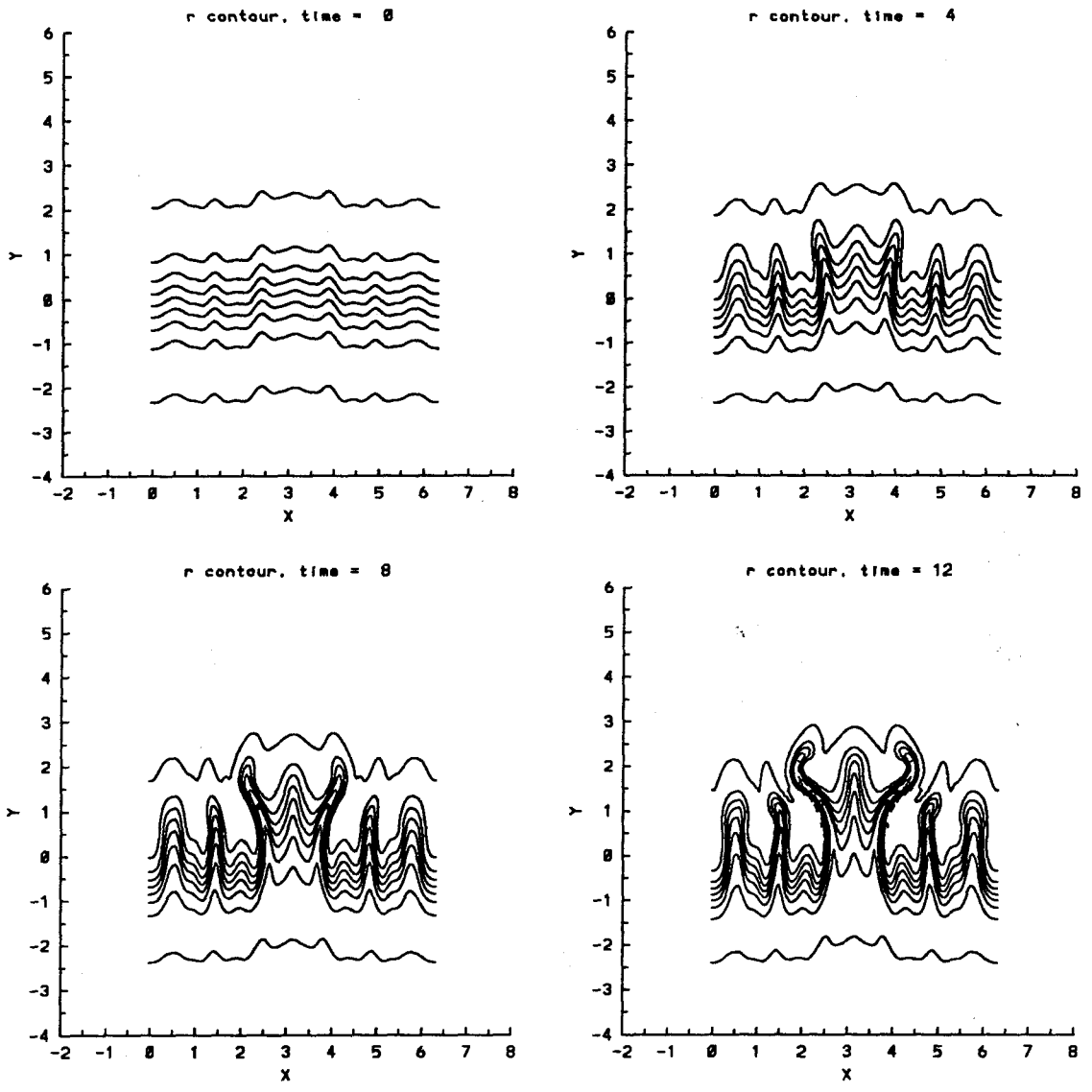

Figure 4.46.3 Time evolution of the density contours for the third initial random profile, A = −0.8, t = 0, 4, 8, 12. The contours are at ρ = 0.11, 0.2, 0.3, 0.4, 0.5, 0.6, 0.7, 0.8, 0.89.

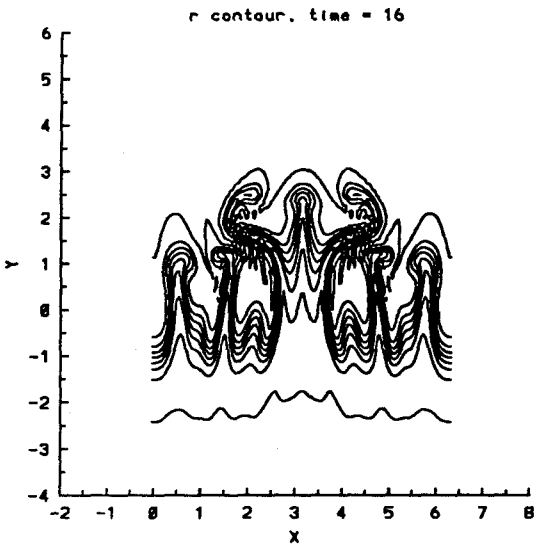

Figure 4.46.4 Time evolution of the density contours for the third initial random profile, A = −0.8, $t = 16$. The contours are at $\rho = 0.11$, 0.2, 0.3, 0.4, 0.5, 0.6, 0.7, 0.8, 0.89.

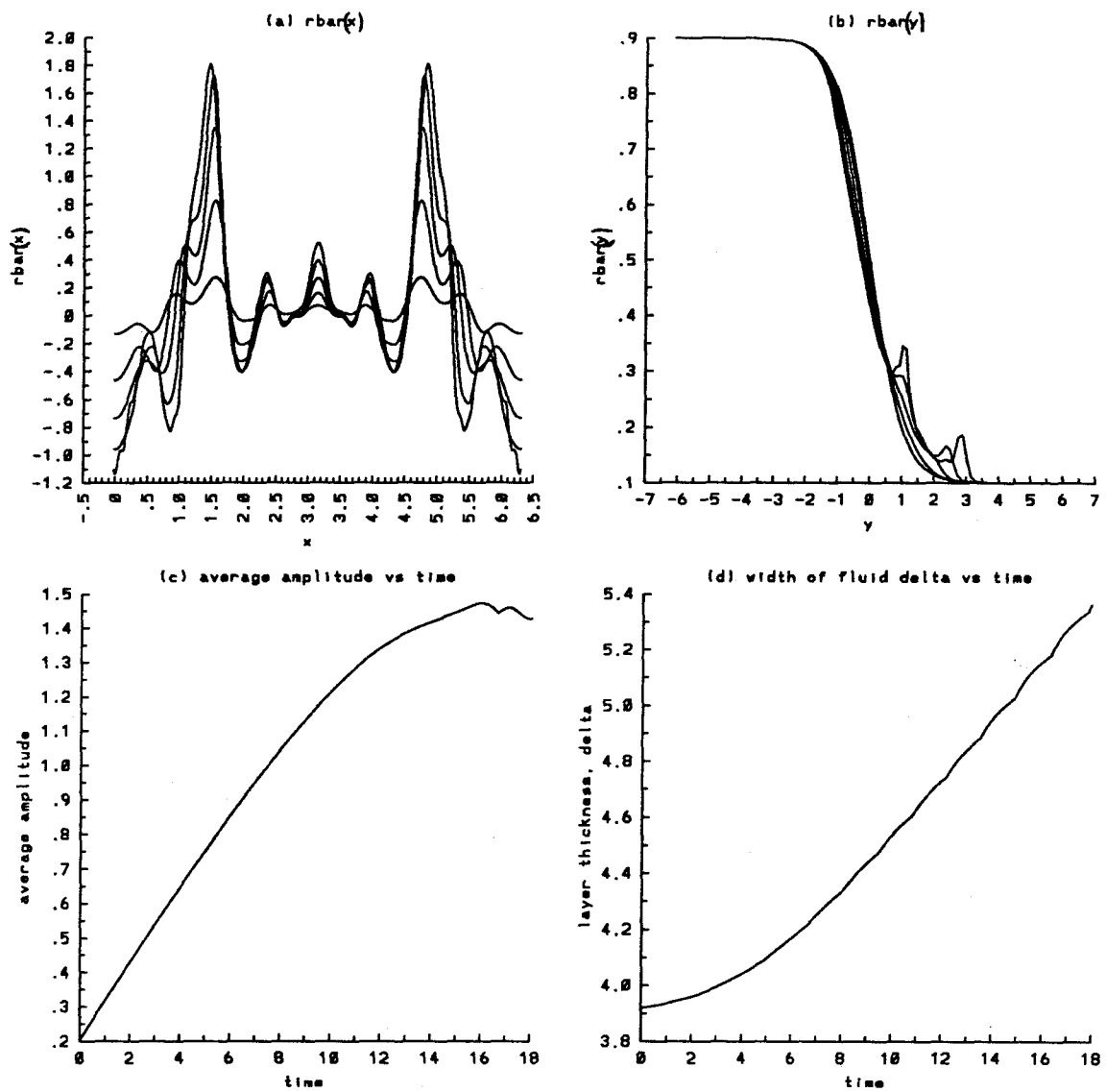

Figure 4.47.1 Time evolution of the average quantities for the fourth initial random profile, A $= -0.8$, $t = 0$ to 17 : a) $\bar{\rho}_y(x)$, b) $\bar{\rho}_x(y)$, c) average amplitude, and d) width of the density layer.

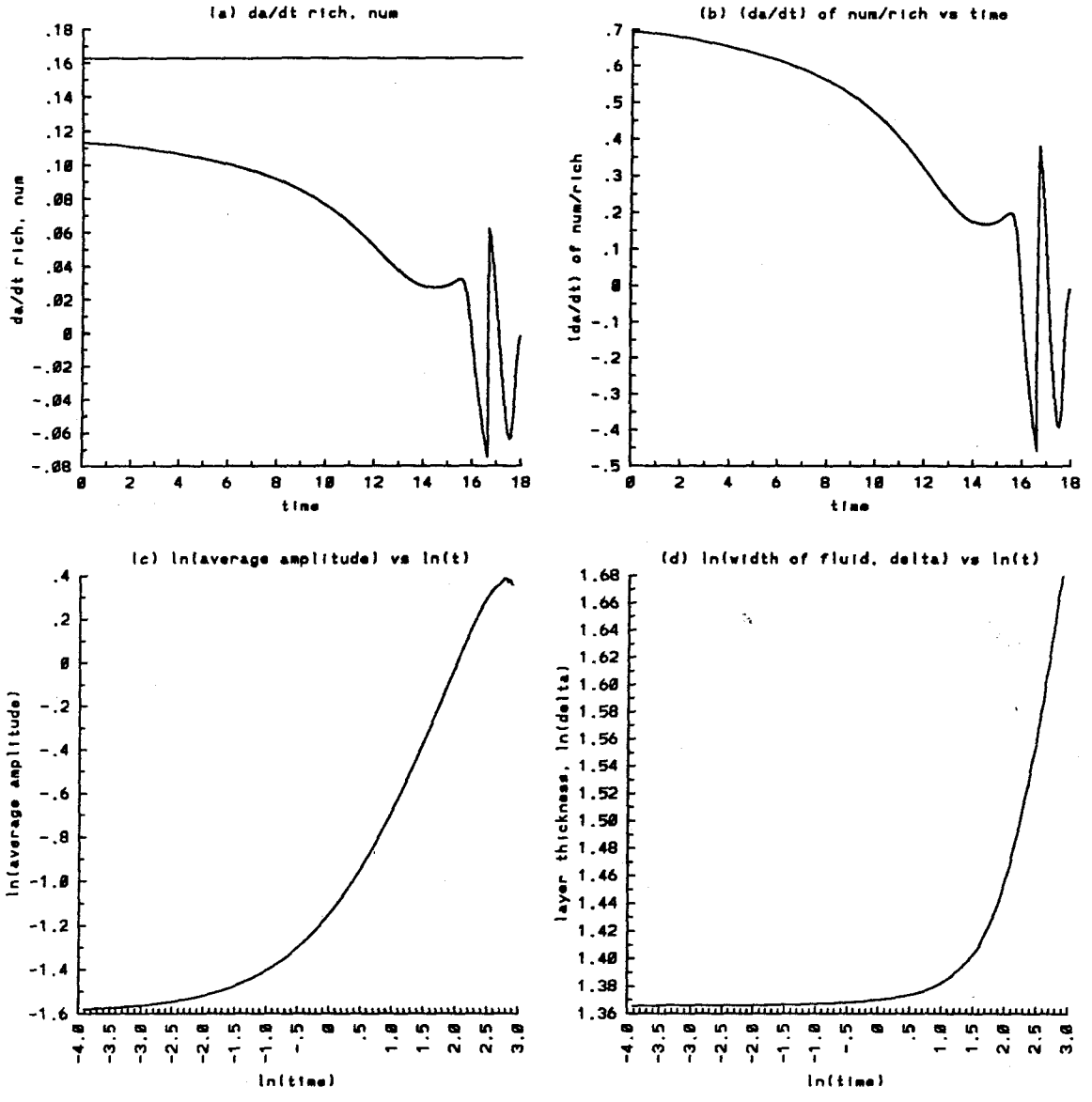

Figure 4.47.2 Time evolution of the average quantities for the fourth initial random profile, A = −0.8, $t = 0$ to 17.98 : a) growth rate da/dt of the average amplitude, numerical and Richtmyer theory (straight line), b) the ratio of the numerical growth rate da/dt over that predicted by Richtmyer theory, c) $\ln(a)$ *vs* $\ln(t)$, d) $\ln(\delta)$ *vs* $\ln(t)$.

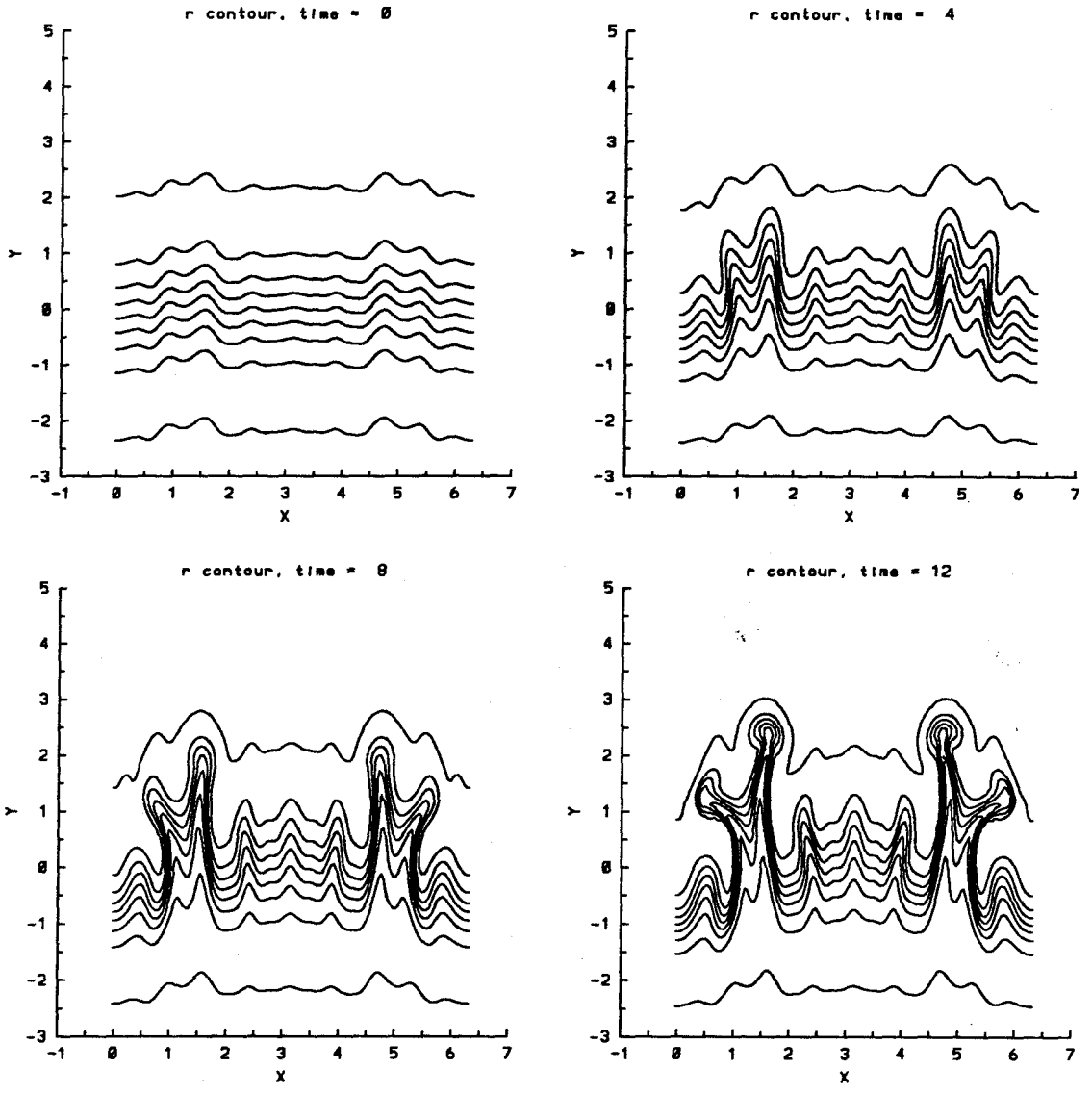

Figure 4.47.3 Time evolution of the density contours for the fourth initial random profile, A = −0.8, t = 0, 4, 8, 12. The contours are at ρ = 0.11, 0.2, 0.3, 0.4, 0.5, 0.6, 0.7, 0.8, 0.89.

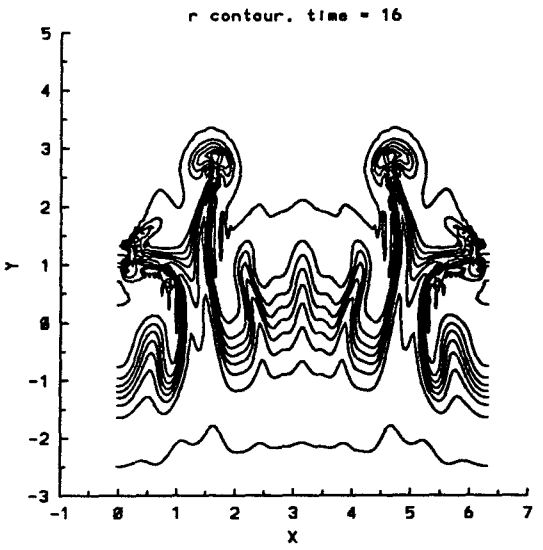

Figure 4.47.4 Time evolution of the density contours for the fourth initial random profile, A $= -0.8$, $t = 16$. The contours are at $\rho = 0.11$, 0.2, 0.3, 0.4, 0.5, 0.6, 0.7, 0.8, 0.89.

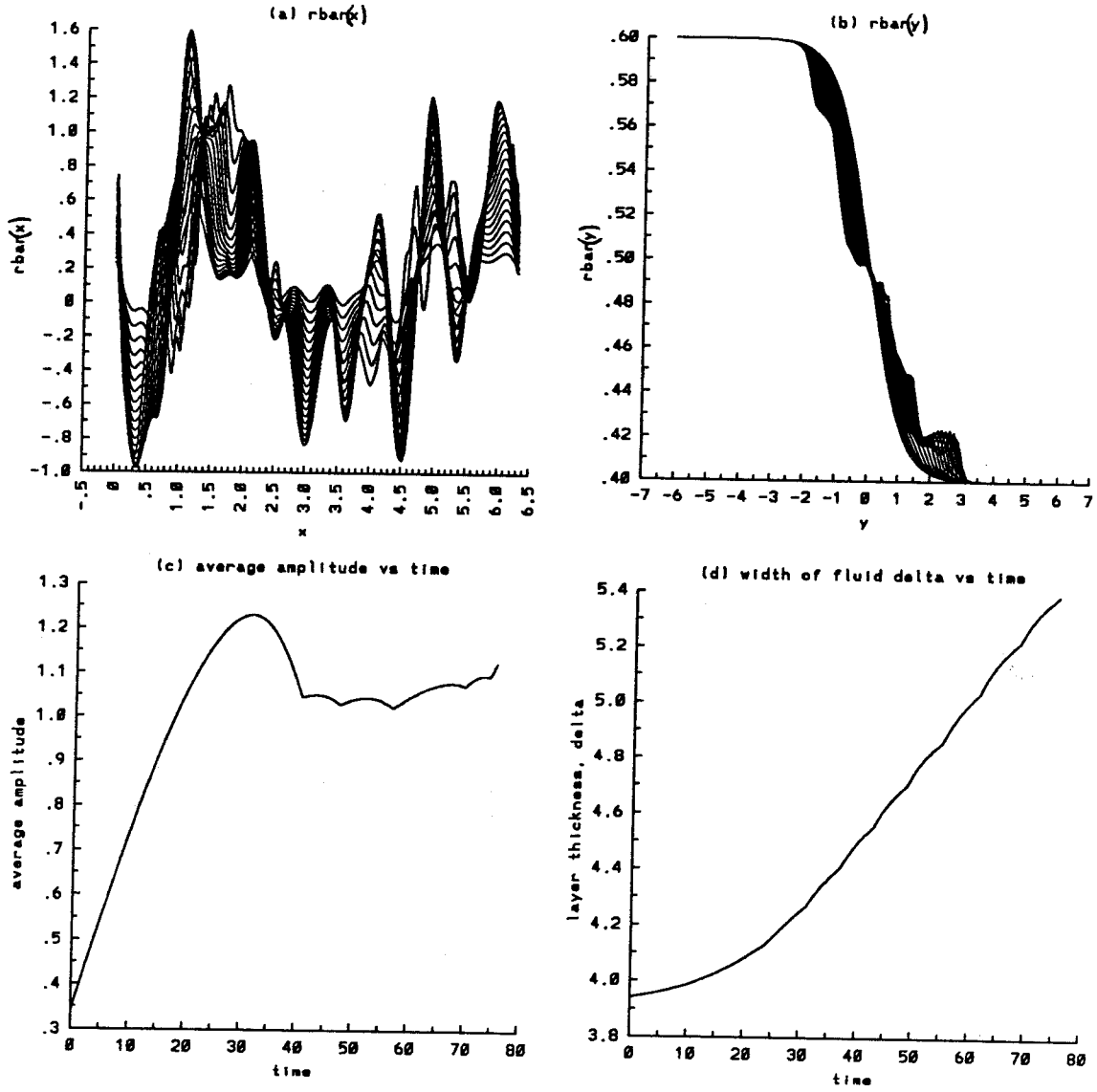

Figure 4.48.1 Time evolution of the average quantities for the fifth initial random profile, A = -0.2, $t = 0$ to 75.4 : a) $\bar{\rho}_y(x)$, b) $\bar{\rho}_x(y)$, c) average amplitude, and d) width of the density layer.

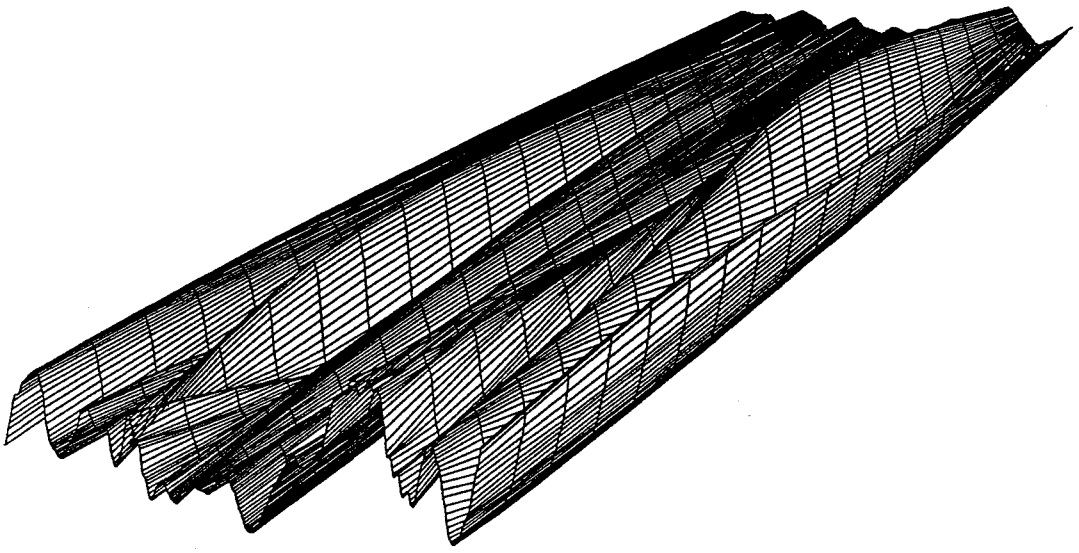

Figure 4.48.1a Three-dimensional surface of $\bar{\rho}_y(x,t)$ for the fifth initial random profile, A $= -0.2$ and $t = 0$, 75.4.

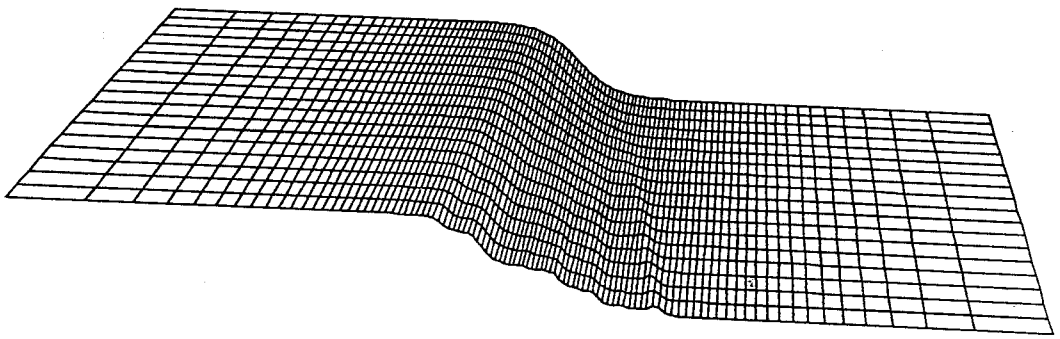

Figure 4.48.1b Three-dimensional surface of $\bar{\rho}_x(y,t)$ for the fifth initial random profile, A $= -0.2$ and $t = 0$, 75.4.

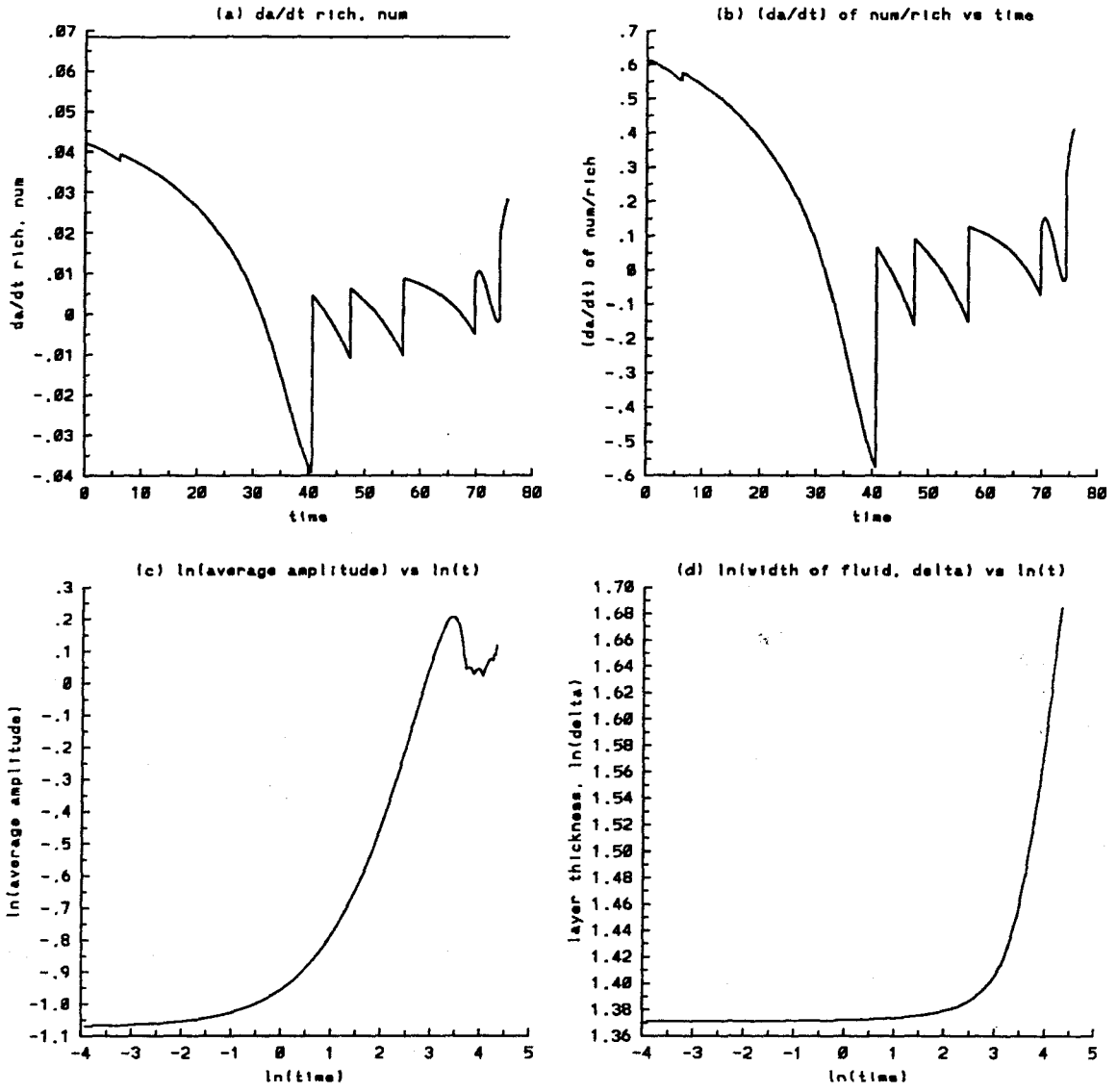

Figure 4.48.2 Time evolution of the average quantities for the fifth initial random profile, A = −0.2, $t = 0$ to 75.4 : a) growth rate da/dt of the average amplitude, numerical and Richtmyer theory (straight line), b) the ratio of the numerical growth rate da/dt over that predicted by Richtmyer theory, c) $\ln(a)$ *vs* $\ln(t)$, d) $\ln(\delta)$ *vs* $\ln(t)$.

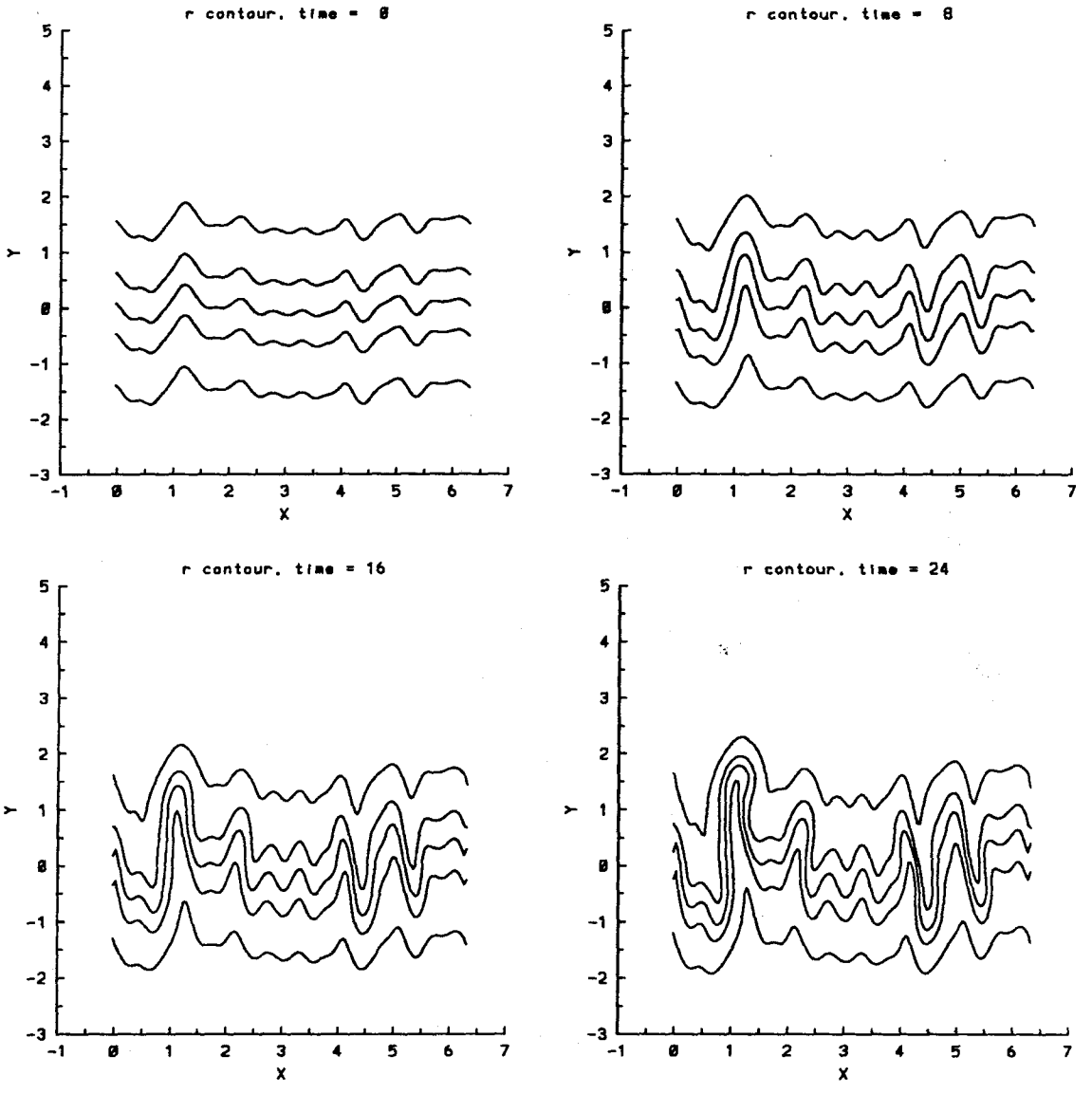

Figure 4.48.3 Time evolution of the density contours for the fifth initial random profile, A = −0.2, t = 0, 8, 16, 24. The contours are at ρ = 0.41, 0.45, 0.50, 0.55, 0.59.

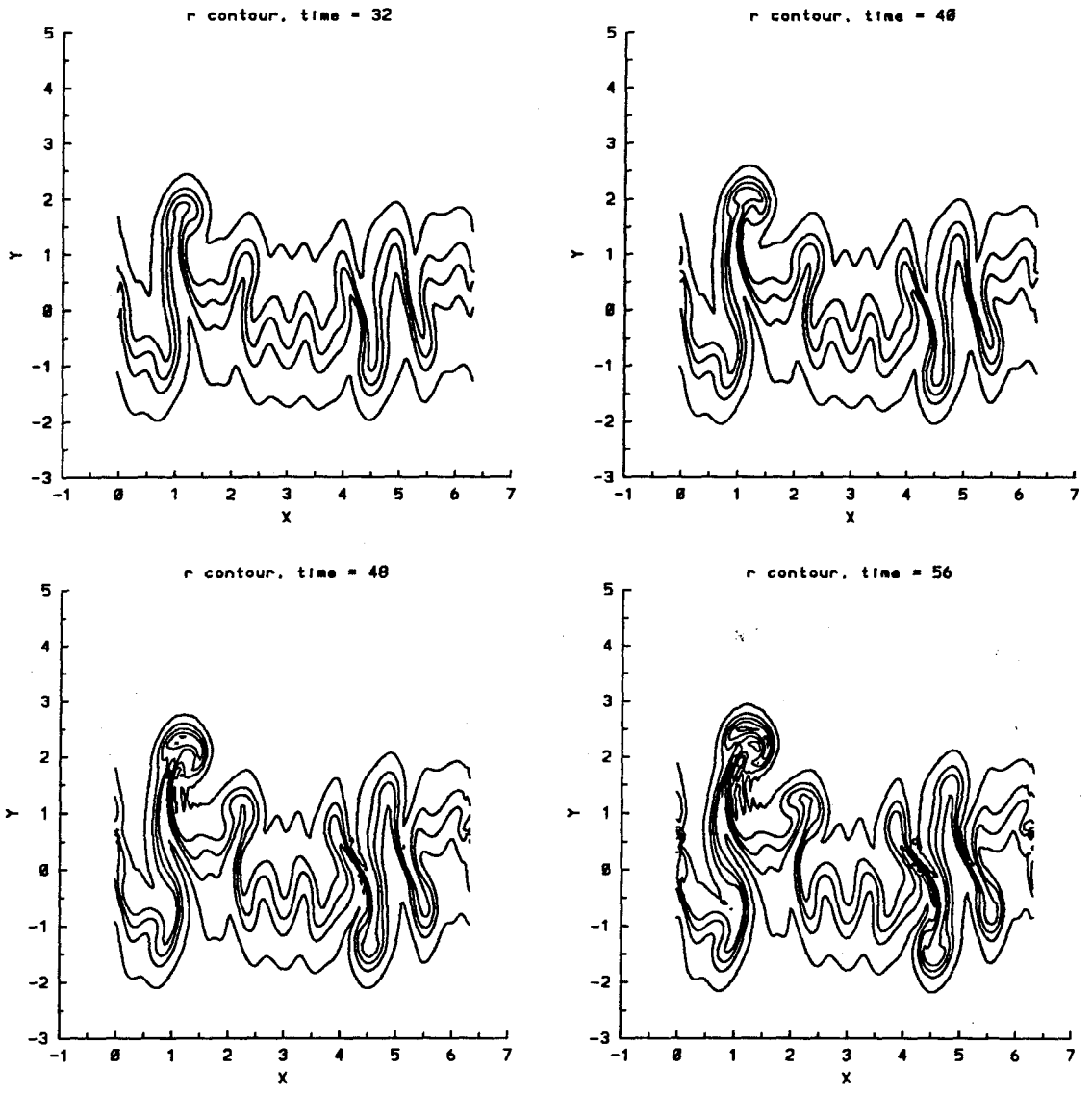

Figure 4.48.4 Time evolution of the density contours for the fifth initial random profile, A = -0.2, $t = 32, 40, 48, 56$. The contours are at $\rho = 0.41, 0.45, 0.50, 0.55, 0.59$.

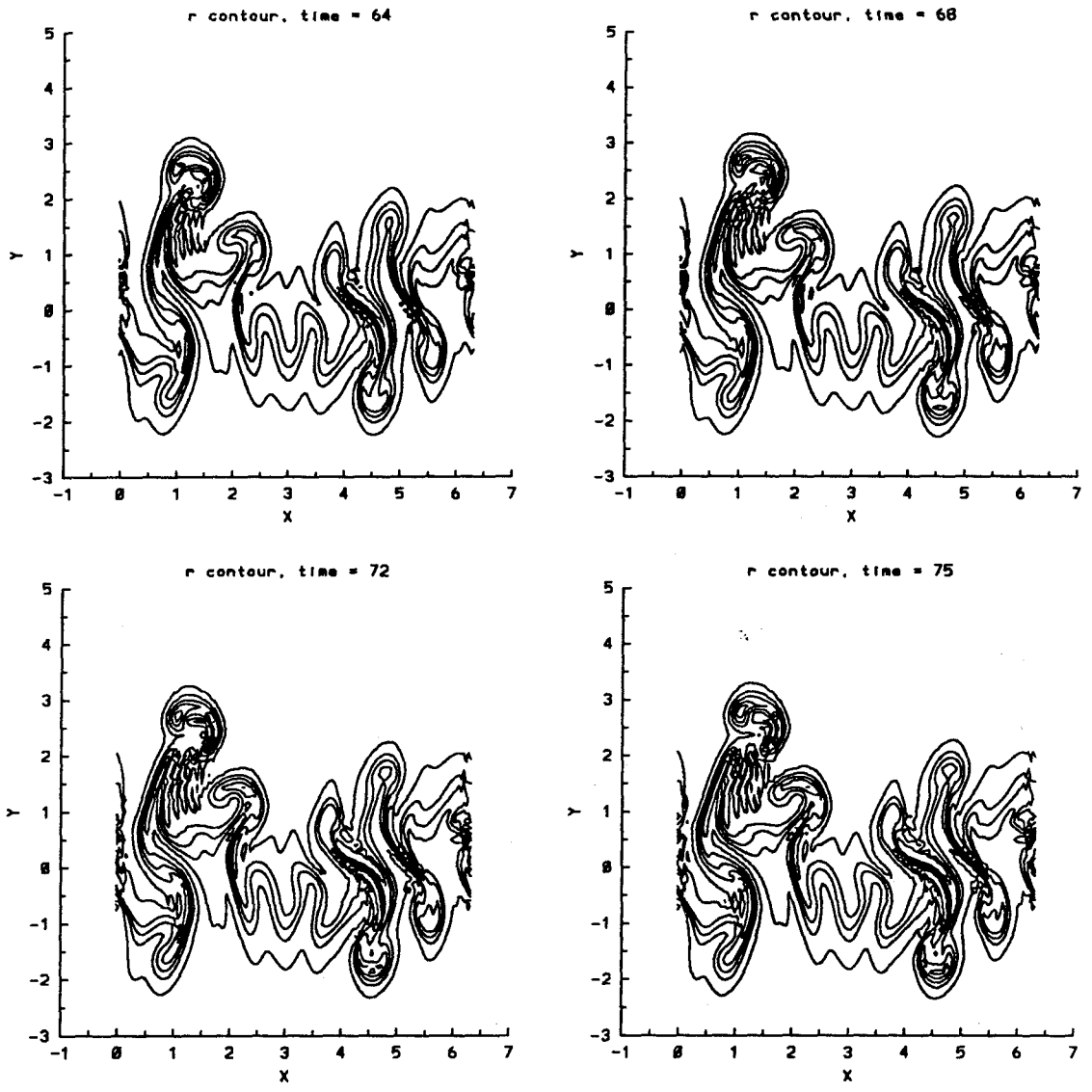

Figure 4.48.5 Time evolution of the density contours for the fifth initial random profile, A = −0.2, t = 64, 68, 72, 75. The contours are at ρ = 0.41, 0.45, 0.50, 0.55, 0.59.

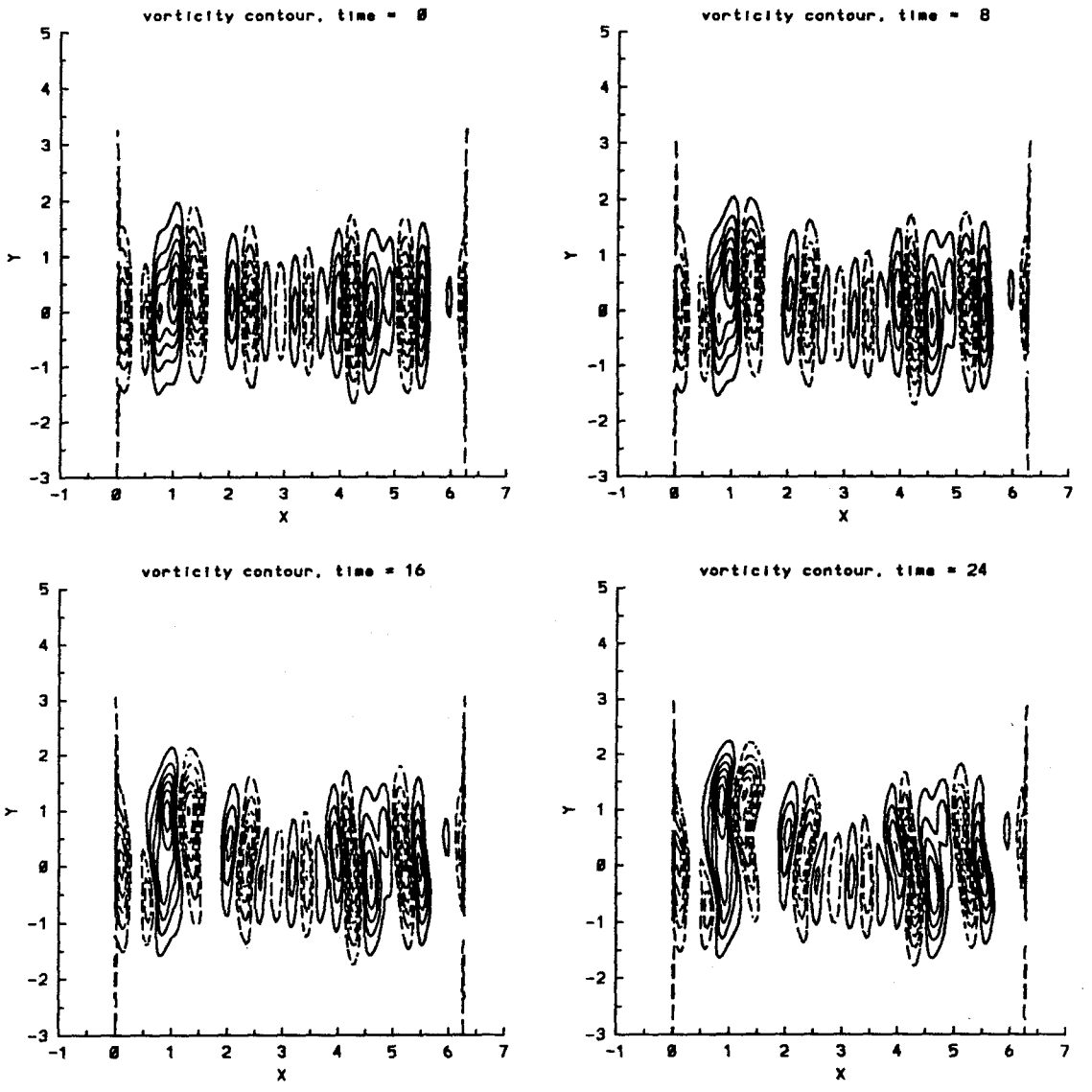

Figure 4.48.3V Time evolution of the vorticity contours for the fifth initial random profile, A = −0.2, t = 0, 8, 16, 24. The contours are at — · — −0.35, −0.30, −0.25, −0.20, −0.15, −0.10, −0.05 and — 0.05, 0.10, 0.15, 0.20, 0.25, 0.30 in that order from the innermost contour line.

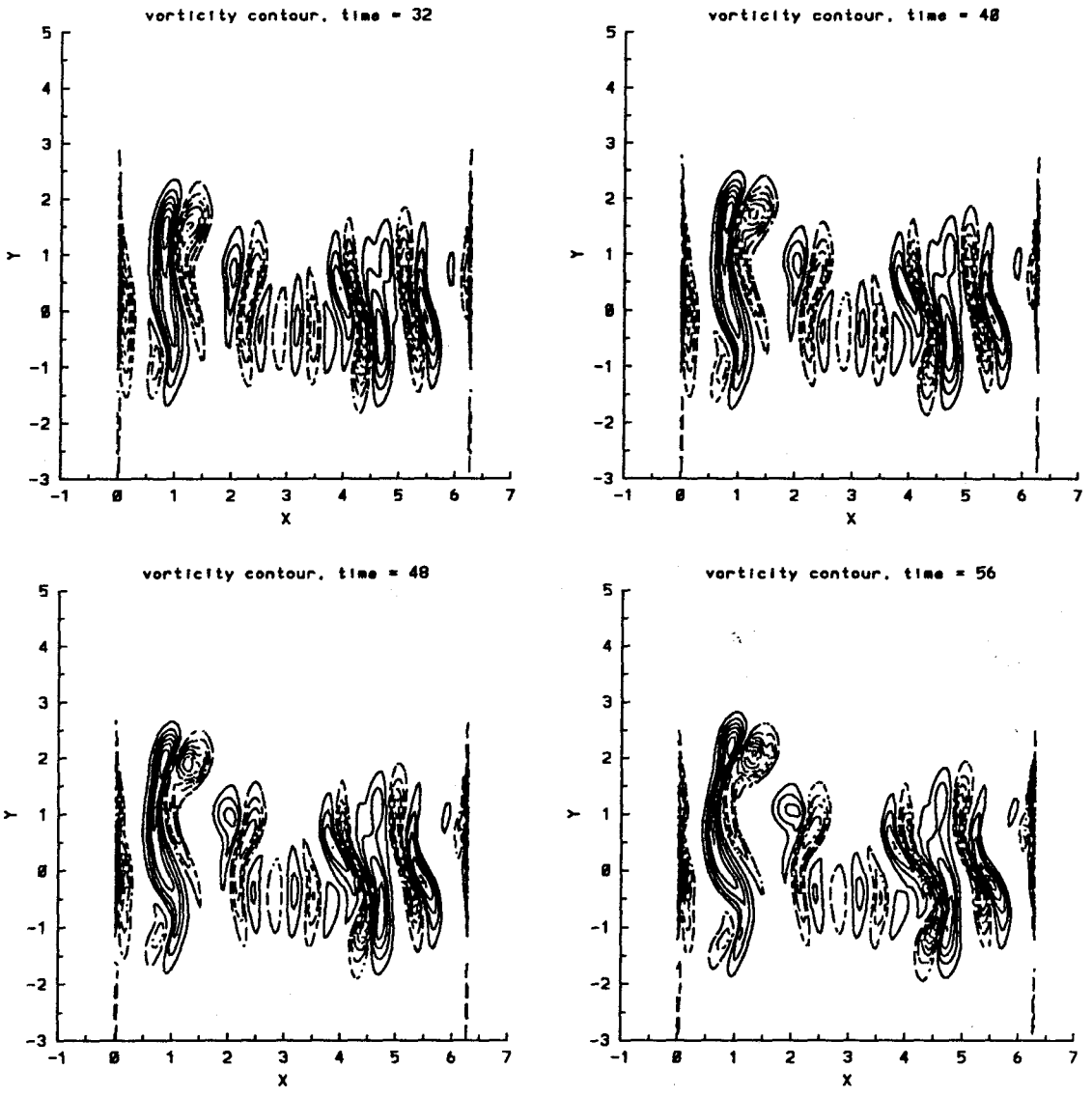

Figure 4.48.4V Time evolution of the vorticity contours for the fifth initial random profile, A = −0.2, t = 32, 40, 48, 56. The contours are from −0.40 to 0.30 for t = 32, −0.55 to 0.30 for t = 40, −0.80 to 0.30 for t = 48, 56 with incremental step size of 0.05. The negative contours are indicated by — · — and positive ones by —. The maximum and minimum vorticities are at the centers of the innermost circles.

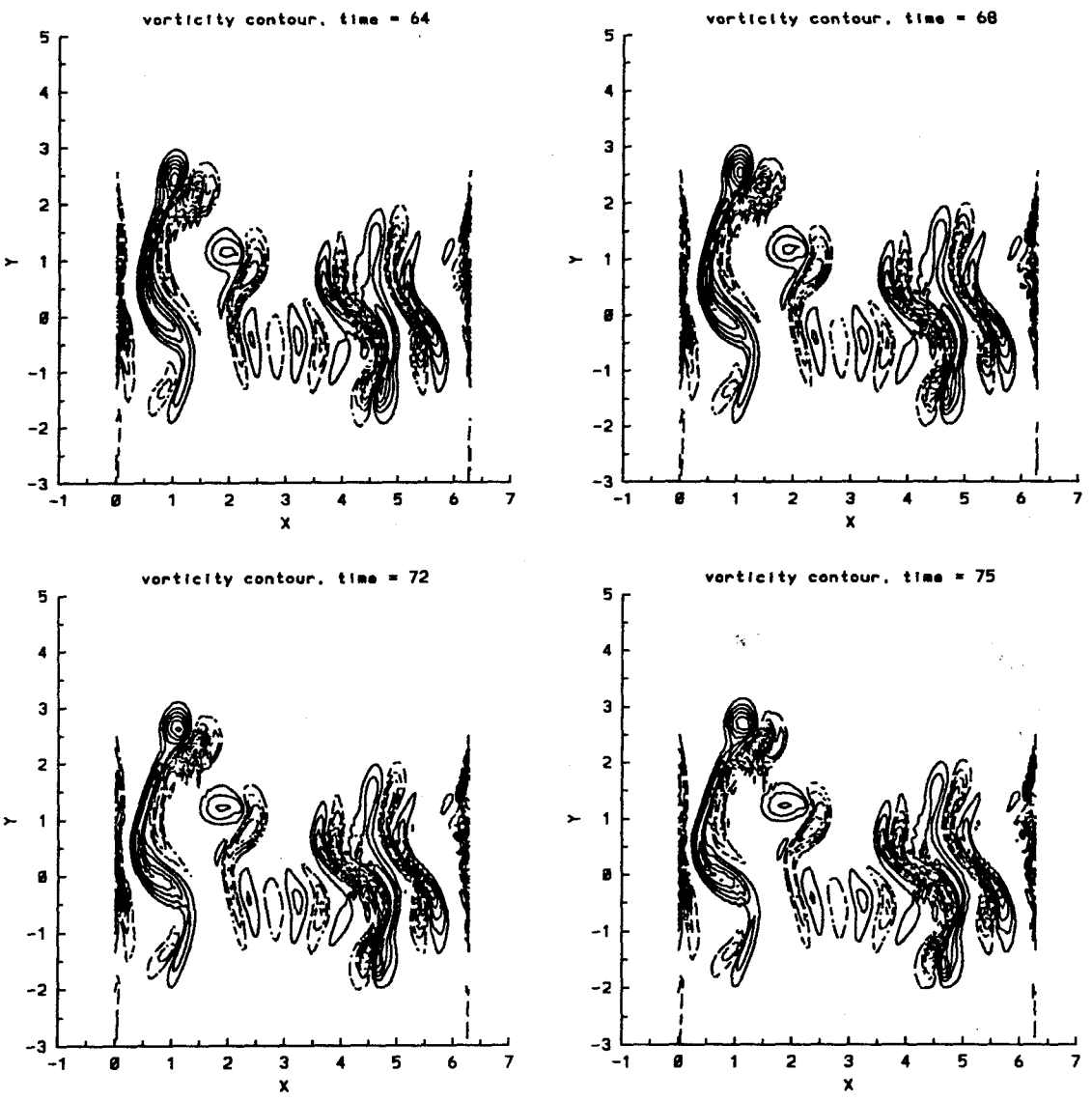

Figure 4.48.5V Time evolution of the vorticity contours for the fifth initial random profile, A = −0.2, t = 64, 68, 72, 75. The contours are from −0.60 to 0.30 t = 64, −0.65 to 0.40 t = 68, −0.60 to 0.60 t = 72, and −0.60 to 0.70 t = 75 with incremental step size of 0.05. The negative contours are indicated by — · — and positive ones by —.

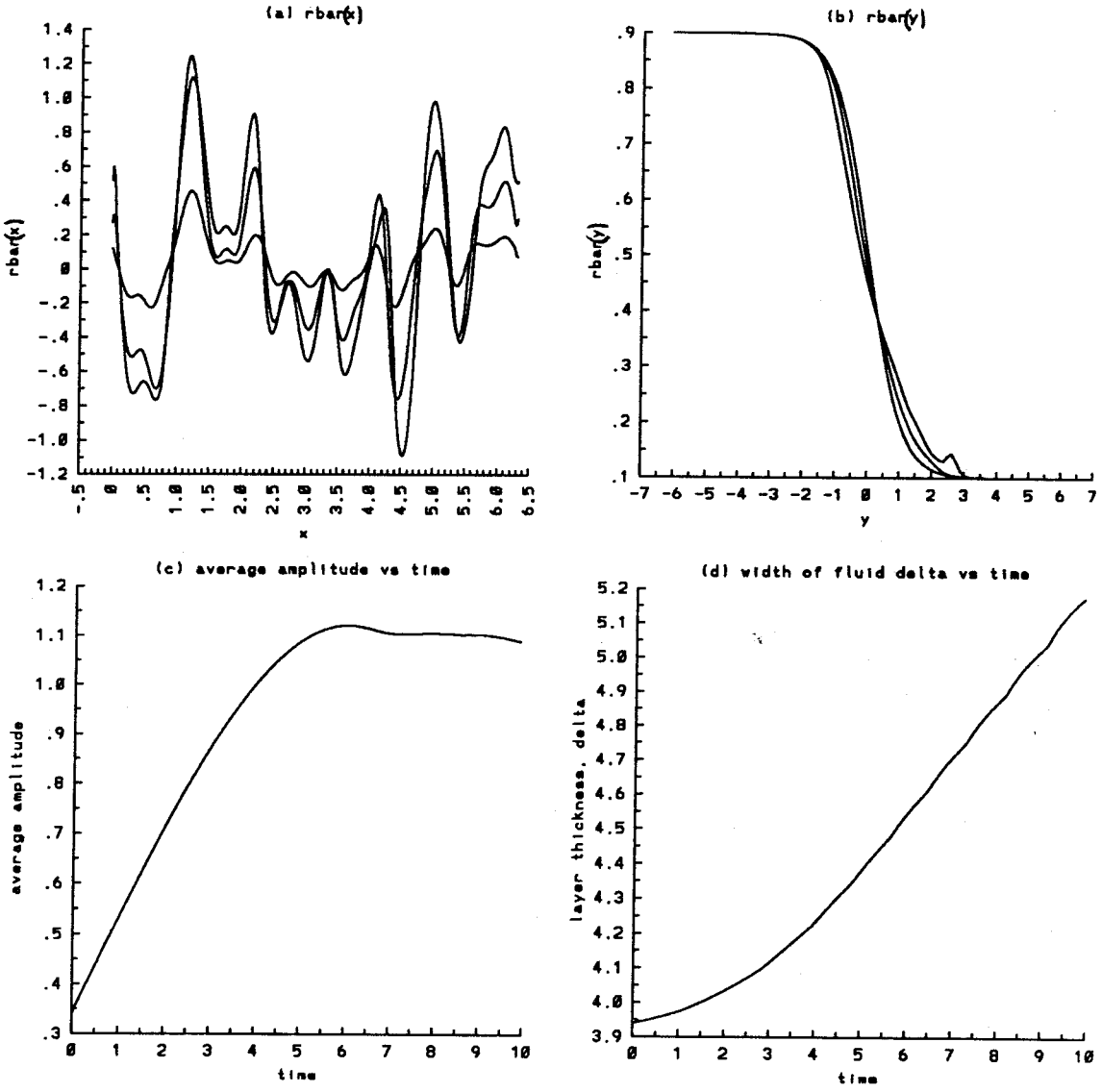

Figure 4.49.1 Time evolution of the average quantities for the fifth initial random profile, A = -0.8, $t = 0$ to 9 : a) $\bar{\rho}_y(x)$, b) $\bar{\rho}_x(y)$, c) average amplitude, and d) width of the density layer.

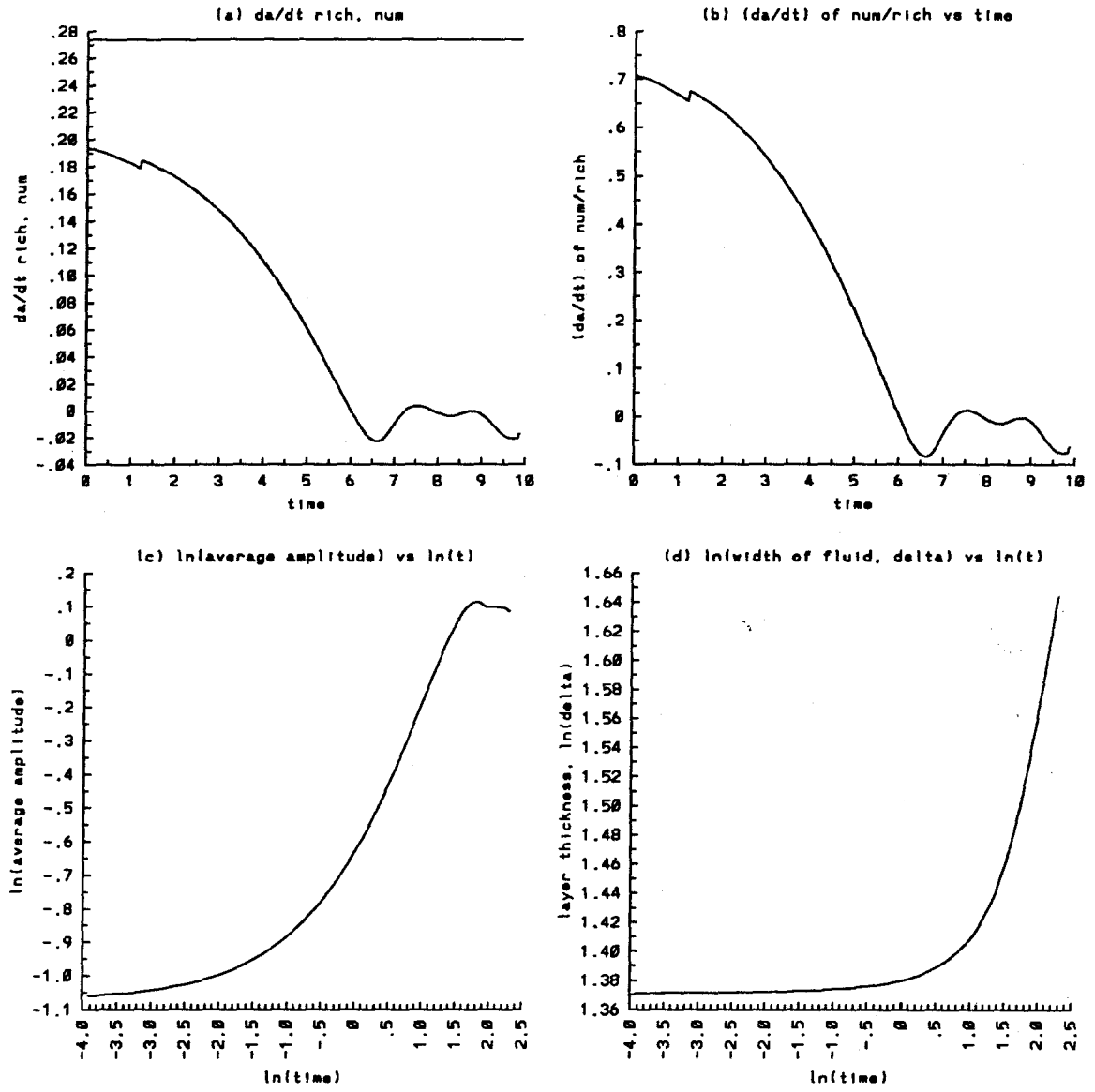

Figure 4.49.2 Time evolution of the average quantities for the fifth initial random profile, A = −0.8, t = 0 to 9.5 : a) growth rate da/dt of the average amplitude, numerical and Richtmyer theory (straight line), b) the ratio of the numerical growth rate da/dt over that predicted by Richtmyer theory, c) $\ln(a)$ *vs* $\ln(t)$, d) $\ln(\delta)$ *vs* $\ln(t)$.

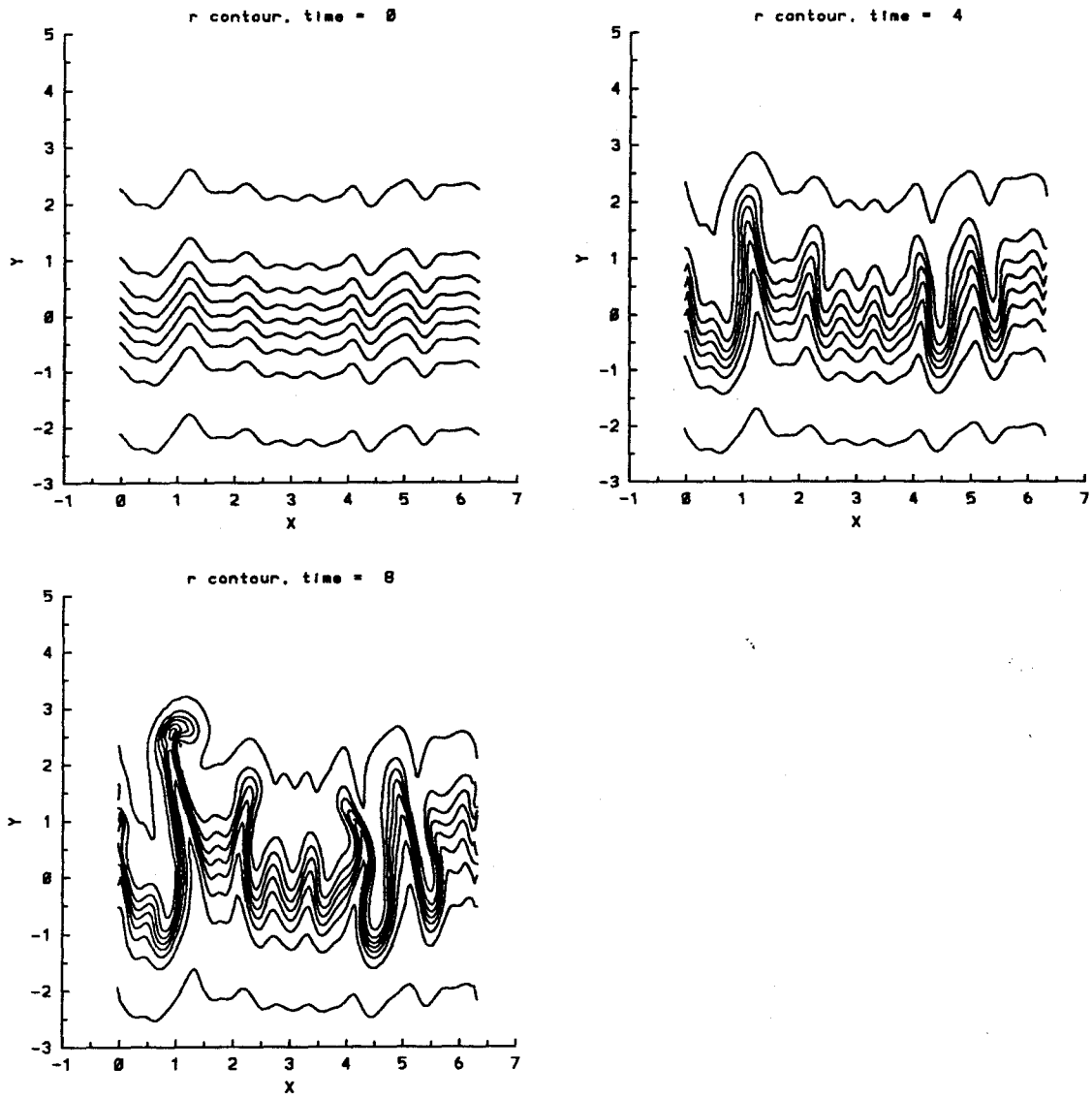

Figure 4.49.3 Time evolution of the density contours for the fifth initial random profile, A = −0.8, t = 0, 4, 8. The contours are at ρ = 0.11, 0.2, 0.3, 0.4, 0.5, 0.6, 0.7, 0.8, 0.89.

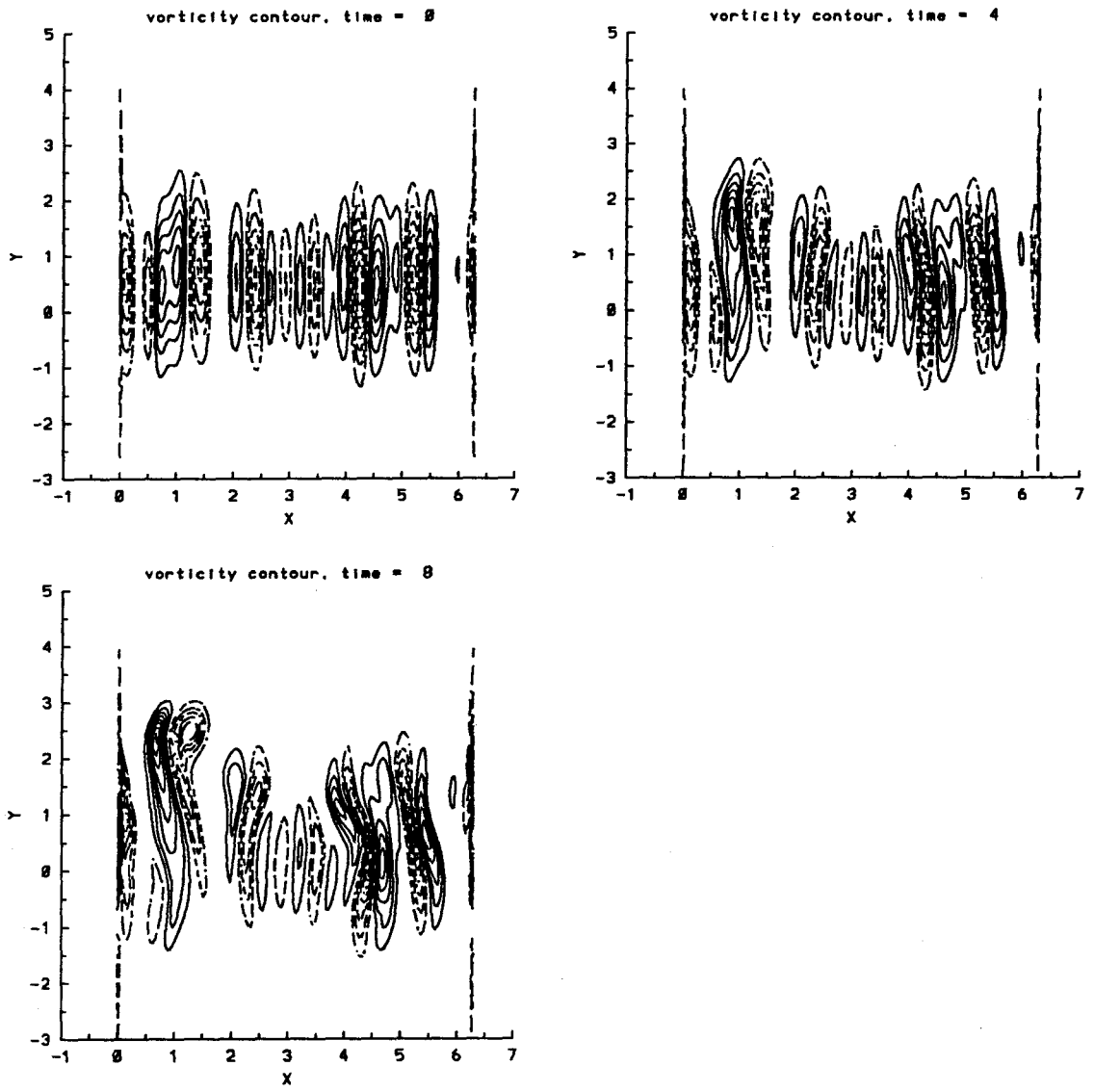

Figure 4.49.3V Time evolution of the vorticity contours for the fifth initial random profile, A = −0.8, t = 0, 4, 8. The contours are from −1.75 to 1.25 for t = 0, −2.0 to 1.50 for t = 4, −2.5 to 2.0 for t = 8, with incremental step size of 0.25. The negative contours are indicated by — · — and positive ones by —. The maximum and minimum vorticities are at the centers of the innermost circles.

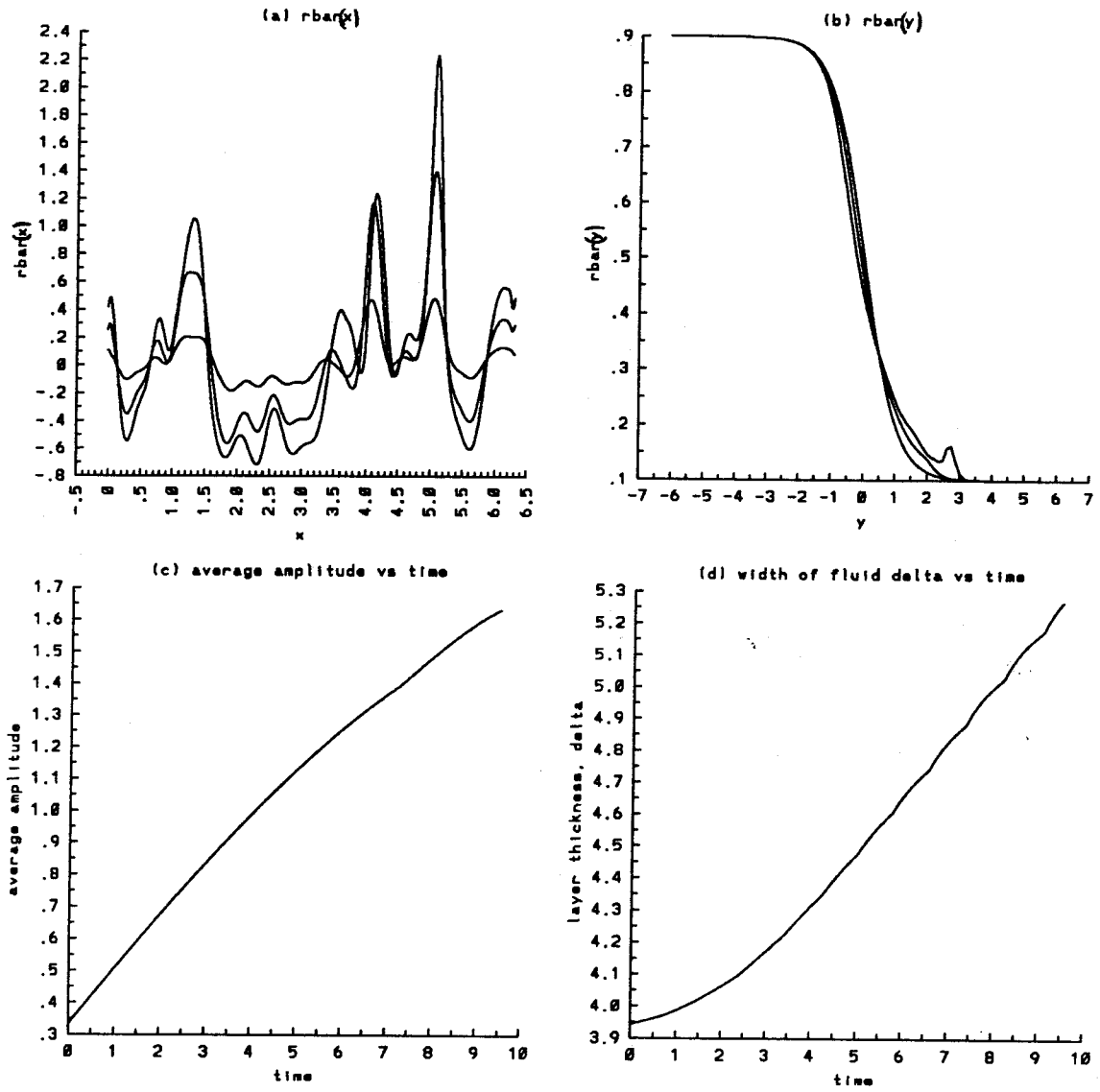

Figure 4.50.1 Time evolution of the average quantities for the sixth initial random profile, A = -0.8, $t = 0$ to 9 : a) $\bar{\rho}_y(x)$, b) $\bar{\rho}_x(y)$, c) average amplitude, and d) width of the density layer.

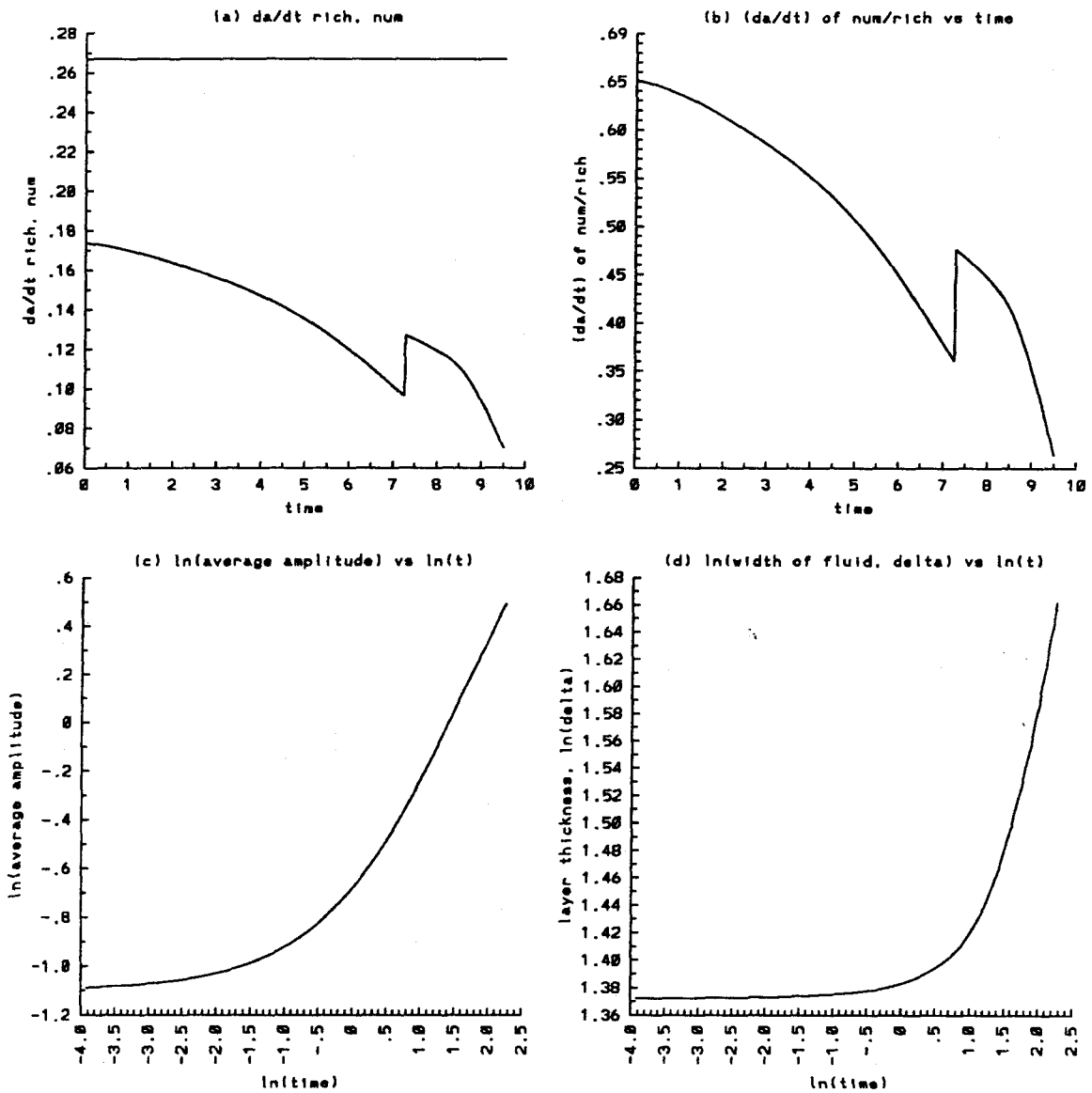

Figure 4.50.2 Time evolution of the average quantities for the sixth initial random profile, A = -0.8, $t = 0$ to 9.5 : a) growth rate da/dt of the average amplitude, numerical and Richtmyer theory (straight line), b) the ratio of the numerical growth rate da/dt over that predicted by Richtmyer theory, c) $\ln(a)$ *vs* $\ln(t)$, d) $\ln(\delta)$ *vs* $\ln(t)$.

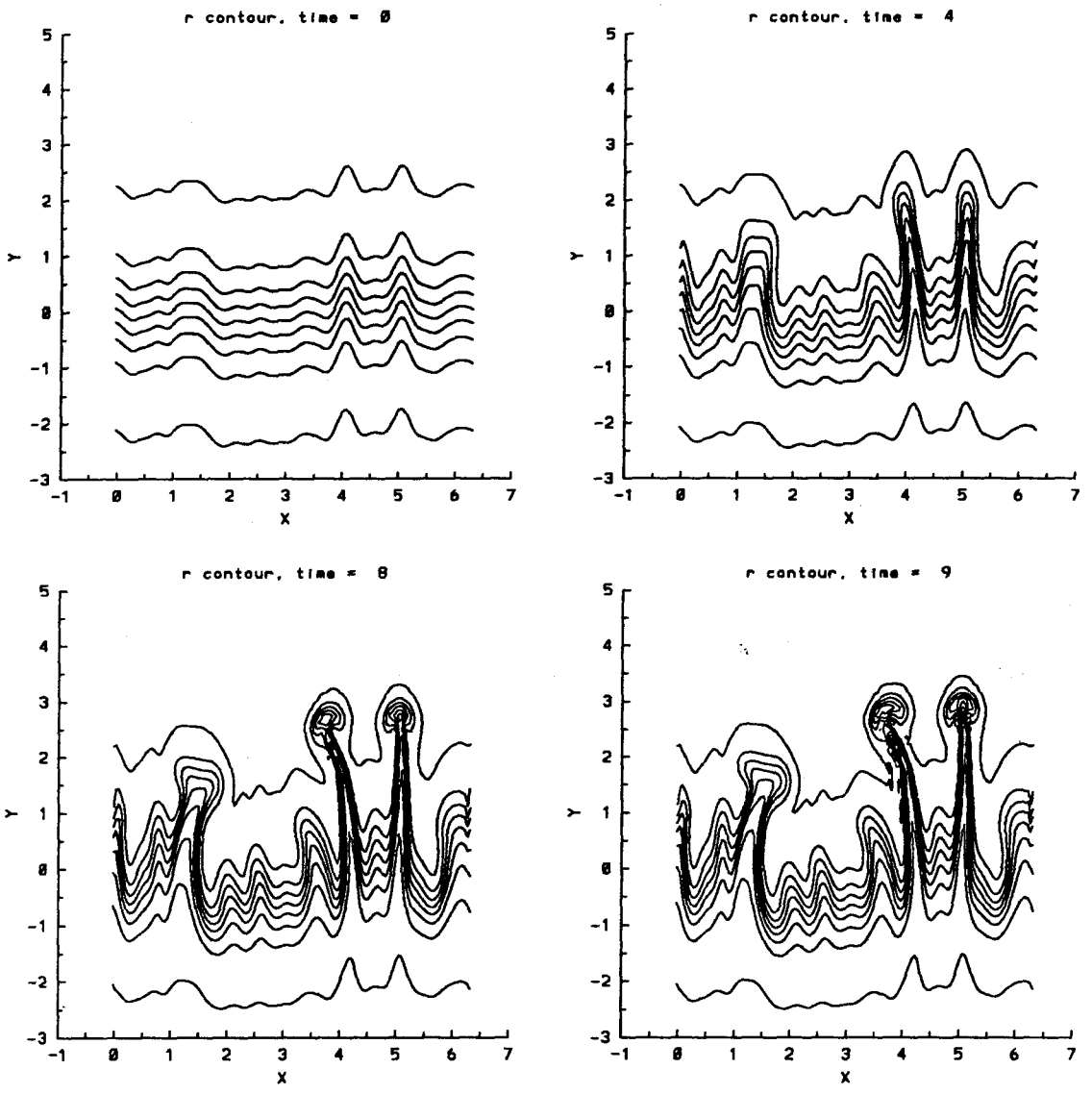

Figure 4.50.3 Time evolution of the density contours for the sixth initial random profile, A = −0.8, t = 0, 4, 8, 9. The contours are at ρ = 0.11, 0.2, 0.3, 0.4, 0.5, 0.6, 0.7, 0.8, 0.89.

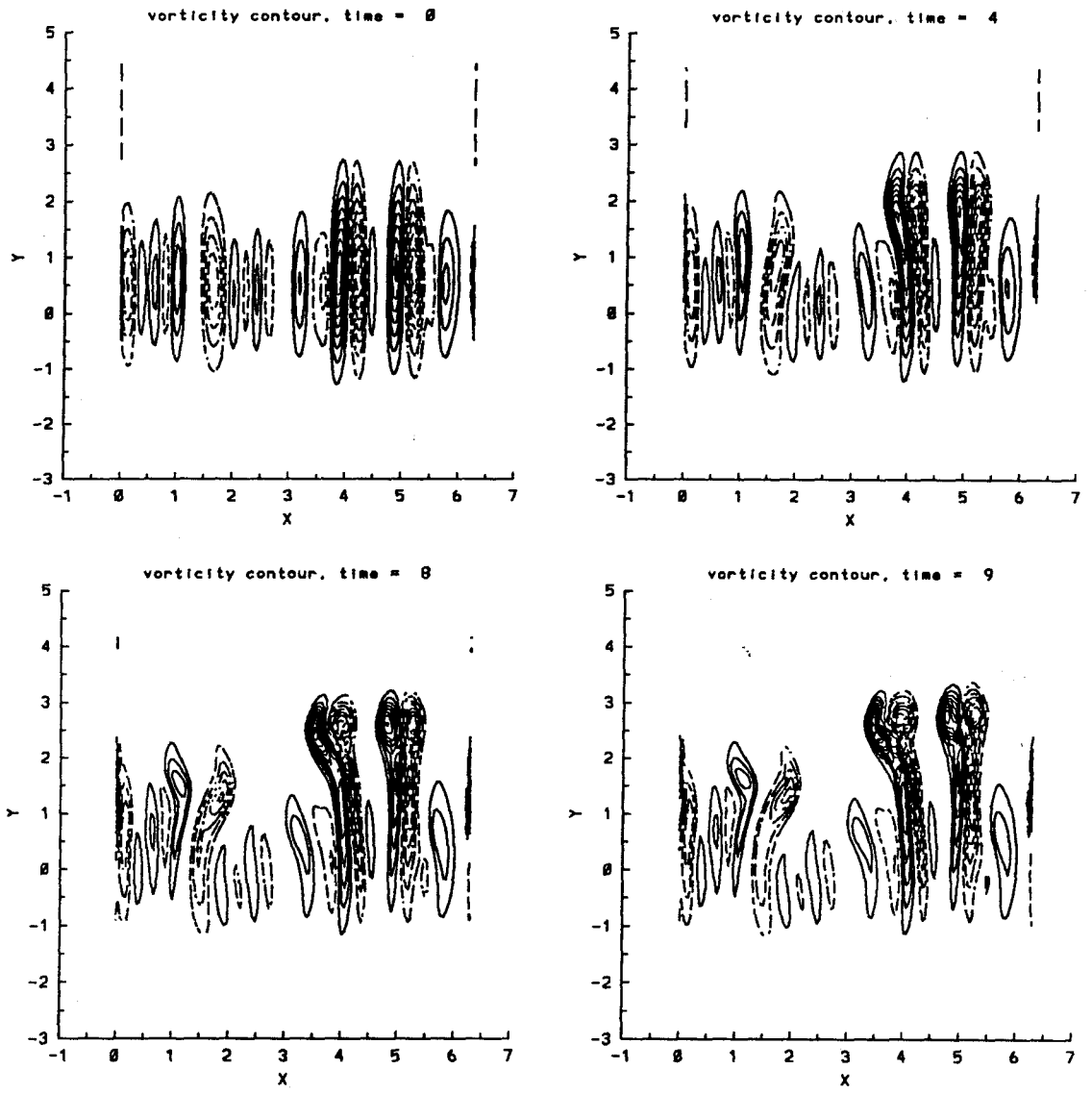

Figure 4.50.3V Time evolution of the vorticity contours for the sixth initial random profile, A = −0.8, t = 0, 4, 8, 9. The contours are from −2.0 to 2.0 t = 0, −1.75 to 2.0 t = 4, −1.75 to 2.5 t = 8, and −2.25 to 2.75 t = 9 with incremental step size of 0.25. The negative contours are indicated by — · — and positive ones by —.

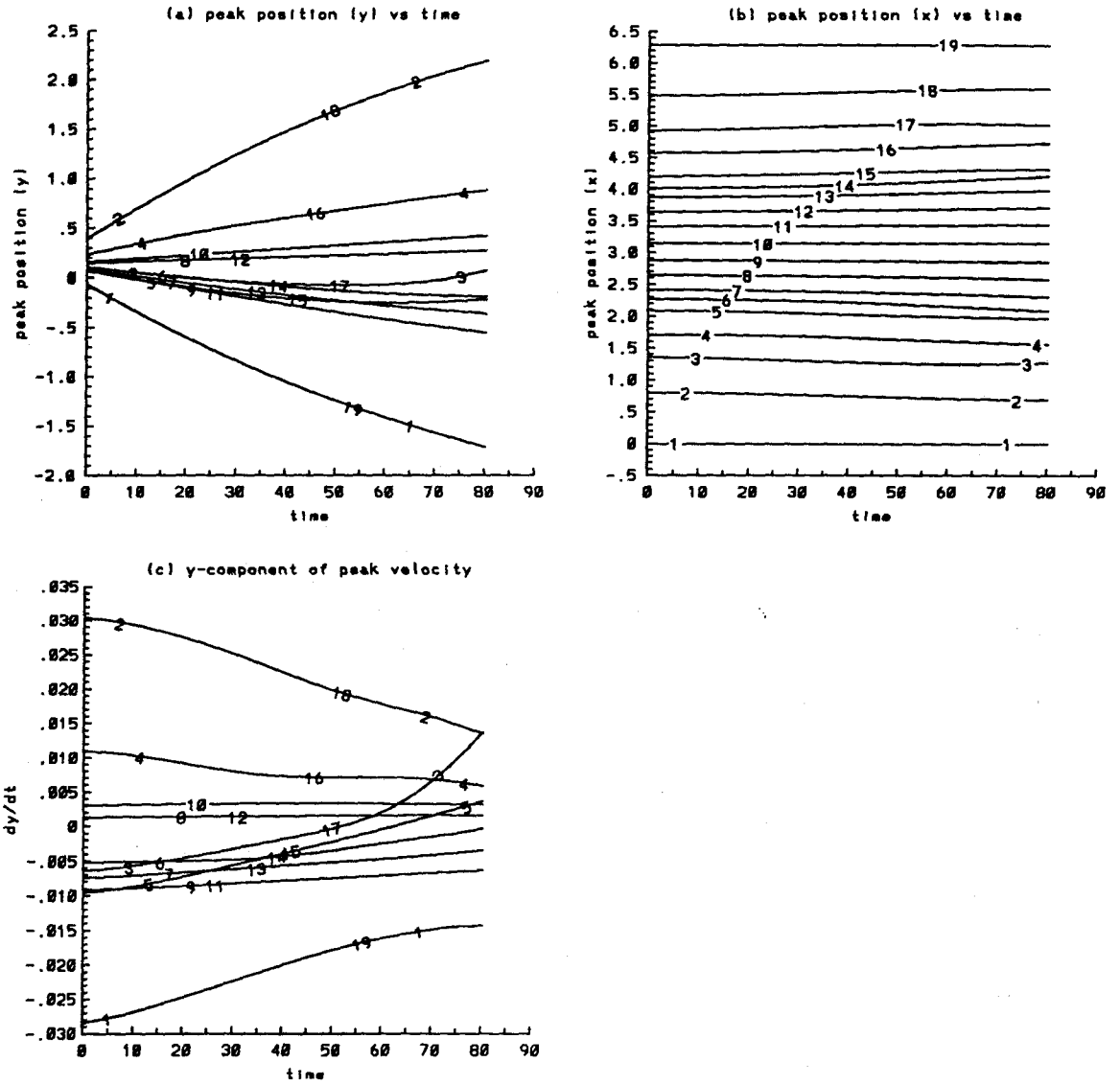

Figure 4.51 Time evolution of the positions and velocities of the average peaks of the second initial random profile, A = −0.2, t = 0 to 89.34 a) y b) x c) dy/dt. The numbers on the curves refer to the peaks on the curves $\bar{\rho}(x)$ versus x.

the emergence of the globules, the growth is in the linear regime. Hence it is proportional to the initial strength of circulation, which is in turn proportional to the density gradient. For all of the multiple scale calculations, the conservation of energy is satisfied as shown in Figure 4.52.5. In the next section, we try to explore the possibility of scaling behavior that governs the late time asymptotic growth of the layer.

4.6.2 Overall growth of the stratified layer

An important issue in this study is the development of a self-similar asymptotic limit independent of the initial random distribution. From Barenblatt's analysis (1983), the propagation of a uniform turbulent layer initially deposited in an inviscid homogeneous fluid is self-similar in time. From a dimensional argument, he found a time exponent of around 2/3 for the thickness of the layer. Due to the presence of large structures in our problem, there may not exist a scaling behavior governing late time growth. Even if there exists a limit, the value of 2/3 for the time exponent is questionable. In an attempt to answer this issue, we plot in Figures 4.52.1, and 4.52.2 the time evolution of the average amplitude a, and the width δ of the stratified layer, and in Figures 4.52.3 and 4.52.4 the terms $\ln(a)$ and $\ln(\delta)$ versus $\ln(t)$ respectively. The curves for a seem to have a slope of 2/3 while for δ the slope is close to 1/4. As seen above, the information from the average amplitude a can be misleading in regard to the growth of the layer. In fact it is the quantity $\delta(t)$ which should exhibit growth varying with time as $t^{2/3}$, if Barenblatt's theory were valid.

4.6.3 Initial growth predicted by linear model

In Figures 4.53 to 4.55, we plot the time evolution of the instability using the linear model for the first initial profile with three different Atwood numbers A = -0.2, -0.5, and -0.8. As in the case of single scale perturbations, the linear model

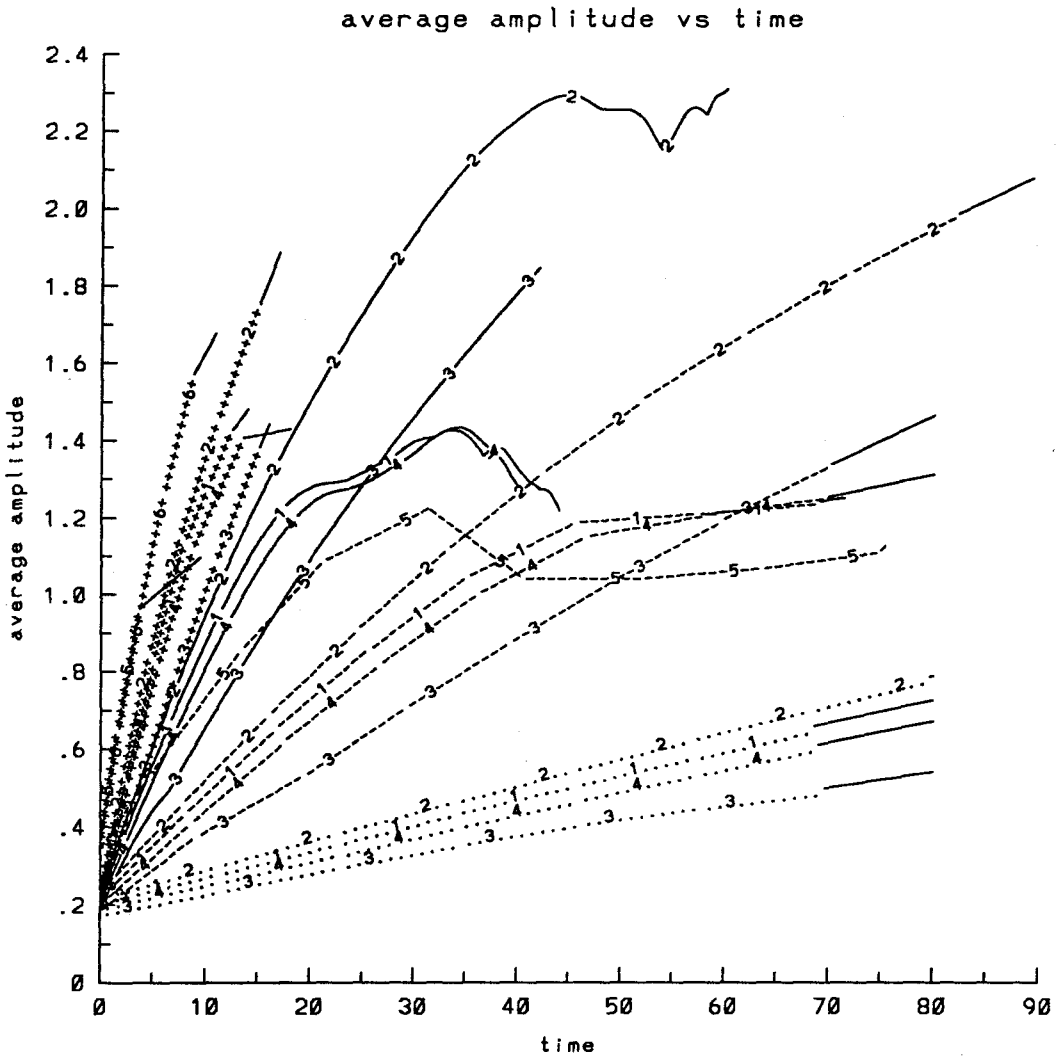

Figure 4.52.1 Time evolution of the average amplitude for six different initial random profiles : $\cdots$ A = – 0.05, – – – A = – 0.2, — A = – 0.5, +++ A = – 0.8. The numbers 1, 2, 3, 4, 5, and 6 on the curves refer to the first, second, third, fourth, fifth, and sixth initial random profiles respectively.

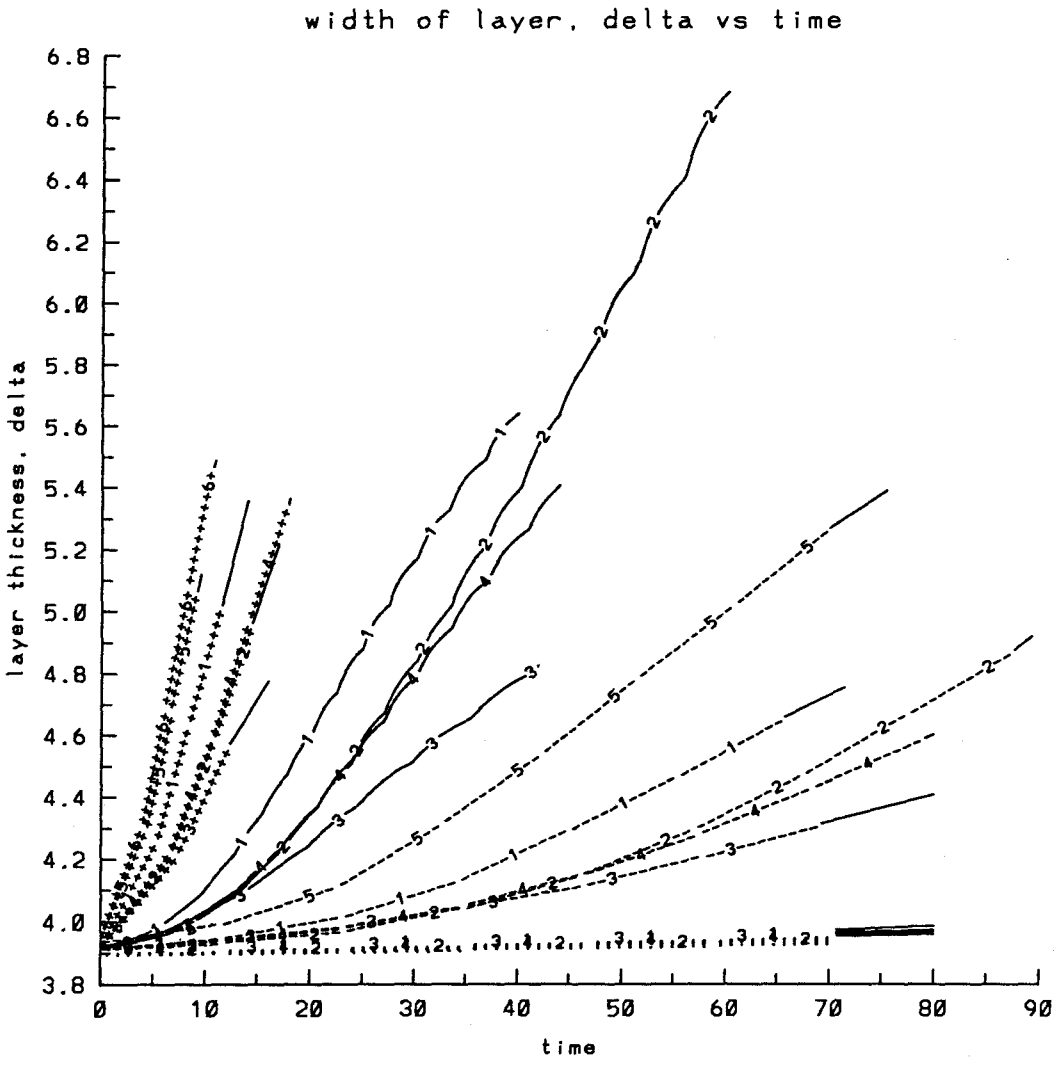

Figure 4.52.2 Time evolution of the width δ of the stratified layer for six different initial random profiles : $\cdots$ A = – 0.05, – – – A = – 0.2, — A = – 0.5, +++ A = – 0.8. The numbers 1, 2, 3, 4, 5, and 6 on the curves refer to the first, second, third, fourth, fifth, and sixth initial random profiles respectively.

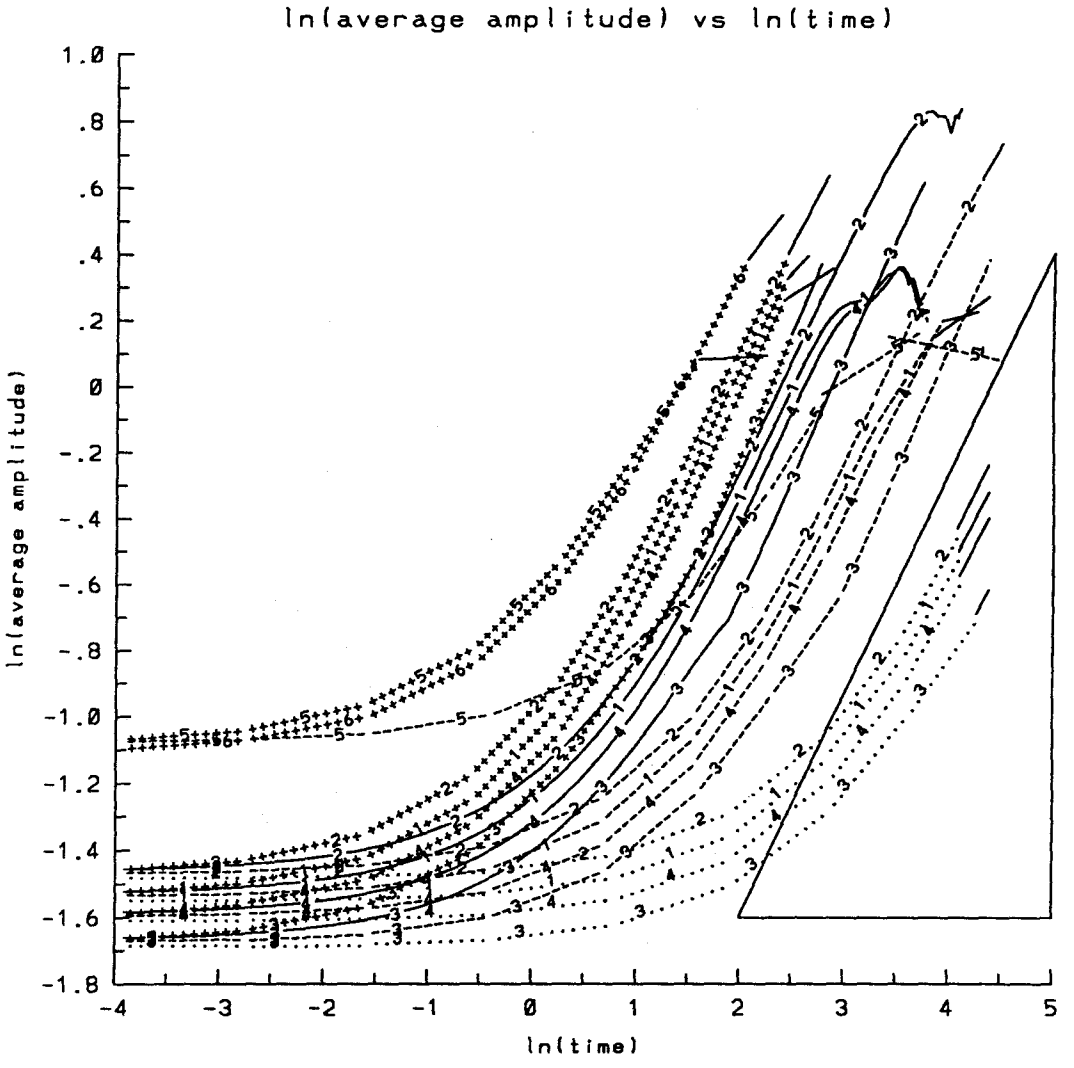

Figure 4.52.3 Combined results of ln(average amplitude) versus ln(time) for six different initial random profiles : $\cdots$ A = – 0.05, – – – A = – 0.2, — A = – 0.5, +++ A = – 0.8. The numbers 1, 2, 3, 4, 5, and 6 on the curves refer to the first, second, third, fourth, fifth, and sixth initial random profiles respectively. The referenced triangle has slope 2/3.

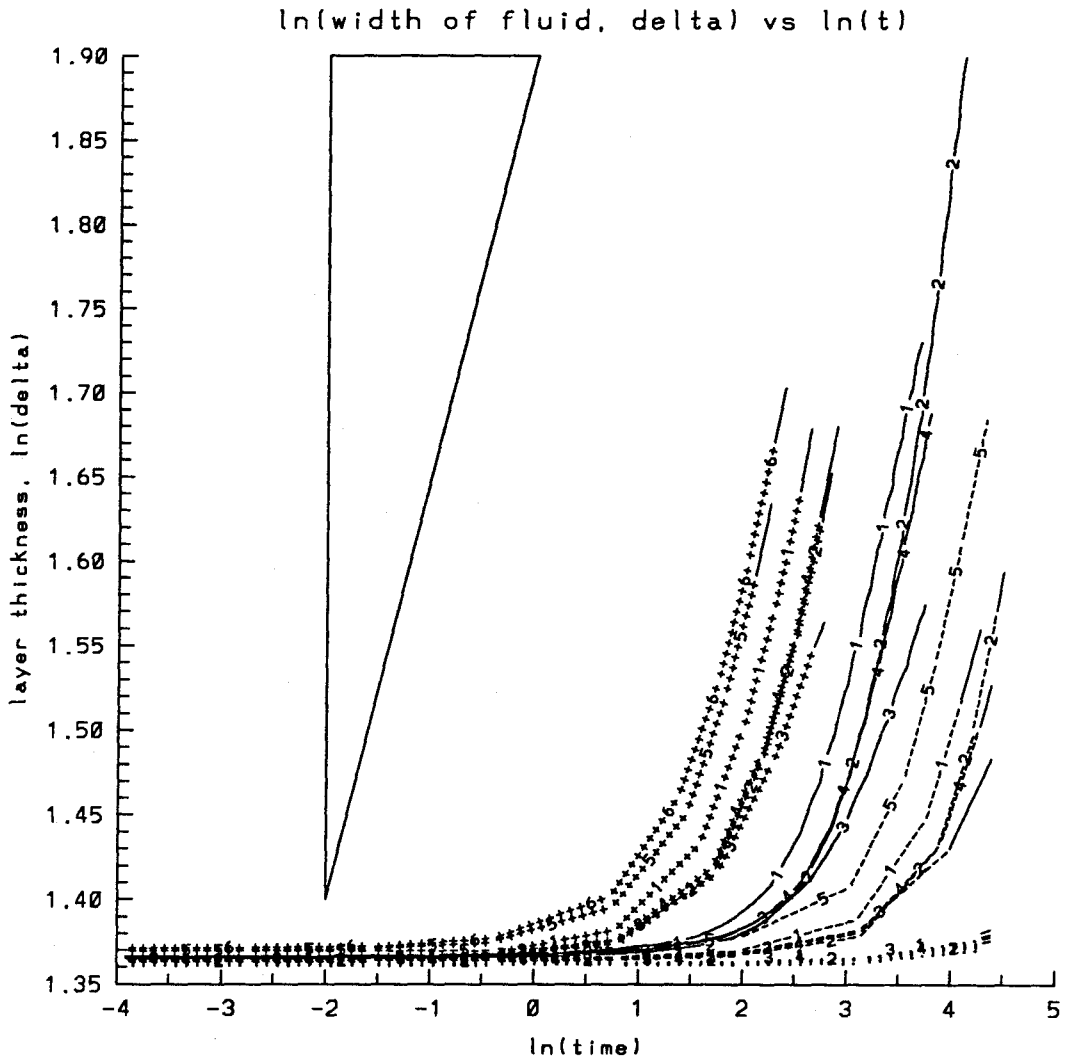

Figure 4.52.4 Combined results of ln(width of stratified layer δ) versus ln(time) for six different initial random profiles : $\cdots$ A = − 0.05, − − − A = − 0.2, — A = − 0.5, +++ A = − 0.8. The numbers 1, 2, 3, 4, 5, and 6 on the curves refer to the first, second, third, fourth, fifth, and sixth initial random profiles respectively. The referenced triangle has slope 1/4.

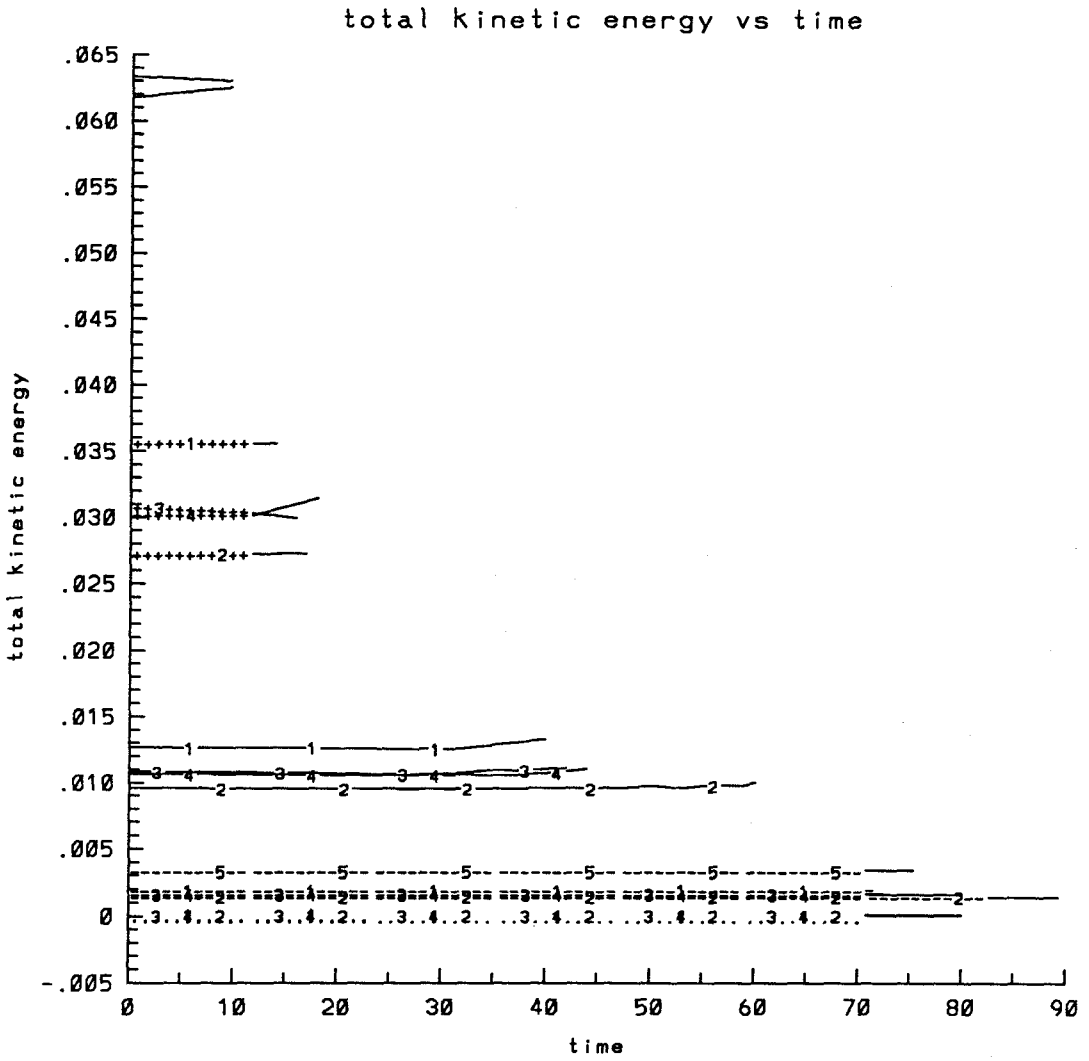

Figure 4.52.5 Time evolution of the total kinetic energy for six different initial random profiles : $\cdots$ A = − 0.05, − − − A = − 0.2, — A = − 0.5, +++ A = − 0.8. The numbers 1, 2, 3, 4, 5, and 6 on the curves refer to the first, second, third, fourth, fifth, and sixth initial random profiles respectively.

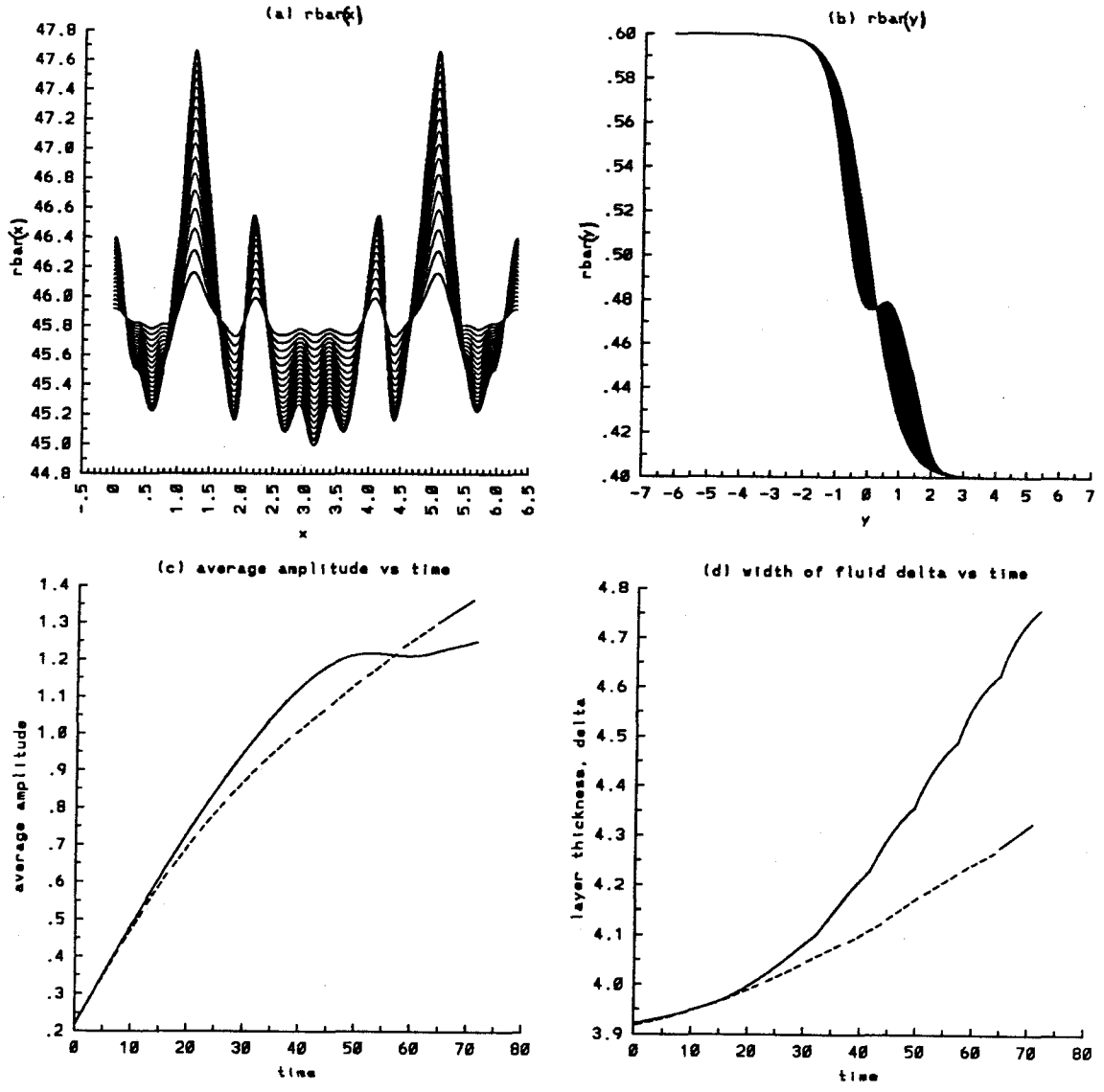

Figure 4.53.1 Time evolution of the average quantities for the first initial random profile, A = -0.2, $t = 0$ to 70.5 : a) $\bar{\rho}_y(x)$, b) $\bar{\rho}_x(y)$. Combined results — numerical simulation, – – – linear model c) average amplitude, and d) width of the density layer.

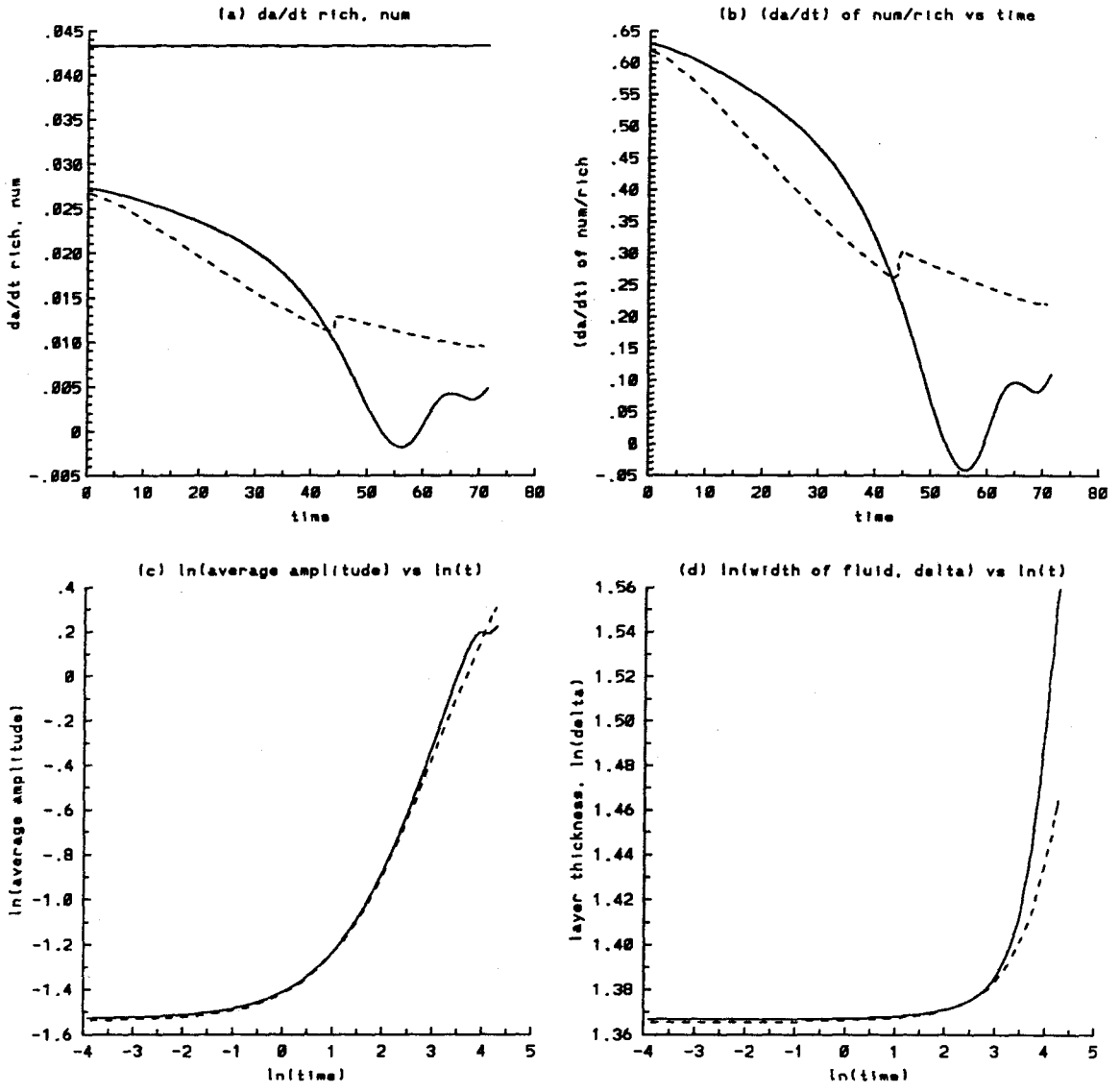

Figure 4.53.2 Time evolution of the average quantities for the first initial random profile, A = −0.2, t = 0 to 70.5. Combined results — numerical simulation, – – – linear model : a) growth rate da/dt of the average amplitude, numerical and Richtmyer theory (straight line), b) the ratio of the numerical growth rate da/dt over that predicted by Richtmyer theory, c) $\ln(a)$ *vs* $\ln(t)$, d) $\ln(\delta)$ *vs* $\ln(t)$.

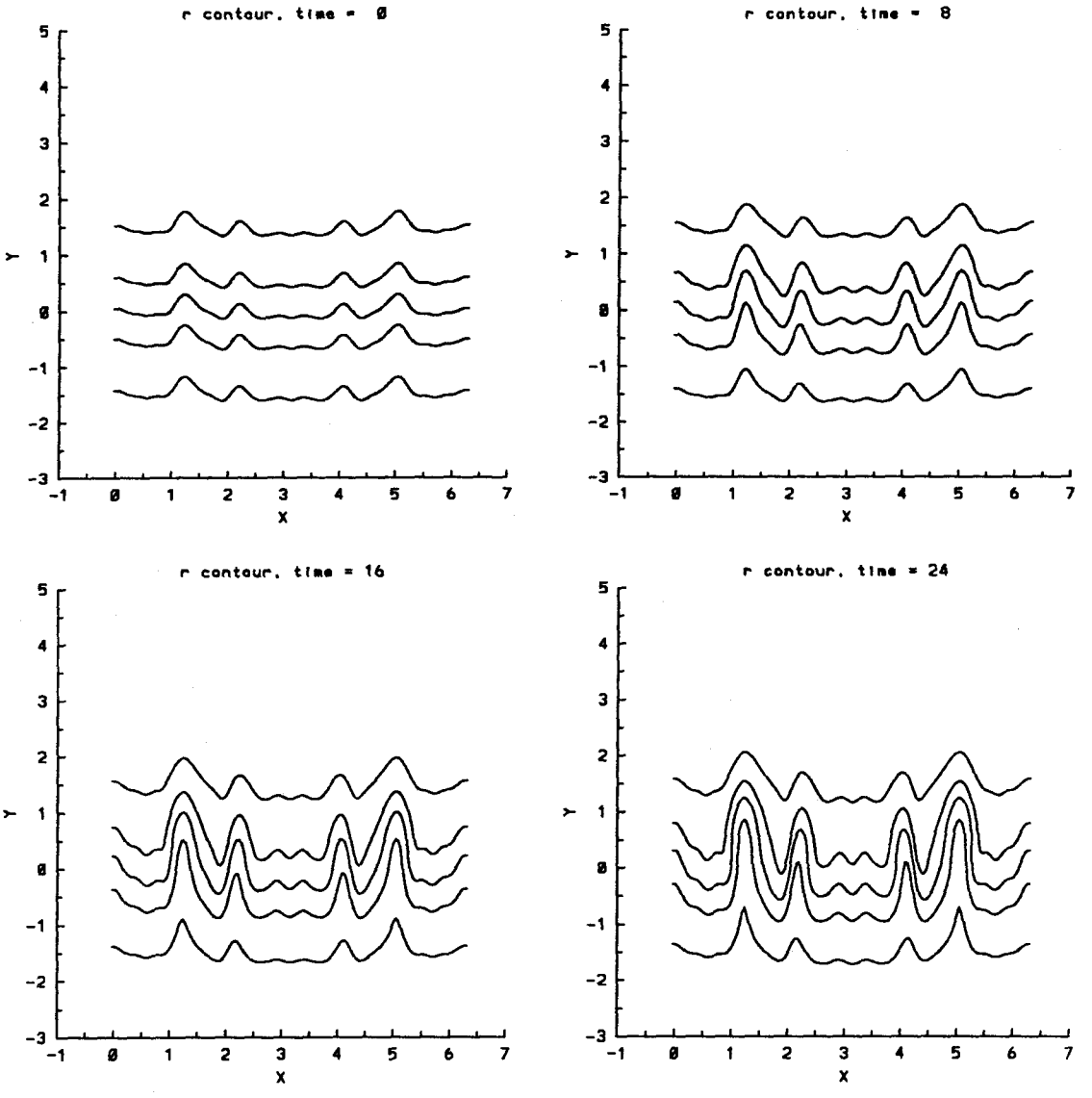

Figure 4.53.3 Time evolution of the density contours for the first initial random profile, A = −0.2, t = 0, 8, 16, 24 using the linear model. The contours are at ρ = 0.41, 0.45, 0.50, 0.55, 0.59.

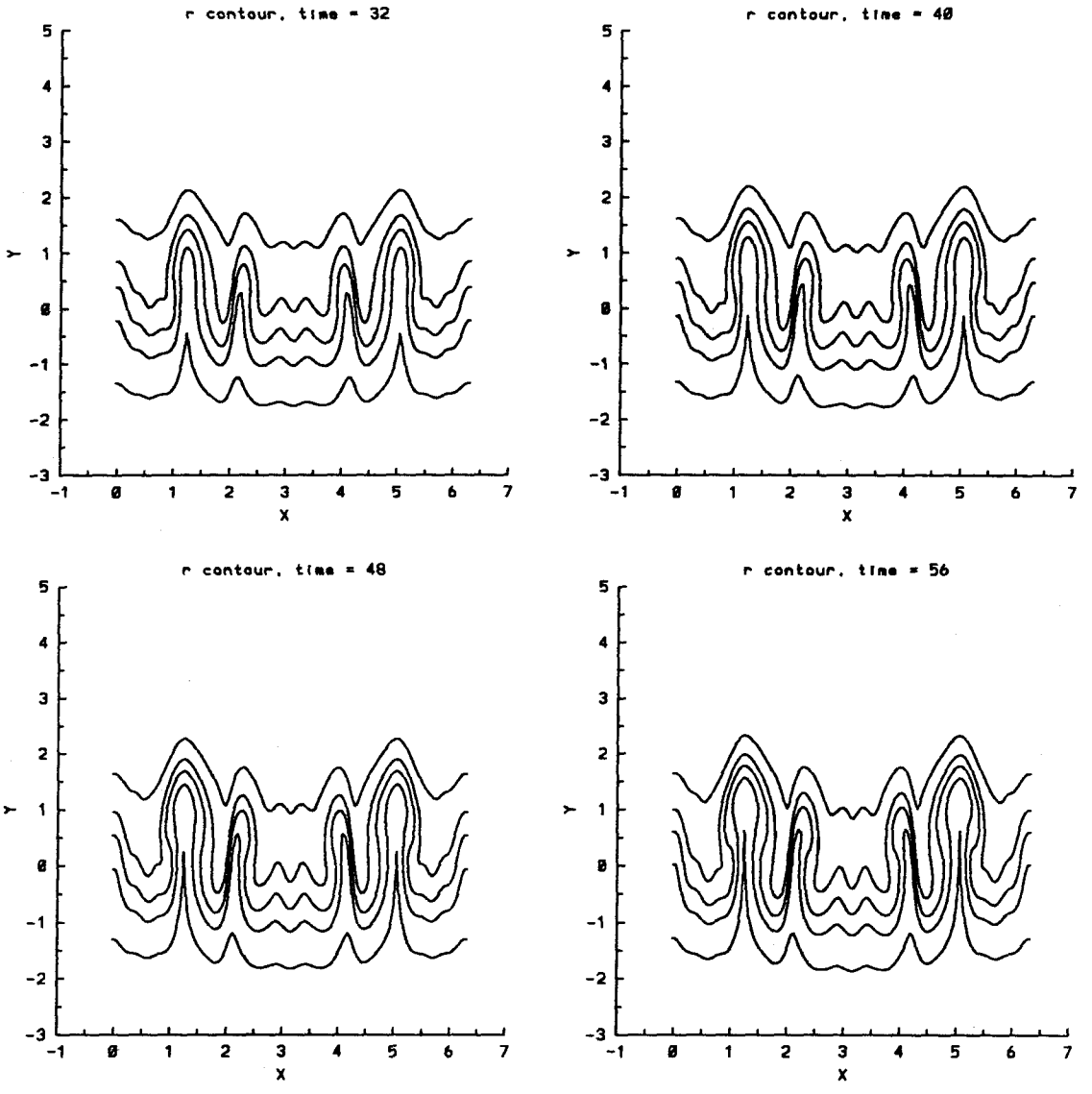

Figure 4.53.4 Time evolution of the density contours for the first initial random profile, A = -0.2, t = 32, 40, 48, 56 using the linear model. The contours are at ρ = 0.41, 0.45, 0.50, 0.55, 0.59.

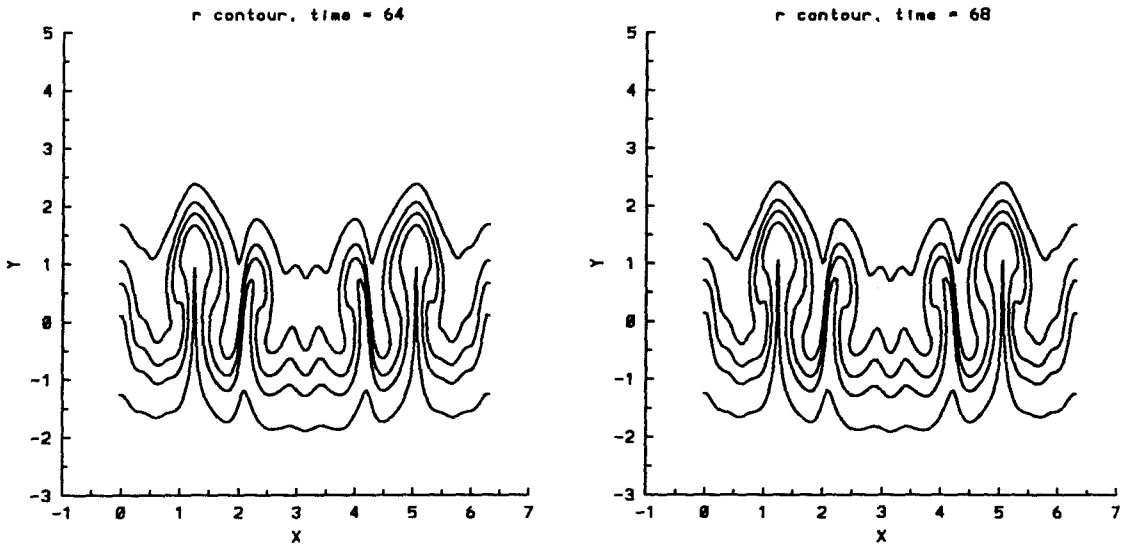

Figure 4.53.5 Time evolution of the density contours for the first initial random profile, A = -0.2, $t = 64$, 68 using the linear model. The contours are at $\rho = 0.41$, 0.45, 0.50, 0.55, 0.59.

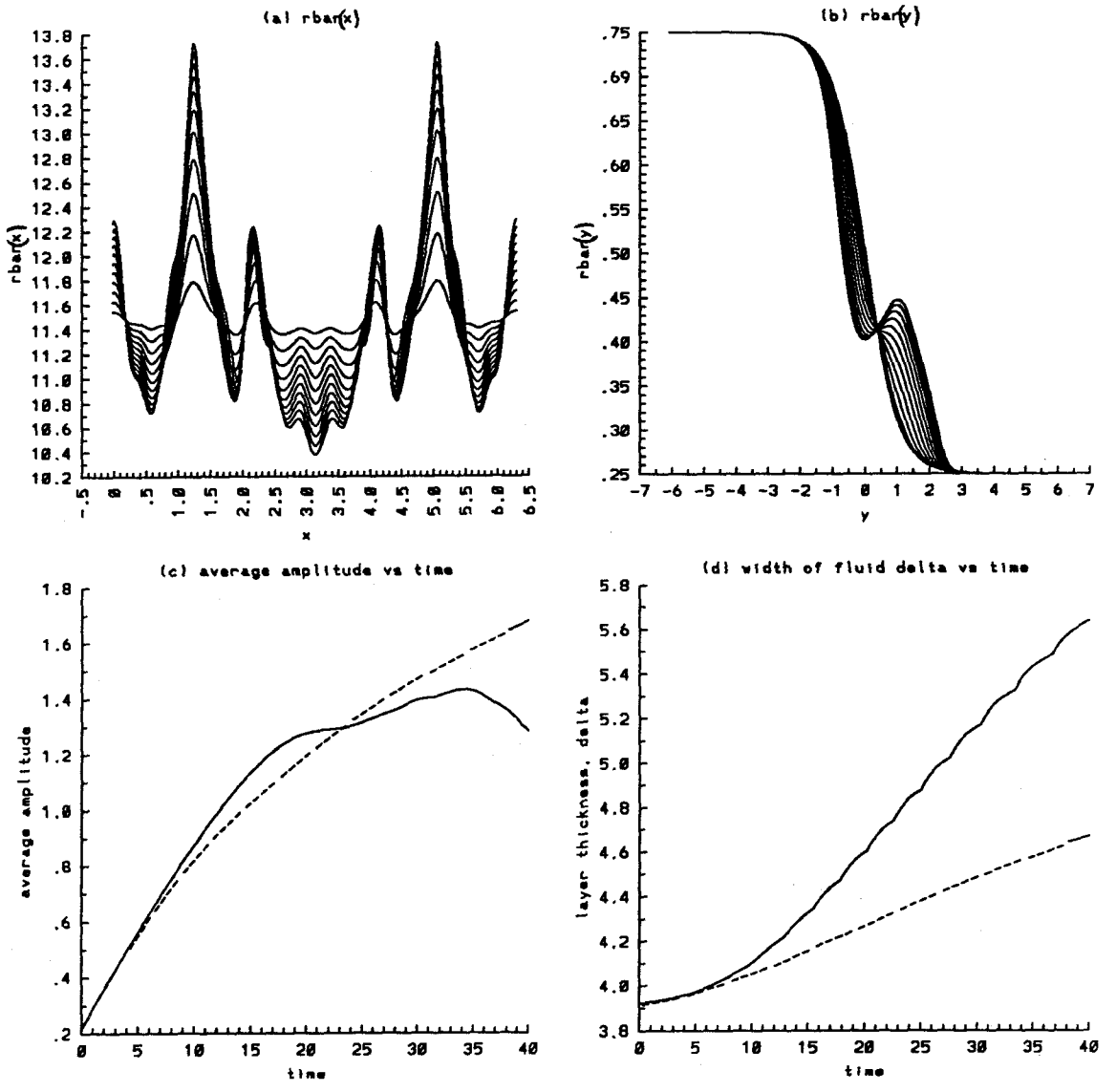

Figure 4.54.1 Time evolution of the average quantities for the first initial random profile, A = -0.5, $t = 0$ to 56 : a) $\bar{\rho}_y(x)$, b) $\bar{\rho}_x(y)$. Combined results — numerical simulation, – – – linear model c) average amplitude, and d) width of the density layer.

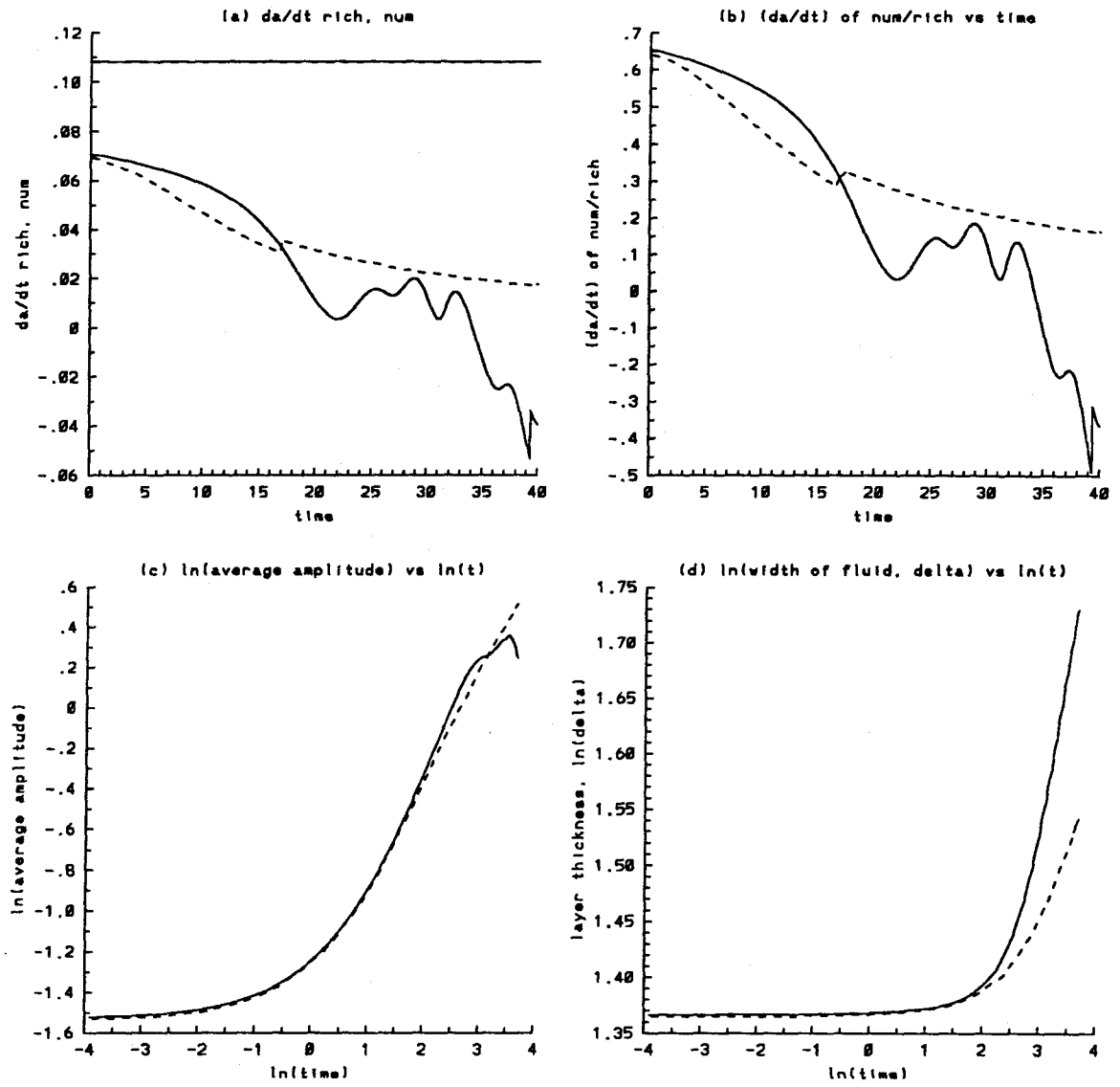

Figure 4.54.2 Time evolution of the average quantities for the first initial random profile, A = −0.5, t = 0 to 56. Combined results — numerical simulation, – – – linear model : a) growth rate da/dt of the average amplitude, numerical and Richtmyer theory (straight line), b) the ratio of the numerical growth rate da/dt over that predicted by Richtmyer theory, c) $\ln(a)$ *vs* $\ln(t)$, d) $\ln(\delta)$ *vs* $\ln(t)$.

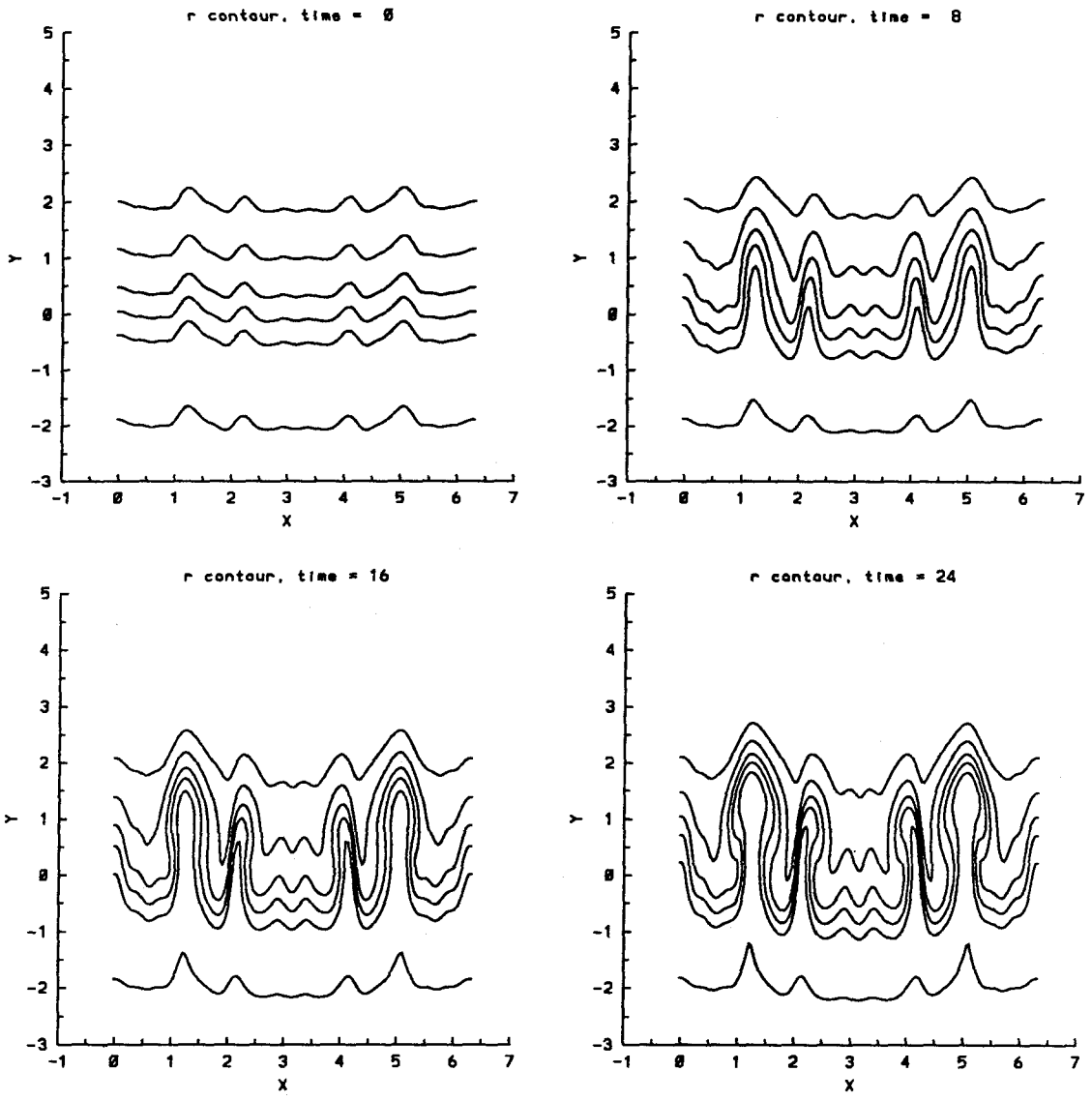

Figure 4.54.3 Time evolution of the density contours for the first initial random profile, A = −0.5, t = 0, 8, 16, 24 using the linear model. The contours are at ρ = 0.26, 0.3, 0.4, 0.5, 0.6, 0.74.

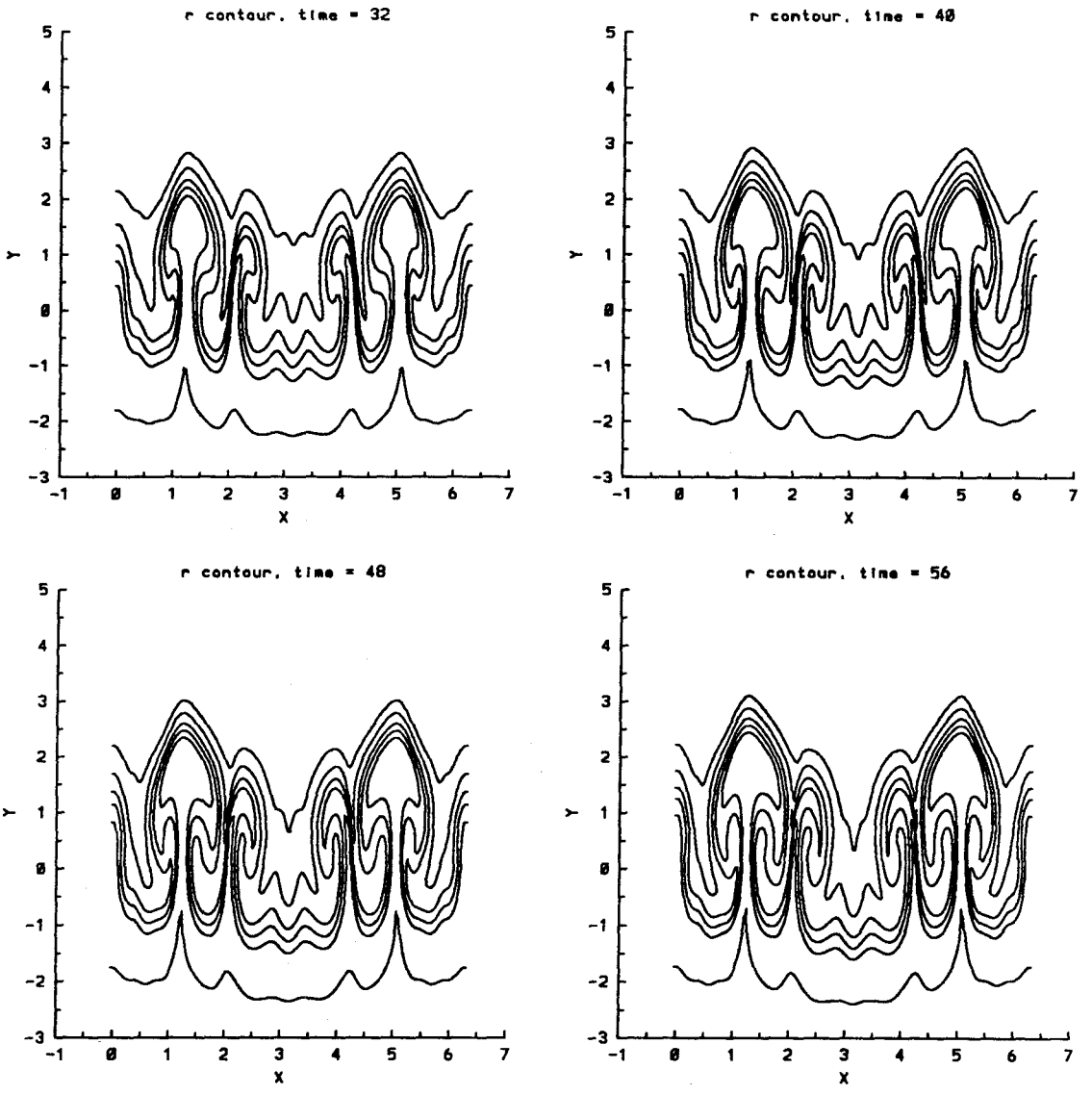

Figure 4.54.4 Time evolution of the density contours for the first initial random profile, A = −0.5, t = 32, 40, 48, 56. The contours are at ρ = 0.26, 0.3, 0.4, 0.5, 0.6, 0.74.

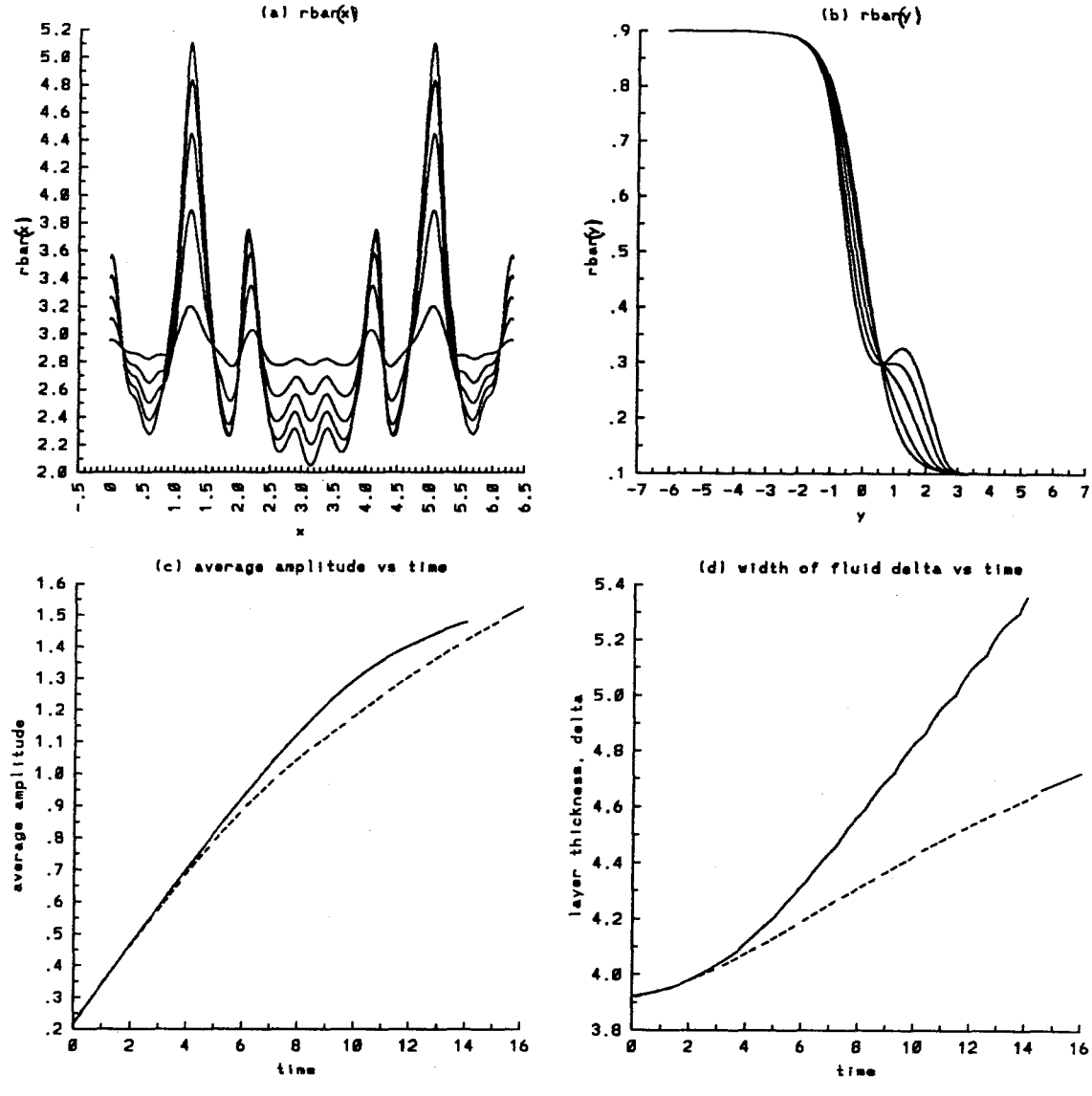

Figure 4.55.1 Time evolution of the average quantities for the first initial random profile, A = −0.8, $t = 0$ to 16 : a) $\bar{\rho}_y(x)$, b) $\bar{\rho}_x(y)$. Combined results — numerical simulation, – – – linear model c) average amplitude, and d) width of the density layer.

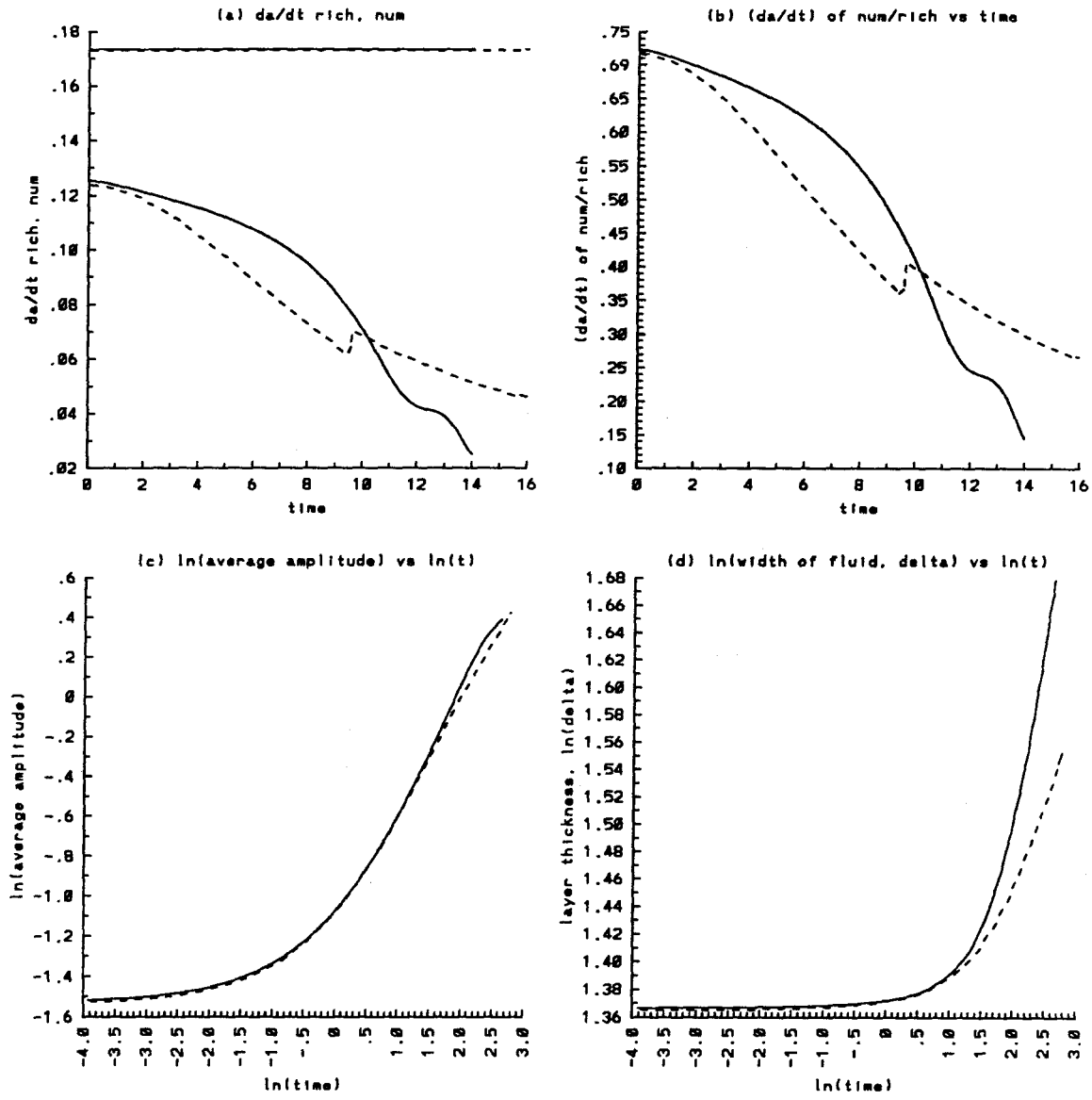

Figure 4.55.2 Time evolution of the average quantities for the first initial random profile, A = −0.8, t = 0 to 16. Combined results — numerical simulation, – – – linear model : a) growth rate da/dt of the average amplitude, numerical and Richtmyer theory (straight line), b) the ratio of the numerical growth rate da/dt over that predicted by Richtmyer theory, c) $\ln(a)$ *vs* $\ln(t)$, d) $\ln(\delta)$ *vs* $\ln(t)$.

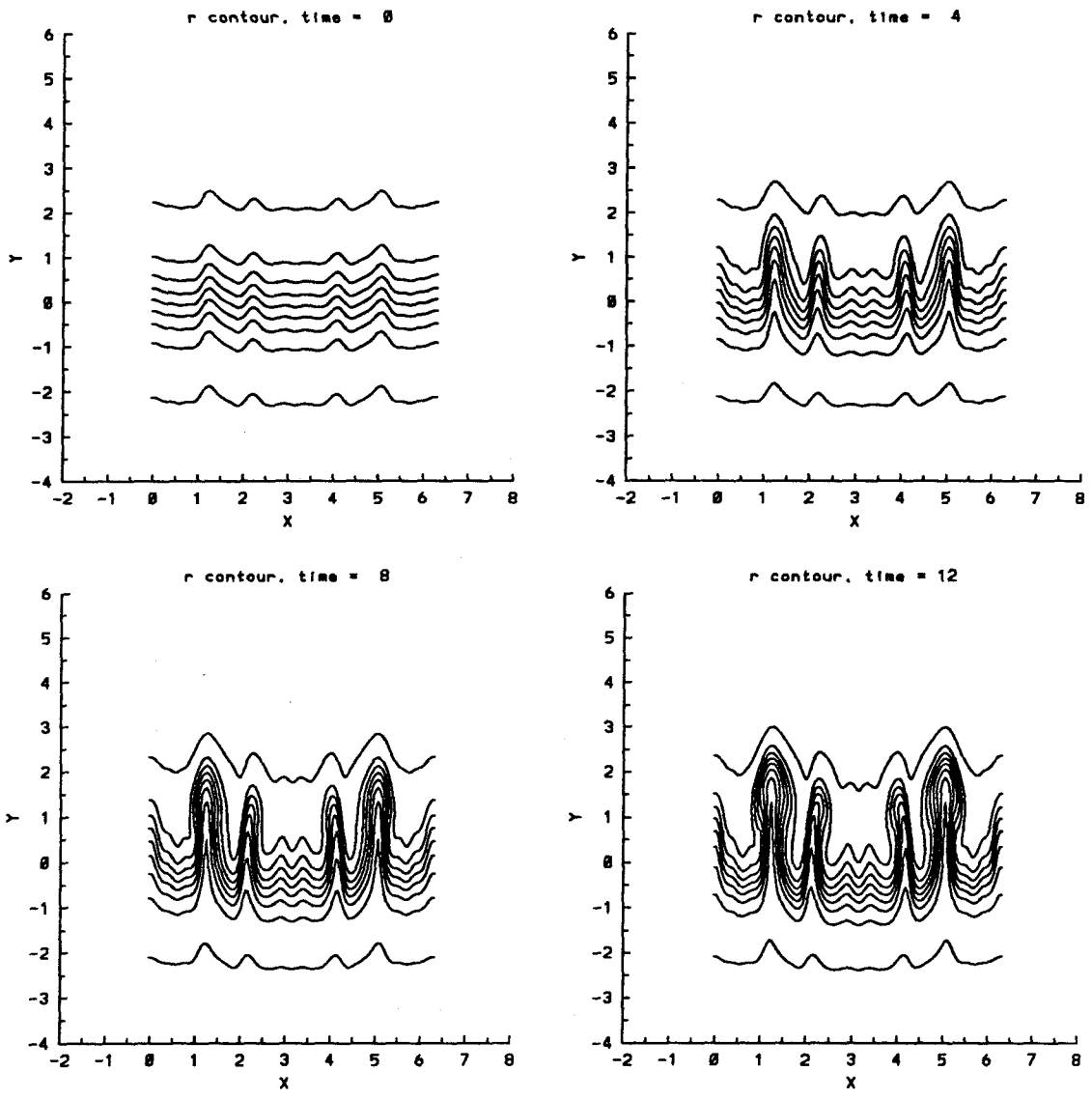

Figure 4.55.3 Time evolution of the density contours for the first initial random profile, A = −0.8, t = 0, 4, 8, 12 using the linear model. The contours are at ρ = 0.11, 0.2, 0.3, 0.4, 0.5, 0.6, 0.7, 0.8, 0.89.

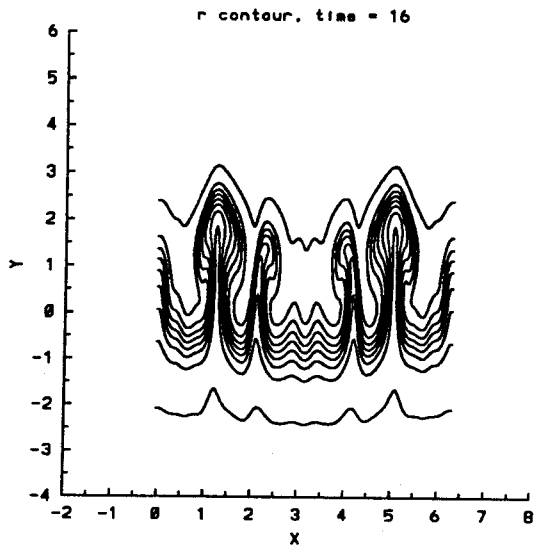

Figure 4.55.4 Time evolution of the density contours for the first initial random profile, A = -0.8, $t = 16$ using the linear model. The contours are at $\rho = 0.11$, 0.2, 0.3, 0.4, 0.5, 0.6, 0.7, 0.8, 0.89.

correctly predicts the average growth of the instability at the initial time. For example, this agreement extends to times of the order of $t = 20$ in the case of A $= -0.2$. This corresponds to travel of the layer over a distance comparable to 5 layer widths. For higher Atwood ratio, the corresponding distances are 2 1/2 and 1 for A $= -0.5, -0.8$ respectively. For long time simulation, it underpredicts the overall growth. From the density contour plot, one obvious limitation of the linear model is its inability to simulate the emergence of the large scale structures. The formation of the globules at late times is therefore definitely a nonlinear effect. Their interaction gives rise to a relatively faster growth than the linear model predicts.

In summary, for an initial random profile, during the first phase of its development, the growth is in the linear regime where the internal peaks interact weakly with each other. The higher the peaks, and the closer they are from the middle horizontal plane of the layer, the faster they grow. As the peaks emerge from the layer, they form fluid globules that roll up. The initial energy deposited in the layer is used to drive the mixing process rather than the growth of the layer. There appears to exist a weak scaling behavior of the layer thickness δ with time exponent of 1/4 in the later development of the instability, which depends mildly on the initial density distributions. A much more definite answer can only be obtained with longer simulations. In the next chapter, we conclude our work by summarizing the results obtained, and discuss some possible alternatives for further study.

CHAPTER 5

CONCLUSIONS

An extensive simulation of the two-dimensional incompressible Richtmyer-Meshkov instability of a continuously stratified fluid is presented in this study as a model of shock induced Richtmyer-Meshkov instability. The initial motion after the passage of the shock is assumed to be equivalent to the motion generated by an impulsive acceleration except for the small effect of compressibility. Using Chisnell's theory (1955) of a shock passing a diffuse interface, we found that the assumption of incompressible impulsive motion is excellent for a weak shock, and small density ratio. Uniform motion of the fluid that is indicative of an impulsive start, however, depends strongly on the density gradient. The smaller the gradient, the more uniform the velocity of the gas becomes. The density profile, on the other hand, depends strongly on the shock strength. A weak shock can modify the characteristic length of the density profile to a great degree, but does not alter significantly the density jump. For a strong shock, both the length and magnitude of the interfacial density gradient are modified. Given the observation that under the conditions discussed above, shock induced motion is equivalent to impulsive motion, we use the velocity field generated by an impulse as an initial condition for our numerical simulation of Richtmyer-Meshkov instability. We note that our simulation is purely incompressible, since as shown in Chapter 2 if the shock is weak, the residence time is short and the subsequent dynamics should be incompressible.

For the simulation, since there is a region of sharp density gradient in the flow domain, we solve the problem on a non-uniform grid. The initial impulsive

acceleration problem is solved by inverting a Poisson-type equation for the pressure. The governing equations in a moving reference frame are discretized using the Crank-Nicholson scheme on all terms. The resulting nonlinear system of equations is solved iteratively by introducing a fictitious pseudo-time problem known as the artificial compressibility method. The numerical scheme is tested using five different techniques which ascertain its accuracy, efficiency, and stability.

For a small single scale perturbation on a sharp interface, our numerical growth rates of the instability are the same as those predicted by Richtmyer theory. For a continuous interface, and similarly for a highly perturbed layer, the Richtmyer formula overpredicts the growth rate as discussed in Chapter 4. The growth rate varies most strongly with variations of the layer thickness. Variation of the growth rate with amplitude and Atwood ratio are less pronounced.

For the single scale problem, with L = 1.0, our simulation covers the range of A from -0.8 to -0.05, and ϵ from 0.2 to 1.0. The numerical growth rates for these cases are about half of the Richtmyer results for the sharp profiles with an equivalent jump in density. The rate decreases in time in proportion to the nonlinear effects. The higher the perturbation amplitude and the Atwood number, the greater the reduction in the growth rate da/dt. The initial behavior is linear over a time equivalent to the traversal of several layer thickness. It is observed that there is no existence of a self-similar long-time asymptotic limit, as in the case of Rayleigh-Taylor instability in the single scale regime. For all cases, we observe the emergence of fluid plumes due to roll-up where the nonlinear effects become significant. This phenomenon causes the overall growth of the layer to decrease, and the initial deposited energy is used to increase the internal mixing of the stratified layer.

For the multiple scale problem, we observe a weak scaling behavior in the growth of the density layer. The layer thickness δ seems to scale with $t^{1/4}$ in contrast to the $t^{2/3}$ power law of Barenblatt even at low Atwood ratio. We believe this is a consequence of the inhomogeneity and anisotropy which is related to the presence of large scale vortices. The late time behavior of the instability is dominated by

the emergence of plumes of fluid, once an internal peak reaches the boundaries of the layer. These fluid globules resemble the nonlinear development of the single scale problem. The formations of the plumes may correspond to weakly interacting single scale modes.

The detailed structure of the time evolution of the incompressible Richtmyer-Meshkov instability has been studied extensively for both of the single and multiple scale problem. Due to the difficulty of resolving the small scales in mixing stages of the instability, we cannot readily extend the simulations at their present resolutions to longer times. This problem can be overcome with enhanced resolution. Since the nonlinear development of the instability is connected to the time evolution of vortex pairs of opposite signed vorticity, it may be possible to construct a model for the late time behavior through the use of vortex dynamics and appropriate modeling of the baroclinic interactions.

APPENDIX

The random numbers r_{k1} used in the multiple scale problem are listed in Table A-1 below.

Table A-1

Random parameters r_{k1} for four initial density distribution.

k	$1st$ profile	$2nd$ profile	$3rd$ profile	$4th$ profile
1	0.2751921	0.3298150	0.9529670	0.6640730
2	0.8888904	0.7173490	0.1626060	0.9854710
3	0.6348671	0.8679210	0.6224670	0.8386250
4	0.4398165	0.8192670	0.6426410	0.3251820
5	0.0007059	0.8600640	0.3859950	0.3385220
6	0.1755233	0.6563750	0.7847900	0.6320470
7	0.9761031	0.2583430	0.9588820	0.4574180
8	0.5681258	0.3082260	0.3315980	0.1176570
9	0.2711180	0.6972540	0.6831200	0.7242860
10	0.5584524	0.5975760	0.2575900	0.9374660
11	0.0573481	0.6791700	0.5677850	0.7264860
12	0.5488701	0.6054280	0.9451590	0.5130380
13	0.9679297	0.9568540	0.0394958	0.3754490
14	0.4032842	0.2474830	0.1942990	0.4602190
15	0.0975372	0.5564400	0.7869740	0.3619470
16	0.4471384	0.3467640	0.6032460	0.1429350
17	0.0023837	0.2345760	0.8757100	0.8710980
18	0.4674150	0.4922850	0.0836847	0.3497710
19	0.7002206	0.0352285	0.1166330	0.5868370
20	0.7126347	0.5981560	0.1046270	0.8136450
21	0.6703379	0.6970640	0.2422350	0.0863009
22	0.8928567	0.0868583	0.6474060	0.4931420
23	0.8535640	0.1167580	0.1775080	0.6293650

Table A-1(*cont'd*)

Random parameters r_{k1} for four initial density distribution.

k	1*st* profile	2*nd* profile	3*rd* profile	4*th* profile
24	0.1796786	0.4968310	0.9111100	0.8493050
25	0.6522657	0.3333960	0.9809520	0.4097850
26	0.2062365	0.1098270	0.4699440	0.0956409
27	0.9303484	0.8252460	0.9024920	0.8438360
28	0.0672049	0.0583677	0.8460980	0.5748300
29	0.0132558	0.7709130	0.6588570	0.1527100
30	0.3187970	0.1898910	0.4803390	0.1316690
31	0.6879703	0.8672080	0.0156801	0.5854020
32	0.9787641	0.5904350	0.6873580	0.8615760
33	0.2030125	0.8597640	0.7575580	0.9781390
34	0.5263962	0.6907290	0.4087590	0.5421870
35	0.2684416	0.9638210	0.3229550	0.3386810
36	0.9025217	0.2730060	0.9637420	0.3884610
37	0.0558552	0.2479040	0.2458840	0.8707220
38	0.5095074	0.3096030	0.5987440	0.4023370
39	0.1983894	0.6606930	0.5912930	0.5534480
40	0.2112587	0.1071700	0.5788170	0.8501400
41	0.7907189	0.5666290	0.2982190	0.6232370
42	0.3332194	0.8906300	0.8560400	0.1824640
43	0.3890564	0.7383150	0.2092770	0.5732810
44	0.6623718	0.5111380	0.4455750	0.4359340
45	0.0111537	0.6301070	0.7486700	0.1972440
46	0.4472364	0.3847200	0.6011690	0.0872308
47	0.1363005	0.3698950	0.5457880	0.2972370
48	0.3978726	0.0359175	0.8713210	0.4610430
49	0.7053255	0.9693060	0.9175900	0.9333250
50	0.6858780	0.1373090	0.1912720	0.0213102
51	0.1205952	0.3030890	0.2301880	0.4353170
52	0.9443885	0.2414900	0.0332621	0.8974640
53	0.2460152	0.6730200	0.6332500	0.7872860
54	0.2680789	0.6489650	0.0594251	0.7442220
55	0.4070292	0.7394200	0.3640520	0.7644790
56	0.2131620	0.0159938	0.2881370	0.7454290
57	0.3906194	0.3663180	0.0539127	0.3042640
58	0.7973894	0.6700200	0.5050870	0.9956230

Table A-1(*cont'd*)

Random parameters r_{k1} for four initial density distribution.

k	1*st* profile	2*nd* profile	3*rd* profile	4*th* profile
59	0.4453065	0.4865920	0.2968580	0.7726590
60	0.5000511	0.3929410	0.4655970	0.8357490
61	0.2811498	0.4873610	0.8183020	0.2556550
62	0.2619754	0.4922710	0.8331750	0.4205810
63	0.0697469	0.4235170	0.3287940	0.8568030
64	0.4855292	0.9375300	0.1868340	0.6276940
65	0.4442337	0.7423630	0.4777340	0.4931760
66	0.0346178	0.4252360	0.4115180	0.2377350
67	0.4992850	0.6802980	0.8630860	0.2988350
68	0.2346851	0.3203810	0.2170190	0.8921940
69	0.7911138	0.1470350	0.8673660	0.5502020
70	0.8727131	0.2306600	0.0322412	0.4708060
71	0.3374714	0.0813921	0.4499450	0.9307080
72	0.1972228	0.2100330	0.8042510	0.0924435
73	0.6176479	0.3453810	0.2295910	0.9111870
74	0.9182732	0.7151320	0.7959290	0.6442160
75	0.5724716	0.0617709	0.0446693	0.0445251
76	0.2074619	0.9490350	0.6230990	0.6675190
77	0.6043094	0.4005110	0.9091990	0.3648400
78	0.6979252	0.6538890	0.3088130	0.1325390
79	0.5770667	0.7475680	0.5620360	0.1294020
80	0.4843374	0.5880580	0.5847250	0.7407560
81	0.8161871	0.9448910	0.5470380	0.7895700
82	0.1229117	0.2796750	0.4358520	0.1618540
83	0.1086531	0.8488480	0.3766750	0.0712566
84	0.6313995	0.4446890	0.8064230	0.2962610
85	0.7029852	0.9759220	0.9699620	0.8691980
86	0.4890907	0.6362230	0.1736890	0.6792960
87	0.3092427	0.6743220	0.5012440	0.3355680
88	0.6368139	0.9337780	0.3967100	0.7162790
89	0.0990231	0.4988120	0.2350740	0.7347920
90	0.4769357	0.7760290	0.1791900	0.1879780
91	0.7054627	0.6025780	0.3536580	0.3132330
92	0.8733616	0.2838600	0.3719450	0.2328900
93	0.2232359	0.0717426	0.7061530	0.1164620

Table A-1(*cont'd*)

Random parameters r_{k1} for four initial density distribution.

k	1*st* profile	2*nd* profile	3*rd* profile	4*th* profile
94	0.1515353	0.2781840	0.2674890	0.6305280
95	0.2085557	0.2902240	0.8062350	0.9578420
96	0.0984391	0.7382770	0.8165190	0.3532260
97	0.6791737	0.6123010	0.6314950	0.8301110
98	0.9625938	0.2745030	0.8362330	0.5586490
99	0.1143797	0.2940850	0.3436660	0.5021530
100	0.4540583	0.9313510	0.3537050	0.9232530
101	0.4550023	0.1972970	0.0512559	0.2097480
102	0.7444305	0.8170820	0.1672410	0.3686480
103	0.1034082	0.7448600	0.4589170	0.3788650
104	0.4668464	0.4301310	0.8943570	0.7267360
105	0.9235027	0.4983330	0.9287220	0.3210250
106	0.7159805	0.7190420	0.4888930	0.4291190
107	0.2407297	0.1422980	0.6303700	0.6046750
108	0.0480459	0.2916960	0.6571930	0.9832160
109	0.8420714	0.1285730	0.0272329	0.5829890
110	0.4807941	0.8829370	0.1427400	0.9739510
111	0.9760485	0.9882400	0.4877620	0.6409270
112	0.4935150	0.7753030	0.2015100	0.6749860
113	0.3527201	0.4227630	0.2175950	0.9384760
114	0.0270369	0.3941020	0.8581300	0.5908800
115	0.1436840	0.0838640	0.2984240	0.6506380
116	0.4837268	0.7902540	0.1174540	0.0325423
117	0.9820763	0.3333360	0.9208430	0.8539210
118	0.7274899	0.2667320	0.2527570	0.3318320
119	0.9625714	0.3887480	0.0348783	0.1689140
120	0.0837702	0.3356210	0.9850060	0.5478490

REFERENCES

Barenblatt, G.I. 1983 Self-Similar Turbulence Propagation from an Instantaneous Plane Source, In: *Non-Linear Dynamics and Turbulence,* edited by G. I. Barenblatt, G. Ioos, and D. D. Joseph, Pitman, Boston, 48.

Bellman, R. & Pennington, R. H. 1954 Effects of Surface Ternsion and Viscosity on Taylor Instability, *Quart. Appl. Math.* **12**, 151.

Birkhoff, G. 1955 Taylor Instability and Laminar Mixing, Los Alamos Scientific Laboratory Rept. LA-1862 and Appendixes LA-1927

Brouillette, M. 1989 On the Interaction of Shock Waves with Contact Surfaces between Gases of Different Densities, Ph. D. Thesis, California Institute of Technology.

Case, K. M. 1960 Taylor Instability of an Inverted Atmosphere, *Phys. Fluids* **3**, 366.

Chandrasekhar, S. 1961 *Hydrodynamic and Hydromagnetic Stability*, Oxford, University Press, Oxford, 433.

Chisnell, R. F. 1955 The Normal Motion of a Shock Wave through a Non-Uniform Medium, *Proc. Roy. Soc.* **A232**, 350.

Chorin, A. J. 1968 Numerical Solution of the Navier-Stokes Equations, *Math. Comp.* **22**, 745.

Courant, R. & Friedrichs, K. O. 1948 *Supersonic Flow and Shock Waves*, Interscience Publishers, Inc., New York.

Davies, R. M. & Taylor, G. I. 1950 *Proc. R. Soc. London* **A200**, 375.

Duff, R. E., Harlow, F. H. & Hirt, C. W. 1962 Effects of Diffusion on Interface Instability between Gases, *Phys. Fluids* **5**, 417.

Harlow, F. H. & Welch, J. E. 1965 Numerical Calculation of Time-Dependent Viscous Incompressible Flow of Fluid with Free Surface, *Phys. Fluids* **8**, 2182.

Lamb, H. 1932 *Hydrodynamics*, Dover Publications, New York.

Landau, L. D. & Lifshitz, E. M. 1959 *Fluid Mechanics*, Pergamon Press, New York.

LeLevier, R., Lasher, G. J. & Bjorklund, F. 1955 Effect of a Density Gradient on Taylor Instability, Rerport UCRL-4459, University of California Radiation Laboratory.

Lewis, D. J. 1950 The Instability of Liquid Surfaces when Accelerated in a Direction Perpendicular to their Planes. II., *Proc. Roy. Soc. London* **A202**, 81.

Lindl, J. D. & Mead, W. C. 1975 Two-Dimensional Simulation of Fluid Instability in Laser-Fusion Pellets, *Phys. Rev. Lett.* **34**, 1273.

Marble, F. E., Hendricks, G. J. & Zukoski, E. E. 1987 Progress Toward Shock Enhancement of Supersonic Combustion Processes, *AIAA Paper* 87-1880.

Markstein, G. H. 1957 A Shock Tube Study of Flame Front-Pressure Wave Interaction, In: *Sixth Symposium (International) on Combustion*, Reinhold, New York, 387.

Meshkov, E. E. 1969 Instability of the Interface of Two Gases Accelerated by a Shock Wave, *Sov. Fluid Dynamics* **4**, 101.

Mikaelian, K. O. 1988 Simulation of the Richtmyer-Meshkov Instability and Turbulent Mixing in Shock-Tube Experiments, Unpubished Report, Lawrence Livermore National Laboratory.

Paterson, S. 1948 The Reflection of a Plane Shock Wave at a Gaseous Interface, *Proc. Phys. Soc.* **61**, 119.

Rayleigh, Lord 1900 Investigation of the Character of the Equilibrium of an Incompressible Heavy Fluid of Variable Density, In: *Scientific Papers*, Vol. 2., Dover, New York, 200.

Read, K. I. 1984 Experimental Investigation of Turbulent Mixing by Rayleigh-Taylor Instability, *Physica* **D12**, 45.

Richtmyer, R. D. 1960 Taylor Instability in Shock Acceleration of Compressible

Fluids, *Comm. Pure Appl. Math.* **8**, 297.

Saffman, P. G. & Meiron, D. I. 1989 Kinetic Energy Generated by the Incompressible Richtmyer-Meshkov Instability in a Continuously Stratified Fluid, *Phys. Fluids* **A1**(11), 1767.

Sharp, D. H. 1984 An Overview of Rayleigh-Taylor Instability, *Physica* **D12**, 3.

Soh, W. Y. & Goodrich, J. 1988 Unsteady Solution of Incompressible Navier-Stokes Equations, *J. Comput. Phys.* **79**, 113.

Sturtevant, B. 1988 Rayleigh-Taylor Instability in Compressible Fluids, In: *Shock Tubes and Waves*, edited by H. Grönig, VCH, Wendheim, Federal Republic of Germany, 89.

Taylor, G. I. 1950 The Instability of Liquid Surfaces when Accelerated in a Direction Perpendicular to their Planes. **I**, *Proc. Roy. Soc.* **A201**, 192.

Youngs, D. L. 1984 Numerical Simulation of Turbulent Mixing by Rayleigh-Taylor Instability, *Physica* **D12**, 32.

Zufiria, J. A. 1987 Bubble Competition in Rayleigh-Taylor Instability, and Vortex-in-Cell Simulation of Bubble Competition in Rayleigh-Taylor Instability, In: *Analytical and Numerical Analysis of Finite Amplitude Richtmyer-Meshkov Instability*, edited by D. I. Meiron, Applied Mathematics Dept., California Institute of Technology, 1989.